Highlights in Theoretical Chemistry 7
Series Editors: Christopher J. Cramer · Donald G. Truhlar

Srihari Keshavamurthy
Stephen Wiggins *Editors*

Gregory S. Ezra

A Festschrift from Theoretical Chemistry Accounts

Springer

Highlights in Theoretical Chemistry

Vol. 7
Series Editors: Ch.J. Cramer • D.G. Truhlar

More information about this series at http://www.springer.com/series/11166

Srihari Keshavamurthy • Stephen Wiggins
Volume Editors

Gregory S. Ezra

A Festschrift from Theoretical Chemistry Accounts

With contributions from

Johnson K. Agbo • R. Stephen Berry • Barry K. Carpenter • Peter Collins
Thomas Engl • Gregory S. Ezra • Stavros C. Farantos • Laurence E. Fried
Pierre Gaspard • Rigoberto Hernandez • Brittany L. Hyland • Nazar Ileri
T. Iwai • Charles Jaffé • Srihari Keshavamurthy • Tamiki Komatsuzaki
Zeb C. Kramer • David M. Leitner • Craig C. Martens
Frédéric A. L. Mauguière • Jesús Palacián • Peter Plößl • Klaus Richter
Alessandro Sergi • Rex T. Skodje • Boris M. Smirnov • John E. Straub
Hiroshi Teramoto • Mikito Toda • Inga S. Ulusoy • Juan Diego Urbina
T. Uzer • Stephen Wiggins • Yao Xu • Patricia Yanguas • Ping Zhang
B. Zhilinskii

Springer

Volume Editors
Srihari Keshavamurthy
Department of Chemistry
Indian Institute of Technology
Kanpur, India

Stephen Wiggins
Department of Mathematics
University of Bristol
Bristol, UK

Originally published in Theor Chem Acc, Volume 133 (2014), Volume 134 (2015)

ISSN 2194-8666 ISSN 2194-8674 (electronic)
Highlights in Theoretical Chemistry
ISBN 978-3-662-47376-4 ISBN 978-3-662-47377-1 (eBook)
DOI 10.1007/978-3-662-47377-1

Library of Congress Control Number: 2015942233

Springer Heidelberg New York Dordrecht London

Printed on acid-free paper

Springer-Verlag GmbH Berlin Heidelberg is part of Springer Science+Business Media (www.springer.com)

Contents

Theor Chem Acc (2015) 134:14
DOI 10.1007/s00214-014-1601-7

PREFACE

Preface to the special collection in honor of Gregory S. Ezra

Srihari Keshavamurthy · Stephen Wiggins

Published online: 24 January 2015

1 A colleague's appreciation: Roger Loring, Cornell University

As is customary in university departments, the doors of faculty offices in Cornell's Department of Chemistry and Chemical Biology indicate the name of the occupant. One of these doors, however, differs from the rest, lacking a name and decorated only with a small photograph of Rodin's Le Penseur. New arrivals to the department, from first-year undergraduates to faculty, soon learn that a thinker can indeed be found within.

Marking Greg Ezra's 60th birthday is also an occasion to recognize that half of that span has been spent at Cornell. Academic generations of undergraduate and graduate students have appreciated the clarity and rigor of his lectures, to say nothing of the preternaturally neat handwriting on the blackboard. A recent A. B. in chemistry who received an academic award wrote a letter of thanks to the benefactor who had endowed the prize. She chose to illustrate a high point of her undergraduate education with a drawing of Greg Ezra at the blackboard placing a "hat" on a letter H. The intellectual incisiveness admired by students is highly valued by Greg's departmental colleagues in settings varying from informal consultations and formal research presentations to committee and faculty meetings. His Cornell colleagues are delighted to join with former and present collaborators, with contributors to this Festschrift, and with theoretical chemists generally in celebrating Greg Ezra's accomplishments and contributions to the field and community.

2 A collaborator's appreciation: Stephen Wiggins, University of Bristol

I have known Greg Ezra for some time, but we have only been seriously collaborating together for the past 7 years or so. I began graduate school at Cornell in 1983 and Greg had already been there for a year as an assistant professor of chemistry. He had recently taken on his first students (Larry Fried and Craig Martens, who have both contributed to this Festschrift). In those days, Cornell was one of the world's hot spots for the development of nonlinear dynamics from the theoretical, applied, and experimental perspectives. There was a sense of something new happening. Guckenheimer and Holmes had just been published and Phil Holmes was teaching his first course from that book, John Hubbard was teaching ordinary differential equations from V. I Arnold's advanced ordinary differential equations book, Eric Siggia was teaching mechanics from V. I. Arnold's classical mechanics book, and Michael Fisher was lecturing on renormalization group theory. It was a time when everybody went to everybody's seminars, and I saw Greg at many of these seminars, discussing with his students. It seems to me that the Cornell environment had a significant influence on the development of Greg's research career in subsequent years. But it did not work out to be the right time for us to begin any type of collaboration since we both had more

Published as part of the special collection of articles celebrating the 60th birthday of Professor Greg Ezra.

S. Keshavamurthy (✉)
Department of Chemistry, Indian Institute of Technology, Kanpur 208 016, India
e-mail: srihari@iitk.ac.in

S. Wiggins (✉)
Department of Mathematics, University of Bristol, Bristol BS8 1TW, UK
e-mail: stephen.wiggins@me.com

pressing concerns (he had to get tenure, and I had to pass qualifying exams). Even though we both went our separate ways, I continued to follow Greg's work over the years, and for reasons, I cannot remember, I sent him an e-mail in 2008 asking some question (that I also cannot remember). This was the start of a very rewarding collaboration that probably could not have happened earlier because I had to develop the type of mathematics that I was doing to a point where it might actually provide useful insight for a problem in chemistry, and I also needed to develop a common language so that I could benefit from his extensive knowledge. This took about 15 years, but it eventually got there.

Working with Greg is the ideal model of what someone would term an interdisciplinary collaboration (although I am not sure either of us have thought of it in that way). I have learned an incredible amount from working with him, and not just about chemistry. His encyclopedic knowledge of classical and quantum mechanics has greatly enriched our work. (It is a running joke now when we write papers that Greg must be falling down on the job if there are less than 100 cited references). When you work with Greg on a project, you will know what you can, and cannot, understand, about the project when it is completed. He is uncompromising and rigorous in his approach to research, and I have appreciated, admired, and benefited from that greatly. But there are aspects to Greg's scholarship that are probably not so well known. Greg is a very serious scholar of the best of twentieth century music (and he can also convince you that vinyl provides a superior listening experience). For example, he can explain in detail the evolution of the drumming style of Ginger Baker, and he has a deep knowledge of the influence of American blues music on the great British rock music of the 1960's.

I am sorry that I did not get to know Greg during my days as a graduate student. But everything has its time, and I feel fortunate that I now have this collaboration, and I wish Greg the best for the next 60 years.

3 A former postdoc's appreciation: Srihari Keshavamurthy, IIT Kanpur

I had the honor of joining Greg Ezra as a fresh postdoc in the winter of 1995. In fact, having met and discussed briefly with Greg on semiclassics in the 1993 Seattle APS meeting, I was convinced that Greg was the person I wanted to work for my postdoc. I have not regretted that decision! Coming from Berkeley, the recent snowstorm in Ithaca was quite an experience for me. I had to meet Greg at his office in the morning and did so by trudging through snow from the motel to Baker laboratories. Two things that I remember from this first meeting—first, I was the only occupant of that part of Baker laboratory and second, Greg had already prepared a list of papers concerned with dynamical tunneling. Greg told me that he would like to understand dynamical tunneling and its influence on molecular spectra and asked me to analyze the highly excited vibrational states of an effective Hamiltonian for water. I remember being immersed in calculating surfaces of sections, computing resonance zones and widths and looking at hundreds of vibrational eigenstates. Interestingly, and thankfully, Greg let me pursue my line of thoughts on the dynamical assignment problem. At the same time, through numerous discussions and gracefully tolerating many of my grandiose ideas, Greg passed on to me his immense knowledge and deep insights into the phenomenon of intramolecular vibrational energy redistribution. I was amazed by Greg's ability to point out a relevant paper irrespective of when it was published—sometimes a hard copy would emerge from one of the stacks on his desk. Equally striking was the fact that he had not only read these papers through, but also had a firm grasp of the limitations of the approach used in these works. This was an important and a very valuable lesson for me and, for that matter, any honest academician. For those who have had the pleasure of reading Greg's papers, it is a bit unnerving to realize that he has most probably read every one of the hundreds of cited references.

An event that occurred within a few months of my coming to Ithaca has left a lasting impression on me in terms of my current research interests. Greg asked me to attend a NATO ASI workshop on Hamiltonian systems with three or more degrees of freedom in June 1995 held in S'Agaro, Spain. This was a one of a kind meeting and a heady one for a young person with people like Arnold, Moser, and Sinai being there. Attending this workshop exposed me to the great beauty of nonlinear dynamics and the challenges of applying them to molecular Hamiltonians—I am yet to recover from this meeting! But then, the challenges remain and it is a great pleasure to see Greg's recent works that take a step closer toward meeting these challenges. In any case, I am forever indebted to Greg for providing me with this unique opportunity.

My own research has benefited immensely from the beautiful insights into classical-quantum correspondence that have come from Greg's work over the years. Perhaps, to a small extent, I have imbibed even some of his writing skills—to quote Samuel Johnson 'language is the dress of thought.' A colleague read a preprint of mine and remarked that "It is a very scholarly piece of work. There is a Greg Ezra style infused in your work. This is good." I take that as a high compliment.

4 A former graduate student's appreciation: Craig Martens, University of California, Irvine

During the summer of 1982, I traveled from Nebraska to Ithaca, NY to begin my graduate studies in chemistry at

Cornell University. I was drawn to that beautiful campus by its long history of being a home to luminaries of science—from Debye and Feynman to the newly minted Nobel Laureate Roald Hoffmann and the television star Carl Sagan—but it was another newcomer that would end up changing the course of my life. This was Greg Ezra, a new assistant professor with a small (and already cluttered) office and a cavernous laboratory equipped with an antique glove box and a single computer terminal. I remember that first talk in Greg's office about his research. Compact and quiet, with an unruly mop of black hair, Greg stood at the blackboard sketching invariant tori and writing equations with his neat handwriting, his eyes bright and intense. I was hooked.

And so began the graduate education of a theoretical chemist. At the time, I did not fully appreciate how special that education was to be. Greg the thesis advisor was not one to give orders or lecture pedantically to his students, and would not dream of being so presumptuous as to comment on ones work habits. Rather, he led by example. A consummate scholar, Greg seemed to have already read (and photocopied) everything. It was rare to visit Greg's office without him recalling a relevant article and extracting it, miraculously, from the center of one of the tall piles of papers that fought for space on every level surface. Greg was embarking on a new research direction, combining semiclassical mechanics with nonlinear dynamics, and was more concerned about learning this new field than about showing off what he knew. He encouraged a continual commitment to intellectual development by attending seminars and reading literature, and made it possible for his students to attend conferences and workshops. He would even go with us to sit in on classes in other departments. And although he did not have a big ego, he set high standards. Greg demanded rigor in science and scholarship, but also for usage of the English language. Writing papers with him was an intense process, sometimes requiring a trip to his office to consult his immense copy of the Oxford Dictionary to determine the fate of a single word.

There were a few things that Greg did not teach his students. Things like overselling your work, ignoring or minimizing previous contributions by others, cranking out numerous mediocre publications, navigating the meta-scientific waters of politics and fashion, and the tireless pursuit of credit and citation. To Greg, the scientists life is one driven by a passion to appreciate the beautiful whole that emerges by seeing the connections between ideas—yours and those of a community of scholars. He taught by example the ideals of hard work, intellectual and personal honesty, optimism, generous sharing of credit with others, and the final authority of the truth and beauty of natural law. I have become older and wiser since leaving Ithaca. But the essential principles and practices that set the high bar I believe a scientist should strive for are things I picked up (and hopefully have not misplaced) long ago from Greg Ezra.

5 Greg Ezra: Scientific autobiography

Ed é subito sera [1]

> Ognuno sta solo cuor della terra
> traffito da un raggio di sole:
> ed é subito sera
>
> Salvatore Quasimodo (1901–1968)

5.1 Beginnings

I was born and raised in northwest London. A bookish and intellectually precocious child, I early on developed the habit of amassing and organizing large amounts of data and information in order to write my own 'encyclopedias'; some of my coworkers will perhaps recognize this trait!

Throughout the course of my education in the UK, I was extremely fortunate to have benefitted from the state run system in place at the time that recognized ability and aptitude in children of modest backgrounds, and facilitated their passage to academically excellent schools. So, I passed from Braintcroft Primary in Neasden to Merchant Taylors' (alma mater of, among others, Edmund Spenser, Clive of India and Boris Karloff) to St. John's college, Oxford, as a Thomas White Scholar. At Merchant Taylors', I received much support and encouragement from several inspiring teachers; in particular, John Dishman and Andy Edge (chemistry), and Alan Whitney (art).

5.2 Apprenticeship

I studied chemistry at Oxford, with equal time devoted to Organic, Inorganic and Physical branches. It became clear early on that I was not cut out to be an experimentalist (despite having a strong interest in synthetic organic chemistry in high school), and so, it was necessary to pick up the mathematics and physics necessary for deeper study of theory on my own initiative.

A first encounter with transition state theory as an undergraduate set the stage for decades of interest in this fascinating topic: After I complained to my tutor that the theory made absolutely no sense (What, precisely, were the assumptions involved? Where, exactly, had the dynamics gone?), it was suggested that I write a research paper to clarify my misgivings on the subject! At this point, the

[1] *And suddenly it's evening* Everyone stands alone at the heart of the world, pierced by a ray of sunlight: and suddenly it's evening Salvatore Quasimodo (1901–1968)

seminal papers of Pechukas and Pollak on periodic orbit dividing surfaces, etc, had not appeared, and I had yet to read Wigner's remarkably lucid treatment of the topic.

Peter Atkins had a profound influence on my intellectual direction through both his textbooks and lectures on quantum mechanics. I therefore joined Peter's research group for my part II (a thesis on multiphoton processes, leading to a lifelong interest in angular momentum and symmetry) and my Ph.D. thesis.

As a Senior Scholar at Christ Church, Oxford, I had the freedom to chart my own course as a graduate student. My research direction was set after I heard an inspiring talk by Brian Sutcliffe on the properties of the Eckart frame (used to separate molecular vibration from rotation), in particular the connection with molecular symmetry properties. This talk was based both on Brian's own work and on the then-recent review by Louck and Galbraith. Already familiar with the Eckart-Sayvetz frame, which generalizes the Eckart frame to non-rigid molecules, I resolved to carry out the same kind of analysis for non-rigid systems. (I was unaware that very similar work was being undertaken by Natanson and Adamov in the Soviet Union at about the same time). Extensive use was made of the theory of induced representations, which I learned from the book of Simon Altmann and the papers and lectures of Harald Fritzer. This work formed the basis for my D. Phil. thesis, and for my continuing interest in the subtleties associated with use of the Eckart condition and with vibration-rotation interaction generally. The puzzling (to me, at the time) observations of Meyer and Günthard on the non-integrability of the conditions for removal of rotation-vibration coupling and many other outstanding problems besides were eventually beautifully elucidated by the seminal work of Guichardet, Iwai, Tachibana and Littlejohn on holonomy in the RV problem.

I had the good fortune to meet Steve Berry during one of his visits to Oxford and went to Chicago to work with Steve as a NATO Postdoc. At Chicago, I worked on a number of projects related to the properties of "floppy molecules" which, following the seminal work of Kellman and Herrick, included the doubly excited Helium atom! While at Chicago I learned how to program a trajectory integration algorithm, and so began to explore the classical mechanics of the Helium atom. Influenced by the work of Percival and others on semiclassical quantization of vibrational levels, my (very näive) plan was to find invariant tori in the Helium atom phase space, and hence obtain quantized levels for 2-electron systems. I very quickly discovered that any randomly selected non-symmetric Helium atom trajectory will apparently autoionize with probability one (!), and that singular Coulomb potentials require application of special but well-established regularization techniques. So, began a long-term interest in the classical and semiclassical mechanics of few-body Coulomb systems, which was to culminate in a few years in the semiclassical quantization of the He atom.

5.3 Vocation

After Chicago, the plan was to return to an academic post in the UK, but the situation in the job market dictated otherwise. I interviewed for a faculty position at a number of US universities, and was offered a job at Cornell, located somewhere in upstate NY in a place called Ithaca. There I have been ever since.

My research at Cornell has covered many aspects of the few-body problem in chemistry and physics. In broad terms, I have been interested in the role of symmetry in physical problems, in classical, semiclassical and quantum approaches to atomic and molecular systems, and in geometrical aspects of Hamiltonian and non-Hamiltonian dynamics.

I have been fortunate to have had a number of talented and creative students and postdocs over the years, several of whom have gone on to distinguished careers in research. I count myself particularly lucky that my first graduate students were Craig Martens and Larry Fried, both of whom worked on problems in semiclassical mechanics. Craig's work on the Fourier quantization of quasiperiodic trajectories in multidimensional systems led us to inquire what power spectra looked like for finite time segments of non-regular trajectories; the resulting method of 'Local Frequency analysis' (a collaborative effort with Mike Davis) has been developed and applied to a number of physical problems since by many others since. Larry's work focussed on the use of Lie-transform perturbation theory to derive simplified Hamiltonians for molecular vibrational problems, in the spirit of earlier work of Swimm-Delos-Jaffé-Shirts-Reinhardt; this work led to an interest in the symplectic geometry of phase space which has informed much of my work since.

A turning point in the Helium atom problem came when I attended a Cornell seminar given by Robert Devaney, who talked about the application of the McGehee 'blow-up' technique to the analysis of the dynamics of the anisotropic Kepler problem. (Steve Wiggins, then a graduate student at Cornell, was also at this very memorable talk.) I was aware that Gutzwiller's periodic orbit quantization technique had been applied to the anisotropic Kepler problem, which was conjectured to be completely chaotic, but was unfamiliar with the various blow-up and regularization techniques used in celestial mechanics. Regularization of pairwise collisions would facilitate numerical integration of He atom trajectories, while analysis of the triple collision manifold would perhaps provide the basis for application of some kind of symbolic dynamics. Numerical work on a (suitably regularized) collinear model for the classical He atom

showed that these approaches worked well and suggested that the system might be completely chaotic, with unstable periodic orbits coded by a complete binary code. My student Jong-Hyun Kim carried out extensive computations of doubly excited resonances in the collinear model, so that by applying the Gutwiller trace formula 'in reverse,' we were able to use the scaled quantum levels to extract information on the nature of the classical periodic orbits contributing to the quantized level structure. Our results definitively showed that it is the 'antisymmetric stretch' po, *not* the 'symmetric stretch' po, as had previously been thought, that is the most important po associated with the manifold of $n = n'$ doubly excited states. The symmetric stretch orbit is in a sense infinitely unstable, and hence does not contribute to the semiclassical spectrum, although it serves as the basis for organizing the classical phase space structure.

These results were presented at the 1990 Trieste conference on Quantum Chaos and published in the proceedings. (A short paper describing these findings was rejected by Physical Review Letters; a full account is given in Kim's unpublished doctoral thesis.) At the Trieste meeting, I was fortunate to meet the late Dieter Wintgen and his students Grigor Tanner and Klaus Richter, who were working on the same problem. They had been using similar techniques to analyze the classical dynamics of He, and I ended up as a co-author on a short paper describing the application of the cycle-expansion technique to the more difficult problem of forward quantization of the He. While this work overturned textbook dogma about the inapplicability of semiclassical quantization to the 2-electron problem, it of course relied on more than a half century of development of semiclassics and classical dynamics! It is also true to say that many aspects of the phase space structure of the 3D He atom remain to be understood.

The problem of comprehending dynamics in multidimensional systems (that is, those with $N \geq 3$ degrees of freedom) has been a central theme of my research. In 1991, Richard Gillilan and I published a study of dividing surfaces and 'turnstiles' in a 4D model of a van der Waals complex dissociation reaction (as a symplectic mapping). One surprise was the possibility of the non-existence of turnstiles (phase space structures mediating passage between bound and unbound regions) in higher dimensions. This work was inspired by a seminal paper of Steve Wiggins on Normally Hyperbolic Invariant Manifolds (NHIMs), which has provided the foundation for much subsequent research in the field.

Another noteworthy excursion into higher dimensional phase space was the study of the Baggot Hamiltonian for the water molecule, carried out in collaboration with Srihari Keshavamurthy.

In the past few years, I have enjoyed a very stimulating and productive collaboration with Steve Wiggins, who is in the Mathematics department at Bristol University, and other members of the 'Bristol group'. We have worked on a number of topics, such as thermostats, higher-index saddles, transition state theory and the gap time formalism, the roaming mechanism, and non-statisticality on organic reaction mechanisms. A major theme of this work is the important role played by NHIMs and related phase space structures in reaction dynamics, long emphasized by Wiggins, and the importance of adopting a phase space perspective for understanding mechanisms and non-statisticality in general. I am particularly pleased to be currently working on the theory of the dynamics of organic reactions with my former Cornell colleague Barry Carpenter, now at Cardiff University, and on roaming dynamics with Stavros Farantos (Iraklion, Greece), whose work on periodic orbit theory I have followed for a long time.

Space does not allow full discussion of the various other projects and topics of interest we have investigated over the years: non-adiabatic dynamics; dynamics of ion-molecule reactions; rotation–vibration interactions; semiclassics for singular potentials; periodic orbit analysis of vibrational spectra; semiclassical theory of nonlinear response functions; geometrical approach to non-Hamiltonian (thermostat) dynamics; quantum monodromy in molecular rotors.

5.4 Avocation

When not teaching or researching, I can often be found playing and performing music as a drummer-percussionist, pursuing anew a youthful interest in the percussive arts. I enjoy playing in a variety of genres such as blues, folk-rock, Middle Eastern and Klezmer music. Making live music in real time with real people is to me a perfect antidote to the alienating and (dis)connected nature of our digital world.

5.5 Sine qua non

The Cornell Chemistry (now Chemistry and Chemical Biology) department is an extraordinary place, and I am singularly fortunate to have been able to spend my career as an independent scientist there. Inhabited by titans such as (the late) Andy Albrecht, Michael Fisher, Jack Freed, Roald Hoffmann, Harold Scheraga, and Ben Widom (to name but a few), and dynamic younger theorists Nandini Ananth, Garnet Chan (now at Princeton), and Roger Loring, it is a uniquely collegial and friendly department. Most important, the department as a whole has a genuine and unwavering commitment to the highest standards of intellectual rigor and scholarship, regardless of research fads or fashions, and to quality teaching. It is a wonderfully supportive environment in which to pursue research on fundamental problems in chemical physics.

I offer my sincere gratitude to all my coworkers past and present for their inspiration and efforts, and especially those friends, colleagues, and collaborators (by no means mutually exclusive categories!) who have contributed their excellent papers to this special issue of TCA. Particular thanks are due to Srihari Keshavamurthy and Steve Wiggins for devoting their time and energy to organizing this Fest. It is indeed humbling to be honored in this way.

Finally, I can hardly begin to thank my wife Sally for many years of support and companionship and for her loving forebearance toward an often-distracted thinker of 'deep thoughts', and our daughters Rachel and Ruth for having enriched our lives immeasurably.

6 Publications of Gregory S. Ezra[2]

1. G.S. Ezra, "On the symmetry properties of nonrigid molecules: a unified approach", Mol. Phys. **38**, 863–875 (1979).
2. G.S. Ezra, "On the symmetry properties of nonrigid molecules:semifactorizability of the isometric group", Mol. Phys. **43**, 773–783 (1981).
3. G.S. Ezra, "Symmetry properties of molecules", Lecture Notes in Chemistry **28** (Springer, 1982).
4. G.S. Ezra, "Symmetry properties of nonrigid molecules", in: Proc. Bielefeld Conf. *Molecular Structure, Rigidity and Potential Energy Surfaces*, 1980, Ed. J. Hinze (Plenum, 1983).
5. G.S. Ezra, "The semidirect product structure of nonrigid molecule symmetry groups", in: Proc. Intl. Conf. *Symmetry and Properties of Nonrigid Molecules*, Ed. J. Maruani (Elsevier, 1983).
6. H.J. Yuh, G. Ezra, P. Rehmus and R.S. Berry, "Electron correlation and Kellman-Herrick quantization in doubly-excited Helium", Phys. Rev. Lett. **47**, 497 (1981).
7. G.S. Ezra and R.S. Berry, "Correlation of two particles on a sphere", Phys. Rev. A **25**, 1513–1527 (1982).
8. G.S. Ezra and R.S. Berry, "Correlation diagrams for rigid and nonrigid five-body and XY_5 six-body systems", J. Chem. Phys. **76**, 3679–3691 (1982).
9. R.S. Berry, G.S. Ezra and G.A. Natanson, "Collective and independent particle motion in simple atoms and molecules: a unification", in: Proc. 4th Intl. Cong. Quantum Chem. 1982 (Reidel, 1983).
10. G.S. Ezra and R.S. Berry, "Collective and independent-particle motion in doubly-excited two-electron atoms", Phys. Rev. A **28**, 1974–1988 (1983).
11. G.S. Ezra and R.S. Berry, "The quantum states of two particles on concentric spheres", Phys. Rev. A **28**, 1989–2000 (1983).
12. G.S. Ezra and R.S. Berry, "Comment on: 'Classification of doubly-excited states of two-electron atoms'", Phys. Rev. Lett. **52**, 1252–1252 (1984).
13. G.A. Natanson, G.S. Ezra, G. Delgado-Barrio and R.S. Berry, "Calculation of rovibrational spectra of water by means of particles-on-concentric-spheres models. I. Ground stretching vibrational state", J. Chem. Phys. **81**, 3400–3406 (1984).
14. G.A. Natanson, G.S. Ezra, G. Delgado-Barrio and R.S. Berry, "Calculation of rovibrational spectra of water by means of particles-on-concentric-spheres models. II. Excited stretching vibrational states", J. Chem. Phys. **84**, 2035–2044 (1986).
15. G.S. Ezra, "The adiabatic approximation for coupled oscillators", Chem. Phys. Lett. **101**, 259–264 (1983).
16. R.S. Tapper, R.L. Whetten, G.S. Ezra and E.R. Grant, "The role of near-resonant intermediate states in two-photon excitation NO_2: origin bands in bent-to-linear transitions", J. Phys. Chem. **88**, 1273–1275 (1984).
17. C.C. Martens and G.S. Ezra, "A simple method for determining the number of isolating integrals in multidimensional systems: computation of the pointwise dimension", Chem. Phys. Lett. **108**, 573–579 (1984).
18. R.L. Whetten, G.S. Ezra and E.R. Grant, "Molecular dynamics beyond the adiabatic approximation: new experiments and theory", Ann. Rev. Phys. Chem. **36**, 277–320 (1985).
19. J. Zwanziger, R.L. Whetten, G.S. Ezra and E.R. Grant, "Semiclassical eigenvalues for a nonadiabatic system", Chem. Phys. Lett. **120**, 106–112 (1985).
20. C.C. Martens and G.S. Ezra, "EBK quantization of nonseparable systems: a Fourier transform method", J. Chem. Phys. **83**, 2990–3001 (1985).
21. L. Bigio, G.S. Ezra and E.R. Grant, "Intramolecular dynamics and multiresonant absorption spectroscopy. II. Power broadening and superposition states in double resonant two-photon excitation", J. Chem. Phys. **83**, 5369–5379 (1985).
22. E.M. Goldfield, P.L. Houston and G.S. Ezra, "Nonadiabatic interactions in the photodissociation of ICN", J. Chem. Phys. **84**, 3120–3129 (1986).
23. J. Santamaria, G. Alvarez Galindo, R. Escribano and G.S. Ezra, "Rotation-vibration separability in the classical motion of triatomics", J. Mol. Struct. **142**, 529–532 (1986).
24. G.S. Ezra, "Interaction between bending vibrations and molecular rotations: a model study", Chem. Phys. Lett. **127**, 492–500 (1986).
25. J. Zwanziger, E.R. Grant and G.S. Ezra, "Semiclassical quantization of a classical analogue for the Jahn-

[2] http://www.chem.cornell.edu/pubs.html.

Teller E×e system", J. Chem. Phys. **85**, 2089–2098 (1986).
26. C.C. Martens and G.S. Ezra, "Uniform quantization of multidimensional systems", in: Proc. 19th Jerusalem Symp. Quantum Chem., *Tunnelling*, Ed. J. Jortner and B. Pullman (Reidel, 1986).
27. C.C. Martens and G.S. Ezra, "Semiclassical mechanics of strongly resonant systems: a Fourier transform approach", J. Chem. Phys. **86**, 279–307 (1987).
28. L. Fried and G.S. Ezra, "PERTURB: a special-purpose algebraic manipulation program for classical perturbation theory", J. Comp. Phys. **8**, 397–411 (1987).
29. L. Fried and G.S. Ezra, "Semiclassical quantization using perturbation theory: algebraic quantization of multidimensional systems", J. Chem. Phys. **86**, 6270–6282 (1987).
30. C.C. Martens and G.S. Ezra, "Classical, quantum mechanical and semiclassical representations of resonant dynamics: a unified treatment", J. Chem. Phys. **87**, 284–301 (1987).
31. G.S. Ezra, C.C. Martens and L.E. Fried, "Semiclassical quantization of polyatomic molecules: some recent developments", J. Phys. Chem. (Invited Feature Article) **91**, 3721–3730 (1987).
32. A. Garcia-Ayllon, C.C. Martens, J. Santamaria and G.S. Ezra, "Semiclassical vibrational transition frequencies for a Hamiltonian with stretch-bend potential energy coupling: application of Fourier methods", J. Phys. Chem. **87**, 6609–6617 (1987).
33. B.G. Sumpter and G.S. Ezra, "Semiclassical rotation-vibration energies for a triatomic molecule: H_2O", Chem. Phys. Lett. **142**, 142–146 (1987).
34. C.C. Martens, M.J. Davis and G.S. Ezra, "Local frequency analysis of chaotic motion in multidimensional systems: energy transport and bottlenecks in planar OCS", Chem. Phys. Lett. **142**, 519–528 (1987).
35. L.E. Fried and G.S. Ezra, "Generalized algebraic quantization: corrections to arbitrary order in $\hbar$", J. Phys. Chem. **92**, 3144–3154 (1988).
36. L.E. Fried and G.S. Ezra, "PERTURB: A program for calculation of vibrational energies using generalized algebraic quantization", Comp. Phys. Comm. **51**, 103–114 (1988) [Invited contribution to Special Issue on Molecular Vibrations].
37. A. Garcia-Ayllon, J. Santamaria and G.S. Ezra, "Sensitivity of IVR to stretch-bend potential energy coupling and stability of periodic orbits", J. Chem. Phys. **89**, 801–811 (1988).
38. B.G. Sumpter, C.C. Martens and G.S. Ezra, "Interaction of molecular rotation with large-amplitude internal motions: a rigid twister model for hydrogen peroxide", J. Phys. Chem. **92**, 7193–7204 (1988).
39. L.E. Fried and G.S. Ezra, "Avoided crossings and resummation of nearly resonant molecular vibrations: reconstruction of an effective secular equation", J. Chem. Phys. **90**, 6378–6390 (1989).
40. C. Getino, B.G. Sumpter, J. Santamaria and G.S. Ezra, "Unimolecular decay lifetimes and intramolecular energy redistribution in HOOH: sensitivity to potential energy surface", J. Phys. Chem. **93**, 3877–3880 (1989).
41. R.M. Benito, F. Borondo, J.H. Kim, B.G. Sumpter and G.S. Ezra, "Comparison of classical and quantum phase space structure of nonrigid molecules: LiCN", Chem. Phys. Lett. **161**, 60–66 (1989).
42. C. Getino, B.G. Sumpter, J. Santamaria and G.S. Ezra, "Ab initio study of stretch-bend coupling in HOOH", J. Phys. Chem. **94**, 3995–4000 (1990).
43. R.E. Gillilan and G.S. Ezra, "Turnstiles, transport and unimolecular decay in multidimensional Hamiltonian maps: application to van der Waals predissociation", J. Chem. Phys. **94**, 2648–2668 (1991).
44. J.H. Kim and G.S. Ezra, "Periodic orbits and the classical-quantum correspondence for doubly-excited states of two-electron atoms", Proc. Trieste Workshop *Quantum Chaos*, pp 436–448, Ed. H. Caldiera, M. Gutzwiller and R. Ramaswamy (World Scientific, 1991).
45. G.S. Ezra, K. Richter, G. Tanner and D. Wintgen, "Semiclassical cycle expansion for the Helium atom", J. Phys. B **24**, L413–L420 (1991).
46. G.S. Ezra, "Classical trajectory studies of intramolecular dynamics: local mode dynamics, rotation-vibration interaction and the structure of multidimensional phase space", in *Intramolecular Dynamics and Nonlinear Dynamics*, pp 1–40, edited by W.L. Hase (JAI Press, 1992).
47. G. Ramachandran and G.S. Ezra, "Vibrational deactivation in planar ion-neutral collisions: a classical trajectory study of the fixed-angle approximation", Chem. Phys. Lett. **199**, 397–402 (1992).
48. G. Ramachandran and G.S. Ezra, "Vibrational deactivation in Kr/O_2^+ collisions: role of complex formation and potential anisotropy", J. Chem. Phys. **97**, 6322–6334 (1992).
49. H. Li, G.S. Ezra and L.A. Philips, "Vibrationally induced axis switching: a novel mechanism for vibration-rotation coupling", J. Chem. Phys. **97**, 5956–5963 (1992).
50. K.M. Atkins and G.S. Ezra, "Semiclassical density of states at symmetric pitchfork bifurcations in coupled quartic oscillators" Phys. Rev. A **50**, 93–97 (1994).
51. R. Manning and G.S. Ezra, "A regularized semiclassical radial propagator for the Coulomb potential", Phys. Rev. A **50**, 954–966 (1994).

52. R.J. Hinde and G.S. Ezra, "Direct and complex forming collisions in a model for the barrierless proton transfer reaction: $CH_3OH + {}^{-}OCH_3 \rightarrow CH_3O^{-} + HOCH_3$", Chem. Phys. Lett. **228**, 333–340 (1994).
53. G. Ramachandran and G.S. Ezra, "Orbiting complex formation in Na^{+}/N_2 collisions: a phase space view"[Invited contribution to S. Rice issue], J. Phys. Chem. **99**, 2435–2443 (1995).
54. K.M. Atkins and G.S. Ezra, "Classical-quantum correspondence and the transition from regular to chaotic dynamics in coupled quartic oscillators", Phys. Rev. E **51**, 1822–1837 (1995).
55. D.C. Rouben and G.S. Ezra, "Periodic orbit analysis of molecular vibrational spectra: 1:1 resonant coupled modes", J. Chem. Phys. **103**, 1375–1383 (1995).
56. G.S. Ezra, "Periodic orbit analysis of molecular vibrational spectra: Spectral patterns and dynamical bifurcations in Fermi resonant systems", J. Chem. Phys. **104**, 26–35 (1996).
57. R. Manning and G.S. Ezra, "A uniform regularized semiclassical propagator for the $1/x^2$ potential", Phys. Rev. A **53**, 661–668 (1996).
58. S. Keshavamurthy and G.S. Ezra, "Analysis of quantum eigenstates in a 3-mode system", in Proc. NATO ASI on *Hamiltonian Systems with Three or More Degrees of Freedom*, p 435–439, ed C. Simo, (Kluwer, 1999).
59. S. Keshavamurthy and G.S. Ezra, "Assigning vibrational spectra of highly-excited molecules: Classical and quantum vibrational dynamics of the H_2O molecule", Chem. Phys. Lett. **259**, 81–90 (1996).
60. S. Keshavamurthy and G.S. Ezra, "Eigenstate assignments and the quantum-classical correspondence for highly-excited states of the Baggot H_2O Hamiltonian", J. Chem. Phys. **107**, 156–179 (1997).
61. G.S. Ezra, "Classical-quantum correspondence and the analysis of highly-excited states: periodic orbits, rational tori and beyond", in *Advances in Classical Trajectory Methods*, Vol. 3, pp 35–72, edited by W.L. Hase (JAI Press, 1998).
62. C.C. Martens, M.J. Davis and G.S. Ezra, "Comment on 'Local Frequency analysis and the structure of classical phase space of the LiNC/LiCN molecular system' [J. Chem. Phys. **108**, 63 (1998)], J. Chem. Phys. **109**, 6507 (1998).
63. M. Tsuchiya and G.S. Ezra, "Global analysis of periodic orbit bifurcations in coupled Morse systems: Time-reversal symmetry, permutational representations and codimension-2 collisions", CHAOS **9**, 819–840 (1999).
64. G. S. Ezra, "Geometric approach to response theory in non-Hamiltonian systems", J. Math. Chem. **32**, 339–359 (2002).
65. G. S. Ezra, "On the statistical mechanics of non-Hamiltonian systems: the generalized Liouville equation, entropy, and time-dependent metrics", J. Math. Chem. **35**, 29–53 (2004).
66. W. G. Noid, G. S. Ezra, and R. F. Loring, "Optical response functions with semiclassical dynamics", J. Chem. Phys. **119**, 1003–1020 (2003).
67. W. G. Noid, G. S. Ezra, and R. F. Loring, "Vibrational echoes: Dephasing, rephasing, and the stability of classical trajectories", J. Phys. Chem. **108**, 6536–6543 (2004).
68. W. G. Noid, G. S. Ezra, and R. F. Loring, "Semiclassical calculation of the vibrational echo", J. Chem. Phys. **120**, 1491–1499 (2004).
69. C. A. Arango, W. W. Kennerly, and G. S. Ezra,"Quantum monodromy for diatomic molecules in combined electrostatic and pulsed nonresonant laser fields",Chem. Phys. Lett. **392**, 486–492 (2004).
70. C. A. Arango, W. W. Kennerly, and G. S. Ezra,"Quantum and classical mechanics of diatomic molecules in tilted fields",J. Chem. Phys. **122**, Art. No. 184303 (2005).
71. C. A. Arango, W. W. Kennerly, and G. S. Ezra,"Semiclassical IVR approach to rotational excitation of nonpolar diatomic molecules by nonresonant laser pulses",Chem. Phys. Lett. **420**, 296–303 (2006).
72. S. A. Deshpande and G. S. Ezra, "On the derivation of the Herman-Kluk propagator",J. Phys. A **39**, 5067–5078 (2006).
73. G. S. Ezra, "Reversible measure-preserving integrators for non-Hamiltonian systems",J. Chem. Phys. **125**, Art. No. 034104 (2006).
74. S. A. Deshpande and G. S. Ezra, "Quantum state reconstruction for rigid rotors",Chem. Phys. Lett. **440**, 341–347 (2007).
75. C. A. Arango and G. S. Ezra, "Classical mechanics of dipolar asymmetric top molecules in collinear static electric and nonresonant linearly polarized laser fields:energy-momentum diagrams, bifurcations and accessible configuration space",Int. J. Bifurc. Chaos **18**, 1127–1149 (2008).
76. J. N. Stember and G. S. Ezra, "Fragmentation kinetics of a Morse oscillator chain under tension", Chem. Phys. **337**, 11–32 (2007).
77. G. S. Ezra and S. Wiggins, "Impenetrable barriers in phase space for deterministic thermostats", J. Phys. A (Fast Track Communication) **42**, 042001 (2009).
78. G. S. Ezra, H. Waalkens and S. Wiggins,"Microcanonical rates, gap times, and phase space dividing surfaces",J. Chem. Phys. **130**, 164118 (2009).
79. G. S. Ezra and S. Wiggins,"Phase space geometry and reaction dynamics near index two saddles", J. Phys. A **42**, 205101 (2009).

80. A. Sergi and G. S. Ezra,, "Bulgac-Kusnezov-Nosé-Hoover thermostats", Phys. Rev. E **81**, 036705 (2010). [cond-mat arXiv:1002.0657]
81. P. Collins, G. S. Ezra and S. Wiggins, "Phase space structure and dynamics for the Hamiltonian isokinetic thermostat", J. Chem. Phys. **133**, 014105 (2010) [cond-mat arXiv:1004.4294].
82. J. N. Stember and G. S. Ezra, "Isomerization kinetics of a strained Morse oscillator ring", Chem. Phys. **381**, 80–87 (2011).
83. A. Sergi and G. S. Ezra, "Algorithms for non-Hamiltonian dynamics", Atti Accad. Pelorit. Pericol. Cl. Sci. Fis. Mat. Nat., Vol. **LXXXVIII**, No. 2, C1C1002002 (2010).
84. G. S. Ezra and S. Wiggins, "Phase space barriers and dividing surfaces in the absence of critical points of the potential energy", preprint [chem-ph arXiv:1011.0913].
85. P. Collins, G. S. Ezra and S. Wiggins, "Index *k* saddles and dividing surfaces in phase space, with applications to isomerization dynamics", J. Chem. Phys. **134**, 244105 (2011).
86. P. Collins, G. S. Ezra and S. Wiggins,"Isomerization dynamics of a buckled nanobeam", Phys. Rev. E **86**, 056218 (2012).
87. F. A. L. Mauguiere, P. Collins, G. S. Ezra and S. Wiggins, "Bond breaking in a Morse chain under tension: fragmentation patterns, higher index saddles and bond healing", J. Chem. Phys. **138**, 134118 (2013).
88. F. A. L. Mauguiere, P. Collins, G. S. Ezra and S. Wiggins, "Bifurcations of Normally Hyperbolic Invariant Manifolds in Analytically Tractable Models and Consequences for Reaction Dynamics", Int. J. Bifurc. Chaos **23**, 1330043 (2013).
89. F. A. L. Mauguiere, P. Collins, G. S. Ezra, S. C. Farantos and S. Wiggins,"Multiple Transition States and Roaming in Ion-Molecule Reactions: a Phase Space Perspective", Chem. Phys. Lett, **592**, 282–287 (2014).
90. P. Collins, B. K. Carpenter, G. S. Ezra and S. Wiggins, "Nonstatistical dynamics on potentials exhibiting reaction path bifurcations and valley-ridge inflection points", J. Chem. Phys. **139**:154108 (2013).
91. F. A. L. Mauguiere, P. Collins, G. S. Ezra, S. C. Farantos and S. Wiggins, "Roaming dynamics in ion-molecule reactions: phase space reaction pathways and geometrical interpretation", J. Chem. Phys. **140**, 134112 (2014).
92. F. A. L. Mauguiere, P. Collins, G. S. Ezra, S. C. Farantos and S. Wiggins,Roaming dynamics in Ketene isomerization,Theoretical Chemistry Accounts **133**, 1507 (2014).
93. P. Collins, Z. C. Kramer, B. K. Carpenter, G. S. Ezra and S. Wiggins, Nonstatistical dynamics on the caldera, J. Chem. Phys. **141**, 034111 (2014).
94. G. S. Ezra and S. Wiggins,"Vladimir Igorevich Arnold: obituary", Physics Today, **63** (12), 74–76 (2010).

Acknowledgments We appreciate and thank all of the authors, and the various reviewers, who contributed to this Festschrift. Finally, the enthusiastic support of Christopher Cramer and help from TCA staff is gratefully acknowledged.

Theor Chem Acc (2014) 133:1507
DOI 10.1007/s00214-014-1507-4

REGULAR ARTICLE

Roaming dynamics in ketene isomerization

Frédéric A. L. Mauguière · Peter Collins · Gregory S. Ezra · Stavros C. Farantos · Stephen Wiggins

Received: 25 March 2014 / Accepted: 19 May 2014 / Published online: 10 June 2014

Abstract A reduced two-dimensional model is used to study ketene isomerization reaction. In light of recent results by Ulusoy et al. (J Phys Chem A 117, 7553, 2013), the present work focuses on the generalization of the roaming mechanism to the ketene isomerization reaction by applying our phase space approach previously used to elucidate the roaming phenomenon in ion–molecule reactions. Roaming is again found be associated with the trapping of trajectories in a phase space region between two dividing surfaces; trajectories are classified as reactive or nonreactive, and are further naturally classified as direct or nondirect (roaming). The latter long-lived trajectories are trapped in the region of nonlinear mechanical resonances, which in turn define alternative reaction pathways in phase space. It is demonstrated that resonances associated with periodic orbits provide a dynamical explanation of the quantum mechanical resonances found in the isomerization rate constant calculations by Gezelter and Miller (J Chem Phys 103, 7868–7876, 1995). Evidence of the trapping of trajectories by 'sticky' resonant periodic orbits is provided by plotting Poincaré surfaces of section, and a gap time analysis is carried out in order to investigate the statistical assumption inherent in transition state theory for ketene isomerization.

Keywords Roaming reaction · Normally hyperbolic invariant manifold · Periodic orbit · Nonlinear resonance · Transition state and dividing surface · Gap time distribution

Dedicated to Professor Greg Ezra and published as part of the special collection of articles celebrating his 60th birthday.

F. A. L. Mauguière · P. Collins · S. Wiggins (✉)
School of Mathematics, University of Bristol,
Bristol BS8 1TW, UK
e-mail: s.wiggins@bristol.ac.uk

F. A. L. Mauguière
e-mail: frederic.mauguiere@bristol.ac.uk

P. Collins
e-mail: Peter.Collins@bristol.ac.uk

G. S. Ezra
Baker Laboratory, Department of Chemistry and Chemical Biology, Cornell University, Ithaca, NY 14853, USA
e-mail: gse1@cornell.edu

S. C. Farantos
Institute of Electronic Structure and Laser, Foundation for Research and Technology - Hellas, Iráklion, Crete 711 10, Greece
e-mail: farantos@iesl.forth.gr

S. C. Farantos
Department of Chemistry, University of Crete, Iráklion, Crete 711 10, Greece

1 Introduction

The photodissociation of ketene, CH_2CO, has been the subject of many studies, both experimental and theoretical. Moore and co-workers, in a series of experiments, have reported many interesting aspects of this reaction [1–3]. The dissociation gives rise to two product fragments, CO and CH_2. However, when the dissociation is observed in molecules for which the two carbons are differentiated by using different isotopes, with for example, $^{12}CH_2^{13}CO$ or $^{13}CH_2^{12}CO$, then the products of the dissociation show in each case a mixture of ^{13}CO and ^{12}CO with co-fragments $^{13}CH_2$ and $^{12}CH_2$. These results show that isomerization (carbon exchange) in ketene has taken place prior to dissociation. The postulated mechanism involved in the

isomerization of ketene is the Wolff rearrangement mechanism [4]. In order to examine this hypothesis, ab initio calculations have been carried out by several authors [1, 5]. These calculations showed that the relevant portion of the potential energy surface (PES) for ketene isomerization has three different minima associated with two symmetrically related formylmethylene species and an oxirene structure situated midway between these structures, respectively [3]. On each side, a high barrier leads to the two isomers of ketene. These findings point out the importance of understanding the isomerization of ketene when studying its dissociation.

Recently, Ulusoy et al. [6, 7] studied the effect of roaming trajectories on the reaction rates for the isomerization of ketene. The *roaming phenomenon* is a recently identified chemical reaction mechanism, which has attracted much attention due to its unusual character. The roaming phenomenon was discovered in the photodissociation of H_2CO [8]. In this process, the formaldehyde molecule can dissociate via two channels: $H_2CO \rightarrow H + HCO$ (radical channel) and $H_2CO \rightarrow H_2 + CO$ (molecular channel). Zee et al. [9] pointed out that, above the threshold for the $H + HCO$ dissociation channel, the CO rotational state distribution exhibited an intriguing "shoulder" at lower rotational levels correlated with a hot vibrational distribution of H_2 co-product. The observed product state distribution did not fit well with the traditional picture of the dissociation of formaldehyde via a well-characterized saddle point transition state for the molecular channel. The roaming mechanism as an alternative reaction pathway, which explains the observations of van Zee and co-workers, was demonstrated both experimentally and in trajectory simulations by Townsend et al. [8]. Following this work, roaming has been identified in the unimolecular dissociation of molecules such as CH_3CHO, CH_3OOH or CH_3CCH, as well as in ion–molecule reactions [10], and it is now recognized as a general phenomenon in reaction dynamics (see refs [11, 12] and references therein).

A common characteristic of systems exhibiting roaming reactions studied so far is the presence of long-range interactions between the fragments of the dissociating molecule. However, the study by Ulusoy et al. [6, 7] discussed the roaming phenomenon in a different context. For ketene isomerization, there are no long-range interactions at play and this raises the question of the broader relevance of the roaming mechanism. Ulusoy et al. [6, 7] in their effort to find trajectories that avoid the minimum energy path (MEP) on the potential energy surface carried out isomerization rate constant calculations at very high energies, accessible neither to experiments [1–3] nor to the quantum mechanical calculations of Gezelter and Miller [13].

In two recent studies [14, 15], we have analysed the roaming phenomenon for ion–molecule reactions. In such reactions, the long-range potential function is dominated by charge-induced dipole interactions; a useful model for these systems is the Chesnavich potential [16]. By investigating the dynamics in its appropriate setting, phase space, we examined the roaming phenomenon in the presence of well-defined dividing surfaces (DSs) and associated reaction pathways in phase space. This approach enabled us to interpret roaming as a trapping phenomenon of trajectories between two DSs and the enhancement of this trapping by the presence of nonlinear mechanical resonances between the different degrees of freedom (DoF) of the system. ketene offers the opportunity to investigate the roaming phenomenon in other type of molecules than those studied up to now, and this is the main purpose of the present article.

The paper is organized as follows. Section 2 presents the reduced dimensional model for ketene isomerization used in our study and originally introduced by Gezelter and Miller [13]. We then analyse the dynamics of ketene isomerization in Sect. 3. In this section, we first discuss the construction of DSs that govern the reactions studied in Sect. 3.1 and then the dynamics in Sect. 3.2. The next Sect. 3.3 investigates the statistical assumption for the dynamics by a gap time analysis. Sect. 3.4 presents a detailed analysis of the trapping mechanism of trajectories between the DSs and the role of the ubiquitous resonances due to bifurcations of periodic orbits. In Sect. 4, roaming observed in the two distinctly different systems, ion–molecule and ketene, is compared. By associating roaming to the phase space structure of the molecule in a dynamically well-defined fashion, we establish its general character as a framework for revealing and exploring new reaction pathways. Finally, Sect. 5 concludes.

2 Reduced dimensional model of ketene isomerization

In this section, we give the details of the Hamiltonian used in our study. A reduced dimensional model for the study of ketene isomerization was proposed several years ago by Gezelter and Miller [13]. In their original paper, they proposed three models for ketene isomerization, retaining one, two and three relevant DoF for describing the isomerization process of ketene amongst the nine DoF of ketene molecule, respectively. They subsequently employed these three models for calculating quantum mechanical isomerization reaction rates. From their study, it appears that a two-dimensional model provides the best agreement when compared with experimental results by Lovejoy et al. [3]. Ulusoy et al. employed this two DoF model in their classical mechanical study [6, 7] of the dynamics of isomerization of ketene, and we use the same model in the present study.

In the Gezelter and Miller model, one of two DoF is identified with the reactive mode and involves mainly oxygen and hydrogen atom motion. The other relevant DoF corresponds to the out-of-plane motion of a hydrogen atom relative to the CCO plane, a motion which has a harmonic frequency of approximately 514 cm^{-1}. Gezelter and Miller used an analytical form for their reduced dimensional potential having several adjustable parameters in it. They fitted these parameters to reproduce the data from *ab initio* calculations obtained by Scott et al. [5]. The resulting potential[1] is expressed as:

$$V(q_F, q_1) = V_{1d}(q_F) + \frac{1}{2}k\left(q_1 + \frac{d}{k}\, q_F^4\right)^2, \tag{1}$$

with

$$V_{1d}(q_F) = a_2\, q_F^2 + a_4\, q_F^4 + a_6\, q_F^6 + c\, q_F^2 \exp(-d_0\, q_F^2). \tag{2}$$

Numerical values of the potential parameters are given in Table1. Figure 1 depicts a contour plot of the potential along with some periodic orbits (see Sect. 3.4). The different equilibrium points (EP) of the potential are listed in Table 2. For each EP, the stability is indicated by the labels CC or CS. A CC label denotes a centre–centre EP, which means that the EP is stable in both directions and the label CS is used for centre-saddle, which means that the EP is stable in one direction and unstable in the other.

The total Hamiltonian is obtained by adding to the above potential a kinetic energy term quadratic in momenta (p_{q_F}, p_{q_1}) conjugate to the coordinates (q_F, q_1), respectively. The resulting Hamiltonian takes the form:

$$H(p_{q_F}, p_{q_1}, q_F, q_1) = \frac{p_{q_F}^2}{2m_{\mathrm{O}}} + \frac{p_{q_1}^2}{2m_{\mathrm{H}}} + V(q_F, q_1), \tag{3}$$

where $m_{\mathrm{O}} = 16$ u and $m_{\mathrm{H}} = 1$ u are the masses of oxygen and hydrogen atom, respectively. This choice of masses was used by Gezelter and Miller [17].

3 Dynamics of ketene isomerization

In this work, we are concerned with the dynamics of isomerization in ketene and its relation to the roaming phenomenon. Recently, Ulusoy et al. reported a study of ketene isomerization where they analysed the impact of roaming trajectories on the rate of the reaction [6, 7]. Up to now, roaming reactions have been identified in the context of reactions involving long-range interactions between two fragments of a dissociating molecule. The study of Ulusoy et al. suggests the possibility of looking at roaming in different reaction dynamics contexts and in this sense represents an important conceptual advance. Recently, we

[1] Note that, the original paper by Gezelter and Miller [13] had a typo in it resulting in a missing factor of one half in front of the second term in the RHS of their Eq. (2.2).

Table 1 Parameters used in the reduced dimensional potential of ketene

Parameter	Value	Units
k	1.0074×10^{-2}	$(E_h a_0^2)$
d	1.9769	$(E_h a_0^5)$
a_2	-2.3597×10^{-3}	$(E_h a_0^2)$
a_4	1.0408×10^{-3}	$(E_h a_0^4)$
a_6	-7.5496×10^{-5}	$(E_h a_0^6)$
c	7.7569×10^{-3}	$(E_h a_0^2)$
d_0	-2.45182×10^{-4}	(a_0^2)

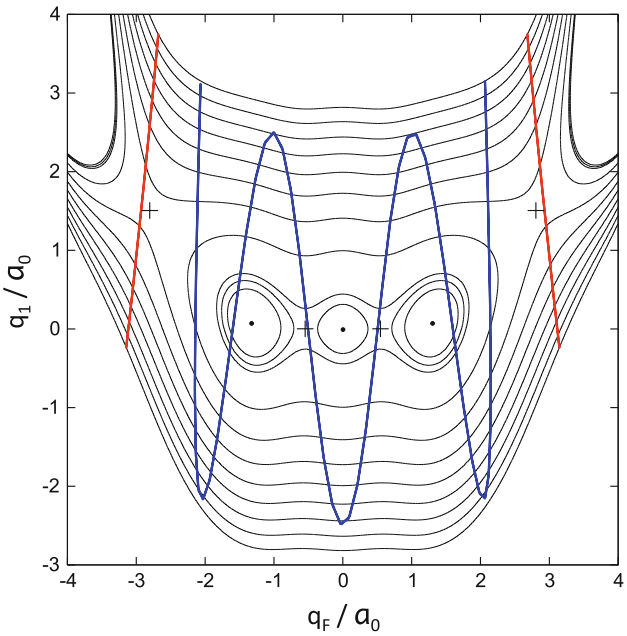

Fig. 1 Contour plot of the PES along with some POs. The *red curves* are the Lyapunov POs, and the *blue* is a 1:6 resonant PO (see text)

Table 2 Equilibrium points of the potential with their stability

Name	q_{F}	q_1	Stability
EP_1	−2.805	1.506	CS
EP_2	−1.325	0.075	CC
EP_3	−0.547	0.002	CS
EP_4	0.0	0.0	CC
EP_5	0.547	0.002	CS
EP_6	1.325	0.075	CC
EP_7	2.805	1.506	CS

Coordinates q_F and q_1 are indicated in Bohr. CS means centre-saddle and CC centre-centre

studied the dynamics of roaming reactions in the context of ion–molecule reactions [14, 15] and proposed a dynamical origin for the roaming phenomenon. Our approach consisted of identifying optimal DSs for the different reactive events possibly occurring in the problem considered. The roaming phenomenon was then identified with the trapping of trajectories between two DSs and enhanced by the presence of nonlinear resonances identified with resonant periodic orbits (POs). In the present work, we extend our methods to study the ketene isomerization reaction and the way roaming appears. To begin, we must first locate the relevant DSs for the problem we consider. The next paragraph is devoted to the definition of proper DSs and how this can be achieved with the help of the so-called normally hyperbolic invariant manifolds (NHIMs).

3.1 Normally hyperbolic invariant manifolds and dividing surfaces

The study of reaction dynamics aims at understanding the associated mechanism at an atomic level of detail in a specific molecular reaction. Eventually, one is interested in computing quantities such as reaction rate constants, which can be compared with experiment. The most popular theory developed for this purpose is transition state theory (TST). TST relies on several fundamental assumptions [18]. One of these assumptions is the existence of a dividing surface, which separates reactants from products and which has the nonrecrossing property. This means that a trajectory initiated at the reactants and crossing this dividing surface must proceed to products without recrossing the dividing surface, and end up as a reactant. The other fundamental assumption of TST is that of statistical dynamics. If one considers the reaction at a specific energy (microcanonical), the statistical assumption requires that throughout the dissociation of the molecule, all phase space points are equally probable on the timescale of reaction [18]. This assumption is equivalent to saying that the redistribution of the energy amongst the different DoF of the system on the reactant side of the DS is fast compared to the rate of the reaction, and this guarantees a single exponential decay for the reaction. We will check this assumption for the ketene model by a gap time analysis in the roaming region (see below).

In our previous study of roaming phenomena, we explained how NHIMs provide a solution to the problem of the nonrecrossing property of the DS. In fact, the problem of constructing a nonrecrossing DS for a two DoF system was solved during the 1970s by Pechukas, Pollak and coworkers [19–22]. They showed that the DS at a specific energy is intimately related to an invariant phase space object, an unstable PO. The periodic orbit defines the bottleneck in phase space through which the reaction occurs, and the DS which intersects trajectories evolving from reactants to products can be shown to have the topology of a hemisphere, whose boundary is the PO. As our present system is a two DoF problem, we will focus on POs and the DSs constructed from them. Nevertheless, this unstable PO is a simple example of a NHIM. Generalization to higher number of DoF has been a major obstacle in the development of the theory, and the question of the construction of DSs for systems with three and more DoF has been given a satisfactory answer only recently. The appropriate construction is built around an invariant phase space object, a NHIM, which is the generalization of the unstable PO of the two DoF case. The NHIM serves as the anchor for the construction of the DS, and this DS constructed in this way can be shown to have the nonrecrossing property [23].

The construction of a nonrecrossing DS for the simple two DoF model of ketene isomerization therefore starts with the location of relevant unstable POs. For the ketene problem, isomerization reaction is completed when the system passes from one ketene well to the other. The model we are dealing with locates the oxirene minimum between the formylmethylene wells. If we consider that the system is initially in the ketene well located on the part of the potential for which $q_F < -3\,a_0$ (the 'left'' ketene well if we look at Fig. 1), then isomerization is completed if the system passes to the other ketene well located on the part of the potential for which $q_F > 3\,a_0$. To accomplish this reaction, we see that the system must pass through two bottlenecks located around the equilibria labelled EP_1 and EP_7 in Table 2. These two EPs are of CS stability type, which means that the linearized vector field at these points (with momenta $p_{q_F} = 0$ and $p_{q_1} = 0$) has one pair of real eigenvalues and one pair of imaginary eigenvalues. This means that in the vicinity of these EPs, there exist unstable POs [24], the so-called Lyapunov POs [25]. In the vicinity of these EPs, the Lyapunov POs exist as families of POs depending on the energy of the system. Representative POs of these families are shown in Fig. 1. These POs are the NHIMs which define the bottlenecks through which the reaction occurs and will serve as anchors for the construction of the nonrecrossing DSs.

The DSs attached to these NHIMs are obtained by considering a fixed value of energy. At each energy, two Lyapunov POs exist, each located in the vicinity of EP_1 and EP_7, respectively. These POs are the equators of the DSs [23] and split the DSs into two hemispheres. One hemisphere intersects trajectories travelling from reactant to products (forward hemisphere) and the other intersects trajectories travelling from products to reactants (backward hemisphere). For concreteness, we consider the Lyapunov

PO at a certain energy in the vicinity of EP_1. This PO projects to a line in configuration space (see Fig. 1). To sample points on the DS, we need to specify the phase space coordinates of the points belonging to the DS at a certain energy. To do so, we move along the PO (the equator of the DS) in configuration space. This fixes the values of q_F and q_1. We then scan the values of one of the momenta p_{q_F} or p_{q_1}. To obtain the value of the remaining phase space coordinate (the remaining momentum), we solve the equation $H(p_{q_F}, p_{q_1}, q_F, q_1) = E$ for the remaining unknown momentum (p_{q_F} or p_{q_1}) and at a specified value of energy, E. Since the kinetic energy is quadratic in the momenta, this equation has two real roots distinguished by their sign. Each root belongs to one of the hemispheres of the DS (forward and backward hemispheres). The result of this sampling procedure is shown in Fig. 2. Panel (a) of this figure is a 3D plot of the forward hemisphere (blue dots) of the DS at energy of 0.01 Hartree above the oxirene minimum. The Lyapunov PO is shown by the green curve. Panel (b) depicts a 2D projection of this hemisphere onto the (q_1, p_{q_1}) plane. At the bottom of this figure, we note that some points belonging to the hemisphere lie out of the area enclosed by the Lyapunov PO (green curve). This is the result of the 'tilting' over of the DS in the coordinates we are using. Because of this fact, to obtain a uniform sampling with full coverage of the hemisphere, we sample momenta in two ways: sampling p_{q_1} with p_{q_F} obtained by solving the energy equation mentioned above, or sampling p_{q_F} and fixing p_{q_1} from the equation of energy.

3.2 Classical trajectory simulations

Our aim is to investigate the dynamics of ketene isomerization and how one can identify and understand the roaming phenomenon in this situation. To do so, we propagated classical trajectories and examined their qualitatively different characters.

If we consider that the system is initially located in the ketene well in the region where $q_F < -3\,a_0$, then the isomerization reaction is completed when the system arrives in the ketene well on the region where $q_F > 3\,a_0$. On its way to complete this reaction, a trajectory has to pass through two bottlenecks, one located in the vicinity of EP_1 and which is defined by the Lyapunov PO we discussed above, and the other located in the vicinity of EP_7 also defined by a Lyapunov PO. We explained above how to construct DSs attached to these two POs. In order to understand the dynamics of the isomerization process, we sampled the DS attached to the Lyapunov PO associated with EP_1. We used these samples as initial conditions for numerically propagating classical trajectories.

As we did in our previous studies [14, 15] of roaming phenomenon, we classified the trajectories into four qualitatively different categories. These different categories of trajectories are defined in relation to the reactive scenario involved in the ketene isomerization. To begin, we note that there are two obvious different types of expected trajectories. First, there are *reactive* trajectories which will complete the isomerization reaction, which means that these type of trajectories will cross the DS located in the vicinity of EP_7. Second, there are *nonreactive* trajectories, which do not complete the isomerization reaction, but instead recross the DS located in the vicinity of EP_1 and end up in the ketene well where they originally came from.

Since we are interested in understanding the roaming phenomenon from a dynamical point of view, we need to specify those characteristics a trajectory should have to be assigned as roaming. The notion of roaming is invoked when a trajectory does not follow the minimum energy path (MEP) or intrinsic reaction coordinate (IRC) [26] of the potential function. In our problem, this departure from traditional understanding of reactivity occurs in trajectories, which do not complete *directly* the isomerization reaction or do not recross *directly* the DS located in the vicinity of EP_1. Instead, the *roaming* trajectories spend more time in the trapping (roaming) region and exhibit oscillations in the q_F direction before eventually finding their way out of the oxirene well region by either crossing

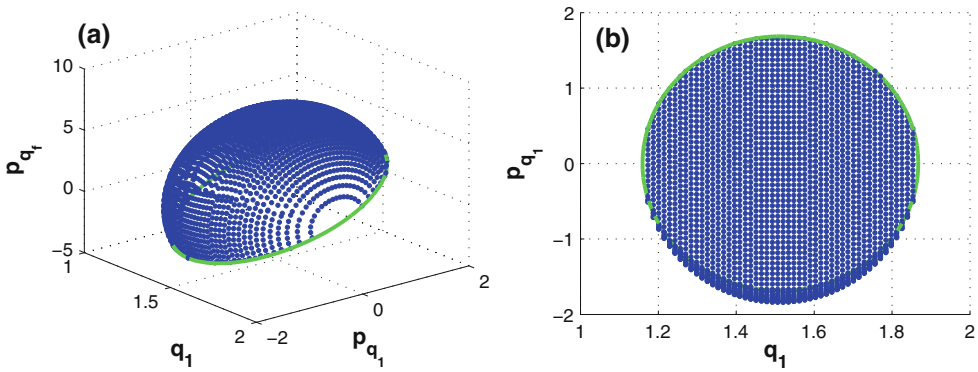

Fig. 2 Forward hemisphere of the dividing surface at the *top left* saddle at energy $E = 0.01$ E_h. **a** 3-D view. **b** Projection on the (q_1, p_{q_1}) plane

the DS located in the vicinity of EP_7 or the DS located in the vicinity of EP_1. To summarize, reactive (which complete the isomerization reaction) and nonreactive (which do not complete isomerization) trajectories are further categorized as direct and roaming. Hence, we have four classes of trajectories: direct reactive, roaming reactive, direct nonreactive and roaming nonreactive. However, in order to quantitatively define a roaming trajectory, we need a criterion to decide when a trajectory exhibits oscillations in the q_F direction before eventually becoming reacting or nonreacting. To achieve this task, we count the number of times a trajectory crosses the symmetry line $q_F = 0$. The precise definitions of the four categories are therefore:

1. Direct reactive trajectories: these trajectories cross the line $q_F = 0$ only once before crossing the DS located in the vicinity of EP_7 and completing the isomerization reaction.
2. Roaming reactive trajectories: these trajectories cross the line $q_F = 0$ at least three times before crossing the DS located in the vicinity of EP_7 and complete the isomerization reaction. Note that a reactive trajectory has to cross the line $q_F = 0$ an odd number of times.
3. Direct nonreactive trajectories: these trajectories cross the line $q_F = 0$ only twice before crossing the DS located in the vicinity of EP_1 and do *not* complete the isomerization reaction.
4. Roaming nonreactive trajectories: these trajectories cross the line $q_F = 0$ at least four times before crossing the DS located in the vicinity of EP_1 and do *not* complete the isomerization reaction. Note that nonreactive trajectories have to cross the line $q_F = 0$ an even number of times.

In Fig. 3, we show representative trajectories from these four categories. Each panel in this figure corresponds to a particular category. Panel (a) shows representative direct reactive trajectories, panel (b) roaming reactive, panel (c) direct nonreactive and panel (d) roaming nonreactive.

At this point, it is interesting to compare the present results on ketene isomerization with those obtained in our previous studies of the roaming phenomenon [14, 15], which were done in the context of an ion–molecule reaction. We see that in the present problem, the natural classification into four different categories of the trajectories fits nicely into the classification provided in the previous studies. Our earlier analyses of the roaming phenomenon pointed out that roaming is related to the appearance of trapped trajectories between two DSs in phase space. This led us to define a roaming region which is the region of phase space between these two DSs, where the roaming occurs. The scenario here for ketene isomerization is similar, and the trapping occurs between the two DSs located in the vicinity of EP_1 and EP_7. These two DSs define a region in phase space, which can be identified with the roaming region we defined in our previous work. Furthermore, we previously described how nonlinear resonances manifest by the presence of certain POs provide the basic mechanism to transfer energy from one DoF to another and enhance the trapping phenomenon in the roaming region. We shall see below that this ingredient of the roaming phenomenon is also present in ketene isomerization and takes also the form of resonant POs. Lastly, we noted in our earlier studies that our approach had strong similarities with Miller's unified approach to reaction mechanisms in the presence of complex formation [27]. Specifically, Miller considered how TST should be

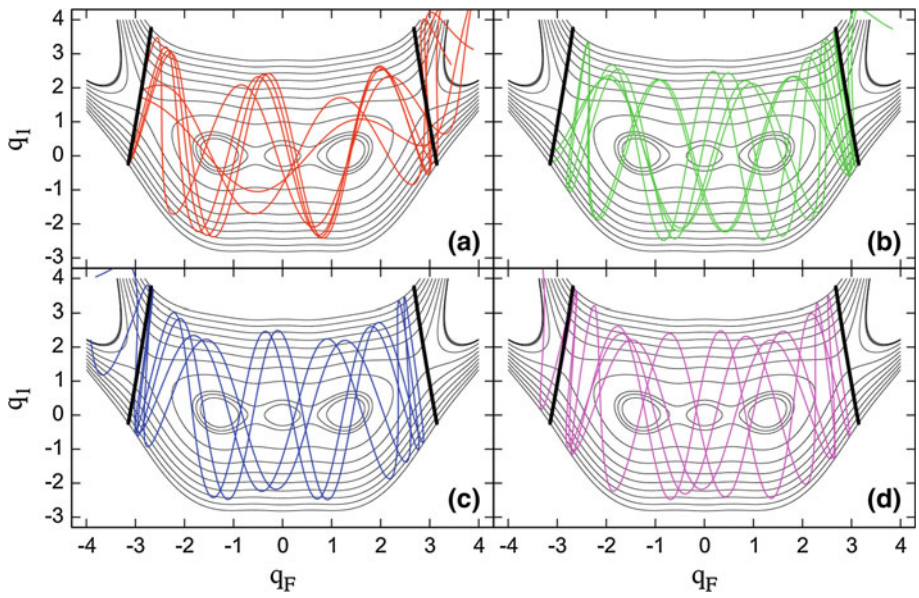

Fig. 3 The four different categories of trajectories at energy $E = 0.04\ E_h$. **a** Direct reactive trajectories. **b** Roaming reactive trajectories. **c** Direct nonreactive trajectories. **d** Roaming nonreactive trajectories

modified in the presence of a complex formation. This led us to investigate the question of the statistical assumption of TST in the roaming region using a gap time analysis, and we now investigate this question for the ketene isomerization.

3.3 Gap time analysis

The relevance of studying gap times in unimolecular reaction is seen in the investigation of the validity of the statistical assumption of TST. This assumption has been the subject of numerous works (see, for example the work of Slater [28, 29], Bunker [30, 31], Bunker and Hase [32], Thiele [33, 34], Dumont and Brumer [35] and DeLeon and co-workers [36, 37]).

In our earlier paper [15], we summarized the gap time approach to reaction rates due to Thiele [33, 34] (see also the discussion in Ref. [38]). The gap time in the ketene isomerization problem is the time s it takes for a trajectory to traverse the roaming region. If we consider a point on the forward hemisphere of the DS located in the vicinity of EP_1 (the hemisphere which intercepts trajectories travelling from the 'left' ketene well to the oxirene well), the gap time of a trajectory initiated at this point is the time it takes for this trajectory to reach either the hemisphere intercepting trajectories travelling from the oxirene well to the 'right' ketene well of the DS located in the vicinity of EP_7 or to reach the backward hemisphere of the DS located in the vicinity of EP_1 (the one which intercepts trajectories travelling from the oxirene well to the 'left' ketene well). An important notion in the gap time formulation of TST is the gap time distribution, $P(s;E)$: the probability that a phase space point on the forward hemisphere of the DS at EP_1 at energy E has a gap time between s and $s+ds$ is equal to $P(s;E)ds$. The statistical assumption of TST is equivalent to the requirement that the gap time distribution is the random, exponential distribution.

$$P(s;E) = k(E)\exp(-k(E)s). \tag{4}$$

This distribution is characterized by a single exponential decay constant $k(E)$, which is a function of the energy.

In addition to the gap time distribution, we also consider the integrated gap time distribution $F(t;E)$, which is defined as the fraction of trajectories with gap times $s \geq t$, and is expressed as

$$F(t;E) = \int_t^{+\infty} \mathrm{d}s\, P(s;E). \tag{5}$$

For the random gap time distribution, the integrated gap time distribution is exponential, $F(t;E) = \exp(-kt)$.

The results of gap time and integrated gap time distributions for ketene isomerization are shown in Figs. 4 and 5. To obtain these figures, we sampled uniformly at a certain energy the forward hemisphere of the DS at EP_1 and propagated trajectories until they exit the roaming region by either crossing the DS at EP_7 or recrossed the DS at EP_1. Figure 4 shows the gap time distributions at different energies measured from the oxirene minimum (see the caption of the figure). For each panel, we have reported the individual gap time distributions of the different categories of trajectories. The red curves represent the distributions for the direct reactive trajectories, the green represent the roaming reactive trajectories, the blue the direct nonreactive and the magenta the roaming nonreactive trajectories. The black curves depict the gap time distributions for all categories taken together. Figure 5 shows the integrated gap time distributions at the same energies as Fig. 4. For each energy, we show two panels presenting the short timescale distributions and the large timescale distributions. The different curves with their colours have the same meaning as in Fig. 4.

As we can see, these two figures exhibit significant deviation from the random gap time distributions as well as exponential integrated gap time distributions, indicating that the statistical assumption of TST is not valid for the ketene isomerization problem and must be corrected in some fashion. To give an idea of the kind of corrections one needs to provide, we plot in Fig. 6 the fractions of the different types of trajectories as a function of the energy. If one were to use the DS at EP_1 to compute the flux needed to evaluate the reaction rate in TST, this flux would have to be corrected by the fractions given in Fig. 6. Indeed, since some trajectories are reflected back to the 'left' ketene well, there are some recrossing trajectories and the real flux is the flux through the DS multiplied by the sum of the fractions of the direct and roaming reactive trajectories.

3.4 Trapping in the roaming region and resonant periodic orbits

We have attributed the roaming phenomenon to trapped trajectories, which follow alternative pathways to those associated with MEPs on the PES. The trapping is due to multiple dividing surfaces and the existence of nonlinear mechanical resonances. Resonances can be traced in phase space by constructing continuation/bifurcation diagrams of periodic orbits starting from principal POs originating from equilibria, minima and saddles, and following them in a parameter space, which may include the total energy, angular momentum, masses or other parameters of interest. This is a well-known strategy in studying nonlinear dynamical systems.

For the ketene isomerization model, we located families of POs that are related to EP1 and EP7 equilibria and the

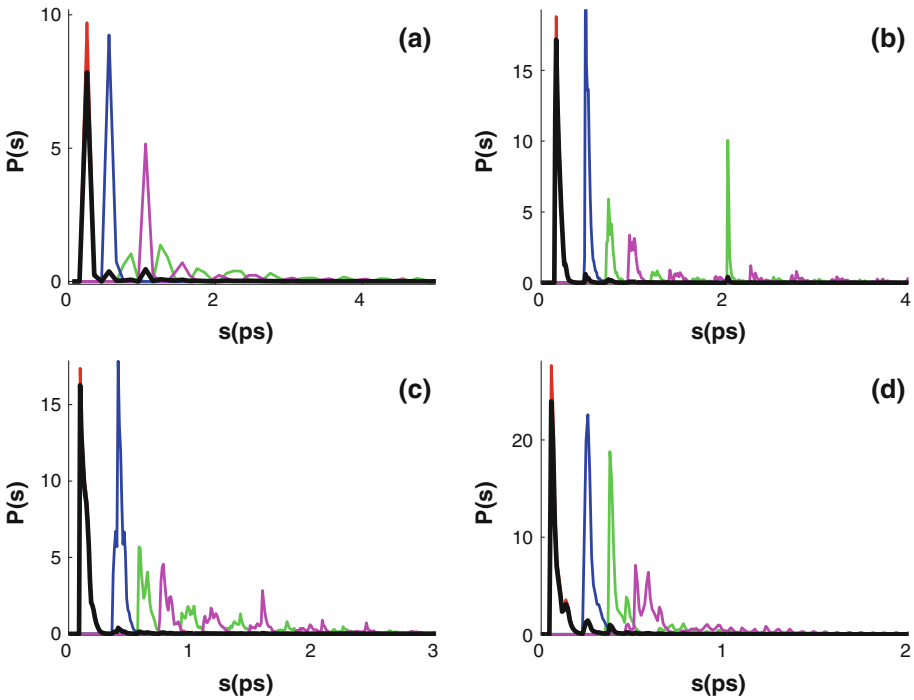

Fig. 4 Gap time distributions. For each energy, we give the number n of trajectories used to compute the distributions. **a** Energy $E = 0.010\ E_h$, $n = 942592$. **b** $E = 0.0150\ E_h$, $n = 941938$. **c** $E = 0.040\ E_h$, $n = 1967165$. **d** $E = 0.150\ E_h$, $n = 1932961$

roaming region at low energies of excitation. These families emanate from a cascade of centre-saddle bifurcations approaching the saddle from energies above the isomerization threshold [39]. The results are shown in a continuation/bifurcation diagram of POs in Fig. 7. This figure depicts the period of the POs found as a function of energy. We also label the POs with respect to their resonance numbers $n : m$, which means that the PO makes n oscillations in q_F direction in the time it performs m oscillations in q_1 direction. To give an idea of the shape of these POs in configuration space, we have plotted the 1:6 resonant PO as a blue line in Fig. 1. It is easy to recognize the impact of this family of POs on the dynamics of ketene from the plots of representative trajectories in Fig. 3. It is worth emphasizing that these periodic orbits are the results of centre-saddle bifurcations. Thus, we expect, and indeed find, stable and unstable branches of POs to appear simultaneously, and these periodic orbits define the resonance region in phase space. A linear stability analysis of periodic orbits reveals the stable/unstable character of nearby trajectories with respect to POs. However, in order to better estimate the size of the resonance zone defined by these periodic orbits, we calculate Poincaré surfaces of section (PSS) [40], and autocorrelation functions from batches of trajectories sampled around the POs.

3.4.1 Poincaré surfaces of section

We have used two different PSS, which give complementary views of the dynamics. The first one (PSS_1) was defined by fixing $q_F = 0$ and recording points when they cross this plane with a momentum $p_{q_F} > 0$. The second one (PSS_F) was chosen at $q_1 = 0$ with momentum $p_{q_1} > 0$. These two PSS are depicted in Fig. 8 for two different energies. Panel (a) is PSS_1 for energy $E = 0.01$ Hartree above oxirene minimum and panel (b) is PSS_F for the same energy. Panels (c) and (d) are the equivalent PSS at energy $E = 0.04$ Hartree above oxirene minimum.

For each panel, we have used different colours for points on the PSSs belonging to trajectories of a different category as were classified above. The colours are consistent with those in the previous plots: hence, red dots denote points belonging to direct reactive trajectories, green dots denote the roaming reactive ones, blue the direct nonreactive and magenta the roaming nonreactive trajectories, respectively. In Fig. 8, we see a clear separation between the red and the other colours with the red concentrated in the middle of the figure. This is consistent with the fact that direct reactive trajectories have their energy mainly distributed on the (q_F, p_{q_F}) DoF. Interestingly, the blue nonreactive direct trajectories appear at the boundary between the red and the roaming trajectories. Such reactivity boundaries have been observed in many studies and in several different contexts (see for example [15, 41–43], and references therein).

On the other hand, the green and magenta points (roaming trajectories) cover the periphery in the plots of PSS_1 indicating that more energy is involved in the (q_1, p_{q_1}) DoF for these types of trajectories. The two plots of PSS_F for the two energies show that the green and magenta dots are concentrated around some islands of

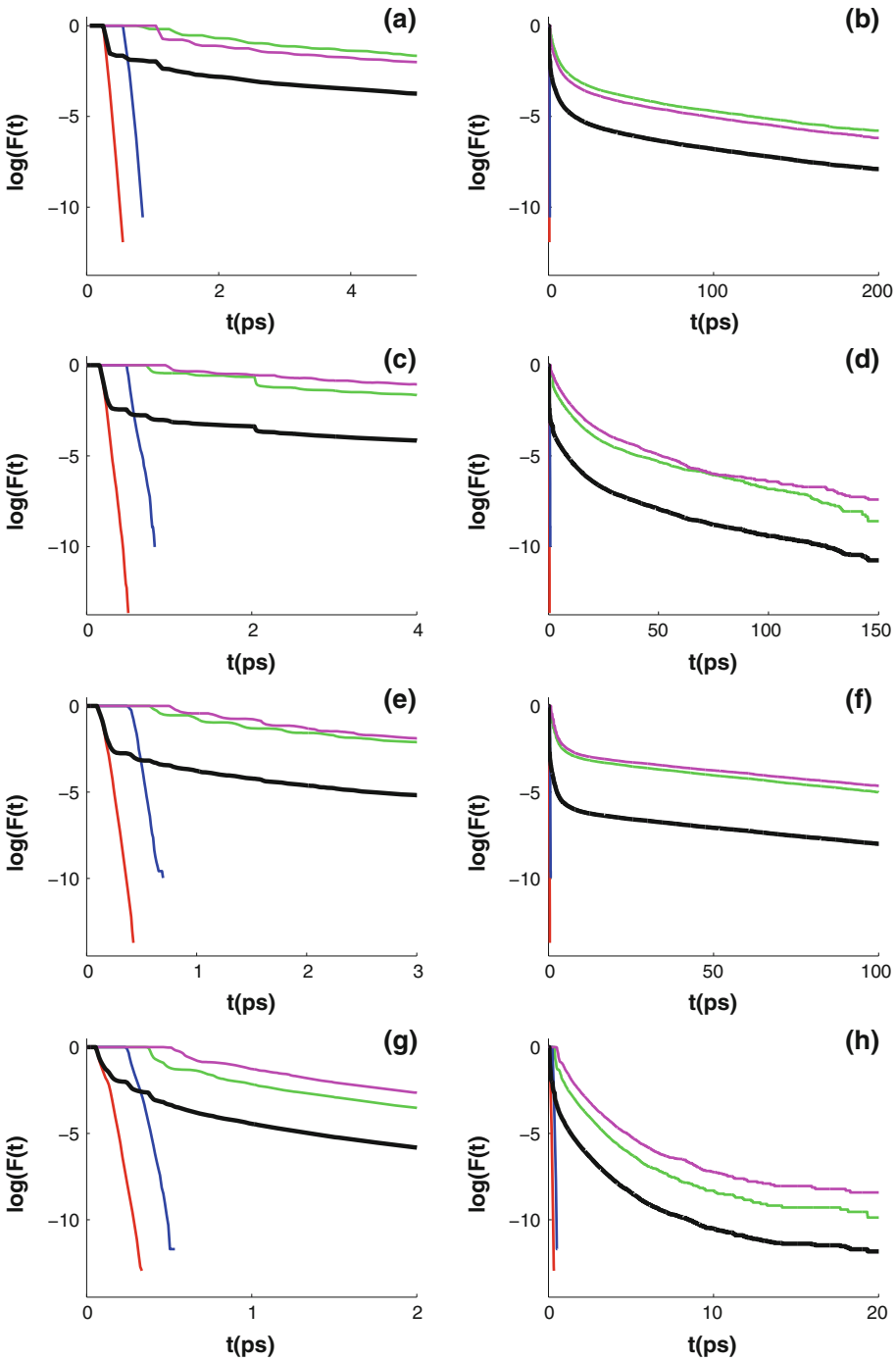

Fig. 5 Lifetime distributions. For each energy, we plot two panels showing the small timescale and the large timescale of the distribution. The number of trajectories used to compute the distributions is as indicated in Fig. 4. **a**, **b** Energy $E = 0.010\ E_h$. **c**, **d** $E = 0.0150\ E_h$. **e**, **f** $E = 0.040\ E_h$. **g**, **h** Energy $E = 0.150\ E_h$

stability (blank area). These blank areas correspond to the stable regions in phase space associated with the stable resonant POs. The large blank area in panel (b) and for the energy $E = 0.01$ Hartree is not accessible to trajectories initiated on the DS at EP_1. However, as energy increases to 0.04 Hartree, this stable area shrinks and the three central blank domains in panel (d) are attributed to trajectories in the vicinity of the three minima, which correspond to oxirene (EP_4) and the two formylmethylene minima (EP_2, EP_6).

3.4.2 *Classical autocorrelation functions*

Quantum calculations of the rate constant of ketene isomerization have shown that there are resonant features that are spaced at 70–80 cm^{-1} apart and with a width of about 10 cm^{-1}. These resonances have been attributed to Feshbach energy transfer or dynamical resonances that occur at energies above the barrier to isomerization [13]. According to Gezelter and Miller [13], 'these dynamical resonances appear because the multimode potential energy surface has

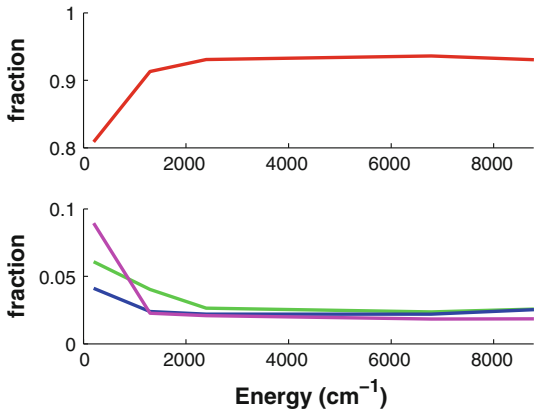

Fig. 6 Fractions of the different trajectories categories as a function of the energy above the barrier for isomerization. The different fractions are computed with the same number of trajectories as indicated in Fig. 4

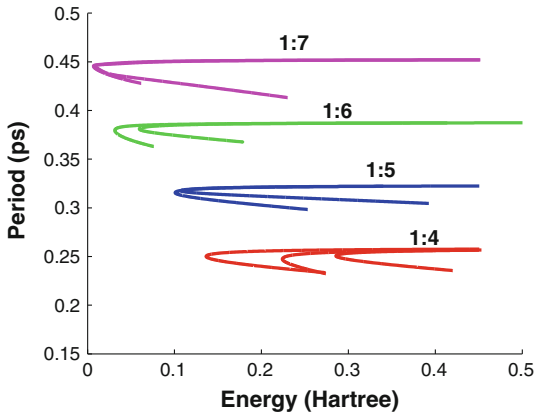

Fig. 7 Continuation/Bifurcation diagram for the resonant periodic orbits in the roaming region

a strongly bent region between the two outer transition states, which acts as a dynamical bottleneck even at total energies above the outer transition state energies'. The present classical trajectory results suggest that these resonances can be identified with the resonant periodic orbits, which are the result of a cascade of centre-saddle bifurcations shown in Fig. 7 [44].

This notion can be verified by calculating the classical analogue ($\Omega(t)$) of the quantum survival probability function ($|C(t)|^2$) for a wavepacket centred on the classical PO. In this case, the correspondence between spectrum and phase space structure is relatively straightforward. We can pass from the quantum to the classical analogue of the autocorrelation function by replacing the trace in the density matrix given in Eq. 7 with an integral over the phase space, and by replacing the density operators ($|\phi(q,t)\rangle\langle\phi(q,t)|$) with classical distribution functions, $\rho(q,p)$, [45, 46].

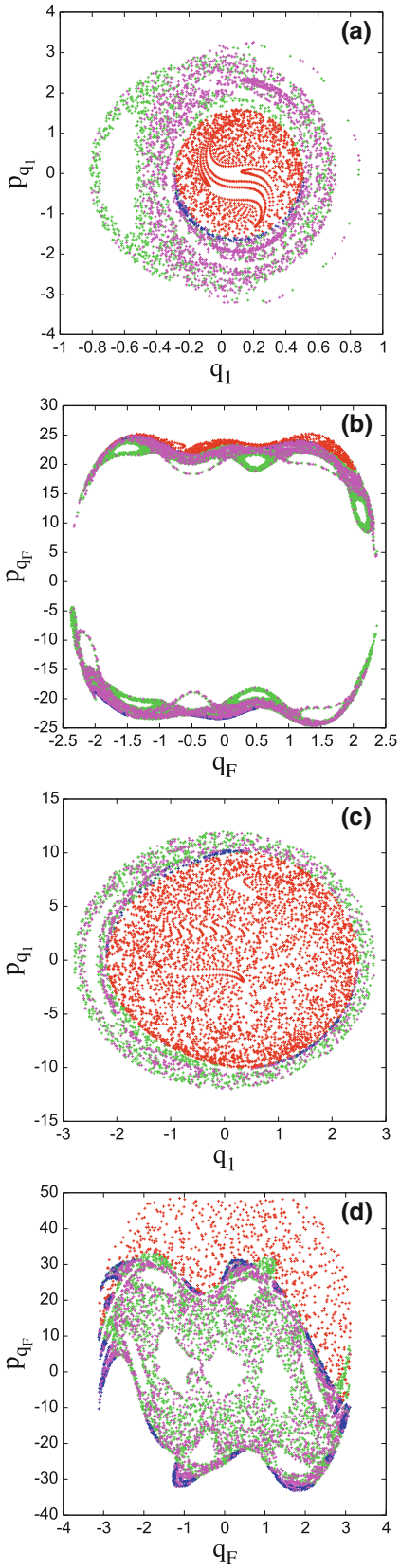

Fig. 8 Poincaré surfaces of sections (PSSs). **a** PSS_1 at $E = 0.010\ E_h$. **b** PSS_F at $E = 0.010\ E_h$. **c** PSS_1 at $E = 0.040\ E_h$. **d** PSS_F at $E = 0.040\ E_h$

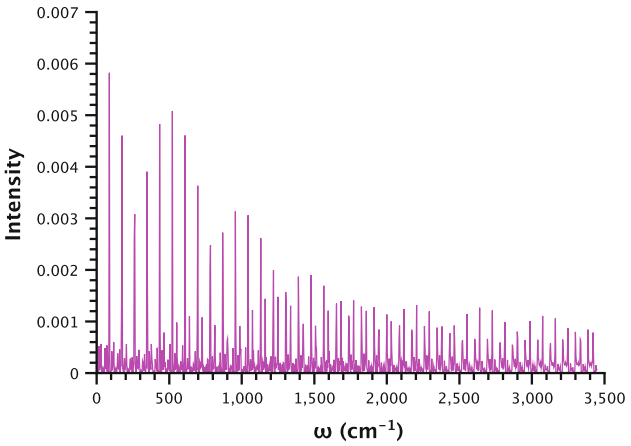

Fig. 9 Autocorrelation function for trajectories in the neighbourhood of 1:6 periodic orbit at energy of 0.04 E_h

$$\Omega(t) = \int \rho[q(0), p(0)]\rho[q(t), p(t)]\mathrm{d}q\mathrm{d}p. \tag{6}$$

$$\begin{aligned} |C(t)|^2 &= |\langle\phi(q,0)|\phi(q,t)\rangle|^2 \\ &= \langle\phi(q,0)|\phi(q,t)\rangle\langle\phi(q,t)|\phi(q,0)\rangle, \end{aligned} \tag{7}$$

In our case, the classical initial distribution $\rho[q(0), p(0)]$ is a Gaussian function of coordinates and momenta. The spectrum is then defined as the Fourier transform,

$$I_c(\omega) = \int e^{i\omega t}\Omega(t)\mathrm{d}t. \tag{8}$$

The classical survival probability function, Eq. 6, and its Fourier transform have been used in studies of molecular spectroscopy and dynamics by Gomez Llorente, Pollak and Taylor [47, 48].

Figure 9 shows a typical spectrum produced by a batch of 1000 trajectories selected from a Gaussian distribution centred on the stable 1:6 PO and at energy 0.04 E_h. The spacing of eigenfrequencies is 83 cm^{-1} and the regularity of the spectrum reflects the regularity of the region of phase space in which the trajectories are trapped. Higher-order POs, like the 1:7, have longer periods and appear at energies closer to the isomerization saddle. Their frequencies match the quantum mechanical frequencies in the interval of 70–80 cm^{-1} found by Gezelter and Miller [13].

4 Phase space reaction pathways and roaming

Reaction pathways are conventionally identified in nuclear configuration space by minimum energy paths on the potential energy surface, since the latter is the fundamental concept used to interpret chemical reactivity [26]. Thus, the presence of multiple saddles on the PES suggests the existence of multiple reaction pathways. However, the development of nonlinear mechanics has enabled the rigorous definition of objects such as reaction pathways and transition states in phase space for polyatomic molecules.

The strategy followed to understand the motions of nonlinear dynamical systems is to reveal the geometry of phase space in a systematic way by first locating equilibria, and from them the emanating principal families of periodic orbits, tori, NHIMs and (un)stable manifolds associated with NHIMs. The latter are key protagonists in controlling reaction fluxes. Both for the isomerization dynamics of ketene and in our previous work on the Chesnavich model for ion–molecule reactions, we have shown that, by defining transition states using the appropriate NHIMs (unstable periodic orbits for 2D molecular models), ordinary (MEP) and roaming reaction pathways emerge within a phase space framework. Similarities between the two type of reactions emphasized in Sect. 3.2; we now point out some significant differences.

ketene belongs to the general type of molecules for which NHIMs are associated with potential energy saddles. The Chesnavich model for ion–molecule reactions is a model, which manifests the existence of NHIMs not associated with potential energy saddles. Indeed, as shown in refs [14, 15], the loose transition state and the tight one are periodic orbits originating from centre-saddle bifurcations. The loose transition state is a rotating-type periodic orbit (relative equilibrium). The tight transition state is a periodic orbit associated with the barrierless MEP for association/dissociation. Hence, for these type of reactions, phase space is mandatory to define reaction pathways, since the potential energy alone is inadequate.

By attributing roaming to trapped trajectories in the region of nonlinear resonances in phase space, we are able to generalize the concept of roaming. From the PSS in Fig. 8 and in the low energy regime (0.01 Hartree), the roaming pathways are determined by the resonances 1:6 and 1:7 as indicated by the types of POs in Fig. 7. From the large number of trajectories run, none penetrates close to the regions of formylmethylene and oxirene. At higher energies (0.04 Hartree), the regular phase space region governed by the equilibria, EP2, EP4 and EP6, shrinks, and the reactive trajectories initiated from the NHIMs of the outer saddle penetrate into this region. In this way, we infer that the new resonances associated with these minima define new roaming reaction pathways. It is worth mentioning that nonlinear resonances associated with centre-saddle bifurcations of periodic orbits have been found to be a general phenomenon in molecular dynamics [44].

Finally, it is essential to stress that, although roaming as an alternative reaction pathway was identified in the dissociation of formaldehyde with long-range interactions between the fragment species, several other molecules with

competing non-MEP have previously been studied [49–55].

5 Summary and conclusions

In this paper, we have used a reduced dimensional model initially proposed by Gezelter and Miller to study the isomerization dynamics of ketene molecule. The study of Ulusoy et al. [6, 7] discussed the connection of ketene isomerization and roaming reactions mechanism. The question of how our previous interpretation of roaming phenomenon [14, 15] fits the ketene isomerization situation naturally arose.

It was found that the previous interpretation of the roaming mechanism in terms of a trapping mechanism of trajectories between two DSs enhanced by nonlinear resonances also fits the ketene isomerization reaction well. We were able to classify classical trajectories into qualitatively different types of trajectories and compute fractions of different types of trajectories; these data could be used to correct the flux in a reaction rate calculation. As in our previous study, the question of statistical dynamics was raised and investigated by gap time analysis. Significant deviation from the statistical assumption of TST was found. In addition, evidence of the trapping mechanism of the trajectories by resonant POs has been given using surfaces of section.

The importance of ketene isomerization stems from the experimental investigations of Moore and co-workers. Furthermore, the quantum mechanical results of Gezelter and Miller are in overall agreement to the experimental results. Our phase space analysis provides further insight into this important system; for example, ketene provides an experimental manifestation of the importance of the centre-saddle bifurcations of periodic orbits.

In the present calculation and for the energies studied, the direct-type reactive trajectories dominate (Fig. 6). However, if oxirene could be isolated and photoexcited into resonant states, the roaming branch of the reaction would then be the dominant one. In other words, knowledge of the phase space structure in a particular range of energies in principle enables us to exert some degree of control over chemical reaction pathways. Analysis of classical phase space as presented here can achieve a degree of resolution not necessarily accessible to experiment. Nevertheless, experimental techniques are continually advancing, and methods may be developed in the future to control roaming pathways [56].

Acknowledgments We wish to thank Dr. D. Gezelter, Prof. W. H. Miller and Prof. R. Hernandez and coworkers for helpful discussions. This work is supported by the National Science Foundation under Grant No. CHE-1223754 (to GSE). FM, PC and SW acknowledge the support of the Office of Naval Research (Grant No. N00014-01-1-0769), the Leverhulme Trust, and the Engineering and Physical Sciences Research Council (Grant No. EP/K000489/1).

References

1. Lovejoy ER, Kim SK, Alvarez RA, Moore CB (1991) J Chem Phys 95:4081
2. Lovejoy ER, Kim SK, Moore CB (1992) Science 256(5063):1541
3. Lovejoy ER, Moore CB (1993) J Chem Phys 98:7846
4. Kirmse W (2002) Eur J Org Chem 2002(14):2193
5. Scott AP, Nobes RH, Schaefer HF III, Radom L (1994) J Am Chem Soc 116(22):10159
6. Ulusoy IS, Stanton JF, Hernandez R (2013) J Phys Chem A 117:7553
7. Ulusoy IS, Stanton JF, Hernandez R (2013) J Phys Chem A 117:10567
8. Townsend D, Lahankar SA, Lee SK, Chambreau SD, Suits AG, Zhang X, Rheinecker J, Harding LB, Bowman JM (2004) Science 306(5699):1158
9. van Zee RD, Foltz MF, Moore CB (1993) J Chem Phys 99:1664
10. Yu HG (2011) Physica Scripta 84(2):028104
11. Bowman JM, Shepler BC (2011) Ann Rev Phys Chem 62:531
12. Bowman JM (2014) Mol Phys. doi:10.1080/00268976.2014.897395
13. Gezelter JD, Miller WH (1995) J Chem Phys 103:7868
14. Mauguière FAL, Collins P, Ezra GS, Farantos SC, Wiggins S (2014) Chem Phys Lett 592:282
15. Mauguière FAL, Collins P, Ezra GS, Farantos SC, Wiggins S (2014) J Chem Phys 140:134112
16. Chesnavich WJ (1986) J Chem Phys 84:2615
17. Gezelter D Private communication
18. Baer T, Hase WL (1996) Unimolecular reaction dynamics. Oxford University Press, New York
19. Pechukas P, McLafferty FJ (1973) J Chem Phys 58(4):1622
20. Pechukas P, Pollak E (1977) J Chem Phys 67(12):5976
21. Pollak E, Pechukas P (1978) J Chem Phys 69:1218
22. Pechukas P, Pollak E (1979) J Chem Phys 71(5):2062
23. Waalkens H, Wiggins S (2004) J Phys A Math Gen 37(35):L435
24. Moser J (1976) Commun Pure Appl Math 29:727
25. Kelley A (1969) Pac J Math 29(2):335
26. Heidrich D (1995) The reaction path in chemistry: current approaches and perspectives. Kluwer, Boston
27. Miller WH (1976) J Chem Phys 65:2216
28. Slater NB (1956) J Chem Phys 24(6):1256
29. Slater NB (1959) Theory of unimolecular reactions. Cornell University Press, Ithaca
30. Bunker DL (1962) J Chem Phys 37:393
31. Bunker DL (1964) J Chem Phys 40:1946
32. Bunker DL, Hase WL (1973) J Chem Phys 59:4621
33. Thiele E (1962) J Chem Phys 36(6):1466
34. Thiele E (1963) J Chem Phys 38(8):1959
35. Dumont RS, Brumer P (1986) J Phys Chem 90:3509
36. DeLeon N, Berne BJ (1981) J Chem Phys 75:3495
37. Berne BJ, DeLeon N, Rosenberg RO (1982) J Phys Chem 86:2166
38. Ezra GS, Waalkens H, Wiggins S (2009) J Chem Phys 130:164118

39. Lin SY, Guo H, Farantos SC (2005) J Chem Phys 122(12):124308
40. Wiggins S (2003) Introduction to applied nonlinear dynamical systems and chaos, 2nd edn. Springer, New York
41. Nagahata Y, Teramoto H, Li C, Kawai S, Komatsuzaki T (2013) Phys Rev E 88:042923
42. Grice M, Andrews B, Chesnavich W (1987) J Chem Phys 87:959
43. Mauguiere F, Collins P, Ezra G, Wiggins S (2013) J Chem Phys 138:134118
44. Farantos SC, Schinke R, Guo H, Joyeux M (2009) Chem Rev 109(9):4248
45. Baranger M (1958) Phys Rev A 111:481
46. Heller EJ, Davis MJ (1980) J Phys Chem 84:1999
47. Gomez Llorente JM, Pollak E (1989) J Chem Phys 90:5406
48. Gomez Llorente JM, Taylor HS (1989) J Chem Phys 91:953
49. Hu X, Hase WL (1989) J Phys Chem 93:6029
50. Sun L, Hase WL (2002) Science 296:875
51. López JG, Vayner G, Lourderaj U, Addepalli SV, Kato S, deJong WA, Windus TL, Hase WL (2007) J Am Chem Soc 129:9976
52. Mikosch J, Trippel S, Eichhorn C, Otto R, Lourderaj U, Zhang JX, Hase WL, Weidemüller M, Wester R (2008) Science 319:183
53. Zhang J, Mikosch J, Trippel S, Otto R, Weidemüller M, Wester R, Hase WL (2010) J Phys Chem Lett 1:2747
54. Carpenter BK (2004) In Moss RA, Platz MS, Jones M Jr (eds) Reactive intermediate chemistry. Wiley, New York, pp 925–960
55. Lourderaj U, Hase WL (2009) J Phys Chem A 113:2236
56. Ashfold MNR, Nahler N, Orr-Ewing A, Vieuxmaire O, Toomes R, Kitsopoulos T, Garcia I, Chestakov D, Wu S, Parker D (2006) Phys Chem Chem Phys 8:26

Theor Chem Acc (2014) 133:1528
DOI 10.1007/s00214-014-1528-z

REGULAR ARTICLE

Revisiting roaming trajectories in ketene isomerization at higher dimensionality

Inga S. Ulusoy · Rigoberto Hernandez

Received: 25 April 2014 / Accepted: 20 June 2014 / Published online: 15 July 2014

Abstract Roaming dynamics have been observed in a three-dimensional model of the ketene isomerization reaction. The roaming trajectories sample the region between the outer potential barriers closest to the respective ketene isomers and involve turning points along the reaction coordinate in a polar representation. These roaming trajectories avoid the intrinsic reaction coordinate and the intermediates to which it is associated. Thus, one-dimensional transition state theory (TST) is generally insufficient as has been confirmed through an analysis of the reactive flux along the dividing surface (DS). A global representation of the DS, however, leads to accurate TST rate constants. The exact and TST microcanonical rates of isomerization have been obtained for the three-dimensional model and compare well to experiment. The global DS is therefore particularly important for obtaining rates in reactions that exhibit roaming. This work thus confirms the findings of our previous two-dimensional treatment of ketene isomerization (Ulusoy et al. in J. Phys. Chem. A 117:7553–7560, 2013).

Keywords Transition state theory · Roaming · Reaction dynamics · Classical trajectories · Reaction rate Theory

1 Introduction

The rate-determining step of a chemical reaction is generally the slowest step along the reaction pathway and can be linked to the point of highest energy along a reaction coordinate—that is, the saddle point of the reaction. In transition state theory (TST), the rate of a chemical reaction is described as the flux through a dividing surface (DS) at the saddle point (or col) [1–4]. The DS ideally separates the phase space into reactant and product regions. The better the choice of the DS, the better is the agreement between the TST and exact rate.

In more general TST, the DS is defined in phase space rather than configuration space [4–7]. For example, for a system with two degrees of freedom (DOF) ($F = 2$), if the transition state (TS) is described as a periodic orbit DS (PODS [8]), then the rates are exact. More generally, the non-recrossing requirement can be satisfied if the TS is a normally hyperbolic invariant manifold (NHIM) for a multidimensional system ($F \geq 3$). The formalism has been extended to barriers containing higher-rank saddles, allowing the treatment of reaction dynamics with multiple saddle points connected through a higher-rank saddle [9, 10].

While many reactions exhibit an energy profile along the reaction path that accommodates the inherent TST assumption of a recrossing-free DS, there may exist alternative mechanisms that circumvent the barrier and lead to non-IRC (internal reaction coordinate) behavior [11, 12]. One such mechanism involves roaming pathways. Therein, one atom or a group of atoms moves around the molecule followed by an "intramolecular" abstraction of an atom or group of atoms. Examples can be found in formaldehyde, acetaldehyde and nitrate molecular dissociation [13–15]. The roaming fragment bypasses the traditional reaction path and avoids the naive TS. The energy profile of the roaming pathway may also not reveal any relevant dynamics in the saddle point region. Thus, roaming dynamics present a challenge to traditional TST [16–19].

Dedicated to Professor Greg Ezra and published as part of the special collection of articles celebrating his 60th birthday.

I. S. Ulusoy · R. Hernandez (✉)
Center for Computational Molecular Science and Technology, School of Chemistry and Biochemistry, Georgia Institute of Technology, Atlanta, GA 30332-0400, USA
e-mail: hernandez@gatech.edu

In a phase-space representation of roaming trajectories, it has been shown by Mauguière et al. [20–22] that roaming trajectories are trajectories which are trapped for an arbitrarily long time between two barriers. The roaming region therefore is defined by two DSs in phase space. Klippenstein et al. [18] showed a similar representation in configuration space for roaming in formaldehyde. These results are consistent with our recent finding [23, 24] that a globalized TS is capable of capturing the rates even in the presence of roaming trajectories.

In the present paper, we extend our work studying the ketene isomerization reaction and the role of roaming trajectories in a multidimensional representation of the model ($F = 3$) [23, 24]. We calculate exact and TST rates for isomerization while finding roaming trajectories in three dimensions. We demonstrate that these trajectories avoid the IRC altogether and are "bound" by two DSs. Flux profiles along the DS are shown, and the implications on traditional one-dimensional (1D) TST are discussed.

2 Theory and methods

2.1 The model system: ketene isomerization

A reduced-dimensional potential for this reaction has already been constructed by Gezelter and Miller [25]. The potential energy is given by

$$V(q_1, q_2, q_F) = V_{1\mathrm{d}}(q_F) + V_{\mathrm{coup}}(q_1, q_2, q_F) \tag{1a}$$

$$V_{1\mathrm{d}}(q_F) = a_2 q_F^2 + a_4 q_F^4 + a_6 q_F^6 + c q_F^2 \exp^{-dq_F^2} \tag{1b}$$

$$V_{\mathrm{coup}}(q_1, q_2, q_F) = \frac{k_1}{2}\left(q_1 + \frac{d_1 q_F^4}{k_1}\right)^2 + \frac{k_2}{2}\left(q_2 + \frac{d_2 q_F^4}{k_2}\right)^2 \tag{1c}$$

The potential contains a one-dimensional term $V_{1\mathrm{d}}(q_F)$ along the reaction coordinate q_F and a coupling term $V_{\mathrm{coup}}(q_1, q_2, q_F)$. The parameters are given in Table 1. A projection of the potential onto the (q_2, q_F) plane is shown in Fig. 1. Other cuts through the potential can be found elsewhere [23–25]. The normal and local modes associated with the DOFs are the coupled in-plane motion of O and H atoms (reaction coordinate q_F), an out-of-plane vibration of the H_a in oxirene (mode q_1), and an in-plane bending vibration of the H_b in oxirene (mode q_2) [23–25].

In the Hamiltonian, we neglect rotational contributions in the kinetic energy term and employ the simple form

$$H = \frac{p_1^2}{2m_1} + \frac{p_2^2}{2m_2} + \frac{p_F^2}{2m_F} + V(q_1, q_2, q_F) \tag{2}$$

Table 1 Parameters contained in the potential function [25]

Parameter	Value
a_2	$-2.3597 \times 10^{-3}\,(E_h a_0^{-2})$
a_4	$1.0408 \times 10^{-3}\,(E_h a_0^{-4})$
a_6	$-7.5496 \times 10^{-5}\,(E_h a_0^{-6})$
c	$7.7569 \times 10^{-3}\,(E_h a_0^{-2})$
d	$1.9769\,(a_0^{-2})$
k_1	$1.0074 \times 10^{-2}\,(E_h a_0^{-2})$
d_1	$-2.45182 \times 10^{-4}\,(E_h a_0^{-5})$
k_2	$2.9044 \times 10^{-2}\,(E_h a_0^{-2})$
d_2	$-8.5436 \times 10^{-4}\,(E_h a_0^{-5})$

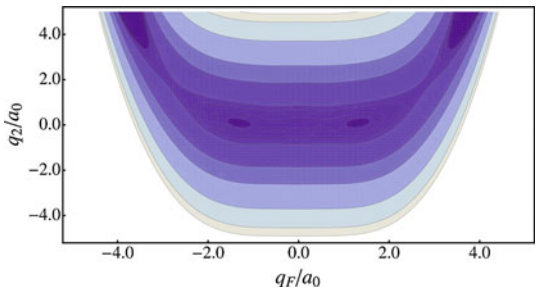

Fig. 1 Contour plot of the ketene isomerization potential projected onto the reaction coordinate q_F and the in-plane bend of H_b, mode q_2

where the momenta p_i are conjugate to positions q_i with associated masses m_i ($i = \{1, \ldots, F\}$). The values employed for the masses are discussed below.

2.2 Exact and TST rates of isomerization

To obtain isomerization rate constants, we calculate classical rates *exactly* by integrating over the reactive phase points at a DS, and *approximately* by employing TST. The DS is denoted through the $(F-1)$ dimensional vector $\mathbf{q}_\mathrm{s}$ between the product and reactant regions on the potential [26, 27]:

$$k_{\mathrm{Flux}}(E) = \frac{1}{\rho_\mathrm{R}(E)\, h^F} \int \mathrm{d}\mathbf{p}\, \mathrm{d}\mathbf{q}_\mathrm{s} (\mathbf{p} \cdot \mathbf{n}_\mathrm{s}) \chi_\mathrm{r}(\mathbf{p}, \mathbf{q}_\mathrm{s}) \delta(E - H(\mathbf{p}, \mathbf{q}_\mathrm{s})) \tag{3}$$

The function $\chi_\mathrm{r}(\mathbf{p}, \mathbf{q}_\mathrm{s})$ is the characteristic function of reactive phase points, $\chi_\mathrm{r}(\mathbf{p}, \mathbf{q}_\mathrm{s}) = 1$ if $(\mathbf{p}, \mathbf{q}_\mathrm{s})$ lies on a reactive trajectory, and $\chi_\mathrm{r}(\mathbf{p}, \mathbf{q}_\mathrm{s}) = 0$ otherwise. The unit vector $\mathbf{n}_\mathrm{s}$ is perpendicular to the DS and points in the direction of product formation. The reactant density of states $\rho_\mathrm{R}(E)$ is assigned the experimentally measured value [28, 29] of 4.5×10^4 states/cm^{-1} for a ketene molecule at an internal energy equal to 28,000 cm^{-1}. The numerator in Eq. 3 can be interpreted as the cumulative reaction probability, $N(E)$.

In the TST approximation, the rate simplifies to a form that requires no information about the dynamics, namely

$$k_{\mathrm{TST}}(E) = \frac{1}{\rho_{\mathrm{R}}(E)\, h^F} \int \mathrm{d}\mathbf{p}\, \mathrm{d}\mathbf{q}_{\mathrm{s}} (\mathbf{p}\cdot n_{\mathrm{s}}) \chi_{+}(\mathbf{p}, \mathbf{q}_{\mathrm{s}}, \mathbf{n}_{\mathrm{s}}) \delta(E - H(\mathbf{p}, \mathbf{q}_{\mathrm{s}})) \tag{4}$$

Here, the characteristic function $\chi_{\mathrm{r}}(\mathbf{p}, \mathbf{q}_{\mathrm{s}})$ is approximated as $\chi_{+}(\mathbf{p}, \mathbf{q}_{\mathrm{s}}, \mathbf{n}_{\mathrm{s}}) = 1$ for momenta $\mathbf{p}\cdot n_{\mathrm{s}} > 0$. Hence, $k_{\mathrm{TST}}(E)$ is an upper bound to the exact classical rate, as is well known [30].

2.3 Methodology

To obtain reaction rates, the integration in Eq. (3) is in principle carried out over all F DOF of the molecule. In order to make trajectory calculations computationally feasible, we employ a reduced-dimensional model where only three DOF are treated explicitly, and the other six DOF are approximated as harmonic oscillator modes and included in the reactive state count via the number of states $G^{\ddagger}(E)$ [31–33], as discussed previously [23, 24]. The vibrational frequencies of the implicit modes are taken from Ref. [34]. Anharmonic corrections for the implicit modes have not been introduced here under the assumption that they are weaker than the coupling to the explicit modes which has also been neglected.

Use of statistical phase-space theory within the RRKM approximation suggests that the total energy E is distributed equally between the implicit and explicit DOF into the correspondingly designated implicit and explicit energies E^{im} and E^{ex}

$$E = E^{\mathrm{im}} + E^{\mathrm{ex}} = \frac{N^{\mathrm{im}}}{F} E + \frac{N^{\mathrm{ex}}}{F} E \tag{5}$$

where N^{ex} and N^{im} denote the number of explicit and implicit DOFs. The energy for the explicit DOF contains a correction term for the zero-point energy for all explicit DOF except the reaction coordinate.

The energies are given relative to an effective zero of energy E_0, which is found to lie approximately at 3,600 cm^{-1} below the barrier (the outer TS). This effective zero of energy impacts only the state count $G^{\ddagger}(E^{\mathrm{im}})$ in so far as it sets the amount of energy to be distributed across the vibrational DOF. Thus, at the barrier, E^{im} is available as kinetic energy for the implicit (harmonic) modes.

The energy in the explicit modes E^{ex} corresponds to that required to activate the reactant above the threshold to reaction. The difference between these energies, $E^{\mathrm{ex}} - E^{\ddagger}$, is the excess energy.

The flux integral of Eq. 3 is now carried out over the $N^{\mathrm{ex}} - 1$ explicit DOF

$$\Gamma(E^{\mathrm{ex}}) = \int \mathrm{d}\mathbf{p}^{\mathrm{ex}}\, \mathrm{d}\mathbf{q}_{\mathrm{s}}^{\mathrm{ex}} (\mathbf{p}^{\mathrm{ex}}\cdot \mathbf{n}_{\mathrm{s}}) \chi_{\mathrm{r}}(\mathbf{p}^{\mathrm{ex}}, \mathbf{q}_{\mathrm{s}}^{\mathrm{ex}}) \delta(E - H^{\mathrm{ex}}(\mathbf{p}^{\mathrm{ex}}, \mathbf{q}_{\mathrm{s}}^{\mathrm{ex}})) \tag{6}$$

Table 2 Vibrational frequencies for the ring-opening mode of $b2$ symmetry in cm^{-1}, as derived from a local harmonic fit to potential $V_{1\mathrm{d}}(q_F)$, using a mass of $m_F = 9580.46$ a.u. (this publication) ($\omega_F^{(1)}$), and a mass of $m_F \approx m_O$ [25] ($\omega_F^{(2)}$), in comparison with ab initio values at the CCSD(T)/6-31G(d) level of theory [34] ($\omega_F^{(3)}$), and at the CCSD(T)/cc-pVTZ level of theory ($\omega_F^{(4)}$) [35]

Structure	$\omega_F^{(1)}$	$\omega_F^{(2)}$	$\omega_F^{(3)}$	$\omega_F^{(4)}$
Oxirene	234	**134**	21	**139**
Iinner TS	246*i*	141*i*	133*i*	–
Formylmethylene	265	152	328	–
Outer TS	**484** *i*	277*i*	**409** *i*	–

The pair of emboldened frequencies in the first and fourth lines highlight the agreement obtained according to the respective choices of the mass along the reaction coordinate

where $\chi_{\mathrm{r}}(\mathbf{p}^{\mathrm{ex}}, \mathbf{q}_{\mathrm{s}}^{\mathrm{ex}})$ has to be replaced by $\chi_{+}(\mathbf{p}^{\mathrm{ex}}, \mathbf{q}_{\mathrm{s}}^{\mathrm{ex}}, \mathbf{n}_{\mathrm{s}})$ for a TST calculation, and the unimolecular rate constant becomes

$$k_{\mathrm{Flux}}(E) = \frac{G^{\ddagger}(E^{\mathrm{im}})\Gamma(E^{\mathrm{ex}})}{\rho_{\mathrm{R}}(E)\, h^{N^{\mathrm{ex}}}} \tag{7}$$

which carries the units of inverse time.

In order to fully specify the Hamiltonian Eq. (2) and the trajectory propagation, masses must be assigned to each DOF. The potential term $V(q_1, q_2, q_F)$ is a fit to *ab initio* energies at relevant points on the potential energy surface (PES) [25, 34, 35]. The coordinate connecting the reactant and product minima across the lowest barrier—the reaction coordinate q_F—is the $b2$ ring deformation mode. The frequency of this normal mode vibration at different points on the PES is very strongly dependent on the level of theory used and basis set employed [34, 35].

The mass associated with this normal mode vibration, m_F, is also strongly dependent on the displacement coordinate. In their original paper, Gezelter and Miller employed a mass of $m_F = 29203.22$ a.u., which roughly corresponds to the mass of an oxygen atom [21, 36]. For an exact treatment, m_F should take on different values at different points on the potential. However, we use the mass associated with the b_2 ring deformation vibration at the oxirene geometry ($m_F = 9580.46$ a.u.), as obtained from a normal mode analysis. To demonstrate the effect of the mass on the dynamic properties of the system, we employ a local harmonic fit to the potential $V_{1\mathrm{d}}(q_F)$ to derive harmonic vibrational frequencies $\omega_F^{(1)}$ at the relevant points of the potential. This frequency can be compared to the vibrational frequency using a mass $m_F \approx m_O$, and the vibrational frequency from a normal mode analysis of the relevant structures at a high level of theory [34]. The results are summarized in Table 2.

Both masses lead to reasonable vibrational frequencies $\omega_F^{(1)}$ and $\omega_F^{(2)}$, where the choice of $m_F \approx m_O$ leads to an improved description of the dynamical properties at the

central region (the oxirene intermediate), and the choice of m_F in accordance with the mass derived from our normal mode analysis results in a better representation at the formylmethylene intermediate/outer TS. Thus, in the choice of a fixed mass to be associated with q_F, either of these choices for m_F are appropriate. Both model systems have been found to contain roaming trajectories [21, 23, 24].

Meanwhile, the masses m_1 and m_2, associated with vibrations of a single hydrogen atom, take the value of 1837.1 a.u., resulting in vibrational frequencies $\omega_1 = 514\,\mathrm{cm}^{-1}$ and $\omega_2 = 873\,\mathrm{cm}^{-1}$.

3 Results

3.1 Rates of isomerization and reactive flux at low energies

The TST (k_{TST}) and exact (k_{Flux}) rates of the ketene isomerization reaction were calculated at low energies using the 3D reduced-dimensional model in Eq. 1. These rates are compared to experiment [37] in Fig. 2 as a function of the excess energy E_{exc}. The latter E_{exc} is defined as the energy above the barrier corresponding to the outer TS and corrected for zero-point vibrational energies [23].

The TST rates for the 3D model are much higher than the experimental rates. This overestimate of the isomerization rate is even more pronounced at higher energies. The exact rates are in very good agreement with the experimental values and are an improvement upon what was seen in the previous 2D model [23, 24]. The large discrepancy between TST rates and exact ones indicates that there are a significant number of recrossings through the DS even at low energies. Below, we investigate the extent to which these recrossings can be attributed to the presence of roaming trajectories. Nevertheless, the experimental rates are very well reproduced by the classical exact rates in our reduced-dimensional model and are even capable of capturing some of the stepwise characteristics of the experimental rates.

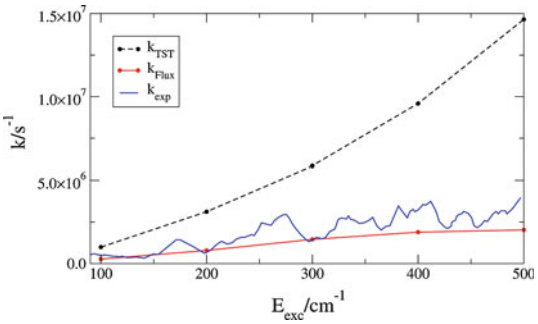

Fig. 2 Microcanonical reaction rates, approximate k_{TST} (*in black*) and exact k_{Flux} (*in red*) rates for the three-dimensional representation of ketene isomerization in comparison with experimental rates [37] (*in blue*)

3.2 Roaming events in a three-dimensional representation of ketene

In moving from a 2D to 3D representation of ketene isomerization, the dimensionality of the roaming dynamics can remain effectively two-dimensional or expand to all three explicit DOFs. We observe two general types of roaming trajectories (RTs): The first type (RT1) exhibits one large swing in the flat region of the potential, following a ridge line of high potential energy far out from the central region of the oxirene intermediate. The second type (RT2) takes a complete turn in the plateau region of the potential before proceeding to the product side. The energies in the explicit modes of the specific roaming trajectories discussed here are $E^{\mathrm{ex}}(\mathrm{RT1}, q_1) = 0.20966\,\mathrm{E}_h$ and $E^{\mathrm{ex}}(\mathrm{RT1}, q_2) = 0.21055\,\mathrm{E}_h$ in the 2D case, and $E^{\mathrm{ex}}(\mathrm{RT1}, q_1, q_2) = 0.37149\,\mathrm{E}_h$ and $E^{\mathrm{ex}}(\mathrm{RT2}, q_1, q_2) = 1.24654\,\mathrm{E}_h$ in the 3D case. While these are seemingly quite high, it is notable that this is due in part to the fact that the explicit orthogonal modes q_1 and q_2 are treated as harmonic oscillators. The orthogonal modes soak up additional energy in order to maintain a vibrational equidistribution.

Representative trajectories of RT1 are shown in Fig. 3a–c. In the case of RT1, the roam can be restricted (without loss of information) to the (q_F, q_1) (a) or (q_F, q_2) (b) planes only when the third DOF—that is q_2 and q_1 in cases a and b, respectively—contains a small percentage of the available energy and gives rise to particle motion that stays close to the potential minimum. In these cases, the roam takes a large swing into the high potential energy region along the second DOF For RT1, roaming can also involve significant motion in all three DOFs, as shown in Fig. 3c. Here, the RT samples the high potential energy region both in q_1 and q_2 . The structures along the roaming path involve an oxirene-like ring structure, where one of the hydrogen atoms is displaced out of the plane, and the other hydrogen swings in-plane. This pathway resembles an alternative pathway to the traditionally observed structures involved in the isomerization of ketene.

Representative trajectories of RT2 are shown in Fig. 3d. In the 3D model, this type of RT only occurs in spaces involving all three DOFs inseparably. Here, the roam takes a full turn on the central region before proceeding to the product side of the potential. This type of trajectory occurs at higher energy than RT1. At even higher energy, there may be other types of RTs, where the roam could take two or three turns over the plateau region of the potential.

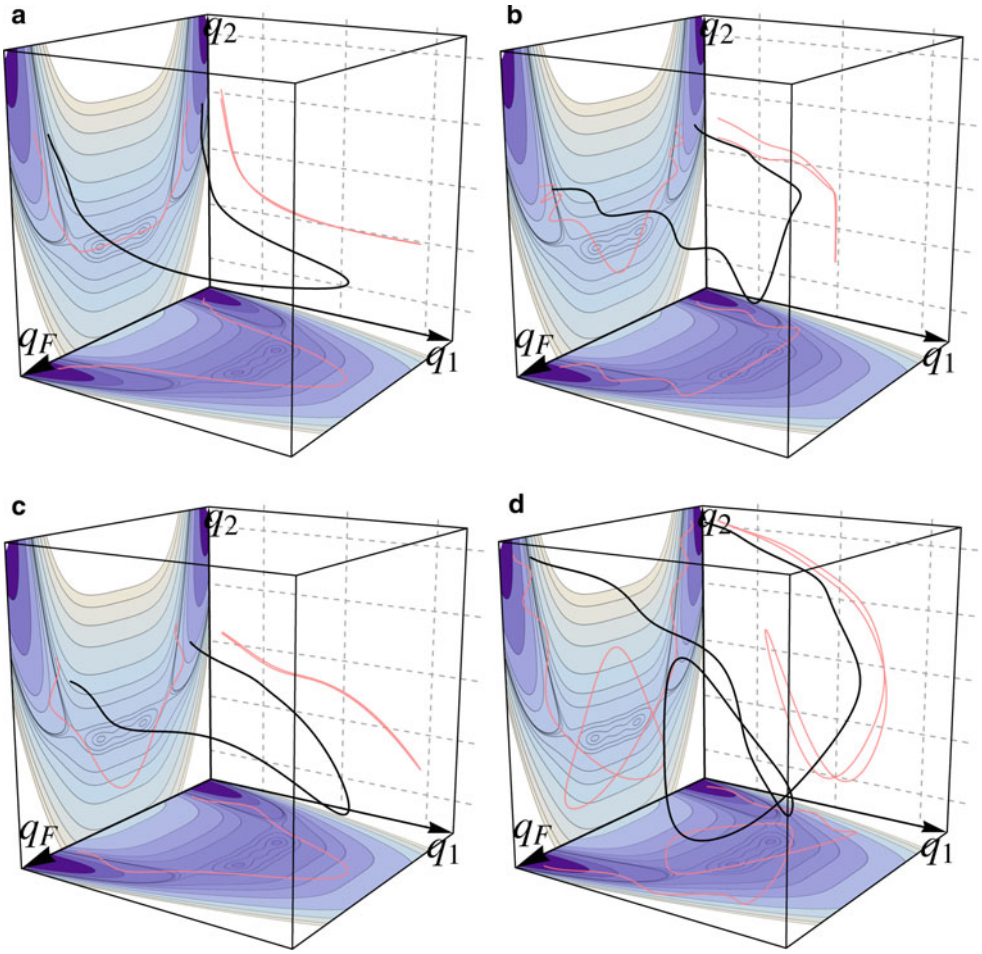

Fig. 3 Roaming trajectory one and two, where the roam occurs in **a** (q_F, q_1), **b** (q_F, q_2), **c** (q_F, q_1, q_2), and **d** (q_F, q_1, q_2) . **a**–**c** are roaming trajectories of type one, where the trajectory takes one large swing in the plateau region of the potential. **d** is a roaming trajectory of type two, where the trajectory takes a complete turn in the plateau region. These trajectories avoid the minimum energy path and involve non-planar structures along the pathway. The energy contours projected onto the (q_F, q_1) and (q_F, q_2) plane are also shown, together with projections of the trajectories onto the (q_F, q_1), (q_F, q_2), and (q_1, q_2) plane

Kinetic energy terms along RT1 are shown in Fig. 4: The total kinetic energy T, and the partial energies, T_F, T_1 and T_2, corresponding to the contributions of the reactive DOF and the coupled DOFs 1 and 2, respectively. The reactant **R**, roaming, and product **P** regions are separated by dashed lines. These are located at the time for which the RT enters the flat region of the potential via the outer TS. The decomposition is shown for the three occurrences of RT1 depicted above, roaming in (q_1, q_2) only (top panel), roaming in (q_F, q_2) only (middle panel), and roaming in (q_F, q_1, q_2) (bottom panel). For all three cases, the decomposition of the kinetic energy indicates that the kinetic energy of the reaction coordinate is low and constant during the roam, and that the kinetic energy in the coupled DOFs exhibit oscillations. Furthermore, after the trajectory has reached the product region, there is a significant contribution of kinetic energy in q_1 and q_2, corresponding to the vibrational energy of the isomerization product. Thus, when the isomerization takes place via the roaming pathway, the product is in a vibrational excited state. This is in contrast to isomerization processes via the IRC, wherein most of the kinetic energy resides in the reaction coordinate q_F, and corresponds to translational energy.

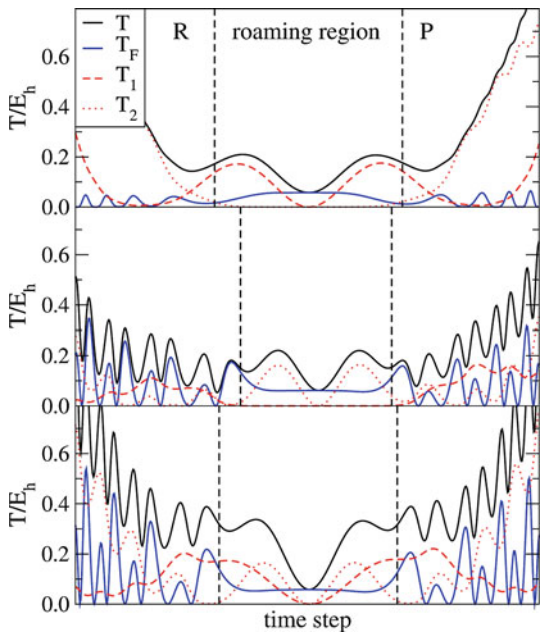

Fig. 4 Kinetic energy along RT1, and the contribution of the three explicit degrees of freedom. *Top panel* roaming in (q_F, q_1) only. *Middle panel* roaming in (q_F, q_2) only. *Bottom panel* roaming in (q_F, q_1, q_2) simultaneously

3.3 Roaming: avoiding the col

The accuracy of the TST reaction rates may be impacted by the extent to which the RTs circumvent the saddle point. Below, we explore several representations of the trajectories that illustrate the extent to which the RTs avoid the saddle as well as document the frequency of such events. We further compare the TST rates to those obtained from the flux calculations as well as identify the fraction of the flux due to the RTs. The observation that this fraction is small suggests that in this case the RTs are playing a small role in the rates.

Polar plots of the RTs are shown in Figs. 5 and 6 superimposed over the contour lines of the potential. The radius corresponds to q_F and the angular coordinate to the out-of-plane angle (for a projection onto the (q_F, q_1) plane) and the in-plane angle (for a projection onto the (q_F, q_2) plane) of hydrogen displacement. In this representation, it is easy to see the outer TS barriers (black dashed curves) that mark the entry and exit into the plateau region of the potential. In the literature [18, 20–22], roaming trajectories have been described as trajectories which are trapped between these two barriers. The IRC is shown as a solid black line and the RT as a solid red line. The RTs sample a large region of the potential between the two barriers, thus spending a significant amount of time in the central region of the potential. In this central region, the RTs follow ridge lines of potential energy parallel to the reaction coordinate. Furthermore, the RTs largely avoid the IRC and cross the barrier far from its col. The RTs are "trapped" between the two potential barriers enclosing the roaming region and exhibit one (RT1) and three (RT2) turning points along the roaming pathway. This behavior is characteristic of roaming and is now seen to be present in both two and three dimensions.

For both RT1 and RT2, there exist a manifold of trajectories. Some of these trajectories cross closer to the col and intermediate, and some of them cross further out. A 2D representation of the ketene model quantifying the extent by which the RTs avoid these regions in configuration space is shown in the top pane of Fig. 7. In the 2D model, the part of the coupling potential $V_{\text{coup}}(q_1, q_2, q_F)$ that depends on q_2 is set to zero. Some of the resulting RTs are shown in the bottom panel in Fig. 7. For each RT sampled, we measure how close the RT approaches the transition state/oxirene intermediate. The point of closest approach (Δq_{TS} and $\Delta q_{\text{Oxirene}}$, respectively) is shown in the figure.

The RTs avoid the col and the intermediate by different amounts of $\Delta q_{\text{TS}}/\Delta q_{\text{Oxirene}}$, where the trajectory (**d**) crossing the furthest out is found at the maximum of the curve.

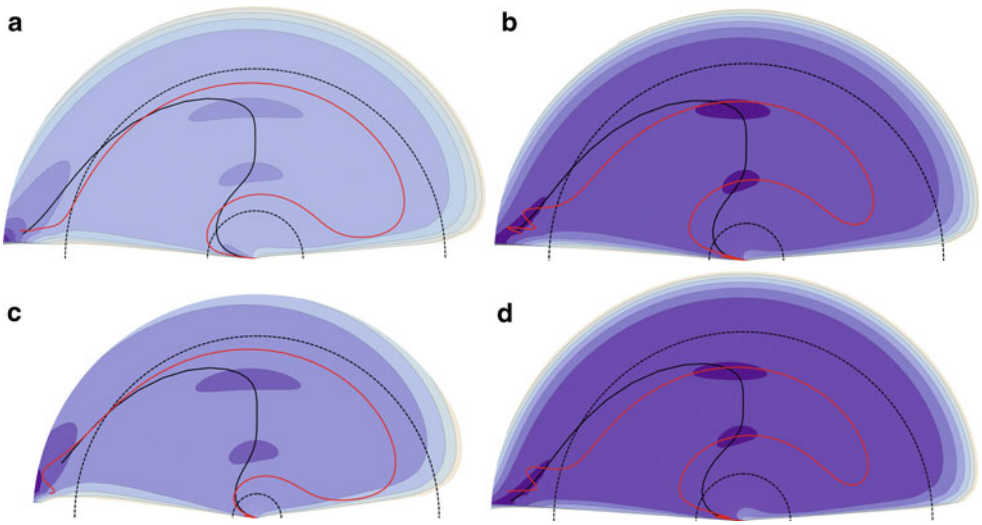

Fig. 5 Polar representation of RT1 (*red line*). Overlaid are the potential contours, where the radius corresponds to q_F and the angle to the out-of-plane angle (for a projection onto the (q_F, q_1) plane) and the in-plane angle (for a projection onto the (q_F, q_2) plane) of hydrogen displacement. The *dashed circles* denote the potential barrier, the *bold line* the IRC. The roam occurs in **a** (q_F, q_1), **b** (q_F, q_2), **c** (q_F, q_1, q_2) (projection onto (q_F, q_1)), **d** (q_F, q_1, q_2) (projection onto (q_F, q_2))

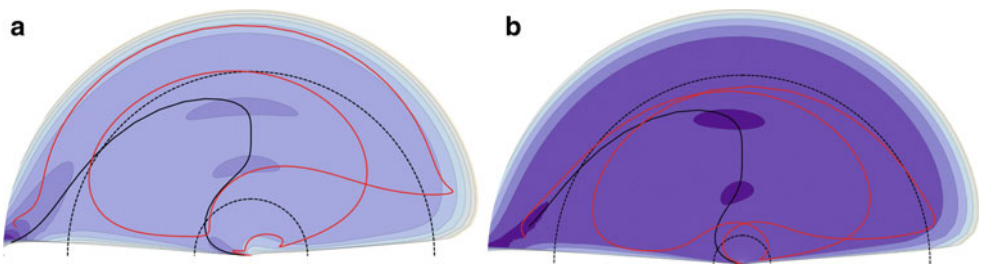

Fig. 6 Polar representation of RT2 (*red line*). A description of the contours can be found in Fig. 5. The trajectory is projected onto **a** (q_F, q_1), **b** (q_F, q_2)

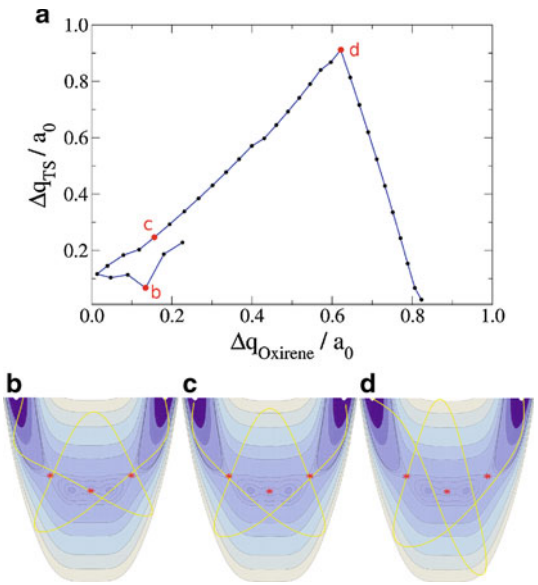

Fig. 7 Roaming trajectories avoiding the col and the oxirene intermediate, for the 2D representation of the model. The quantities Δq_{TS} and $\Delta q_{Oxirene}$ quantify the point of closest approach of the RT to the transition state and the oxirene intermediate when the trajectory follows the general direction of the IRC. When the RT moves perpendicular to the reaction coordinate, as is the case when the RT takes its swing in the roaming region, the approach of the transition state is not counted since it is a potential minimum in that direction. Three RT of the manifold are shown in the *bottom panel*, where their values of $\Delta q_{TS}/\Delta q_{Oxirene}$ are indicated on the *plot*. The outer TS and oxirene intermediate are marked on the potential contours by *red stars*

In order to investigate the impact on the TST rates due to the RTs that avoid the col, the momentum contributions to the reactive and TST flux along the DS at high energy ($E^{im} = 1.2557\,E_h$) are shown in Fig. 8. This is the energy at which the type RT2 appears. These RTs can recross the DS and therefore impact the TST result. The momentum contribution to the flux is projected onto the (q_F, q_1) plane, and the magnitude of the arrow corresponds to the (scaled) magnitude of the momentum contribution at that point. The different colors designate different contributions to the flux integral; here, red arrows designate the contributions to the TST flux, blue to the net reactive flux, and yellow designates contributions to the net reactive flux arising from roaming trajectories.

The magnitude of the net reactive flux is about one-third to one-half of the magnitude of the TST flux. Thus, about one-half to two-thirds of trajectories crossing the DS in product direction can be attributed to recrossings and lead to an overestimate of the TST rate. At the edge of the DS for positive q_1, the momentum contribution to the reactive flux points in reactant direction, which means that the net reactive flux at these points starts out in reactant direction. This leads to a further overestimate of the TST rate. However, the discrepancy of the momentum contributions to the TST and exact rate cannot be attributed to roaming trajectories: The momentum contributions of the roaming trajectories to the reactive flux are very small. Setting the overall TST momentum contributions to 100 %, the net flux corresponds to 40 % of the TST flux where the roaming contributions account for 0.002 %.

More generally, in traditional 1D TST, the reaction rate is obtained from the flux at the saddle only, and the other DOFs are completely decoupled in this representation. This very straightforward approach can certainly be adopted in cases when the barrier is high and the transition state "tight," but cannot be employed as the standard routine to derive rate constants without a priori knowledge about the phase space around the barrier. In cases with small barriers associated with a soft potential, as is the case here, 1D TST will lead to a significant overestimate of the rate constant. An improved estimate of the TST rate constant can be obtained from TST using a DS over which the flux is integrated as in Eq. (4). In this approach, the reactive DOF is allowed to couple to the other DOFs present in the system, and an improved representation of the reactive flux is obtained. By employing variational TST (VTST [38]), a routine for the derivation of a "good" DS is available which

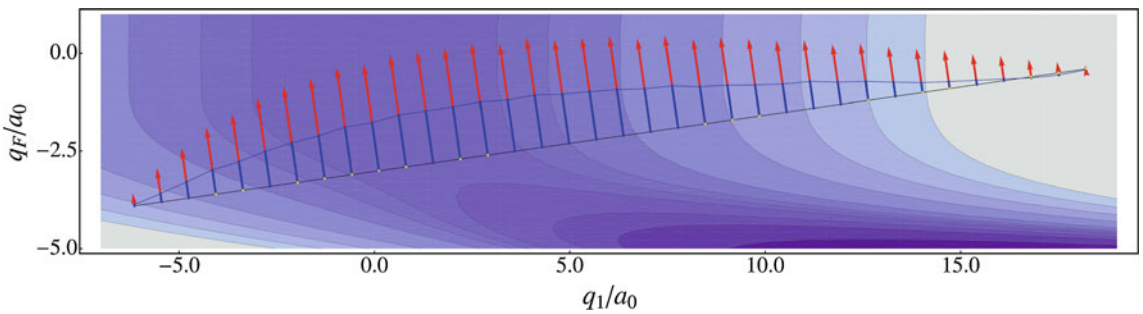

Fig. 8 Momentum contribution ($\mathbf{p}^{ex} \cdot \mathbf{n}_s$) to the flux along the DS at the energy of roaming trajectory type two. The flux at each point of the DS is color-coded according to its contribution to k_{TST} (*red*) and k_{Flux} (*blue*). The contributions of roaming trajectories to the net reactive flux are shown in *yellow*

takes into account the configuration space topology around the saddle. This leads to a DS similar to the one depicted in Fig. 8, where the amount of recrossing trajectories is minimized. This approach can be improved by defining the DS in phase space, which in our example here would lead to a curved DS when depicted in configuration space. This DS is dependent on the potential energy of the system and would lead to an optimal description of the TST rate and perhaps one with no recrossings [4, 30, 39–45]. To simplify the theoretical treatment, we do not take curvature of the DS into account, but employ a DS derived from the periodic orbit at low energies. From the flux profile in Fig. 8, it becomes apparent that most of the reactive flux is captured quite well by this DS. The RTs cross the DS further out and lead to recrossings, but their impact can be minimized by a well-chosen DS in which the number of recrossings is minimized. The deviation of the TST rate and the exact rate can be attributed to recrossings, where the (by far) majority of the recrossings is not due to the presence of roaming trajectories in the present case. These recrossings may be due to non-ergodic behavior of the system; the RTs are an example of such a behavior. To further investigate the non-ergodicity of the system, a detailed analysis of the phase-space dynamics and stability would be required and is beyond the scope of this work.

In summary, in the present model system, the RTs can be captured on a single DS and thereby included in the TST rates. The recrossings from the RTs do contribute to an overestimate of the TST rate in addition to that from the recrossings of other trajectories. The contribution from the roaming recrossings, however, is comparatively insignificant because their momentum contributions are very small.

4 Conclusion

In the present work, we have added a third dimension to the 2D model used earlier to obtain the rates of the ketene isomerization reaction. Not surprisingly, the 3D model generally maintains the good agreement seen in the calculated classical microcanonical rate constants in comparison with experimental data. The addition of a third dimension, however, opens the possibility of more complex dynamics that can give rise to errors in the TST rates. In particular, the effect of roaming trajectories has generally been seen to be more significant at full dimensionality [19], and hence, exploring its effect on higher dimensionality as done here is important to better understand roaming effects on rates.

We have confirmed that the roaming trajectories previously found in the 2D model are also present in three dimensions, where the roam can involve only two or all three DOFs. Using a polar representation of the coordinates, we found that the roaming trajectories stray far from the IRC and sample a large portion of the potential energy landscape following ridge lines of the potential energy surface. The roaming trajectories are "trapped" between the two potential barriers enclosing the roaming region and exhibit one (RT1) and three (RT2) turning points along the roaming pathway.

Using a flux profile of the reactive flux along the DS, we demonstrated that 1D TST, as determined by the "col," is generally insufficient. It is certainly violated by non-IRC processes, and more gravely by the existence of roaming. TST based on *global* DSs has been seen to be capable of addressing trajectories that cross far from the col. In the present case of ketene, TST dividing surfaces living in 2D and 3D are sufficiently global to capture most of the flux necessary to obtain the rates. The question of whether such holds true for more complex dissociation pathways such as that seen in formaldehyde is a challenge to future work. The existence of roaming trajectories creates a further challenge to TST when they access exit channels leading to different reaction products than those available over the col of the IRC. These, in turn, may be addressable through a TST with the inclusion of topologically disconnected DSs that address the additional exit channels, and the verification of this conjecture is a second challenge to future work.

Acknowledgments It a pleasure to publish this article in honor of Greg Ezra. This work has been partially supported by the Air Force Office of Scientific Research through Grant No. FA9550-12-1-0483. I. U. acknowledges the Alexander von Humboldt Foundation, Germany, for support through a Feodor Lynen Fellowship. This work used the HPC resources (Stampede) at the Texas Advanced Computing Center (TACC) at the University of Texas at Austin through XSEDE allocation under award No. TG-CTS090079. We are also grateful to Prof. J. Daniel Gezelter for discussions [36] about the energetics and masses associated with the ketene surface.

References

1. Pechukas P (1981) Transition state theory. Annu Rev Phys Chem 32:159. doi:10.1146/annurev.pc.32.100181.001111
2. Bartsch T, Hernandez R, Uzer T (2005) Transition state in a noisy environment. Phys Rev Lett 95:058301. doi:10.1103/PhysRevLett.95.058301
3. Bartsch T, Uzer T, Hernandez R (2005) Stochastic transition states: reaction geometry amidst noise. J Chem Phys 123:204102. doi:10.1063/1.2109827
4. Hernandez R, Bartsch T, Uzer T (2010) Transition state theory in liquids beyond planar dividing surfaces. Chem Phys 370:270. doi:10.1016/j.chemphys.2010.01.016
5. Keck JC (1967) Variational theory of reaction rates. Adv Chem Phys 13:85
6. Pollak E, Talkner P (2005) Reaction rate theory: what it was, where it is today, and where is it going? Chaos 15:026116
7. Uzer T, Jaffé C, Palacían J, Yanguas P, Wiggins S (2002) The geometry of reaction dynamics. Nonlinearity 15:957
8. Pechukas P, McLafferty FJ (1973) On transition state theory and the classical mechanics of collinear collisions. J Chem Phys 58:1622

9. Ezra GS, Wiggins S (2009) Phase-space geometry and reaction dynamics near index 2 saddles. J Phys A: Math Theor 42:205101
10. Collins P, Ezra GS, Wiggins S (2011) Index k saddles and dividing surfaces in phase space with applications to isomerization dynamics. J Chem Phys 134:244105
11. Sun L, Song K, Hase WL (2002) A s_{N2} reaction that avoids its deep potential energy minimum. Science 296:875. doi: 10.1126/science.1068053
12. Lourderaj U, Hase WL (2009) Theoretical and computational studies of non-rrkm unimolecular dynamics. J Phys Chem A 113:2236. doi:10.1021/jp806659f
13. Townsend D, Lahankar SA, Lee SK, Chambreau SD, Suits AG, Zhang X, Rheinecker JL, Harding LB, Bowman JM (2004) The roaming atom: straying from the reaction path in formaldehyde decomposition. Science 306:1158. doi:10.1126/science.1104386
14. Heazlewood BR, Jordan MJT, Kable SH, Selby TM, Osborn DL, Shepler BC, Braams BJ, Bowman JM (2008) Roaming is the dominant mechanism for molecular products in acetaldehyde photodissociation. Proc Natl Acad Sci USA 105(35):12719. doi:10.1073/pnas.0802769105
15. Grubb MP, Warter ML, Xiao H, Maeda S, Morokuma K, North SW (2012) No straight path: Roaming in both ground- and excited-state photolytic channels of $NO_3 \rightarrow NO + O_2$. Science 335:1075. doi: 10.1126/science.1216911
16. Shepler BC, Han Y, Bowman JM (2011) Are roaming and conventional saddle points for H_2CO and CH_3CHO dissociation to molecular products isolated from each other? J Phys Chem Lett 2:834. doi: 10.1021/jz2002138
17. Harding LB, Klippenstein SJ, Jasper AW (2012) Separability of tight and roaming pathways to molecular decomposition. J Phys Chem A 116:6967. doi:10.1021/jp303581k
18. Klippenstein SJ, Georgievskii Y, Harding LB (2011) Statistical theory for the kinetics and dynamics of roaming reactions. J Phys Chem A 115:14370. doi:10.1021/jp208347j
19. Bowman JM (2014) Roaming. Mol Phys doi:10.1080/00268976.2014.897395
20. Maugière FAL, Collins P, Ezra G, Farantos SC, Wiggins S (2014) Multiple transition states and roaming in ion-molecule reactions: a phase space perspective. Chem Phys Lett 592:282. doi:10.1016/j.cplett.2013.12.051
21. Maugière FAL, Collins P, Ezra G, Farantos SC, Wiggins S (2014) Roaming dynamics in ketene isomerization. Theor Chem Acc 133:1507. doi:10.1007/s00214-014-1507-4
22. Maugière FAL, Collins P, Ezra G, Farantos SC, Wiggins S (2014) Roaming dynamics in ion-molecule reactions: phase space reaction pathways and geometrical interpretation. J Chem Phys 140:134112. doi:10.1063/1.4870060
23. Ulusoy IS, Stanton JF, Hernandez R (2013) Effects of roaming trajectories on the transition state theory rates of a reduced-dimensional model of ketene isomerization. J Phys Chem A 117:7553. doi:10.1021/jp402322h
24. Ulusoy IS, Stanton JF, Hernandez R (2013) Correction to 'effects of roaming trajectories on the transition state theory rates of a reduced-dimensional model of ketene isomerization'. J Phys Chem A 117:10567. doi:10.1021/jp408997z
25. Gezelter JD, Miller WH (1995) Resonant features in the energy dependence of the rate of ketene isomerization. J Chem Phys 103:7868. doi:10.1063/1.470204
26. Miller WH (1998) Direct and correct calculation of canonical and microcanonical rate constants for chemical reactions. J Phys Chem A 102:793
27. Miller WH, Hernandez R, Handy NC, Jayatilaka D, Willetts A (1990) Ab initio calculation of anharmonic constants for a transition state, with application to semiclassical transition state tunneling probabilities. Chem Phys Lett 172:62. doi:10.1016/0009-2614(92)85491-R
28. Kim SK, Lovejoy ER, Moore CB (1995) Transition state vibrational level thresholds for the dissociation of triplet ketene. J Chem Phys 102(8):3202. doi:10.1063/1.468631
29. Lovejoy ER, Kim SK, Moore CB (1992) Observation of transition-state vibrational thresholds in the rate of dissociation of ketene. Science 256(5063):1541. doi:10.1126/science.256.5063.1541
30. Hernandez R (1994) A combined use of perturbation theory and diagonalization: application to bound energy levels and semiclassical rate theory. J Chem Phys 101:9534. doi:10.1063/1.467985
31. Whitten GZ, Rabinovitch BS (1963) Accurate and facile approximation for vibrational energy-level sums. J Chem Phys 38(10):2466. doi:10.1063/1.1733526
32. Whitten GZ, Rabinovitch BS (1964) Approximation for rotation–vibration energy level sums. J Chem Phys 41(6):1883. doi:10.1063/1.1726175
33. Tardy DC, Rabinovitch BS, Whitten GZ (1968) Vibration-rotation energy-level density calculations. J Chem Phys 48(3):1427. doi:10.1063/1.1668840
34. Scott AP, Nobes RH, Schaefer HF III, Radom L (1994) The Wolff rearrangement: the relevant portion of the oxirene-ketene potential energy hypersurface. J Am Chem Soc 116(22):10159. doi:10.1021/ja00101a039
35. Vacek G, Garlbraith JM, Yamaguchi Y III (1994) Oxirene: to be or not to be? J Phys Chem 98:8660
36. Gezelter JD (2014) (private communication)
37. Lovejoy ER, Moore CB (1993) Structures in the energy dependence of the rate constant for ketene isomerization. J Chem Phys 98(10):7846. doi:10.1063/1.464592
38. Truhlar DG, Garrett BC (1984) Variational transition state theory. Annu Rev Phys Chem 35:159. doi:10.1146/annurev.pc.35.100184.001111
39. De Leon N, Mehta MA, Topper RQ (1991) Cylindrical manifolds in phase space as mediators of chemical reaction dynamics and kinetics. I. Theory. J Chem Phys 94(12):8310
40. Hernandez R, Miller WH (1993) Semiclassical transition state theory. A new perspective. Chem Phys Lett 214:129. doi:10.1016/0009-2614(93)90071-8
41. Uzer T, Jaffé C, Palacián J, Yanguas P, Wiggins S (2002) The geometry of reaction dynamics. Nonlinearity 15(4):957. doi:10.1088/0951-7715/15/4/301
42. Komatsuzaki T, Berry RS (2002) Chemical reaction dynamics: many-body chaos and regularity. Adv Chem Phys 123:79
43. Waalkens H, Wiggins S (2004) Direct construction of a dividing surface of minimal flux for multi-degree-of-freedom systems that cannot be recrossed. J Phys A 37(35):L435
44. Li CB, Shoujiguchi A, Toda M, Komatsuzaki T (2006) Definability of no-return transition states in the high-energy regime above the reaction threshold. Phys Rev Lett 97(2):028302
45. Çiftçi U, Waalkens H (2013) Reaction dynamics through kinetic transition states. Phys Rev Lett 110:233201. doi:10.1103/PhysRevLett.110.233201

Theor Chem Acc (2014) 133:1536
DOI 10.1007/s00214-014-1536-z

REGULAR ARTICLE

Toward a quantum trajectory-based rate theory

Brittany L. Hyland · Craig C. Martens

Received: 29 April 2014 / Accepted: 2 July 2014 / Published online: 12 August 2014

Abstract We describe a new approach to incorporating quantum effects into chemical reaction rate theory using quantum trajectories. Our development is based on the entangled trajectory molecular dynamics method for simulating quantum processes using trajectory integration and ensemble averaging. By making dynamical approximations similar to those underlying classical transition state theory, quantum corrections are incorporated analytically into the quantum rate expression. We focus on a simple model of quantum decay in a metastable system and consider the deep tunneling limit where the classical rate vanishes and the process is entirely quantum mechanical. We compare our approximate estimate with the well-known WKB tunneling rate and find qualitative agreement.

Keywords Reaction rate theory · Quantum tunneling · Transition state theory

1 Introduction

A rigorous theoretical description of quantum dynamical processes in molecular systems is provided by solutions to the time-dependent Schrödinger equation [1]. In practice, however, direct quantum mechanical simulation becomes intractable as the complexity of the system increases. Approximations must inevitably be made to solve problems involving many degrees of freedom or infrequent events. Classical molecular dynamics (MD) is commonly employed to model many-body molecular systems [2] and provides an excellent approximation for phenomena where the particle masses and thermal energies make quantum effects such as interference and tunneling negligible.

The direct dynamical simulation of slow processes involving infrequent events is a challenge even for classical mechanics. Despite the relative simplicity and numerical efficiency of solving classical equations of motion relative to the time-dependent Schrödinger equation, capturing infrequent events in MD simulations can easily become beyond reach of a direct approach. The frontal assault of direct simulation must be complemented by a more sophisticated combination of both statistical and dynamical theories; this combination constitutes reaction rate theory [3–6].

The development of the theory of chemical reaction rates has a long history and is still an active area of research. The concept of a barrier separating the reactants and products of a chemical reaction goes back to studies of the temperature dependence of thermal rate constants by Arrhenius [7]. Eyring, Polyani, Wigner, and others connected this idea to the dynamics on a potential energy surface and combined dynamical and statistical mechanical concepts [8–12]. Transition state theory emerges in the limit were these dynamical details are simplified to the computation of the rate of crossing a critical bottleneck configuration that acts as a point of no return in the evolution of the reaction process [3–6].

The conventional concept of a transition state is a configuration space dividing surface separating reactants and

Dedicated to Professor Greg Ezra and published as part of the special collection of articles celebrating his 60th birthday.

B. L. Hyland
Department of Physics and Astronomy, University of California, Irvine, Irvine, CA 92697-4574, USA
e-mail: bhyland@uci.edu

C. C. Martens (✉)
Department of Chemistry, University of California, Irvine, Irvine, CA 92697-2025, USA
e-mail: cmartens@uci.edu

products [3–6]. For a one-dimensional system, this corresponds simply to a critical coordinate value $q = q_B$, where q_B is the coordinate of the top of the barrier of the potential function $V(q)$ separating configurations corresponding to reactant and product structures. It is remarkable that, early in the development of reaction rate theory, Wigner, Keck, and others considered reaction dynamics more generally in phase space. They defined surfaces $S(q,p)$ dividing reactants and products that were expressed as functions of both the coordinates q and their conjugate momenta p [12, 13]. As transition state theory and other statistical approaches to chemical reaction rates developed, the configuration space transition state was usually found to be appropriate, and phase space theory took a secondary role. More recently, research in the field of nonlinear dynamics has clarified the roles of chaos, non-ergodicity, and transport in Hamiltonian and dissipative systems and its relation to intramolecular dynamics and chemical rate processes, and the early phase space perspective has again become relevant [14–18]. Greg Ezra and his collaborators have been leaders in applying rigorous dynamical systems theory to the problem of reaction rates in multidimensional and non-Hamiltonian systems [19–22], in the spirit of Wigner and other early pioneers.

Much of our understanding of chemical reaction rate theory is based on classical mechanics. However, when the temperature is low or light particles such as H atoms are involved, quantum effects can be significant. Considerable research effort has been directed at developing quantum mechanical versions of chemical rate theories [23–25]. The dynamical approximation of a sharp dividing surface in phase space is difficult to reconcile with quantum uncertainty, and so the formulation of a quantum transition state theory has been challenging. Quantum rate theories remain a very active current research area (see, e.g., [26]).

In this paper, we explore a new approach to incorporating quantum effects into chemical rate processes. We base our treatment on the entangled trajectory molecular dynamics (ETMD) approach to simulating quantum dynamical processes using trajectory integration and ensemble averaging [27–34]. In the ETMD approach, quantum effects appear as an entanglement between ensemble members which are absent in the classical limit. In our previous work, we evaluate these intra-ensemble interactions numerically from the evolving ensemble. Here, we adopt additional approximations that allow these effects to be incorporated analytically into a transition state-like rate theory. In general, we anticipate that this approach can combine both thermal and quantum effects in rate processes. As a first step, we focus here on a simple model of tunneling decay in a metastable system. We consider the deep tunneling limit, where the classical rate vanishes, and the process is entirely quantum mechanical. We compare our approximate estimate with the WKB tunneling rate [35] and find qualitative agreement.

The organization of this paper is as follows. In Sect. 2, we review classical Liouville dynamics and the phase space Wigner representation of quantum mechanics. Section 3 describes the ETMD methodology, while Sect. 4 presents a quantum rate theory based on the ETMD formulation of quantum mechanics in terms of phase space trajectory dynamics. We discuss the results in Sect. 5.

2 Quantum mechanics in phase space

The ETMD method is based on solving the equation of motion for the Wigner function using a classical-like approach of trajectory integration and ensemble averaging [27–34]. From the perspective of a trajectory ensemble, quantum effects emerge from a non-classical breakdown of the statistical independence of the trajectories, and an *entanglement* of the evolution of the ensemble as a whole. Before developing ETMD, we briefly review the connection between classical phase space probability densities and independent Hamiltonian trajectories.

The evolution of a classical probability distribution $\rho(q,p,t)$ in phase space is described by the classical Liouville equation [36, 37]

$$\frac{\partial \rho}{\partial t} = \{H, \rho\}, \tag{1}$$

where q and p are the canonical coordinate and momentum, respectively, H is the system Hamiltonian, and $\{H, \rho\}$ is the Poisson bracket of H and ρ, defined as

$$\{H, \rho\} \equiv \frac{\partial H}{\partial q}\frac{\partial \rho}{\partial p} - \frac{\partial \rho}{\partial q}\frac{\partial H}{\partial p}. \tag{2}$$

In the context of a classical MD simulation, solution of the Liouville equation is accomplished by generating an ensemble of N distinct initial conditions $q_k(0)$ and $p_k(0)$ $(k = 1, 2, \ldots, N)$ sampled from the given initial probability distribution $\rho(q,p,0)$. Trajectories in phase space are then computed by integrating Hamilton's equations,

$$\dot{q} = \frac{\partial H}{\partial p} \tag{3}$$

$$\dot{p} = -\frac{\partial H}{\partial q} \tag{4}$$

using the $q_k(0)$ and $p_k(0)$ as initial data. Aside from statistical error due to a finite N, the distribution $\rho(q,p,t)$ is given exactly by the local phase space density of the evolving trajectories $(q_k(t), p_k(t))$ around the point (q,p).

The quantum analog of the phase space probability density $\rho(q,p,t)$ is the Wigner function $\rho_{\rm W}(q,p,t)$ [38–40], given in terms of the time-dependent wave function $\psi(q,t)$ by

$$\rho_{\rm W}(q,p,t) = \frac{1}{2\pi\hbar}\int_{-\infty}^{\infty} \psi^*(q+\tfrac{y}{2},t)\psi(q-\tfrac{y}{2},t)\mathrm{e}^{ipy/\hbar}\,\mathrm{d}y. \tag{5}$$

The Wigner function obeys the equation of motion

$$\frac{\partial\rho_{\rm W}}{\partial t} = -\frac{p}{m}\frac{\partial\rho_{\rm W}}{\partial q} + \int_{-\infty}^{\infty} J(q,p-\xi)\rho_{\rm W}(q,\xi,t)\mathrm{d}\xi, \tag{6}$$

where

$$J(q,p) = \frac{i}{2\pi\hbar^2}\int_{-\infty}^{\infty}\left[V(q+\tfrac{y}{2}) - V(q-\tfrac{y}{2})\right]\mathrm{e}^{-ipy/\hbar}\,\mathrm{d}y. \tag{7}$$

Equation (6) emphasizes the fundamental non-locality of quantum mechanics: The time rate of change of $\rho_{\rm W}$ at point (q,p) depends on the value of $\rho_{\rm W}$ over a range of momentum values $\xi \neq p$. For a potential $V(q)$ with a power series expansion in q, the integrand in Eq. (6) can be expanded [38, 39], leading to the equation of motion as a power series in $\hbar$,

$$\frac{\partial\rho_{\rm W}}{\partial t} = -\frac{p}{m}\frac{\partial\rho_{\rm W}}{\partial q} + V'(q)\frac{\partial\rho_{\rm W}}{\partial p} - \frac{\hbar^2}{24}V'''(q)\frac{\partial^3\rho_{\rm W}}{\partial p^3} + \cdots, \tag{8}$$

where prime denotes the derivative with respect to q. The higher-order terms not shown involve successively higher even powers of $\hbar$, odd derivatives of V with respect to q, and corresponding derivatives of $\rho_{\rm W}$ with respect to p. In the classical ($\hbar \to 0$) limit, the Wigner function becomes a solution of Eq. (1), the classical Liouville equation for probability distributions in phase space. The Wigner representation is an exact and faithful description of quantum mechanics; the Wigner function $\rho_{\rm W}(q,p,t)$ contains the same information about observable quantities as does $\psi(q,t)$.

The Wigner function $\rho_{\rm W}$ is the quantum analog of the classical phase space probability density ρ. Its role as a probability density is complicated, however, by the fact that $\rho_{\rm W}$, although always real, can assume negative values. Faithful representations of quantum mechanics *do* exist, however, that are built on positive probability distributions in phase space. An example is the Husimi representation [39], based on the Wigner function smoothed with a minimum uncertainty phase space.

The non-locality of quantum mechanics forbids an arbitrarily fine subdivision of the quantum distribution into individual independent elements as is possible in classical mechanics. Instead, quantum mechanics insists that the entire state be propagated as a unified whole. If a trajectory ensemble representation of non-local quantum motion is to be achieved, the statistical independence of the trajectories must be given up and the individual members of the ensemble must *interact* with each other. We review the ETMD method of incorporating those interactions in numerical simulations in the next section.

3 Entangled trajectory molecular dynamics

The equations of motion for the ETMD trajectory ensemble are derived by viewing the quantum Liouville equation as a continuity equation in phase space,

$$\frac{\partial\rho_{\rm W}}{\partial t} + \nabla\cdot\mathbf{j} = 0. \tag{9}$$

Trajectory equations of motion are then derived by relating the current $\mathbf{j}$ to a phase space vector field $\mathbf{v}$ through

$$\mathbf{j} = \mathbf{v}\,\rho_{\rm W}. \tag{10}$$

This establishes the rules by which the ensemble representing the Wigner function must move in order to satisfy the evolution of $\rho_{\rm W}$. We first consider the classical limit, where $\rho_{\rm W} \to \rho$, the classical phase space probability density. Here, the $\hbar$-dependent terms in Eq. (8) vanish, and the phase space density obeys the classical Liouville equation [36, 37]:

$$\frac{\partial\rho}{\partial t} = \{H,\rho\} \equiv -\nabla\cdot\mathbf{j} \tag{11}$$

By noting that $\partial\dot{q}/\partial q + \partial\dot{p}/\partial p = 0$, we can identify the phase space current vector as

$$\mathbf{j} = \begin{pmatrix} \partial H/\partial p \\ -\partial H/\partial q \end{pmatrix}\rho. \tag{12}$$

Division by ρ then gives the familiar classical independent evolution of phase space trajectories under conventional Hamiltonian's equations $\dot{q} = \mathbf{v}_q = \partial H/\partial p$, $\dot{p} = \mathbf{v}_p = -\partial H/\partial q$. This occurs because of the cancellation of ρ from the expression for the phase space vector field $\mathbf{v}$ when $\mathbf{j} = \mathbf{v}\rho$ in Eq. (12) is divided by ρ.

We now turn to the quantum Liouville equation in the Wigner representation. The continuity condition now involves the full equation of motion, Eq. (8). Writing the divergence of the current as

$$\begin{aligned}\nabla\cdot\mathbf{j} = &\frac{\partial}{\partial q}\left(\frac{\partial H}{\partial p}\rho_{\rm W}\right) \\ &+ \frac{\partial}{\partial p}\left(-V'(q)\rho_{\rm W} + \frac{\hbar^2}{24}V'''(q)\frac{\partial^2\rho_{\rm W}}{\partial p^2} + \cdots\right)\end{aligned} \tag{13}$$

and dividing the corresponding current by $\rho_{\rm W}$, we arrive at the equations of motion for the trajectory at point (q,p):

$$\dot{q} = v_q = \frac{p}{m}$$
$$\dot{p} = v_p = -V'(q) + \frac{\hbar^2}{24} V'''(q) \frac{1}{\rho_{\mathrm{W}}} \frac{\partial^2 \rho_{\mathrm{W}}}{\partial p^2} + \cdots . \tag{14}$$

Note that in this case ρ_{W} *does not cancel out of the equations*. In marked contrast with classical Hamiltonian dynamics, the vector field now depends on the global state of the system as well as on the phase point (q, p).

A consequence of the additional ρ_{W}-dependent contribution to the force is that individual trajectory energies are not conserved.

$$\frac{\mathrm{d}H}{\mathrm{d}t} = \dot{q} \frac{\partial H}{\partial q} + \dot{p} \frac{\partial H}{\partial p}$$
$$= \frac{p}{m} \left(\frac{\hbar^2}{24} V'''(q) \frac{1}{\rho_{\mathrm{W}}} \frac{\partial^2 \rho_{\mathrm{W}}}{\partial p^2} + \cdots \right) \neq 0 \tag{15}$$

This is acceptable—and in fact essential—if quantum effects are going to be represented by the method. Energy conservation is only required *on average*. It is straightforward to show from Eq. (14) that the ensemble average $\langle \dot{p} \rangle = \mathrm{Tr}(\dot{p} \rho_{\mathrm{W}}) = -\langle V' \rangle$, and thus the method obeys Ehrenfest's theorem, while the average energy $\langle E \rangle = \mathrm{Tr}(H \rho_{\mathrm{W}})$ is independent of time. The individual trajectories, however, behave non-classically.

The ETMD method implements this formalism in terms of a finite trajectory ensemble that approximately represents the continuous distribution function ρ_{W}:

$$\rho_{\mathrm{W}}(q, p, t) = \frac{1}{N} \sum_{j=1}^{N} \delta(q - q_j(t)) \delta(p - p_j(t)). \tag{16}$$

This ansatz is an approximate one, as the exact Wigner function ρ_{W} can become negative. In practice, smoothing over a minimum uncertainty region of phase space yields a positive quantity from the Wigner function, and the numerical methods employed to solve the ETMD equations of motion incorporate such smoothing by dressing each δ -function in Eq. (16) with a minimum uncertainty phase space Gaussian. The details of the methodology and results illustrating its accuracy can be found in Refs. [27–34].

The ETMD approach allows accurate simulation of manifestly quantum mechanical phenomena such as tunneling to be achieved in a trajectory ensemble context. In the next section, we describe an alternative application of the ETMD formalism in an approximate analytic theory of quantum rate processes.

4 Quantum trajectory transition state theory

Classical reaction rate theories combine elements of dynamics and statistics in an approximate representation of slow processes that cannot be simulated by direct time-dependent methods. In this section, we address the problem of adding quantum corrections to classical rate theories by modifying the underlying phase space dynamics using the ETMD formalism. In general, an approach that incorporates both classical components and quantum corrections to the overall rate process can be imagined. Here, we focus on the limiting case of purely quantum tunneling from a metastable potential. In this most challenging case, the classical rate vanishes and the entire decay process is due to quantum effects.

We consider the quantum decay of a system initially confined in a metastable potential, given by

$$V(q) = \frac{1}{2} m \omega^2 q^2 - \frac{1}{3} b q^3. \tag{17}$$

The critical points of the potential satisfy $V'(q) = 0$, with solutions $q = 0, q = m\omega^2/b$. The solution $q = 0$ corresponds to the potential minimum, while $q_{\mathrm{B}} \equiv m\omega^2/b$ corresponds to the barrier. The barrier height $V_o = V(q_{\mathrm{B}})$ is then given by

$$V_o = V(q_{\mathrm{B}}) = \frac{(m\omega^2)^3}{6b^2} = \frac{1}{6} m\omega^2 q_{\mathrm{B}}^2. \tag{18}$$

Direct simulations of time-dependent tunneling of a quantum wave packet in this system are presented in Refs. [27–34], where it was demonstrated that the ETMD equations of motion can indeed capture the non-classical component of decay from this metastable system. Here, we consider the limiting case of deep tunneling at zero temperature, where the system decays from the approximately harmonic and stationary ground state $\psi_0(q)$ of the quadratic part of the potential with zero point energy $\frac{1}{2}\hbar\omega$ through the barrier of height V_0. In this limit, $V_o/\hbar\omega \gg 1$.

The tunneling rate for this system can be calculated by WKB and instanton methods, and is given by [35]

$$k = \frac{\omega}{2\pi} \sqrt{\frac{V_o}{\hbar\omega}} 12\sqrt{6\pi}\, \mathrm{e}^{-\frac{36}{5}\frac{V_0}{\hbar\omega}}. \tag{19}$$

Our goal is to derive an analogous expression using the ideas underlying classical transition state theory combined with modifications of the classical dynamics by quantum effects as expressed by the ETMD formalism.

In conventional transition state theory, the dividing surface is a critical coordinate: $S(q) = q - q_{\mathrm{B}}$, where q_{B} corresponds to the coordinate value of the barrier. For our problem, it is the classical conservation of energy that prevents escape from the region of phase space within the potential well and below the barrier, and so we use a dividing surface defined in terms of the Hamiltonian: $S(q, p) = H(q, p) - V_o$, where $V_o = V(q_{\mathrm{B}})$ is the barrier height. The idea of using a generalized phase space transition state goes back to Wigner's early work [12], as well as in treatment of condensed phase reactions in the case of

weak coupling between the system and the environment [5], leading to energy diffusion being the rate limiting process. In the context of unimolecular dissociation reactions, Gray, Rice, and Davis employed the zeroth-order separatrix of weakly bound complexes as a generalized transition state in their *Alternative RRKM* approach [15, 16]. We use this perspective as the starting point for our development.

The rate content is given in the alternative RRKM formalism by

$$k = -\frac{\dot{N}}{N}, \tag{20}$$

where $N(t)$ is the normalized phase population within the dividing surface defined by $S(q,p) = 0$:

$$N(t) = \int\int \mathrm{d}q\mathrm{d}p\,\theta(-S(q,p))\rho_{\mathrm{W}}(q,p). \tag{21}$$

Here, $\theta(x)$ is the Heaviside step function, so the integrand is nonzero for the region $S(q,p) < 0$. The reactant region is defined as the accessible part of phase space below the dissociation energy. For the metastable potential in Eq. (17), this corresponds to the region of phase space within the well and below the barrier:

$$S(q,p) = H(q,p) - V_o, \tag{22}$$

where $H(q,p) = \frac{p^2}{2m} + V(q)$ is the Hamiltonian of the system. For our estimate of the deep tunneling rate out of the metastable potential well, we replace in Eq. (21) the classical (canonical or microcanonical) phase space distribution $\rho(q,p)$ by the Wigner function $\rho_{\mathrm{W}}(q,p)$ of the approximate metastable ground state $\psi_0(q)$ of the system. In this limit, the ratio of the quantum of energy to the barrier height $\hbar\omega/V_o \to 0$, and the ground state can be approximated by a harmonic oscillator wave function. In this limit, the Wigner function becomes

$$\rho_{\mathrm{W}}^{(o)}(q,p) = \frac{1}{\pi\hbar}\exp\left(-\frac{p^2}{2\sigma_p^2} - \frac{q^2}{2\sigma_2^2}\right). \tag{23}$$

Here, $\sigma_q = \sqrt{\hbar/2m\omega}$ and $\sigma_p = \sqrt{\hbar m\omega/2}$ are the minimum uncertainty values of coordinate and momenta, respectively, which obey $\sigma_q\sigma_p = \hbar/2$.

We first evaluate the numerator of the rate expression, Eq. (20). The time rate of change of the normalized well population is given by

$$\dot{N}(t) = -\int\int \mathrm{d}q\mathrm{d}p\,\dot{S}\delta(S)\rho_{\mathrm{W}}(q,p), \tag{24}$$

where $\frac{\mathrm{d}}{\mathrm{d}t}\theta(-S) = -\delta(S)\dot{S}$, and, by the chain rule,

$$\dot{S} = \frac{\partial S}{\partial q}\dot{q} + \frac{\partial S}{\partial p}\dot{p}. \tag{25}$$

The dividing surface is $S = H - V_o$. Classical Hamiltonian dynamics leave the Hamiltonian invariant, so in the classical limit, $\dot{S} = \{H,H\} = 0$. In this limit, the rate of escape across the separatrix is identically zero. The quantum trajectory equations of motion, however, do not preserve the Hamiltonian, so quantum effects will lead to crossing of the $S(q,p) = 0$ separatrix.

We now estimate the quantum trajectory motion across the separatrix. For the cubic potential, $V'''(q) = -2b$, and so the equations of motion in Eq. (14) reduce to

$$\begin{aligned}\dot{q} &= \frac{\partial H}{\partial p}\\ \dot{p} &= -\frac{\partial H}{\partial q} - \frac{\hbar^2 b}{12}\frac{1}{\rho_{\mathrm{W}}}\frac{\partial^2\rho_{\mathrm{W}}}{\partial p^2}.\end{aligned} \tag{26}$$

In Refs. [27–34], we perform direct simulations of time-dependent Wigner functions represented by trajectory ensembles. There, we calculate the instantaneous $\rho_{\mathrm{W}}(q,p,t)$ from the evolving ensemble at each time step to determine the quantum force on each of its members. The method presents numerical challenges, as there are interactions between the ensemble members that are absent in the classical limit. Nonetheless, the approach gives accurate results for model problems involving quantum tunneling. Here, we pursue a simple but approximate theory and use a perturbative approach to approximate these forces in the limit where the slow decay of the system causes negligible changes to the Wigner function. We thus take $\rho_{\mathrm{W}} \simeq \rho_{\mathrm{W}}^{(o)}$, given by Eq. (23), in the entangled trajectory equations of motion. The differential equations for q and p then become

$$\begin{aligned}\dot{q} &= \frac{\partial H}{\partial p}\\ \dot{p} &= -\frac{\partial H}{\partial q} + \frac{\hbar^2 b}{12\sigma_p^2}\left(1 - \frac{p^2}{\sigma_p^2}\right).\end{aligned} \tag{27}$$

The approximation of replacing the full evolving $\rho_{\mathrm{W}}(q,p,t)$, supported by the entire evolving trajectory ensemble, with the *given* $\rho_{\mathrm{W}}^{(o)}(q,p)$ effectively "disentangles" the trajectory ensemble, and replaces the full intra-ensemble interactions with an external "quantum force." This greatly simplifies numerical solution of the equations and allows analytical estimates of the dynamics of escape to be made.

The time rate of change of the dividing surface $\dot{S}$ can be expressed in terms of the quantum external force:

$$\dot{S} = \{H,H\} + \frac{\partial H}{\partial p}F^Q \tag{28}$$

or just

$$\dot{S} = \frac{p}{m}F^Q \tag{29}$$

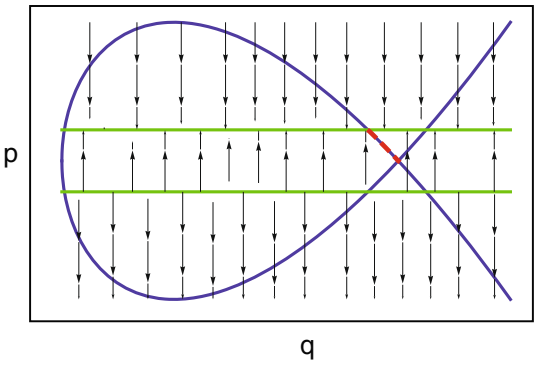

Fig. 1 Phase portrait of the metastable quadratic plus cubic oscillator. The separatrix defined by $H(q,p) = V_o$ is shown by the *thick blue curve*, where V_o is the barrier height. Also shown is the quantum contribution to the phase space vector field $\mathbf{v} = (0, F^Q)$, in addition to *green lines* $p = \pm\sigma_p$, along which the quantum force F^Q vanishes. The *red dashed portion* of the separatrix is the reactive region, defined below. See the text for discussion

where

$$F^Q(p) = \frac{\hbar^2 b}{12\sigma_p^2}\left(1 - \frac{p^2}{\sigma_p^2}\right) = f_o\left(1 - \frac{p^2}{\sigma_p^2}\right) \tag{30}$$

is the external quantum force. The expression consists of the product of a constant with units of force and a dimensionless factor that depends on the dynamical variable p. The strength can be expressed as

$$f_o = \frac{\hbar^2 b}{12\sigma_p^2} = \frac{\hbar\omega}{6q_{\mathrm{B}}}. \tag{31}$$

This is proportional to the ratio of the quantum of energy $\hbar\omega$ and the characteristic classical displacement $q_{\mathrm{B}} = \sqrt{6V_o/m\omega^2}$, and so f_o is a small quantity that decreases with increasing barrier height. In terms of the dimensionless small parameter $\hbar\omega/V_o$, the coefficient becomes

$$f_o = \frac{\hbar\omega}{6\sqrt{12}\,\sigma_q}\sqrt{\frac{\hbar\omega}{V_o}}. \tag{32}$$

Figure 1 shows a view of the phase portrait of the metastable system for $m = 1$, $\omega = 1$, and $V_o = 5$. The separatrix $H(q,p) = V_o$ is indicated as a thick blue curve. In addition, the quantum contribution to the vector field F^Q, given by Eq. (30), is depicted, as well as two horizontal green lines at $p = \pm\sigma_p$, along which $F^Q(p) = 0$. The red dashed segment indicates the reactive portion of the separatrix, which we define below.

In Fig. 2, we show the results of numerical solution of the perturbative quantum trajectory equations of motion given in Eq. (27). Parameters are $m = 1$, $\omega = 1$, and $V_o = 1$. A uniform grid of initial conditions inside of the separatrix $S(q,p) = 0$ are generated and then propagated using the equations of motion, Eq. (27). The value of V_o chosen is quite small, far from the deep tunneling limit, to illustrate clearly the nature of the dynamics. (For larger V_o the escape rate becomes too small for direct simulation.) Trajectories that are inside of the separatrix are shown in green, while those outside are depicted in blue. The non-classical separatrix crossing predicted by the vector field shown in Fig. 1 is clearly observed to occur for segments of the separatrix in both the upper and lower half planes of the phase portrait. Importantly, however, it is seen that the trajectories crossing $S(q,p) = 0$ for $p < 0$ do not escape directly, but rather are drawn back into the bound region as the classical portion of the dynamics brings them into the upper half plane. All trajectories that escape permanently do so by crossing the segment of the separatrix near but to the left of the barrier top, with $0 \le p \le \sigma_p$. This constitutes the reactive portion of the separatrix. For larger values of V_o, the qualitative structure of the dynamics remains valid, but the fraction of escaping trajectories becomes correspondingly smaller.

In Fig. 3, we show schematically the structure of the relevant portion of the phase space, near the critical point at the top of the barrier. In the limit $\hbar\omega/V_o \to 0$, this region corresponds to the portion of phase space where the potential $V(q)$ is well approximated by an inverted harmonic potential,

$$V(q) \simeq V_o - \frac{1}{2}m\omega^2(q - q_{\mathrm{B}})^2, \tag{33}$$

and so the stable and unstable manifolds of the fixed point $(q,p) = (q_{\mathrm{B}}, 0)$ are linear. In particular, the reactive portion of the separatrix is given by the curve

$$p(q) = -m\omega(q - q_{\mathrm{B}}) \tag{34}$$

for $q_{\mathrm{B}} - \sigma_q \le q \le q_{\mathrm{B}}$, as indicated in the figure.

The numerator in the rate expression can now be evaluated. We make a transition state theory-like approximation, and assume that the flux can be estimated by calculating the outward phase space flow across the reactive segment of the separatrix identified above. We denote this restriction of the integral by introducing a characteristic function $\chi_R(q,p)$ which is nonzero on the reactive portion of the linearized separatrix indicated in Fig. 3. The numerator then becomes

$$\dot{N} = -f_o \int\int \mathrm{d}q\mathrm{d}p \frac{p}{m}\left(1 - \frac{p^2}{\sigma_p^2}\right)\delta(H(q,p) - V_o)\rho_{\mathrm{W}}^{(o)}(q,p)\chi_R(q,p). \tag{35}$$

Integrating over momentum and using the δ function relation

$$\delta(f(x)) = \sum_i \frac{1}{|f'(x_i)|}\delta(x - x_i), \tag{36}$$

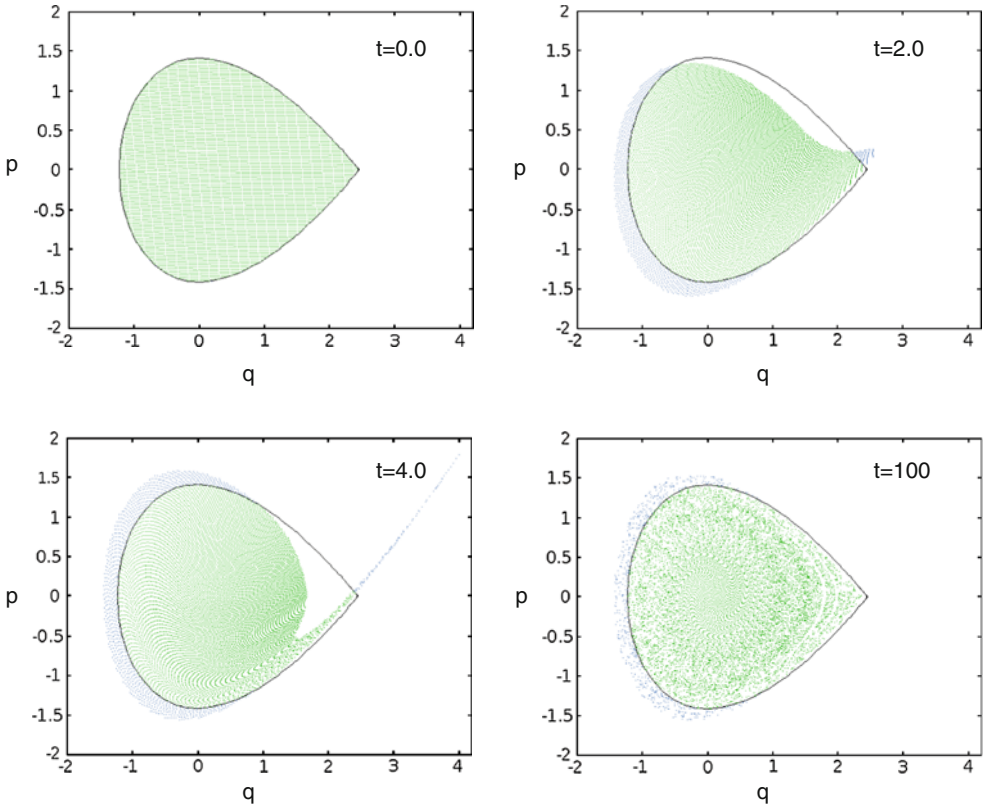

Fig. 2 Four snapshots of the dynamics of the perturbative quantum trajectory equations of motion given in Eq. (27). Parameters are $m = 1$, $\omega = 1$, and $V_o = 1$. A uniform grid of initial conditions inside of the separatrix $S(q,p) = 0$ are generated and then propagated using the equations of motion. Frames with $t = 0$, $t = 2.0$, $t = 4.0$, and $t = 100$ are shown. *Points* inside of the separatrix are *green* in *color*, while those that are outside are shown in *blue*. It is observed that all trajectories escaping to the right of the barrier depart thorough the reactive portion of the positive separatrix, as defined in the text

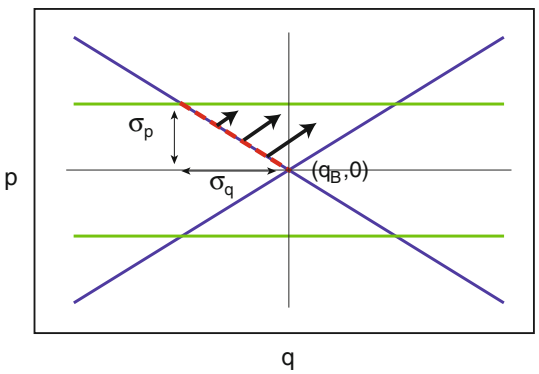

Fig. 3 Schematic structure of the relevant reactive portion of the phase space, near the critical point at the top of the barrier. The linearized separatrix is indicated in *blue*, while the reactive segment of the separatrix, through which all dissociating trajectories leave before crossing the barrier at $q = q_B$, is depicted as a *red dashed line*. Also shown are the lines $p = \pm\sigma_p$ (in *green*). See the text for discussion

where $f(x_i) = 0$, we obtain

$$\dot{N} = -f_0 \int \mathrm{d}q \left(1 - \frac{p(q)^2}{\sigma_p^2}\right) \rho_{\mathrm{W}}^{(o)}(q, p(q)) \chi_R(q, p(q)). \tag{37}$$

In the limit $V_o/\hbar\omega \to \infty$, the reactive portion of the separatrix is within σ_q of the barrier top. This deviation of q from q_B vanishes in comparison with q_B itself. We thus evaluate the Wigner function at the fixed point in phase space corresponding to the barrier top:

$$\begin{aligned}\rho_{\mathrm{W}}^{(o)}(q,p) \simeq \rho_{\mathrm{W}}^{(o)}(q_B,0) &= \frac{1}{\pi\hbar} \exp\left(-\frac{q_B^2}{2\sigma_q^2}\right) \\ &= \frac{1}{\pi\hbar} \exp\left(-\frac{6V_o}{\hbar\omega}\right)\end{aligned} \tag{38}$$

The momentum $p(q)$ is given by Eq. (34), and writing the integral in terms of $y = q - q_B$, we obtain

$$\begin{aligned}\dot{N} &= -\frac{f_0}{\pi\hbar} \exp\left(-\frac{6V_o}{\hbar\omega}\right) \int_{-\sigma_q}^{0} \left(1 - \frac{y^2}{\sigma_q^2}\right) \mathrm{d}y \\ &= -\frac{f}{\pi\hbar} \frac{2\sigma_q}{3} \exp\left(-\frac{6V_o}{\hbar\omega}\right).\end{aligned} \tag{39}$$

By evaluating f_o using Eq. (32), this becomes

$$\dot{N} = -\frac{\omega}{2\pi} \frac{2}{9\sqrt{12}} \sqrt{\frac{\hbar\omega}{V_o}} \exp\left(-\frac{6V_o}{\hbar\omega}\right). \tag{40}$$

Returning now to the expression for the rate, Eq. (20), we need to evaluate the denominator N, which represents the reactive fraction of the phase space within the $H(q,p) = V_o$ separatrix. Here, the quantum nature of the deep tunneling limit requires a different approach than employed in classical rate theories based on assumtions of ergodicity derived from chaotic dynamics. In constructing corrections to the classical Alternative RRKM approach of Ref. [16], areas of quasiperiodicity that cannot be reached by trajectories in the reactive phase space regions must be excluded. In our application, there is only a single quantum state within the region defining the denominator, and so we estimate the reactive normalized fraction of phase space

$$N = \frac{\Phi_{\text{react}}}{\Phi_{\text{tot}}} \tag{41}$$

as the ratio of the minimum uncertainty area to the total area within the separatrix. Thus,

$$\Phi_{\text{react}} = \sigma_q \sigma_p = \frac{\hbar}{2} \tag{42}$$

and

$$\Phi_{\text{tot}} = \frac{1}{2\pi} \oint p(q, V_o) \mathrm{d}q \tag{43}$$

where $p(q,E) = \sqrt{2m(E - V(q))}$. Aside from a factor of 2π, Φ_{tot} is just the action appearing in the WKB and instanton rate estimates [35]:

$$\Phi_{\text{tot}} = \frac{1}{2\pi} \frac{36}{5} \frac{V_o}{\omega}. \tag{44}$$

The quantity $\Phi_{\text{tot}}/\hbar$ corresponds to a semiclassical estimate of the total number of bound states within the potential well. The denominator N is then

$$N = \frac{\Phi_{\text{react}}}{\Phi_{\text{tot}}} = \frac{10\pi}{72} \frac{\hbar\omega}{V_o} \tag{45}$$

Putting the pieces together, our estimate for the rate constant $k = -\dot{N}/N$ finally becomes

$$k = \frac{\omega}{2\pi} \sqrt{\frac{V_o}{\hbar\omega}} \frac{16}{10\pi\sqrt{12}} \exp\left(-\frac{6V_o}{\hbar\omega}\right). \tag{46}$$

5 Discussion

The rate estimate in Eq. (46) consists of a prefactor and an exponent, both of which depend on the parameter $V_o/\hbar\omega$. Our quantum trajectory-based analysis correctly captures the scaling of both the prefactor and the exponent with $V_o/\hbar\omega$, although the numerical factors are not captured quantitatively. The WKB exponential factor is $\exp(-36V_o/5\hbar\omega)$ while the present analysis yields $\exp(-36V_o/6\hbar\omega) = \exp(-6V_o/\hbar\omega)$. Evaluating the approximate ground state Wigner function $\rho_{\text{W}}^{(o)}$ at the barrier in phase space leads to an overestimate of the exponential rate dependence. The result of the present analysis is, however, much better than a classical Boltzmann-like estimate, based on an effective temperature $k_{\text{B}}T = \hbar\omega/2$, which gives an exponential factor of $\exp(-2V_o/\hbar\omega)$. The prefactor in Eq. (46) has the correct $\sqrt{V_o/\hbar\omega}$ dependence, but the numerical factor we determine (~0.15) is significantly smaller than the corresponding WKB factor (~52).

Although the results of our analysis do not quantitatively reproduce the WKB tunneling rate, the scaling of both the prefactor and exponent with the problem's relevant dimensionless parameter $V_o/\hbar\omega$ are correctly reproduced. This level of agreement is encouraging in light of the simplifications, assumptions, and approximations that underlie the present work. The exercise of casting the manifestly quantum mechanical phenomenon of tunneling within a phase space theory of trajectory dynamics and ensemble averaging highlights both classical mechanical analogs of quantum phenomena and the sharp distinctions between the classical and quantum worlds.

In future work, we hope to extend the present approach and consider a combination of both thermal and quantum effects in a theory of reaction rates, along with refinements of the dynamical approximations and relevant phase space dividing surfaces underlying the theory. It would also be interesting to develop a similar rate theory formulated in terms of quantum trajectories in the context of Bohmian dynamics [41, 42].

Acknowledgments This material is based upon work supported by the National Science Foundation under CHE-0614005 and CHE-0802913. One of us (C. M.) has spent a career investigating nonlinear dynamical processes in chemical systems from classical, semiclassical, and quantum mechanical perspectives. That road began in 1982, as a graduate student in Greg Ezra's research group. Greg's example of curiosity, intelligence, scholarship, deep thinking, and high standards set a high bar for a new scientist to strive for. And he has influenced (in his quiet way, from his office above Cayuga Lake) every step I have since taken along that road. It is therefore an honor and a pleasure to dedicate this paper to him.

References

1. Cohen-Tannoudji C, Diu B, Laloe F (1977) Quantum mechanics. Wiley, New York
2. Allen MP, Tildesley DJ (1987) Computer simulation of liquids. Clarendon Press, Oxford
3. Laidler KJ, King MC (1983) J Phys Chem 87:2657
4. Berne BJ, Borkovec M, Straub JE (1988) J Phys Chem 92:3711
5. Hänggi P, Talkner P, Borkovec M (1990) Reviews of modern physics 62:251
6. Pollak E, Talkner P (2005) Chaos Interdiscip J Nonlinear Sci 15:026116
7. Arrhenius S, Phys Z (1889) Chemistry 4:226
8. Eyring H (1935) J Chem Phys 3:107

9. Evans MG, Polanyi M (1935) Trans Faraday Soc 31:875
10. Wigner E (1937) J Chem Phys 5:720
11. Wigner E (1938) Trans Faraday Soc 34:29
12. Wigner EP (1939) J Chem Phys 7:646
13. Keck JC (1967) Adv Chem Phys 13:85
14. Lichtenberg AJ, Lieberman MA (1992) Regul Chaotic Dyn, 2nd edn. Springer, Berlin
15. Davis MJ, Gray SK (1986) J Chem Phys 84:5389
16. Gray SK, Rice SA, Davis MJ (1986) J Phys Chem 90:3470
17. Toda M, Komatsuzaki T, Konishi T, Berry RS, Rise SA (eds) (2005) Advances in chemical physics, vol 130: geometric structures of phase space in multidimensional chaos. Wiley-Interscience. Hoboken
18. Waalkens H, Schubert R, Wiggins S (2007) Nonlinearity 21:R1
19. Martens C, Davis M, Ezra G (1987) Chem Phys Lett 142:519
20. Gillilan RE, Ezra GS (1991) J Chem Phys 94:2648
21. Ezra GS, Waalkens H, Wiggins S (2009) J Chem Phys 130:164118
22. Collins P, Ezra GS, Wiggins S (2010) J Chem Phys 133:014105
23. Voth GA, Chandler D, Miller WH (1989) J Chem Phys 91:7749
24. Miller WH (1998) Faraday Discuss 110:1
25. Weiss U (1999) Quantum dissipative systems. World Scientific, Singapore
26. Hele TJH, Althorpe SC (2013) J Chem Phys 138(8):084108
27. Donoso A, Martens CC (2001) Phys Rev Lett 87:223202
28. Donoso A, Martens CC (2002) Int J Quantum Chem 87:1348
29. Donoso A, Martens CC (2002) J Chem Phys 116:10598
30. Donoso A, Zheng Y, Martens CC (2003) J Chem Phys 119:5010
31. López H, Martens CC, Donoso A (2006) J Chem Phys 1125:154111
32. Wang A, Zheng Y, Ren W, Martens CC (2009) Phys Chem Chem Phys 11:1588
33. Martens CC, Donoso A, Zheng Y (2009) In: Shalashilin D, de Miranda MP (eds) Multidimensional quantum dynamics with trajectories. CCP6
34. Hogan P, Wart AV, Donoso A, Martens CC (2010) Chem Phys 370:20
35. Ankerhold J (2007) Quantum tunneling in complex systems. Springer, Berlin
36. McQuarrie DA (1976) Statistical mechanics. HarperCollins, New York
37. Goldstein H (1980) Classical mechanics, 2nd edn. Addison-Wesley, Reading
38. Wigner EP (1932) Phys Rev 40:749
39. Takahashi K (1989) Prog Theor Phys Suppl 98:109
40. Lee HW (1995) Phys Rep 259:147
41. Loperore CL, Wyatt RE (1999) Phys Rev Lett 82:5190
42. Wyatt RE (2005) Quantum dynamics with trajectories. Springer, New York

Theor Chem Acc (2015) 134:1592
DOI 10.1007/s00214-014-1592-4

REGULAR ARTICLE

Semiclassical quantization of atomic systems through their normal form: the hydrogen atom

Charles Jaffé · Jesús Palacián · Patricia Yanguas · T. Uzer

Received: 19 May 2014 / Accepted: 30 October 2014 / Published online: 21 November 2014

Abstract Over a century after Bohr's the initial quantization of hydrogen, the semiclassical quantization of atomic systems still represents a challenge. In the present paper, we re-examine the semiclassical quantization of hydrogen asking the question: *How can hydrogen be quantized without making use of its separability?* The approach adopted was to explicitly a construct transformation from the physical variable to the action-angle variables. The initial difficulty encountered is the lack of an equilibrium point on the potential energy surface. To surmount this difficulty, it is noted that the circular periodic orbits are relative equilibria. In a rotating frame, the relative equilibria become critical points in the phase flow. It is shown that the flow in the vicinity of the critical point is stable. The Lie–Deprit transformation is then used to transform the system into normal form, following which the semiclassical quantization is straightforward.

Keywords Semiclassical quantization · Hydrogen · Normal form · Canonical transformation · Relative equilibria · Rotating frame

Dedicated to Professor Greg Ezra and published as part of the special collection of articles celebrating his 60th birthday.

C. Jaffé (✉)
Department of Chemistry, West Virginia University, Morgantown, WV 26506-6045, USA
e-mail: cjaffe@mail.wvu.edu

J. Palacián · P. Yanguas
Departamento de Ingeniería Matemática e Informática, Universidad Pública de Navarra, Pamplona 3100, Spain

T. Uzer
Center for Nonlinear Sciences, School of Physics, Georgia Institute of Technology, Atlanta, GA 30332-0430, USA

1 Introduction

The hydrogen atom and Rydberg systems continue to be a source of discovery to this day. This is surprising as last year was the centennial of the publication of Niels Bohr landmark paper [1] on the quantization of the hydrogen atom. This remarkable paper represents the height of what has become known as the old quantum theory [2, 3]. It was an extraordinary time. The question of the constitution of atoms and molecules was one of the major issues of the day. While the atomic theory of matter had been widely accepted, such basic properties as the size and mass of atoms were only just being measured.

The internal structure of atoms were a matter of great debate. In 1904, two fundamentally different models were proposed. The atomic model proposed by Nagaoka [4] is based upon Maxwell's model of the rings of Saturn [5]. He proposes that atoms consist of a very massive, positively charged core surrounded by a large number of negatively charged particles placed on a circle forming a regular polygon. This and similar models are commonly referred to as Saturnian models. Thomson, on the other hand, proposed that atoms consist of a number of negatively charges particles embedded in a sphere of a positively charged medium [6]. This became known as the plum pudding model with the negatively charged particles being the 'plums.' In 1909, under the direction of Rutherford, Geiger and Marsden [7] performed an experiment scattering alpha particles by gold atoms. The experiment was conceived in an effort to determine the properties of the 'plums.' The results of the experiment were inconsistent with Thomson's plum pudding model and lead Rutherford in 1911 to propose his planetary model of atoms [8]. It was Rutherford's planetary model of hydrogen that Bohr quantized in 1913 [1].

With the astonishing success of Bohr's quantization of hydrogen, attention was turned to helium and other larger, more complex systems. Within months, Bohr published two additional papers: the first discussing multi-electron atoms [9] and the second discussing molecules [10]. In 1917, Einstein [11] published an insightful paper generalizing Sommerfeld's quantization conditions [12] to nonseparable systems. In a footnote, Einstein observes that other methods will have to be used if the dynamics are not integrable. By the end of the decade, it had become apparent that Bohr's initial success with hydrogen was unlikely to be repeated with helium [13] and this failure in turn lead to the development of quantum mechanics. In the intervening years, since the development of quantum mechanics, quantization of helium [14] and similar problems [15] have been re-examined in an effort to understand the failure of the old quantum theory. The conclusion is that these difficulties centered around the theory's failure to correctly account for the zero-point motion and for the theory's inability to treat nonclassical effects such as tunneling [16]. In a similar effort, Ezra et al. [17] addresses the issue raised by Einstein concerning the quantization of the nonintegrable dynamics. Ezra observed that the highly doubly excited states of helium met Einstein's criteria and then applied Gutzwiller's trace formula [18] to obtain semiclassical energy levels.

The present work re-examines this conundrum from a different perspective. Instead of searching for periodic orbits (or more correctly, invariant tori) that satisfy the Einstein–Brillouin–Keller (EBK) quantization conditions, we turn the problem on its head and re-examine the semiclassical quantization of hydrogen asking the question: *How would one quantize hydrogen if one did not take advantage of its separability in spherical coordinates?* Our hope is that this will give insight into the quantization of more complex systems where separability is not feasible.

The semiclassical quantization of molecular vibrations is standard fare today [16, 18, 19]. The approach taken is very simple. One first finds the classical stationary points and then determines their stability properties. With this information, it is then possible to transform the Hamiltonian into a normal form after which the quantization follows immediately. A fundamental difference between molecular and atomic systems is that the atomic systems do not possess stationary points, and consequently, the above approach is not feasible. In atomic problems, instead of stationary points, one looks for relative equilibria. These are found by transforming the system into a rotating frame where the relative equilibria appear as stationary points. Once the stability properties of the relative equilibrium are determined, the system is transformed into normal form and again the quantization follows immediately. The major difference between the atomic and molecular problems is that in the molecular one, the Hamiltonian is expanded about an equilibrium point, while in the atomic problem, the Hamiltonian is expanded about a periodic orbit.

2 Einstein–Brillouin–Keller quantization conditions

The EBK semiclassical quantization conditions can be traced back to the conditions proposed by Bohr [1]. Einstein's contribution [11] was the generalization of the quantization conditions, as proposed by Bohr and Sommerfeld [12], to nonseparable systems. Brillouin provided the connection to the Wentzel–Kramers–Brillouin formalism [20], and Keller provided for the inclusion of Maslov's index [16, 21] in the quantization conditions.

For the hydrogen atom, the quantization conditions for the radial-action variables are as follows:

$$\begin{aligned} J_\phi &= \hbar\left(n_\phi + \frac{\alpha_\phi}{4}\right) = \hbar n_\phi \\ J_\theta &= \hbar\left(n_\theta + \frac{\alpha_\theta}{4}\right) = \hbar\left(n_\theta + \frac{1}{2}\right) \\ J_r &= \hbar\left(n_r + \frac{\alpha_r}{4}\right) = \hbar\left(n_r + \frac{1}{2}\right) \end{aligned} \tag{1}$$

where Maslov's indices [16, 21] are given as follows: $\alpha_\phi = 0$ as the dynamics in the ϕ-mode are rotational, the dynamics of both the r-mode, and the θ-mode are librational and consequently $\alpha_\theta = \alpha_r = 2$. As for the range of the quantum numbers, as the ϕ-mode is a rotation, n_ϕ can take both positive and negative values $n_\phi = 0, \pm 1, \pm 2, \ldots$, the θ- and the r-mode are both librations and the quantum numbers can only take zero and positive values, $n_\theta = 0, 1, 2, \ldots$ and $n_r = 0, 1, 2, \ldots$.

It is convenient to introduce a different set of action-angle variable. They are defined by the following transformation.

$$\begin{aligned} L_z &= J_\phi \\ L &= J_\phi + J_\theta \\ N &= J_\phi + J_\theta + J_r. \end{aligned} \tag{2}$$

L_z is the projection of the angular momentum on the z axis, L is the total angular momentum, and N is the principle action. The quantization conditions for these new variable are given by

$$\begin{aligned} L_z &= \hbar\ell_z \quad \text{for} \quad \ell_z = 0, \pm 1, \ldots, \pm\ell \\ L &= \hbar(\ell + 1/2) \quad \text{for} \quad \ell = 0, 1, \ldots, n' \\ N &= \hbar(n' + 1) \quad \text{for} \quad n' = 0, 1, \ldots. \end{aligned} \tag{3}$$

One more step remains to putting the quantization conditions into the traditional form. This involves incorporating Maslov's index into the principal quantum number, i.e., $n = n' + 1$, then one obtains

$$
\begin{aligned}
L_z &= \hbar\ell_z \quad \text{for} \quad \ell_z = 0, \pm 1, \ldots, \pm\ell \\
L &= \hbar(\ell + 1/2) \quad \text{for} \quad \ell = 0, 1, \ldots, n-1 \\
N &= \hbar n \quad \text{for} \quad n = 1, 2, \ldots .
\end{aligned} \tag{4}
$$

In the next section, the traditional approach to the treatment of hydrogen is reviewed. Here, the radial-action variables are obtained as solutions of the Hamilton–Jacobi equation. In the fourth section, the classical action variables are obtained as a consequence of transforming the system into normal form (i.e., normalizing the system). In both cases, once the action variables are in hand, the semiclassical quantization proceeds without hitch.

3 The traditional approach

In the traditional approach [2] to the quantization of the hydrogen atom, the starting point is the Hamilton–Jacobi equation

$$
\frac{1}{2}\left(\left(\frac{\partial S}{\partial r}\right)^2 + \frac{1}{r^2}\left(\left(\frac{\partial S}{\partial \theta}\right)^2 + \frac{1}{\sin^2\phi}\left(\frac{\partial S}{\partial \phi}\right)^2\right)\right) - \frac{1}{r} = E.
$$

Here, S is Hamilton's principal function or the classical action. The classical action is a generating function of the second type [22]. It defines the transformation between spherical variables $(r, \theta, \phi, p_r, p_\theta, p_\phi)$ and the action-angle variables $(J_r, J_\theta, J_\phi, \varphi_r, \varphi_\theta, \varphi_\phi)$. Thus, the classical action is a function of the spherical coordinates and the action variables $S(r, \theta, \phi; J_r, J_\theta, J_\phi)$.

The solution to the Hamilton–Jacobi equation is obtained by method of separation of variables. It is assumed that the classical action can be written as

$$
\begin{aligned}
S(r, \theta, \phi; J_r, J_\theta, J_\phi) = {} & S_r(r; J_r, J_\theta) + S_\theta(\theta; J_\theta, J_\phi) \\
& + S_\phi(\phi; J_\phi).
\end{aligned}
$$

Substituting this expression into the Hamilton–Jacobi equation allows for the separation of the system into three one-dimensional differential equations which are readily integrated:

$$
\begin{aligned}
\frac{\mathrm{d}S_\phi}{\mathrm{d}\phi} &= C_\phi \\
\frac{\mathrm{d}S_\theta}{\mathrm{d}\theta} &= \pm\sqrt{C_\theta^2 - \frac{C_\phi^2}{\sin^2\theta}} \\
\frac{\mathrm{d}S_r}{\mathrm{d}r} &= \pm\sqrt{2C_r + \frac{1}{r} - \frac{C_\theta^2}{r^2}}
\end{aligned}
$$

where the separation constants are, respectively, the projection of the angular momentum on the z axis $C_\phi = L_z$, the angular momentum $C_\theta = L$, and the total energy $C_r = E$.

To quantize the system, these three constants of the motion need to be expressed as functions of the quantized action variables, Eq. (1). This can be achieved by evaluating the three action integrals and then inverting the results. By definition, the action integrals are

$$
\begin{aligned}
J_\phi &= \frac{1}{2\pi}\oint p_\phi \mathrm{d}\phi = \frac{1}{2\pi}\int_0^{2\pi} C_\phi \mathrm{d}\phi = L_z \\
J_\theta &= \frac{1}{2\pi}\oint p_\theta \mathrm{d}\theta = \frac{1}{\pi}\int_{\theta_-}^{\theta_+} \sqrt{C_\theta^2 - \frac{C_\phi^2}{\sin^2\theta}} = L - L_z \\
J_r &= \frac{1}{2\pi}\oint p_r \mathrm{d}r = \frac{1}{\pi}\int_{r_-}^{r_+} \sqrt{2C_r + \frac{1}{r} - \frac{C_\theta^2}{r^2}} = \frac{1}{\sqrt{-2E}} - L.
\end{aligned}
$$

Inverting yields

$$
\begin{aligned}
L_z &= J_\phi \\
L &= J_\theta + J_\phi \\
E &= -\frac{1}{2(J_r + J_\theta + J_\phi)^2}.
\end{aligned} \tag{5}
$$

Application of the quantizations conditions given in Eq. (4) yields the traditional results

$$
\begin{aligned}
L_z &= \hbar\ell_z \quad \text{for} \quad \ell_z = 0, \pm 1, \ldots, \pm\ell \\
L &= \hbar(\ell + 1/2) \quad \text{for} \quad \ell = 0, 1, \ldots, n-1 \\
E &= -\frac{1}{2\hbar^2 n^2} \quad \text{for} \quad n = 1, 2, \ldots .
\end{aligned} \tag{6}
$$

4 An alternative approach

The alternative approach adopted in this section was suggested by the study of the dynamics of the rings of Saturn, for examples, see Meyer and Schmidt [23] and references cited therein. In these studies, the typical model of the ring consists of n light (low mass) bodies placed in a regular polygon surrounding a very massive central body with the bodies interacting via the gravitational force. This model, which is commonly referred to as the $(n + 1)$-body problem, has been studied extensively and can be traced back to Maxwell [5]. An analogous model for Coulombic systems was proposed by Nagaoka [4] as a model of structure of atoms.

Typically, the first step in the analysis of the dynamics in the $(n + 1)$-body problem is to transform the system into a rotating frame. Within this rotating frame, the n light bodies will be at a critical point if they are placed at the vertices of a regular polygon centered on the massive body. The dynamics in the vicinity of this critical point is most conveniently studied in this rotating frame. Once the critical points are identified, a canonical transformation, constructed via an iterative process, transforms the Hamiltonian into a function of the action-angle variables. It should be noted that these critical points are central configurations of the $(n + 1)$-body problem [24].

The hydrogen atom can be viewed as an $(n + 1)$-body problem in the limiting case where n is equal to one. The

dynamical solutions of this system are well known. To see that consider the circular periodic orbits: The dynamics on these orbits are uniform; this implies that the angle of rotation develops linearly in time. They form a one-parameter family, take the parameter to be the angular momentum L. The angular momentum is an integral of the motion and is to be quantized, $L = \hbar(\ell + 1/2)$ for $\ell = 0, 1, 2, \ldots$. Consequently, to study the dynamics of states having a given (quantized) value of the angular momentum, one needs to examine the dynamics within the rotating frame associated with the circular periodic orbit having angular momentum L. This orbit will have a radius of $\rho_0 = L^2$ and a frequency $\omega_0 = L^{-3}$.

4.1 Transformation into rotating frame

As a starting point, consider the Hamiltonian function expressed in cylindrical coordinates

$$H = \frac{1}{2}\left(p_\rho^2 + \frac{p_\theta^2}{\rho^2} + p_z^2\right) - \frac{1}{\sqrt{\rho^2 + z^2}}$$

where the z axis has been chosen to coincide with the angular momentum vector. The transformation into the rotating frame is given by

$$\begin{aligned}
\rho &\to \rho' \\
\theta &\to \theta' - \omega_0 t \\
z &\to z'.
\end{aligned}$$

In the rotating frame, the Hamiltonian is

$$K = \frac{1}{2}\left(p_\rho^2 + \frac{p_\theta^2}{\rho^2} + p_z^2\right) - \frac{1}{\sqrt{\rho^2 + z^2}} - \omega_0 p_\theta$$

where the primes have been dropped.

4.2 Stability of the relative equilibrium

Consider the rotating frame associated with a particular value L of the angular momentum, it is simple to demonstrate that the relative equilibria forms a circle of critical points. That is, the phase points on the circle $p_\rho = 0, p_\theta = L, p_z = 0, \rho = L^2, 0 \le \theta < 2\pi$, and $z = 0$ defines a one-parameter family of critical points. In this case, the angle θ can be used as the parameter. The questions of the stability of these critical points and of the nature of the dynamics in their immediate vicinity are investigated by linearizing the equations of motion about the critical point $(\rho = L^2, \theta = \pi/2, z = 0, p_\rho = 0, p_\theta = L, p_z = 0)$. This yields

$$\dot{Z} = J\nabla^2 H \cdot Z$$

where Z is a vector in phase space

$$Z = \begin{pmatrix} \Delta Q \\ \Delta P \end{pmatrix}$$

with

$$\Delta Q = \begin{pmatrix} \Delta\rho \\ \Delta\theta \\ \Delta z \end{pmatrix}, \quad \Delta P = \begin{pmatrix} \Delta p_\rho \\ \Delta p_\theta \\ \Delta p_z \end{pmatrix} \quad \text{and} \quad J = \begin{pmatrix} 0 & I \\ -I & 0 \end{pmatrix},$$

I being the 3×3 identity matrix and $\nabla^2 H$ the Hessian of the Hamiltonian evaluated at the critical point. The Hessian is

$$\nabla^2 H = \left(\begin{array}{ccc|ccc}
L^{-6} & 0 & 0 & 0 & -2L^{-5} & 0 \\
0 & 0 & 0 & 0 & 0 & 0 \\
0 & 0 & L^{-6} & 0 & 0 & 0 \\
\hline
0 & 0 & 0 & 1 & 0 & 0 \\
-2L^{-5} & 0 & 0 & 0 & L^{-4} & 0 \\
0 & 0 & 0 & 0 & 0 & 1
\end{array}\right) \tag{7}$$

The stability of the critical points is determined by the eigenvalues of the stability matrix $J\nabla^2 H$. The quadratic approximation of the Hamiltonian which is consistent with Eq. (7) is

$$\begin{aligned}
K_2 = &\frac{1}{2}\left(p_\rho^2 + L^{-6}\rho^2\right) + \frac{1}{2}L^{-4}p_\theta^2 - 2L^{-5}\rho p_\theta \\
&+ \frac{1}{2}\left(p_z^2 + L^{-6}z^2\right).
\end{aligned}$$

The eigenvalues are obtained in two steps. First, a canonical transformation which diagonalizes the Hessian matrix is introduced. This is followed by a second canonical transformation which introduces complex variables and results in the diagonalization of the stability matrix. The first transformation is

$$\begin{aligned}
\rho &\to L^{3/2}\rho' + 2Lp_{\theta'} \\
\theta &\to \theta' + 2L^{-1/2}p_{\rho'} \\
z &\to L^{3/2}z' \\
p_\rho &\to L^{-3/2}p_{\rho'} \\
p_\theta &\to p_{\theta'} \\
p_z &\to L^{-3/2}p_{z'}.
\end{aligned}$$

The transformed Hessian is

$$\nabla^2 H = \left(\begin{array}{ccc|ccc}
L^{-3} & 0 & 0 & 0 & 0 & 0 \\
0 & 0 & 0 & 0 & 0 & 0 \\
0 & 0 & L^{-3} & 0 & 0 & 0 \\
\hline
0 & 0 & 0 & L^{-3} & 0 & 0 \\
0 & 0 & 0 & 0 & -3L^{-4} & 0 \\
0 & 0 & 0 & 0 & 0 & L^{-3}
\end{array}\right) \tag{8}$$

The quadratic approximation of the Hamiltonian consistent with Eq. (8) is

$$K_2 = \frac{1}{2}L^{-3}\left(p_\rho^2 + \rho^2\right) - \frac{3}{2}L^{-4}p_\theta^2 + \frac{1}{2}L^{-3}\left(p_z^2 + z^2\right)$$

where the primes have been dropped. In the transformed variables, the critical point is located at $(\rho = -L^{1/2}, \theta = \pi/2, z = 0, p_\rho = 0, p_\theta = L, p_z = 0)$.

The full Hamiltonian K is independent of the new variable θ, and thus, the conjugate momentum P_θ is a constant of the motion with a value of L. This is a consequence of the rotation being uniform about the z axis. Consider this degree of freedom first. The linearized equations of motion for this degree of freedom are $\dot{Z} = J\nabla^2 HZ$ where $Z = \begin{pmatrix} \Delta\theta \\ \Delta p_\theta \end{pmatrix}$ and

$$\left(J\nabla^2 H\right)_\theta = \begin{pmatrix} 0 & 3L^{-4} \\ 0 & 0 \end{pmatrix}.$$

As the determinate of this matrix is equal to zero, it cannot be diagonalized. The matrix $\left(J\nabla^2 H\right)_\theta$ has two eigenvalues, both equal to zero. The first of these is associated with the eigenvector $\begin{pmatrix} \Delta\theta \\ 0 \end{pmatrix}$. This eigenvector corresponds to a perturbation along the relative equilibrium, that is, the perturbed trajectory is simply another point on the relative equilibrium. The second zero (generalized) eigenvalue is not associated with a physical eigenvector. If such an eigenvector existed, then it would necessarily be orthogonal to the first eigenvector. Consequently, it must involve a change in the value of L which is not allowed; thus, a second eigenvector does not exist.

The Hessian of the remaining modes is

$$\left(\nabla^2 H\right)_{\rho,z} = \left(\begin{array}{cc|cc} L^{-3} & 0 & 0 & 0 \\ 0 & L^{-3} & 0 & 0 \\ \hline 0 & 0 & L^{-3} & 0 \\ 0 & 0 & 0 & L^{-3} \end{array}\right) \tag{9}$$

and the quadratic approximation of the Hamiltonian consistent with Eq. (9) is

$$K_2 = \frac{1}{2}L^{-3}\left(p_\rho^2 + \rho^2\right) - \frac{3}{2L^2} + \frac{1}{2}L^{-3}\left(p_z^2 + z^2\right).$$

The second transformation is designed to put the Hessian into a form such that when it is multiplied by J, it is diagonal. This transformation is

$$\rho = \sqrt{\frac{1}{2}}(\xi_1 + \imath\eta_1)$$
$$p_\rho = \imath\sqrt{\frac{1}{2}}(\xi_1 - \imath\eta_1)$$
$$z = \sqrt{\frac{1}{2}}(\xi_2 + \imath\eta_2)$$
$$p_z = \imath\sqrt{\frac{1}{2}}(\xi_2 - \imath\eta_2).$$

The transformed Hessian is

$$\left(\nabla^2 H\right)_{\rho,z} = \left(\begin{array}{cc|cc} 0 & 0 & \imath L^{-3} & 0 \\ 0 & 0 & 0 & \imath L^{-3} \\ \hline \imath L^{-3} & 0 & 0 & 0 \\ 0 & \imath L^{-3} & 0 & 0 \end{array}\right) \tag{10}$$

and the quadratic approximation of the Hamiltonian consistent with Eq. (10) is

$$K_2 = \imath L^{-3}\eta_1\xi_1 + \imath L^{-3}\eta_2\xi_2 - \frac{3}{2L^2}.$$

Multiplying the Hessian by J yields the stability matrix

$$\left(J\nabla^2 H\right)_{\rho,z} = \left(\begin{array}{cc|cc} -\imath L^{-3} & 0 & 0 & 0 \\ 0 & -\imath L^{-3} & 0 & 0 \\ \hline 0 & 0 & \imath L^{-3} & 0 \\ 0 & 0 & 0 & \imath L^{-3} \end{array}\right)$$

which is diagonal.

Let us note that the pairs of eigenvalues associated with both the ρ and z mode are purely imaginary and are complex conjugates. As none of the six eigenvalues $(0, 0, \imath L^{-3}, -\imath L^{-3}, \imath L^{-3}, -\imath L^{-3})$ have a positive real part, the critical point is said to be linearly stable. Also observe that not only are the ρ- and z-modes degenerate, i.e., their frequencies (eigenvalues) are identical, but they also oscillate with the same frequency as the rotating frame is rotating, that is, $L^{-3} = \omega_0$. This will be of significance in the subsequent discussion.

4.3 Transformation to normal form

In order to prepare for the transformation into normal form, one must first shift the origin to the critical point and then expand the Hamiltonian in a power series about the critical point,

$$K = \sum_{n=0}^{\infty} \varepsilon^n K_{n+2}$$

where the K_{n+2} are homogenous polynomials of order $n + 2$ having the form

$$K_{n+2} = \sum_{\ell_1+\ell_2+\ell_3+\ell_4=n+2} c_{\ell_1,\ell_2,\ell_3,\ell_4}\xi_1^{\ell_1}\eta_1^{\ell_2}\xi_2^{\ell_3}\eta_2^{\ell_4}.$$

The goal is to transform to a new set of variables such that the new Hamiltonian has the form

$$\mathscr{K} = \sum_{n=0}^{\infty} \varepsilon^n \mathscr{K}_{n+2}$$

with $\mathscr{K}_2 = K_2$ and $\{\mathscr{K}_2, \mathscr{K}_{n+2}\} = 0$ where $\{\ ,\ \}$ are the Poisson brackets.

This was accomplished using the Lie–Deprit transformation [25]. The procedure is discussed by Meyer et al. [26] and Palacián and Yanguas [27] in detail.

The coefficients are

$$\mathscr{K}_{2n+3} = 0$$

and

$$\mathscr{K}_{2n+2} = -\frac{n+2}{2L^2}\left(\frac{-\pi_0}{L}\right)^{n+1}$$

for $n = 0, 1, \ldots$ and where $\pi_0 = \imath\xi_1\eta_1 + \imath\xi_2\eta_2$.

The procedure is formal and is usually carried out up to a certain finite order. However, in this case due to the simplicity of the terms, the resulting expression at any order is easily inferred. The transformed Hamiltonian is

$$\mathscr{K} = -\frac{1}{2L^2}\sum_{n=1}^{\infty}(n+1)\left(-\frac{\pi_0}{L}\right)^n - \frac{3}{2L^2}.$$

Extending the sum to include $n = 0$ yields

$$\mathscr{K} = -\frac{1}{2L^2}\sum_{n=0}^{\infty}(n+1)\left(-\frac{\pi_0}{L}\right)^n - \frac{1}{L^2}.$$

The infinite sum is readily evaluated when $|\pi_0/L| < 1$. We get

$$\mathscr{K} = -\frac{1}{2L^2}\frac{1}{\left(1+\frac{\pi_0}{L}\right)^2} - \frac{1}{L^2},$$

which is simplified to obtain

$$\mathscr{K} = -\frac{1}{2}\frac{1}{(L+\pi_0)^2} - \frac{1}{L^2}.$$

Finally transforming back to the non-rotating frame yields

$$H = -\frac{1}{2}\frac{1}{(L+\pi_0)^2}.$$

4.4 Semiclassical quantization

In order to quantize the dynamics, we need to express the results as functions of the action variables given in either Eqs. (1) or (4). The first step is to recognize that the quantity π_0 is equal to the radial action. In order to see this recall that

$$\pi_0 = \imath\xi_1\eta_1 + \imath\xi_2\eta_2.$$

Transforming back into real variables gives

$$\pi_0 = \frac{1}{2}\left(p_\rho^2 + \rho^2\right) + \frac{1}{2}\left(p_z^2 + z^2\right).$$

Next transform into polar coordinates

$$\pi_0 = \frac{1}{2}\left(p_r^2 + \frac{p_\theta^2}{r^2} + r^2\right) = J_r.$$

From this, it is immediately evident that π_0 is the radial action, and thus, the Hamiltonian becomes

$$H = -\frac{1}{2}\frac{1}{(L+J_r)^2} = -\frac{1}{2}\frac{1}{N^2},$$

where Eq. (2) has been used.

At this point, two of the classical action variables that are to be quantized have been identified. They are the angular momentum L and the total action N. The third classical action to be quantized is the projection of the total angular momentum on one of the fixed axes in the rotating frame.

The projection of the angular momentum onto the x axis L_x is the most convenient to examine. The projection is given by

$$L_x(t) = \rho(t)p_z(t) - z(t)p_\rho(t) \tag{11}$$

where the expression is evaluated along a trajectory. To accomplish this, it is necessary to first write down the solutions of the equations of motion. As a starting point, consider the orbits having $L_x = 0$. These orbits are straight lines that pass through the origin. The angle of intersection at the origin is determined by the partitioning of the energy between the two modes. As the system being considered is invariant under rotation, the actual angle is immaterial. Choosing this angle to be $\pi/4(45°)$ greatly simplifies the algebra. In these circumstances, the solution has the form

$$\begin{aligned} \rho(t) &= x_0\sin(\omega t + \varphi_0) \\ p_\rho(t) &= \omega x_0\cos(\omega t + \varphi_0) \\ z(t) &= x_0\sin(\omega t) \\ p_z(t) &= \omega x_0\cos(\omega t) \end{aligned} \tag{12}$$

where φ_0 is the difference in the phase of the two oscillators. The amplitude x_0 will be determined presently.

When the phase angle φ_0 is equal to zero, the orbit is a straight (diagonal) line. This corresponds to $L_x = 0$. On the other hand, if the phase angle is equal to $\pi/2$, then the orbit is circular and $L_x = L$. To illustrate this, substitute the solution Eqs. (12) into (11). This yields

$$L_x = \omega x_0^2\sin\varphi_0.$$

Observe that L_x is a constant of the motion as expected and is equal to zero for $\varphi_0 = 0$ as expected. The amplitude of the oscillation x_0 is determined by observing that $L = L_z$ for $\varphi_0 = \pi/2$. This yields $x_0 = \sqrt{L/\omega}$.

5 Discussion

The quantization conditions applied here and applied in the traditional approach (see Eqs. 2–4) are identical and consequently both yield the same set of quantized energy levels (Eq. 6). A difficulty encountered in this discussion stems

from the fact that the solutions for the hydrogen atom are periodic orbits and the EBK quantization conditions are applicable to invariant tori. The difficulties are resolved when one recognizes that the dynamics of hydrogen are degenerate, i.e., and that there are families of quantizable periodic orbits which fill invariant tori. In other words, the quantized periodic orbits identified in the traditional approach are not unique, but rather, there are families of periodic orbits which satisfy the quantization conditions which fill the invariant tori.

In addition to obtaining expressions for the quantized constants of the motion, the normal form approach advocated here also yields the generating function of the transformation to action and angle variables. This is analogous to the Hamilton's principle function found in the traditional approach. The transformation equations, that is, the physical variables as functions of the action-angle variables, are readily obtained once the generating function is in hand. Quantizing these transformation equations, that is, setting the action variables equal to their quantized values, yields a set of three-tori corresponding to the quantum mechanical wave functions. The three angle variables parameterize the surface of this invariant torus.

The dynamics on the three-torus comprises a two-parameter family of periodic orbits. The Hamiltonian is a function of the total action N alone. Consequently, the angle variable ϕ_N associated with the total action develops linearly in time. The remaining two angle variables are constants of the motion as the Hamiltonian is not a function of their conjugate momenta. These two angles ϕ_L and ϕ_{L_z} can be taken to be the parameters.

6 Summary

The hydrogen atom is amenable to quantization via normal form. The approach taken differs significantly from that encountered in the semiclassical quantization of molecular vibrations. The potential energy surfaces of molecular systems possess stationary (equilibrium) points about which one expands the Hamiltonian in normal form. Atomic potentials do not possess stationary points. In their place, one finds relative equilibria. Consequently, the atomic Hamiltonian is expanded in normal form about the relative equilibria.

A principle difference in the analysis is the introduction of the rotating frame. The quantization of the angular momentum occurs when one is chooses which rotating frame in which work. In other words, one quantizes the states in different angular momentum manifold separately. Thus, we can associate the S states with the first rotating frame, the P states with the next and so on.

References

1. Bohr N (1913) Philos Mag (Ser 6) 26:1
2. Born M (1927) The mechanics of the atom. G. Bell and Sons, London. Translated by J. W. Fisher with revisions by D. R. Hartree
3. Pauling L, Wilson EB Jr (1935) Introduction to quantum mechanics. McGraw-Hill, London
4. Nagaoka H (1904) Philos Mag (Ser 6) 7:445
5. Maxwell JC (1859) On the stability of the motion of Saturn's rings. MacMillan, London
6. Thomson JJ (1904) Philos Mag (Ser 6) 7:237
7. Geiger H, Marsden E (1909) Proc R Soc Lond A 82:495
8. Rutherford E (1911) Philos Mag (Ser 6) 21:699
9. Bohr N (1913) Philos Mag (Ser 6) 26:476
10. Bohr N (1913) Philos Mag (Ser 6) 26:857
11. Einstein A (1979) Verh It Phys Ges 19, 82 (1917). (Engl. transl.: Jaffé C, JILA Report no. 116, Joint Institute of Laboratory Astrophysics, University of Colorado)
12. Sommerfeld A (1919) Atombau und Spektrallinien. Friedrich Vieweg und Sohn, Braunschweig
13. van Vleck JD (1922) Philos Mag (Ser 6) 44:842
14. Leopold JG, Percival IC (1980) J Phys B Atom Mol Phys 13:1037
15. Strand MP, Reinhardt WP (1979) J Chem Phys 70:3812
16. Percival IC (1977) Advances in chemical physics, vol 36, chap. 1. Wiley, New York
17. Ezra GS, Richter K, Tanner G, Wintgen D (1991) J Phys B Atom Mol Opt Phys 24:L413
18. Gutzwiller MC (1991) Chaos in classical and quantum mechanics. Interdisciplinary applied mathematics, vol 1. Springer, Berlin
19. Jaffé C, Reinhardt WP (1982) J Chem Phys 77:5191
20. Child MS (1991) Semiclassical mechanics with molecular applications. Clarendon Press, Oxford
21. Maslov VP (1972) Théorie des perturbation et méthodes et asymptotiques (Dunod)
22. Goldstein H (1980) Classical mechanics. Addison-Wesley, Reading
23. Meyer KR, Schmidt DS (1993) Celest Mech 55:289
24. Saari DG (2005) Collisions, rings, and other Newtonian N-body problems, CBMS regional conference series in mathematics, vol 104. American Mathematical Society, Providence
25. Deprit A (1969) Celest Mech 1:12
26. Meyer K, Hall G, Offin D (2009) Introduction to Hamiltonian dynamical systems and the N-body problem, applied mathematical sciences, vol 90, 2nd edn. Springer, Berlin
27. Palacián J, Yanguas P (2000) Nonlinearity 13:1021

Theor Chem Acc (2014) 133:1530
DOI 10.1007/s00214-014-1530-5

REGULAR ARTICLE

A semiclassical adiabatic calculation of state densities for molecules exhibiting torsion: application to hydrogen peroxide and its isotopomers

Zeb C. Kramer · Rex T. Skodje

Received: 29 April 2014 / Accepted: 25 June 2014 / Published online: 11 July 2014

Abstract A practical computational method is discussed for obtaining the rotational–vibrational molecular state densities of molecules with large amplitude torsional degrees of freedom (DoFs). This method goes beyond the traditional harmonic oscillator/rigid rotor or separable hindered rotor approximations in that it includes coupling between the torsion, the remaining vibrational modes, and the overall rotation. The method is based on the vibrationally adiabatic approximation whereby the torsional motion is assumed to be slow compared to the remaining vibrational DoFs although the nonseparability may be large. The torsional coordinate therefore parameterizes the rotational constants and the effective vibrational potential. A semiclassical method is then introduced to calculate the total state density in which the torsion is treated classically while the remaining coordinates are treated quantum mechanically. The method is also formulated for reactive problems in which the density of states is parameterized by a second large amplitude degree of freedom, the reaction coordinate. The performance of the method is assessed using the dissociation reaction of the hydrogen peroxide molecule and its isotopomers. It is found that the method performs well based on numerical tests. The torsional nonseparability is found to yield errors of factors of 2–3 in the statistical rate coefficient when compared with results of traditional separable models.

Keywords State sum · RRKM theory · Torsion

1 Introduction

Efficient and accurate computations of molecular densities of states and canonical partition functions are crucial for calculating thermodynamic properties and rate coefficients in statistical theories of chemical reactions such as RRKM and TST [1]. However, the success of such theories depends upon the accuracy of the computed state sums of the reactants and the activated complex. Calculations of molecular state sums and partition functions are quite routine [2–6] and can be easily accomplished when the internal DoFs are separable and well approximated by simple harmonic oscillators (HOs) or rigid rotor (RR) models. While HO–RR methods are useful as simple first approximations and have proven remarkably robust in many applications, they are often unsuited for obtaining accurate state sums of highly coupled and anharmonic systems. In principle, given an accurate potential energy surface (PES), the energy spectrum of such systems can be calculated using a quantum determination. However, the determination of the rovibrational energy spectrum of even modest size molecules can be computationally demanding and may be impossible for large systems at high excitation required for reactivity. It follows that practical approximate treatments more sophisticated than the simple HO–RR model that account for coupling and anharmonicity are often necessary.

Torsional DoFs, often internal hindered rotations of two molecular moieties about a chemical bond, are an important

Dedicated to Professor Greg Ezra and published as part of the special collection of articles celebrating his 60th birthday.

Z. C. Kramer · R. T. Skodje (✉)
Department of Chemistry and Biochemistry,
University of Colorado, Boulder, CO 80309-0215, USA
e-mail: rex.skodje@colorado.edu

Present Address:
Z. C. Kramer
Baker Laboratory, Department of Chemistry and Chemical Biology, Cornell University, Ithaca, NY, USA

class of motion for which the HO–RR approximation is generally poor. Development of methods for incorporating torsion into molecular state sums and partition functions is a long-standing problem in statistical mechanics. The most significant and popular example of such work was done by Pitzer and Gwinn [7–9] who introduced a separable hindered rotor approximation. The original and extended version of this method varies smoothly between a quantum harmonic approximation at low temperature to a classical hindered or rigid rotor approximation at high temperature. Such treatments, however, rely on the torsional mode being separable, which is often not the case [10]. Indeed, motion along a torsional coordinate can result in significant distortion of the internal molecular environment and a significant change of the local shape of the PES. It is a significant challenge to devise a computationally tractable method that can handle high levels of coupling while maintaining a quantum framework [11]. There may be several molecular conformers along a reaction coordinate, each of which may contribute to a state sum. Some treatment of the torsion and its coupling to the other DoFs is necessary in such a case and is the subject of this work. We note there is considerable effort currently being devoted to the development of such techniques using a variety of approaches [12–17]. Here, we discuss the method we have recently proposed that is based on a separation of timescales (i.e., vibrational adiabatic) approximation.

Torsional motion usually corresponds to a low-frequency normal mode that is reasonably well separated from the other higher-frequency motions. Therefore, this separation of timescales suggests a natural approach to treat the torsion, and its coupling is via an adiabatic separation from the higher-frequency DoFs. In this picture, the frequencies of harmonic normal modes are functions of the torsional coordinate. This method is reminiscent of the reaction path Hamiltonian (RPH) approach in which vibrations and rotations of the collision complex are adiabatically separated along a large amplitude (slow) reaction coordinate [18]. Indeed, the use of the RPH for torsional motion has been considered previously by Quack et al. [19]. For nonzero angular momentum, the external rotational DoFs must also be considered. Motion along a torsional coordinate may highly distort molecular shape and therefore change the principal moments of inertia. In this work, we include centrifugal coupling by allowing the principal moments of inertia needed in the state sums to vary with the torsional coordinate. For analysis of the activated complex in a statistical rate coefficient calculation, we note that in many cases, the character of the transition state dividing surface may need to be reformulated from its simplest approximate conception as a hyperplane in normal mode coordinates centered at the first-order saddle point (SP) on the PES. The transition state here shall be considered as a hyperplane orthogonal to the reaction coordinate and *parameterized* by the torsional coordinate. In this form, the transition state is no longer associated with a single point on the PES, the SP, but rather the ridgeline on the PES along the torsional coordinate passing through the SP. This is not unlike the notion of a reaction surface [20]. This configuration space construction of the dividing surface provides a practical approximation to account for the contribution of reactive flux across the dividing surface at all values of the torsional coordinate. Quantum tunneling effects are quite readily incorporated into this picture as well.

The quantum adiabatic treatment of the density of states for an N-dimensional problem involves solving the time-independent Schrodinger equation (TISE) for the collection of $N-1$ "fast" DoFs at each value of the slow torsional coordinate, τ. In many cases, the fast DoFs can be approximated as separable and harmonic with frequencies that are functions of the torsional coordinate. The energy levels as a function of τ are trivially obtained, and so a one-dimensional adiabatic potential energy curve, $V(\tau)$, for each set of quantum numbers, $\nu_1\nu_2\ldots\nu_{N-1}$, can be generated. More generally, if the $N-1$ fast DoF problem can be solved or accurately approximated, then the N-dimensional dynamics can be represented by a set of one-dimensional ($1d$) adiabatic potentials. The TISE for each of these $1d$ τ potential energy curves can be solved to find the energy levels of the full system. Obviously, the $1d$ potential curves need not be harmonic since the torsional potential and the frequencies may be strongly anharmonic. Thus, the $1d$ TISE generally needs to be solved numerically. While such $1d$ problems are straightforward to solve, the process can become quire cumbersome if the number of adiabatic states becomes large even for the simple hydrogen peroxide molecule, HOOH, used as an example in this work. At level of excitation appropriate to unimolecular reaction, i.e., ~20,000 cm^{-1}, there are thousands of contributing vibrational states. If we include the rotational state-dependent centrifugal distorsion of $V(\tau)$ as well, the number of distinct TISEs can become quite overwhelming. In order to circumvent this difficulty, we propose in this work to treat the torsional degree of freedom (DOF) semiclassically. We maintain the quantum description of the "fast" DoFs and the external rotations while performing the two-dimensional integral over the torsional phase space in the state summations and partition functions.

In a previous study, we investigated the complex-forming reaction $HO_2 + HO_2 \rightarrow HOOH + O_2$ using the adiabatic approach [21]. Here, we consider the influence of the torsional motion on the statistical description of the hydrogen peroxide molecule HOOH and its isotopomers HOOD and DOOD. The hydrogen peroxide species provides a good problem for study since it is the simplest molecule to exhibit torsion. Furthermore, its spectroscopy has been

thoroughly studied in all its isotopic variants [22]. Theoretically, a high-quality potential energy surface (PES) is available due to Kuhn et al. [23]. The equilibrium geometry of the HOOH molecule is nonplanar, which leads to a double-barrier potential energy profile along the dihedral angle. The higher barrier to internal rotation, in the cis configuration, is approximately 7.6 kcal/mol. The O–O bond can rupture at excitation energies of 48.4 kcal/mol and higher. In additional to numerous theoretical treatments of HOOH [19, 24–30] including our recent six-dimensional wave packet treatment of the reaction dynamics [31] and the high-level treatment of vibrational dynamics and tunneling by Luckhaus [24], there have been experimental studies carried out for this system which provide useful data for comparison [32–42].

In Sect. 2, we present the formal theory of the adiabatic approach to the computation of thermodynamics functions with the emphasis on the high amplitude torsional motion. For simplicity, only cases with a single torsional DoF are addressed which is all that is required for the hydrogen peroxide problem. An algorithm is presented for the computation of rotational–vibrational state sums with the torsional motion adiabatically coupled to the remaining rotational–vibrational DoFs. The calculations are made feasible with the introduction of a semiclassical technique for the torsional state sum that obviates the need for repeated diagonalization of the vibrationally adiabatic Hamiltonian. The methodology required for reactive problems is introduced in Sect. 3. In this case, the density of states is now written as an explicit function of two slow coordinates, the torsion and the reaction coordinates. A technique to include quantum tunneling through the reactive ridge is discussed. In Sect. 4, the numerical results for the hydrogen peroxide molecule are presented. It is found that molecular partition functions and thermodynamic functions change by 10–20 % when the torsional coupling is included. The RRKM reaction rate coefficient changes by a larger amount, on the order of a factor of 2. Section 5 presents a brief conclusion.

2 Adiabatic method for bound systems

In this section, we develop the semiclassical adiabatic method to compute state sums for bound molecules that possess a large amplitude motion. Examples of such large amplitude motion include torsion or more a general isomerization defined by a path of steepest descent from a SP [18]. We make no restriction on the identity of the large amplitude motion, but we shall use internal rotation in the HOOH example that follows later.

Consider a bound polyatomic molecule consisting of n atoms. We assume that the molecule is nonlinear and it contains a large amplitude torsional DoF described by the coordinate τ and that the torsional coordinate can be identified with a normal mode near the minimum of the potential well, although this is not strictly necessary. The full molecular Hamiltonian, of dimension $3n$, can be approximately separated into three terms describing the overall translation, the overall rotation, and the internal motions [43]

$$\widehat{H}_{\mathrm{tot}} = \widehat{H}_{\mathrm{trans}} + \widehat{H}_{\mathrm{rot}}(\tau) + \widehat{H}_{\mathrm{vib}}\left(\widehat{p}_\tau, \tau, \widehat{\boldsymbol{p}}, \widehat{\boldsymbol{q}}\right) \tag{2.1}$$

the $3n - 7$ small amplitude motions' momenta and coordinates are represented by the vectors $\widehat{\boldsymbol{p}}$ and $\widehat{\boldsymbol{q}}$, respectively. We expect that the most significant rotation–vibration coupling is due to the molecular distortion occurring with the large amplitude torsional motion which is reflected in the τ-dependence of the rotational constants. This effect is included in our treatment, but the remaining rotation–vibration coupling, such as Coriolis coupling, is neglected. We note that the RPH treatment of torsion in the work of Quack et al. [19] retains a more complete description of the rotational dynamics since their interest was in analyzing spectra.

In order to solve the time-independent Schrödinger equation (TISE) for the vibrational dynamics (the rotational motion will be considered later), we assume an adiabatic separation between τ and the fast coordinates $\boldsymbol{q}$, so that each vibrational eigenstate is of product form $\psi(\tau)\phi(\boldsymbol{q}; \tau)$. The TISE for the internal molecular motions can then be split into two individual equations for the "fast" DoFs and the slow coordinate τ. The TISE for the "fast" vibrations takes the following form when we omit the torsional kinetic energy

$$\widehat{H}_{\mathrm{vib}}\left(\widehat{p}_\tau = 0, \tau, \widehat{\boldsymbol{p}}, \boldsymbol{q}\right)\phi_{\boldsymbol{n}}(\boldsymbol{q}; \tau) = \varepsilon_{\boldsymbol{n}}(\tau)\phi_{\boldsymbol{n}}(\boldsymbol{q}; \tau) \tag{2.2}$$

where hereafter we shall neglect the "vib" subscript when referring to the Hamiltonian for the internal motions. For the large amplitude τ,

$$\left(\widehat{T}_\tau + \varepsilon_{\boldsymbol{n}}(\tau)\right)\psi_{\boldsymbol{n},n_\tau}(\tau) = E(n_\tau, \boldsymbol{n})\psi_{\boldsymbol{n},n_\tau}(\tau) \tag{2.3}$$

where $\widehat{T}_\tau$ is the kinetic energy operator for τ and $\boldsymbol{n} = (n_1, n_2, \ldots, n_{3n-7})$ are the quantum numbers for the "fast" vibrational DoFs. The approximate vibrational eigenstates of the molecule are given by $E(n_\tau, \boldsymbol{n})$ in Eq. (2.3).

Given the eigenvalues of the vibrational Hamiltonian, the cumulative sum of states and the density of vibrational states can be found as,

$$G(E) = \sum_i \Theta(E - E_i) = \mathrm{Tr}\left[\Theta\left(E - \widehat{H}\right)\right] \tag{2.4}$$

$$\rho(E) = \frac{\mathrm{d}}{\mathrm{d}E}G(E) = \mathrm{Tr}\left[\delta\left(E - \widehat{H}\right)\right] \tag{2.5}$$

where the E_i are the exact energy eigenvalues obtained from the solutions of the TISEs from Eqs. (2.2) and (2.3). The functions Θ and δ are the Heaviside step function and the Dirac delta function, respectively. The canonical partition function can be obtained from the density of states via

$$Q(E) = \int_0^\infty \rho(E) e^{-\frac{E}{k_B T}} dE \tag{2.6}$$

The solutions of the TISE in Eq. (2.2) for the energy eigenvalues $\varepsilon_{\boldsymbol{n}}(\tau)$ of the "fast" vibrational DoFs are assumed to be well described by a separable approximation or through a low-order perturbation treatment at a given value of τ. The large amplitude motion τ, however, is not expected to be separable. In order to obtain the adiabatic energy eigenvalues $E(n_\tau, \boldsymbol{n})$, the TISE from Eq. (2.2) must be solved at each value of τ for every set of quantum numbers $\boldsymbol{n}$ of the "fast" DoFs up to a sufficiently high excitation energy. This divide and conquer strategy allows us to obtain the energy spectrum $E(n_\tau, \boldsymbol{n})$ in the adiabatic approximation. This procedure is not burdensome for small systems, such as triatomics, but for polyatomics of significant size, the number of $1d$ τ-TISEs can become huge. The purpose of the semiclassical adiabatic method in this work is to obtain accurate state sums for the adiabatically separated system while avoiding the need to solve a large number on $1d$ TISEs.

The cumulative sum of states is expressed in the classical picture as an integral over the molecular phase space volume,

$$G_{\text{class}}(E) = \frac{1}{h^{3n-6}} \int \Theta(E - H) \prod_{i=1}^{3n-6} \mathrm{d}p_i \mathrm{d}q_i \tag{2.7}$$

It is known that the classical sum of states does not properly account for zero-point energy, and the error in the classical approximation can become enormous for large systems. Therefore, it is preferable to treat quantum mechanically the high-frequency DoFs that have large zero-point energy. For the low-frequency motions, such as our designated large amplitude motion τ, the zero-point energy errors are modest and the classical picture presents a computational advantage. We create a classical-quantum mixed state sum representation, where the "fast" DoFs are kept in the quantally traced Heaviside operator but the τ motion is treated as an integral over its phase space volume,

$$G_{\text{mix}}(E) = \frac{1}{h} \int \left[Tr' \Theta(E - H_{mix}) \right] \mathrm{d}p_\tau \mathrm{d}\tau \tag{2.8}$$

The mixed Hamiltonian operator in the trace is given by,

$$H_{\text{mix}} = T_\tau + \widehat{H}\left(p_\tau = 0, \tau, \widehat{\boldsymbol{p}}, \widehat{\boldsymbol{q}}\right) \tag{2.9}$$

and T_τ is now the classical expression for the kinetic energy of the large amplitude DOF rather than the quantum operator of Eq. (2.3). We make the additional assumption that T_τ is independent of the $\boldsymbol{q}$ DoFs or that the $\boldsymbol{q}$ dependence can be averaged without significant error. The trace in Eq. (2.8) is no longer over all internal DoFs as the τ motion is left out, which we denote with the primed trace notation. The integrand in Eq. (2.8) is simply the quantum cumulative sum of states over the $3n - 7$ "fast" DoFs, $\widetilde{G}(\varepsilon_{\text{fast}}, \tau)$, where $\varepsilon_{\text{fast}}$ is the portion of the energy partitioned to the high-frequency modes, so that we can abbreviate the cumulative sum of states expression as,

$$G_{\text{mix}}(E) = \frac{1}{h} \int \widetilde{G}(E - T_\tau, \tau) \mathrm{d}p_\tau \mathrm{d}\tau \tag{2.10}$$

where E is the total energy of the system consistent with our definition of $\widetilde{G}$ above. As a practical note, the energy argument in Eq. (2.10) depends upon how the energy zero is set and the torsional potential energy is defined in the energy zero (see below).

The simplest and most convenient approximation for obtaining the state sum for the fast DoFs is to treat them as a collection of harmonic oscillators. These DoFs can be defined as the normal modes. However, since the τ DOF is not necessarily identified with a single normal mode and the shape of the potential energy surface may vary significantly as a function of τ, the fast DoFs are treated as instantaneous normal modes that vary with τ. The instantaneous normal modes are found by diagonalizing a force constant matrix from which the overall translations and rotations *and* the τ-coordinate have been projected out,

$$\boldsymbol{F}_{\text{proj}} = \mathbb{Q}\boldsymbol{F}\mathbb{Q}^{-1} \tag{2.11}$$

where $\boldsymbol{F}$ is the Hessian matrix in mass-weighted Cartesian coordinates of the full configuration space and $\mathbb{Q}$ is the projection operator responsible for removing the translation, rotation, and τ DoFs. The projector is constructed as a product of one-dimensional projectors that locally eliminate the subspaces for translation, overall rotation, and the τ-motion; the projector and the instantaneous normal modes are functions of τ [18]. The projected force constant matrix in Eq. (2.11) is diagonalized at each value of τ to determine the instantaneous normal modes and frequencies of the fast DoFs as functions of τ. The Hamiltonian operator of the adiabatically separated fast harmonic modes in mass-weighted coordinates $\widehat{\boldsymbol{q}}$ is

$$\widehat{H}_{\text{mix}} = \left(\frac{p_\tau^2}{2I_\tau} + V(\tau) \right) + \left(\sum_{i=1}^{3n-7} \frac{\widehat{p}_i^2 + \omega_i^2(\tau)\widehat{q}_i^2}{2} \right) \tag{2.12}$$

where $V(\tau) = V(\tau, \boldsymbol{q} = 0)$, and we have associated T_τ with a generic torsional kinetic energy term and will continue to

do so for the rest of this work. In this approximation, the fast DOF sum of states $\widetilde{G}(E - T_\tau, \tau)$ can be very efficiently computed using the Beyer–Swinehart algorithm [5, 6] as a function of the energy and τ.

While the τ DOF is likely to have a small zero-point energy, there is still expected to be some error from the classical treatment of the τ motion in Eq. (2.10). Marcus and Rice [3] devised an approximate correction to this problem, and we incorporate it into our state count for the fast DoF,

$$G_{\mathrm{mix}}(E) = \frac{1}{h}\int \widetilde{G}\big(E + \varepsilon_0^\tau - T_\tau, \tau\big)\mathrm{d}p_\tau \mathrm{d}\tau \tag{2.13}$$

where we have added a term, ε_0^τ, to the energy expression that is the zero-point energy of the τ mode meant to account for the undercounting of states by the classical expression. The corresponding density of states is obtained by differentiation of $G_{\mathrm{mix}}(E)$ using finite difference or by differentiating a local polynomial fit of $G_{\mathrm{mix}}(E)$.

The overall rotation can be incorporated into the semiclassical adiabatic method by treating the molecule as a symmetric top in which two of the moments of inertia are set equal to their geometric mean. The rotational energies are found using the quantum expression for the symmetric top. The symmetric top moments of inertia are obtained from a principal axes analysis at the geometry $(\tau, \boldsymbol{q} = 0)$ for each value of τ and are denoted $I_u(\tau)$ and $I_d(\tau)$. These moments of inertia are allowed to vary with τ, thus permitting some coupling of the internal and rotational coordinates. However, except this variation with τ, the external rotations are considered to be separable. The rotational energy levels are given by [43]

$$\begin{aligned} E_{Jk} &= \frac{\hbar^2 J(J+1)}{2I_d(\tau)} + \hbar^2 k^2 \cdot \left(\frac{1}{2I_u(\tau)} - \frac{1}{2I_d(\tau)}\right) \\ & J = 0, 1, 2, \ldots, k = -J, \ldots, J \end{aligned} \tag{2.14}$$

where each energy level E_{Jk} is $d_{Jk} = 2J + 1$ degenerate. The total internal cumulative sum of states for given E and J, which does not include the d_{Jk} degeneracy factor,

$$\begin{aligned} G_{\mathrm{mix}}(E, J) = \frac{1}{h}\int \widetilde{G}\left(E + \varepsilon_0^\tau - \frac{p_\tau^2}{2I_\tau(\tau)} - \frac{\hbar^2 J(J+1)}{2I_d(\tau)}, \tau\right)\mathrm{d}p_\tau \mathrm{d}\tau \\ + 2\sum_{k=1}^{J}\frac{1}{h}\int \widetilde{G}\left(E + \varepsilon_0^\tau - \frac{p_\tau^2}{2I_\tau(\tau)} - \frac{\hbar^2 J(J+1)}{2I_d(\tau)} \right. \\ \left. -\hbar^2 k^2 \cdot \left(\frac{1}{2I_u(\tau)} - \frac{1}{2I_d(\tau)}\right), \tau\right)\mathrm{d}p_\tau \mathrm{d}\tau \end{aligned} \tag{2.15}$$

This expression may appear somewhat daunting; however, it can be computed relatively efficiently by pre-calculating the quantity $\widetilde{G}(\epsilon, \tau)$ in the expression at the integration quadrature grid points of τ and ε. The phase space integral over p_τ in Eqs. (2.10) or (2.15) can then be performed quickly over p_τ at each value of τ by one-dimensional interpolation in the energy. Any appropriate symmetry factor σ accounting for the interchange of identical particles along the course of a DoF should divide the quantity in Eq. (2.15).

In order to assess the accuracy of the semiclassical adiabatic algorithm, we consider the very simple model problem posed by the generalized harmonic system,

$$H = \frac{P_\tau^2}{2} + \frac{\omega_\tau^2 \tau^2}{2} + \sum_{i=1}^{N-1}\left(\frac{P_i^2}{2} + \frac{\omega_i^2(\tau) q_i^2}{2}\right) \tag{2.16}$$

where

$$\omega_i(\tau) = \omega_i^0 + \frac{1}{2}\delta_i \tau^2 \tag{2.17}$$

with ω_τ and ω_i^0 being constants. The potential is a sixth-order polynomial, and the exact eigenvalues are not analytically known. However, the levels in the vibrationally adiabatic approximation can be computed exactly. In the limit where the frequency ω_τ is low compared to the remaining $N - 1$ frequencies, the effective Hamiltonian for the τ-DOF is

$$\begin{aligned} V_{\mathrm{ad}}(n_1, \ldots, n_{N-1}; \tau) &= \frac{1}{2}\omega_\tau^2 \tau^2 + \sum_{i=1}^{N-1}\hbar\omega_i(\tau)\left(n_i + \frac{1}{2}\right) \\ &= \frac{1}{2}\left(\omega_\tau^2 + \sum_{i=1}^{N-1}\hbar\delta_i\left(n_i + \frac{1}{2}\right)\right)\tau^2 \\ &\quad + E_0(n_1, n_2, \ldots) \end{aligned} \tag{2.18}$$

where

$$E_0(n_1, n_2, \ldots) = \sum_{i=1}^{N-1}\hbar\omega_i^0\left(n_i + \frac{1}{2}\right) \tag{2.19}$$

Hence, the adiabatic levels are given by

$$E_{\mathrm{ad}}(n_\tau, n_1, n_2, \ldots) = \hbar\omega_{\mathrm{eff}}\left(n_\tau + \frac{1}{2}\right) + E_0(n_1, n_2, \ldots) \tag{2.20}$$

with

$$\omega_{\mathrm{eff}} = \sqrt{\omega_\tau^2 + \sum_{i=1}^{N-1}\hbar\delta_i\left(n_i + \frac{1}{2}\right)} \tag{2.21}$$

If we assume that ω_{eff} does not become too large, the adiabatic approximation is expected to be accurate.

As a preliminary test, we have evaluated the state densities for the harmonic system with $N = 3$, $\omega_\tau = 1$, $\omega_1^0 = 4$, $\omega_2^0 = 5$, $\delta_1 = 0.1$ and $\delta_2 = 0.11$. In Fig. 1, we show the "exact" adiabatic cumulative state density using Eq. (2.20) with the orange line. The semiclassical result obtained using Eq. (2.13) is given by the yellow line and

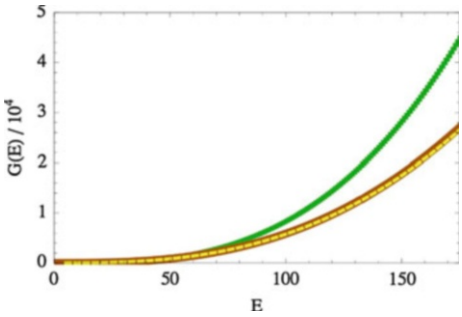

Fig. 1 The cumulative sum of states for a system of three coupled harmonic oscillators. The Hamiltonian is given by Eq. (2.16) with $\omega_\tau = 1, \omega_1^0 = 4, \omega_2^0 = 5, \delta_1 = 0.1$ and $\delta_2 = 0.11$. The *orange line* is the semiclassical adiabatic method, Eq. (2.13). The *green line* is the uncoupled harmonic description based on the potential minimum. The *dashed yellow line* is the "exact" adiabatic state count obtained by a full state sum of the levels in Eq. (2.20)

is seen to be virtually indistinguishable from the exact adiabatic result. For reference, we have also plotted the traditional separable (quantum) harmonic approximation in Fig. 1 which clearly shows serious error. From this result and other similar tests, it seems that the semiclassical model is capable of accurately reproducing the adiabatic state counting without the need to explicitly evaluate the energy levels for the myriad adiabatic potential curves $V_{\rm ad}(n_1, \ldots, n_{N-1}; \tau)$.

3 Adiabatic method for reactive systems

Extension of the semiclassical adiabatic method to reactive systems is straightforward. In the reactive problem, however, there is no longer only one slow coordinate but two: the τ mode and the reaction coordinate s. The reaction coordinate can be defined as the steepest descent path from the saddle point or another method convenient to the problem. In any case, now τ and s are separated adiabatically from the other "fast" $\boldsymbol{q}$-motions in the system. To obtain the rate coefficient, the cumulative sum of states must be computed as a function of the reaction coordinate, $G(E, J; s)$, which is the state sum over the $3n - 8$ $\boldsymbol{q}$-motions and the τ motion. For a unimolecular reaction where the transition state bottleneck occurs at $s = s_0$, so that $G^{\ddagger}(E, J) = G(E, J; s_0)$, the energy and angular momentum-resolved rate coefficient is [4]

$$k(E, J) = \frac{G^{\ddagger}(E, J)}{h\rho(E, J)} \tag{3.1}$$

where $\rho(E, J)$ is the reactant density of states.

In our semiclassical adiabatic method, we propose to view the transition state dividing surface as a function of the torsional coordinate τ. Rather than associating the transition state in the usual way, with a configuration space saddle point X_0, it is associated with a ridgeline of saddle points $X_0(\tau)$ defined by $\nabla V = 0$ at fixed τ. In this case, a reaction surface [20] replaces a reaction path and is composed of the union of all the individual paths of steepest descent (at fixed τ) that issue from the reduced saddle points on the ridgeline. Along each reaction path of fixed τ, we carry out an instantaneous normal mode analysis of the projected mass-weighted hessian matrix from Eq. (2.11), as discussed in the previous section, but now we project out the reaction coordinate motion from the force constant matrix in addition to translation, external rotation, and the τ motion. From this normal mode analysis, the $3n - 8$ frequencies of the "fast" modes are obtained. By treating the fast modes as quantum harmonic oscillators and the slow modes, (s, τ), classically, the semiclassical mixed Hamiltonian for the system can be written,

$$H_{\rm mix} = \frac{p_\tau^2}{2I_\tau} + \frac{p_s^2}{2\mu_s} + V(\tau, s) + \sum_{i=1}^{3n-8} \frac{\widehat{p}_i^2 + \omega_i^2(\tau, s)\widehat{q}_i^2}{2} \tag{3.2}$$

Making the assumption that the transition state dividing surface lies along the ridgeline defined by $s = s_0$, the vibrational cumulative sum of states for the system is obtained by,

$$G_{\rm mix}^{\ddagger}(E) = \frac{1}{h} \int \widetilde{G}^{\ddagger}\left(E + \varepsilon_0^{\tau} - \frac{p_\tau^2}{2I_\tau}, \tau, s = s_0\right) \mathrm{d}p_\tau \mathrm{d}\tau \tag{3.3}$$

where $\widetilde{G}^{\ddagger}(\epsilon, \tau)$ is the trace over the $3n - 8$ fast DoFs using the transition state frequencies $\omega_i(\tau, s = s_0)$ and ε_0^{τ} is found on the potential $V(\tau, s = s_0)$.

The overall rotations are incorporated in the reactive approximation almost identically to the way discussed in the bound problem. The symmetric top approximation is made, and the necessary moments of inertia required for the state sum are obtained by a principal axes analysis at fixed τ and for $s = s_0$. The expression for the transition state cumulative sum of states is then,

$$\begin{aligned} &G_{\rm mix}^{\ddagger}(E, J) \\ &= \frac{1}{h} \int \widetilde{G}\left(E + \varepsilon_0^{\tau}(s = s_0) - \frac{p_\tau^2}{2I_\tau(\tau, s_0)} - \frac{\hbar^2 J(J+1)}{2I_d(\tau, s_0)}, \tau, s = s_0\right) \mathrm{d}p_\tau \mathrm{d}\tau \\ &\quad + 2\sum_{k=1}^{J} \frac{1}{h} \int \widetilde{G}\left(E + \varepsilon_0^{\tau} - \frac{p_\tau^2}{2I_\tau(\tau, s_0)} - \frac{\hbar^2 J(J+1)}{2I_d(\tau, s_0)}\right. \\ &\quad \left. -\hbar^2 k^2 \cdot \left(\frac{1}{2I_u(\tau, s_0)} - \frac{1}{2I_d(\tau, s_0)}\right), \tau, s = s_0\right) \mathrm{d}p_\tau \mathrm{d}\tau \end{aligned} \tag{3.4}$$

The degeneracy factor associated with the quantum numbers J and k, d_{Jk}, is not incorporated into the expression above. In the reactive problem, this expression can be used to obtain the RRKM rate coefficient in Eq. (3.1).

As a last brief topic in this section, we discuss how to incorporate quantum tunneling into the semiclassical adiabatic method. The usual method for incorporating tunneling into an RRKM rate coefficient for a unimolecular reaction involves constructing the cumulative sum of states at the transition state as a convolution of the density of states at the transition state with the quantum transmission probability at the reaction coordinate translational energy $\epsilon_{s-\mathrm{trans}}, P(\epsilon_{s-\mathrm{trans}})$. Thus, we have

$$G^{\ddagger}_{\mathrm{tunnel}}(E) = \int_{E_{\mathrm{TS}}}^{\infty} \rho^{\ddagger}(\varepsilon) \cdot P(E-\varepsilon)\mathrm{d}\varepsilon \tag{3.5}$$

where the density of states is constructed from a state count not including tunneling,

$$\rho^{\ddagger}(\varepsilon) = \frac{\mathrm{d}G^{\ddagger}(\varepsilon)}{\mathrm{d}\varepsilon} \tag{3.6}$$

and ε is the energy available to the $3n-8$ fast DoF [4]. For our adiabatic approximation, we assume that the tunneling occurs through the transition state ridge at a fixed value of the τ coordinate. The tunneling probability can then be calculated at each dynamically frozen value of τ to obtain a function $P(E-\varepsilon, \tau)$ by applying a traditional tunneling method [44, 45] to the constrained-τ system. In the semiclassical adiabatic method, we modify Eq. (3.5) so that we obtain the fast modes' sum of states with the integrated tunneling effect at fixed τ,

$$\widetilde{G}^{\ddagger}_{\mathrm{tunnel}}\left(E', \tau\right) = \int_{E_{\mathrm{TS}(\tau)}}^{\infty} \widetilde{\rho}^{\ddagger}(\varepsilon, \tau) \cdot P(E-\varepsilon, \tau)\mathrm{d}\varepsilon \tag{3.7}$$

where,

$$\widetilde{\rho}(E, \tau) = \mathrm{d}\widetilde{G}(E, \tau)/\mathrm{d}E \tag{3.8}$$

The $\widetilde{G}$ in the equation above is the fast coordinate sum of states at fixed τ with no tunneling correction. The RRKM constant with tunneling can then be obtained by substituting the expression in Eq. (3.7) into our expression for the full transition state cumulative sum of states in Eq. (3.4) or Eq. (3.3) for $J = 0$.

4 Hydrogen peroxide and isotopomers

The hydrogen peroxide molecule is one of the simplest systems with a torsional coordinate. An accurate potential energy surface for this system was determined by Kuhn et al. [23] that has been used in several classical and quantum dynamics studies [24, 29, 31]. The definition of the torsion coordinate as the dihedral angle in the HOOH molecule is shown in Fig. 2. Two symmetry-related nonplanar equilibrium geometries of the HOOH molecule

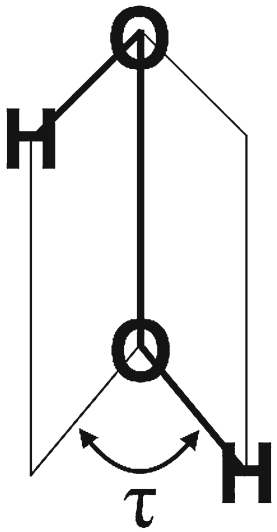

Fig. 2 The torsion coordinate τ for HOOH is defined to be the dihedral angle

occur with $\tau = 114°, 246°$. The τ potential energy curve, computed by varying τ and optimizing all other DoFs, is shown in Fig. 3a. The highest barrier to internal rotation has a value of 7.6 kcal mol^{-1} occurs when the hydrogens are in the cis configuration. A smaller barrier of 1.0 kcal mol^{-1} is found when the hydrogens are in a trans-configuration. Much fundamental experimental [32–40] and theoretical work [23, 24, 26–31] has been done, primarily in the context of looking at energy flow and randomization in vibrationally excited molecules, examining the dissociation of HOOH into OH radicals. The barrier to dissociation into separated OH radicals is 48.4 kcal mol^{-1} on the PES of Kuhn et al. [23]. Although the nonseparable torsional coupling in HOOH is somewhat modest, the existence of an analytical potential and the simplicity of the system makes it ideal for an example study. In addition, the coupling to the torsion is sufficient to have a clear influence on the state sums and is clearly distinguishable from the predictions of the HO–RR and separable hindered rotor (HR) models. We will also look at the effect of isotopic substitutions of deuterium for hydrogen on the state sums, and specifically, we consider the isotopomers HOOD and DOOD. In the following, we shall explore the properties and state sums of the bound forms of HOOH and its isotopomers and compare our semiclassical adiabatic model to the predictions of the simpler approximations.

The equilibrium configuration frequencies for each of the isotopomers are given in Table 1. The lowest frequency normal mode has significant torsional character and is compared in Table 1 with the actual instantaneous frequency of the torsion in the equilibrium geometry. In all cases, the

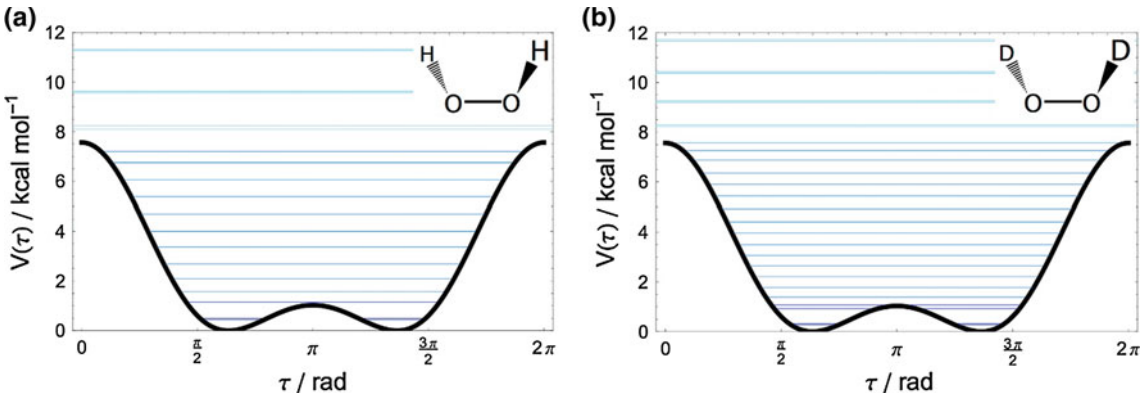

Fig. 3 The torsional 1*d* potential energy curve for the isotopomers. **a** HOOH and **b** DOOD. The torsional energy levels of the separable torsion model are superimposed as *blue lines*. No zero-point energy from higher-frequency modes is included

Table 1 Relevant molecular properties from the hydrogen peroxide PES of Kuhn et al. [23]

	O–X stretch	O–X stretch	∠OOX bend	∠OOX bend	O–O stretch	Torsion
HOOH	3,777	3,762	1,453	1,297	888	392/397
HOOD	3,770	2,746	1,386	1,003	887	343/344
DOOD	2,752	2,738	1,066	959	886	287/281
	B_τ	B_1^{ext}	B_2^{ext}	B_3^{ext}	$B_{2/3}^{\text{eff}}$	ΔE_{diss}
HOOH	37.23	10.15	0.88	0.85	0.87	16,927
HOOD	27.93	7.14	0.84	0.79	0.82	17,143
DOOD	18.62	5.53	0.79	0.75	0.77	17,369

The normal mode frequencies are given for each isotopomer. For the torsion, the frequencies of the normal mode and the pure torsional mode (along the dihedral angle) are both given (normal/pure). The molecular rotational constants and torsional rotational constant are given. The dissociation energy is defined to be zero-point corrected energy difference between the infinitely separated XO radicals and the XOOX molecule. All quantities in cm^{-1}

agreement is within 1 %. In order to obtain torsional energy levels for a separable hindered rotor approximation to use in later state sums for the HR approximation and to illustrate the torsional energy spectrum, a 1*d* potential energy curve,$V(\tau)$, is made by optimizing all other DoFs at a given τ. This potential was used in the diagonalization a torsional Schrödinger equation,

$$\left[-\frac{\hbar^2}{2I_\tau}\frac{d^2}{d\tau^2}+V(\tau)\right]\psi_k(\tau)=\varepsilon_k\psi_k(\tau) \tag{4.1}$$

where the torsional moment of inertia is given as a reduced moment of the two moments of inertia of the OH bonds rotating around the OO bond axis,

$$I_\tau=\frac{I_1^{\text{OH}}\cdot I_2^{\text{OH}}}{I_1^{\text{OH}}+I_2^{\text{OH}}} \tag{4.2}$$

with

$$I_1^{\text{OH}}=m_H\left(r_{1,\text{OH}}\sin\theta_1\right)^2 \tag{4.3a}$$

$$I_2^{\text{OH}}=m_H\left(r_{2,\text{OH}}\sin\theta_2\right)^2 \tag{4.3b}$$

where the $r_{i,\text{OH}}$s are the OH (or OD) bond lengths and θ_is are the OOH(D) bond angles. The energy levels calculated for HOOH and DOOD are superimposed on the torsional PESs shown in Fig. 3a, b. There are one pair of even and odd states below the lower torsional barrier for HOOH and two pairs of such states for DOOD. There are 13 bound states below the higher barrier in the torsional coordinate for HOOH and 19 for DOOD. At energies higher than the upper torsional barrier, the states become widely spaced pairs similar to the rigid rotor.

At each value of τ, the potential energy was minimized with respect to all other DoFs and a normal mode analysis was performed at this constrained stationary point by calculating the projected mass-weighted Hessian matrix. In this way, the normal mode frequencies were determined as a function of τ and a quadratic representation of the potential in terms of the instantaneous normal modes, $q_i(i=1\ldots5)$, and the torsional DOF is constructed

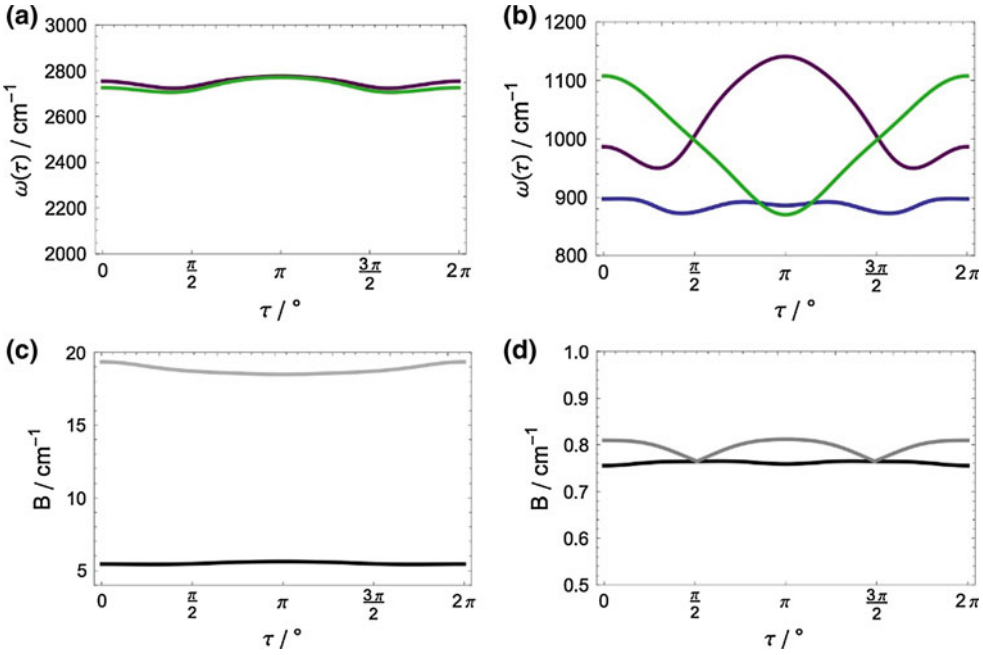

Fig. 4 Normal mode frequencies and rotational constants for DOOD. **a** The O–D stretch frequencies. **b** The OOD bend frequencies, *green* and *purple*, and the O–O stretch frequency, *blue*. **c** The torsion rotational constant, *gray*, and the largest external rotational constant, *black*. **d** The two smaller external rotational constants. The analogous results for HOOH and HOOD are not shown but are similar

$$V = V(\tau) + \frac{1}{2}\sum_{i=1}^{5}\omega_i^2(\tau)q_i^2 \tag{4.4}$$

The first term in Eq. (4.4), $V(\tau)$, is the 1d torsional potential shown in Fig. 3. The normal mode frequencies depend upon the isotopomer, but trends are quite similar. The OH and OD stretching frequencies vary little with the torsion, but the bending frequencies show a strong dependence in all the isotopomers where frequency variations of ~20 % are observed. The change in the O–O stretch frequency is much more moderate, approximately 3 %. The largest rotational constant for HOOH has a very weak dependence upon τ, but the two smaller rotational constants vary more strongly, ~10 %. The torsional (internal) rotation constant (obtained from I_τ of Eq. (4.2)) varies by ~10 % as well. The torsion-dependent normal mode frequencies and external rotational constants are shown in Fig. 4 for DOOD which qualitatively resembles the variations in HOOH and HOOD.

The cumulative sum of states for HOOH and DOOD is shown in Fig. 5 on two different energy scales. The semiclassical adiabatic method, SA, results are shown along with cumulative state sums obtained from the simple harmonic state count, with frequencies obtained at the potential minimum, a factor of 2 is used to account for the two torsional wells, and the rotational is treated as a symmetric top. Also shown is the result obtained when the separable torsional levels are used in the state count algorithm along with the harmonic oscillator levels of the other normal modes using the frequencies and B-constants of the equilibrium geometry. We refer to this method as HR, for hindered rotor.

The results for all three isotopomers are quite similar. At low energies, the SA method gives a larger state count than the HO and HR approximations. By $E = 20$ kcal mol^{-1}, the HO and the HR methods still give a smaller sum of states than the SA method and are in error by around 10 %. At the higher energies, see Fig. 5c, d, the HO approximation overcounts the sum of states since it neglects the torsional anharmonicity and the wide spacing of the rigid rotor states of the torsions when the energy is larger than the upper torsional barrier height, for reference see Fig. 3. The overcounting is largest for the HOOH isotopomer and smallest for DOOD. The separable hindered rotor method HR consistently undercounts the sum of states relative the SA method at all energies as HR fails to account for the variation in the (non-torsion) normal mode frequencies and the rotational constants over the torsion coordinate. The effects of deuterium substitution are also clearly evident from comparing Fig. 5a, c with b, d, respectively, where state sum increases significantly for DOOD over HOOH.

A similar pattern of result is seen for the densities of states, $\rho(E)$, shown in Fig. 6. The differences between the SA method and the HO and HR methods are more pronounced for $\rho(E)$ versus $G(E)$. The HO results are consistently lower than SA at low energies, but increase at high energy. The HR remains lower than SA over all the entire energy range.

The canonical partition function can be obtained from the Boltzmann average of the density of states. This can be easily incorporated directly into the semiclassical adiabatic state counting algorithm using the expression obtained by integration by parts:

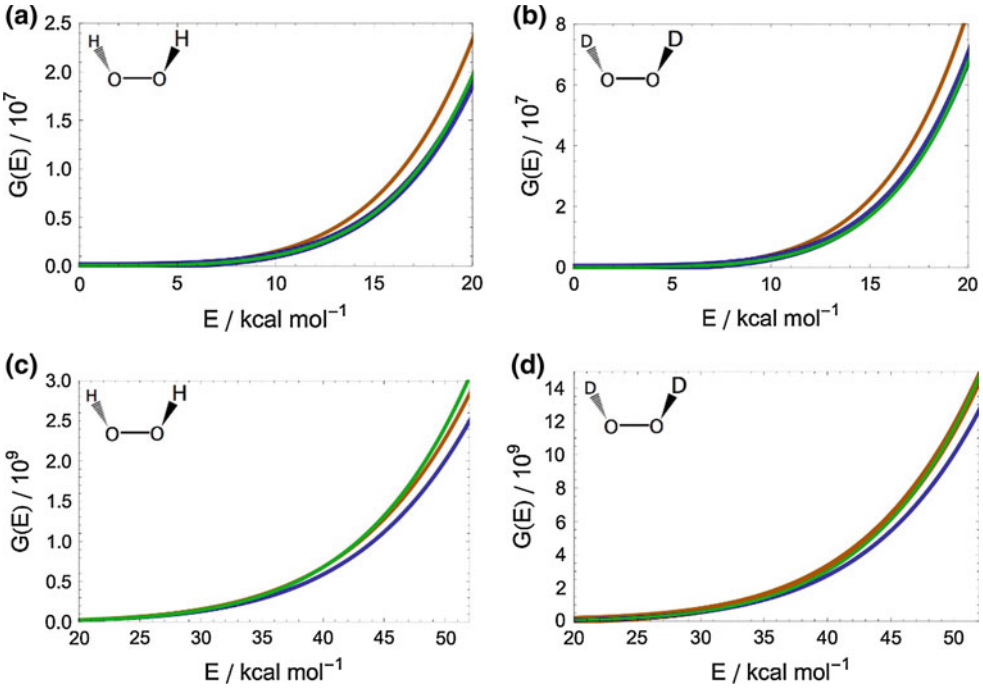

Fig. 5 The cumulative sum of states for HOOH and DOOD. Panels **a** and **b** show a lower energy scale and panels **c** and **d** show a higher energy scale. The harmonic approximation (HO) is in *green*, the separable torsion (HR) model is in *blue*, and the semiclassical adiabatic (SA) method is in *orange*. The cumulative state sum for HOOD is not shown. The energy E is the energy above zero point

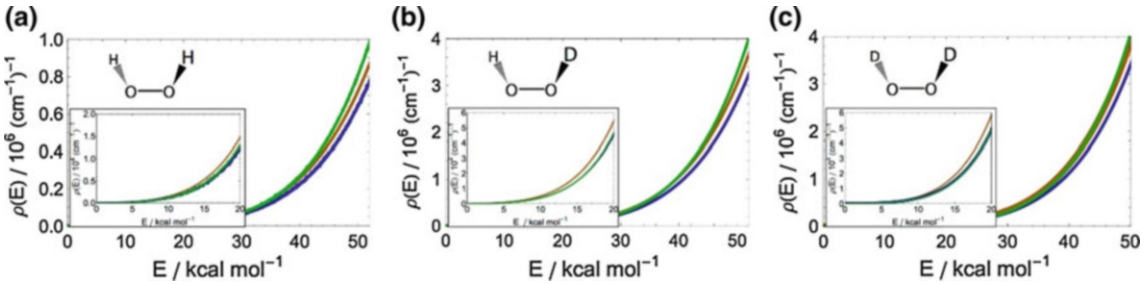

Fig. 6 The density of states for HOOH, HOOD, and DOOD. The *inset* graphs show the densities of states on a lower energy scale. HO is in *green*, HR is in *blue*, and SA is in *orange*

$$Q(T) = \int_0^\infty \rho(E) e^{-\frac{E}{k_B T}} dE = \frac{1}{k_B T} \int_0^\infty G(E) e^{-\frac{E}{k_B T}} dE - G(0) \tag{4.5}$$

where the zero of energy is taken to be the zero-point energy of the molecule. To compare the results of the SA approximation, the partition function was also computed under the HO and HR approximations. The results show that the larger number of states counted by the SA approximation at low energies, where the canonical state weighting is higher, results in a larger value of the partition function over the calculated energy range. The harmonic oscillator approximation (HO) is consistently too low while the Pitzer Gwinn approximation (HR) lies between the HO and SA approximations. The effect due to isotopic substitution is readily observed between the three curves as the partition function rises much more quickly in HOOD and DOOD, see the scale of the ordinate axes in Fig. 7. The relative quality of the three approximations is the same for each isotopomer.

In order to illustrate the performance of the semiclassical adiabatic method for reactive problems, we apply it to the dissociation of HOOH into separated hydroxyl radicals, HOOH → 2OH, and the analogous reaction of DOOD. The absolute energy of dissociation of HOOH on the potential of Kuhn et al. [23] is 54.4 kcal mol^{-1}, but it is substantially lowered by zero-point energy correction to 48.4 kcal mol^{-1}. Deuterium substitutions of the hydrogens in the HOOH molecule raise the dissociation energy to 49.0 kcal mol^{-1} in HOOD and 49.7 kcal mol^{-1} in DOOD which leads to a kinetic isotope effect in the rate coefficients.

The dissociation of the HOOH molecule involves the rupture of the weak O–O bond. The relaxed (i.e., geometry optimized) potential energy curve along the O–O bond distance (effectively the reaction coordinate) is shown in Fig. 8. As seen in the figure, a small cusp

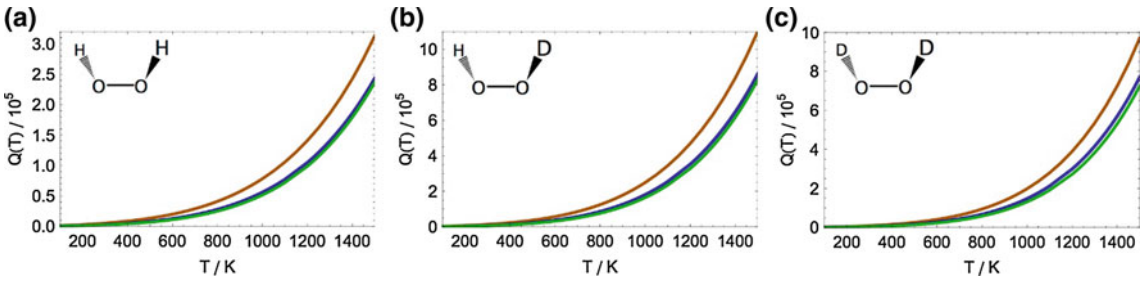

Fig. 7 The canonical partition functions for HOOH, HOOD, and DOOD over a range of temperatures. The harmonic oscillator with rigid rotor asymmetric top approximation is in *green*, the Pitzer Gwinn separable hindered rotor with rigid rotor asymmetric top approximation is in *blue*, and SA is in *orange*

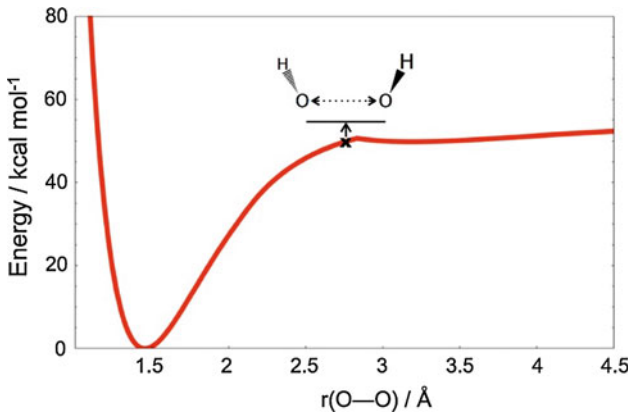

Fig. 8 The potential energy along the O–O bond length obtained by optimizing the geometry at fixed O–O values. The nominal transition state is indicated with an "*x*" and is located just before the potential kink

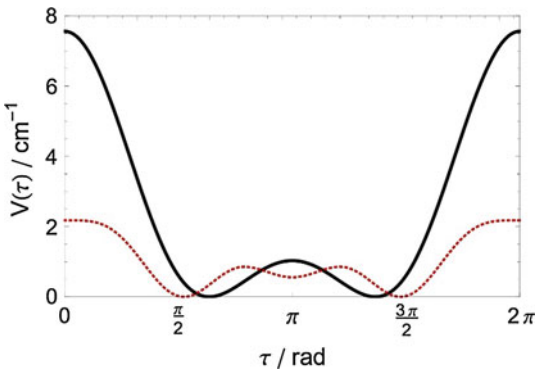

Fig. 9 The torsional 1*d* potential energy curve (*solid black curve*) for the HOOH reactant and the potential along the transition state ridge line (*dashed red curve*). The potential curves are plotted with a common zero of energy set to the minimum energy versus τ

appears in the exit channel potential, a fact also reported by Kuhn et al. [23]. This cusp lies in the vicinity of the transition state and creates some practical difficulties in defining a transition state dividing surface. Thus, in place of the usual variational scheme, we have simply adopted an approximate transition state at an O–O bond distance of $5.2a_0$ (2.75 Å), just before the cusp. The transition state ridge thus corresponds to freezing the reaction coordinate at this O–O bond distance as the torsion varies. Since the TS is actually slightly below the dissociation energy, we have excluded the states in the TS state sum, $G^{\ddagger}(E)$ in Eq. (3.4), that lie below the dissociation energy. Our primary objective here is to evaluate our reactive SA method compared to the less rigorous HO and HR methods, and the use of these approximations to the TS will not affect this comparison.

The torsion ridgeline tracing the transition state dividing surface is shown in Fig. 9 along with the torsional potential energy contour of the reactant for comparison. It can be seen that the separation of the OH fragments at the TS leads to a decrease in the torsional barriers compared to the torsional potential of the reactant. The cis configuration still corresponds to a maximum, but this maximum is now much broader and its height is just over 2 kcal mol^{-1}. There are three torsional minima on the TS ridgeline: the trans-configuration and the two symmetry-related configurations where the O–H bonds point in perpendicular directions. Considerable anharmonicity of the TS ridge line is apparent from Fig. 9 so that an accurate description of the torsion DoF is critical.

The microcanonical rate constant, from Eq. (3.1), was computed for a large range of values of overall angular momentum quantum number J. The density of states of the reactant, $\rho(E, J)$, was computed by numerical differentiation of the sum of states $G(E, J)$, which was smoothed by polynomial fitting for the HO and HR methods. A comparison of the SA method to the HO method and the HR method is shown in Fig. 10 for the $J = 0$ case for both the HOOH and the DOOD reactions. The results for several higher values of J are shown in Fig. 11. The kinetic isotope effect (KIE) is clearly evident in these plots, where, for one thing, the reaction threshold for the DOOD is higher than

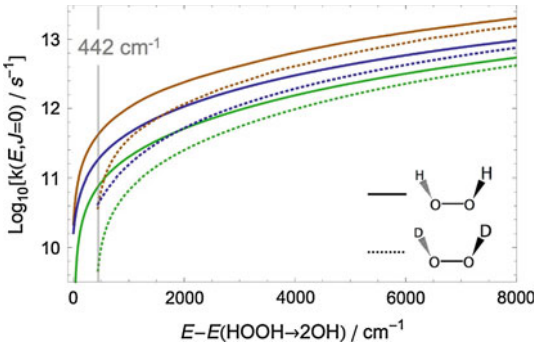

Fig. 10 The $J = 0$ microcanonical rate coefficients of the dissociation of HOOH into OH radicals (*solid lines*), and DOOD into OD radicals (*dashed lines*) computed using RRKM theory. The *orange curves* are the semiclassical adiabatic method, the *green curves* are the harmonic approximation, and the *blue curves* are the separable torsion model. Energies are relative to the (zero-point corrected) HOOH dissociation energy 48.40 kcal mol^{-1}

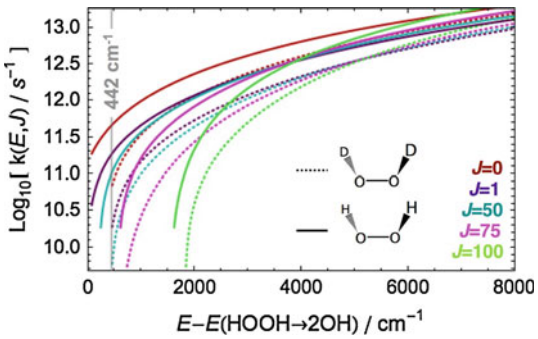

Fig. 11 The angular momentum-resolved microcanonical RRKM rate coefficients of the dissociation of HOOH into OH radicals (*solid lines*), and DOOD into OD radicals (*dashed lines*) using the semiclassical adiabatic method for several values of total angular momentum, J. Energies are relative to the (zero-point corrected) HOOH dissociation energy 48.4 kcal mol^{-1}, and the DOOD dissociation energy is noted in the figure

HOOH. It is also apparent that the larger reactant density of states for DOOD reduces the dissociation rate relative to that of HOOH over the energy range shown. However, at higher energy, the difference between the dissociation rate coefficients for the two isotopomers decreases. The performance of the three different approximation methods for the dissociation rate coefficient does not seem to strongly depend upon the isotopomer. The HO approximation is seen to underestimate the value of the $J = 0$ rate coefficient over the energy range. This is likely due to the HO overestimation of the reactant density of states, $\rho(E, J)$, at the dissociation energy given the trends shown in Fig. 6. The separable HR method is more robust and predicts a higher rate of dissociation for both isotopomers. This method still underestimates the rate coefficient relative to the SA method. Over most of the energy range shown in Fig. 10, the SA method predicts a rate of dissociation greater than the HO result by a factor of ~3 to 6 for both isotopomers and greater than the HR result by factor of around 1.5–3. Both the HO and the HR methods completely neglect the coupling of the other DoFs to the torsional coordinate, though the HR method does more accurately treat the torsional motion itself. The importance of this coupling to the dissociation reaction and the necessity for an accurate treatment of torsional coupling effects in rate coefficient is clear.

5 Conclusions

We have considered a new scheme to incorporate anharmonicity and mode coupling into quantum state sums for systems possessing a large amplitude DoF such as a torsion. This method is based on the presumed timescale separation between the torsional mode and the remaining high-frequency vibrations. While the commonly used separable approximations, like the harmonic oscillator/rigid rotor method, are quite often useful in the statistical modeling of reactions, they should be used cautiously. Furthermore, more rigorous inclusion of anharmonicity such as employed in methods using Monte Carlo sampling of molecular geometries [11] may be based on classical mechanics and thus neglect quantum effects. The semiclassical adiabatic method developed here accounts for torsional coupling at a quantum level while circumventing the necessity for repeated quantum determinations of torsional eigenenergies for the excited states of the molecule. The method also leads to some new insight into reactions that may have multiple transition states due to multiple conformers associated with the torsional coordinate.

We calculated the density of states for the HOOH and its isotopomers, HOOD and DOOD, using the SA method, and compared the results to the conventional separable HO and HR models. Both the HO and HR models showed a deviation from the SA model. At low energies, the HO model underestimated the state density due to the omission of mode coupling, while at high energies, it over counted the state density due to its omission of torsional anharmonicity. The HR approximation predicted a state density that was too low due to the neglect of mode coupling. It is clear that while the differences between the SA model and the separable models are on the order of 10–20 %, these differences are quite possibly amenable to experimental verification.

We have studied the statistical RRKM rate coefficients for hydrogen peroxide dissociation using our method. The results were compared to the conventional HO and HR models over a broad range of energies for reactions of

HOOH and HOOD. The rate coefficients predicted by the methods were found to be significantly different. The HO underestimates the rate by a factor of 3–6 indicating that the harmonic treatment of torsion at the TS is clearly a poor approximation. The hindered rotor approximation reduces the error to a factor of 1.5–3. We find that the differences between the separable models and the semiclassical adiabatic model are much greater for the rate coefficient than for the state densities of the bound molecule. This is due to both the increased torsion coupling at higher reagent energies and the importance of torsional coupling at the TS.

It is clear that the semiclassical adiabatic method is at an early stage of development. It is quite important, in future work, to consider the role of multiple torsional coordinates. Indeed, as the reagent molecules become large, as in the combustion chemistry of complex fuels, we expect there will be many high-amplitude internal coordinates that must be appropriately accounted for in an accurate rate calculation.

Acknowledgments We are grateful to the Chinese Academy of Sciences for support through the program for visiting professorships for senior international scientists. We also acknowledge support from the National Science Foundation and summer support from Argonne National Laboratory.

References

1. Truhlar DG, Hase WL, Hynes JT (1983) J Phys Chem 87:2664
2. McQuarrie DW (2000) Statistical mechanics. University Science Books, Sausalito
3. Marcus RA, Rice OK (1951) J Phys Colloid Chem 55:894
4. Holbrook KA, Pilling MJ, Robertson ST (1996) Unimolecular reactions, 2nd edn. Wiley, New York
5. Beyer T, Swinehart DF (1973) Commun ACM 16:379
6. Stein SE, Rabinovitch BS (1973) J Chem Phys 58:2438
7. Pitzer KS, Gwinn WD (1942) J Chem Phys 10:428
8. Ellingson BA, Lynch VA, Mielke SL, Truhlar DG (2006) J Chem Phys 125:084305
9. Pfaendtner J, Yu X, Broadbelt LJ (2007) Theor Chem Acct 118:881
10. Lin CY, Izgorodine EI, Coote ML (2008) J Phys Chem A 112:1956
11. Kamarchik E, Jasper AW (2013) J Phys Chem Lett 4:2430
12. Lynch VA, Mielke SL, Truhlar DG (2005) J Phys Chem A 109:10092
13. Vansteenkiste P, Van Neck D, Van Speybroeck V, Waroquier M (2006) J Chem Phys 124:044314
14. Sharma S, Raman S, Green WH (2010) J Phys Chem A 114:5689
15. Reinisch G, Leyssale LM, Vignoles GL (2010) J Chem Phys 133:154112
16. Wang WJ, Zhao Y (2012) J Chem Phys 137:214306
17. Zheng J, Yu T, Papajak E, Alecue IM, Mielke SL, Truhlar DG (2011) Phys Chem Chem Phys 13:10885–10907
18. Miller WH, Handy NC, Adams JE (1980) J Chem Phys 72:99
19. Fehrensen B, Luckhaus D, Quack M (1999) Chem Phys Lett 300:312
20. Carrington T, Miller WH (1984) J Chem Phys 81:3942
21. Zhou DDY, Han KL, Zhang PY, Harding LB, Davis MJ, Skodje RT (2012) J Phys Chem A 116:2089
22. Koput J, Carter S, Handy NC (1998) J Phys Chem A 102:6325
23. Kuhn B, Rizzo TR, Luckhaus D, Quack M, Suhm MA (1999) J Chem Phys 111:2565
24. Luckhaus D (2000) J Chem Phys 113:1329
25. Uzer T, Hynes JT, Reinhardt WP (1985) Chem Phys Lett 117:600
26. Getino C, Sumpter BG, Santamaria J, Ezra GS (1989) J Phys Chem 93:3877
27. Guo Y, Thompson DL (2003) Chem Phys Lett 382:654
28. Colbert DT, Sibert EL (1991) J Chem Phys 94:6519
29. Troe J, Ushakov VG, Chem P (2008) Chem Phys 10:3915
30. Kramer ZC, Skodje RT (2014) In: Han KL, Chu T (eds) Reaction rate constant computations: theories and applications, chapter 6. Royal Society of Chemistry Publishing, p 133
31. Wang CR, Zhang DH, Skodje RT (2012) J Chem Phys 136:164314
32. Rizzo TR, Hayden CC, Crim FF (1984) J Chem Phys 81:4501
33. Butler LJ, Ticich TM, Likar MD, Crim FF (1986) J Chem Phys 85:2331
34. Ticich TM, Rizzo TR, Dubal H-R, Crim FF (1986) J Chem Phys 84:1508
35. Crim FF (1990) Science 249:1387
36. Luo X, Rieger PT, Perry DS, Rizzo TR (1988) J Chem Phys 89:4448
37. Luo X, Rizzo TR (1991) J Chem Phys 94:889
38. Luo X, Rizzo TR (1992) J Chem Phys 96:5659
39. Kuhn B, Rizzo TR (2000) J Chem Phys 112:7461
40. Kappel C, Luther K, Troe J (2002) Phys Chem Chem Phys 4:4392
41. Flaud JM, Camy-Peyret C, Johns JWC, Carli B (1992) J. Chem. Phys. 91:1504
42. Camy-Peyret C, Flaud JM, Johns JWC, Noel M (1992) J Mol Spectros 155:84
43. Wilson EB, Decius JC, Cross PC (1955) Molecular vibrations. Dover, New York
44. Skodje RT, Truhlar DG, Garrett BC (1981) J Phys Chem 85:3019
45. Skodje RT, Garrett BC, Truhlar DG (1982) J Chem Phys 77:5955

Theor Chem Acc (2014) 133:1563
DOI 10.1007/s00214-014-1563-9

REGULAR ARTICLE

The semiclassical propagator in fermionic Fock space

Thomas Engl · Peter Plößl · Juan Diego Urbina · Klaus Richter

Received: 19 May 2014 / Accepted: 6 August 2014 / Published online: 10 September 2014

Abstract We present a rigorous derivation of a semiclassical propagator for anticommuting (fermionic) degrees of freedom, starting from an exact representation in terms of Grassmann variables. As a key feature of our approach, the anticommuting variables are integrated out exactly, and an exact path integral representation of the fermionic propagator in terms of commuting variables is constructed. Since our approach is *not* based on auxiliary (Hubbard–Stratonovich) fields, it surpasses the calculation of fermionic determinants yielding a standard form $\int \mathscr{D}[\psi,\psi^*]\mathrm{e}^{iR[\psi,\psi^*]}$ with real actions for the propagator. These two features allow us to provide a rigorous definition of the classical limit of interacting fermionic fields and therefore to achieve the long-standing goal of a theoretically sound construction of a semiclassical van Vleck–Gutzwiller propagator in fermionic Fock space. As an application, we use our propagator to investigate how the different universality classes (orthogonal, unitary and symplectic) affect generic many-body interference effects in the transition probabilities between Fock states of interacting fermionic systems.

Keywords Path integral · Semiclassical · Fermions · classical limit

1 Introduction

Semiclassical techniques attempt to describe quantum phenomena using only classical information as input (besides $\hbar$), but keeping all the kinematical and interpretational aspects of quantum mechanics untouched. Semiclassical methods should therefore be distinguished from quasi-classical approaches, which are based on the quantum-classical correspondence and do not only use classical information, but also try to export classical concepts to approximate quantum mechanics. The epitome of the quasi-classical approach is the use of the Ehrenfest theorem to approximate the quantum mechanical evolution of wave packets, with systematic corrections given by the Wigner–Moyal expansion [1].

Semiclassical methods, as understood in this contribution, attempt to link classical and quantum mechanics in a more abstract, less direct way. While for the quasi-classical program, quantum mechanics is used to construct quantities with a direct classical counterpart (like the trajectory defined by the mean position and momentum of a wavepacket), the semiclassical program employs information extracted from classical trajectories (like their actions and stabilities) to construct quantum mechanical objects. This difference becomes very explicit when we use semiclassical methods to construct quantum objects without classical analog, such as probability amplitudes.

A major goal of the semiclassical program is the construction of the semiclassical propagator K^{sc}, the asymptotic form (when $\hbar \to 0$) of the quantum mechanical propagator

$$K(\mathbf{q},\mathbf{q}',t) = \langle \mathbf{q}|\mathrm{e}^{-\frac{i}{\hbar}\hat{H}t}|\mathbf{q}'\rangle, \tag{1}$$

defined as the matrix element of the time-evolution operator [2].

As reviewed in [3], the challenge to construct a semiclassical propagator has a long history. Although already in 1926 it was clear for Pauli, Dirac and van Vleck that the quantum mechanical propagator can be approximated by

Dedicated to Professor Greg Ezra and published as part of the special collection of articles celebrating his 60th birthday.

T. Engl (✉) · P. Plößl · J. D. Urbina · K. Richter
Institut für Theoretische Physik, Universität Regensburg, 93040 Regensburg, Germany
e-mail: thomas.engl@physik.uni-regensburg.de

an object of the form $K^{\mathrm{sc}} \sim \mathrm{e}^{\frac{i}{\hbar}R}$ with the classical action R appearing as a phase, it took more than 40 years before Gutzwiller [4] completed the rigorous construction of the semiclassical propagator from Feynman's path integral. In its final form, it reads [5]

$$K^{\mathrm{sc}}(\mathbf{q},\mathbf{q}',t) = \sum_{\gamma} A_{\gamma}(\mathbf{q},\mathbf{q}',t)\mathrm{e}^{\frac{i}{\hbar}R_{\gamma}(\mathbf{q},\mathbf{q}',t)+i\mu_{\gamma}\frac{\pi}{2}} \tag{2}$$

where the sum extends over the set of solutions γ of the classical problem to join the classical configurations $\mathbf{q}'$ and $\mathbf{q}$ in time t. As envisioned by Dirac, R is the classical action of the trajectory, while A is related to its variations with respect to the initial and final configurations, and μ is the number of focal points of the trajectory γ.

The derivation of the van Vleck–Gutzwiller propagator marks the starting point of modern semiclassical methods [1, 3, 6]. They have been able not only to capture but also to successfully describe interference phenomena, i.e., wave effects impossible to describe using quasi-classical techniques.

By Fourier-transforming K^{sc} we get the semiclassical (Gutzwiller) Green's function, the starting point to describe stationary properties of quantum systems in the semiclassical limit, and in particular to understand the emergence of universal fluctuations in the spectra and eigenfunctions of classically chaotic quantum systems [3, 6]. Also, the early semiclassical notion of the theory of molecular collisions [7] and related approaches in mesoscopic condensed matter to describe quantum transport [8, 9] (for reviews see [10–12]) connect the van Vleck–Gutzwiller propagator, or the semiclassical Green function, with the single-particle S-matrix in terms of transition amplitudes for transmission and reflection.

The success of the semiclassical methods has been restricted, however, predominantly to quantum systems that admit a first-quantization description. In fact, the generalization of the van Vleck–Gutzwiller propagator to describe systems of interacting particles does not pose any conceptual challenge, as the classical limit of the theory is very well understood. The semiclassical propagator is now an established tool to describe quantum dynamics of molecular systems [13–16] and mesoscopic electronic systems [17].

Technical, but not conceptual, problems arise when indistinguishability comes into play. Here, the semiclassical calculation of ground and (doubly) excited states in helium by Ezra et al. [18] marks a successful step in coping with strongly interacting two-electron dynamics. The number of classical paths we need to construct to calculate the transition amplitude between different (anti-) symmetrized configurations of a quantum system, however, grows extremely fast with the number of particles [19]. The same vast increase of the number of classical trajectories that have to be taken into account, affects the coupled coherent state approach [20], which has been developed for the treatment of fermionic many-body systems in phase space. In this approach, the wave function is expanded in a (large) set of Slater determinants of single-particle coherent states with randomly selected initial conditions. The coherent states are then evolved along the corresponding classical trajectory.

Moreover, for fermionic systems with spin orbit interactions, hybrid semiclassical approaches exist, which describe the orbital motion of non-interacting particles in phase space, while the spin is treated in a second-quantized approach using spin coherent states [21–28].

Importantly, the emergence of mean-field behavior, an expected simplification of the description when the number of particles is large, cannot be rigorously included in a natural way if one sticks to the first-quantized picture where the total number of particles N is not defined by the quantum many-body state but is an external parameter determining the dimensionality $D = Nd$, where d is the spatial dimension, of the system and thereby fixing the structure of the very space where the system lives.

These remarks indicate already a possible solution of the problem. If a second-quantized picture in Fock space is adopted instead, both quantum indistinguishability and flexibility in the number of particles are automatically included at the kinematic level: the Fock space of quantum states is by definition spanned by states which are correctly (anti-) symmetrized, and the number of particles is simply another observable represented by a hermitian operator [29]. When invoking a Fock space description, this change of perspective implies for the semiclassical program that particles appear as an emergent concept, derived from the more fundamental degree of freedom: the quantum field [30].

The development of a semiclassical program for bosonic fields has received powerful impact from the experimental realization of their discrete version in the context of cold-atom physics [31]. In fact, the theoretical model that describes microscopically a system of interacting bosons on a lattice, the so-called Bose-Hubbard model [32], is a special realization of an interacting bosonic field. Here, again, the complementarity between quasi-classical and semiclassical approaches has been apparent. Quasi-classical methods as the ones used in [33] work well as long as quantum interference does not come into play and eventually dominates the dynamics. However, a rigorous derivation of the van Vleck–Gutzwiller propagator in bosonic Fock space was achieved only recently [34].

It is fair to say that the situation in the fermionic case is more desperate. Already a quasi-classical approach faces a fundamental problem: how to define a sensible classical limit if the fermionic fields must obey the Pauli principle and therefore admit only non-commutative descriptions? The attempts and achievements to associate commuting variables to fermionic operators that spans from the 1970s well into the 2010s, are still lacking a rigorous microscopic

derivation, indicating the complexity of the problem [35–38]. The importance of the Chemical Physics community in this program has been obvious: electronic degrees of freedom are fundamental in the realm of molecular reactions. Moreover, chemical reactions require, in principle, simulations with anticommuting variables.

In order to avoid these anticommuting variables, in a series of important papers, Miller and collaborators proposed to use a heuristic generalization of the Heisenberg prescription [36, 37, 39] to construct the classical limit of fermionic degrees of freedom (for recent applications see [40, 41]). It is a remarkable and valuable feature of this approach that it associates correct signs to expressions involving anticommuting fermionic operators $\hat{c}, \hat{c}^\dagger$ and respects the Pauli principle. In the simplest example, these key features can be seen in the mapping $F \to F^{\rm cl}$ between operators $F(\hat{c}, \hat{c}^\dagger)$ and classical phase-space functions $F^{\rm cl}(\sqrt{n}\mathrm{e}^{i\theta}, \sqrt{n}\mathrm{e}^{-i\theta})$, which gives for $i \neq j$

$$\begin{aligned} \hat{c}_i^\dagger \hat{c}_j &\to \sqrt{n_i n_j (1-n_i)(1-n_j)}\mathrm{e}^{-i(\theta_i-\theta_j)}, \\ \hat{c}_j \hat{c}_i^\dagger &\to -\sqrt{n_i n_j (1-n_i)(1-n_j)}\mathrm{e}^{-i(\theta_i-\theta_j)}. \end{aligned} \tag{3}$$

The (in general continuous) classical phase-space variables $0 \leq n \leq 1$ are naturally interpreted as classical fermionic occupation numbers with the angles θ as their corresponding canonically conjugated variables.

However, as it is obvious from Eq. (3), the classical Hamiltonian obtained in this way has the physical Fock states, defined by

$$n_i = 0 \text{ or } 1 \quad \text{for all } i, \tag{4}$$

as fixed points of the dynamics and the corresponding semiclassical propagator is then trivially incorrect in the relevant case where it connects physical Fock states. Moreover, as discussed at length in Sect. 3, approaching the classical limit from the quantum side by means of a formal path integral in terms of the fermionic states (introduced by Klauder [35]),

$$|b\rangle = \sqrt{1-|b|^2}|0\rangle + b\hat{c}^\dagger|0\rangle, \quad \text{with complex } b, \tag{5}$$

shows that Eq. (3) can be rigorously obtained from an exact path integral representation in terms of the commuting fields b. This indicates that in a representation where Eq. (3) holds, the quantum mechanical propagation between Fock states is *not* supported by classical trajectories and the semiclassical limit is problematic.

This complication may be due to the fact that in Klauder's representation the path integral is *restricted*, namely, the integration over the variables b are defined inside the unit disk instead of over the whole complex plane. A heuristic incorporation of Langer corrections proposed in [39],

$$\sqrt{n(1-n)} \to \sqrt{\left(n+\frac{1}{2}\right)\left(\frac{3}{2}-n\right)}, \tag{6}$$

lifts the problem and actually leads to a classical limit that gives, for example, agreement with first-order quantum perturbation theory by using classical perturbation theory.

As this volume commemorates Greg Ezra's contributions to the description of atomic and molecular dynamics, we would like to mention that Ezra's pioneering work on the Langer correction to the semiclassical propagator [42] could possibly provide the key to make rigorous the promising proposal presented in [37]. It is then tempting to check whether Ezra's insight into Langer corrections within the path integral formalism in first-quantized systems with would help to make Miller's approach justified from first principles [43].

Here, we follow a different route and present what we believe to be the first microscopic derivation of the exact propagator between N-particle fermionic Fock states in terms of path integrals over commuting, unrestricted classical fields. Our path integral not only incorporates and generalizes Miller's mapping $F \to F^{\rm cl}$ "teaching" the classsical limit of large N about anticommuting operators, but it is supported in the semiclassical limit by classical paths. No extra assumptions or corrections are required.

As we will discuss in Sect. 3, the thus derived classical Hamiltonian corresponds to an approximation of the Holstein-Primakoff transformation for a single particle in a two-level system, used in [44].

After briefly introducing Grassmann variables in Sect. 2, in Sect. 3, we present our derivation of the exact path integral for fermionic systems. Armed with this object, in Sect. 4 we follow the typical semiclassical program: we identify both the effective Planck's constant and the classical limit of the theory from the phase of the path's amplitude in the path integral and evaluate the path integral in stationary phase approximation to obtain a van Vleck–Gutzwiller type propagator for interacting fermionic fields. The presentation will be restricted to spin-1/2 systems, although a generalization to higher spins is straight forward. Finally, in Sect. 5, we use the thus derived semiclassical propagator to calculate the transition probability from one fermionic Fock state to another one for systems without time reversal symmetry, for systems diagonal in spin space but time reversal invariant, as well as for time reversal invariant spin-1/2 systems non-diagonal in spin space.

Technical details of the derivation of our main results, namely the exact complex path integral representation of the fermionic propagator in terms of commuting fields, Eq. (19), the classical Hamiltonian Eq. (22) and the van Vleck propagator, Eqs. (56, 64) can be found in the appendices.

2 Grassmann coherent states

In order to derive the path integral representation for the fermionic propagator in Fock space, we will use Grassmann

coherent states in intermediate steps. They are defined as the eigenstates of the fermionic annihilation operators [29],

$$\hat{c}_j|\boldsymbol{\zeta}\rangle = \zeta_j|\boldsymbol{\zeta}\rangle. \tag{7}$$

Here, $\hat{c}_j$ and $\hat{c}_j^\dagger$ annihilates and creates, respectively, a particle in the j-th single-particle state, two states which coincide in the orbital degrees of freedom, but differ in the spin degree of freedom are accounted for as different single-particle states, and are therefore labeled by different indexes j.

However, due to the antisymmetry and the Pauli exclusion principle, the eigenvalues of the coherent states have to be (complex) anticommuting numbers, called Grassmann numbers [29, 45], i.e., for two of these numbers ζ and χ

$$\zeta\chi = -\chi\zeta. \tag{8}$$

They also anticommute with the creation and annihilation operators,

$$\zeta\hat{c}_j = -\hat{c}_j\zeta, \quad \zeta\hat{c}_j^\dagger = -\hat{c}_j^\dagger\zeta, \tag{9}$$

while they commute with regular complex numbers. The anticommuting property also implies $\zeta^2 = 0$.

Integration over a complex Grassmann number is defined by

$$\int \mathrm{d}\zeta^* \mathrm{d}\zeta 1 = \int \mathrm{d}\zeta^* \mathrm{d}\zeta\zeta = \int \mathrm{d}\zeta^* \mathrm{d}\zeta\zeta^* = 0, \tag{10}$$

$$\int \mathrm{d}\zeta^* \mathrm{d}\zeta\zeta\zeta^* = 1. \tag{11}$$

With the properties of the Grassmann numbers, it is possible to show that the fermionic coherent states are given by [29]

$$|\boldsymbol{\zeta}\rangle = \exp\left(-\frac{1}{2}\boldsymbol{\zeta}^*\cdot\boldsymbol{\zeta}\right)\prod_j\left(1-\zeta_j\hat{c}_j^\dagger\right)|0\rangle, \tag{12}$$

where $|0\rangle$ denotes the fermionic vacuum state. Moreover, they satisfy

$$\langle\boldsymbol{\zeta}|\boldsymbol{\chi}\rangle = \exp\left[\sum_j\left(-\frac{1}{2}\zeta_j^*\zeta_j - \frac{1}{2}\chi_j^*\chi_j + \zeta_j^*\chi_j\right)\right], \tag{13}$$

$$\langle\mathbf{n}|\boldsymbol{\zeta}\rangle = \exp\left(-\frac{1}{2}\boldsymbol{\zeta}^*\cdot\boldsymbol{\zeta}\right)\prod_j{}'\,\zeta_j^{n_j}, \tag{14}$$

$$\int \mathrm{d}\boldsymbol{\zeta}^* \int \mathrm{d}\boldsymbol{\zeta}|\boldsymbol{\zeta}\rangle\langle\boldsymbol{\zeta}| = 1, \tag{15}$$

with $|\mathbf{n}\rangle$ being an arbitrary Fock state, such that $n_j \in \{0,1\}$ is the occupation of the j-th single-particle state. The prime at the product indicates that the order of the individual factors is reversed, i.e., the factor corresponding to the largest possible value is the most left one, while the $j = 1$ term is the most right one.

3 The path integral in complex variables

3.1 Derivation

The aim of this part is to derive a path integral representation of the propagator in Fock space,

$$K\left(\mathbf{n}^{(f)},\mathbf{n}^{(i)};t_f\right) = \left\langle\mathbf{n}^{(f)}\middle|\exp\left(-\frac{\mathrm{i}}{\hbar}\hat{H}t_f\right)\middle|\mathbf{n}^{(i)}\right\rangle, \tag{16}$$

to which the stationary phase approximation can be applied. Note that for simplicity of presentation, the Hamiltonian has been chosen time independent, although the following calculations are also valid for the time dependent case.

The path integral representation is usually achieved by applying the Trotter Formula [46], which replaces the exponential in Eq. (16) by the product of infinitely many propagators with an infinitesimally small time step and by inserting the unit operator between two adjacent factors. Since the resolution of unity for Fock states is given by a sum, rather than an integral, they are not suitable for the construction of a path integral. This makes the coherent states the natural choice for the representation of the unit operator. However, when applying the semiclassical approximation to the coherent state path integral, one ends up with grassmannian equations of motion. On the other hand, it is desirable to have complex equations of motion leading to a real action. In order to achieve this, one has to find a way to replace the integrals over Grassmann variables by integrals over complex ones.

Here, we will give a rough description of the procedure, which allows for such a transformation from Grassmann to complex integrals. However, it turns out that some of the steps contain a certain freedom of choice. The final path integral will then depend on the individual choices made during the derivation. The derivation for the specific choice presented later in this publication, is then carried out in Appendix 1.

After applying Trotter's formula [46], the first step is to insert *two* unit operators in terms of fermionic coherent states between two adjacent exponentials,

$$\begin{aligned}
&K\left(\mathbf{n}^{(f)},\mathbf{n}^{(i)};t_f\right)\\
&= \lim_{M\to\infty}\left[\prod_{m=0}^{M}\left(\int \mathrm{d}\boldsymbol{\zeta}^{(m)*}\int \mathrm{d}\boldsymbol{\zeta}^{(m)}\int \mathrm{d}\boldsymbol{\chi}^{(m)*}\int \mathrm{d}\boldsymbol{\chi}^{(m)}\right)\right]\\
&\quad\times\left[\prod_{m=0}^{M-1}\left\langle\boldsymbol{\zeta}^{(m+1)}\middle|\exp\left(-\frac{\mathrm{i}\tau}{\hbar}\hat{H}\right)\middle|\boldsymbol{\chi}^{(m)}\right\rangle\left\langle\boldsymbol{\chi}^{(m)}|\boldsymbol{\zeta}^{(m)}\right\rangle\right]\\
&\quad\times\left\langle\mathbf{n}^{(f)}|\boldsymbol{\chi}^{(M)}\right\rangle\left\langle\boldsymbol{\chi}^{(M)}|\boldsymbol{\zeta}^{(M)}\right\rangle\left\langle\boldsymbol{\zeta}^{(0)}|\mathbf{n}^{(i)}\right\rangle,
\end{aligned} \tag{17}$$

where $\tau = t_f/M$.

Next, in order to replace the Grassmann integrals by complex ones, one has to insert complex integrals such that the overlap $\langle \boldsymbol{\chi}^{(m)} | \boldsymbol{\zeta}^{(m)} \rangle$ can be written as an integral over a product of two factors, with the first one depending only on $\boldsymbol{\chi}^{(m)}$ and the second one on $\boldsymbol{\zeta}^{(m)}$. Here, integrals of the form

$$\int_{\mathbb{C}} \mathrm{d}\phi \int_{\mathbb{C}} \mathrm{d}\mu \exp\left(-|\phi|^2 - |\mu|^2 + \phi^* \mu\right) \phi^k \left(\mu^*\right)^{k'} = \pi^2 k! \delta_{kk'} \tag{18}$$

will be used, since this choice allows us to construct a path integral, which for intermediate times has the same form as the one for bosons in coherent state representation [29] (see Appendix 1).

After this insertion, we can decouple $\boldsymbol{\zeta}^{(m+1)}$ and $\boldsymbol{\chi}^{(m)}$ from $\boldsymbol{\zeta}^{(m)}$ and $\boldsymbol{\chi}^{(m-1)}$ in Eq. (17), such that the integrand for the propagator becomes a product, in which the m-th factor only depends on $\boldsymbol{\zeta}^{(m)}$ and $\boldsymbol{\chi}^{(m-1)}$. Therefore, the insertion of these integrals allows us to integrate out the Grassmann variables exactly after expanding the exponential up to linear order in τ.

At this point, it is important to note that not only the choice of the inserted integrals is not unique, but that, when choosing e.g. integrals of the form (18), there is a certain freedom in choosing the combinations of k and k'. With the choices cf. Appendix 1, one arrives at

$$\begin{aligned} K\left(\mathbf{n}^{(f)}, \mathbf{n}^{(i)}; t_f\right) = & \left[\prod_{j:n_j^{(i)}=1} \int_0^{2\pi} \frac{\mathrm{d}\theta_j^{(0)}}{2\pi} \exp\left(-\mathrm{i}\theta_j^{(0)}\right) \right] \\ \times & \left(\prod_{j:n_j^{(f)}=1} \int_{\mathbb{C}} \frac{\mathrm{d}\phi_j^{(M)}}{\pi} \phi_j^{(M)} \right) \left(\prod_{m=1}^{M-1} \prod_j \int_{\mathbb{C}} \frac{\mathrm{d}\phi_j^{(m)}}{\pi} \right) \\ \times & \exp\left\{ \sum_{m=1}^{M} \left[-\left|\phi^{(m)}\right|^2 + \phi^{(m)*} \cdot \phi^{(m-1)} - \frac{\mathrm{i}\tau}{\hbar} H_{cl}\left(\phi^{(m)*}, \phi^{(m-1)}\right) \right] \right\}, \end{aligned} \tag{19}$$

where at final time the integrals over those $\phi_j^{(M)}$ corresponding to empty single-particle states, i.e., for those j where $n_j^{(f)} = 0$, are already evaluated exactly and therefore have to be set to zero in Eq. (19). In fact, the integrals over those components do not even have to be inserted right from the beginning, since

$$\int \mathrm{d}\chi_j^{(M)*} \int \mathrm{d}\chi_j^{(M)} \exp\left(-\chi_j^{(M)*} \chi_j^{(M)}\right) \left(1 + \chi_j^{(M)*} \zeta_j^{(M)}\right) = 1. \tag{20}$$

The exact integration over the finally unoccupied states is necessary, since the stationarity conditions will not give solutions for the phases of these components and therefore, these integrals can not be performed in a stationary phase approximation. For the same reason, the integrations over those $\phi_j^{(0)}$ with $n_j^{(i)} = 0$ are already performed exactly. This means that effects due to vacuum fluctuations [47], i.e., the spontaneous creation and annihilation of particles out of the vacuum, are treated exactly. Furthermore, for $m = 0$, the integrations over the amplitudes $J_j^{(0)} = |\phi_j^{(0)}|^2$ for the initially occupied single-particle states j are performed exactly (see Appendix 1 for details of this exact integration). As a matter of fact, these integrals could also be included in the stationary phase approximation, which would eventually result in a multiplication of our result for the semiclassical propagator with a factor $\alpha = \mathrm{e}^N/(\sqrt{2\pi})^N$, where N is the total number of particles, which is the N-th power of Stirling's approximation of $n!$ for $n = 1$.

Now one might raise the question, why the initial amplitudes related to occupied states are integrated out, but not the final ones. Actually, the amplitudes of $\phi_j^{(M)}$ for occupied sites could also be integrated out, which would result in dividing the result for the semiclassical approximation by the same factor α. However, we choose not to perform them, in order to be in accordance with the usual first-quantized semiclassical approach, where the path integral, to which the stationary phase approximation is applied, consists of one integration (over the canonical variables chosen as basis) less than those over their canonical conjugate variables. For instance, the path integral for the propagator in configuration space consists (before taking the limit $M \to \infty$) of M momentum integrals and $M - 1$ position integrals. Moreover, our choice is supported by the fact that it leads to the exact result if the quantum Hamiltonian is diagonal and non-interacting.

When comparing the path integral with the corresponding one in first quantization, Eq. (2), the phases $\theta_j^{(0)}$ would correspond to the initial momenta of the path. The role of $\phi^{(M)}$, however, is much more sophisticated. Its phases again correspond to the final momenta, while its amplitude should somehow correspond to the final position. Yet, the value of the latter is not fixed to $n_j^{(f)} = 1$, which would be the expected boundary condition for the paths. This boundary condition is hidden in the integration over $\phi_j^{(M)}$ and is determined by the extra factor $\phi_j^{(M)}$ of the integrand. In a stationary phase analysis of the integrand, which will be performed below, one finally recognizes that indeed both, the stationarity condition of phase and amplitude of $\phi_j^{(M)}$, are required in order to get the correct boundary condition. Thus, the boundary condition at final time is indeed hidden in the full integral over $\phi_j^{(M)}$.

Finally, it should be noted that the classical Hamiltonian H_{cl} is not unique, but again depends on the way chosen to construct the path integral in complex variables. There remains a certain freedom to weigh individual terms in the classical Hamiltonian differently, which might help in studying effects related to particular parts of the Hamiltonian. For instance, in the Hamiltonian given in Eq. (118) in "Appendix 3.1", the interaction, single-particle energies and the antisymmetry under particle exchange are

weighted exponentially, while the Pauli principle is given by an exponential suppression of hopping processes leading to occupations of one single-particle state by more than one particle. However, due to the exponential factor in the diagonal term of the single-particle part of the Hamiltonian, processes quantum mechanically forbidden by the Pauli principle are further suppressed energetically. This energetical suppression essentially corresponds to the heuristic inclusion of a Pauli potential [38, 48–51], i.e., a potential, which hinders two electrons to occupy the same single-particle state.

For the quantum Hamiltonian considered here,

$$\hat{H} = \sum_{\alpha,\beta} h_{\alpha\beta}\hat{c}_\alpha^\dagger \hat{c}_\beta + \sum_{\substack{\alpha,\beta \\ \alpha\neq\beta}} U_{\alpha\beta}\hat{c}_\alpha^\dagger \hat{c}_\beta^\dagger \hat{c}_\beta \hat{c}_\alpha. \tag{21}$$

one possible classical Hamiltonian is given by

$$\begin{aligned} &H_{cl}(\mu,\phi) \\ &= \sum_\alpha h_{\alpha\alpha}\mu_\alpha\phi_\alpha + \sum_{\substack{\alpha,\beta \\ \alpha\neq\beta}} U_{\alpha\beta}\mu_\alpha\mu_\beta\phi_\alpha\phi_\beta + \sum_{\substack{\alpha,\beta \\ \alpha\neq\beta}} h_{\alpha\beta}\mu_\alpha\phi_\beta \\ &\quad \times \exp\left(-\mu_\alpha\phi_\alpha - \mu_\beta\phi_\beta\right)\prod_j^{\alpha,\beta}\left(1-2\mu_j\phi_j\right), \end{aligned} \tag{22}$$

where the product in the last line runs only over those values of j, which are lying between α and β, excluding α and β themselves. The case $\mu = \phi^*$, i.e.,

$$\begin{aligned} &H_{cl}\left(\phi^*,\phi\right) \\ &= \sum_\alpha h_{\alpha\alpha}|\phi_\alpha|^2 + \sum_{\substack{\alpha,\beta \\ \alpha\neq\beta}} U_{\alpha\beta}|\phi_\alpha|^2|\phi_\beta|^2 + \sum_{\substack{\alpha,\beta \\ \alpha\neq\beta}} h_{\alpha\beta}\phi_\alpha^*\phi_\beta \\ &\quad \times \exp\left(-|\phi_\alpha|^2 - |\phi_\beta|^2\right)\prod_j^{\alpha,\beta}\left(1-2|\phi_j|^2\right), \end{aligned} \tag{23}$$

will be of particular importance for the continuum limit. It is instructive to compare it with the classical electron analog model (CEAM) obtained from Miller's mapping which gives in this case

$$\begin{aligned} &H_{cl}^{\mathrm{CEAM}}\left(\phi^*,\phi\right) \\ &= \sum_\alpha h_{\alpha\alpha}|\phi_\alpha|^2 + \sum_{\substack{\alpha,\beta \\ \alpha\neq\beta}} U_{\alpha\beta}|\phi_\alpha|^2|\phi_\beta|^2 + \sum_{\substack{\alpha,\beta \\ \alpha\neq\beta}} h_{\alpha\beta}\phi_\alpha^*\phi_\beta \\ &\quad \times \sqrt{(1-|\phi_\alpha|^2)(1-|\phi_\beta|^2)}\prod_j^{\alpha,\beta}\left(1-2|\phi_j|^2\right), \end{aligned} \tag{24}$$

in terms of the, now *restricted*, variables ϕ_α with $|\phi_\alpha|^2 \leq 1$.

In Eq. (22), the factors $1-2\mu_j\phi_j$ are a consequence of the anticommutativity of the creation and annihilation operators (and the Grassmannians) and thus account for the antisymmetry of the fermions under particle exchange. Consider for example the following two processes for the scattering of two particles in the states 1 and 2 into the states 2 and 3: in the first process, the particle in state 1 is scattered into state 3, with the second particle staying in state 2, while in the second one the particle in state 2 is scattered into state 3 and the particle in state 1 is scattered into state 2. These two processes are the same up to an exchange of the two particles. Therefore, these two processes have to yield the same contribution, but with a different sign. On the other hand, if state 2 is empty, while a particle is scattered from state 1 to state 3, there is no corresponding process resulting from an odd number of exchanges of particles, and thus, the contribution has always to be the same. In general, a process where a particle is scattered from state α to state β with $|\alpha-\beta| > 1$, has to be multiplied by a factor of -1 for each occupied state j between α and β . However, classically the occupations are not restricted to 0 and 1, but can be any number, such that one ends up with a factor interpolating between the two extreme values $+1$ for the case without a particle in state j and -1 for the case where state j is occupied. Furthermore, the exponential in the non-diagonal part of the single-particle term accounts for the Pauli principle by the exponential suppression of processes, which lead to an enhanced number of particles within one single-particle state.

A (certainly not complete) list of further possible classical Hamiltonians corresponding to the quantum Hamiltonian (21) can be found in Appendix 3.

It is furthermore instructive to see how our approach treats the extreme case of a *single* electron, $N = 1$, where the state space is spanned by two discrete states and anticommutation of the fermionic fields does not play a role. In this situation, our results can be directly compared with existing exact mappings between systems with $n = 2$ discrete states and a quantum top with total angular momentum s such that $n = (2s+1)/2$. In the Chemical Physics community, these so-called Meyer–Miller–Stock–Thoss (MMST) methods [36, 41, 44, 52] have been successfully used to describe non-adiabatic transitions of the nuclear dynamics between two potential surfaces corresponding to two discrete many-body states of the electrons. The MMST method maps the dynamics of a two-level system into the problem of a spinning particle, which can be in turn mapped into a set of harmonic oscillators by means of the Schwinger representation of angular momentum (see [44]). In this way, a classical picture for two-level systems is obtained, as a basis for standard (continuous) semiclassical approaches.

Our result for the classical limit of a single electron, included in Eq. (23), appears naturally within the MMST approach as an approximate version of the Holstein-Primakoff transformation, see [44] for details and [21] for an application to spin transport. As it is also shown there, this classical limit, however, gives unsatisfactory results

when used as starting point of a semiclassical calculation of the time evolution of quantum observables. This apparent drawback is fully resolved when taking into account, as shown in detail here, that the semiclassical limit where our result holds is defined by $N \to \infty$. Therefore, the application of our methods to the limiting case $N = 1$ is expected to poorly compare with exact quantum mechanical results. However, the main motivation of the present work is to deal semiclassically with anticommuting variables, not with few discrete degrees of freedom as in [44].

3.2 Comparison with CEAM and Klauder's approach

Miller's heuristic approach can actually be verified by extracting the classical Hamiltonian from another path integral representation. This is by extending the *b*-fermionic states introduced by Klauder in [35],

$$|b\rangle = \sqrt{1 - |b|^2}|0\rangle + b|1\rangle, \tag{25}$$

to the case of multiple single-particle states and define (see also [53])

$$|\mathbf{b}\rangle = \prod_j \left(\sqrt{1 - |b_j|^2}\hat{1} + b_j \hat{c}_j^\dagger\right)|0\rangle. \tag{26}$$

These states define an overcomplete basis for the fermionic Hilbert space, as they form the identity

$$\left(\prod_j \int_{\mathbb{D}} \frac{\mathrm{d}b_j^{(m)}}{\pi}\right)|\mathbf{b}\rangle\langle\mathbf{b}| = \hat{1} \tag{27}$$

where $\mathbb{D}$ denotes the unit disk in the complex plane, and therefore can be used to construct a path integral representation of the propagator in terms of paths $\mathbf{b}(t)$ in the space of commuting variables $\mathbf{b}$.

The steps of the derivation of the path integral in this basis correspond to those one follows to construct the fermionic path integral using coherent states [29, 35]. After reaching a form where the classical Hamiltonian can be read off from an action functional giving the phase of the quantum propagator, we obtain

$$H_{cl}^{\text{Klauder}}(\mathbf{b}^*, \mathbf{b}) = \left\langle \mathbf{b}\middle|\hat{H}\middle|\mathbf{b}\right\rangle. \tag{28}$$

A short calculation finally shows that the classical Hamiltonian (28) obtained using Klauder's representation is equal to Miller's, Eq. (24), i.e.,

$$H_{cl}^{\text{Klauder}}(\mathbf{b}^*, \mathbf{b}) = H_{cl}^{\text{CEAM}}(\mathbf{b}^*, \mathbf{b}). \tag{29}$$

thus providing a rigorous construction of the classical limit of the approach by Miller and coworkers [37].

In principle, having at hand a classical Hamiltonian as the one in Eq. (24), a semiclassical analysis of the path integral in *b*-representation along the lines presented bellow can be carried out. The first step is to consider the classical equations of motion

$$i\hbar\frac{d}{dt}\mathbf{b}(t) = \frac{\partial}{\partial \mathbf{b}^*}H_{cl}^{\text{CEAM}}(\mathbf{b}^*, \mathbf{b}), \tag{30}$$

which can be canonically transformed into

$$i\hbar\frac{d}{dt}n_j(t) = \frac{\partial}{\partial\theta_j}H_{cl}^{\text{CEAM}}(\mathbf{b}^*, \mathbf{b})\Big|_{b=\sqrt{n}\exp(i\theta)} \tag{31}$$

$$i\hbar\frac{d}{dt}\theta_j(t) = -\frac{\partial}{\partial n_j}H_{cl}^{\text{CEAM}}(\mathbf{b}^*, \mathbf{b})\Big|_{b=\sqrt{n}\exp(i\theta)}. \tag{32}$$

Without loss of generality, we consider the many-body Hamiltonian (21). Inspection of the associated equations of motion readily shows that the classical occupations $n_j = |b_j|^2$ evolve in time only through the terms that depend on the phases θ_j. Here is where the classical limit $H_{cl}^{\text{CEAM}}(\mathbf{b}^*, \mathbf{b})$ is problematic: due to the presence of the "Pauli" factors $\sqrt{n(1-n)}$ in Eq. (24) we trivially obtain

$$\frac{d}{dt}n_j(t)\Big|_{n=0 \text{ or } 1} = 0. \tag{33}$$

Therefore, the classical phase-space manifolds associated with the physical Fock states, which are defined by precisely the condition $n = 0$ or 1, do not evolve in time and there is no way to connect the quantum and classical dynamics, neither at the quasi-classical, nor at the semiclassical level. Remarkably, the classical limit as given for example in Eq. (22) circumvents this problem by allowing arbitrarily high classical occupation numbers, but penalizing them in a smooth (but exponentially strong) manner.

It is important to stress that there is no reason why classical occupations must be bounded, exactly as there is no reason why they have to take only integer values. In both cases, we are apparently violating what is just a classical picture of the fermionic degrees of freedom. However, fermionic fields are essentially non-classical objects and we are satisfied with being able to *define* a consistent classical limit by pure formal manipulations. Adopting this pragmatical point of view of defining the classical limit formally through the exact path integral, the fields ϕ_α in Eq. (23) do not need to fit our expectations on how the classical limit should look like. All that we ask them for is to correctly describe the propagation between physical Fock states.

4 Semiclassical approximation

The reason for the semiclassical approach to any quantum system to be rooted in the path integral formulation is that

it accomplishes simultaneously three major goals. First, it allows us to identify the classical limit of the theory. Second, it serves as the starting point of a systematic stationary phase analysis that eventually leads to the semiclassical propagator. Third, *it is in the structure of the action functional where* $\hbar_{\rm eff}$ *can be identified*. The effective Planck constant is not only the dimensionless parameter that defines the classical limit $\hbar_{\rm eff} \to 0$, but also the small parameter that makes the whole semiclassical approach valid. It appears non-perturbatively, if the characteristic path integral representation of the propagator,

$$K \sim \int \mathscr{D}[\cdot] \mathrm{e}^{R[\cdot]/\hbar}, \tag{34}$$

is written in terms of a dimensionless action $\tilde{R}$,

$$K \sim \int \mathscr{D}[\cdot] \mathrm{e}^{\tilde{R}[\cdot]/\hbar_{\rm eff}}. \tag{35}$$

Inspection of the exponents in Eq. (19) shows that Planck's constant $\hbar$ actually plays a minor role in our case. Clearly, $\hbar$ can be absorbed simply by a redefinition of the parameters of the Hamiltonian (note that this is not the case in the usual phase-space path integral). In order to identify $\hbar_{\rm eff}$, we rescale all the fields in such a way that the exponent appearing in Eq. (19) takes the form $\tilde{R}/\hbar_{\rm eff}$ with $\tilde{R} = \mathscr{O}(1)$. Following this recipe, Eq. (19) leads to

$$\hbar_{\rm eff} = N^{-1}, \tag{36}$$

showing that in the present approach *the classical limit corresponds to the limit of large number of particles*. In the following, we complete the stationary analysis of the exact propagator valid in this $N \gg 1$ limit.

In Eq. (19) all integrals, that can and should be carried out exactly, are already performed, except for the integration over the initial phase of the first occupied single-particle state. This integration has to be done exactly because of the $U(1)$ gauge symmetry, i.e., the freedom to multiply the wave function by an arbitrary global phase. In order to perform this integration, one first has to substitute the integrations over the real and imaginary part of $\phi_j^{(m)}$ by those over its modulus squared $J_j^{(m)}$ and phase $\varphi_j^{(m)}$ and then has to substitute the latter by $\theta_j^{(m)} - \theta_{j_1}^{(0)}$, where j_1 denotes the first initially occupied single-particle state,

$$j_1 = \min\left\{ j \in \{1, 2, \ldots\} : n_j^{(i)} = 1 \right\}. \tag{37}$$

These substitutions can be summarized as

$$\phi_j^{(m)} = \sqrt{J_j^{(m)}} \exp\left[\mathrm{i}\left(\theta_j^{(m)} - \theta_{j_1}^{(0)} \right) \right], \tag{38}$$

for all j and $m \geq 1$, while for $m = 0$,

$$\phi_j^{(0)} = n_j^{(i)} \exp\left[\mathrm{i}\left(\theta_j^{(0)} - \theta_{j_1}^{(0)} \right) \right] \qquad \text{if } j \neq j_1, \tag{39}$$

$$\phi_{j_1}^{(0)} = \exp\left(\mathrm{i}\theta_{j_1}^{(0)} \right). \tag{40}$$

After these substitutions, it is easy to see that the remaining dependence of the path integral on the global phase $\theta_{j_1}^{(0)}$ is given by $\exp[\mathrm{i}(N_f - N_i)\theta_{j_1}^{(0)}]$, with $N_{i/f} = \sum_j n_j^{(i/f)}$ being the initial, respectively, final total number of particles. Therefore, the integration over the global phase simply yields a factor $2\pi\delta_{N_f,N_i}$, which accounts for the conservation of the total particle number. The remaining integrals over $J_j^{(m)}$ and $\theta_j^{(m)}$ are then performed in stationary phase approximation, where (similar to the derivation of Stirling's approximation) for consistency and in order to include the behavior of the integrand especially for small occupations correctly, it is important to include the factors

$$\sqrt{J_j^{(m)}} = \exp\left[\log\left(J_j^{(m)} \right)/2 \right] \tag{41}$$

in the stationarity analysis. For intermediate times, $1 \leq m < M$, the stationarity conditions for $J_j^{(m)}$ and $\theta_j^{(m)}$ can be combined to the conditions

$$\mathrm{i}\hbar\left(\phi_j^{(m)} - \phi_j^{(m-1)} \right) = \tau \frac{\partial H_{cl}\left(\phi^{(m)*}, \phi^{(m-1)} \right)}{\partial \phi_j^{(m)*}}, \tag{42}$$

$$-\mathrm{i}\hbar\left(\phi_j^{(m+1)*} - \phi_j^{(m)*} \right) = \tau \frac{\partial H_{cl}\left(\phi^{(m+1)*}, \phi^{(m)} \right)}{\partial \phi_j^{(m)}}. \tag{43}$$

In the same way, the conditions for $m = M$ can be written in the form of Eq. (42) with $m = M$ as well as the boundary condition

$$J_j^{(M)} = n_j^{(f)}. \tag{44}$$

Note that a linear combination of the stationarity conditions for $\theta_j^{(M)}$ and $J_j^{(M)}$ is required to get the stationary phase conditions in this form.

Since the integration over the initial phase is performed only for occupied states, and the amplitude of $\phi_j^{(0)}$ is equal to the initial occupation of the site $n_j^{(i)}$, the stationarity condition for $\theta_j^{(0)}$ yields Eq. (43) with $m = 0$. When finally taking the continuous limit $\tau \to 0$, these conditions result in the equations of motion

$$\mathrm{i}\hbar\dot{\phi}(t) = \frac{\partial H_{cl}(\phi^*(t), \phi(t))}{\partial \phi^*(t)}, \tag{45}$$

$$-\mathrm{i}\hbar\dot{\phi}^*(t) = \frac{\partial H_{cl}(\phi^*(t), \phi(t))}{\partial \phi(t)}, \tag{46}$$

along with the boundary conditions

$$\left|\phi_j(0)\right|^2 = n_j^{(i)}, \quad \left|\phi_j(t_f)\right|^2 = n_j^{(f)} \tag{47}$$

with $\phi_{j_1}(0) = 1$. It is important to note that the equations of motion (45) and (46) are complex conjugates of each other, such that for J single-particle states we get J complex (or correspondingly $2J$ real) equations of motion with $2J$ real boundary conditions. Therefore one can always find at least one solution without the complexification necessary for the bosonic coherent state propagator [33, 54]. Therefore, the classical Hamiltonian and action will also be real.

We also point out the key difference in the role of the boundary conditions in Eq. (47) when compared with the derivation of the classical limit from the path integral in the standard first-quantized case. In the latter case, *boundary conditions are imposed at the level of the path integral* and therefore are not subject to the stationary phase conditions. Contrary to the bosonic case where this observation remains true [34], here again we encounter that the classical limit of fermionic fields displays counter-intuitive features: the boundary conditions (47) that allow for multiple solutions of (45, 46) are themselves obtained from a stationary phase argument, and the corresponding quantum fluctuations must be considered at the same footing as the fluctuations around the classical solutions.

Evaluating the exponent of the path integral along the stationary point (including all additional phase factors originating from the boundary terms $m = 1, M$) then yields the classical action

$$R_\gamma\left(\mathbf{n}^{(f)}, \mathbf{n}^{(i)}; t_f\right) = \int_0^{t_f} \mathrm{d}t\left[\hbar\boldsymbol{\theta}(t)\cdot\dot{\mathbf{J}}(t) - H_{cl}\left(\phi^*(t), \phi(t)\right)\right], \quad (48)$$

of the mean-field trajectories defined by the equations of motion (45) and the boundary conditions (47). In Eq. (48) the real functions $\boldsymbol{\theta}(t)$ and $\mathbf{J}(t)$ are defined through

$$\phi_j(t) = \sqrt{J_j(t)}\exp\left(\mathrm{i}\theta_j(t)\right). \quad (49)$$

It is worth to note, that the equations of motion (45, 46) in these variables can also be written as the real equations

$$\dot{\mathbf{J}}(t) = \frac{2}{\hbar}\frac{\partial H_{cl}(\phi^*(t), \phi(t))}{\partial\boldsymbol{\theta}(t)}, \quad (50)$$

$$\dot{\boldsymbol{\theta}}(t) = -\frac{2}{\hbar}\frac{\partial H_{cl}(\phi^*(t), \phi(t))}{\partial\mathbf{J}(t)}, \quad (51)$$

where $\phi_j^*(t)$ and $\phi_j(t)$ should be understood as functions of $J_j(t)$ and $\theta_j(t)$ according to Eq. (49). Thus, the classical trajectory lives on a symplectic manifold in phase space, which is here defined as $\{(\mathbf{J}, \boldsymbol{\theta}) : J_{j=1,2,\ldots} \in [0, \infty), \theta_{j=1,2,\ldots} \in [0, 2\pi)\}$. Moreover, the theory of canonical transformations [55] can be applied to show that the Poincaré-Cartan 1-form

$$\boldsymbol{\theta}\cdot\mathrm{d}\mathbf{J} - H\mathrm{d}t \quad (52)$$

is invariant under canonical transformations.

The derivatives of the action can be found by applying the equations of motion to the integrand to read

$$\frac{\partial R_\gamma\left(\mathbf{n}^{(f)}, \mathbf{n}^{(i)}; t_f\right)}{\partial\mathbf{n}^{(i)}} = -\hbar\boldsymbol{\theta}(0), \quad (53)$$

$$\frac{\partial R_\gamma\left(\mathbf{n}^{(f)}, \mathbf{n}^{(i)}; t_f\right)}{\partial\mathbf{n}^{(f)}} = \hbar\boldsymbol{\theta}(t_f), \quad (54)$$

$$\frac{\partial R_\gamma\left(\mathbf{n}^{(f)}, \mathbf{n}^{(i)}; t_f\right)}{\partial t_f} = -E_\gamma, \quad (55)$$

where $E_\gamma = H_{cl}(\phi^*(0), \phi(0))$ is the energy of the trajectory.

Finally, the propagator Eq. (16) reads

$$K^{\mathrm{sc}}\left(\mathbf{n}^{(f)}, \mathbf{n}^{(i)}; t_f\right) = \sum_\gamma \mathscr{A}_\gamma \exp\left[\frac{\mathrm{i}}{\hbar}R_\gamma\left(\mathbf{n}^{(f)}, \mathbf{n}^{(i)}; t_f\right)\right], \quad (56)$$

where the sum runs over all "classical paths" γ which satisfy the equations of motion (45) and the boundary conditions (47), while $\mathscr{A}_\gamma$ is given by the still pending integrations over the second variation of the paths.

As is shown in Appendix 2, $\mathscr{A}_\gamma$ can be written as

$$\mathscr{A}_\gamma = \frac{1}{\sqrt{2\pi}^{N-1}}\exp\left\{\frac{\mathrm{i}}{2\hbar}\int_0^{t_f}\mathrm{d}t\mathrm{Tr}\left[\frac{\partial^2 H_{cl}}{\partial\phi(t)^2}\mathbf{X}(t)\right]\right\}$$
$$\det\left\{\mathbf{I}_N + \exp\left[-2\mathrm{i}\mathrm{diag}\left(\mathbf{P}_f\boldsymbol{\theta}(t_f)\right)\right]\mathbf{P}_f\mathbf{X}(t_f)\mathbf{P}_f^{\mathrm{T}}\right\}^{-\frac{1}{2}}, \quad (57)$$

with $N = N_i = N_f$ being the total particle number and $\mathbf{I}_N$ the $N \times N$ unit matrix. Moreover, $\mathbf{P}_f$ is the matrix of the projector onto the subspace of the states which are occupied at final time, such that e.g.

$$\mathbf{P}_f\mathbf{n}^{(f)} = (\underbrace{1, \ldots, 1}_{N})^{\mathrm{T}}. \quad (58)$$

For later reference, we also define $\mathbf{P}_i$, which is defined in the same way as $\mathbf{P}_f$, but selecting the initially occupied single-particle states, as well as the complements $\bar{\mathbf{P}}_{i/f}$ of $\mathbf{P}_{i/f}$. With these matrices, one can also define the (orthonormal) matrix

$$\mathbf{Q}_{i/f} = \begin{pmatrix}\bar{\mathbf{P}}_{i/f}\\ \mathbf{P}_{i/f}\end{pmatrix}, \quad (59)$$

shifting all components of a vector corresponding to an initially (finally) unoccupied single-particle state in front of all the others.

Finally, in Eq. (57) $\mathbf{X}(t)$ satisfies the differential equation

$$\dot{\mathbf{X}}(t) = \frac{\mathrm{i}}{\hbar}\frac{\partial^2 H_{cl}}{\partial\phi^*(t)^2} - \frac{\mathrm{i}}{\hbar}\frac{\partial^2 H_{cl}}{\partial\phi^*(t)\partial\phi(t)}\mathbf{X}(t)$$
$$-\frac{\mathrm{i}}{\hbar}\mathbf{X}(t)\frac{\partial^2 H_{cl}}{\partial\phi(t)\partial\phi^*(t)} + \frac{\mathrm{i}}{\hbar}\mathbf{X}(t)\frac{\partial^2 H_{cl}}{\partial\phi(t)^2}\mathbf{X}(t), \quad (60)$$

with initial condition

$$\mathbf{X}(0) = \mathbf{Q}_i^{\mathrm{T}} \begin{pmatrix} 0 & \\ & \exp\left[2\mathrm{i}\mathrm{diag}\left(\mathbf{P}_i'\boldsymbol{\theta}(0)\right)\right] \end{pmatrix} \mathbf{Q}_i. \tag{61}$$

The same differential equation, however with different initial conditions, was encountered previously in derivations of a semiclassical propagator for bosonic many-body systems in coherent state representation [33, 54]. The solutions given there indicate, how to find $\mathbf{X}(t)$: Consider a solution $\boldsymbol{\psi}(t)$ of the equations of motion with initial conditions $\mathbf{Y}$ and $\mathbf{W}$, whereby each pair (Y_j, W_j) are canonically conjugate variables. Possibilities for the choice of these pairs are e.g. $(\Re\psi_j(0), \Im\psi_j(0))$, where $\Re$ and $\Im$ denote the real and imaginary part, respectively, $(|\psi_j(0)|, \arg\psi_j(0))$ with $\arg\psi$ denoting the phase of ψ, or $(\psi_j(0), \psi_j^*(0))$. Then, the differential equation (60) is solved by the function

$$-\frac{\partial\boldsymbol{\psi}(t)}{\partial\mathbf{W}}\left(\frac{\partial\boldsymbol{\psi}^*(t)}{\partial\mathbf{W}}\right)^{-1}, \tag{62}$$

evaluated at the initial conditions corresponding to the trajectory γ.

Finally, in order to find the solution for $\mathbf{X}(t)$, the variables $\mathbf{Y}$ and $\mathbf{W}$ need to be chosen such that for $t = 0$, Eq. (62) also satisfies the initial condition (61), which yields

$$(Y_j, W_j) = \begin{cases} (\psi_j(0), \psi_j^*(0)), & \text{if } n_j^{(i)} = 0 \text{ or } j = j_1 \\ (n_j^{(i)}, \theta_j), & \text{else.} \end{cases} \tag{63}$$

Eventually, the semiclassical amplitude $\mathscr{A}_\gamma$ can be written as

$$\begin{aligned} \mathscr{A}_\gamma = & \sqrt{\det\left[\frac{1}{2\pi\mathrm{i}\hbar}\frac{\partial^2 R_\gamma}{\partial\left(\mathbf{P}_f'\mathbf{n}^{(f)}\right)\partial\left(\mathbf{P}_i'\mathbf{n}^{(i)}\right)}\right]} \\ & \times\sqrt{\det\mathbf{Q}_f\mathbf{Q}_i}\exp\left(\frac{\mathrm{i}}{2\hbar}\int_0^{t_f}\mathrm{d}t\mathrm{Tr}\frac{\partial^2 H_{cl}}{\partial\phi^*\partial\phi}\right) \\ & \times\exp\left(\frac{\mathrm{i}}{2}\sum_{j:n_j^{(f)}=1}\theta_j(t_f) - \frac{\mathrm{i}}{2}\sum_{j:n_j^{(i)}=1}\theta_j(0)\right) \\ & \times\det\left(\mathbf{A}-\mathbf{B}\mathbf{C}^{-1}\mathbf{D}\right)^{-\frac{1}{2}}. \end{aligned} \tag{64}$$

with $\mathbf{P}_i'$ and $\mathbf{P}_f'$ being the matrices resulting from $\mathbf{P}_i$ and $\mathbf{P}_f$, respectively, by removing the first line. The determinant consisting of the matrices

$$\mathbf{A} = \frac{\partial\left(\bar{\mathbf{P}}_f\phi^*(t_f), J_{\min\left\{j\in\{1,2,\ldots\}:n_j^{(f)}=1\right\}}(t_f)\right)}{\partial\left(\bar{\mathbf{P}}_i'\phi^*(0)\right)}, \tag{65}$$

$$\mathbf{B} = \frac{\partial\left(\bar{\mathbf{P}}_f\phi^*(t_f), J_{\min\left\{j\in\{1,2,\ldots\}:n_j^{(f)}=1\right\}}(t_f)\right)}{\partial\left(\mathbf{P}_i'\boldsymbol{\theta}(0)\right)}, \tag{66}$$

$$\mathbf{C} = \frac{\partial\left(\mathbf{P}_f'\mathbf{J}(t_f)\right)}{\partial\left(\mathbf{P}_i'\boldsymbol{\theta}(0)\right)}, \tag{67}$$

$$\mathbf{D} = \frac{\partial\left(\mathbf{P}_f'\mathbf{J}(t_f)\right)}{\partial\left(\bar{\mathbf{P}}_i'\phi^*(0)\right)}. \tag{68}$$

accounts for the vacuum fluctuations that have been treated exactly. Note that in Eq. (64), the Solari-Kochetov extra-phase

$$\exp\left(\frac{\mathrm{i}}{2\hbar}\int_0^{t_f}\mathrm{d}t\mathrm{Tr}\frac{\partial^2 H_{cl}}{\partial\phi^*\partial\phi}\right) \tag{69}$$

typically arises in a semiclassical approximation of the propagator in coherent state representation [33, 56–58], while in the standard (first quantized) van-Vleck–Gutzwiller propagator [5], this phase is absent, due to the Weyl (symmetric) ordering of the Hamiltonian with respect to position and momentum operators. For Bosons, the Solari-Kochetov phase can be absorbed in the action by replacing the bosonic creation and annihilation operators according to $\hat{a}_j^\dagger\hat{a}_{j'} \to (\hat{a}_j^\dagger\hat{a}_{j'} + \hat{a}_{j'}\hat{a}_j^\dagger)/2$ [33], which corresponds to Weyl ordering of the quantum Hamiltonian. In the same way, for the propagator in spin coherent states, this phase is absent in Weyl ordering [59]. However, this vanishing of the Solari-Kochetov phase in these cases is due to the fact that the classical Hamiltonian is obtained out of the quantum one by the simple replacements $\hat{a}_j^\dagger \to \phi_j^*$ and $\hat{a}_j \to \phi_j$, which is not valid here. Therefore, it seems that here this phase can not be eliminated by changing the chosen ordering of the fermionic creation and annihilation operators.

Due to their definition Eq. (59), the determinants $\det\mathbf{Q}_{i/f}$ depend only on the choice of the initial and final occupations and accept only the values ± 1. Note that this sign also depends on the definition of the Fock states, while the product of both depends only on the relative changes between the initial and final state and therefore is independent of the exact choice of ordering of the single-particle states.

It is important to notice that in Eq. (64) the determinant $\det(\mathbf{A}-\mathbf{B}\mathbf{C}^{-1}\mathbf{D})$ depends only on the derivatives of the values of the trajectory at final time with respect to the initial conditions and should, therefore, be possible to calculate in an actual application. Moreover, we expect that this determinant is just the product of the exponentials of the final and initial phases of the final unoccupied states, which can be set to zero. Thus, we assume this determinant to be equal to one. However, up to now, we did not succeed in proofing this conjecture rigorously and therefore, we will keep this determinant in the following.

5 Transition probability

5.1 General semiclassical treatment

Knowing the propagator enables us, in principle, to calculate the quantum probability to measure the Fock state $\mathbf{n}^{(f)}$ after preparing the system of spin-1/2 particles in the initial Fock state $\mathbf{n}^{(i)}$ and letting it evolve for some time t. Computing this probability is usually non-trivial, since the single-particle states can on the one hand be chosen arbitrarily, and may thus not necessarily be eigenstates of the single-particle Hamiltonian, and on the other hand, interactions in general induce a coupling between different single-particle states. This probability is given by the modulus square of the overlap between the time evolved state and $\left|\mathbf{n}^{(f)}\right\rangle$,

$$P\left(\mathbf{n}^{(f)},\mathbf{n}^{(i)};t_f\right)=\left|\left\langle\mathbf{n}^{(f)}\middle|\hat{K}\left(t_f\right)\middle|\mathbf{n}^{(i)}\right\rangle\right|^2. \tag{70}$$

Using the semiclassical approximation (56), it is given by a double sum over trajectories,

$$P\left(\mathbf{n}^{(f)},\mathbf{n}^{(i)};t_f\right)\approx\sum_{\gamma,\gamma'}\mathscr{A}_\gamma\mathscr{A}^*_{\gamma'}\exp\left[\frac{\mathrm{i}}{\hbar}\left(R_\gamma-R_{\gamma'}\right)\right]. \tag{71}$$

Upon applying an energy or disorder average, the action difference gives rise to huge oscillations, such that most contributions to the averaged double sum will cancel, except if the paths γ and γ' are correlated. The types of trajectory pairs, which we will consider in the following are depicted in Fig. 1. The simplest type of correlation arises for $\gamma=\gamma'$. This is known as the diagonal approximation [60]. The second derivatives of the action with respect to the initial and final Fock state in the prefactor can then be used to transform the sum over trajectories into an integration over the initial phases. Then, the diagonal approximation yields,

$$P_{cl}\left(\mathbf{n}^{(f)},\mathbf{n}^{(i)};t_f\right)=\int_0^{2\pi}\mathrm{d}^{N-1}\theta^{(i)}\,\det\left(\mathbf{A}-\mathbf{B}\mathbf{C}^{-1}\mathbf{D}\right)^{-1}\times\delta\left(\left|\phi(t_f)\right|^2-\mathbf{n}^{(f)}\right), \tag{72}$$

which we will refer to as classical probability. Here, $\phi(t)$ is the solution of the equations of motion Eq. (45) with the initial condition $\phi_j(0)=\sqrt{n_j^{(i)}}\exp\left(\mathrm{i}\theta_j^{(i)}\right)$. It is worth to notice that the exact treatment of the vacuum fluctuations gives rise to a renormalization of the transition probability by the additional factor $\det\left(\mathbf{A}-\mathbf{B}\mathbf{C}^{-1}\mathbf{D}\right)^{-1}$.

Further pairs of correlated trajectories are those given by γ and its time reverse, $\gamma'=\mathscr{T}\gamma$. However, the time reverse of a trajectory exists only if the system is time reversal symmetric. Moreover, the initial and final occupations, respectively, of both trajectories in the double sum

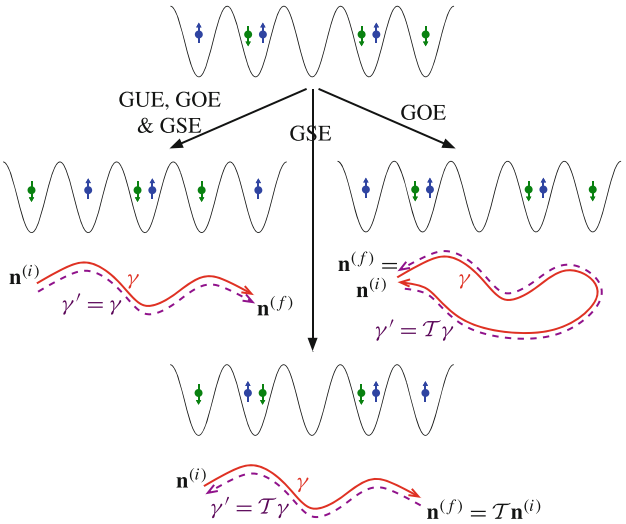

Fig. 1 The quantum transition in a system of spin-1/2 particles in the semiclassical limit. A trajectory γ is paired with a partner trajectory γ', where γ' can be either γ itself, or its time reverse. The annotations at the arrows indicate the symmetry class required for the corresponding pairing to be present

of Eq. (71) have to be the same. On the other hand, if γ has initial occupations $\mathbf{n}^{(i)}$ and final occupations $\mathbf{n}^{(f)}$, the initial occupations of its time reverse are given by the time reverse of $\mathbf{n}^{(f)}$ and the final ones by the time reverse of $\mathbf{n}^{(i)}$. Therefore, in order to pair γ with its time reverse, we need time reversal symmetry and also the final Fock state has to be the time reverse of the initial one. To this end, one has to replace the sum over trajectories from $\mathbf{n}^{(i)}$ to $\mathbf{n}^{(f)}$ by a sum over trajectories ending at the Fock state $\mathscr{T}\mathbf{n}^{(i)}$ originating from time reversing the initial one. To this end, the actions in the exponential need to be expanded in the final Fock state around $\mathscr{T}\mathbf{n}^{(i)}$ up to linear order, while the prefactor is assumed to vary only very slightly with $\mathbf{n}^{(f)}$, such that it can be simply replaced by $\mathscr{T}\mathbf{n}^{(i)}$. For pairs $\gamma'=\mathscr{T}\gamma$ this procedure then gives the contribution

$$\sum_\gamma\mathscr{A}_\gamma\mathscr{A}^*_{\mathscr{T}\gamma}\exp\left(\frac{\mathrm{i}}{\hbar}\Delta R\right)\times\exp\left[\mathrm{i}\left(\boldsymbol{\theta}^{(\gamma)}(t_f)-\boldsymbol{\theta}^{(\mathscr{T}\gamma)}(t_f)\right)\cdot\left(\mathbf{n}^{(f)}-\mathscr{T}\mathbf{n}^{(i)}\right)\right], \tag{73}$$

with the difference $\Delta R=R_\gamma-R_{\mathscr{T}\gamma}$ in the actions of γ and $\mathscr{T}\gamma$. Since for time reversal symmetric systems, the energy of a trajectory and its time reverse is the same, we easily get

$$\Delta R=\hbar\int_0^{t_f}\mathrm{d}t\left(\boldsymbol{\theta}^{(\gamma)}\cdot\dot{\mathbf{j}}^{(\gamma)}-\boldsymbol{\theta}^{(\mathscr{T}\gamma)}\cdot\dot{\mathbf{j}}^{(\mathscr{T}\gamma)}\right). \tag{74}$$

In the next steps, we assume—in accordance with the cases considered below—that the difference ΔR, is independent

of the trajectory. This is usually the case, since the second part of the integral in the action difference can be related with the first one by making use of the nature of the time reversal operation. However, as we will see later, ΔR does not vanish in general. Moreover, we can savely assume that $\boldsymbol{\theta}^{(\mathcal{T}\gamma)}(t_f)$ depends on the initial phases of γ, only (and through them on the initial Fock state).

Upon disorder average, the phases $\theta_j^{(\gamma)}(t_f)$ behave, for chaotic systems, like linearly distributed random variables between 0 and 2π. Thus, treating them as random variables and performing the average, yields a $\delta_{\mathbf{n}^{(f)},\mathcal{T}\mathbf{n}^{(i)}}$, such that one gets after utilizing the second derivative of the action again

$$P_{cl}\left(\mathbf{n}^{(f)},\mathbf{n}^{(i)};t_f\right)\delta_{\mathbf{n}^{(f)},\mathcal{T}\mathbf{n}^{(i)}}\exp\left(\frac{\mathrm{i}}{\hbar}\Delta R\right). \tag{75}$$

The action difference ΔR strongly depends on whether the system is diagonal in spin space or not.

5.2 Systems diagonal in spin space

If the system is diagonal in spin space, i.e., the Hamiltonian does not consist of terms giving rise to spin-flips, the time reversal operation amounts to a complex conjugation only, and therefore

$$\mathcal{T}\mathbf{n}^{(i)}=\mathbf{n}^{(i)}. \tag{76}$$

It also implies that, on the classical level, the time reverse of $\phi(t)$ is given by $\phi^*(t_f-t)$. With this information, it is easy to prove that time-reversed paths have the same action, $\Delta R=0$. Thus, in semiclassical approximation, the averaged transition probability for a spin-diagonal system is given by

$$P\left(\mathbf{n}^{(f)},\mathbf{n}^{(i)};t_f\right)\approx P_{cl}\left(\mathbf{n}^{(f)},\mathbf{n}^{(i)};t_f\right)\left(1+\delta_{\mathbf{n}^{(f)},\mathbf{n}^{(i)}}\right). \tag{77}$$

This is, apart from the renormalization of the classical transition probability due to the exact treatment of the vacuum (see Eq. (72)), exactly the same result found previously for bosonic, spinless systems [34].

5.3 Systems non-diagonal in spin space

If the system's Hamiltonian is non-diagonal in spin space, the time reversal operation is not just complex conjugation, but also demands an exchange of the spin-up and spin-down components while at the same time introducing a relative minus sign between them,

$$\hat{T}=\left[\prod_j\left(-\mathrm{i}\hat{\sigma}_{j,y}\right)\right]\hat{K}. \tag{78}$$

Here $\hat{\sigma}_{j,y}$ is the y-Pauli matrix for the j-th state and $\hat{K}$ denotes complex conjugation. Important examples of systems with such time reversal operations are for instance systems with a Rashba spin-orbit coupling [61], which is of key importance in semiconductor spintronics, but more recently has also been realized using ultra-cold atoms [62].

On the classical level, this means that the time reversal of $\phi=(\phi_\uparrow,\phi_\downarrow)^{\mathrm{T}}$, where $\phi_{\uparrow(\downarrow)}$ is the vector containing all spin-up (spin-down) components of ϕ, is given by

$$\mathcal{T}\begin{pmatrix}\phi_\uparrow(t)\\ \phi_\downarrow(t)\end{pmatrix}=\begin{pmatrix}-\phi_\downarrow^*(t_f-t)\\ \phi_\uparrow^*(t_f-t)\end{pmatrix}, \tag{79}$$

and therefore also

$$\mathcal{T}\mathbf{n}^{(i)}=\mathcal{T}\begin{pmatrix}\mathbf{n}_\uparrow^{(i)}\\ \mathbf{n}_\downarrow^{(i)}\end{pmatrix}=\begin{pmatrix}\mathbf{n}_\downarrow^{(i)}\\ \mathbf{n}_\uparrow^{(i)}\end{pmatrix}. \tag{80}$$

For the action difference, this yields

$$\Delta R=\pi\hbar\sum_j\left[\left(\mathcal{T}\mathbf{n}^{(i)}\right)_{j,\uparrow}-n_{j,\uparrow}^{(i)}\right]=\pi\hbar\left(N_\downarrow-N_\uparrow\right), \tag{81}$$

where $N_{\uparrow(\downarrow)}$ is the total number of spin-up (spin-down) particles in the initial state.

Thus, invoking the widely used nomenclature of the random matrix symmetry classes and quantum chaos [6], one finally finds for the averaged transition probability in semiclassical approximation

$$P\left(\mathbf{n}^{(f)},\mathbf{n}^{(i)};t_f\right)=P^{(cl)}\left(\mathbf{n}^{(f)},\mathbf{n}^{(i)};t_f\right)\begin{cases}1 & ,\text{GUE}\\ \left[1+\delta_{\mathbf{n}^{(f)},\mathbf{n}^{(i)}}\right] & ,\text{GOE}\\ \left[1+(-1)^N\delta_{\mathbf{n}_\downarrow^{(f)},\mathbf{n}_\uparrow^{(i)}}\delta_{\mathbf{n}_\downarrow^{(f)},\mathbf{n}_\uparrow^{(i)}}\right] & ,\text{GSE.}\end{cases} \tag{82}$$

Here, GUE (Gaussian Unitary Ensemble) means that the average runs over systems without time reversal symmetry, while for GOE (Gaussian Orthogonal Ensemble) and GSE (Gaussian Symplectic Ensemble) the average is over time reversal invariant spin-1/2 systems, which are diagonal and non-diagonal in spin space, respectively. This result and in particular the origin of the deltas is illustrated in Fig. 1.

It is important to note that, the probability to find $\mathbf{n}^{(f)}=\mathcal{T}\mathbf{n}^{(i)}$ is zero on average for the GSE case, if N is odd. However, the transition probability is a strictly positive quantity. Therefore, in order to become zero on average, it has to be zero for each disorder realization. In other words, for a time reversal symmetric system, which is non-diagonal in spin space, the transition from an initial Fock state to its spin reversed version is semiclassically prohibited,

$$\left\langle\hat{T}\mathbf{n}^{(i)}|\hat{K}\left(t_f\right)|\mathbf{n}^{(i)}\right\rangle=0 \tag{83}$$

for an odd total number of particles. This is consistent with

$$\left\langle\hat{T}\mathbf{n}|\hat{H}|\mathbf{n}\right\rangle=0. \tag{84}$$

Similar to the proof of Kramer's degeneracy [2], one can show that Eq. (84) implies that for an odd number of particles and a symplectic time reversal symmetry, the transition from a Fock state to its spin reversed version is exactly forbidden quantum mechanically.

On the other hand, if the total number of particles is even, and hence the total spin is integer, the transition probability is always enhanced by a factor of two compared to the classical one, if the final Fock state is the time-reversed version of the initial one.

6 Conclusions

We presented a rigorous derivation of fermionic path integrals representing quantum transition amplitudes in Fock space in terms of unrestricted, commuting complex fields. In the context of semiclassical approaches, we believe that this result represents an important improvement over previous approaches. First, we replace the anticommuting (Grassmann) variables, usually assumed to be the most natural representation of a fermionic path integral, by complex variables in the path integral. In this way, the propagator can be given a direct physical interpretation as a complex-valued amplitude. Second, the path integral is unrestricted (defined over the whole complex plane) and therefore avoids the complications due to the definition of path integrals in compact phase spaces.

Most notably, in the approach presented here, a Hamiltonian classical limit can be identified which leads to real actions and therefore explicit interference. After applying the stationary phase approximations to the path integral. In the semiclassical limit (of large particle number), we are able to derive as our major result a van Vleck–Gutzwiller type propagator for fermionic quantum fields.

In contrast to the approaches of [37, 39], here the semiclassical approximation as well as the classical limit is obtained from an exact path integral. However, there is still a freedom of choice for the classical Hamiltonian, which should be investigated further. Hence, we do not exclude the possibility, that by a certain choice, the classical limits of [37, 39] can be recovered. Moreover, it remains to be explored, which classical limit is best suited for calculations and simulations. This may actually even depend on the actual problem at hand.

In Sect. 5, we applied our results to the calculation of transition probabilities in the fermionic Fock space, and found a rich dependence of many-body interference effects on the universality class of the system. For systems with spin-orbit interaction that belong to the symplectic class, our results predict the exact cancelation of the transition probability between time-reversed many-body states, if the total number of particles is odd. This prediction that can be independently demonstrated to be a consequence of Kramer's degeneracy, is a very stringent test for the correctness of our approach. If the total particle number is even, however, the same transition is not only allowed, but its probability is enhanced by a factor of two compared to the transitions to other states. For systems without spin-flip mechanisms, we recover the coherent backscattering previously found for bosons [34]. Upon destroying time reversal symmetry all these effects vanish, and the transition probability profile can be assumed to be more or less constant for all Fock states.

Finally, we would like to note that, although the path integral Eq. (19) is restricted to the particle picture, i.e., to the case that a particle is defined through an occupied single-particle state, it is also possible to construct a path integral in the hole picture (for more details see "Appendix 3.2"), where a particle is defined as an unoccupied single-particle state.

The *major* principle restriction of applicability of our approach is that the number of fermions $N \gg 1$ should be large enough (our experience in the bosonic case indicates that $N \sim 10$ is enough). Therefore, within this regime, electronic systems such as quantum dots, coupled discrete systems like spin chains modeled by Heisenberg or Ising type Hamiltonians, and molecular systems described by a discrete set of single-particle orbitals can be addressed. Still, then exist practical limitations of semiclassical approaches in concrete applications, related, e.g., to the solution of the shooting problem and the correct evaluation of amplitudes and Maslov indexes. We hope that our approach is still beneficial for the Chemical Physics community.

Finally, we remark that for treating emergent universal quantum fluctuations in mesoscopic systems we only need to verify that the classical limit displays chaotic behavior, a substantially easier task.

Further applications of the semiclassical methods along the lines presented here like the description of many-body spin echoes [63] are presently under investigation.

Acknowledgments We thank T. Guhr, P. Schlagheck, S. Essert and S. Smirnov for useful discussions. This work was financially supported by the Deutsche Forschungsgemeinschaft wihtin FOR 760 and SPP 1666.

Appendix 1: Derivation of the path integral

For simplicity, in this section, we assume a quantum hamiltonian given by

$$\hat{H} = \sum_{\alpha,\beta} h_{\alpha\beta} \hat{c}_\alpha^\dagger \hat{c}_\beta + \sum_{\substack{\alpha,\beta \\ \alpha \neq \beta}} U_{\alpha\beta} \hat{c}_\alpha^\dagger \hat{c}_\beta^\dagger \hat{c}_\beta \hat{c}_\alpha. \tag{85}$$

The result for a non-diagonal interaction $U_{\alpha\beta\gamma\nu}$, however, is given in Appendix 3 In order to get from Eq. (17) to the

complex path integral Eq. (19), the following two integrals with $j,j' \in \mathbb{N}_0$, will be inserted:

$$\int_0^{2\pi} \mathrm{d}\theta \int \mathrm{d}^2\phi \exp\left(-|\phi|^2 + \phi^* \mathrm{e}^{\mathrm{i}\theta} - \mathrm{i}j\theta\right)\phi^{j'} = 2\pi^2 \delta_{j,j'} \quad (86)$$

$$\int \mathrm{d}^2\phi \int \mathrm{d}^2\mu \exp\left(-|\phi|^2 - |\mu|^2 + \phi^*\mu\right)\phi^j \left(\mu^*\right)^{j'} = \pi^2 j! \delta_{j,j'}, \quad (87)$$

for the unoccupied ones, it is important to notice, that the term $\chi_j^{(0)\,*}\zeta_j^{(0)}$ does vanish when integrating over $\boldsymbol{\zeta}^{(0)}$. This is because of the properties of the Grassmann integrals Eq. (10) and the fact, that there is no $\zeta_j^{(0)\,*}$ for those components, for which $n_j^{(i)} = 0$.

The thus obtained expression is the starting point for an iterative insertion of integrals of the form of Eq. (87). For $1 \leq m < M$, an evaluation of the overlaps and matrix elements of Eq. (17) containing $\boldsymbol{\zeta}^{(m)}$ yields the following expression:

$$\begin{aligned}
&\left[\prod_{j=1}^{J}\left(1 + \chi_j^{(m)\,*}\zeta_j^{(m)}\right)\right] \\
&\times \left[1 - \frac{\mathrm{i}\tau}{\hbar}\sum_{\alpha,\beta=1}^{J}\left(h_{\alpha\beta}^{(m-1)}\zeta_\alpha^{(m)\,*}\chi_\beta^{(m-1)} + U_{\alpha\beta}^{(m-1)}\zeta_\alpha^{(m)\,*}\zeta_\beta^{(m)\,*}\chi_\beta^{(m-1)}\chi_\alpha^{(m-1)}\right)\right]\prod_{j=1}^{J}\left(1 + \zeta_j^{(m)\,*}\chi_j^{(m-1)}\right) \\
&= \left[a^{(m)} - \frac{\mathrm{i}\tau}{\hbar}\sum_{\alpha} h_{\alpha\alpha}^{(m-1)} b_\alpha^{(m)} - \frac{\mathrm{i}\tau}{\hbar}\sum_{\substack{\alpha,\beta \\ \alpha\neq\beta}} h_{\alpha\beta}^{(m-1)} c_{\alpha\beta}^{(m)} - \frac{\mathrm{i}\tau}{\hbar}\sum_{\substack{\alpha,\beta \\ \alpha\neq\beta}} U_{\alpha\beta}^{(m-1)} d_{\alpha\beta}^{(m)}\right]\prod_{j=1}^{J}\left(1 + \zeta_j^{(m)\,*}\chi_j^{(m-1)}\right).
\end{aligned} \quad (89)$$

Thereby $\mathrm{d}^2\mu = \mathrm{d}\Re\mu\mathrm{d}\Im\mu$, i.e., the integrations over ϕ and, in the second case, over μ run over the whole complex plane. One should notice, that the first of these two integrals is just the second one, but with the modulus of μ already integrated out.

The first of these two integrals is used to decouple $\boldsymbol{\zeta}^{(0)}$ from $\boldsymbol{\zeta}^{(1)}$ by the following identity:

$$\begin{aligned}
&\int \mathrm{d}^{2J}\zeta^{(0)} \exp\left(-\boldsymbol{\zeta}^{(0)\,*}\cdot\boldsymbol{\zeta}^{(0)}\right)\left[\prod_{j=1}^{J}\left(1 + \chi_j^{(0)\,*}\zeta_j^{(0)}\right)\right] \\
&\times \prod_{j=1}^{J}\left(\zeta_j^{(0)\,*}\right)^{n_j^{(i)}} = \int \frac{\mathrm{d}^{2N_i}\phi^{(0)}}{\pi^{N_i}}\int_0^{2\pi}\frac{\mathrm{d}^{N_i}\theta^{(i)}}{(2\pi)^{N_i}}\int \mathrm{d}^{2J}\zeta^{(0)} \\
&\times \exp\left(-\boldsymbol{\zeta}^{(0)\,*}\cdot\boldsymbol{\zeta}^{(0)} - \left|\phi^{(0)}\right|^2 + \phi^{(0)\,*}\cdot\mu^{(0)}\right) \\
&\times \left[\prod_{j=1}^{J}\left(1 + \chi_j^{(0)\,*}\phi_j^{(0)}\right)\right]\left[\prod_{j=0}^{J-1}\left(1 + \zeta_{J-j}^{(0)}\mu_{J-j}^{(0)\,*}\right)\right]\prod_{j=1}^{J}\left(\zeta_j^{(0)\,*}\right)^{n_j^{(i)}},
\end{aligned} \quad (88)$$

with $\mu_j^{(0)} = n_j^{(i)}\exp(\mathrm{i}\theta_j^{(i)})$ for all $j \in \{1,\ldots,J\}$, where J is the number of single-particle states taken into account. Note that here, for the initially unoccupied single-particle states, the phases $\theta_j^{(i)}$ are arbitrary but fixed, e.g. to zero, while the integration runs only over those initial phases $\theta_j^{(i)}$, for which $n_l^{(i)} = 1$. In this way, the integrals, that have to be performed exactly, in order to get a reasonable and correct semiclassical approximation for the propagator are already done, and do not have to be carried out later.

For the $N_i = \sum_{j=1}^{J} n_j^{(i)}$ initially occupied single-particle states, the identity follows directly from Eq. (86), while

With the help of the integral Eq. (87), the coefficients $a^{(m)}$, $b^{(m)}$, $c^{(m)}$ and $d^{(m)}$ can successively—starting from $m = 1$ – be written as

$$\begin{aligned}
a^{(m)} &= \int \frac{\mathrm{d}^{2J}\mu^{(m)}}{\pi^J}\int \frac{\mathrm{d}^{2J}\phi^{(m)}}{\pi^J}\left[\prod_{j=1}^{J}\left(1 + \chi_j^{(m)\,*}\phi_j^{(m)}\right)\right] \\
&\times \exp\left(-\left|\phi^{(m)}\right|^2 - \left|\mu^{(m)}\right|^2 + \phi^{(m)\,*}\cdot\mu^{(m)}\right) \\
&\times \prod_{j=0}^{J-1}\left[1 + \zeta_{J-j}^{(m)}\sum_{k=1}^{\infty}\frac{1}{k!}\left(\mu_{J-j}^{(m)\,*}\right)^k\left(\phi_{J-j}^{(m-1)}\right)^{k-1}\right],
\end{aligned} \quad (90)$$

$$\begin{aligned}
b_\alpha^{(m)} &= \int \frac{\mathrm{d}^{2J}\mu^{(m)}}{\pi^J}\int \frac{\mathrm{d}^{2J}\phi^{(m)}}{\pi^J}\exp\left(-\left|\phi^{(m)}\right|^2\right) \\
&\times \exp\left(-\left|\mu^{(m)}\right|^2 + \phi^{(m)\,*}\cdot\mu^{(m)}\right)\zeta_\alpha^{(m)\,*}\chi_\alpha^{(m-1)} \\
&\times \left\{\prod_{j=0}^{J-\alpha-1}\left[1 + \zeta_{J-j}^{(m)}\sum_{k=1}^{\infty}\frac{1}{k!}\left(\mu_{J-j}^{(m)\,*}\right)^k\left(\phi_{J-j}^{(m-1)}\right)^{k-1}\right]\right\} \\
&\times \left[1 + \zeta_\alpha^{(m)}\sum_{k=1}^{\infty}c_k^{(1)}\left(\phi_\alpha^{(m-1)}\right)\left(\mu_\alpha^{(m)\,*}\right)^k\right] \\
&\times \left\{\prod_{j=J-\alpha+1}^{J-1}\left[1 + \zeta_{J-j}^{(m)}\sum_{k=1}^{\infty}\frac{1}{k!}\left(\mu_{J-j}^{(m)\,*}\right)^k\left(\phi_{J-j}^{(m-1)}\right)^{k-1}\right]\right\} \\
&\times \left[\prod_{j=1}^{J}\left(1 + \chi_j^{(m)\,*}\phi_j^{(m)}\right)\right],
\end{aligned} \quad (91)$$

$$
\begin{aligned}
c_{\alpha\beta}^{(m)} = & \int \frac{\mathrm{d}^{2J}\mu^{(m)}}{\pi^J} \int \frac{\mathrm{d}^{2J}\phi^{(m)}}{\pi^J} \\
& \times \exp\left(-\left|\phi^{(m)}\right|^2 - \left|\mu^{(m)}\right|^2 + \phi^{(m)\,*}\cdot\mu^{(m)}\right) \zeta_\alpha^{(m)\,*}\chi_\beta^{(m-1)} \\
& \times \left\{\prod_{j=0}^{J-\max(\alpha,\beta)-1}\left[1+\zeta_{J-j}^{(m)}\sum_{k=1}^{\infty}\frac{1}{k!}\left(\mu_{J-j}^{(m)\,*}\right)^k\left(\phi_{J-j}^{(m-1)}\right)^{k-1}\right]\right\} \\
& \times \left[1+\zeta_{\max(\alpha,\beta)}^{(m)}\sum_{k=1}^{\infty}c_k^{(2)}\left(\phi_{\max(\alpha,\beta)}^{(m-1)}\right)\left(\mu_{\max(\alpha,\beta)}^{(m)\,*}\right)^k\right] \\
& \times \left\{\prod_{j=J-\max(\alpha,\beta)+1}^{J-\min(\alpha,\beta)-1}\left[1+\zeta_{J-j}^{(m)}\sum_{k=1}^{\infty}c_k^{(3)}\left(\phi_{J-j}^{(m-1)}\right)\left(\mu_{J-j}^{(m)\,*}\right)^k\right]\right\} \\
& \times \left[1+\zeta_{\min(\alpha,\beta)}^{(m)}\sum_{k=1}^{\infty}c_k^{(2)}\left(\phi_{\min(\alpha,\beta)}^{(m-1)}\right)\left(\mu_{\min(\alpha,\beta)}^{(m)\,*}\right)^k\right] \\
& \times \left\{\prod_{j=J-\min(\alpha,\beta)+1}^{J-1}\left[1+\zeta_{J-j}^{(m)}\sum_{k=1}^{\infty}\frac{1}{k!}\left(\mu_{J-j}^{(m)\,*}\right)^k\left(\phi_{J-j}^{(m-1)}\right)^{k-1}\right]\right\} \\
& \times \left[\prod_{j=1}^{J}\left(1+\chi_j^{(m)\,*}\phi_j^{(m)}\right)\right]
\end{aligned}
\tag{92}
$$

$$
\begin{aligned}
d_{\alpha\beta}^{(m)} = & \int \frac{\mathrm{d}^{2J}\mu^{(m)}}{\pi^J} \int \frac{\mathrm{d}^{2J}\phi^{(m)}}{\pi^J} \\
& \times \exp\left(-\left|\phi^{(m)}\right|^2 - \left|\mu^{(m)}\right|^2 + \phi^{(m)\,*}\cdot\mu^{(m)}\right) \\
& \times \left[\prod_{j=1}^{J}\left(1+\chi_j^{(m)\,*}\phi_j^{(m)}\right)\right]\zeta_\alpha^{(m)\,*}\zeta_\beta^{(m)\,*}\chi_\beta^{(m-1)}\chi_\alpha^{(m-1)} \\
& \times \left\{\prod_{j=0}^{J-\max(\alpha,\beta)-1}\left[1+\zeta_{J-j}^{(m)}\sum_{k=1}^{\infty}\frac{1}{k!}\left(\mu_{J-j}^{(m)\,*}\right)^k\left(\phi_{J-j}^{(m-1)}\right)^{k-1}\right]\right\} \\
& \times \left[1+\zeta_{\max(\alpha,\beta)}^{(m)}\sum_{k=1}^{\infty}c_k^{(4)}\left(\phi_{\max(\alpha,\beta)}^{(m-1)}\right)\left(\mu_{\max(\alpha,\beta)}^{(m)\,*}\right)^k\right] \\
& \times \left\{\prod_{j=J-\max(\alpha,\beta)+1}^{J-\min(\alpha,\beta)-1}\left[1+\zeta_{J-j}^{(m)}\sum_{k=1}^{\infty}\frac{1}{k!}\left(\mu_{J-j}^{(m)\,*}\right)^k\left(\phi_{J-j}^{(m-1)}\right)^{k-1}\right]\right\} \\
& \times \left[1+\zeta_{\min(\alpha,\beta)}^{(m)}\sum_{k=1}^{\infty}c_k^{(4)}\left(\phi_{\min(\alpha,\beta)}^{(m-1)}\right)\left(\mu_{\min(\alpha,\beta)}^{(m)\,*}\right)^k\right] \\
& \times \left\{\prod_{j=J-\min(\alpha,\beta)+1}^{J-1}\left[1+\zeta_{J-j}^{(m)}\sum_{k=1}^{\infty}\frac{1}{k!}\left(\mu_{J-j}^{(m)\,*}\right)^k\left(\phi_{J-j}^{(m-1)}\right)^{k-1}\right]\right\},
\end{aligned}
\tag{93}
$$

with $c_1^{(1)} = c_1^{(2)} = c_1^{(3)} = c_1^{(4)} = 1$.

It is important to notice, that the integral over $\phi^{(m)}$ and $\mu^{(m)}$ selects only the $k = 1$ terms of the occurring sums. Therefore, the terms with $k \geq 2$ can be varied, in order to modify the final path integral in the desired way.

Finally, for $m = M$, a similar argument as for $m = 0$ allows to restrict the integrals over $\phi^{(M)}$ again to those $N_f = \sum_{j=1}^{J} n_j^{(f)}$ components with $n_j^{(f)} = 1$, while setting all the other components of $\phi^{(M)}$ to zero.

After this the m-th factor in the product over the timesteps only depends on $\boldsymbol{\zeta}^{(m+1)}$ and $\boldsymbol{\chi}^{(m)}$, such that one can easily integrate out the intermediate Grassmann variables $\boldsymbol{\zeta}^{(1)}, \ldots, \boldsymbol{\zeta}^{(M)}$ and $\boldsymbol{\chi}^{(0)}, \ldots, \boldsymbol{\chi}^{(M-1)}$ by using

$$
\begin{aligned}
& \int \mathrm{d}^{2J}\zeta \int \mathrm{d}^{2J}\chi \exp\left(-\boldsymbol{\zeta}^*\cdot\boldsymbol{\zeta} - \boldsymbol{\chi}^*\cdot\boldsymbol{\chi}\right) \\
& \quad \times \left[\prod_{j=0}^{J-1}\left(1+\zeta_{J-j}f_{J-j}^{(m)}\right)\right] \\
& \quad \times \left[\prod_{j=1}^{J}\left(1+\zeta_j{}^*\chi_j\right)\right]\left[\prod_{j=1}^{J}\left(1+\chi_j{}^*\phi_j^{(m)}\right)\right] \\
& = \prod_{j=1}^{J}\left(1+f_j^{(m)}\phi_j^{(m)}\right),
\end{aligned}
\tag{94}
$$

$$
\begin{aligned}
& \int \mathrm{d}^{2J}\zeta \int \mathrm{d}^{2J}\chi \exp\left(-\boldsymbol{\zeta}^*\cdot\boldsymbol{\zeta} - \boldsymbol{\chi}^*\cdot\boldsymbol{\chi}\right) \\
& \quad \times \left[\prod_{j=0}^{J-1}\left(1+\zeta_{J-j}f_{J-j}^{(m)}\right)\right] \\
& \quad \times \left[\prod_{j=1}^{J}\left(1+\zeta_j{}^*\chi_j\right)\right]\left[\prod_{j=1}^{J}\left(1+\chi_j{}^*\phi_j^{(m)}\right)\right]\zeta_\alpha{}^*\chi_\beta \\
& = f_\alpha^{(m)}\phi_\beta^{(m)}\left[\prod_{j=1}^{\min(\alpha,\beta)-1}\left(1+f_j^{(m)}\phi_j^{(m)}\right)\right] \\
& \quad \times \left[\prod_{j=\max(\alpha,\beta)+1}^{J}\left(1+f_j^{(m)}\phi_j^{(m)}\right)\right]\prod_{j=\min(\alpha,\beta)+1}^{\max(\alpha,\beta)-1}\left(1-f_j^{(m)}\phi_j^{(m)}\right),
\end{aligned}
\tag{95}
$$

$$
\begin{aligned}
& \int \mathrm{d}^{2J}\zeta \int \mathrm{d}^{2J}\chi \exp\left(-\boldsymbol{\zeta}^*\cdot\boldsymbol{\zeta} - \boldsymbol{\chi}^*\cdot\boldsymbol{\chi}\right) \\
& \quad \times \left[\prod_{j=0}^{J-1}\left(1+\zeta_{J-j}f_{J-j}^{(m)}\right)\right] \\
& \quad \times \left[\prod_{j=1}^{J}\left(1+\zeta_j{}^*\chi_j\right)\right]\left[\prod_{j=1}^{J}\left(1+\chi_j{}^*\phi_j^{(m)}\right)\right]\zeta_\alpha{}^*\zeta_\beta{}^*\chi_\beta\chi_\alpha \\
& \quad = f_\alpha^{(m)}f_\beta^{(m)}\phi_\beta^{(m)}\phi_\alpha^{(m)}\prod_{\substack{j=1 \\ j\neq\alpha,\beta}}^{J}\left(1+f_j^{(m)}\phi_j^{(m)}\right).
\end{aligned}
\tag{96}
$$

Moreover, the integrals over $\boldsymbol{\zeta}^{(0)}$ and $\boldsymbol{\chi}^{(M)}$ yield

$$
\begin{aligned}
& \int \mathrm{d}^{2J}\zeta^{(0)} \exp\left(-\boldsymbol{\zeta}^{(0)\,*}\cdot\boldsymbol{\zeta}^{(0)}\right)\left[\prod_{j=0}^{J-1}\left(1+\zeta_{J-j}^{(0)}\mu_{J-j}^{(0)\,*}\right)\right] \\
& \quad \times \prod_{j=1}^{J}\left(\zeta_j^{(0)\,*}\right)^{n_j^{(i)}} = \prod_{j:n_j^{(i)}=1}\mu_j^{(0)\,*}
\end{aligned}
\tag{97}
$$

$$\int \mathrm{d}^{2J}\chi^{(M)} \exp\left(-\boldsymbol{\chi}^{(M)\,*}\cdot\boldsymbol{\chi}^{(M)}\right)\left[\prod_{j=0}^{J-1}\left(\chi_{J-j}^{(M)}\right)^{n_{J-j}^{(f)}}\right] \times\prod_{j=1}^{J}\left(1+\chi_j^{(M)}\,\phi_j^{(M)\,*}\right)=\prod_{j:n_j^{(f)}=1}\phi_j^{(M)} \tag{98}$$

After performing these integrals, one notices, that the inserted integrals have been chosen such, that the resulting sums can be performed and yield exponentials, such that the propagator is, after integrating out $\mu^{(1)},\ldots,\mu^{(M)}$ as well as $\phi^{(0)}$ and undo the expansion in τ, given by the path integral Eq. (19), where the classical Hamiltonian is given by

$$\begin{aligned} H_{cl}(\mu^*,\phi) &= \sum_{\alpha} h_{\alpha\alpha}\,\mu_\alpha{}^*\phi_\alpha f_1(\mu_\alpha{}^*,\phi_\alpha)\\ &+\sum_{\substack{\alpha,\beta\\ \alpha\neq\beta}} U_{\alpha\beta}\,\mu_\alpha{}^*\mu_\beta{}^*\phi_\alpha\phi_\beta f_3(\mu_\alpha{}^*,\phi_\alpha) f_3(\mu_\beta{}^*,\phi_\beta)\\ &+\sum_{\substack{\alpha,\beta\\ \alpha\neq\beta}} h_{\alpha\beta}\,\mu_\alpha{}^*\phi_\beta f_2(\mu_\alpha{}^*,\phi_\alpha)\exp\left(-\mu_\beta{}^*\phi_\beta\right)\\ &\times\prod_{l}^{\alpha,\beta} g(\mu_l{}^*,\phi_l), \end{aligned} \tag{99}$$

where f_1, f_2, f_3 and g are arbitrary analytic functions satisfying the following conditions:

$$f_1(0,\phi)=f_2(0,\phi)=f_3(0,\phi)=1 \tag{100}$$

$$g(0,\phi)=1 \tag{101}$$

$$\left.\frac{\partial}{\partial\mu^*}g(\mu^*,\phi)\right|_{\mu^*=0}=-2\phi. \tag{102}$$

Moreover, as in Sect. 3, the product in the third line runs only over those values of j, which are lying between α and β, excluding α and β themselves,

$$\prod_{j}^{\alpha,\beta}\ldots=\prod_{j=\min(\alpha,\beta)+1}^{\max(\alpha,\beta)-1}\ldots \tag{103}$$

Appendix 2: The semiclassical amplitude

The semiclassical amplitude is given by the integral over the exponential of the second variation of the path integral around the classical path which can be written as,

$$\begin{aligned} \mathscr{A}_\gamma = \lim_{M\to\infty}\frac{1}{(2\pi)^{2N-1+(M-1)J}}&\int \mathrm{d}^{N-1}\delta\theta^{(0)}\int \mathrm{d}^{N}\delta J^{(M)}\int \mathrm{d}^{N}\delta\theta^{(M)}\int \mathrm{d}^{J}\delta J^{(1)}\int \mathrm{d}^{J}\delta\theta^{(1)}\cdots\int \mathrm{d}^{J}\delta J^{(M-1)}\int \mathrm{d}^{J}\delta\theta^{(M-1)}\\ &\times\exp\left\{-\frac{1}{2}\delta\boldsymbol{\theta}^{(0)}\mathbf{P}_i'\frac{\partial\phi^{(0)}}{\partial\boldsymbol{\theta}^{(i)}}\left[-\exp\left[-2\mathrm{idiag}\left(\boldsymbol{\theta}^{(i)}\right)\right]+\frac{\mathrm{i}\tau}{\hbar}\frac{\partial^2 H^{(cl)\,(0)}}{\partial{\phi^{(0)}}^2}\right]\frac{\partial\phi^{(0)}}{\partial\boldsymbol{\theta}^{(i)}}\mathbf{P}_i'^{\mathrm{T}}\delta\boldsymbol{\theta}^{(0)}\right.\\ &-\frac{1}{2}\begin{pmatrix}\delta\boldsymbol{\theta}^{(M)}\mathbf{P}_f\\ \delta\mathbf{J}^{(M)}\mathbf{P}_f\end{pmatrix}\mathbf{O}^{(M)\,\mathrm{T}}\begin{pmatrix}\exp\left[-2\mathrm{idiag}\left(\boldsymbol{\theta}^{(M)}\right)\right] & \mathbf{I}_J\\ \mathbf{I}_J & \frac{\mathrm{i}\tau}{\hbar}\frac{\partial^2 H^{(cl)\,(M-1)}}{\partial\,{\phi^{(M)}}^{*2}}\end{pmatrix}\mathbf{O}^{(M)}\begin{pmatrix}\mathbf{P}_f^{\mathrm{T}}\delta\boldsymbol{\theta}^{(M)}\\ \mathbf{P}_f^{\mathrm{T}}\delta\mathbf{J}^{(M)}\end{pmatrix}\\ &-\frac{1}{2}\sum_{m=1}^{M-1}\begin{pmatrix}\delta\boldsymbol{\theta}^{(m)}\\ \delta\mathbf{J}^{(m)}\end{pmatrix}\mathbf{O}^{(m)\,\mathrm{T}}\begin{pmatrix}\frac{\mathrm{i}\tau}{\hbar}\frac{\partial^2 H^{(cl)\,(m)}}{\partial{\phi^{(m)}}^2} & \mathbf{I}_J\\ \mathbf{I}_J & \frac{\mathrm{i}\tau}{\hbar}\frac{\partial^2 H^{(cl)\,(m-1)}}{\partial\,{\phi^{(m)}}^{*2}}\end{pmatrix}\mathbf{O}^{(m)}\begin{pmatrix}\delta\boldsymbol{\theta}^{(m)}\\ \delta\mathbf{J}^{(m)}\end{pmatrix}\\ &+\begin{pmatrix}\delta\boldsymbol{\theta}^{(1)}\\ \delta\mathbf{J}^{(1)}\end{pmatrix}\mathbf{O}^{(1)\,\mathrm{T}}\begin{pmatrix}0\\ \mathbf{I}_J-\frac{\mathrm{i}\tau}{\hbar}\frac{\partial^2 H^{(cl)\,(0)}}{\partial\,{\phi^{(1)}}^*\partial\phi^{(0)}}\end{pmatrix}\frac{\partial\phi^{(0)}}{\partial\boldsymbol{\theta}^{(i)}}\mathbf{P}_i'^{\mathrm{T}}\delta\boldsymbol{\theta}^{(i)}\\ &+\begin{pmatrix}\delta\boldsymbol{\theta}^{(M)}\mathbf{P}_f\\ \delta\mathbf{J}^{(M)}\mathbf{P}_f\end{pmatrix}\mathbf{O}^{(M)\,\mathrm{T}}\begin{pmatrix}0 & 0\\ \mathbf{I}_J-\frac{\mathrm{i}\tau}{\hbar}\frac{\partial^2 H^{(cl)\,(M-1)}}{\partial\,{\phi^{(M)}}^*\partial\phi^{(M-1)}} & 0\end{pmatrix}\mathbf{O}^{(M-1)}\begin{pmatrix}\delta\boldsymbol{\theta}^{(M-1)}\\ \delta\mathbf{J}^{(M-1)}\end{pmatrix}\\ &\left.+\sum_{m=1}^{M-2}\begin{pmatrix}\delta\boldsymbol{\theta}^{(m)}\\ \delta\mathbf{J}^{(m)}\end{pmatrix}\mathbf{O}^{(m)\,\mathrm{T}}\begin{pmatrix}0 & 0\\ \mathbf{I}_J-\frac{\mathrm{i}\tau}{\hbar}\frac{\partial^2 H^{(cl)\,(m)}}{\partial\,{\phi^{(m+1)}}^*\partial\phi^{(m)}} & 0\end{pmatrix}\mathbf{O}^{(m)}\begin{pmatrix}\delta\boldsymbol{\theta}^{(m)}\\ \delta\mathbf{J}^{(m)}\end{pmatrix}\right\}, \end{aligned} \tag{104}$$

with

$$\mathbf{O}^{(m)} = \begin{pmatrix} \frac{\partial \phi^{(m)}}{\partial \boldsymbol{\theta}^{(m)}} & \frac{\partial \phi^{(m)}}{\partial \mathbf{J}^{(m)}} \\ \frac{\partial \phi^{(m)\,*}}{\partial \boldsymbol{\theta}^{(m)}} & \frac{\partial \phi^{(m)\,*}}{\partial \mathbf{J}^{(m)}} \end{pmatrix}. \tag{105}$$

Moreover, diag($\mathbf{v}$) is the diagonal $d \times d$-matrix for which the (j,j)-th entry is equal to v_j, where d is the dimensionality of the vector $\mathbf{v}$ and $\mathbf{P}_{i/f}$ and $\mathbf{P}'_{i/f}$ are defined as the $N \times J$ and $(N-1) \times J$-matrices, respectively, which project onto the subspace of initially and finally occupied single-particle states, with the latter excluding the first occupied one,

$$\left(\mathbf{P}_{i/f}\right)_{lj} = \delta_{j_l^{(\prime)} j} \tag{106}$$

$$\left(\mathbf{P}'_{i/f}\right)_{lj} = \delta_{j_{l+1}^{(\prime)} j}, \tag{107}$$

where $j_1 < \cdots < j_N \in \left\{ j \in \{1,\ldots,J\} : n_j^{(i)} = 1 \right\}$ and $j'_1 < \cdots < j'_N \in \left\{ j \in \{1,\ldots,J\} : n_j^{(f)} = 1 \right\}$ are the initially, respectively finally, occupied single-particle states.

For later reference, we also define $\bar{\mathbf{P}}_{i/f}$ as the complement of $\mathbf{P}_{i/f}$ as well as

$$\mathbf{Q}_{i/f} = \begin{pmatrix} \bar{\mathbf{P}}_{i/f} \\ \mathbf{P}_{i/f} \end{pmatrix}, \tag{108}$$

which are the (orthogonal) matrices, which put the components corresponding to initially and finally unoccupied single-particle states to the first $J-N$ positions, and those corresponding to occupied single-particle states to the last N positions, i.e.,

$$\mathbf{Q}_{i/f}\mathbf{n}^{(i/f)} = (\underbrace{0,\ldots,0}_{J-N},\underbrace{1,\ldots,1}_{N})^{\mathrm{T}}. \tag{109}$$

The integral over $\delta\boldsymbol{\theta}^{(0)}$ is given by

$$\begin{aligned}
&\frac{1}{(2\pi)^{N-1}} \int \mathrm{d}^{N-1}\delta\theta^{(0)} \exp\left\{ -\frac{1}{2}\delta\boldsymbol{\theta}^{(0)}\mathbf{P}_i' \frac{\partial\phi^{(0)}}{\partial\boldsymbol{\theta}^{(i)}} \right. \\
&\quad \times \left(-\exp\left[-2\mathrm{idiag}\left(\boldsymbol{\theta}^{(i)}\right)\right] + \frac{\mathrm{i}\tau}{\hbar}\frac{\partial^2 H^{(cl)\,(0)}}{\partial\phi^{(0)\,2}} \right) \frac{\partial\phi^{(0)}}{\partial\boldsymbol{\theta}^{(i)}} \mathbf{P}_i'^{\mathrm{T}} \delta\boldsymbol{\theta}^{(0)} \\
&\quad + \begin{pmatrix} \delta\boldsymbol{\theta}^{(1)} \\ \delta\mathbf{J}^{(1)} \end{pmatrix} \mathbf{O}^{(1)\,\mathrm{T}} \begin{pmatrix} 0 \\ \mathbf{I}_J - \frac{\mathrm{i}\tau}{\hbar}\frac{\partial^2 H^{(cl)\,(0)}}{\partial\phi^{(1)\,*}\partial\phi^{(0)}} \end{pmatrix} \frac{\partial\phi^{(0)}}{\partial\boldsymbol{\theta}^{(i)}} \mathbf{P}_i'^{\mathrm{T}} \delta\boldsymbol{\theta}^{(i)} \\
&\quad \left. - \frac{1}{2} \begin{pmatrix} \delta\boldsymbol{\theta}^{(1)} \\ \delta\mathbf{J}^{(1)} \end{pmatrix} \mathbf{O}^{(1)\,\mathrm{T}} \begin{pmatrix} \frac{\mathrm{i}\tau}{\hbar}\frac{\partial^2 H^{(cl)\,(1)}}{\partial\phi^{(1)\,2}} & \mathbf{I}_J \\ \mathbf{I}_J & \frac{\mathrm{i}\tau}{\hbar}\frac{\partial^2 H^{(cl)\,(0)}}{\partial\phi^{(1)\,*2}} \end{pmatrix} \mathbf{O}^{(1)} \begin{pmatrix} \delta\boldsymbol{\theta}^{(1)} \\ \delta\mathbf{J}^{(1)} \end{pmatrix} \right\} \\
&= \frac{1}{\sqrt{2\pi}^{N-1}} \left\{ \det\left[\mathbf{I}_J - \frac{\partial^2 H^{(cl)\,(0)}}{\partial\left(\mathbf{P}_i\phi^{(0)}\right)^2} \exp\left[2\mathrm{idiag}\left(\boldsymbol{\theta}^{(i)}\right)\right] \right] \right\}^{-1} \\
&\quad \times \exp\left\{ -\frac{1}{2} \begin{pmatrix} \delta\boldsymbol{\theta}^{(1)} \\ \delta\mathbf{J}^{(1)} \end{pmatrix} \mathbf{O}^{(1)\,\mathrm{T}} \begin{pmatrix} \frac{\mathrm{i}\tau}{\hbar}\frac{\partial^2 H^{(cl)\,(1)}}{\partial\phi^{(1)\,2}} & \mathbf{I}_J \\ \mathbf{I}_J & \mathbf{X}^{(1)} \end{pmatrix} \mathbf{O}^{(1)} \begin{pmatrix} \delta\boldsymbol{\theta}^{(1)} \\ \delta\mathbf{J}^{(1)} \end{pmatrix} \right\},
\end{aligned} \tag{110}$$

where $\mathbf{X}^{(1)}$ is defined as

$$\begin{aligned}
\mathbf{X}^{(1)} &= \frac{\mathrm{i}\tau}{\hbar}\frac{\partial^2 H^{(cl)\,(0)}}{\partial\phi^{(1)\,*2}} + \left(\mathbf{I}_J - \frac{\mathrm{i}\tau}{\hbar}\frac{\partial^2 H^{(cl)\,(0)}}{\partial\phi^{(1)\,*}\partial\phi^{(0)}} \right) \mathbf{P}_i'^{\mathrm{T}} \\
&\quad \times \left\{ \exp\left[-2\mathrm{idiag}\left(\mathbf{P}_i'\boldsymbol{\theta}^{(i)}\right)\right] - \frac{\mathrm{i}\tau}{\hbar}\frac{\partial^2 H^{(cl)\,(0)}}{\partial\left(\mathbf{P}_i'\phi^{(0)}\right)^2} \right\}^{-1} \\
&\quad \times \mathbf{P}_i' \left(\mathbf{I}_J - \frac{\mathrm{i}\tau}{\hbar}\frac{\partial^2 H^{(cl)\,(0)}}{\partial\phi^{(0)}\partial\phi^{(1)\,*}} \right)
\end{aligned} \tag{111}$$

It can be shown, that Eq. (111) can also be written as

$$\begin{aligned}
\mathbf{X}^{(1)} &= \frac{\mathrm{i}\tau}{\hbar}\frac{\partial^2 H^{(cl)\,(0)}}{\partial\phi^{(1)\,*2}} + \left(\mathbf{I}_J - \frac{\mathrm{i}\tau}{\hbar}\frac{\partial^2 H^{(cl)\,(0)}}{\partial\phi^{(1)\,*}\partial\phi^{(0)}} \right) \mathbf{X}^{(0)} \\
&\quad \times \left(\mathbf{I}_J - \frac{\mathrm{i}\tau}{\hbar}\frac{\partial^2 H^{(cl)\,(0)}}{\partial\phi^{(0)\,2}}\mathbf{X}^{(0)} \right)^{-1} \left(\mathbf{I}_J - \frac{\mathrm{i}\tau}{\hbar}\frac{\partial^2 H^{(cl)\,(0)}}{\partial\phi^{(0)}\partial\phi^{(1)\,*}} \right),
\end{aligned} \tag{112}$$

with

$$\mathbf{X}^{(0)} = \mathbf{Q}_i^{\mathrm{T}} \begin{pmatrix} 0 & \\ & \exp\left[2\mathrm{idiag}\left(\mathbf{P}_i'\boldsymbol{\theta}^{(i)}\right)\right] \end{pmatrix} \mathbf{Q}_i. \tag{113}$$

Now, consider the integral

$$\begin{aligned}
&\frac{1}{(2\pi)^J} \int \mathrm{d}^J\delta J^{(m)} \int \mathrm{d}^J\delta\theta^{(m)} \exp\left\{ -\frac{1}{2} \begin{pmatrix} \delta\boldsymbol{\theta}^{(m+1)} \\ \delta\mathbf{J}^{(m+1)} \end{pmatrix} \right. \\
&\quad \times \mathbf{O}^{(m+1)\,\mathrm{T}} \begin{pmatrix} \frac{\mathrm{i}\tau}{\hbar}\frac{\partial^2 H^{(cl)\,(m+1)}}{\partial\phi^{(m+1)\,2}} & \mathbf{I}_J \\ \mathbf{I}_J & \frac{\mathrm{i}\tau}{\hbar}\frac{\partial^2 H^{(cl)\,(m)}}{\partial\phi^{(m+1)\,*2}} \end{pmatrix} \mathbf{O}^{(m+1)} \begin{pmatrix} \delta\boldsymbol{\theta}^{(m+1)} \\ \delta\mathbf{J}^{(m+1)} \end{pmatrix} \\
&\quad - \frac{1}{2} \begin{pmatrix} \delta\boldsymbol{\theta}^{(m)} \\ \delta\mathbf{J}^{(m)} \end{pmatrix} \mathbf{O}^{(m)\,\mathrm{T}} \begin{pmatrix} \frac{\mathrm{i}\tau}{\hbar}\frac{\partial^2 H^{(cl)\,(m)}}{\partial\phi^{(m)\,2}} & \mathbf{I}_J \\ \mathbf{I}_J & X^{(m)} \end{pmatrix} \mathbf{O}^{(m)} \begin{pmatrix} \delta\boldsymbol{\theta}^{(m)} \\ \delta\mathbf{J}^{(m)} \end{pmatrix} \\
&\quad \left. + \begin{pmatrix} \delta\boldsymbol{\theta}^{(m+1)} \\ \delta\mathbf{J}^{(m+1)} \end{pmatrix} \mathbf{O}^{(m+1)\,\mathrm{T}} \begin{pmatrix} 0 & 0 \\ \mathbf{I}_J - \frac{\mathrm{i}\tau}{\hbar}\frac{\partial^2 H^{(cl)\,(m)}}{\partial\phi^{(m+1)\,*}\partial\phi^{(m)}} & 0 \end{pmatrix} \mathbf{O}^{(m)} \begin{pmatrix} \delta\boldsymbol{\theta}^{(m)} \\ \delta\mathbf{J}^{(m)} \end{pmatrix} \right\} \\
&= \left\{ \det\left[\mathbf{I}_J - \frac{\mathrm{i}\tau}{\hbar}\frac{\partial^2 H^{(cl)\,(m)}}{\partial\phi^{(m)\,2}}\mathbf{X}^{(m)} \right] \right\}^{-1} \exp\left\{ -\frac{1}{2} \begin{pmatrix} \delta\boldsymbol{\theta}^{(m+1)} \\ \delta\mathbf{J}^{(m+1)} \end{pmatrix} \right. \\
&\quad \left. \times \mathbf{O}^{(m+1)\,\mathrm{T}} \begin{pmatrix} \frac{\mathrm{i}\tau}{\hbar}\frac{\partial^2 H^{(cl)\,(m+1)}}{\partial\phi^{(m+1)\,2}} & \mathbf{I}_J \\ \mathbf{I}_J & \mathbf{X}^{(m+1)} \end{pmatrix} \mathbf{O}^{(m+1)} \begin{pmatrix} \delta\boldsymbol{\theta}^{(m+1)} \\ \delta\mathbf{J}^{(m+1)} \end{pmatrix} \right\}
\end{aligned} \tag{114}$$

with

$$\begin{aligned}
\mathbf{X}^{(m+1)} &= \frac{\mathrm{i}\tau}{\hbar}\frac{\partial^2 H^{(cl)\,(m)}}{\partial\phi^{(m+1)\,*2}} + \left(\mathbf{I}_J - \frac{\mathrm{i}\tau}{\hbar}\frac{\partial^2 H^{(cl)\,(m)}}{\partial\phi^{(m+1)\,*}\partial\phi^{(m)}} \right) \mathbf{X}^{(m)} \\
&\quad \times \left(\mathbf{I}_J - \frac{\mathrm{i}\tau}{\hbar}\frac{\partial^2 H^{(cl)\,(m)}}{\partial\phi^{(m)\,2}}\mathbf{X}^{(m)} \right)^{-1} \left(\mathbf{I}_J - \frac{\mathrm{i}\tau}{\hbar}\frac{\partial^2 H^{(cl)\,(m)}}{\partial\phi^{(m)}\partial\phi^{(m+1)\,*}} \right).
\end{aligned} \tag{115}$$

For $m = 1$ this is exactly the integral in Eq. (104) after integrating out $\delta\boldsymbol{\theta}^{(0)}$ and thus defines $\mathbf{X}^{(2)}$. One then recognizes, that after the m-th integration, the integral is again of the form of Eq. (114) up to the $(M-1)$-th integration. With this observation, the semiclassical amplitude is given by

$$\mathscr{A}_\gamma = \lim_{M\to\infty} \frac{1}{(2\pi)^{\frac{3N-1}{2}}} \int \mathrm{d}^N J^{(M)} \int \mathrm{d}^N \theta^{(M)} \prod_{m=0}^{M-1} \sqrt{\det\left(\mathbf{I}_J - \frac{\mathrm{i}\tau}{\hbar}\frac{\partial^2 H^{(cl)(m)}}{\partial \phi^{(m)2}}\mathbf{X}^{(m)}\right)}^{-1}$$
$$\times \exp\left\{-\frac{1}{2}\begin{pmatrix}\delta\boldsymbol{\theta}^{(M)}\mathbf{P}_f \\ \delta\mathbf{J}^{(M)}\mathbf{P}_f\end{pmatrix}\mathbf{O}^{(M)\mathrm{T}}\begin{pmatrix}\exp\left[-2\mathrm{idiag}\left(\boldsymbol{\theta}^{(M)}\right)\right] & \mathbf{I}_J \\ \mathbf{I}_J & X^{(M)}\end{pmatrix}\mathbf{O}^{(M)}\begin{pmatrix}\mathbf{P}_f^{\mathrm{T}}\delta\boldsymbol{\theta}^{(M)} \\ \mathbf{P}_f^{\mathrm{T}}\delta\mathbf{J}^{(M)}\end{pmatrix}\right\}$$
$$= \lim_{M\to\infty} \frac{1}{\sqrt{2\pi}^{N-1}}\left[\prod_{m=0}^{M-1}\sqrt{\det\left(\mathbf{I}_J - \frac{\mathrm{i}\tau}{\hbar}\frac{\partial^2 H^{(cl)(m)}}{\partial \phi^{(m)2}}\mathbf{X}^{(m)}\right)}^{-1}\right]\sqrt{\det\left(\mathbf{I}_N - \exp\left[-2\mathrm{idiag}\left(\mathbf{P}_f\boldsymbol{\theta}^{(M)}\right)\right]\mathbf{P}_f\mathbf{X}^{(M)}\mathbf{P}_f^{\mathrm{T}}\right)}^{-1}. \tag{116}$$

In the continuous limit, the discrete set of $\mathbf{X}^{(m)}$ turns into a function of time $\mathbf{X}(t)$, and (by expanding it up to first order in τ) is given by Eq. (60), and the semiclassical amplitude can be written in the form given in Eq. (57).

Appendix 3: Possible classical Hamiltonians

In this part, we state different possibilities for the classical hamiltonian as can be derived out of similar calculations as in Appendix 1 without going further into detail.

Appendix 3.1: Classical Hamiltonians in the particle picture

First, we present two possibilities arising directly from the derivation presented in Appendix 1, but restrict ourselves to those, which contain μ and ϕ in a symmetric way and omitting the one already stated in Sect. 3. These examples shall just illustrate, which kinds of classical Hamiltonians are possible:

$$H_{cl}^{(1)}\left(\mu^*,\phi\right) = \sum_\alpha h_{\alpha\alpha}\,{\mu_\alpha}^*\phi_\alpha \cos\left({\mu_\alpha}^*\phi_\alpha\right) + \sum_{\substack{\alpha,\beta\\ \alpha\neq\beta}} U_{\alpha\beta}\,{\mu_\alpha}^*{\mu_\beta}^*\phi_\alpha\phi_\beta + \sum_{\substack{\alpha,\beta\\ \alpha\neq\beta}} h_{\alpha\beta}\,{\mu_\alpha}^*\phi_\beta \exp\left(-\sum_{l=\min(\alpha,\beta)}^{\max(\alpha,\beta)}{\mu_l}^*\phi_l\right), \tag{117}$$

$$H_{cl}^{(2)}\left(\mu^*,\phi\right) = \sum_\alpha h_{\alpha\alpha}\,{\mu_\alpha}^*\phi_\alpha \exp\left({\mu_\alpha}^*\phi_\alpha\right) + \sum_{\substack{\alpha,\beta\\ \alpha\neq\beta}} h_{\alpha\beta}\,{\mu_\alpha}^*\phi_\beta \exp\left(-{\mu_\beta}^*\phi_\beta - {\mu_\alpha}^*\phi_\alpha\right) \times \prod_{l=\min(\alpha,\beta)+1}^{\max(\alpha,\beta)-1}\left[1-\sinh\left(2{\mu_l}^*\phi_l\right)\right] + \sum_{\substack{\alpha,\beta\\ \alpha\neq\beta}} U_{\alpha\beta}\,{\mu_\alpha}^*{\mu_\beta}^*\phi_\alpha\phi_\beta \cosh\left({\mu_\alpha}^*\phi_\alpha\right)\cosh\left({\mu_\beta}^*\phi_\beta\right), \tag{118}$$

Next, consider the more general case, that the quantum Hamiltonian is written in the form

$$\hat{H} = \sum_{\alpha,\beta} h_{\alpha\beta}\hat{c}_\alpha^\dagger\hat{c}_\beta + \sum_{\substack{\alpha,\beta,\rho,\nu\\ \alpha\neq\beta,\rho\neq\nu}} U_{\alpha\beta\rho\nu}\hat{c}_\alpha^\dagger\hat{c}_\beta^\dagger\hat{c}_\rho\hat{c}_\nu. \tag{119}$$

By splitting the interaction term also into (pairwise) diagonal and non-diagonal terms, one can in a similar way as in Sect. 7 construct the following classical Hamiltonian

$$
\begin{aligned}
H_{cl}\left(\mu^*,\phi\right) = & \sum_{\alpha} h_{\alpha\alpha}\,{\mu_\alpha}^*\phi_\alpha f_1\left({\mu_\alpha}^*,\phi_\alpha\right) \\
& + \sum_{\substack{\alpha,\beta \\ \alpha\neq\beta}} h_{\alpha\beta}\,{\mu_\alpha}^*\phi_\beta f_2\left({\mu_\alpha}^*,\phi_\alpha\right)\exp\left(-{\mu_\beta}^*\phi_\beta\right)\prod_{l=\min(\alpha,\beta)+1}^{\max(\alpha,\beta)-1} g\left({\mu_l}^*,\phi_l\right) \\
& + \sum_{\substack{\alpha,\beta \\ \alpha\neq\beta}} U_{\alpha\beta\beta\alpha}\,{\mu_\alpha}^*{\mu_\beta}^*\phi_\alpha\phi_\beta f_3\left({\mu_\alpha}^*,\phi_\alpha\right)f_3\left({\mu_\beta}^*,\phi_\beta\right) \\
& + \sum_{\substack{\alpha,\beta,\rho \\ \alpha\neq\beta,\rho\neq\alpha,\rho\neq\beta}} [\Theta(\beta-\alpha)\Theta(\beta-\rho)+\Theta(\alpha-\beta)\Theta(\rho-\beta) \\
& -\Theta(\alpha-\beta)\Theta(\beta-\rho)-\Theta(\beta-\alpha)\Theta(\rho-\beta)] \\
& \times\left(U_{\alpha\beta\beta\rho}-U_{\alpha\beta\rho\beta}\right){\mu_\alpha}^*{\mu_\beta}^*\phi_\beta\phi_\rho f_1\left({\mu_\alpha}^*,\phi_\alpha\right)f_2\left({\mu_\alpha}^*,\phi_\alpha\right) \\
& \times\exp\left(-{\mu_\rho}^*\phi_\rho\right)\prod_{j=\min(\alpha,\rho)+1}^{\max(\alpha,\rho)-1} g\left({\mu_j}^*,\phi_j\right) \\
& + \sum_{\substack{\alpha,\beta,\rho \\ \alpha\neq\beta,\rho\neq\alpha,\rho\neq\beta}} [\Theta(\beta-\alpha)\Theta(\rho-\alpha) \\
& +\Theta(\alpha-\beta)\Theta(\alpha-\rho)-\Theta(\alpha-\beta)\Theta(\rho-\alpha)-\Theta(\beta-\alpha)\Theta(\alpha-\rho)] \\
& \left(U_{\alpha\beta\rho\alpha}-U_{\alpha\beta\alpha\rho}\right){\mu_\alpha}^*{\mu_\beta}^*\phi_\alpha\phi_\rho f_1\left({\mu_\alpha}^*,\phi_\alpha\right)f_2\left({\mu_\beta}^*,\phi_\beta\right) \\
& \times\exp\left(-{\mu_\rho}^*\phi_\rho\right)\prod_{j=\min(\beta,\rho)+1}^{\max(\beta,\rho)-1} g\left({\mu_j}^*,\phi_j\right) \\
& + \sum_{\substack{\alpha,\beta,\rho,\nu \\ \alpha\neq\beta,\alpha\neq\rho,\alpha\neq\nu,\beta\neq\rho,\beta\neq\nu,\rho\neq\nu}} [\Theta(\beta-\alpha) \\
& -\Theta(\alpha-\beta)][\Theta(\rho-\nu)-\Theta(\nu-\rho)]U_{\alpha\beta\rho\nu}\,{\mu_\alpha}^*{\mu_\beta}^*\phi_\rho\phi_\nu f_2 \\
& \times\left({\mu_\alpha}^*,\phi_\alpha\right)f_2\left({\mu_\beta}^*,\phi_\beta\right)\exp\left(-{\mu_\rho}^*\phi_\rho-{\mu_\nu}^*\phi_\nu\right) \\
& \times\left[\prod_{l=\min(\alpha,\beta,\rho,\nu)+1}^{\min\left\{\{\alpha,\beta,\rho,\nu\}\setminus\{\min(\alpha,\beta,\rho,\nu)\}\right\}-1} g\left({\mu_j}^*,\phi_j\right)\right]\left[\prod_{l=\max\left\{\{\alpha,\beta,\rho,\nu\}\setminus\{\max(\alpha,\beta,\rho,\nu)\}\right\}+1}^{\max(\alpha,\beta,\rho,\nu)-1} g\left({\mu_j}^*,\phi_j\right)\right],
\end{aligned}
\tag{120}
$$

where f_1, f_2, f_3 and g are again arbitrary analytic functions satisfying Eqs. (100–102). Thereby, one should notice, that

$$\min\left\{\{\alpha,\beta,\rho,\nu\}\setminus\{\min(\alpha,\beta,\rho,\nu)\}\right\}$$

is the second smallest number out of the set $\{\alpha,\beta,\rho,\nu\}$ and

$$\max\left\{\{\alpha,\beta,\rho,\nu\}\setminus\{\max(\alpha,\beta,\rho,\nu)\}\right\}$$

the second largest number out of the set $\{\alpha,\beta,\rho,\nu\}$.

Appendix 3.2: Classical Hamiltonians in the hole picture

The cases considered above, we call particle picture, since the boundary conditions are such, that $\left|\phi_j\right|^2 = 1$ corresponds to the j-th single-particle state being occupied, while $\left|\phi_j\right|^2 = 0$ corresponds to the j-th single-particle state being empty. However, the role of occupied and unoccupied states can be reversed, if Eqs. (88) are replaced by

$$\int \mathrm{d}^{2J}\zeta^{(0)} \exp\left(-\boldsymbol{\zeta}^{(0)\,*}\cdot\boldsymbol{\zeta}^{(0)}\right)\left[\prod_{j=1}^{J}\left(1+\chi_j^{(0)\,*}\zeta_j^{(0)}\right)\right]\prod_{j=1}^{J}\left(\zeta_j^{(0)\,*}\right)^{n_j^{(i)}}$$
$$=\int\frac{\mathrm{d}^{2(J-N_i)}\phi^{(0)}}{\pi^{J-N_i}}\int_0^{2\pi}\frac{\mathrm{d}^{J-N_i}\theta^{(i)}}{(2\pi)^{J-N_i}}\int \mathrm{d}^{2J}\zeta^{(0)}\exp\left(-\boldsymbol{\zeta}^{(0)\,*}\cdot\boldsymbol{\zeta}^{(0)}-\left|\phi^{(0)}\right|^2+\phi^{(0)\,*}\cdot\mu^{(0)}\right)$$
$$\times\left[\prod_{j=1}^{J}\left(\phi_j^{(0)}+\chi_j^{(0)\,*}\right)\right]\left[\prod_{j=0}^{J-1}\left(\mu_{J-j}^{(0)\,*}+\zeta_{J-j}^{(0)}\right)\right]\prod_{j=1}^{J}\left(\zeta_j^{(0)\,*}\right)^{n_j^{(i)}}, \tag{121}$$

where the integrations over $\boldsymbol{\theta}^{(i)}$ and $\phi^{(0)}$ run over those components, which are initially empty $\mu_j^{(0)}=(1-n_j^{(i)})\exp(\mathrm{i}\theta_j^{(i)})$, as well as

$$a^{(m)}=\int\frac{\mathrm{d}^{2J}\mu^{(m)}}{\pi^J}\int\frac{\mathrm{d}^{2J}\phi^{(m)}}{\pi^J}\left[\prod_{j=1}^{J}\left(\phi_j^{(m)}\right)+\chi_j^{(m)\,*}\right]$$
$$\times\exp\left(-\left|\phi^{(m)}\right|^2-\left|\mu^{(m)}\right|^2+\phi^{(m)\,*}\cdot\mu^{(m)}\right)\prod_{j=0}^{J-1}\left[\sum_{k=1}^{\infty}\frac{1}{k!}\left(\mu_{J-j}^{(m)\,*}\right)^k\left(\phi_{J-j}^{(m-1)}\right)^{k-1}+\zeta_{J-j}^{(m)}\right], \tag{122}$$

$$b_\alpha^{(m)}=\int\frac{\mathrm{d}^{2J}\mu^{(m)}}{\pi^J}\int\frac{\mathrm{d}^{2J}\phi^{(m)}}{\pi^J}$$
$$\times\exp\left(-\left|\phi^{(m)}\right|^2-\left|\mu^{(m)}\right|^2+\phi^{(m)\,*}\cdot\mu^{(m)}\right)\zeta_\alpha^{(m)\,*}\chi_\alpha^{(m-1)}\left\{\prod_{j=0}^{J-\alpha-1}\left[\sum_{k=1}^{\infty}\frac{1}{k!}\left(\mu_{J-j}^{(m)\,*}\right)^k\left(\phi_{J-j}^{(m-1)}\right)^{k-1}+\zeta_{J-j}^{(m)}\right]\right\}$$
$$\times\left[\sum_{k=1}^{\infty}c_k^{(1)}\left(\phi_\alpha^{(m-1)}\right)\left(\mu_\alpha^{(m)\,*}\right)^k+\zeta_\alpha^{(m)}\right]\left\{\prod_{j=J-\alpha+1}^{J-1}\left[\sum_{k=1}^{\infty}\frac{1}{k!}\left(\mu_{J-j}^{(m)\,*}\right)^k\left(\phi_{J-j}^{(m-1)}\right)^{k-1}+\zeta_{J-j}^{(m)}\right]\right\}$$
$$\times\left[\prod_{j=1}^{J}\left(\phi_j^{(m)}+\chi_j^{(m)\,*}\right)\right], \tag{123}$$

$$c_{\alpha\beta}^{(m)}=\int\frac{\mathrm{d}^{2J}\mu^{(m)}}{\pi^J}\int\frac{\mathrm{d}^{2J}\phi^{(m)}}{\pi^J}\exp\left(-\left|\phi^{(m)}\right|^2-\left|\mu^{(m)}\right|^2+\phi^{(m)\,*}\cdot\mu^{(m)}\right)\zeta_\alpha^{(m)\,*}\chi_\beta^{(m-1)}$$
$$\times\left\{\prod_{j=0}^{J-\max(\alpha,\beta)-1}\left[\sum_{k=1}^{\infty}\frac{1}{k!}\left(\mu_{J-j}^{(m)\,*}\right)^k\left(\phi_{J-j}^{(m-1)}\right)^{k-1}+\zeta_{J-j}^{(m)}\right]\right\}\times\left[\sum_{k=1}^{\infty}c_k^{(2)}\left(\phi_{\max(\alpha,\beta)}^{(m-1)}\right)\left(\mu_{\max(\alpha,\beta)}^{(m)\,*}\right)^k+\zeta_{\max(\alpha,\beta)}^{(m)}\right]$$
$$\times\left\{\prod_{j=J-\max(\alpha,\beta)+1}^{J-\min(\alpha,\beta)-1}\left[\sum_{k=1}^{\infty}c_k^{(3)}\left(\phi_{J-j}^{(m-1)}\right)\left(\mu_{J-j}^{(m)\,*}\right)^k+\zeta_{J-j}^{(m)}\right]\right\}$$
$$\times\left[\sum_{k=1}^{\infty}c_k^{(2)}\left(\phi_{\min(\alpha,\beta)}^{(m-1)}\right)\left(\mu_{\min(\alpha,\beta)}^{(m)\,*}\right)^k+\zeta_{\min(\alpha,\beta)}^{(m)}\right]\times\left\{\prod_{j=J-\min(\alpha,\beta)+1}^{J-1}\left[\sum_{k=1}^{\infty}\frac{1}{k!}\left(\mu_{J-j}^{(m)\,*}\right)^k\left(\phi_{J-j}^{(m-1)}\right)^{k-1}+\zeta_{J-j}^{(m)}\right]\right\}$$
$$\times\left[\prod_{j=1}^{J}\left(\phi_j^{(m)}+\chi_j^{(m)\,*}\right)\right] \tag{124}$$

$$
\begin{aligned}
d_{\alpha\beta}^{(m)} = & \int \frac{\mathrm{d}^{2J}\mu^{(m)}}{\pi^J} \int \frac{\mathrm{d}^{2J}\phi^{(m)}}{\pi^J} \exp\left(-\left|\phi^{(m)}\right|^2 - \left|\mu^{(m)}\right|^2 + \phi^{(m)\,*} \cdot \mu^{(m)}\right) \\
& \times \left[\prod_{j=1}^{J}\left(\phi_j^{(m)} + \chi_j^{(m)\,*}\right)\right] \zeta_\alpha^{(m)\,*} \zeta_\beta^{(m)\,*} \chi_\beta^{(m-1)} \chi_\alpha^{(m-1)} \times \left\{\prod_{j=0}^{J-\max(\alpha,\beta)-1}\left[\sum_{k=1}^{\infty}\frac{1}{k!}\left(\mu_{J-j}^{(m)\,*}\right)^k\left(\phi_{J-j}^{(m-1)}\right)^{k-1} + \zeta_{J-j}^{(m)}\right]\right\} \\
& \times \left[\sum_{k=1}^{\infty} c_k^{(4)}\left(\phi_{\max(\alpha,\beta)}^{(m-1)}\right)\left(\mu_{\max(\alpha,\beta)}^{(m)\,*}\right)^k + \zeta_{\max(\alpha,\beta)}^{(m)}\right] \times \left\{\prod_{j=J-\max(\alpha,\beta)+1}^{J-\min(\alpha,\beta)-1}\left[\sum_{k=1}^{\infty}\frac{1}{k!}\left(\mu_{J-j}^{(m)\,*}\right)^k\left(\phi_{J-j}^{(m-1)}\right)^{k-1} + \zeta_{J-j}^{(m)}\right]\right\} \\
& \times \left[\sum_{k=1}^{\infty} c_k^{(4)}\left(\phi_{\min(\alpha,\beta)}^{(m-1)}\right)\left(\mu_{\min(\alpha,\beta)}^{(m)\,*}\right)^k + \zeta_{\min(\alpha,\beta)}^{(m)}\right] \times \left\{\prod_{j=J-\min(\alpha,\beta)+1}^{J-1}\left[\sum_{k=1}^{\infty}\frac{1}{k!}\left(\mu_{J-j}^{(m)\,*}\right)^k\left(\phi_{J-j}^{(m-1)}\right)^{k-1} + \zeta_{J-j}^{(m)}\right]\right\},
\end{aligned}
\tag{125}
$$

Inserting the integrals like this results in the following path integral:

$$
\begin{aligned}
K\left(\mathbf{n}^{(f)}, \mathbf{n}^{(i)}; t_f\right) = & \left[\prod_{j:n_j^{(i)}=0}\int_0^{2\pi}\frac{\mathrm{d}\theta_j^{(0)}}{2\pi}\exp\left(-\mathrm{i}\theta_j^{(0)}\right)\right]\left[\prod_{m=1}^{M-1}\prod_j\int_{\mathbb{C}}\frac{\mathrm{d}\phi_j^{(m)}}{\pi}\exp\left(-\left|\phi_j^{(m)}\right|^2\right)\right] \\
& \times \left[\prod_{j:n_j^{(f)}=0}\int_{\mathbb{C}}\frac{\mathrm{d}\phi_j^{(M)}}{\pi}\phi_j^{(M)}\exp\left(-\left|\phi_j^{(M)}\right|^2\right)\right] \\
& \times \exp\left\{\sum_{m=1}^{M}\left[\phi^{(m)*}\cdot\phi^{(m-1)} - \frac{\mathrm{i}\tau}{\hbar}H_{cl}\left(\phi^{(m)*}, \phi^{(m-1)}\right)\right]\right\},
\end{aligned}
\tag{126}
$$

with the classical hamiltonian

$$
\begin{aligned}
& H^{(cl)(m)}\left(\mu^*, \phi\right) \\
& \quad = \sum_{\alpha=1}^{J} h_{\alpha\alpha}^{(m)} \exp\left(-\mu_\alpha{}^*\phi_\alpha\right) \\
& \qquad + \sum_{\substack{\alpha,\beta=1 \\ \alpha\neq\beta}}^{J} U_{\alpha\beta}^{(m)} \exp\left(-\mu_\alpha{}^*\phi_\alpha - \mu_\beta{}^*\phi_\beta\right) \\
& \qquad + \sum_{\substack{\alpha,\beta=1 \\ \alpha\neq\beta}}^{J} h_{\alpha\beta}^{(m)} \mu_\beta{}^*\phi_\alpha \exp\left(-\mu_\alpha{}^*\phi_\alpha\right) f\left(\mu_\beta{}^*, \phi_\beta\right) \\
& \qquad \times \prod_{j=\min(\alpha,\beta)+1}^{\max(\alpha,\beta)-1} g\left(\mu_j{}^*, \phi_j\right),
\end{aligned}
\tag{127}
$$

where f and g are arbitrary analytical functions satisfying

$$
f(0, \phi) = 1 \tag{128}
$$

$$
g(0, \phi) = -1 \tag{129}
$$

$$
\left.\frac{\partial}{\partial \mu^*} g\left(\mu^*, \phi\right)\right|_{\mu^*=0} = 2\phi. \tag{130}
$$

References

1. Brack M, Bhaduri R (1997) Semiclassical physics, 1st edn. Westview Press, Boulder
2. Sakurai JJ, Napolitano JJ (2010) Modern quantum mechanics, 2nd edn. Addison-Wesley, Boston
3. Gutzwiller MC (1991) Chaos in classical and quantum mechanics, 1st edn. Springer, New York
4. Schulman LS (1996) Techniques and applications of path integration. Wiley, New York
5. Gutzwiller MC (1967) J Math Phys 8:1979
6. Haake F (2010) Quantum signatures of chaos, 3rd edn. Springer, Berlin
7. Miller WH (1974) Adv Chem Phys 25:69
8. Baranger HU, Jalabert RA, Stone AD (1993) Phys Rev Lett 70:3876
9. Richter K, Sieber M (2002) Phys Rev Lett 89:206801
10. Richter K (2000) Semiclassical theory of mesoscopic quantum systems. Springer, Berlin
11. Jalabert RA (2000) Proc Int Sch Phys "Enrico Fermi" 143:145
12. Waltner D (2012) Semiclassical approach to mesoscopic systems. Springer, Berlin
13. Miller WH (1975) Adv Chem Phys 30:77
14. Heller EJ (1991) J Chem Phys 94:2723
15. Stock G, Thoss M (1997) Phys Rev Lett 78:578
16. Wang H, Thoss M, Miller WH (2000) J Chem Phys 112:47
17. Ullmo D (2008) Rep Prog Phys 71:026001
18. Ezra GS, Richter K, Tanner G, Wintgen D (1991) J Phys B At Mol Opt Phys 24:L413

19. Hummel Q, Urbina JD, Richter K (2013) J Phys A Math Theor 47:01510
20. Kirrander A, Shalashilin DV (2011) Phys Rev A 84:033406
21. Paul T (2002) Semiklassik für spinabhängigen Transport in inhomogenen Magnetfeldern. Diploma thesis, Universität Regensburg
22. Littlejohn RG, Flynn WG (1991) Phys Rev A 44:5239
23. Littlejohn RG, Flynn WG (1992) Phys Rev A 45:7697
24. Mathur H, Stone AD (1992) Phys Rev Lett 68:2964
25. Bolte J, Glaser R, Keppeler S (2001) Ann Phys 293:1
26. Pletyukhov M, Amann C, Mehta M, Brack M (2002) Phys Rev Lett 89:116601
27. Pletyukhov M, Zaitsev O (2003) J Phys A Math Gen 36:5181
28. Zaitsev O, Frustaglia D, Richter K (2005) Phys Rev B 72:155325
29. Negele JW, Orland H (1988) Quantum many-particle systems. Addison-Wesley, Boston
30. Weinberg S (2005) The quantum theory of fields, volume 1: foundations. Cambridge University Press, Cambridge
31. Lewenstein M, Sanpera A, Ahufinger V (2012) Ultracold atoms in optical lattices: simulating quantum many-body systems. Oxford University Press, Oxford
32. Lewenstein M, Sanpera A, Ahufinger V, Damski B, Sen(De) A, Sen U (2007) Adv Phys 56:243
33. Baranger M, de Aguiar MAM, Keck F, Korsch HJ, Schellhaaß B (2001) J Phys A Math Gen 34:7227
34. Engl T, Dujardin J, Argüelles A, Schlagheck P, Richter K, Urbina JD (2014) Phys Rev Lett 112:140403
35. Klauder JR (1960) Ann Phys 11:123
36. Meyer H, Miller WH (1979) J Chem Phys 71:2156
37. Miller WH, White KA (1986) J Chem Phys 84:5059
38. Grossmann F, Buchholz M, Pollak E, Nest M (2014) Phys Rev A 89:032104
39. Li B, Miller WH (2012) J Chem Phys 137:154107
40. Swenson DWH, Levy T, Cohen G, Rabani E, Miller WH (2011) J Chem Phys 134:164103
41. Li B, Wilner EY, Thoss M, Rabani E, Miller WH (2014) J Chem Phys 140:104110
42. Manning RS, Ezra GS (1996) Phys Rev A 53:661
43. The authors tried, so far unsuccessfully, to establish such a link.
44. Thoss M, Stock G (1999) Phys Rev A 59:64
45. Berezin FA (1966) The method of second quantization. Academic Press, New York
46. Trotter HF (1959) Proc Am Math Soc 10:545
47. Nolting W (2009) Fundamentals of many-body physics: principles and methods. Springer, New York
48. Wilets L, Henley EM, Kraft M, Mackellar A (1977) Nucl Phys A 282:341
49. Dorso C, Duarte S, Randrup J (1987) Phys Lett B 188:287
50. Boal DH, Glosli JN (1988) Phys Rev C 38:1870
51. Latora V, Belkacem M, Bonasera A (1994) Phys Rev Lett 73:1765
52. Sun X, Miller WH (1997) J Chem Phys 106:6346
53. Levein RD (2000) Proc Natl Acad Sci USA 97:1965
54. Braun C, Garg A (2007) J Math Phys 48:032104
55. Tabor M (1989) Chaos and integrability in nonlinear dynamics: an introduction, 1st edn. Wiley, New York
56. Solari HG (1987) J Math Phys 28:1097
57. Kochetov EA (1995) J Math Phys 36:4667
58. Vieira V, Sacramento P (1995) Nucl Phys B 448:331
59. Pletyukhov M (2004) J Math Phys 45:1859
60. Berry MV (1985) Proc R Soc Lond A 400:229
61. Bychkov YA, Rashba EI (1984) J Phys C Solid State Phys 17:6039
62. Lin YJ, Jimenez-Garcia K, Spielman IB (2011) Nature 471:83
63. Engl T, Urbina JD, Richter K (in preparation)

Theor Chem Acc (2014) 133:1571
DOI 10.1007/s00214-014-1571-9

REGULAR ARTICLE

A new method to improve validity range of Lie canonical perturbation theory: with a central focus on a concept of non-blow-up region

Hiroshi Teramoto · Mikito Toda · Tamiki Komatsuzaki

Received: 12 May 2014 / Accepted: 21 August 2014 / Published online: 13 September 2014

Abstract Validity ranges of Lie canonical perturbation theory (LCPT) are investigated in terms of non-blow-up regions. We investigate how the validity ranges depend on the perturbation order in two systems, one of which is a simple Hamiltonian system with one degree of freedom and the other is a HCN molecule. Our analysis of the former system indicates that non-blow-up regions become reduced in size as the perturbation order increases. In case of LCPT by Dragt and Finn and that by Deprit, the non-blow-up regions enclose the region inside the separatrix of the Hamiltonian, but it may not be the case for LCPT by Hori. We also analyze how well the actions constructed by these LCPTs approximate the true action of the Hamiltonian in the non-blow-up regions and find that the conventional truncated LCPT does not work over the whole region inside the separatrix, whereas LCPT by Dragt and Finn without truncation does. Our analysis of the latter system indicates that non-blow-up regions do not necessarily cover the whole regions inside the HCN well. We propose a new perturbation method to improve non-blow-up regions and validity ranges inside them. Our method is free from blowing up and retains the same normal form as the conventional LCPT. We demonstrate our method in the two systems and show that the actions constructed by our method have larger validity ranges than those by the conventional and our previous methods proposed in Teramoto and Komatsuzaki (J Chem Phys 129:094302, 2008; Phys Rev E 78:017202, 2008).

Keywords Lie canonical perturbation theory · Non-blow-up region · HCN isomerization

Dedicated to Professor Greg Ezra and published as part of the special collection of articles celebrating his 60th birthday.

H. Teramoto · T. Komatsuzaki (✉)
Molecule and Life Nonlinear Sciences Laboratory,
Research Institute for Electronic Science, Hokkaido University,
Kita 20 Nishi 10, Kita-ku, Sapporo 001-0020, Japan
e-mail: tamiki@es.hokudai.ac.jp

H. Teramoto
e-mail: teramoto@es.hokudai.ac.jp

M. Toda
Nonequilibrium Dynamics Laboratory, Research group
of Physics, Division of Natural Science,
Nara Women's University, Nara 630-8506, Japan
e-mail: toda@ki-rin.phys.nara-wu.ac.jp

1 Introduction

Canonical transformations are coordinate transformations in the phase space of Hamiltonian systems that preserve symplectic two forms, i.e., preserving the form of Hamiltonian equations of motions. Canonical perturbation theory (CPT) is one of the fundamental theories of solving nonlinear dynamical problems that is carried by perturbation from integrable systems through some canonical transformation. CPT has often been applied for seeking for integrals of motions, adiabatic invariants and a better and simpler description of the systems [3]. The traditional canonical transformation is by mixed-variable generating function composed of old and new canonical variables. The most traditional Poincaré-Von Zeipel CPT [3, 4] based on the mixed-variable generating function approach, however, imposes a major impediment to implementing higher order perturbations. Among CPTs, Lie canonical perturbation theory (LCPT) originally developed by Hori [5, 6] and Deprit [7], later by Dragt and Finn [8], is very powerful in that canonical transformation is carried by a series of operations of Poisson brackets avoiding

cumbersome generating function of mixed variables where complete inversion from the old to the new canonical variables is rather straightforward. Their mutual relation and their computational efficiency have also been investigated [4, 9–14]. These different formats result in the same normal form Hamiltonian but can result in different normal form transformations. The convergence or divergence of the normal form and normal form transformation of order infinity has been investigated in the previous studies [15–27] under various conditions. Under some of these conditions, the normal form and normal form transformation converges globally, but, since generic Hamiltonians are non-integrable [28], in most cases, there is no hope to seek for (nontrivial) global integral of motions without any symmetries. Under such circumstance, what one can do best is to look into a better and simpler local description of the system in question. LCPT has been applied to seeking for such local descriptions in a perturbative manner from integrable solutions and shown to be versatile in various types of Hamiltonian in the research fields such as celestial mechanics [29, 30], atomic physics [31, 32] and cluster physics [33–39]. For example, in the context of chemical reaction dynamics, LCPT has been applied to seeking (locally-)no-return transition state and the associated reaction coordinate buried in the phase space for many-degrees of freedom Hamiltonian systems such as intramolecular proton transfer in malonaldehyde [40, 41], argon cluster isomerization [33–39], $O(^1D) + N_2O \rightarrow NO + NO$ [42], a hydrogen atom in crossed electric and magnetic fields [32, 43], HCN isomerization [1, 2, 44–46] and so forth. LCPT was generalized to dissipative systems such as multidimensional (generalized) Langevin formulation to describe reactions under thermal fluctuation, in which no-return transition state can be obtained by incorporating nonlinearity of the system and interactions with heat bath [47–54]. The pioneering studies on semiclassical analog of LCPT was also carried out in late 1980s for multidimensional resonant, nonresonant and nearly resonant systems [55–57]: They presented a method for deriving corrections in powers of Planck's constant by the reflection of the underlying (near) divergence properties of classical chaos, which was found to be effective even at low-order corrections in improving the accuracy of the energy eigenvalues. Recently, their semiclassical studies were extended to the analyses of reaction dynamics over a rank-one saddle under a time-dependent external field (optimally controlled laser pulse), and it was found that optimally controlled laser pulse corresponds to modulating the boundary of the reaction in the phase space so as to catch the system excited in the reactant well and then to release it into the product [58]. This method provides a new protocol to design the laser field facilitated by the classical phase space picture [59].

However, in most cases, the convergence radii of these LCPTs are limited even for finite order of perturbations [60], and the convergence radii shrink to zero as the perturbation order increases. In a context of chemical reaction dynamics, molecules exhibit larger amplitude motions as their energies increase. For these molecules to surmount the reaction barriers, they must have large enough energies. Therefore, to describe and understand the chemical reaction dynamics, it is vital to develop a perturbation method that is valid not only in the very vicinity of their equilibrium structures but also in regions far from them. In a broader context, if we succeed in obtaining a better estimation for approximate invariants of motion, we would be able to analyze dynamics not only for near-integrable systems but also for systems with mixed phase space, i.e., those systems which exhibit both chaotic and regular behavior.

In the study of systems with mixed phase space, one of the crucial problems is to find boundaries between chaotic and regular behavior. For systems of more than two degrees of freedom, it is well known that the KAM tori do not divide the equi-energy surface into two separate regions. In fact, Arnold showed, for a specific model Hamiltonian, that trajectories detour around KAM tori, thereby leading to the motion along the resonances [61]. Such motions are now called the Arnold diffusion [62–64]. Moreover, it is known that the resonances constitute a network called the Arnold web [3, 31, 65–70], where the motion across the resonances gives rise to faster diffusion especially around resonance junctions [71, 72]. Thus, in the analysis of the dynamics on the Arnold web, it is crucial to find those regions which trap trajectories for a finite but longer duration [73], since distribution of resonances plays a key role for statistical features of the reaction dynamics [74, 75]. Then, better approximate invariants would offer a clue to find how chaotic and regular regions are distributed in the phase space.

Another important issue in systems of mixed phase space is the transport in the phase space [76–78], i.e., to understand how different regions of the phase space are dynamically connected. In chemistry, reaction processes are nothing but the transport from a potential well to another one via a saddle region. Thus, we face the problem of what kind of phase space structures connect dynamics in a well to that in another one [79]. In such studies, we need to construct better action variables, if any, in different regions of the phase space so that validity ranges of different sets of variables overlap with each other. Then, we could investigate the connection based on the transformation between different sets of the approximate invariants corresponding to different regions of the phase space.

Teramoto et al. [1, 2] proposed a method that makes LCPT valid in wider regions than those in the previous method and demonstrated it in a highly excited HCN molecule. The crux is to calculate canonical transformation in

each order of LCPT without any truncation errors. However, validity ranges of their method are also limited by non-blow-up regions. Validity range of a LCPT is a subset of phase space where the resulting normal form is valid. For example, if the normal form is to construct slowly varying actions, center manifolds or stable and unstable manifolds, the validity range of the LCPT is a region where the resulting normal form describes these objects within a given accuracy needed to describe systems. Non-blow-up region of LCPT is a subset of initial conditions in the phase space where the results of the perturbation are finite. Non-blow-up region limits the validity ranges of LCPT because the results should be at least finite to validate them. To improve their method further, it is important to understand these concepts. Section 2 is devoted to an illustration of these concepts in a simple one-degree-of-freedom Hamiltonian system and elucidations of these concepts along with their numerical demonstrations. In Sect. 3, we propose a new perturbation method to avoid blowing up while retaining the normal forms and demonstrate it in Sect. 4. Section 5 is devoted to conclusions and discussions.

2 Non-blow-up regions of Lie canonical perturbation theory, LCPT

2.1 An illustration of a validity range of LCPT for a one-dimensional Hamiltonian system

To illustrate non-blow-up regions of LCPT, let us investigate a simple Hamiltonian system. Let (q,p) be a coordinate and its conjugate momentum with a Hamiltonian represented by

$$H(q,p) = \frac{1}{2}\left(p^2+q^2\right) + \left(2p^2q - q^3\right). \tag{1}$$

LCPT seeks for a canonical transformation $(q,p) \mapsto (Q,P)$ so that the Hamiltonian [Eq. (1)] in terms of the new coordinate (Q,P) becomes simple in a certain sense. There exist several conventions for the simplicities [12] and normal forms that attain them.[1] In this specific example, the leading order of normal form would be like

$$\bar{H}(Q,P) = \frac{1}{2}\left(P^2+Q^2\right) + O(4), \tag{2}$$

[$O(4)$ means a collection of terms of order quartic and those of higher than quartic with respect to P and Q.] such that it has the same quadratic terms but does not have terms of order cubic. To obtain the normal form, LCPT seeks for a canonical transformation generated by a generating function $F(q,p)$, i.e.,

$$Q(q,p) = e^{-\{F(q,p),\cdot\}}q, \tag{3}$$

$$P(q,p) = e^{-\{F(q,p),\cdot\}}p, \tag{4}$$

where $\{\cdot,\cdot\}$ is Poisson bracket defined as

$$\{A(q,p),B(q,p)\} = \frac{\partial A(q,p)}{\partial q}\frac{\partial B(q,p)}{\partial p} - \frac{\partial A(q,p)}{\partial p}\frac{\partial B(q,p)}{\partial q}. \tag{5}$$

A benefit for Lie canonical transformation is that the inverse transformation $(Q,P) \to (q,p)$ can be easily written as

$$q(Q,P) = e^{\{F(Q,P),\cdot\}}Q, \tag{6}$$

$$p(Q,P) = e^{\{F(Q,P),\cdot\}}P. \tag{7}$$

This can be evaluated using the following relation,

$$\begin{aligned}\left\{A'(Q,P),B'(Q,P)\right\} &= \frac{\partial A'(Q(q,p),P(q,p))}{\partial q}\frac{\partial B'(Q(q,p),P(q,p))}{\partial p} \\ &\quad - \frac{\partial A'(Q(q,p),P(q,p))}{\partial p}\frac{\partial B'(Q(q,p),P(q,p))}{\partial q}, \\ &= \frac{\partial A'(Q,P)}{\partial Q}\frac{\partial B'(Q,P)}{\partial P} - \frac{\partial A'(Q,P)}{\partial P}\frac{\partial B'(Q,P)}{\partial Q},\end{aligned} \tag{8}$$

which holds for arbitrary differentiable functions $A'(Q,P)$ and $B'(Q,P)$ if the transformation $(q,p) \mapsto (Q,P)$ is a canonical transformation [80]. using Eq. (8), the leading order expression of Eqs. (6) and (7) can be written as

$$q(Q,P) = Q - \frac{\partial F(Q,P)}{\partial P} + \cdots, \tag{9}$$

$$p(Q,P) = P + \frac{\partial F(Q,P)}{\partial Q} + \cdots. \tag{10}$$

By plugging the leading order expression in Eq. (1), we get

$$\begin{aligned}\bar{H}(Q,P) = H(p,q) &= \frac{1}{2}\left(Q^2+P^2\right) + \left(2P^2Q - Q^3\right) \\ &\quad - Q\frac{\partial F(Q,P)}{\partial P} + P\frac{\partial F(Q,P)}{\partial Q} + \cdots.\end{aligned} \tag{11}$$

To eliminate the cubic term of Eq. (11), the generating function $F(Q,P)$ should satisfy

$$\left(2P^2Q - Q^3\right) - Q\frac{\partial F(Q,P)}{\partial P} + P\frac{\partial F(Q,P)}{\partial Q} = 0. \tag{12}$$

[1] In a context of chemistry, people are often interested in extracting slowly varying action variables, i.e., adiabatic invariants. It is because these variables determine the slowest time scale of intramolecular vibrational relaxation and chemical reaction triggered by that. For this purpose, the desired normal form would be the one that maximally decouples these action variables from those of the other degrees of freedom.

Equation (12) can have multiple solutions but, in this specific case, the conventional semi-simple normal form requires

1. $F(Q,P)$ is of order cubic.
2. $F(Q,P) \in \mathrm{Im}(-Q\frac{\partial}{\partial P} + P\frac{\partial}{\partial Q}) = \mathrm{Im}\{H_2(Q,P),\cdot\}$, where $H_2(Q,P) = \frac{1}{2}(P^2+Q^2)$ is the quadratic term of Eq. (2) and $\mathrm{Im}\,A$ is the image of the operator A, i.e., $\mathrm{Im}\,A = \{f|\exists g, f = Ag\}$.

By these requirements, Eq. (12) has an unique solution, $F(Q,P) = -PQ^2$. By plugging this in Eq. (11), the $\cdots$ terms in Eq. (11) become of order quartic or higher than quartic, and thus, the canonical transformation generated by the generating function $F(Q,P)$ is actually what we sought for. In this case, we can *exactly* calculate the canonical transformation [Eqs. (3) and (4)] and we get

$$Q(q,p) = \frac{q}{1+q}, \tag{13}$$

$$P(q,p) = p(q+1)^2, \tag{14}$$

using the fact that the canonical transformations can be calculated by integrating the following differential equations up to $\epsilon = 1$,

$$\frac{dq(\epsilon)}{d\epsilon} = \frac{\partial F(q(\epsilon),p(\epsilon))}{\partial p}, \tag{15}$$

$$\frac{dp(\epsilon)}{d\epsilon} = -\frac{\partial F(q(\epsilon),p(\epsilon))}{\partial q}, \tag{16}$$

starting from the initial condition $(q(0),p(0)) = (q,p)$ at $\epsilon = 0$. Then, $Q(q,p)$ and $P(q,p)$ can be obtained as $(Q(q,p),P(q,p)) = (q(1),p(1))$.

Note that the canonical transformation has a set of singular points at $q = -1$. Therefore, the maximally connected component containing the origin and where the canonical transformation is well-defined is $\mathrm{Dom}_F = \{(q,p)|-1 < q\}$. We call Dom_F the non-blow-up region of the canonical transformation generated by F. As long as one uses the formal power series of the canonical transformation, its domain of convergence cannot go beyond this region, and thus, this region limits the validity range of Lie canonical perturbation theory. To illustrate this, let us consider the power series expansion of the canonical transformation [Eqs. (13) and (14)],

$$Q(q,p) = \sum_{l=0}^{\infty}(-1)^l q^{l+1}, \tag{17}$$

$$P(q,p) = pq^2 + 2pq + p. \tag{18}$$

The region where this expansion converges is $\{(q,p)|-1 < q < 1\}$, which is strictly smaller than Dom_F. Roughly speaking, the convergence radius of a canonical transformation is determined by the shortest distance between the expansion origin and the singularity of the canonical transformation, and the expansion converges only within an isotropic circle of the radius.[2] However, if its non-blow-up region extends anisotropically in the phase space, like the current example, the non-blow-up region can be much larger than the region where the expansion converges.

2.2 Non-blow-up regions of LCPT for n-dimensional Hamiltonian systems

Let $\mathbf{q} = (q_1,\ldots,q_n)$ be coordinates in an n-dimensional Hamiltonian system and $\mathbf{p} = (p_1,\ldots,p_n)$ be their conjugate momenta with a Hamiltonian $H(\mathbf{q},\mathbf{p})$, which is analytic in a neighborhood of the origin $(\mathbf{q},\mathbf{p}) = \mathbf{0}$. In addition, let the Hamiltonian have a stationary point at the origin $(\mathbf{q},\mathbf{p}) = \mathbf{0}$, i.e., $(\frac{\partial H(\mathbf{q},\mathbf{p})}{\partial \mathbf{p}}, -\frac{\partial H(\mathbf{q},\mathbf{p})}{\partial \mathbf{q}})|_{(\mathbf{q},\mathbf{p})=\mathbf{0}} = \mathbf{0}$. Without loss of generality, the value of the Hamiltonian at the origin can be set to zero, i.e., $H(\mathbf{0},\mathbf{0}) = 0$. Under these settings, in a neighborhood of the origin, the Hamiltonian can be written as

$$H(\mathbf{q},\mathbf{p}) = \sum_{k=2}^{\infty} H_k(\mathbf{q},\mathbf{p}) \tag{19}$$

where $H_k(\mathbf{q},\mathbf{p})$ is a homogeneous polynomial of order k with respect to $(\mathbf{q},\mathbf{p})$. Depending on the form of $H_2(\mathbf{q},\mathbf{p})$, several types of normal forms have been proposed, such as, semi-simple normal form, inner product normal form [12]. There also exist several types of the normalization procedures to realize the normal forms [12]. Here, we use the normalization procedure due to Dragt and Finn [82], which is classified as format 2a in [12].[3] However, our method works for other procedures classified into format 2 in [12]. The procedure of Dragt and Finn aims at normalizing the Hamiltonian [Eq. (19)] by the following consecutive Lie canonical transformations

$$\mathbf{Q}^{(m)}(\mathbf{q},\mathbf{p}) = e^{-\{F_m,\cdot\}}e^{-\{F_{m-1},\cdot\}}\cdots e^{-\{F_3,\cdot\}}\mathbf{q}, \tag{20}$$

$$\mathbf{P}^{(m)}(\mathbf{q},\mathbf{p}) = e^{-\{F_m,\cdot\}}e^{-\{F_{m-1},\cdot\}}\cdots e^{-\{F_3,\cdot\}}\mathbf{p}, \tag{21}$$

[2] Note that if the generating function F is real analytic, $Q(q,p)$ and $P(q,p)$ are also real analytic in Dom_F [81].

[3] In this book, the existing types of perturbations are classified to the five formats, format 1a, 1b, 2a, 2b and 2c, depending on whether they use generating function or not, iterative or recursive. LCPTs by Dragt and Finn, Hori and Deprit are classified into format 2a, 2b and 2c, respectively. For details of the classification, see [12] in Sect. 3.2.

generated by the generating functions $F_m, F_{m-1}, \ldots, F_3$ where F_k $(3 \leq k \leq m)$ is a homogeneous polynomial of order k with respect to $(\mathbf{q}, \mathbf{p})$. The non-blow-up region U_m of the LCPT is

$$\begin{aligned} U_m &= \mathrm{Dom}_{F_3} \cap \bigcap_{k=4}^{m} e^{\{F_3,\cdot\}} \ldots e^{\{F_{k-1},\cdot\}} \mathrm{Dom}_{F_k}, \\ &= \mathrm{Dom}_{F_3} \cap e^{\{F_3,\cdot\}} \mathrm{Dom}_{F_4} \cap \cdots \cap e^{\{F_3,\cdot\}} \ldots e^{\{F_{m-1},\cdot\}} \mathrm{Dom}_{F_m}, \end{aligned} \tag{22}$$

that is, an intersection between Dom_{F_3} and $e^{\{F_3,\cdot\}} \ldots e^{\{F_{k-1},\cdot\}} \mathrm{Dom}_{F_k}$ $(k = 4, \ldots, m)$, which is the non-blow-up region Dom_{F_k} pulled back to the space spanned by the original phase space variables, $\mathbf{p}$ and $\mathbf{q}$.

In general, we have $U_{m_1} \subseteq U_{m_2}$ for $m_1 \geq m_2$, and thus, the non-blow-up region shrinks as the perturbation order $m (m > 3)$ increases. The question of how the non-blow-up region shrinks depends on specific forms of the generating functions but, in general, if k $(k \geq 3)$ is odd and if $\mathbf{0}$ is an isolated critical point of $F_k(\mathbf{q}, \mathbf{p})$,[4] the differential equation induced by $F_k(\mathbf{q}, \mathbf{p})$,

$$\frac{d\mathbf{q}}{d\epsilon} = \frac{\partial F_k(\mathbf{q}, \mathbf{p})}{\partial \mathbf{p}}, \tag{23}$$

$$\frac{d\mathbf{p}}{d\epsilon} = -\frac{\partial F_k(\mathbf{q}, \mathbf{p})}{\partial \mathbf{q}}, \tag{24}$$

is unbounded, i.e., there is at least one unbounded solution [83].[5] If the unbounded solution blows up in a finite time, it can be shown that non-blow-up region of the canonical transformation generated by F_k is not equal to the whole phase space. The reason is the following. Let k be an odd integer that is larger than 2 and $(\mathbf{q}(\epsilon), \mathbf{p}(\epsilon))$ be one of the solutions of the differential equation that blows up at ϵ^*. Then,

$$\left(\mathbf{q}'(\epsilon), \mathbf{p}'(\epsilon)\right) = \left(\epsilon^*\right)^{\frac{1}{k-2}} \left(\mathbf{q}\left(\epsilon^* \epsilon\right), \mathbf{p}\left(\epsilon^* \epsilon\right)\right) \tag{25}$$

is also the solution of the differential equation that blows up at $\epsilon = 1$.

2.3 A demonstration of how the non-blow-up region U_m depends on the perturbation order m

In this section, we provide two examples of how the non-blow-up region U_m shrinks as the perturbation order m increases. First, we evaluate non-blow-up regions of LCPT by Dragt and Finn in a Hamiltonian [Eq. (1)] in Sect. 2.3.1 and compare them with those of LCPTs by Hori and by Deprit. The relation between these LCPTs has been discussed in [4, 9–14], and comparison has been made in terms of the computational complexity [4, 14], generalizability to non-autonomous Hamiltonian systems [4] and to an abstract setting of graded Lie algebras [12, 13]. Here, these LCPTs are compared in terms of their non-blow-up regions and validity ranges. In Sect. 2.3.2, we evaluate non-blow-up regions in a HCN molecule. In both the examples, we use a blow-up technique to integrate the differential equation in Eqs. (23) and (24) shown in Sect. 6.1 in Appendix. In the calculation of generating functions, we used an algorithm of Broer [14] for LCPT by Dragt and Finn and the triangle algorithms [10, 12] for LCPTs by Hori and Deprit.

2.3.1 Non-blow-up regions in a Hamiltonian [Eq. (1)]

In this section, we investigate how the non-blow-up region U_m depends on the perturbation order m. To investigate their relation to the phase space topology of the Hamiltonian [Eq. (1)], we plot contour lines of the Hamiltonian in Fig. 1a in the energy range $[-0.1, 0.4]$. This Hamiltonian has four fixed points, one of which is elliptic and the other three are hyperbolic. The elliptic fixed point is located at the origin $(q, p) = \mathbf{0}$ and the other three are located at $(\frac{1}{3}, 0)$, $(-\frac{1}{4}, \sqrt{\frac{7}{32}})$ and $(-\frac{1}{4}, -\sqrt{\frac{7}{32}})$, respectively. The one located at $(\frac{1}{3}, 0)$ has an energy $\frac{1}{54}$ that is smaller than that of the other two hyperbolic fixed points, and thus, the closest separatrix from the origin is made up of the stable and unstable manifolds of the hyperbolic fixed point $(\frac{1}{3}, 0)$. In Fig. 1b, we plot non-blow-up regions U_m $(m = 5, 10, 15, 20)$ of LCPT by Dragt and Finn in the Hamiltonian [Eq. (1)] along with the separatrix of the Hamiltonian. From this figure, U_m shrinks as m increases and U_m converges into the region inside the separatrix. To see if the similar behavior can be seen in other types of perturbation theory, we compare non-blow-up regions of LCPT by Hori, and that by Deprit which are classified as format 2b and 2c in [12], respectively. The former one seeks for the canonical perturbation of the form

$$\tilde{Q}^{(m)}(q, p) = e^{-\sum_{k=3}^{m} \left\{\tilde{F}_k, \cdot\right\}} q, \tag{26}$$

$$\tilde{P}^{(m)}(q, p) = e^{-\sum_{k=3}^{m} \left\{\tilde{F}_k, \cdot\right\}} p, \tag{27}$$

where $\tilde{F}_k(q, p)$ $(k = 3, \ldots, m)$ is a homogeneous polynomial of order k with respect to q and p. The generating function $\tilde{F}_k(q, p)$ $(k = 3, \ldots, m)$ is determined by the conventional manner (see [12]). $\tilde{Q}^{(m)}(q, p)$ and $\tilde{P}^{(m)}(q, p)$ can be obtained by integrating the differential equations

[4] $\mathbf{0}$ is an isolated critical point of $F_k(\mathbf{q}, \mathbf{p})$ if $F_k(\mathbf{q}, \mathbf{p})$ has a critical (stationary) point at $\mathbf{0}$ and there exists an open neighborhood of $\mathbf{0}$ within which there is no critical point other than $\mathbf{0}$.

[5] See COROLLARY in [83] in p. 1921. Note that k in this manuscript corresponds to $k + 1$ in their notation.

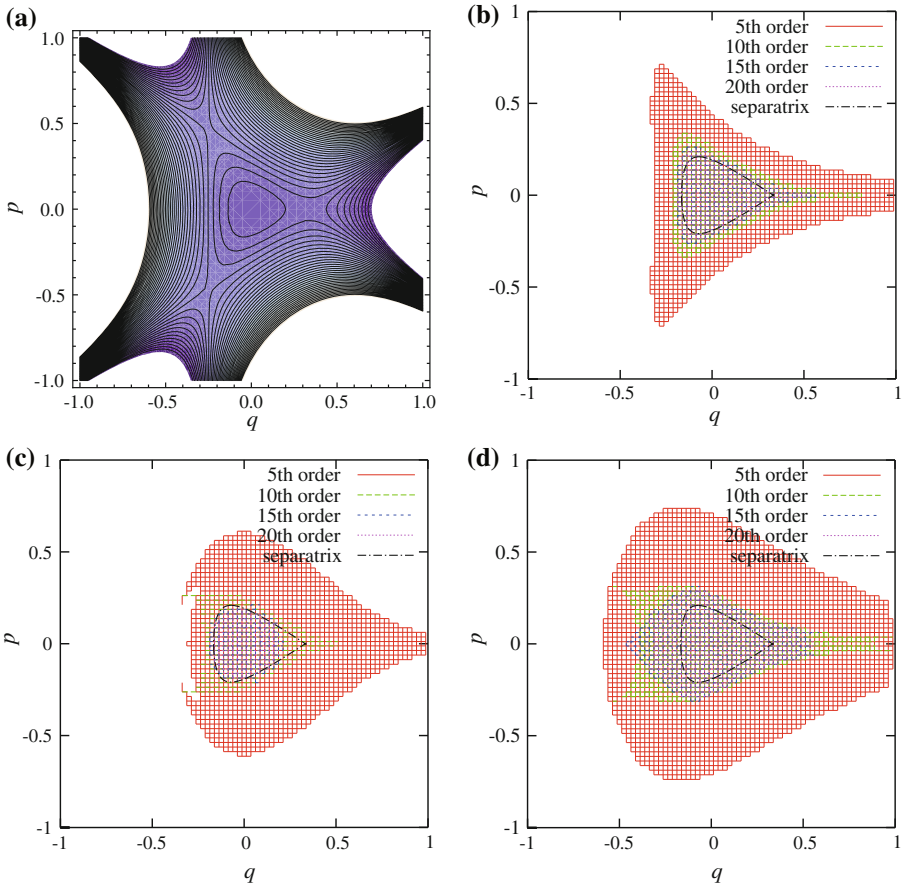

Fig. 1 **a** Contour lines of the Hamiltonian [Eq. (1)], **b**, **c**, **d** non-blow-up regions of LCPT by **b** Dragt and Finn U_m ($m = 5, 10, 15, 20$), **c** Hori $\tilde{U}_m$ ($m = 5, 10, 15, 20$), and, **d** Deprit $\hat{U}_m$ ($m = 5, 10, 15, 20$), along with the separatrix of the Hamiltonian [Eq. (1)]

$$\frac{dq(\epsilon)}{d\epsilon} = \frac{\partial \sum_{k=3}^{m} \tilde{F}_k(q(\epsilon), p(\epsilon))}{\partial p}, \tag{28}$$

$$\frac{dp(\epsilon)}{d\epsilon} = -\frac{\partial \sum_{k=3}^{m} \tilde{F}_k(q(\epsilon), p(\epsilon))}{\partial q}. \tag{29}$$

up to $\epsilon = 1$ starting from $(q(0), p(0)) = (q, p)$ at $\epsilon = 0$ and by putting

$$\left(\tilde{Q}^{(m)}(q,p), \tilde{P}^{(m)}(q,p)\right) = (q(1), p(1)). \tag{30}$$

The latter one seeks for a canonical transformation generated by the generating function $W^{(m)}(\epsilon, q, p) = \sum_{k=3}^{m} \frac{\epsilon^{k-3}}{(k-3)!} \hat{F}_k(q,p)$, where $\hat{F}_k(q,p)$ is a homogeneous polynomial of order k. In this case, the new variables $(\hat{Q}^{(m)}(q,p), \hat{P}^{(m)}(q,p))$ can be obtained by integrating the differential equation,

$$\frac{dq(\epsilon)}{d\epsilon} = \frac{\partial W^{(m)}(\epsilon, q(\epsilon), p(\epsilon))}{\partial p}, \tag{31}$$

$$\frac{dp(\epsilon)}{d\epsilon} = -\frac{\partial W^{(m)}(\epsilon, q(\epsilon), p(\epsilon))}{\partial q}, \tag{32}$$

until $\epsilon = 1$, starting from the initial condition $(q(0), p(0)) = (q, p)$ at $\epsilon = 0$. Then, $(\hat{Q}^{(m)}(q,p), \hat{P}^{(m)}(q,p))$ can be obtained as $(\hat{Q}^{(m)}(q,p), \hat{P}^{(m)}(q,p)) = (q(1), p(1))$. In these cases, we also define non-blow-up regions of the LCPT of order m, $\tilde{U}_m$ (Hori) and $\hat{U}_m$ (Deprit) as the set of the initial conditions where the solutions of the canonical transformations generated by these generating functions are bounded. In Fig. 1c, d, we plot $\tilde{U}_m$ and $\hat{U}_m$ for $m = 5, 10, 15$ and 20. For Hori's LCPT, the non-blow-up regions $\tilde{U}_{15}$ and $\tilde{U}_{20}$ do not cover the whole region inside the separatrix, whereas those of Deprit's LCPT cover relatively wide regions in the phase space. In this specific example, LCPT by Dragt and Finn and that by Deprit have wider non-blow-up regions up to the perturbation order 20th than that by Hori. More systematic study is needed to determine the best format of all the possible formats of LCPT (some of them is listed in [12]) that leads to the widest non-blow-up region among them.

To investigate validity ranges of the LCPTs, we compare the action variables constructed using the LCPTs with the true action inside the separatrix. Here, the true action is defined as

$$I = \frac{1}{2\pi} \int_{\{(q,p)|H(q,p)\le E, \text{inside the separatrix}\}} dqdp, \tag{33}$$

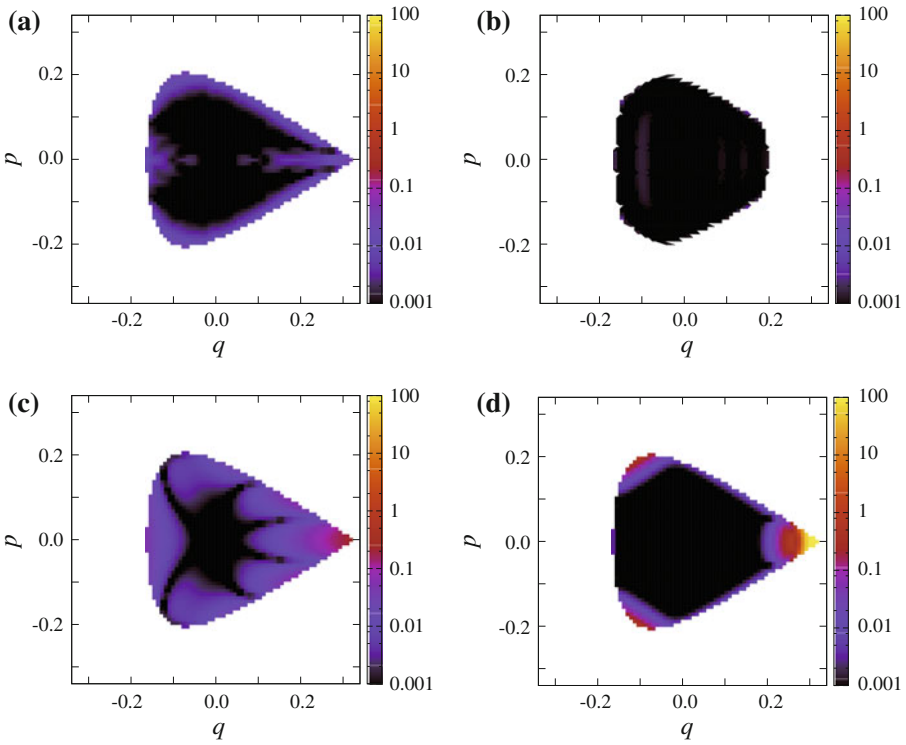

Fig. 2 The relative error between the true action I and **a** $I^{(20)}$ (Dragt and Finn), **b** $\tilde{I}^{(20)}$ (Hori), **c** $\hat{I}^{(20)}$ (Deprit) and **d** $I^{(20)}_{\rm trunc}$ (Dragt and Finn, truncated), plotted inside the separatrix

[80] while the actions constructed by LCPTs are denoted as $I^{(20)} = \frac{1}{2}((p^{(20)})^2 + (q^{(20)})^2)$ (Dragt and Finn), $\tilde{I}^{(20)} = \frac{1}{2}((\tilde{p}^{(20)})^2 + (\tilde{q}^{(20)})^2)$ (Hori), and $\hat{I}^{(20)} = \frac{1}{2}((\hat{p}^{(20)})^2 + (\hat{q}^{(20)})^2)$ (Deprit) with $I^{(20)}_{\rm trunc} = \frac{1}{2}((p^{(20)}_{\rm trunc})^2 + (q^{(20)}_{\rm trunc})^2)$ (Dragt and Finn, truncated), respectively, where $p^{(20)}_{\rm trunc}$ and $q^{(20)}_{\rm trunc}$ are constructed as follows. First, expand the canonical transformation Eqs. (20) and (21) with respect to **q** and **p**, and then, truncated it at the order 21-st, which is the conventional prescription used in [32]. These actions are close with each other within $O(E^{\frac{21}{2}})$. It is because the Hamiltonian (1) can be written as $H(q,p) = H_{\rm int}(I^{(20)}) + O(21)$ [this symbol O is the same as that defined in Eq. (2)] in terms of these actions, and, thus, the following equation

$$\begin{aligned} I &= \frac{1}{2\pi}\int_{\{(q,p)|H_{\rm int}(I^{(20)})\le E,\text{inside the separatrix}\}} dqdp + O\left(E^{\frac{20+1}{2}}\right), \\ &= \frac{1}{2\pi}\int_{\{(q,p)|H_{\rm int}(I^{(20)})\le E,\text{inside the separatrix}\}} dI^{(20)}d\Theta^{(20)} + O\left(E^{\frac{21}{2}}\right), \\ &= \int_{\{I|H_{\rm int}(I)\le E\}} dI^{(20)} + O\left(E^{\frac{21}{2}}\right), \\ &= I^{(20)} + O\left(E^{\frac{21}{2}}\right), \end{aligned} \tag{34}$$

holds, where $\Theta^{(20)} = \arctan\frac{q^{(20)}}{p^{(20)}}$ is an angle variable that is conjugate to $I^{(20)}$. To derive the last equality, we use the fact that $H_{\rm int}(I')$ is monotonically increasing with respect to I'. Therefore, the difference between the action $I^{(20)}$ and the true action is $O(E^{\frac{21}{2}})$. The same is true for the other actions.

Note that, at energies above that of the separatrix, contour lines of the Hamiltonian do not enclose finite regions, and, thus, the true action is defined only inside the separatrix. However, the actions constructed using the LCPTs are well-defined inside their non-blow-up regions and we call them actions in what follows. In Fig. 2a–d, we show their relative errors from the true action I, defined as (a) $\frac{|I^{(20)}-I|}{I}$ (Dragt and Finn), (b) $\frac{|\tilde{I}^{(20)}-I|}{I}$ (Hori), (c) $\frac{|\hat{I}^{(20)}-I|}{I}$ (Deprit), and (d) $\frac{|I^{(20)}_{\rm trunc}-I|}{I}$ (Dragt and Finn, truncated), respectively. This comparison shows that the truncated one $I^{(20)}_{\rm trunc}$ cannot describe the true action properly at the region close to the separatrix (the relative error exceeds 100.), whereas $I^{(20)}$ describes the action inside the separatrix within 1 % error. This tendency does not change even if the perturbation order is increased further. In addition, $\hat{I}^{(20)}$ (Deprit) has larger errors than $I^{(20)}$ (Dragt and Finn), whereas $\tilde{I}^{(20)}$ (Hori) has errors comparable to those of $I^{(20)}$ (Dragt and Finn) has inside of the non-blow-up region $\tilde{U}_{20}$. More systematic study is needed to be done, but, in this specific example, the LCPT by Dragt and Finn leads to the best result among all, regarding the width of the non-blow-up region and the accuracy inside of it. Therefore, we use the LCPT by Dragt and Finn in what follows.

2.3.2 *Non-blow-up regions in a HCN molecule*

The schematic figure of this molecule is shown in Fig. 3. This molecule consists of three atoms H, C and N.

Restricting to the zero total angular momentum, the Hamiltonian can be described by the following three degrees of freedom (dofs), r (distance between C and N atom), R (distance between H and the center of mass of C and N) and γ (angle between H and C as seen from the center of mass of C and N) in the Jacobi coordinate. The corresponding Hamiltonian is

$$H = \frac{1}{2\mu}p_r^2 + \frac{1}{2m}p_R^2 + \frac{1}{2}\left(\frac{1}{\mu r^2} + \frac{1}{mR^2}\right)p_\gamma^2 + V(r, R, \gamma) \tag{35}$$

where $\mu = (m_C m_N)/(m_C + m_N)$ is the reduced mass of the CN diatom, $m = (m_H(m_C + m_N))/((m_H + m_C + m_N))$ the reduced mass of the full system and the potential $V(r, R, \gamma)$ is taken from Murrell et al. [84]. This molecule has two minima that have collinear configurations, one is called HCN and the other is CNH. The potential energy of the saddle located in between the HCN and CNH wells is -0.444 kcal/mol. The HCN and CNH well and the saddle point that lies between the two wells correspond to $\gamma \approx 0, \approx \pi$ and $\gamma \approx \pm 1.168$ rad., respectively. In Fig. 4, we show intersections between non-blow-up regions U_m $(m = 4, 8, 12, 16)$ and $p_r = p_\gamma, p_R = 0, H = -0.430$ kcal/mol projected on the coordinate space (r, R, γ) using ParaView [85], version 4.10. In Fig. 4, the boundary of the energetically accessible region is plotted in a transparent surface. This surface looks like a bottle, and its neck corresponds to the saddle region $\gamma \approx 1.168$ (rad.). This figure indicates that non-blow-up regions disappear at the saddle region and, at the perturbation of order 16th, U_{16} cannot cover the whole region inside HCN basin $\gamma = -1.168 \sim 1.168$ (rad.).

3 A method of how to improve non-blow-up regions

In this section, we propose a method to improve validity ranges of Lie canonical perturbation theory. In this section and in what follows, we assume $H_2(\mathbf{q}, \mathbf{p})$ can be written as $\frac{1}{2}\sum_{i=1}^n \omega_i(q_i^2 + p_i^2)$, which holds if the origin $(\mathbf{q}, \mathbf{p}) = \mathbf{0}$ is an elliptic fixed point, where ω_i $(\omega_i > 0)$ is a linear frequency of the ith mode. However, it is straightforward to generalize this method to the other types of fixed points. We propose generating functions of a form $\check{F}_k(\mathbf{q}, \mathbf{p}) = (1 - \exp(-\frac{\alpha_k}{H_2^l}))F_k(\mathbf{q}, \mathbf{p})$ where $F_k(\mathbf{q}, \mathbf{p})$ $(k = 3, \ldots, m)$ are the generating functions of LCPT by Dragt and Finn and l and α_k $(k = 3, \ldots, m)$ are positive real numbers.

First, note that the new generating function $\check{F}_k(\mathbf{q}, \mathbf{p})$ has the same Taylor coefficients as $F_k(\mathbf{q}, \mathbf{p})$, and thus, the resulting Hamiltonian $\check{H}^{(m)} = e^{-\{\check{F}_m, \cdot\}} \ldots e^{-\{\check{F}_3, \cdot\}} H$ has the same normal form as $H^{(m)} = e^{-\{F_m, \cdot\}} \ldots e^{-\{F_3, \cdot\}} H$ up to the order m.

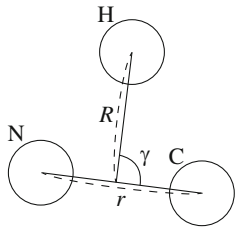

Fig. 3 A schematical figure of HCN molecule

Second, due to the factor $(1 - \exp(-\frac{\alpha_k}{H_2^l}))$ in front of the generating function, the canonical transformation generated by the new generating function is free from blowing up. To show this, it is sufficient to show that all the solutions of the following differential equations $(3 \le k \le m)$,

$$\frac{d\mathbf{q}}{d\epsilon} = \frac{\partial \check{F}_k(\mathbf{q}, \mathbf{p})}{\partial \mathbf{p}}, \tag{36}$$

$$\frac{d\mathbf{p}}{d\epsilon} = -\frac{\partial \check{F}_k(\mathbf{q}, \mathbf{p})}{\partial \mathbf{q}}, \tag{37}$$

do not blow up for $\epsilon \in [0, 1]$. It is because the results of LCPT should be finite if the solutions do not blow up for all $k = 3, \ldots, m$. To show this, it is sufficient to show $r_\omega = \|(\mathbf{q}, \mathbf{p})\|_\omega$ is bounded within the unit time by the time evolution of Eqs. (36) and (37) where $\|\cdot\|_\omega$ is a norm induced by a weighted inner product

$$\langle (\mathbf{q}', \mathbf{p}'), (\mathbf{q}, \mathbf{p}) \rangle = \sum_{i=1}^n \omega_i (q_i' q_i + p_i' p_i). \tag{38}$$

It can be evaluated as

$$\left| \frac{d \log r_\omega}{d\epsilon} \right| \le C_k r_\omega^{k-2} \left(1 - \exp\left(-\frac{2^l \alpha_k}{r_\omega^{2l}}\right)\right), \tag{39}$$

where we set

$$C_k = \max_{\|\mathbf{e}\|_\omega = 1} \|\nabla F_k(\mathbf{e})\|_\omega, \tag{40}$$

which is a finite number. Under the condition $l \ge \frac{k-2}{2}$, the right-hand side of Eq. (39) is bounded, and thus, r_ω has a finite growth rate during the unit time interval. The detailed derivation of Eq. (39) is shown in Sect. 6.2 in Appendix. The condition $l \ge \frac{k-2}{2}$ is a sufficient condition for non-blow-up because if $l \ge \frac{k-2}{2}$ holds, the right-hand side of Eq. (39) has a finite limit $\lim_{r_\omega \to \infty} 2^l \alpha_k C_k r_\omega^{k-2-2l}$, and, thus, it has a finite maximum value in $[0, \infty]$.

Note that the canonical transformation generated by $\check{F}_k$ is no longer analytic. This is due to the fact that the factor $(1 - \exp(-\frac{\alpha_k}{H_2^l}))$ is not analytic at the origin $(\mathbf{q}, \mathbf{p}) = \mathbf{0}$.

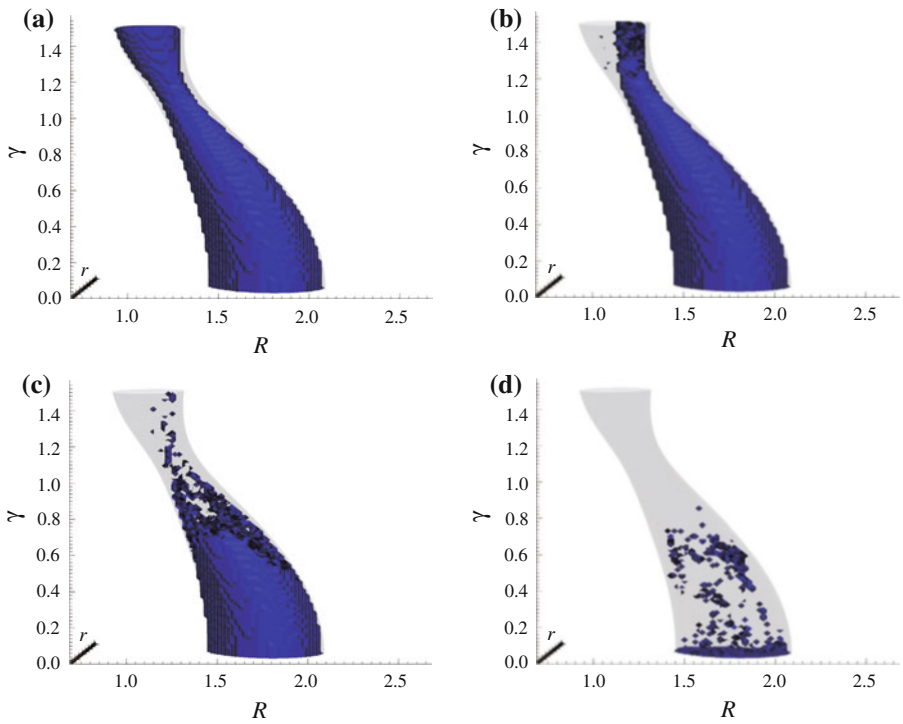

Fig. 4 Non-blow-up regions of LCPT by Dragt and Finn: intersections between U_m and $p_r = p_\gamma, p_R = 0, H = -0.430$ kcal/mol projected on the coordinate space (r, R, γ), **a** $m = 4$, **b** $m = 8$, **c** $m = 12$ and **d** $m = 16$

In general, the normal form of the Hamiltonian is merely a formal power series, and, at best, it is an asymptotic power series with respect to the normalized action-angle variables. This indicates non-existence of analytic canonical transformation that leads to the desired normal form because its existence implies that the original Hamiltonian depends analytically on the normalized action-angle variables. Contrastingly, due to the Borel-Ritt theorem [12], for every formal power series, there exists a C^∞ function (which is not necessarily analytic) whose Taylor coefficients are the same as those of the formal power series. Therefore, there may be a canonical transformation of C^∞ that leads to the desired normal form. This is one of the reasons why we seek for a non-analytic canonical transformation. A method of how to determine l and α_k $(k = 3, \ldots, m)$ is shown in Sect. 6.3 in "Appendix".

4 Demonstration of our method to improve the validity range

In this section, we demonstrate how our method works for the two systems.

4.1 Demonstration of our method in the Hamiltonian system [Eq. (1)]

In Fig. 5a, b, we show that the two actions $I^{(20)}$ and $\check{I}^{(20)}$ along with the true action I, where $\check{I}^{(20)}$ is defined as

$$\check{I}^{(20)} = \frac{1}{2}\left(\left(\check{p}^{(20)}\right)^2 + \left(\check{q}^{(20)}\right)^2\right). \tag{41}$$

This figure indicates that the action $\check{I}^{(20)}$ extends smoothly to the outside of the non-blow-up region U_{20}, whereas $I^{(20)}$ has some spurious peaks indicated by the circles in Fig. 5a′. To investigate how the action $\check{I}^{(20)}$ describes the dynamics for the outside region of the separatrix, we superpose the contour surface of $\check{I}^{(20)}$ with the contour lines of the Hamiltonian in Fig. 6a. The separatrix is indicated by the pink dotted line in this figure. This figure indicates that the two contour lines are roughly parallel with each other. To quantify it, we plot $\left|\frac{\{\check{I}^{(20)},H\}}{\check{I}^{(20)}}\right|$ and $\left|\frac{\{I^{(20)}_{\rm trunc},H\}}{I^{(20)}_{\rm trunc}}\right|$ in Fig. 6b, c, respectively. If the contour lines of the actions and the Hamiltonian are parallel with each other, this quantity should be zero. This figure indicates that $\left|\frac{\{\check{I}^{(20)},H\}}{\check{I}^{(20)}}\right|$ is smaller than $\left|\frac{\{I^{(20)}_{\rm trunc},H\}}{I^{(20)}_{\rm trunc}}\right|$ by more than 100 times for the outside of the separatrix, whereas $\left|\frac{\{\check{I}^{(20)},H\}}{\check{I}^{(20)}}\right|$ is < 0.1 in the plotted region. Here, we use $I^{(20)}_{\rm trunc}$ as a reference to compare because the non-blow-up region U_{20} is almost the same as the region inside the separatrix (see Fig. 1b), and, thus, it cannot be used to compare with $\check{I}^{(20)}$ outside of the separatrix. Again, note that the true action defined as Eq. (33) does not exist outside of the separatrix

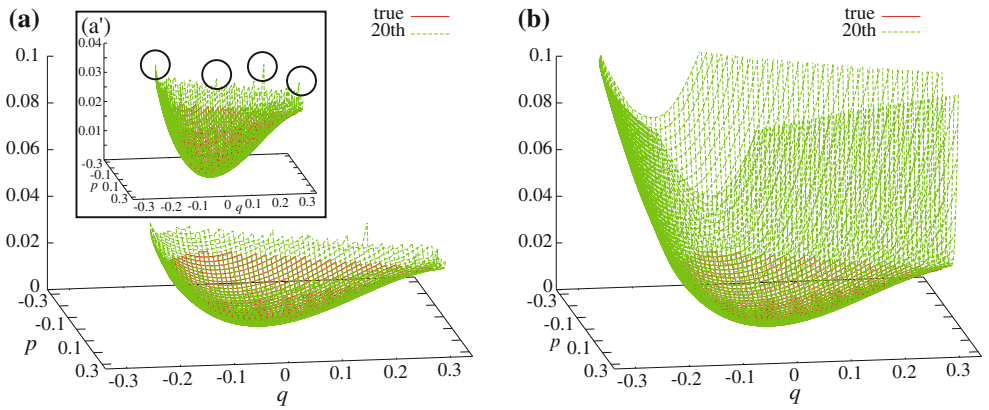

Fig. 5 The actions **a** $I^{(20)}$, **b** $\check{I}^{(20)}$ plotted with the true action I, a' a magnified figure of **a** with spurious peaks indicated by the *black circles*

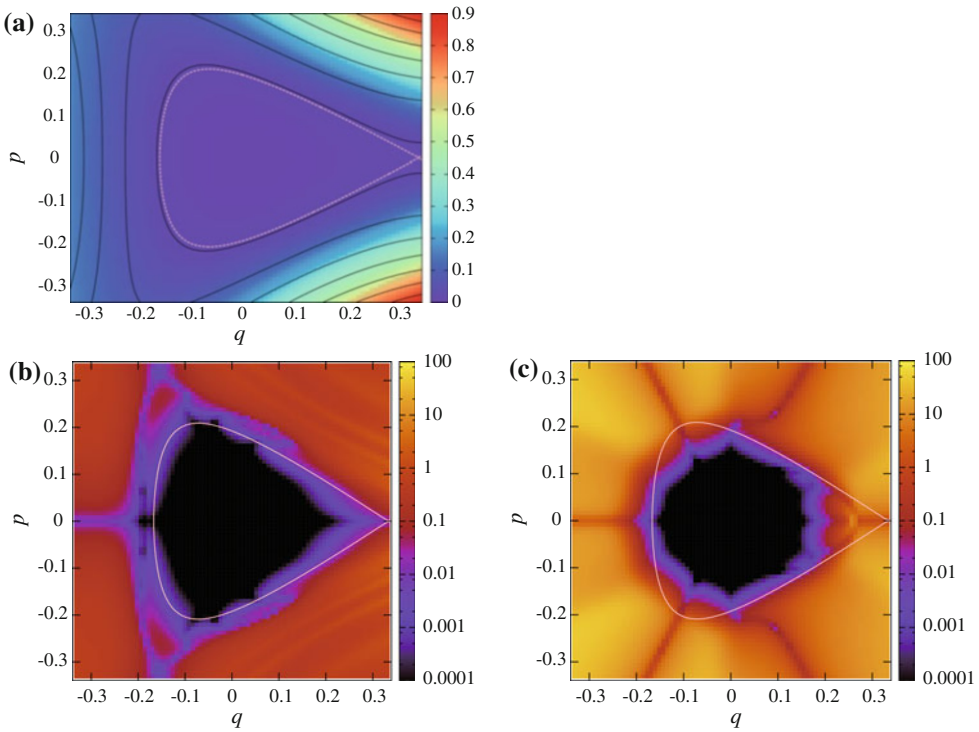

Fig. 6 **a** The contour surface of the action $\check{I}^{(20)}$ plotted with the contour lines of the Hamiltonian in *black lines* (the separatrix is indicated by the *pink dotted curve*), **b**, **c** the Poisson brackets **b** $\left|\left\{\check{I}^{(20)}, H\right\}/\check{I}^{(20)}\right|$ and **c** $\left|\left\{I^{(20)}_{\mathrm{trunc}}, H\right\}/I^{(20)}_{\mathrm{trunc}}\right|$ with the separatrix indicated by the *pink dotted curve*

but the action $\check{I}^{(20)}$ is well defined even outside of the separatrix and serves as an approximate integral of motion, i.e., $\left|\left\{\check{I}^{(20)}, H\right\}\right| \leq 0.1 \times \check{I}^{(20)}$.

4.2 Demonstration of our method in the HCN molecule

In this section, we apply our method to the HCN molecule to demonstrate how our method improves the behavior of the action variables. To demonstrate it, we calculate the actions $I_i^{(7)}$ $(i = 1, 2, 3)$, $\check{I}_i^{(7)}$ $(i = 1, 2, 3)$ and $I^{(7)}_{\mathrm{trunc},i}$ $(i = 1, 2, 3)$ along a trajectory at energy -0.430 kcal/mol, which is beyond the potential energy of the saddle located in between HCN and CNH. Roughly speaking, the third mode $(i = 3)$ corresponds to the γ direction that leads to structural transitions between HCN and CNH and the other modes $i = 1, 2$ are the bath modes that weakly couple to the third mode. The perturbation order 7th is shown to be sufficient to obtain converged actions [1, 2] at this energy. In Fig. 7a, b, we show a typical trajectory of (a) r, R and (b) γ, respectively. The phase space region $-1.168 \leq \gamma \leq 1.168\,(\mathrm{mod}\,2\pi)$ corresponds to the HCN well, and this trajectory shows two structural transitions between HCN and CNH at the time instances indicated by the arrows, i.e., $t = 8.671$ (fs) and $t = 6.697 \times 10^1$ (fs), in Fig. 7b. In the HCN well, we show how the actions evolve in time along the trajectory

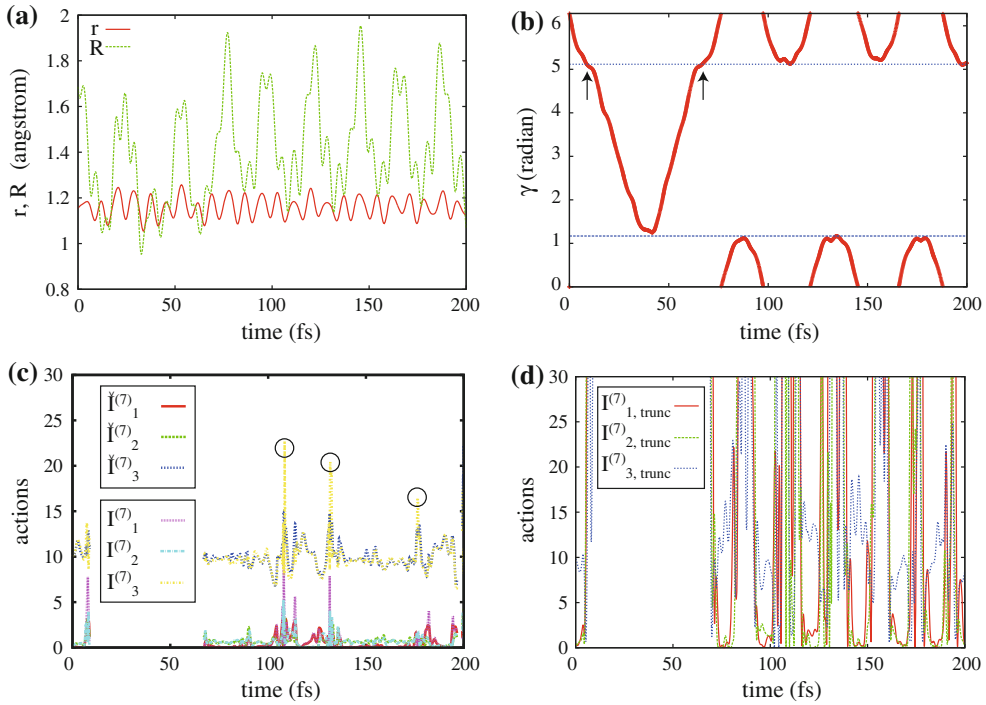

Fig. 7 **a**, **b** Time series of **a** r and R and **b** γ along a trajectory for 2.000×10^2 (fs) with the *arrows* that indicate time instances when the trajectory exits from the HCN well ($t = 8.671$ (fs)) and enters the well ($t = 6.697 \times 10^1$ (fs)), **c** the actions $I_i^{(7)}$ $(i = 1, 2, 3)$ and $\check{I}_i^{(7)}$ $(i = 1, 2, 3)$ with spurious peaks of $I_3^{(7)}$ indicated by the *circles*, **d** the actions $I_{\mathrm{trunc},i}^{(7)}$ $(i = 1, 2, 3)$

in Fig. 7c ($I_i^{(7)}$ $(i = 1, 2, 3)$, $\check{I}_i^{(7)}$ $(i = 1, 2, 3)$) and (d) ($I_{\mathrm{trunc},i}^{(7)}$ $(i = 1, 2, 3)$). The actions $I_{\mathrm{trunc},i}^{(7)}$ $(i = 1, 2, 3)$ change abruptly in time, and it is very difficult to extract any insight from the actions, but the actions shown in Fig. 7c indicate the existence of the slowly varying actions. However, the actions $I_i^{(7)}$ $(i = 1, 2, 3)$ have spurious peaks as indicated by the circles in Fig. 7c. These peaks appear when the trajectory comes very close to the edge of the HCN well ($\gamma \approx 1.168$ or $\gamma \approx 2\pi - 1.168$). Contrastingly, the actions $\check{I}_i^{(7)}$ $(i = 1, 2, 3)$ are free from these spurious peaks. Further study is needed to quantify the difference between the two, but this demonstration indicates potentiality for our method to suppress these spurious peaks on the edge of non-blow-up regions.

5 Conclusions and discussions

Validity ranges of LCPT have been investigated in terms of non-blow-up regions. Non-blow-up region of LCPT is a subset of initial conditions in the phase space where the results of the perturbation are finite. Non-blow-up region limits the validity ranges of LCPT because the results should be at least finite to validate them. We have investigated how the validity ranges depend on the perturbation order in two systems, one of which is a simple Hamiltonian system with one degree of freedom and the other is a HCN molecule. Our analysis of the former system indicates that non-blow-up regions become reduced in size as the perturbation order increases. In case of LCPT by Dragt and Finn and that by Deprit, the non-blow-up regions enclose the region inside the separatrix of the Hamiltonian, but it may not be the case for LCPT by Hori. We have also analyzed how well the actions constructed by these LCPTs approximate the true action of the Hamiltonian in the non-blow-up regions and have found that the conventional truncated LCPT does not work over the whole region inside the separatrix, whereas Dragt and Finn's without truncation does. In addition, LCPT by Dragt and Finn leads to smaller errors than those by Deprit. Regarding the width of the non-blow-up region and the accuracy inside it, LCPT by Dragt and Finn leads to the best results among the three. Our analysis of the latter system indicates that non-blow-up regions do not necessarily cover the whole region inside the HCN well.

We have proposed a new perturbation method to improve non-blow-up regions and validity ranges inside them. Our method is free from blowing up and retains the same normal form as the conventional LCPT. We demonstrated our method in the two systems and showed that the actions constructed by our method have larger validity ranges than those by the conventional ones and our previous method

proposed in [1, 2]. Previously, Padé approximations have also been used to improve validity ranges of LCPT [86–91]. Empirically, these approximations work well and poles of the Padé approximation tend to clump together in the regions where chaotic motion is observed, such as separatrices or other chaotic regions [86, 89]. However, even for an entire function that is analytic in the whole complex plane, its Padé approximation can diverge everywhere [92], and thus, it may not be a reliable method to investigate the phase space geometry. In addition, Teramoto et al. [1, 2] demonstrated that Padé approximation does not work for a highly excited HCN molecule. Contrastingly, our method is free from such a spurious diverging behavior and works even for such highly excited molecules. Some other possible methods to improve validity ranges are using different styles of normalization [12, 93] and using Kolmogorov normal form [94–97]. Both of the methods can be used combining with our method.

Our method can be applied to various subjects in dynamical reaction theory. For example, it would enable us to estimate the time evolution of action variables more precisely than the existing methods, since the action variables constructed by our method are free from blowing up. Thus, it provides us with a new methodology to visualize the Arnold web leading to a better understanding of the dynamical mechanism of intramolecular vibrational-energy redistribution (IVR) [98]. Moreover, the method can be used to investigate how the region around the potential saddle and the well are connected dynamically, since the actions thus constructed offer a better approximation of the real dynamics locally even beyond the separatrix. Therefore, we could evaluate how the stable/unstable manifolds emanating from the normally hyperbolic invariant manifold (NHIM) around the saddle look like in the well even when the energy of the reactive mode is larger than that of the saddle. It would make it possible to understand how the reactive mode obtains energy to go over the saddle from the well and how it loses energy to end up in the well. Results of these studies will be published in near future in separate papers.

Acknowledgments We would like to dedicate this article to continuous stimulating and pioneering works by Professor Greg. Ezra in the research field of classical and semiclassical chemical dynamics. HT would like thank Professor Kazuyuki Yagasaki and Zin Arai for their valuable comments on the definition of the action in the Hamiltonian with one degree of freedom and Professor Turgay Uzer for his comment on the Padé approximation as an alternative method for improving the validity range. This work has been supported by JSPS, the Cooperative Research Program of "Network Joint Research Center for Materials and Devices", Research Center for Computational Science, Okazaki, Japan, and Grant-in-Aid for challenging Exploratory Research (to TK), and Grant-in-Aid for Scientific Research (B) (to TK) from the Ministry of Education, Culture, Sports, Science and Technology, and Nara Women's University Intramural Grant for Project Research (to MT), Grant-in-Aid for challenging Exploratory Research (to MT), and Grant-in-Aid for Scientific Research (C) (to MT) from the Ministry of Education, Culture, Sports, Science and Technology.

Appendix

A blow-up method to solve Eqs. (23) and (24)

It is difficult to solve Eqs. (23) and (24) directly because their right-hand sides are of order $k-1$ with respect to $\mathbf{q}$ and $\mathbf{p}$ and increase rapidly as $\mathbf{q}$ and $\mathbf{p}$ increase. To solve the differential equation, we introduce the following blow-up coordinates [83], r and $\mathbf{e}$ such that $(\mathbf{q},\mathbf{p}) = r\mathbf{e}$ and $\mathbf{e}\cdot\mathbf{e} = 1$. In addition to them, we introduce a scaled virtual time s so that ϵ increases slower as the solution approaches to the infinity such that $d\epsilon = \frac{1}{r^{(k-2)}}ds$. In terms of the blow-up coordinates and the scaled virtual time, Eqs. (23) and (24) can be written as

$$\frac{d\log r}{ds} = \Theta_k(\mathbf{e}), \tag{42}$$

$$\frac{d\mathbf{e}}{ds} = \left(\left.\frac{\partial F_k(\mathbf{q},\mathbf{p})}{\partial \mathbf{p}}\right|_{(\mathbf{q},\mathbf{p})=\mathbf{e}}, -\left.\frac{\partial F_k(\mathbf{q},\mathbf{p})}{\partial \mathbf{q}}\right|_{(\mathbf{q},\mathbf{p})=\mathbf{e}}\right) - \Theta_k(\mathbf{e})\mathbf{e}, \tag{43}$$

$$\frac{d\epsilon}{ds} = \frac{1}{r^{(k-2)}}, \tag{44}$$

where $\Theta_k(\mathbf{e})$ is defined as

$$\Theta_k(\mathbf{e}) = \mathbf{e}\cdot\left(\left.\frac{\partial F_k(\mathbf{q},\mathbf{p})}{\partial \mathbf{p}}\right|_{(\mathbf{q},\mathbf{p})=\mathbf{e}}, -\left.\frac{\partial F_k(\mathbf{q},\mathbf{p})}{\partial \mathbf{q}}\right|_{(\mathbf{q},\mathbf{p})=\mathbf{e}}\right). \tag{45}$$

Equations (42), (43) and (44) can be solved stably because norms of their right-hand sides are bounded by a finite value, i.e., $\max_{\mathbf{e}\cdot\mathbf{e}=1}\|\nabla F_k\|$, where $\|\cdot\|$ is Euclidean norm. In this paper, we integrate this differential equation using Stepper Dropper853 [99], which is 8th order Runge-Kutta method with step size control under the constraint $\mathbf{e}\cdot\mathbf{e} = 1$ until $\epsilon \leq 1$. We use the double precision to integrate them and if the value of $\log r$ exceeds the logarithm of the maximum value of `double` defined in the standard `C++` library [100],

```
std :: numeric_limits < double >:: infty()
```

that is `1.79769e+308` in our current environment, we regard the solution as one that blows up.

This method can be also used to solve differential equations induced by generating functions in LCPTs by Hori [Eqs. (28) and (29)] and Deprit [Eqs. (31) and (32)]. However, those generating functions are not homogeneous polynomials, and thus, this method needs to be adopted for them. To solve them accurately, we decompose the phase space into two regions: One is a region where the highest order terms in the generating function dominate and the other is its complement. In the former region, by

introducing the blow-up coordinate and the scaled virtual time, the differential equations can be written as Eqs. (42), (43) and (44) plus some correction terms of order $1/r$. They can be integrated in the same manner as above. In the latter region, since the lower order terms still dominate, we can directly integrate the differential equations.

A derivation of Eq. (39)

The ϵ-derivative of r_ω can be calculated as follows,

$$\begin{aligned}\frac{dr_\omega}{d\epsilon} &= \frac{1}{r_\omega}\sum_{i=1}^{n}\omega_i\left(q_i\frac{dq_i}{d\epsilon}+p_i\frac{dp_i}{d\epsilon}\right),\\ &= \frac{1}{r_\omega}\sum_{i=1}^{n}\omega_i\left(q_i\frac{\partial \check{F}_k}{\partial p_i}-p_i\frac{\partial \check{F}_k}{\partial q_i}\right),\\ &= \frac{1}{r_\omega}\sum_{i=1}^{n}\omega_i\left(q_i\frac{\partial F_k}{\partial p_i}-p_i\frac{\partial F_k}{\partial q_i}\right)\left(1-\exp\left(-\frac{2^l\alpha_k}{r_\omega^{2l}}\right)\right).\end{aligned} \tag{46}$$

Define $\mathbf{e}$ as $(\mathbf{q},\mathbf{p}) = r_\omega\mathbf{e}$, then, $\|\mathbf{e}\|_\omega = 1$ holds. using this, we get

$$\begin{aligned}\frac{dr_\omega}{d\epsilon} &= \sum_{i=1}^{n}\omega_i\left(e_i\frac{\partial F_k}{\partial p_i}-e_{i+n}\frac{\partial F_k}{\partial q_i}\right)\left(1-\exp\left(-\frac{2^l\alpha_k}{r_\omega^{2l}}\right)\right),\\ &= r_\omega^{k-1}\sum_{i=1}^{n}\omega_i\left(e_i\left.\frac{\partial F_k}{\partial p_i}\right|_{(\mathbf{q},\mathbf{p})=\mathbf{e}}-e_{i+n}\left.\frac{\partial F_k}{\partial q_i}\right|_{(\mathbf{q},\mathbf{p})=\mathbf{e}}\right)\\ &\quad\times\left(1-\exp\left(-\frac{2^l\alpha_k}{r_\omega^{2l}}\right)\right).\end{aligned}$$

Finally, we get

$$\left|\frac{d\log r_\omega}{d\epsilon}\right| \le r_\omega^{k-2}\left(1-\exp\left(-\frac{2^l\alpha_k}{r_\omega^{2l}}\right)\right)\max_{\|\mathbf{e}\|_\omega=1}\|\nabla F(\mathbf{e})\|_\omega. \tag{47}$$

using the following inequality,

$$\begin{aligned}&-\max_{\|\mathbf{e}\|_\omega=1}\|\nabla F(\mathbf{e})\|_\omega\\ &\le \sum_{i=1}^{n}\omega_i\left(e_i\left.\frac{\partial F_k}{\partial p_i}\right|_{(\mathbf{q},\mathbf{p})=\mathbf{e}}-e_{i+n}\left.\frac{\partial F_k}{\partial q_i}\right|_{(\mathbf{q},\mathbf{p})=\mathbf{e}}\right)\\ &\le \max_{\|\mathbf{e}\|_\omega=1}\|\nabla F(\mathbf{e})\|_\omega.\end{aligned} \tag{48}$$

A method to determine l and α_k $(k = 3,\ldots,m)$ in Sect. 3

As pointed out in Sect. 3, the condition $l \ge \frac{k-2}{2}$ is a sufficient condition for the right-hand side of Eq. (39) is bounded. Here, we choose $l = k-2$ for simplicity, but this choice may not be the best choice. Further study is needed to find an optimal power l. Under this choice, the maximum value of the right-hand side of Eq. (39) can be evaluated as $2^{\frac{k-2}{2}}C_k\alpha_k^{\frac{1}{2}}f^*$ and this maximum is attained at $r_\omega = \sqrt{2\alpha_k^{\frac{1}{k-2}}}r^*$, where $f^*\,(\approx 6.38173\times10^{-1})$ and $r^*\,(\approx 8.92135\times10^{-1})$ the maximum and the argument that attains the maximum of the function $f(r) = r(1-\exp(\frac{1}{r^2}))$ $(r \ge 0)$, respectively.

For the right-hand side of Eq. (39) to be of order 1, i.e., $2^{\frac{k-2}{2}}C_k\alpha_k^{\frac{1}{2}}f^* \sim 1$, α_k should satisfy $\alpha_k \sim \frac{1}{2^{k-2}}(\frac{1}{f^*C_k})^2$. This is how we determine α_k $(k = 3,\ldots,m)$. If the α_k is chosen as this,

$$\left|\frac{r_\omega^{(k+1)}-r_\omega^{(k)}}{r_\omega^{(k)}}\right| \lesssim 1 \tag{49}$$

holds for $k = 3,\ldots,m-1$. This should hold if $(k+1)$th order perturbation acts as a correction to the result up to the kth order perturbation.

Note that, if α_k becomes smaller, the deviation between F_k and $\check{F}_k$ becomes larger. Therefore, it is favorable if α_k is chosen as large as possible. Since α_k is inversely proportional to C_k^2, it may also be important to suppress the growth of F_k without normalizing near-resonant terms in LCPT.

References

1. Teramoto H, Komatsuzaki T (2008) Exploring remnant of invariants buried in a deep potential well in chemical reactions. J Chem Phys 129:094302
2. Teramoto H, Komatsuzaki T (2008) Probing remnants of invariant s to mediate energy exchange in highly-chaotic many-dimensional systems. Phys Rev E 78:017202
3. Lichtenberg AJ, Lieberman MA (1991) Regular and chaotic dynamics, 2nd edn. Springer, New York
4. Cary JR (1981) Lie transform perturbation theory for Hamiltonian systems. Phys Rev 79:129
5. Hori G (1966) Theory of general perturbations with unspecified canonical variables. Publ Astron Soc Jpn 18:287
6. Hori G (1967) Non-linear coupling of two harmonic oscillations. Publ Astron Soc Jpn 19:229
7. Deprit A (1969) Canonical transformations depending on a small parameter. Celest Mech 1:12
8. Dragt AJ, Finn JM (1976) Lie series and invariant functions for analytic symplectic maps. J Math Phys 17:2215
9. Campbell JA, Jefferys WH (1970) Equivalence of the perturbation theories of Hori and Deprit. Celest Mech 2:467
10. Marsman WA (1970) A new algorithm for the Lie transformation. Celest Mech 3:81
11. Koseleff PV (1994) Comparison between Deprit and Dragt-Finn perturbation methods. Celest Mech Dyn Astron 58:17
12. Murdock J (2003) Normal forms and unfoldings for local dynamical systems. Springer monographs in mathematics, 1st edn. Springer, New York
13. Sanders JA, Verhulst F, Murdock J (2007) Averaging methods in nonlinear dynamical systems. Applied mathematical sciences, 2nd edn. Springer, New York

14. Broer H, Hoveijn I, Lunter G, Vegter G (2003) Bifurcations in Hamiltonian Systems. Lecture notes in mathematics, vol 1806. Springer, Berlin
15. Siegel CL (1941) On the integrals of canonical systems. Ann Math 42:806
16. Bryuno AD (1975) Normal form of real differential equations. Math Notes 18:722
17. Bryuno AD (1982) Divergence of a real normalizing transformation. Math Notes 31:207
18. Ito H (1989) Convergence of Birkhoff normal forms for integrable systems. Comment Math Helv 64:412
19. Ito H (1992) Integrability of Hamiltonian systems and Birkhoff normal forms in the simple resonance case. Math Ann 292:411
20. Bruno AD, Walcher S (1994) Symmetries and convergence of normalizing transformations. J Math Anal Appl 183:571
21. Cicogna G (1996) On the convergence of normalizing transformations in the presence of symmetries. J Math Anal Appl 199:243
22. Kappeler T, Kodama Y, Némethi A (1998) On the Birkhoff normal form of a completely integrable Hamiltonian system near a fixed point with resonance. Ann Scuola Norm Sup Pisa Cl Sci XXVI:623
23. Walcher S (2000) On convergent normal form transformations in presence of symmetries. J Math Anal Appl 244:17
24. Pérez-Marco P (2001) Total convergence or general divergence in small divisors. Commun Math Phys 223:451
25. Cicogna G, Walcher S (2002) Convergence of normal form transformations: the role of symmetries. Acta Appl Math 70:95
26. Zung NT (2005) Convergence versus integrability in Birkhoff normal form. Ann Math 161:141
27. Chiba H (2009) Extension and unification of singular perturbation methods for ODEs based on the renormalization group method. SIAM J Appl Dyn Syst 8:1066
28. Markus L, Meyer KR (1974) Generic hamiltonian dynamical systems are neither integrable nor ergodic. Mem Am Math Soc 144
29. Koon WS, Lo MW, Marsden JE, Ross SD (2000) Heteroclinic connections between periodic orbits and resonance transitions in celestial mechanics. Chaos 10:427
30. Jaffe C, Ross SD, Lo MW, Marsden J, Farrelly D, Uzer T (2002) Statistical theory of asteroid escape rates. Phys Rev Lett 89:011101
31. von Milczewski J, Diercksen GHF, Uzer T (1996) Computation of the Arnol'd Web for the hydrogen atom in crossed electric and magnetic fields. Phys Rev Lett 76:2890
32. Uzer T, Jaffé C, Palacián J, Yanguas P, Wiggins S (2002) The geometry of reaction dynamics. Nonlinearity 15:957
33. Komatsuzaki T, Berry RS (1999) Regularity in chaotic reaction paths. I . Ar_6. J Chem Phys 110:9160–9173
34. Komatsuzaki T, Berry RS (1999) Regularity in chaotic reaction path II : Ar_6—energy dependence and visualization of the reaction bottleneck. Phys Chem Chem Phy. 1:1387
35. Komatsuzaki T, Berry RS (2000) Local regularity and nonrecrossing path in transition states—a new strategy in chemical reaction theories. J Mol Struct (Theochem) 506:55
36. Komatsuzaki T, Berry RS (2001) Regularity in chaotic reaction paths. III: local invariances at the reaction bottleneck. J Chem Phys 115:4105
37. Komatsuzaki T, Berry RS (2001) Dynamical hierarchy in transition states: why and how does a system climb over the mountain? Proc Natl Acad Sci USA 98:7666
38. Komatsuzaki T, Berry RS (2002) A dynamical propensity rule of transitions in chemical reactions. J Phys Chem A 106:10945
39. Komatsuzaki T, Berry RS (2002) Chemical reaction dynamics: many-body chaos and regularity. Adv Chem Phys 123:79
40. Komatsuzaki T, Nagaoka M (1996) Study on "regularity" of the barrier recrossing motion. J Chem Phys 105:10838
41. Komatsuzaki T, Nagaoka M (1997) A dividing surface free from a barrier recrossing motion in many-body systems. Chem Phys Lett 265:91
42. Kawai S, Fujimura Y, Kajimoto O, Yamashita T, Li C-B, Komatsuzaki T, Toda M (2007) Dimension reduction for extracting geometrical structure of multidimensional phase space: application to fast energy exchange in the reaction $O(^1D) + N_2O \rightarrow NO + NO$. Phys Rev A 75:022714
43. Kawai S, Komatsuzaki T (2010) Robust existence of a reaction boundary to separate the fate of a chemical reaction. Phys Rev Lett 105:048304
44. Jaffé C, Kawai S, Palacián J, Yanguas P, Uzer T (2005) A new look at the transition state: Wigner's dynamical perspective revisited. Adv Chem Phys 130:171
45. Li C-B, Matsunaga Y, Toda M, Komatsuzaki T (2005) Phase space reaction network on a multisaddle energy landscape: Hcn isomerization. J Chem Phys 123:184301
46. Waalkens H, Burbanks A, Wiggins S (2004) Phase space conduits for reaction in multidimensional systems, HCN isomerization in three dimensions. J Chem Phys 121:6207
47. Bartsch T, Hernandez R, Uzer T (2005) Transition state in a noisy environment. Phys Rev Lett 95:058301
48. Bartsch T, Uzer T, Hernandez R (2005) Stochastic transition states: reaction geometry amidst noise. J Chem Phys 123:204102
49. Bartsch T, Uzer T, Moix JM, Hernandez R (2006) Identifying reactive trajectories using a moving transition state. J Chem Phys 124:244310
50. Kawai S, Komatsuzaki T (2009) Dynamical reaction coordinate buried in thermal fluctuation i: time-dependent normal form theory for multidimensional underdamped langevin equation. J Chem Phys 131:224505
51. Kawai S, Komatsuzaki T (2009) Dynamical reaction coordinate buried in thermal fluctuation ii: numerical examples. J Chem Phys 131:224506
52. Kawai S, Komatsuzaki T (2010) Hierarchy of reaction dynamics in a thermally fluctuating environment. Phys Chem Chem Phys 12:7626–7635
53. Kawai S, Komatsuzaki T (2010) Nonlinear dynamical effects on reaction rate constants in thermally fluctuating environments. Phys Chem Chem Phys 12:7636–7647
54. Kawai S, Komatsuzaki T (2010) Dynamical reaction coordinate in thermally fluctuating environment in the framework of multidimensional generalized langevin equations. Phys Chem Chem Phys 12:15382–15391
55. Fried LE, Ezra GS (1987) Semiclassical quantization using perturbation theory: algebraic quantization of multidimensional systems. J Chem Phys 86:6270
56. Fried LE, Ezra GS (1988) Perturb: a special-purpose algebraic manipulation program for classical perturbation theory. Comput Phys Commun 51:103
57. Fried LE, Ezra GS (1988) Semiclassical quantization of polyatomic molecules: some recent developments. J Phys Chem 92:3144
58. Kawai S, Komatsuzaki T (2011) Quantum reaction boundary to mediate reactions in laser fields. J Chem Phys 134:024317
59. Kawai S, Komatsuzaki T (2012) Laser control of chemical reactions by phase space structures. Bull Chem Soc Jpn 85:854–861
60. Giorgilli A, Galgani L (1985) Rigorous estimates for the series expansions of hamiltonian perturbation theory. Celest Mech 37:95
61. Arnold V (1964) Instabilities in dynamical systems with several degrees of freedom. Sov Math Dokl 5:581
62. Chirikov BV (1979) A universal instability of many-dimensional oscillator systems. Phys Rep 52:263
63. Guzzo M, Lega E, Froeschlé C (2009) A numerical study of the topology of normally hyperbolic invariant manifolds supporting arnold diffusion in quasi-integrable systems. Phys D 238:1797

64. Cincottaa PM, Efthymiopoulosb C, Giordanoa CM, Mestrea MF (2014) Chirikov and nekhoroshev diffusion estimates: bridging the two sides of the river. Phys D 266:49
65. Martens CC, Davis MJ, Ezra GS (1987) Local frequency analysis of chaotic motion in multidimensional systems: energy transport and bottlenecks in planar OCS. Chem Phys Lett 142:519
66. Atkins KM, Logan DE (1992) Intersecting resonances as a route to chaos: classical and quantum studies of a three-oscillator model. Phys Lett A 162:255
67. Froeschlé C, Guzzo M, Lega E (2000) Graphical evolution of the arnold web: from order to chaos. Science 289:2108
68. Chandre C, Wiggins S, Uzer T (2003) Time-frequency analysis of chaotic systems. Phys D 181:171
69. Shojiguchi A, Li C-B, Komastuzaki T, Toda M (2006) Wavelet analysis and Arnold web picture for detecting energy transfer in a Hamiltonian dynamical system. Laser Phys 17:1097
70. Arnold VI, Kozlov VV, Neishtadt AI (2006) Mathematical aspects of classical and celestial mechanics. Encyclopedia of mathematical sciences, 3rd edn. Springer, Berlin
71. Laskar J (1993) Frequency analysis for multi-dimensional systems. Global dynamics and diffusion. Phys D 67:257
72. Honjo S, Kaneko K (2003) Structure of resonances and transport in multidimensional Hamiltonian dynamical systems. Adv Chem Phys 130B:437
73. Semparithi A, Keshavamurthy S (2006) Intramolecular vibrational energy redistribution as state space diffusion: classical-quantum correspondence. J Chem Phys 125:141101
74. Shojiguchi A, Li C-B, Komastuzaki T, Toda M (2007) Fractional behavior in nonergodic reaction processes of isomerization. Phys Rev E75:035204(R)
75. Shojiguchi A, Li C-B, Komastuzaki T, Toda M (2007) Fractional behavior in multidimensional Hamiltonian systems describing reactions. Phys Rev E76:056205
76. Wiggins S (1990) On the geometry of transport in phase space I. Transport in k-degree-of-freedom Hamiltonian systems, $2 \leq k \leq \infty$. Phys D 44:471
77. Gillilan RE, Ezra GS (1991) Transport and turnstiles in multidimensional hamiltonian mappings for unimolecular fragmentation: application to van der Waals predissociation. J Chem Phys 94:2648
78. Toda M (1995) Crisis in chaotic scattering of a highly excited van der waals complex. Phys Rev Lett 74:2670
79. Shojiguchi A, Li C-B, Komastuzaki T, Toda M (2008) Dynamical foundation and limitation of statistical reaction theory. Commun Nonlinear Sci Numer Simul 13:857
80. Goldstein H, Poole CP Jr, Safko JL (2001) Classical mechanics, 3rd edn. Addison-Wesley, Boston
81. Coddington EE (1984) Theory of ordinary differential equations. Krieger Pub Co, Huntington
82. Dragt AJ, Finn JM (1979) Normal form mirror machine hamiltonians. J Math Phys 20:2649
83. Coleman CS (1984) Boundedness and unboundedness in polynomial differential systems. Nonlinear Anal Theory Methods Appl 8:1287
84. Murrell JN, Carter S, Halonen LO (1982) Frequency optimized potential energy functions for the ground-state surfaces of hcn and hcp. J Mol Spectrosc 93:307
85. Ahrens J, Geveci B, Law C (2005) ParaView: an end-user tool for large data visualization. In: Hansen C, Johnson C (eds) The visualization handbook. Academic Press, London, p 717
86. Shirts RB, Reinhardt WP (1982) Approximate constants of motion for classically chaotic vibrational dynamics: vague tori, semiclassical quantization, and classical intramolecular energy flow. J Chem Phys 77:5204
87. Ali MK, Wood WR, Devitt JS (1986) On the summation of the Birkhoff–Gustavson normal form of an anharmonic oscillator. J Math Phys 27:1806
88. Ali MK, Wood WR (1987) The Birkhoff–Gustavson normal form of Double-Well anharmonic oscillators. Prog Theor Phys 78:766
89. Robnik M (1993) On the Padé approximations to the Birkhoff–Gustavson normal form. J Phys A Math Gen 26:7427
90. Li CB, Shojiguchi A, Toda M, Komatsuzaki T (2006) Definability of no-return transition states in high energy regime above threshold. Phys Rev Lett 97:028302
91. Teramoto H, Takatsuka K (2007) Local integrals and their globally connected invariant structure in phase space giving rise to a promoting mode of chemical reaction. J Chem Phys 126:124110
92. Baker GA Jr, Graves-Morris P (1996) Padé approximants, 2nd edn. Cambridge University Press, Cambridge
93. Kaluža M, Robnik M (1992) Improved accuracy of the Birkhoff–Gustavson normal form and its convergence properties. J Phys A Math Gen 25:5311
94. Arnold VI (1963) Proof of a theorem of A. N. Kolmogorov on the invariance of quasi-periodic motions under small perturbations of the Hamiltonian. Russ Math Surv 18:9
95. Howland RA (1977) An accelerated eliminations technique for the solution of perturbed Hamiltonian systems. Celest Mech 15:327
96. Howland RA, Richardson DL (1984) The Hamiltonian transformation in quadratic Lie transforms. Celest Mech 32:99
97. Gabern F, Jorba À, Locatelli U (2005) On the construction of the Kolmogorov normal form for the Trojan asteroids. Nonlinearity 18:1705
98. Uzer T (1991) Theories of intramolecular vibrational energy transfer. Phys Rep 199:73
99. Press WH, Teukolosky SA, Vetterling WT, Flannery BP (2007) Numerical recipes, the art of scientific computing. International series of monographs on chemistry, 3rd edn. Cambridge University Press, Cambridge
100. Strpistrup B (2008) Programming: principles and practice using C++, 3rd edn. Addison-Wesley Professional, Boston

Theor Chem Acc (2014) 133:1519
DOI 10.1007/s00214-014-1519-0

REGULAR ARTICLE

Signatures of classical bifurcations in the quantum scattering resonances of dissociating molecules

Pierre Gaspard

Received: 29 April 2014 / Accepted: 9 June 2014 / Published online: 22 June 2014

Abstract A study is reported of the quantum scattering resonances of dissociating molecules using a semiclassical approach based on periodic-orbit theory. The dynamics takes place on a potential energy surface with an energy barrier separating two channels of dissociation. Above the barrier, the unstable symmetric-stretch periodic orbit may undergo a supercritical pitchfork bifurcation, leading to a classically chaotic regime. Signatures of the bifurcation appear in the spectrum of resonances, which have a shorter lifetime than classically expected. A method is proposed to evaluate semiclassically the energy and lifetime of the quantum resonances in this intermediate regime.

Keywords Quantum scattering theory · Classical dynamics · Bifurcations and chaos

1 Introduction

It is a great privilege and pleasure to contribute to this special volume in honor of Gregory Ezra who has so many theoretical achievements in the classical and quantum dynamics of molecules. Methods of dynamical systems theory and semiclassical quantization have proved to be very powerful to understand the rovibrational dynamics of stable and dissociating molecules. If the former are characterized by discrete energy spectra in their ground state, the latter have continuous spectra with possible resonances. Quantum resonances appear at specific energies, and their width is inversely proportional to their lifetime. They manifest themselves in collisions, as well as in dissociations, and are thus called scattering resonances. They play a fundamental role in our understanding of unimolecular reactions and transition-state theory.

Since the seventies, much effort has been devoted to the semiclassical quantization of classically chaotic dynamics, in particular, using periodic-orbit theory [1–11]. These methods have also been applied to scattering processes such as unimolecular reactions [12–14]. Remarkably, the transition state of dissociating molecules is spanned by periodic orbits that are unstable and form a chaotic saddle over large energy ranges. Yet, bifurcations happen at specific energies where the periodic orbits may become stable and form so-called Kolmogorov–Arnold–Moser (KAM) elliptic islands [15]. Several types of bifurcations have been identified including the supercritical and subcritical pitchfork bifurcations [12–14]. At such bifurcations, the spectrum of quantum scattering resonances undergoes changes, which are difficult to investigate in terms of standard periodic-orbit theory because it fails for stable periodic orbits.

The purpose of the present paper is to show that the semiclassical theory can be extended to obtain the quantum scattering resonances close to pitchfork bifurcations. The vehicle of our study is the collinear dynamics of HgI_2 on the potential energy surface considered by Zewail and coworkers [16, 17]. In previous work [12–14], the classical and quantum dynamics of this system have been analyzed in terms of periodic-orbit theory, showing that the classical dynamics has a single unstable periodic orbit below a critical energy and becomes fully chaotic above. The quantum scattering resonances have been calculated using

Dedicated to Professor Greg Ezra and published as part of the special collection of articles celebrating his 60th birthday.

P. Gaspard (✉)
Center for Nonlinear Phenomena and Complex Systems,
Université Libre de Bruxelles, Code Postal 231, Campus Plaine,
1050 Brussels, Belgium
e-mail: gaspard@ulb.ac.be

standard periodic-orbit theory in the periodic and chaotic regimes. Here, the semiclassical theory is developed at the pitchfork bifurcation in between both regimes and a local approximation is obtained for the quantum scattering resonances, completing in this way previous work [12–14]. Semiclassical theory has the advantage of providing compact analytical expressions describing series of scattering resonances.

This paper is organized as follows. Section 2 is devoted to the semiclassical theory in order to determine the dynamics and the quantum scattering resonances of unimolecular reactions. In Sect. 3, the semiclassical theory is developed to obtain the quantum scattering resonances close to a supercritical pitchfork bifurcation using the transfer operator method [4–6, 18, 19]. In Sect. 4, the theory is applied to the dissociation of HgI_2, which manifests such a bifurcation in the classical dynamics of its transition state. Conclusions are drawn in Sect. 5.

2 Semiclassical periodic-orbit theory of molecular dissociation

2.1 Classical dynamics

The dissociation of triatomic molecules—or the reaction between an atom and a diatomic molecule—takes place on a potential energy surface typically presenting an energy barrier between two valleys, in which the molecular fragments separate. The passage is open above a critical energy where a saddle point exists.

The classical dynamics of the reaction can be studied in the phase space of atomic positions and linear momenta. Since the total energy and the total angular momentum are conserved, the phase space can be decomposed into shells where the trajectories remain. Reacting systems are of scattering type in the sense that the centers of mass of the fragments move in free flight at a large distance from each other. The motion is thus unbounded and most of the trajectories are coming from and running away toward infinity. Nevertheless, there might exist invariant sets of bounded trajectories that remain trapped at finite distance. Such invariant sets may be composed of a single or infinitely many trajectories. In the former case, the trajectory is unstable and periodic or reduced to the saddle point. In the latter case, the invariant set contains many stable or unstable periodic orbits. The periodic orbits are stable of elliptic type if the invariant set forms KAM islands [15]. All the periodic orbits are unstable of hyperbolic type if the invariant set is a fully chaotic saddle. Remarkably, such chaotic invariant sets may exist over large energy ranges in the dynamics of dissociating molecules such as HgI_2 or CO_2 [11–14]. These chaotic saddles appear after that the unique unstable periodic orbit existing at energies just above the saddle point has undergone bifurcations.

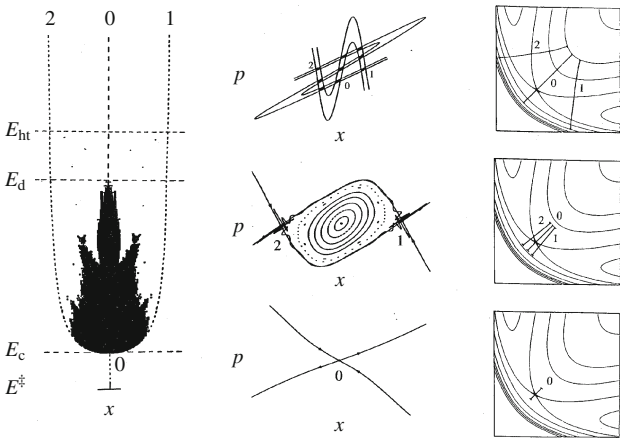

Fig. 1 Supercritical pitchfork bifurcation scenario for symmetric ABA molecules: on the *left*, bifurcation diagram in the plane of the energy E versus the position x. The critical energies are, respectively, the energy $E^{\ddagger}$ of the saddle point, the energy E_c of the pitchfork bifurcation, the energy E_d where the symmetric-stretch periodic orbit becomes unstable again, and the energy E_{ht} of the last heteroclinic tangencies, after which the invariant set becomes fully chaotic. On the *center*, typical phase portraits in some Poincaré surface of section (x, p) in the different regimes. On the *right*, the shortest periodic orbits in position space (r_{AB}, r_{BA}). This scenario is observed to occur in the classical dynamics of HgI_2 [11–13]

The classical dynamics can be analyzed in the phase space by taking a Poincaré surface of section [20–22] in a plane transverse to the symmetric-stretch periodic orbit. For the collinear dynamics of a triatomic molecule, the phase space has dimension six. Eliminating the motion of the center of mass and using energy conservation, we remain with a phase space of dimension three, so that the Poincaré surface of section is bidimensional and easy to depict.

Figure 1 shows the bifurcation scenario in symmetric molecules ABA, such as HgI_2, where a supercritical pitchfork bifurcation happens. Below the bifurcation, the unstable periodic orbit corresponds to the symmetric-stretch motion of the triatomic molecule. This periodic orbit becomes stable of elliptic type at the bifurcation where two new unstable periodic orbits appear corresponding to asymmetric-stretch movements. Thereafter, the symmetric-stretch periodic orbit is surrounded by a KAM elliptic island, which extends between the two new unstable periodic orbits. As energy increases, the island itself undergoes successive bifurcations, which destabilize the orbits. After the last heteroclinic tangencies, the invariant set becomes a fully chaotic saddle composed of unstable orbits of hyperbolic type. In this chaotic regime, all the orbits are in one-to-one correspondence with bi-infinite sequences

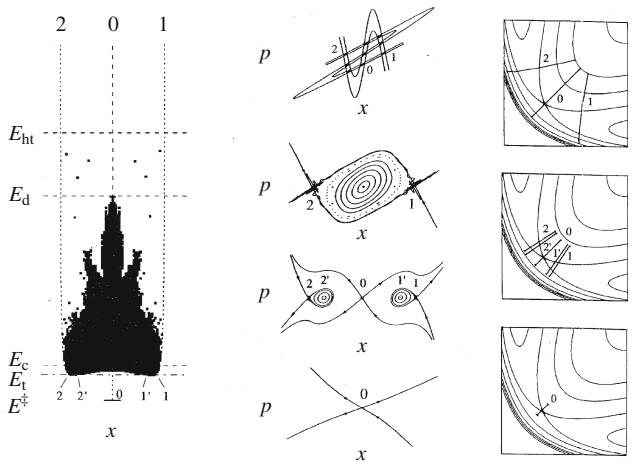

Fig. 2 Subcritical pitchfork bifurcation scenario for symmetric ABA molecules represented by the same diagrams as in Fig. 1. Here, E_t denotes the critical energy of two saddle-center tangent bifurcations preceding the subcritical pitchfork bifurcation at E_c. This scenario is observed to occur in the classical dynamics of CO_2 [11, 14]

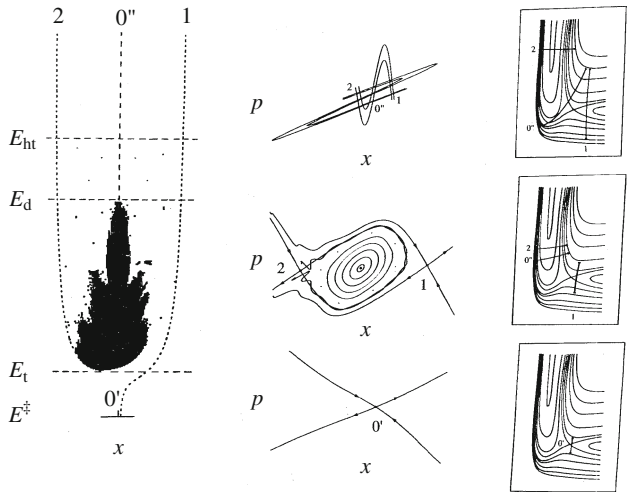

Fig. 3 Saddle-center tangent bifurcation scenario for non-symmetric ABC molecules represented by the same diagrams as in Fig. 1. Here, E_t denotes the critical energy of the saddle-center tangent bifurcation

$$\boldsymbol{\omega} = \cdots \omega_{-2}\omega_{-1} \cdot \omega_0\omega_1\omega_2 \cdots \tag{1}$$

made of three possible symbols $\omega_k \in \{0, 1, 2\}$. The symbol $\omega_k = 0$ is associated with a passage close to the symmetric-stretch periodic orbit and the symbols $\omega_k = 1$ or 2 with a passage near by either one or the other of the two asymmetric-stretch periodic orbits. It is fascinating to observe that this symbolic dynamics captures all the trapped trajectories over a very large range at high energies.

Figure 2 depicts the scenario in other symmetric molecules ABA, such as CO_2, where the pitchfork bifurcation is subcritical and preceded by two saddle-center tangent bifurcations giving birth to a pair of small KAM islands merging together at the subcritical pitchfork bifurcation. Again, the main KAM island is bordered by the two unstable periodic orbits of asymmetric-stretch type, and the scenario at high energy is similar to the previous one with a fully chaotic saddle based on three symbols.

In the case of a non-symmetric molecule ABC, a different scenario is observed. Since the symmetry is broken, the pitchfork bifurcation is replaced by a saddle-center tangent bifurcation giving birth to the main KAM island, while the unstable periodic orbit continues to exist from lower to higher energies, as shown in Fig. 3.

An important remark is that the main KAM elliptic island has a small phase-space extension in light–heavy–light molecules, but a larger extension in heavy–light–heavy ones such as the HCl_2 or HI_2 radicals.

Already the classical dynamics allows us to estimate the lifetime of dissociating molecules by considering the escape of a statistical ensemble of trajectories from the region near the saddle point. The number N_t of trajectories that are still found in this region at a given time t is decaying at a rate, which defines a unimolecular reaction rate as

$$k_t \equiv -\frac{1}{N_t}\frac{\mathrm{d}N_t}{\mathrm{d}t}\,. \tag{2}$$

If the classical dynamics features a KAM elliptic island, the decay of N_t is known to be non-exponential [23]. In particular, N_t may converge to a non-vanishing value in the long-time limit if the elliptic island has a positive volume in a three-dimensional energy shell. Most remarkably, the decay is exponential if the invariant set of trapped trajectories contains a single hyperbolic periodic orbit or is a fully chaotic saddle. In such generic circumstances, a unimolecular reaction rate characterizing the long-time decay can be rigorously defined already in the classical dynamics: $\gamma_{\mathrm{cl}} = \lim_{t\to\infty} k_t$. This rate is equal to the so-called escape rate of dynamical systems theory [24]. It can be expressed as the difference between the positive Lyapunov exponent λ measuring the sensitivity to initial conditions and the Kolmogorov–Sinai (KS) entropy per unit time h_{KS} characterizing the randomness of the chaotic dynamics in the invariant set [24, 25]

$$\gamma_{\mathrm{cl}} = \lambda - h_{\mathrm{KS}}\,. \tag{3}$$

These quantities vary with energy. If the invariant set contains a single periodic orbit, the KS entropy vanishes, $h_{\mathrm{KS}} = 0$, and the unimolecular reaction rate is thus given by the positive Lyapunov exponent: $\gamma_{\mathrm{cl}} = \lambda$. More generally, the classical decay of the number N_t can be decomposed in terms of exponential decays associated with the so-called Pollicott–Ruelle resonances of the classical dynamics [10, 11].

We notice that the invariant set also controls the dynamics of binary reactions. In the periodic regime, the

stable and unstable manifolds of the single unstable periodic orbit constitute phase-space barriers to the reaction [26]. Similar phase-space barriers have been recently discovered, which are associated with higher-index saddles [27]. If the saddle is chaotic, its stable and unstable manifolds form a fractal set, hence the complexity of the classical reaction dynamics.

2.2 Quantum dynamics

Of course, all these classical results have to be reconsidered at the light of quantum mechanics. The sharp classical trajectory structures are replaced by smooth wavefunction features. Every classical structure with a phase-space area smaller than Planck's constant $\hbar$ has no quantum correspondence. Only the classical structures extending in phase space over scales larger than Planck's constant are susceptible to emerge out of quantum-mechanical waves. Accordingly, the KAM elliptic islands generated in the aforementioned bifurcation scenarios are smoothed out if they have an area smaller than Planck's constant. This is the case for light–heavy–light dissociating molecules such as HgI_2 and CO_2 where we should thus expect that the quantization can be carried out semiclassically with a few classical orbits approximating the dynamics over scales larger than Planck's constant $\hbar$.

Quantum mechanically, the configuration of a triatomic molecule is described by a wavefunction $\psi(\mathbf{r}_1, \mathbf{r}_2, \mathbf{r}_3, t)$ ruled by Schrödinger's equation

$$i\,\hbar\,\partial_t \psi = \hat{H}\,\psi\,, \tag{4}$$

where $\hat{H}$ is the Hamiltonian operator. For a dissociating molecule, the energy spectrum is continuous, $\hat{H}\phi_E = E\phi_E$, extending upwards from the lowest zero-point energy $E = 0$ in the valleys of dissociation, so that a wave packet can be decomposed as

$$\psi_t = \int_0^\infty \mathrm{d}E\, c(E)\, \mathrm{e}^{-iEt/\hbar}\, \phi_E \tag{5}$$

with some function $c(E)$ determined by the initial wave packet ψ_0. At energies above the saddle point, the spectrum may feature resonances corresponding to complex energies, $E_n = \mathcal{E}_n - i\Gamma_n/2$, with an imaginary part giving their width Γ_n and lifetime $\tau_n = \hbar/\Gamma_n$. These resonances can be obtained as generalized eigenstates of the Hamiltonian operator

$$\hat{H}\,\phi_n = E_n\,\phi_n = \left(\mathcal{E}_n - i\,\frac{\Gamma_n}{2}\right)\phi_n\,, \tag{6}$$

allowing us to decompose the forward time evolution of a wave packet into a sum of exponentially decaying functions:

$$\psi_t = \sum_n c_n\, \mathrm{e}^{-i(\mathcal{E}_n - i\Gamma_n/2)t/\hbar}\, \phi_n + O(t^{-v}) \tag{7}$$

up to a possible power-law decay [10]. The expansion (7) is obtained by deforming the integration path of Eq. (5) from real to complex energies in order to pick up the exponentially decaying contributions of the resonances and the algebraic tail $O(t^{-v})$ due to the branch point at $E = 0$ [28, 29]. The magnitude of this latter is proportional to the probability amplitude of the initial wave packet at $E = 0$, which describes the quasi-free flight of the molecular fragments in the dissociation valleys [30].

The quantum scattering resonances can be obtained semiclassically using Gutzwiller's trace formula if all the periodic orbits in the invariant set of trapped trajectories are unstable of hyperbolic type [2]. As previously shown [4–14], the scattering resonances are thus given as the zeroes at complex energy of the Gutzwiller–Voros zeta function

$$Z(E) = \prod_{m=0}^{\infty} \prod_p \left[1 - \frac{\mathrm{e}^{\frac{i}{\hbar}S_p(E) - i\frac{\pi}{2}\mu_p}}{|\Lambda_p(E)|^{1/2}\Lambda_p(E)^m}\right] = 0\,, \tag{8}$$

which is a product over all the prime periodic orbits $\{p\}$, i.e., the periodic orbits that are not repeating themselves in phase space [2, 3]. These orbits are characterized by their reduced action

$$S_p(E) = \oint_p \mathbf{p}\cdot \mathrm{d}\mathbf{q}\,, \tag{9}$$

their Maslov index μ_p, and their instability factor $\Lambda_p(E)$ with respect to the linearized classical dynamics. The period of each orbit is given by

$$T_p(E) = \frac{\mathrm{d}}{\mathrm{d}E} S_p(E)\,, \tag{10}$$

and the Lyapunov exponent characterizing the sensitivity to initial conditions in the vicinity of the periodic orbit by

$$\lambda_p(E) = \frac{1}{T_p(E)} \ln|\Lambda_p(E)|\,, \tag{11}$$

which is positive for unstable periodic orbits of hyperbolic type.

It turns out that it is enough to consider the leading factor with $m = 0$ in the infinite product over the integer m in order to obtain good semiclassical approximations for the main quantum scattering resonances. In particular, for an invariant set composed of a single unstable periodic orbit, the main scattering resonances are given by the zeroes of the unique factor with $m = 0$ in the zeta function (8). Using the relation $\exp(2\pi i n) = 1$ for any integer n, the scattering resonances are given by the complex zeroes of

$$S(E) = 2\pi\hbar\left(n + \frac{\mu}{4}\right) - i\,\frac{\hbar}{2}\ln|\Lambda(E)|\,, \tag{12}$$

with $n = 0, 1, 2, ...$ and $\mu = 2$ for the symmetric-stretch periodic orbit. Since the imaginary part of the energy is usually smaller than its real part, the action can be expanded around the energy of the resonances, $\mathrm{Re}\, E_n = \mathcal{E}_n$ satisfying $S(\mathcal{E}_n) = 2\pi\hbar(n + 1/2)$, so that the widths of the resonance are determined by the Lyapunov exponent of the periodic orbit: $\Gamma_n = \hbar\lambda(\mathcal{E}_n)$. Consequently, in this periodic regime where the KS entropy vanishes $h_{\mathrm{KS}} = 0$, the lifetimes $\tau_n = \hbar/\Gamma_n = 1/\lambda(\mathcal{E}_n)$ of the quantum scattering resonances coincide with the classical lifetime given by the inverse of the escape rate (3): $\tau_{\mathrm{cl}} = 1/\gamma_{\mathrm{cl}} = 1/\lambda$.

At energies very close to the critical energy $E^{\ddagger}$ of the saddle point, we notice that the reduced action can be approximated by a linear function of the energy as $S(E) \simeq T^{\ddagger}(E - E^{\ddagger})$. Replacing in Eq. (12), the scattering resonances are estimated to be

$$E_n \simeq E^{\ddagger} + \hbar\omega^{\ddagger}\left(n + \frac{1}{2}\right) - i\,\frac{\hbar}{2}\,\lambda^{\ddagger}\,, \tag{13}$$

with $n = 0, 1, 2, ...$ and the angular frequency $\omega^{\ddagger} = 2\pi/T^{\ddagger}$ in the symmetric-stretch direction of the saddle point. Accordingly, we recover the expression expected from the harmonic approximation at the saddle point.

If the invariant set is fully chaotic and in correspondence with the triadic symbolic dynamics (1), semiclassical approximation for the resonances can be obtained as the zeroes of

$$1 - \sum_{p\in\{0,1,2\}} \frac{\mathrm{e}^{\frac{i}{\hbar}S_p(E) - i\frac{\pi}{2}\mu_p}}{|\Lambda_p(E)|^{1/2}} \simeq 0\,, \tag{14}$$

the higher-order terms being negligible in the zeta function (8) if the periodic orbits are unstable enough. In this regard, the resonances are determined by interferences between the quantum amplitudes associated with the three shortest periodic orbits $p \in \{0, 1, 2\}$, which describe the symmetric stretch $p = 0$ with $\mu_0 = 3$ and the asymmetric stretches $p = 1, 2$ with $\mu_1 = \mu_2 = 2$. In the chaotic regime where $h_{\mathrm{KS}} \neq 0$, the quantum lifetimes may be longer than the classically expected lifetime $\tau_{\mathrm{cl}} = 1/\gamma_{\mathrm{cl}}$ given in terms of the escape rate (3). This lengthening is due to quantum interferences described by Eq. (14) between the multiple periodic orbits composing the chaotic saddle. Such interferences do not exist in the periodic regime where the quantum and classical lifetimes thus coincide. In both the classical and chaotic regimes, the spectrum of quantum scattering resonances is gapped as $\mathrm{Im}\, E_n = -\Gamma_n/2 \leq -\hbar\gamma_{\mathrm{q}}/2$ by the quantum escape rate defined as

$$\gamma_{\mathrm{q}} = \lambda^{(1/2)} - 2\,h_{\mathrm{KS}}^{(1/2)} \tag{15}$$

where the superscript $(1/2)$ means that the Lyapunov exponent and the KS entropy are defined with respect to a probability distribution where the orbits are weighted by the absolute value of their quantum amplitude, $|\Lambda_p(E)|^{-1/2}$ [4–6, 10, 11]. In comparison with the classical escape rate (3), Eq. (15) has an additional factor of 2 multiplying the KS entropy because classical dynamics evolves probabilities given by squaring the quantum amplitudes. In the periodic regime where $h_{\mathrm{KS}} = h_{\mathrm{KS}}^{(1/2)} = 0$, the quantum escape rate reduces to the classical one: $\gamma_{\mathrm{q}} = \lambda^{(1/2)} = \lambda = \gamma_{\mathrm{cl}}$.

These methods have been applied to obtain the scattering resonances of HgI_2 and CO_2 [10–14].

3 Semiclassical quantization near a supercritical pitchfork bifurcation

At the critical energy $E = E_{\mathrm{c}}$ of a supercritical pitchfork bifurcation, the unique unstable periodic orbit of symmetric-stretch motion becomes stable of elliptic type, so that its Lyapunov exponent vanishes, $\lambda(E_{\mathrm{c}}) = 0$, and its instability factor becomes equal to unity $|\Lambda(E_{\mathrm{c}})| = 1$. In this case, the Gutzwiller–Voros zeta function (8) no longer provides a reliable approximation for the quantization and other methods are required. Local and uniform approximations have been developed for bounded systems with discrete energy spectra [31–33]. Here, we extend these methods to open systems with continuous spectra and resonances.

In order to describe the pitchfork bifurcation of the symmetric-stretch periodic orbit, we consider the quantum analog of a classical Poincaré first-return map in a surface of section transverse to the orbit [5, 10, 18, 19]. The quantum transfer operator from and to a section in configuration space can be taken as

$$\psi_{k+1}(x) = \hat{Q}\,\psi_k(x) = \int \frac{\mathrm{d}x'}{\sqrt{2\pi i\hbar}}\,\mathrm{e}^{\frac{i}{\hbar}F(x,x') - i\frac{\pi}{2}\mu}\,\psi_k(x')\,, \tag{16}$$

with the generating function

$$F(x, x') = \frac{1}{2}\,(x - x')^2 - v(x') + F_0\,, \tag{17}$$

and the Maslov index $\mu = 2$ because the paths undergo two turning points before their return in the surface of section. The corresponding classical map can be written as

$$\begin{cases} p_{k+1} = p_k - \dfrac{\mathrm{d}v}{\mathrm{d}x}(x_k)\,, \\ x_{k+1} = x_k + p_{k+1}\,. \end{cases} \tag{18}$$

In order to describe a supercritical pitchfork bifurcation, the effective potential is taken as

$$v(x) = \frac{\chi}{2}\,x^2 - \frac{\alpha}{4}\,x^4 \tag{19}$$

where $\alpha > 0$ is a positive constant coefficient while $\chi(E)$ is a parameter varying with the energy E and changing sign at the bifurcation energy $E = E_c$ [10–14]. The classical map (18) has thus the following form:

$$\begin{cases} p_{k+1} = p_k - \chi x_k + \alpha x_k^3, \\ x_{k+1} = p_k + (1-\chi) x_k + \alpha x_k^3 . \end{cases} \tag{20}$$

We notice that α has the units of the inverse of an action, i.e., the units of $\hbar^{-1}$.

If $\chi < 0$, this map admits a unique unstable fixed point, $x = p = 0$, which is characterized by the instability factor

$$\Lambda_0 = 1 - \frac{\chi}{2} + \sqrt{\frac{\chi^2}{4} - \chi} > 1 , \tag{21}$$

and the reduced action $S_0 = F_0$.

If $\chi > 0$, this map has three fixed points: $x = p = 0$ which is now stable of elliptic type and two new satellite fixed points at $p = 0$ and $x = \pm\sqrt{\chi/\alpha}$ which are unstable with the instability factors

$$\Lambda_{1,2} = 1 + \chi + \sqrt{\chi^2 + 2\chi} > 1 , \tag{22}$$

and the reduced actions $S_{1,2} = F_0 - \chi^2/(4\alpha)$.

The behavior is similar to the continuous-time classical dynamics of symmetric molecules such as HgI_2 , and we can thus identify the reduced action and instability factors of the map with those of the continuous-time dynamics. This allows us to obtain the energy dependence of the parameter F_0 in the generating function (17) from the reduced action of the symmetric-stretch periodic orbit, $F_0(E) = S_0(E)$, and the energy dependence of the parameter χ in the effective potential (19) from the instability factor of this orbit also:

$$\chi(E) = 2 - \Lambda_0(E) - \Lambda_0(E)^{-1} . \tag{23}$$

This parameter vanishes as $\chi(E) \propto E - E_c$ at the bifurcation. It is negative below and positive above. The constant coefficient α is obtained from the difference between the reduced actions of the symmetric- and asymmetric-stretch periodic orbits in the limit where the energy E reaches the critical energy E_c:

$$\alpha = \lim_{E \to E_c} \frac{\chi(E)^2}{4\big[S_0(E) - S_{1,2}(E)\big]} . \tag{24}$$

Now that the suitable energy dependence has been given to the quantum transfer operator (16), the scattering resonances are obtained as the zeroes of the characteristic determinant of this transfer operator:

$$\det\big[\hat{I} - \hat{Q}(E)\big] = 0 , \tag{25}$$

at complex energies $E = E_n$ [5, 10]. Using the relation

$$\ln\det(\hat{I} - \hat{Q}) = \mathrm{tr}\ln(\hat{I} - \hat{Q}) , \tag{26}$$

the determinant (25) can be expanded in a series involving the trace of the powers of the transfer operator as

$$\begin{aligned} \det(\hat{I} - \hat{Q}) &= \exp\left(- \sum_{k=1}^{\infty} \frac{1}{k} \,\mathrm{tr}\,\hat{Q}^k \right) \\ &= 1 - \mathrm{tr}\,\hat{Q} - \frac{1}{2}\left[\mathrm{tr}\,\hat{Q}^2 - \big(\mathrm{tr}\,\hat{Q}\big)^2 \right] + \cdots \end{aligned} \tag{27}$$

Let us suppose that the terms get smaller and smaller as their power in $\hat{Q}$ increases. The first approximation to consider would thus be

$$1 - \mathrm{tr}\,\hat{Q}(E) \simeq 0 . \tag{28}$$

Now, the trace of the transfer operator (16) can be calculated as

$$\begin{aligned} \mathrm{tr}\,\hat{Q} &= \int \frac{\mathrm{d}x}{\sqrt{2\pi i\hbar}}\, \mathrm{e}^{\frac{i}{\hbar}F(x,x) - i\frac{\pi}{2}\mu} \\ &= \mathrm{e}^{\frac{i}{\hbar}F_0 - i\frac{\pi}{2}\mu} \int_{-\infty}^{+\infty} \frac{\mathrm{d}x}{\sqrt{2\pi i\hbar}}\, \mathrm{e}^{-i\,v(x)/\hbar} \\ &= \mathrm{e}^{\frac{i}{\hbar}F_0 - i\frac{\pi}{2}\mu} \int_{-\infty}^{+\infty} \frac{\mathrm{d}x}{\sqrt{2\pi i\hbar}}\, \exp\left(-\frac{i\chi}{2\hbar}\, x^2 + \frac{i\alpha}{4\hbar}\, x^4 \right) , \end{aligned} \tag{29}$$

which is known to be given by

$$\mathrm{tr}\,\hat{Q} = \mathrm{e}^{\frac{i}{\hbar}F_0 - i\frac{\pi}{2}\mu} \sqrt{\frac{\pi\chi}{8i\hbar\alpha}}\, \mathrm{e}^{-\frac{i\chi^2}{8\hbar\alpha}} \left[\mathrm{e}^{i\frac{\pi}{8}} J_{-\frac{1}{4}}\left(\frac{\chi^2}{8\hbar\alpha}\right) + \mathrm{e}^{-i\frac{\pi}{8}} J_{\frac{1}{4}}\left(\frac{\chi^2}{8\hbar\alpha}\right) \right] , \tag{30}$$

in terms of the Bessel functions of fractional order $J_{\pm\frac{1}{4}}(z)$ [32, 33].

Close to the pitchfork bifurcation, the parameter $\chi(E)$ is vanishing and the Bessel functions can be approximated by their Taylor series

$$J_v(z) \simeq \frac{1}{\Gamma(v+1)} \left(\frac{z}{2}\right)^v \tag{31}$$

where $\Gamma(v+1)$ is the gamma function of argument $v+1$ [34]. Within this approximation, we get

$$\mathrm{tr}\,\hat{Q} = \mathrm{e}^{\frac{i}{\hbar}F_0 - i\frac{\pi}{2}\mu - i\frac{\pi}{8}} \frac{\Gamma(\frac{1}{4})}{2\,\pi^{1/2}\hbar^{1/4}\alpha^{1/4}} + O(\chi) \tag{32}$$

where we used the relation $\Gamma(\frac{1}{4})\Gamma(\frac{3}{4}) = \pi\sqrt{2}$. Using the identification of the parameter F_0 with the reduced action of the bifurcating symmetric-stretch periodic orbit, $F_0 = S(E)$, and $\mu = 2$, we obtain the result that the scattering resonances close to the pitchfork bifurcation should be given as the zeroes of

$$S(E) = 2\pi\hbar\left(n + \frac{1}{2} + \frac{1}{16}\right) - i\,\hbar\,\ln\frac{2\,\pi^{1/2}\hbar^{1/4}\alpha^{1/4}}{\Gamma(\frac{1}{4})} , \tag{33}$$

with $n = 0, 1, 2, \ldots$ and under the condition that $\hbar\alpha > \left[\Gamma(\frac{1}{4})/(2\sqrt{\pi})\right]^4 = 1.09422\ldots$

4 The case of HgI_2

The previous results are applied to the dissociation process

$$h\nu + \mathrm{HgI}_2(X^1\Sigma_g^+) \rightarrow [\mathrm{IHgI}]^{\ddagger} \rightarrow \mathrm{HgI}(X^2\Sigma^+) + \mathrm{I}(^2P_{3/2})\,, \tag{34}$$

reported by Zewail and coworkers [16, 17]. The collinear dynamics is modeled according to the Hamiltonian:

$$\hat{H} = \frac{1}{2\mu_{\mathrm{HgI}}}\left(\hat{p}_1^2 + \hat{p}_2^2\right) - \frac{1}{m_{\mathrm{Hg}}}\,\hat{p}_1\,\hat{p}_2 + V(r_1, r_2)\,, \tag{35}$$

with the damped Morse potential for two degrees of freedom proposed in Ref. [17] and the reduced mass $\mu_{\mathrm{HgI}} = (m_{\mathrm{Hg}}^{-1} + m_{\mathrm{I}}^{-1})^{-1}$. The origin of the energy scale is taken at the critical energy $E^{\ddagger} = 0$ of the saddle point. Time and energy units are chosen, respectively, as femtosecond and cm^{-1}. In these units, Planck's constant has the value $\hbar = 5308.84$ fs cm^{-1}.

The dynamics of the Hamiltonian system (35) has been analyzed with classical, semiclassical, and wavepacket methods in Refs. [11–13]. This analysis has shown the existence of a supercritical pitchfork bifurcation at the critical energy $E_c = 523\ \mathrm{cm}^{-1}$ where the single unstable symmetric-stretch periodic orbit becomes stable of elliptic type over the small energy range $E_c < E < 548\ \mathrm{cm}^{-1}$. In this range, this orbit is surrounded by a small KAM island, which is bordered by two unstable asymmetric-stretch periodic orbits born at the pitchfork bifurcation. The KAM elliptic island undergoes further bifurcations until the last heteroclinic tangencies at $E = 575\ \mathrm{cm}^{-1}$, above which the invariant set is fully chaotic and described by the triadic symbolic dynamics (1).

Figure 4 shows the periods and Lyapunov exponents of the three periodic orbits of shortest period, namely the symmetric-stretch periodic orbit $p = 0$ and the two asymmetric-stretch periodic orbits $p = 1$ and $p = 2$. We see in Fig. 4b that their Lyapunov exponents are vanishing at the pitchfork bifurcation. The Lyapunov exponent of $p = 0$ remains equal to zero in the interval $E_c < E < 548\ \mathrm{cm}^{-1}$ where this orbit is elliptic. Figure 4b also shows the classical escape rate (3), which is equal to the Lyapunov exponent of $p = 0$ in the periodic regime for $E < E_c$. In the chaotic regime, the escape rate is smaller than the Lyapunov exponents because of dynamical randomness characterized by the KS entropy in Eq. (3). The energy dependences of the period and the coefficient $\chi(E)$ for the symmetric-stretch periodic orbit $p = 0$ are well described by the fits

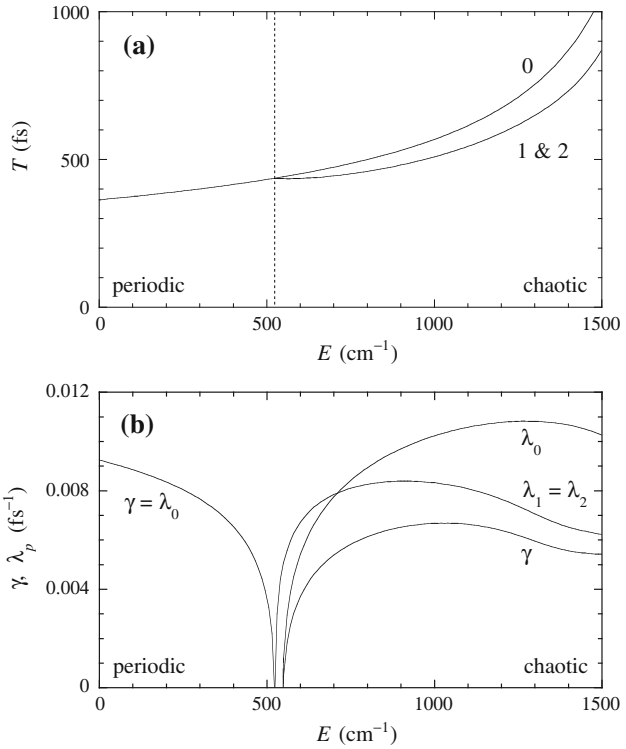

Fig. 4 Characteristic quantities of classical dynamics for the Hamiltonian (35) of HgI_2 versus energy: **a** The periods of the symmetric-stretch periodic orbit $p = 0$ and the asymmetric-stretch periodic orbits $p = 1$ and $p = 2$ existing above the supercritical pitchfork bifurcation at $E_c = 523\ \mathrm{cm}^{-1}$. **b** The Lyapunov exponents λ_p of the three periodic orbits, together with the classical escape rate (3).

$$T(E) = 435.57 + 0.17557\,\Delta E + 7.15 \times 10^{-5}\,\Delta E^2\,, \tag{36}$$

$$\chi(E) = 0.13732\,\Delta E + 2.6733 \times 10^{-4}\,\Delta E^2 + 1.9897 \times 10^{-7}\,\Delta E^3\,, \tag{37}$$

with $\Delta E = E - E_c$ and the chosen units. The reduced action of this periodic orbit is obtained by integrating the polynomial fit (36) over energy:

$$S(E) = \int_0^E T(E')\,\mathrm{d}E'\,. \tag{38}$$

A similar fit has been carried out for the common period of the asymmetric-stretch periodic orbits $p = 1$ and $p = 2$ in order to get with Eq. (24) the value of the coefficient

$$\alpha = 0.038113/(\mathrm{fs\ cm}^{-1})\,, \tag{39}$$

which is positive so that the pitchfork bifurcation is supercritical.

The quantum scattering resonances have been calculated by wavepacket propagation using a numerical integration of the Schrödinger equation (filled circles in Fig. 5) [12].

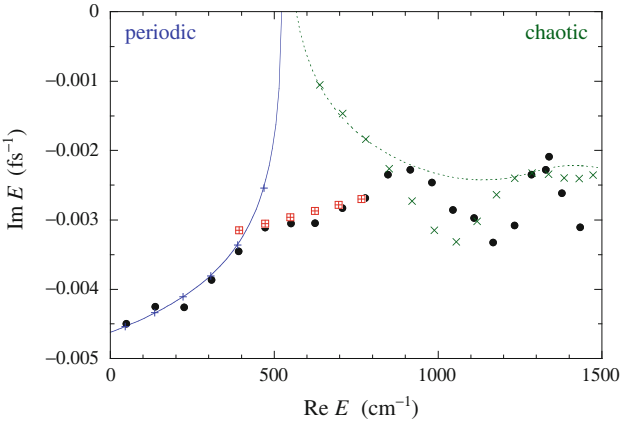

Fig. 5 Scattering resonances of the Hamiltonian (35) of HgI_2 obtained with different methods. The values obtained with the wavefunction method in Ref. [12] are depicted by filled circles. The pluses are the semiclassical approximations given by the zeroes of Eq. (12) in the periodic regime. The solid line corresponds to the gap $\mathrm{Im}\,E = -\hbar\,\lambda_0(\mathrm{Re}\,E)/2$ in terms of the Lyapunov exponent λ_0 of the symmetric-stretch periodic orbit $p = 0$. The crosses are the semiclassical approximations given by the zeroes of the zeta function (14) in the chaotic regime [12, 13]. In this regime, the dashed line gives the gap $\mathrm{Im}\,E = -\hbar\,\gamma_q(\mathrm{Re}\,E)/2$ in terms of the quantum escape rate (15). In the intermediate regime, the crossed squares depict the local approximation here obtained with the formula (33)

In the classically periodic regime, the resonances can be obtained semiclassically using Eq. (12) (pluses in Fig. 5). These resonances are located on the line, $\mathrm{Im}\,E_n = -\Gamma_n/2 = -\hbar\,\lambda_0(\mathrm{Re}\,E_n)/2$, which is determined by the Lyapunov exponent $\lambda_0(E)$ of the symmetric-stretch periodic orbit $p = 0$. This line in Fig. 5 forms the gap (15) in the resonance spectrum.

In the classically chaotic regime, semiclassical approximations for the resonances are given by the zeroes of the zeta function (14) using the characteristic quantities of the three shortest periodic orbits (crosses in Fig. 5) [12]. In this regime, the gap in the resonance spectrum is evaluated in terms of the quantum escape rate defined by Eq. (15) (dashed line in Fig. 5) [11].

We observe that the gap is closed in the intermediate regime between the pitchfork bifurcation at $E_c = 523\ \mathrm{cm}^{-1}$ and the energy $E \simeq 568\ \mathrm{cm}^{-1}$ where the quantum escape rate (15) becomes positive. We notice that this energy interval includes the one where the Lyapunov exponents are vanishing. However, the KAM elliptic island existing in this intermediate regime has an area smaller than Planck's constant $\hbar$, so that the quantum-mechanical wavefunction ignores these non-hyperbolic classical features and escapes nevertheless.

In this intermediate regime, the method of Sect. 3 applies. Using the fits (36)–(37) and the value (39) of the coefficient α in the formula (33), a local approximation is obtained for the quantum scattering resonances (crossed squares in Fig. 5 and values in Table 1). The comparison with the values from the wavefunction method shows that the formula (33) gives a good approximation for the energy and lifetime of the resonances in the intermediate regime. Instead of vanishing as expected from the behavior of the Lyapunov exponents, the imaginary part of the complex energies keeps a nonzero value consistent with the results of the numerical integration of Schrödinger's equation.

Table 1 Scattering resonances of the Hamiltonian (35) of HgI_2

n	$\mathrm{Re}\,E_n^{(\mathrm{wf})}$ (cm^{-1})	$\tau_n^{(\mathrm{wf})}$ (fs)	$\mathrm{Re}\,E_n^{(\mathrm{sc})}$ (cm^{-1})	$\tau_n^{(\mathrm{sc})}$ (fs)
0	47.8	111.1	–	–
1	136.9	117.6	–	–
2	225.2	117.3	–	–
3	308.6	129.5	–	–
4	391.5	144.9	393.5	158.6
5	472.2	160.8	472.8	163.6
6	551.2	163.8	549.8	168.7
7	624.7	164.1	624.4	174.0
8	708.2	176.8	696.7	179.4
9	777.9	186.2	766.9	184.9

The values $\{E_n^{(\mathrm{wf})}\}$ are obtained with the wavefunction method in Ref. [12] and $\{E_n^{(\mathrm{sc})}\}$ with the formula (33). The imaginary parts of the complex energies are given in terms of the lifetimes by $\mathrm{Im}\,E_n = -\hbar/(2\tau_n)$ with $\hbar = 5308.84$ fs cm^{-1}

5 Conclusions

In this paper, a study is reported of the quantum scattering resonances of dissociating molecules in the intermediate regime where a pitchfork bifurcation happens in the classical dynamics.

Below this bifurcation, the only classical trajectory existing above the energy barrier is the unstable symmetric-stretch periodic orbit $p = 0$. This orbit becomes stable and surrounded by a small KAM elliptic island at the bifurcation. This island is bordered by two unstable asymmetric-stretch periodic orbits $p = 1$ and $p = 2$. At higher energies, further bifurcations occur leading to the formation of a fully chaotic saddle described by the triadic symbolic dynamics based on the three aforementioned periodic orbits $p = 0, 1, 2$.

In the classically periodic and chaotic regimes, the quantum scattering resonances can be obtained to a good approximation with the standard periodic-orbit theory. Since this theory makes use of the Lyapunov exponents that are vanishing at the bifurcation, another method is required in the intermediate regime near the bifurcation. Such a method is here developed thanks to a local approximation valid close to the supercritical pitchfork

bifurcation. In this way, an analytical formula is obtained for the scattering resonances in the intermediate regime. This formula is applied to the dissociation of HgI_2 where a supercritical pitchfork bifurcation manifests itself. The results are in agreement with the values of the quantum scattering resonances obtained with the numerical simulation of wavepacket propagation ruled by the Schrödinger equation.

Further work is needed to see whether the approximation can be improved and whether other bifurcations can be analyzed similarly.

Acknowledgments This research is financially supported by the Université Libre de Bruxelles and the Belgian Federal Government under the Interuniversity Attraction Pole Project P7/18 "DYGEST".

References

1. Berry MV (1981) Ann Phys 131:163
2. Gutzwiller MC (1990) Chaos in classical and quantum mechanics. Springer, New York
3. Voros A (1988) J Phys A 21:685
4. Gaspard P, Rice SA (1989) J Chem Phys 90:2225
5. Gaspard P, Rice SA (1989) J Chem Phys 90:2242
6. Gaspard P, Rice SA (1989) J Chem Phys 90:2255
7. Cvitanović P, Eckhardt B (1989) Phys Rev Lett 63:823
8. Ezra GS, Richter K, Tanner G, Wintgen D (1991) J Phys B 24:L413
9. Gaspard P, Rice SA (1993) Phys Rev A 48:54
10. Gaspard P, Alonso D, Burghardt I (1995) Adv Chem Phys 90:105
11. Gaspard P, Burghardt I (1997) Adv Chem Phys 101:491
12. Burghardt I, Gaspard P (1994) J Chem Phys 100:6395
13. Burghardt I, Gaspard P (1995) J Phys Chem 99:2732
14. Burghardt I, Gaspard P (1997) Chem Phys 225:259
15. Arnold VI, Avez A (1968) Ergodic problems in classical mechanics. Benjamin, New York
16. Dantus M, Bowman RM, Gruebele M, Zewail AH (1989) J Chem Phys 91:7437
17. Gruebele M, Roberts G, Zewail AH (1990) Philos Trans R Soc Lond Ser A 332:35
18. Bogomolny EB (1992) Chaos 2:5
19. Bogomolny EB (1992) Nonlinearity 5:805
20. Wiggins S (1988) Global bifurcations and chaos. Springer, New York
21. Wiggins S (1992) Chaotic transport in dynamical systems. Springer, New York
22. Nicolis G (1995) Introduction to nonlinear science. Cambridge University Press, Cambridge
23. Gaspard P, Rice SA (1989) J Phys Chem 93:6947
24. Eckmann J-P, Ruelle D (1985) Rev Mod Phys 57:617
25. Kantz H, Grassberger P (1985) Phys D 17:75
26. Pechukas P, Pollak E (1978) J Chem Phys 69:1218
27. Collins P, Ezra GS, Wiggins S (2011) J Chem Phys 134:244105
28. Taylor JR (2000) Scattering theory: the quantum theory of nonrelativistic collisions. Dover, New York
29. Bohm A (1981) J Math Phys 22:2813
30. Rosenfeld L (1965) Nucl Phys 70:1
31. de Almeida AMO, Hannay JH (1987) J Phys A 20:5873
32. Atkins KM, Ezra GS (1994) Phys Rev A 50:93
33. Schomerus H, Sieber M (1997) J Phys A 30:4537
34. Abramowitz M, Stegun IA (1972) Handbook of mathematical functions. Dover, New York

Theor Chem Acc (2014) 133:1501
DOI 10.1007/s00214-014-1501-x

REGULAR ARTICLE

Topological phase transitions in the vibration–rotation dynamics of an isolated molecule

T. Iwai · B. Zhilinskii

Received: 21 March 2014 / Accepted: 7 May 2014 / Published online: 22 May 2014

Abstract One of the characteristic features of rotation–vibration dynamics is the existence of a variety of energy bands which result from organization of energy levels into bands depending on control parameters. Symmetry and topology aspects of the organization of energy bands and generic modifications of this structure for molecular systems with symmetry are discussed in a way parallel to the description of topological quantum transitions extensively studied in condensed matter physics. A special class of axially symmetric molecular systems is analyzed. It is shown that only a finite number of different band structures are possible for rotation–vibration problem with a finite number of vibrational states in the case of continuous axial symmetry, whereas for problems with finite group symmetry an arbitrary large number of different band structures are formally allowed.

Keywords Energy band · Chern number · Rotation–vibration

1 Introduction

It is well known that macroscopic systems can exist in different phases depending on such control parameters as temperature, pressure, external fields,... Phase transitions between different states of matter are tightly related to symmetry. Landau theory of second-order phase transitions is, probably, the best known example of symmetry breaking associated with qualitative modification of properties of macroscopic thermodynamic systems. Recently, new interesting states of matter associated with qualitatively different properties were discovered like quantum Hall effect [21, 24] or topological insulators [19]. The specificity of these new phases is due to modification of some topological characteristics of matter accompanying the phase transition. The associated phase transitions were named topological phase transitions [6, 14, 20].

For finite particle quantum systems, the problem of qualitative characterization of dynamical behavior can be considered as an analog to classification of different phases of matter and phase transitions between them [32]. Quantum bifurcations which are largely discussed in vibrational and rotational structure of rather small isolated molecules are close in spirit to second-order thermodynamic phase transitions, especially from the point of view of the symmetry breaking aspect [33]. Different possible symmetry breaking phenomena are completely classified, for example, for rotational problems for isolated molecules depending on one control parameter [25], and this classification is parallel to the symmetry classification of second-order thermodynamic phase transitions for crystals.

Quantum monodromy for a simple isolated molecular system [7, 31] was shown to be an important qualitative feature which is clearly manifested in the patterns formed by joint spectra of several mutually commuting (or even almost commuting) variables [8, 27, 28]. While its classical counterpart, the Hamiltonian monodromy, is strictly defined for integrable approximations, the Hamiltonian monodromy is shown to persist owing to its topological

Dedicated to Professor Greg Ezra and published as part of the special collection of articles celebrating his 60th birthday.

T. Iwai
Kyoto University, Kyoto, Japan
e-mail: iwai.toshihiro.63u@st.kyoto-u.ac.jp

B. Zhilinskii (✉)
Université du Littoral, 59140 Dunkerque, France
e-mail: zhilin@univ-littoral.fr

origin even in slightly non-integrable cases [4]. The proof of this fact is similar to the application of the KAM theory showing that regular tori for completely integrable systems still persist under small non-integrable deformation.

The present paper deals with such qualitative characteristics of rovibrational molecular problems as band structure and its modifications [9, 10, 15, 26]. Section 2 gives a brief review of the construction of semi-quantum models using the rotation–vibration problem and of the associated notion of energy bands using as example the rotation–vibration structure of a tetrahedral molecule CF_4 which is well known from experimental studies and brute force calculations. The two slightly different basic questions are posed:

1. What system of isolated bands can be formed under presence of some symmetry requirements?
2. What kind of rearrangement of band structure is allowed under the variation of control parameters in the presence of symmetry?

In order to characterize isolated bands by a topological invariant, the Chern number of the associated fiber bundle, namely the eigenline bundle of the effective matrix Hamiltonians, is used [9, 10, 15]. Possible values of Chern numbers depend on the symmetry of the problem [16, 34].

Rearrangement of the band structure under the variation of control parameters of effective Hamiltonians is well discussed by constructing iso-Chern domains [17, 18], separated by walls, and by studying the wall-crossing phenomenon [22] through local approximation of a Hamiltonian in question along with the orbit structure of the symmetry group action on dynamical variables [23]. The local approximation for "delta-Chern" invariant is close in spirit to the simplest model used by Berry to demonstrate the existence of adiabatic quantum phase [2, 11] but the interpretation of so obtained topological invariant is different and is based on the initial conjecture [26] on a relation between the phenomenon of rearrangement of energy bands in molecules and the modification of such a topological invariant as the Chern number.

The case of axial symmetry is studied in Sect. 3 and compared with previously studied cases of a finite symmetry group.

Possible physical and mathematical generalizations of the discussed approach are outlined in Sect. 4.

2 Full quantum and semi-quantum models: basic notions

In order to explain "semi-quantum" model, we start with a phenomenological formal construction of an effective Hamiltonian using two subsets of dynamical variables: "rapid" variables q and "slow" variables Q. "Rapid" variables are associated with inter-molecular dynamics characterized by relatively high energy excitations. "Slow" variables describe a molecular subsystem with low energy excitations and with high density of the corresponding energy spectrum. Although it is a common practice to explain in similar terms the separation of electronic and nuclear variables in molecular problems, we mainly apply below this construction to rotational and vibrational variables. Taking into account, the fact that vibrational excitations are typically much higher than the rotational excitations, we can restrict ourselves to the model including only a finite (and in fact rather small) number of vibrational quantum states. At the same time in spite of the fact that the number of rotational states associated with each vibrational state is finite for any chosen value of the integral of motion, the square of the rotational angular momentum, J^2, the density of rotational states within multiplet is rather high and this allows us to use classical description of the rotational subsystem in place of a quantum one. As a result, the semi-quantum model of a certain part of the rotation–vibration system of states consists in treating a classical rotational problem combined with a chosen finite set of quantum vibrational states. It corresponds to a classical limit over rotational variables for effective quantum rotation–vibration Hamiltonian for a finite set of vibrational states. We illustrate here the correspondence between a quantum effective Hamiltonian and a semi-quantum model on a concrete molecular example exhibiting band structure and its reorganization associated with redistribution of energy levels between different bands.

One such representative molecular example [3] is shown in Fig. 1. This figure shows only a part of the rotational structure of closely lying v_3 and $2v_4$ bands of the tetrahedral CF_4 molecule. Three branches of v_3 vibrational state (split by Coriolis interaction) at low J-values are situated at lower energies than six components of $2v_4$ state. The internal structure of each band is formed by rotational 6-, 8-, and 12-fold quasi-degenerate clusters and is not relevant to the present discussion of band rearrangements [13, 32]. In contrast, the number of energy levels in the band is a very important characteristics. The lower band shown in Fig. 1 at $J = 29$ (the left side of Fig. 1) consists of $2J + 3$ energy levels and corresponds to the effective rotational quantum number $R = J + 1$. The upper band represented in Fig. 1 at $J = 29$ consists of $2J + 5$ energy levels and corresponds to the effective rotational quantum number $R = J + 2$. At $J = 38$ (the right side of Fig. 1) the lower branch (among two branches represented in this figure) consists of $2J + 5$ energy levels and corresponds to the effective rotational quantum number $R = J + 2$, whereas the higher in energy branch at $J = 38$

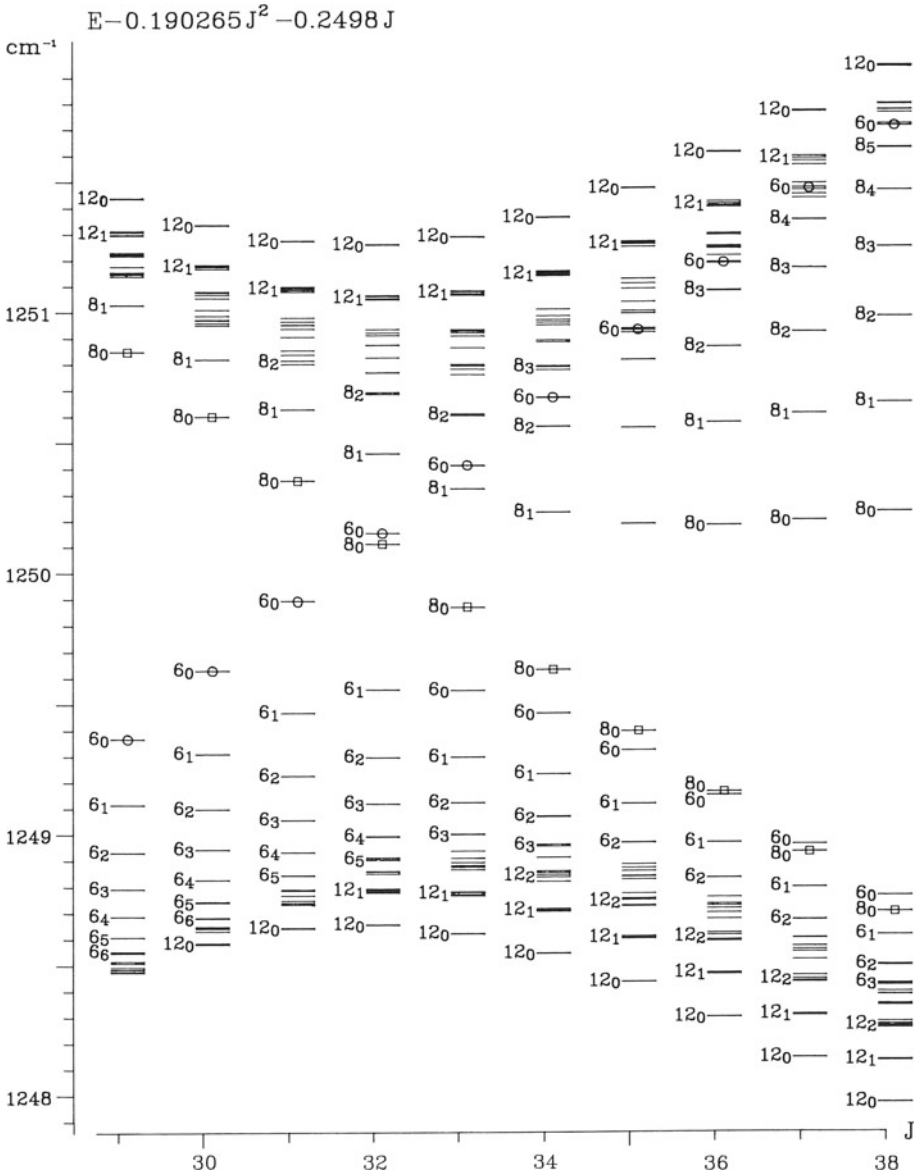

Fig. 1 Upper branch of v_3 and lower branch of $2v_4$ bands of CF_4 molecule with T_d point symmetry group of the equilibrium configuration. 6_i, 8_j, 12_k are labels for 6-, 8-, and 12-fold rotational clusters characterized by the projection $\alpha = J - M$, $\alpha = i, j, k$ on C_4, C_3, and C_2 axes, respectively

region consists of $2J + 3$ energy levels and corresponds to effective rotational quantum number $R = J + 1$. The qualitative effect of the rearrangement of the band structure under the variation of one control parameter, J, is well known in molecular spectroscopy and can be qualified as a generic phenomenon. In order to demonstrate the similarity of this phenomenon with the topological phase transitions in condensed matter, we need to pass from the effective quantum description to a semi-quantum model of this phenomenon.

Let us discuss the correspondence between full quantum and semi-quantum descriptions on the example of v_3 and $2v_4$ bands of the CF_4 molecule. The rotational structure of the upper component of the v_3 triply degenerate band and of the lower branch of the $2v_4$ system of bands of the CF_4 molecule clearly shows the redistribution of energy levels under the increase of J value from $J = 29$ till $J = 38$ (the region shown in Fig. 1). One sequence of eightfold quasi-degenerate rotational clusters goes from the upper branch to the lower one under the J increase. Simultaneously, along almost the same J values, one sequence of sixfold degenerate clusters goes from the lower branch to the upper one. As a result of this redistribution of energy levels, the lower in energy branch at $J = 38$ consists of $2J + 5$ energy levels and can be attributed to $R = J + 2$, whereas the upper in energy branch has $2J + 3$ energy levels and can be labeled by $R = J + 1$.

A complete effective quantum Hamiltonian describing all three branches of v_3 and six branches of $2v_4$ (both v_3 and v_4 are triply degenerate) system of rovibrational energy levels can be written as a linear combination of operators constructed in terms of vibrational and rotational

irreducible tensor operators respecting the symmetry of the problem. Alternatively, it can be put in the form of a 9×9 matrix Hamiltonian associated with nine vibrational states (three components of v_3 state and six components of $2v_4$ state), whose matrix elements are functions of rotational operators. For one chosen value of J, the rotational operators are represented as $(2J+1) \times (2J+1)$ matrices, so that the effective Hamiltonian takes the form of a square matrix of order $9(2J+1)$. If we replace the quantum rotational operators by their classical analogs, we obtain a "semi-quantum" model Hamiltonian which is a 9×9 matrix with its matrix elements being functions defined on the classical phase space for rotational variables. As soon as we can fix the J^2, the classical phase space for rotational variables is nothing else but the two-dimensional sphere defined in J_x, J_y, J_z variables as $J_x^2 + J_y^2 + J_z^2 = J^2$.

We now have a matrix Hamiltonian defined over two-dimensional sphere and depending on extra parameters. There are phenomenological parameters of the effective Hamiltonian which can be, for example, fitted to reproduce experimental data and kept fixed for a chosen molecular system. Of special importance is a physically meaningful parameter such as J^2, the square root J of which can be used as a parameter for the description of evolution of the rovibrational structure under rotational excitation. Such evolution is demonstrated in Fig. 1 where the system of energy levels is plotted against rotational quantum number J. This figure clearly shows the presence of energy bands and their rearrangement under the variation of a control parameter J. In order to formulate more accurately the concept of energy bands and their rearrangement, we need to introduce mathematically more precise language.

The system of eigenspaces of our matrix Hamiltonian forms a vector bundle of rank 9 with a base space being a classical phase space for rotational variables, i.e., a two-dimensional sphere S^2. This means that nine complex eigenspaces are associated with each point of the base space. In order for these eigenspaces to be defined unambiguously, it is necessary that corresponding eigenvalues are non-degenerate. Let us suppose that eigenvalues are non-degenerate everywhere on the sphere. In such a case, the vector bundle can be considered as a direct sum of isolated individual eigenline bundles associated with respective eigenvalues. It is known that globally each complex eigenline bundle can be characterized by a topological invariant, the Chern number, which is an integer number, positive, negative, or zero. The trivial line bundle has its Chern number equal to zero.

It is important to note that the absence of degeneracy points between eigenvalues of a matrix Hamiltonian defined over the two-dimensional sphere is a generic situation if the value of the rotational angular momentum J is fixed. This is because the codimension of degeneracy of two eigenvalues of an Hermitian matrix is three [1, 5], and because for a fixed J value the effective Hamiltonian depends only on two "parameters," the coordinates of a point on the two-dimensional sphere (point of a classical phase space for rotational variables). Consequently, at fixed J values, degeneracies are absent in general and then associated eigenline bundles are defined, each of which is characterized by a topological invariant, its Chern number. To each eigenline bundle so constructed for a semi-quantum model, there corresponds one energy band, i.e., the energy surface $E_n(\theta, \phi)$ defined on the classical phase space, S^2 (here θ, ϕ are two spherical angles used as variables characterizing the position of a point of S^2 classical phase space). Note that so defined energy bands $E_n(\theta, \phi)$ and $E_m(\theta, \phi)$, $n \neq m$ can overlap in energy even in the absence of degeneracy points. The degeneracy means that there exists a point (θ_0, ϕ_0) on the sphere such that $E_n(\theta_0, \phi_0) = E_m(\theta_0, \phi_0)$, whereas overlapping means that there exist at least two distinct points (θ_1, ϕ_1) and (θ_2, ϕ_2) such that $E_n(\theta_1, \phi_1) = E_m(\theta_2, \phi_2)$. It is clear that specific quantum effects can appear when within the semi-quantum model the energy bands are isolated but overlapping. We are interested here in more serious effects manifesting themselves in the full quantum model in association with formation of degeneracy points of energy bands.

If we take the J as a control parameter (serving as a scaling factor for the semi-quantum Hamiltonian) and study one-parameter family of effective Hamiltonians depending on J, isolated degeneracies could appear for some values of J at some points on the sphere on account of the codimensionality of degeneracy. (Remind that the codimension of degeneracy point is three.) For such J-values, eigenline bundles are not defined over S^2, since the eigenspace associated with the degenerate eigenvalue does not naturally split into a direct sum of one-dimensional linear spaces at the degeneracy point of S^2. This means that the control parameter space (in our example this is the J line) is divided into connected regions by singular values of J, the values of J corresponding to formation of degeneracy points on S^2. Each connected region filled by regular values of control parameter (i.e., values for which there are no degeneracy points of eigenvalues) is named an "iso-Chern" domain because if we vary the control parameter value within this regular region, the topological invariant of the eigenline bundle cannot change. In general, values of control parameters corresponding to formation of degeneracy points on S^2 form "walls" between iso-Chern domains in the space of control parameters. In order to describe qualitative modification of eigenline bundles and hence quantitative modification of Chern numbers, we have to study what happens when the control parameters vary

along a path crossing a wall separating different iso-Chern domains in the space of control parameters. Apparently, the serious modifications occur only in a local three-dimensional neighborhood of the degeneracy point characterized by specific values of $(\theta_0, \phi_0, \lambda_0)$, two coordinates of degeneracy point on the classical phase space and one value of the control parameter measured along the path crossing the wall between iso-Chern domains. In addition, we need to remember that in the presence of a finite symmetry group acting on the classical phase space S^2, if there is a degeneracy point on S^2 every point of the orbit by the symmetry group is a degeneracy point as well. Thus, it is necessary to take into account the stratification of the phase space by the action of symmetry group. The stratification of the rotational phase space by the symmetry group for spherical top molecules with tetrahedral or cubic symmetry is well known. Owing to invariance of rotational variables with respect to space inversion, the action of T_d point symmetry group on the rotational sphere is equivalent to the action of the octahedral point group O on the space sphere. There are three isolated orbits formed, respectively, by points with C_4, C_3, and C_2 local symmetry and generic orbits with trivial C_1 symmetry. The C_4 orbit consists of 6 equivalent points on the sphere, the C_3 orbit consists of 8 points and the C_2 orbit consists of 12 points. The number of points in a generic C_1 orbit is equal to the group order, 24. This means that the effect of formation of degeneracy points belonging to some orbit of the group action can be written as an effect of one local degeneracy point multiplied by the number of points forming the orbit of the symmetry group action.

The effect of crossing the wall between different iso-Chern domains in the control parameter space can be represented in the form of "delta-Chern" contribution from each isolated degeneracy point. It was shown that the crossing of the wall along a path gives rise to a Chern number modification by ± 1 from each generic degeneracy point [17]. In full quantum picture, this phenomenon manifests itself through the redistribution of one quantum level between two bands forming degeneracy point in the semi-quantum model [9]. Taking into account the symmetry group G of the problem and the local symmetry (or stabilizer), $G_0 \subset G$, of the degeneracy point, we can express the global "delta-Chern" contribution Δc_1 as

$$\Delta c_1 = \frac{|G|}{|G_0|}\delta. \tag{1}$$

Here $|G|$ and $|G_0|$ are orders of groups G and G_0; δ is the local delta-Chern contribution from one isolated degeneracy point with stabilizer G_0. The absolute value of δ depends on the order of the degeneracy point. In generic situation, the degeneracy point between two energy surfaces is nothing else but a conical intersection point and it is associated with $\delta = \pm 1$. To be precise in the sign of this local delta-Chern contribution, is a much more subtle problem [17, 18]. At the same time from the pattern of energy levels, it is often easy to interpret a very characteristic behavior of energy levels as a function of "control parameter," J, in terms of topological invariant, the Chern number. Let us discuss the pattern formed by rotation–vibration energy levels of the CF_4 molecule represented in Fig. 1 in these terms. The sequence of sixfold rotational clusters going from the lower energy band to the upper one should be associated (within the semi-quantum model) with formation of degeneracy points with C_4 local symmetry at $J \sim 32$. At approximately the same J value another degeneracy point with C_3 local symmetry (in fact eight equivalent points forming orbit with C_3 local symmetry group) should be formed. Appearance of this point in the semi-quantum model is associated with the redistribution of the eightfold cluster between two bands within a fully quantum description. Degeneracy point appears in the semi-quantum model for an isolated J-value. Appearance of degeneracy points with C_4 and with C_3 local symmetries is independent and naturally the corresponding J-values are not obliged to be integers. Two schematic scenarios can be suggested depending on relative order of J-values associated with formation of C_4 and C_3 degeneracy points. Figure 2 represents these two scenario. Two energy bands clearly seen in quantum energy level pattern at $J = 29$ are labeled according to the idea of the semi-quantum model by respective Chern numbers c_1U for the upper band and by c_1L for the lower band. Modification of the topology of individual bands in the semi-quantum model is reflected by the modification of the number of quantum levels within each band as compared to standard $2J + 1$ values for pure rotational multiplet.

The modification of the topological Chern invariant by one within the semi-quantum model is associated with the modification of the number of quantum energy levels by one in an isolated energy band for a full quantum picture [9]. This means that we can convert the topological invariant c_1 into more standard spectroscopic characteristics, effective rotational quantum number R by relating R, J, and c_1 through

$$R = J + c_1/2. \tag{2}$$

It is quite natural that topologically trivial bands associated in the semi-quantum model with $c_1 = 0$ Chern number correspond in a full quantum picture to isolated energy bands consisting of $2J + 1$ rotational energy levels. Nevertheless, in case of degenerate vibrational states, it is not possible to split the whole rotational structure into several isolated bands consisting each of $2J + 1$ energy levels. This effect can be easily seen by studying the

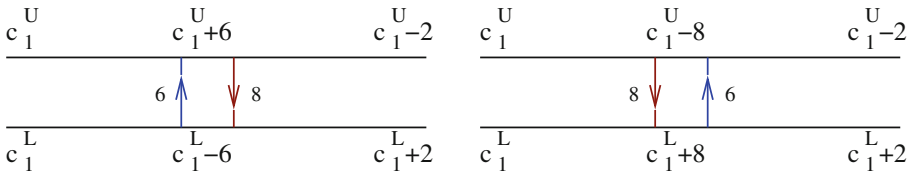

Fig. 2 Possible scenario for modification of topological invariants of isolated bands within semi-quantum model for rotation–vibration bands of CF_4 molecule shown in Fig. 1

decomposition of the whole set of rovibrational states into individual rotational multiplets.

The whole set of rotation–vibration levels for vibrational state belonging to degenerate representation Γ_n of dimension n of the symmetry group G can be classified by irreducible representations of the symmetry group G by reducing the (J) representation of the rotational SO(3) group to rotational subgroup G and by multiplying the so obtained reducible representation by Γ_n and decomposing the resultant representation into irreps of G,

$$\Gamma_n \times (J) = \Gamma_n \times \sum_i m_i \Gamma_i = \sum_j d_j \Gamma_j = \sum_k^n \gamma_k \times \left(J + c_1^{(k)}/2\right), \tag{3}$$

where γ_k is one of the one-dimensional representations of G.[1] In order to check whether the decomposition of the whole set of so obtained representations into several isolated rotational multiplets is possible for a finite group G, it is necessary to verify whether this set can be split into the sum $\sum_k (J + \Delta_k) \times \gamma_k$, where each $(J + \Delta_k)$ representation of the SO(3) group is considered as a reducible representation of the symmetry group G. Expression (3) should be checked for finite groups G for all (J). But in fact, it is sufficient to check it out only for a finite number of J-values because of a cyclic structure of the decomposition of irreducible representations (J) of SO(3) group into irreps of its finite subgroup. The minimal number $J_{\min}$ of representations (J) to be checked can be estimated from relation $J_{\min} = |G|/2$, where $|G|$ is the order of group G, or more precisely, the order of the image of the group G in the studied representation.

Expression (3) gives therefore an interesting possibility to impose restrictions on possible values of Chern numbers of individual bands in the presence of invariance of the rotation–vibration problem under a finite symmetry group. To formulate these restrictions more accurately let us consider first the rotation–vibration problem for the tetrahedral molecule in a doubly degenerate E-vibrational state. Expression (3) reads in this case

[1] The number of one-dimensional representations of a group is equal to the order of Abelianization, i.e., the order of the Abelian group $G/[G,G]$, the quotient of G by the commutator $[G,G]$.

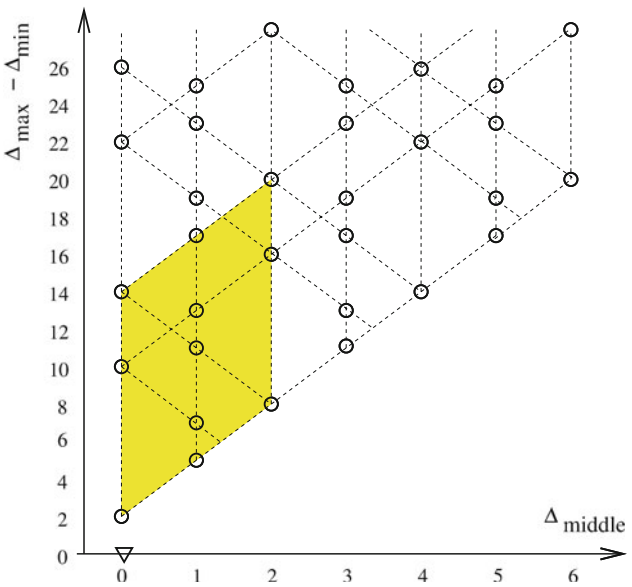

Fig. 3 Possible decompositions of rotational structure for triply degenerate vibrational F state into three isolated bands

$$E \times (J) = (J + \Delta)_g + (J - \Delta)_u; \quad \Delta = \pm 2 \bmod 6. \tag{4}$$

Here $(J + \Delta)_\alpha$, $\alpha = g, u$ means that the vibrational symmetry for isolated band is of type A_1 or A_2, abbreviated for simplicity as g or u, because there are only two different one-dimensional irreducible representations. Taking into account (2), we can rewrite condition (3) in terms of equivalent restriction on topological invariants, Chern numbers, for isolated line bundles into which the rotational structure of a doubly degenerate vibrational E state can be split. Namely we have $c_1^E = \pm 4 \bmod 12$. Note that the realization of the decomposition with a given Δ or c_1 for a fully quantum problem is possible only if $J \geq \Delta$. The suggestion to avoid this inconvenience in quantum classical correspondence is formulated in the next section by introducing the "ghost" band. The semi-quantum model has no such restriction, and we can say that formally an infinite number of possibilities exist for a decomposition of rotational structure for E vibrational state. Naturally the sum of Δ or c_1 over two isolated bands obtained after splitting of the rotational structure of E state equals zero.

Thus, only one number is sufficient to characterize topological invariants for two bands.

The case of triply degenerate vibrational state is more complicated. Now to describe all possible decompositions of the rotational structure of a triply degenerate vibrational state, we need two parameters because the sum of Δ or c_1 over all three components is zero. It is suitable to write Eq. (3) in this case as [18, 23, 34]

$$F \times (J) = (J + \Delta_{\max}) + (J + \Delta_{\mathrm{mid}}) + (J + \Delta_{\min}); \quad \Delta_{\max} + \Delta_{\mathrm{mid}} + \Delta_{\min} = 0. \tag{5}$$

Eq. (5) is written in a simplified form because it does not take into account the difference between two three-dimensional representations F_1 and F_2 and one-dimensional representations A_i. But the possible values of Δ_i, shown in Fig. 3 are identical for F_1 and F_2.

It is also interesting to see the regularity in the possible values of Δ. In fact the whole pattern of possible Δ values can be reconstructed from an "elementary cell" represented in Fig. 3 by hatching.

We can now summarize our discussion of the CF_4 molecule from the point of view of correspondence between the rotational structure of several vibrational states in terms of effective fully quantum Hamiltonian and that in terms of semi-quantum model. The notion of an energy band which is empirically used for the quantum problem finds its justification within the semi-quantum construction which allows us to associate with each isolated energy band a topological invariant and to split the space of control parameters into iso-Chern domains and walls between them. Going from the quantum Hamiltonian to a semi-quantum model and studying the wall-crossing enables one to characterize for the quantum problem the transformation from one qualitative type of internal dynamics to another one and to relate this transformation to a precise topological invariant "delta-Chern." Possible values of delta-Chern are strongly related to the symmetry group of the problem, in particular with the stratification of the classical phase space for rotational motion by the symmetry group action. Different possible decompositions of the rotation–vibration energy level system into an elementary band system are described in terms of possible decompositions of trivial vector bundles into a sum of eigenline bundles with specific Chern numbers whose choice is restricted by symmetry.

Qualitative modifications of the band structure in isolated molecules are therefore similar to topological phase transitions intensively studied in solid state physics. The analysis made in this section uses essentially the fact that the symmetry group of the problem is finite. An important consequence of this assumption is a formally infinite number of possible non-equivalent reorganizations of band structure and infinite choices of possible different band structures compatible with a given initial finite set of vibrational states for sufficiently high J-values.

3 Band structure in the presence of axial symmetry

We now return to the analysis of the semi-quantum model describing rotation vibration structure in the presence of axial symmetry. To simplify the analysis, we will consider the SO(2) rotational group as an invariance group of the problem. An effective rotation–vibration Hamiltonian under study describes rotational structure of K vibrational states whose symmetry with respect to the SO(2) group is given by a reducible representation written in the form $m_1 \oplus m_2 \oplus \cdots \oplus m_K$. Here, we are reminded of the fact that the SO(2) group is Abelian and all its irreducible representations are one-dimensional. For a chosen value of the rotational angular momentum, J, there are $2J + 1$ rotational functions which span the irreducible representation (J) of the SO(3) group. The decomposition of the representation (J) of SO(3) group into irreps of SO(2) subgroup, which is supposed to be the symmetry group of the problem is given by the well-known relation

$$(J) = \sum_{m=-J}^{J} m. \tag{6}$$

This means that the complete set of rotation–vibration states of the effective Hamiltonian under study spans the reducible representation of the SO(2) group

$$\left(\sum_{i=1}^{K} m_i\right) \otimes (J) = \sum_{i=1}^{K} \sum_{m=-J+m_i}^{J+m_i} m. \tag{7}$$

This reducible representation is fixed by the formulation of the effective problem and relevant for the full quantum effective problem and for the semi-quantum model. The questions which we want to answer now are:

1. What system of bands is possible for this problem?
2. What kind of elementary rearrangements of bands are allowed under variation of a control parameter? (We can take as a control parameter the absolute value of J.)
3. How to describe the rearrangement of band structure by the topological invariant, the Chern number?

We start by looking at simplest interesting case of effective Hamiltonian, namely the Hamiltonian for two vibrational states.

To specify the problem, we need to define symmetry types of vibrational states and construct the complete set of rotation–vibration functions for a given value of the integral of motion, J. For two vibrational states of m_1 and m_2

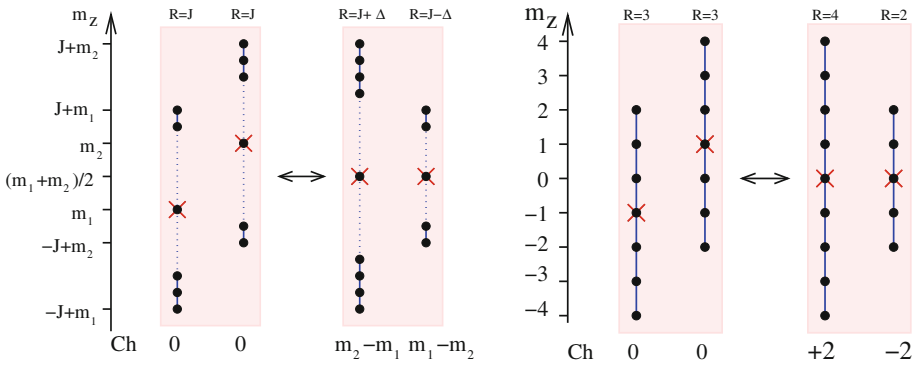

Fig. 4 Two possible band systems are allowed for rotational structure of two vibrational states in the presence of SO(2) symmetry for a fixed *J*-value. *R* is effective rotational quantum number for an isolated band. *Left subfigure* general case of two vibrational states transforming according m_1 and m_2 representations of SO(2). *Right subfigure* concrete realization for $m_1 = -1, m_2 = +1$ and $J = 3$. m_z indicates the symmetry of rotation–vibration state. "Ch" means Chern number for an isolated band. $\Delta = (m_2 - m_1)/2$. *Cross* shows the center of each individual band. Note that the whole set of upper ends of bands remains invariant under band rearrangement as well as the collection of lower ends of bands

symmetry and for a given J value for rotation, the $2(2J + 1)$ rotation–vibration basis functions schematically shown in Fig. 4, left subfigure, can be grouped into two sets each consisting of $2J + 1$ states or into two subsets consisting of different number of basis functions. In order to interpret each subset as a rotational multiplet with some effective rotational number R, it is necessary that each multiplet is formed by a consecutive m values and the same decomposition should be valid for any sufficiently high J values. Taking $J \geq |m_2 - m_1|/2$ we obtain the representation of the basis set shown in Fig. 4 with $m_1 \leq m_2$ and $J + m_1 \geq -J + m_2$. In Fig. 4, each of the bullets represents a basis function. The total number of the basis functions is kept before and after the rearrangement, but we have to note that the basis functions themselves are not literally identical before and after the rearrangement.

To relate the decomposition of the basis of rotation–vibration functions with a bundle structure associated with the semi-quantum model, we note that the decomposition into two groups with the same number of functions, one of which has SO(2) labels varying from $-J + m_1$ to $J + m_1$ and the other from $-J + m_2$ to $J + m_2$ corresponds to the construction of two trivial vector bundles over the sphere with zero Chern number for each. If the decomposition is changed, the only one alternative decomposition into two bands is possible. One band covers the space consisting of basis functions with SO(2) labels varying from $-J + m_1$ till $J + m_2$ whereas another band covers the space formed by functions with SO(2) labels varying from $-J + m_2$ till $J + m_1$. Obviously such a decomposition is possible if $J \geq |m_2 - m_1|/2$. This is quite natural for a semi-quantum model, since the J-values have been necessarily assumed to be high when going to a classical limit over rotational variables for forming the semi-quantum model. The Chern numbers for these two bands become equal to $\pm(m_2 - m_1)$. It is important to note that these two bands can be considered as effective rotational multiplets associated with vibrational states transforming according to an irreducible representation $m = (m_1 + m_2)/2$ of the symmetry group SO(2).

Nevertheless, formally, the description of the reorganization of energy bands can be given even in the case of $J < |m_2 - m_1|/2$. To illustrate such a possibility let us look at an example of two rotational multiplets with vibrational symmetry $m_1 = -5$ and $m_2 = +5$. Normally, for $J \geq 5$ we have two possibilities to form two bands.

1. We can have two bands with the same number of states, $2J + 1$, with vibrational symmetries $m_1 = -5$, $m_2 = +5$, and with the trivial Chern number zero.
2. We can form two bands composed by different number of quantum states and corresponding to different effective rotational quantum number, $R = J - 5$ and $R = J + 5$, and the vibrational symmetry $m = 0$. In the classical limit these two bands have Chern numbers $\pm(m_1 - m_2) = \pm 10$.

For $J < |m_1 - m_2|/2$, i.e., in the considered case for $J < 5$, two isolated bands with the same number of quantum states in each band exist, but between these two bands, there exist an interval of m values which are not associated with quantum states. Figure 5 illustrates the situation for the general case of $J < |m_1 - m_2|/2$ and for the concrete case of $J = 3$ and $m_1 = -5$, $m_2 = +5$. To keep formally the possibility to reorganize the bands, we introduce "ghost" states which fill the interval between two bands and interpret the resulting system as formed by two virtual bands: one with energy states with $-J + m_1 \leq m \leq J + m_2$ and another with "ghost" states with $J + m_1 + 1 \leq m \leq -$

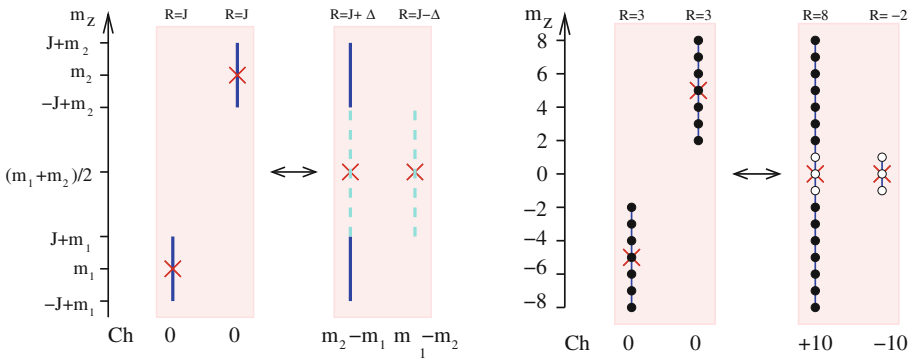

Fig. 5 The interpretation of two possible band systems which are allowed for rotational structure of two vibrational states in the presence of SO(2) symmetry for a fixed J-value in case of $J < |m_2 - m_1|/2$. *Left subfigure* general case of two vibrational states transforming according m_1 and m_2 representations of SO(2). "Ghost band" and the annihilated part of the only observed band are shown by *dash line*. *Right subfigure* concrete realization for $m_1 = -5, m_2 = +5$ and $J = 3$. States which belong to ghost band and to annihilated part of the observed band are shown by *empty dots*. m_z indicates the symmetry of rotation–vibration state. "Ch" means Chern number for an isolated band. $\Delta = (m_2 - m_1)/2$. *Cross* shows the center of each individual band

$J + m_2 - 1$. Figure 5, right illustrates the general situation for $J = 3$ and $m_i = \pm 5$. The two bands after rearrangement correspond to $R = J \pm (m_2 - m_1)/2$, i.e., for $R = 8$ and $R = -2$. The band with $R = -2$ is interpreted as a "ghost band," which does not appear as a system of really observable states but as a formal band which annihilates the same number of quantum states from the other band and the overall system of energy levels consists of really observable states. The band with $R = 8$ has only 14 observable states instead of the formal number $2R + 1 = 17$, because three states, namely those associated with $m = 0, \pm 1$ are annihilated by the "ghost band".

The suggested interpretation allows us to use the classical limit for the description of the rearrangement of bands for any J value. Physically, this means that for low J values, it is still possible to have two topologically different situations. One corresponds to splitting of observable levels into two bands with trivial Chern number 0 and with the effective rotational quantum number $R = J$ for both bands. The both bands are observable in this case. Another situation corresponds to formation of only one observable band with nontrivial Chern number c and with the effective rotational number $R_o = J + c/2$. The second band becomes "ghost," i.e., unobservable. The "ghost" band is characterized by a negative value of $R_g = J - c/2 \leq -1$ and, consequently, by the negative number of quantum states, $2R_g + 1 \leq -1$. This negative number of states for the "ghost" band leads to the fact that the number of observable quantum states for the observable band is different form $2R_o + 1 = 2J + c + 1$ and equals $4J + 2$. The number $4J + 2$ is the total number of observed energy levels for a given J value within the model of two bands. The difference between the number of observed states and the formal number of states expressed in terms of J and Chern number suggests to name this band a "fractional" band.

Note that the "ghosts" are used to compensate unphysical degrees of freedom [12] and lead, in particular, to the appearance of negative spins [29, 30]. In our interpretation of the band structure at low J values, $J < |m_1 - m_2|/2$, we replace actually the classical problem with two degrees of freedom (one degree of freedom is associated with the projection of angular momentum and another with two components of vibrational states) by an effective observable problem with one degree of freedom (projection of effective rotational momentum R). The "ghost" band corresponding to a negative R_g value causes the appearance of the difference between the number of "physically observable states," i.e., $4J + 2$, and formally associated with the only observable band $2R_o + 1$. The ratio between the really observable states in the "fractional" band with R_o quantum number and the virtual number of states in the band, $2R_o + 1$, i.e., $\frac{4J+2}{2R_o+1}$ increases when J varies from 0 till $J = |m_1 - m_2|/2$. For $J = |m_1 - m_2|/2$ the "ghost" band is materialized. Its quantum number R_g becomes equal to 0 and remains positive for higher J values. Simultaneously with materialization of the "ghost" band, the fractional band becomes a normal band with the number of observable states equal to $2J + c + 1$. In the presence of the "ghost" band the observable "fractional" band can be characterized by a fractional quantum factor $\frac{4J+2}{2R_o+1}$ which can be expressed explicitly in terms of J, m_1, m_2. Namely, we have for the fractional factor ν_{J,m_1,m_2} the following expression

$$\nu_{J,m_1,m_2} = \frac{4J + 2}{2J + |m_1 - m_2| + 1}, \quad J < |m_1 - m_2|/2, \tag{8}$$

which is valid only in the presence of a "ghost" band. For $J = |m_1 - m_2|/2$, the ghost band is materialized and becoming normal band with $R = 0$, i.e., with one

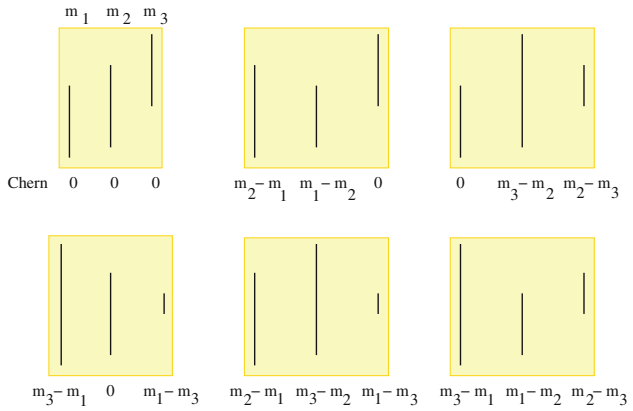

Fig. 6 Six possible band structures for rotation–vibration energy levels for three vibrational states transforming according three different irreducible representations m_1, m_2, m_3 of the SO(2) symmetry group

observable quantum state. To extend expression (8) for $J \geq |m_1 - m_2|/2$ we need to subtract from the numerator the number of states belonging to another band, namely $2J - |m_1 - m_2| + 1$. This gives for all $J \geq |m_1 - m_2|/2$ the fractional factor 1.

4 Generalizations

Generalization of our analysis to the case of an arbitrary number of vibrational states in the presence of a continuous SO(2) symmetry is straightforward. For N vibrational bands belonging to different m_i vibrational representations the total of $N!$ different possible band structures are possible because we can form a band by combining any lower end at $-J - m_i$ with an arbitrary upper end at $J + m_j$. Six alternative band structures for the rotation–vibration energy level system formed by three vibrational states are represented in Fig. 6.

Again we should note that the indicated in Fig. 6 six band structures correspond to the case of sufficiently high J values. At low J it is possible that there exist one or two "ghost" bands and only two or even one band remain observable. The best way to see possible band structures for low J-values is to make a continuation in J: Starting with a sufficiently high J value, we lower the J value, keeping invariant the topological structure, i.e., Chern numbers, to look for effective rotational quantum numbers expressed in terms of J and Chern numbers.

To characterize the band structure for rotation–vibration problem for N vibrational states belonging to $m_1, m_2, \ldots, m_N$ irreducible representations of the SO(2) symmetry group we need to specify for each band within the semi-quantum approach the Chern number and the position of the center of band. As an initial band system, we can take bands with zero Chern numbers and with band centers $m_1, m_2, \ldots, m_N$. Since the number of bands before and after rearrangement is supposed to be conserved within the semi-quantum models under study, different band structures correspond to different permutations of the ends of bands so that we can classify band structures in exactly the same way as permutations of N objects, i.e., by the cycle structure of permutations. For two bands, there are only two classes, 1^2 and 2. Table 1 describes two possible band structures for two bands. In case of N bands, we can name "irreducible band structures" all systems of bands associated with cyclic permutations of maximal length, N. There are $(N-1)!$ such band systems. All other band structures are associated with rearrangements between subsets of initially trivial bands. Irreducible band structures for models with three and four bands are given in Tables 2 and 3.

Each band structure can be associated with a classifying operator in such a way that the same eigenvalue of the classifying operators corresponds to all quantum states belonging to the same band and different eigenvalues correspond to different bands. The simplest example of such a classifying operator naturally appears in a particular case when all "vibrational states" form a reducible representation of the SO(2) group which can be considered as an irreducible representation (S) of SU(2) or SO(3) group. The coupled basis in this case is the eigenbasis of

Table 1 Band structures for a model with two quantum states with SO(2) symmetry m_1, m_2

Cycle	Chern number		Band center	
1^2	0	0	m_1	m_2
2	$m_2 - m_1$	$m_1 - m_2$	$\frac{m_1+m_2}{2}$	$\frac{m_1+m_2}{2}$

First line of the table shows the trivial band structure. Second line gives the only possible alternative case. Chern numbers and center positions for each of two bands are given for sufficiently high N values

Table 2 Irreducible band structures associated with cyclic structure 3 of permutation group S_3 for a model with three quantum states with SO(2) symmetry m_1, m_2, m_3

Cycle	Chern number			Band center		
1^3	0	0	0	m_1	m_2	m_3
3	$m_2 - m_1$	$m_3 - m_2$	$m_1 - m_3$	$\frac{m_1+m_2}{2}$	$\frac{m_2+m_3}{2}$	$\frac{m_3+m_1}{2}$
	$m_3 - m_1$	$m_2 - m_3$	$m_1 - m_2$	$\frac{m_1+m_3}{2}$	$\frac{m_2+m_3}{2}$	$\frac{m_1+m_2}{2}$

First line of the table shows the trivial band structure. Two irreducible cases follow below. Chern numbers and center positions for each of three bands are given for two possible irreducible band structures for sufficiently high N values

Table 3 Irreducible band structures associated with cyclic structure 4 of permutation group S_4 for a model with four quantum states with SO(2) symmetry m_1, m_2, m_3, m_4

Cycle	Chern number				Band center			
1^4	0	0	0	0	m_1	m_2	m_3	m_4
4	$m_2 - m_1$	$m_3 - m_2$	$m_4 - m_3$	$m_1 - m_4$	$\frac{m_1+m_2}{2}$	$\frac{m_2+m_3}{2}$	$\frac{m_3+m_4}{2}$	$\frac{m_1+m_4}{2}$
	$m_4 - m_1$	$m_3 - m_4$	$m_2 - m_3$	$m_1 - m_2$	$\frac{m_1+m_4}{2}$	$\frac{m_3+m_4}{2}$	$\frac{m_2+m_3}{2}$	$\frac{m_1+m_2}{2}$
	$m_2 - m_1$	$m_4 - m_2$	$m_3 - m_4$	$m_1 - m_3$	$\frac{m_2+m_1}{2}$	$\frac{m_4+m_2}{2}$	$\frac{m_3+m_4}{2}$	$\frac{m_1+m_3}{2}$
	$m_3 - m_1$	$m_4 - m_3$	$m_2 - m_4$	$m_1 - m_2$	$\frac{m_3+m_1}{2}$	$\frac{m_4+m_3}{2}$	$\frac{m_2+m_4}{2}$	$\frac{m_1+m_2}{2}$
	$m_3 - m_1$	$m_2 - m_3$	$m_4 - m_2$	$m_1 - m_4$	$\frac{m_3+m_1}{2}$	$\frac{m_2+m_3}{2}$	$\frac{m_4+m_2}{2}$	$\frac{m_1+m_4}{2}$
	$m_4 - m_1$	$m_2 - m_4$	$m_3 - m_2$	$m_1 - m_3$	$\frac{m_4+m_1}{2}$	$\frac{m_2+m_4}{2}$	$\frac{m_3+m_2}{2}$	$\frac{m_1+m_3}{2}$

First line of the table shows the trivial band structure. Six irreducible cases follow below. Chern numbers and center positions for each of four bands are given for all six possible irreducible band structures for sufficiently high N values

$\mathbf{SJ} = (\mathbf{R}^2 - \mathbf{J}^2 - \mathbf{S}^2)/2$ operator. The transformation between an uncoupled and a coupled basis of two angular momenta $\mathbf{S}$ and $\mathbf{J}$ can be considered as a well-known example of a transformation between two different band structures. A classifying operator for one (uncoupled) band structure is the S_z operator. Each of its eigenvalues is $2J + 1$ degenerate and corresponds to a band with trivial Chern number 0. The classifying operator for coupled basis is $\mathbf{SJ}$. If $J \geq S$ there are $2S + 1$ bands characterized by quantum number $R = J + S, J + S - 1, \ldots, J - S$. From the point of view of the semi-quantum model, these bands are characterized by topological invariants, Chern numbers, $2S$, $2(S-1)$, $\ldots, 2(-S)$.

A generalization of the present angular momentum coupling is possible to the case of a weighted action of the symmetry group SO(2) on vibrational and rotational variables. A weighted action is defined in such a manner that SO(2) invariant subspaces are given by

$$W^{(\ell)}_{J,S} = \mathrm{span}\{|k\rangle \otimes |r\rangle; k + 2r = \ell, |k| \leq J, |r| \leq S\}. \qquad (9)$$

In particular, vibrational states with $m_1 = -1$, $m_2 = 1$ are comparable with the *effective* spin $S = 1/2$. In a similar way, four vibrational states with symmetry ± 1, ± 3 are comparable with the *effective* spin $S = 3/2$. However, in this case, the transformation to the coupled basis with respect to a certain classifying operator describes only one among $4! = 24$ possible bases. All these 24 band structures are listed in Table 4.

The band system corresponding to angular momentum coupling between J and *effective* spin $S = 3/2$ in presence of weighted symmetry is associated with the cycle structure 2^2 of the group of permutation S_4 (see line 10 in Table 4).

Up to now we have discussed different possible band structures but did not touch the question of "elementary," i.e., generic transformations between different band structures.

The rearrangement of band structure is possible within semi-quantum model through formation of degeneracy points of different eigenvalues of a matrix Hamiltonian. Generically, the formation of degeneracy points is possible only between two eigenvalues. Consequently, an "elementary rearrangement" occurs between two neighboring in energy bands.

In order to give a concrete simplest form of the local Hamiltonian associated with the formation of a degeneracy point and with a point on the path crossing (in the control parameter space) the wall between iso-Chern domains let us take an example of two vibrational states belonging to two irreducible representations of the SO(2) group $\pm k$ and suppose that the rotational momentum N is sufficiently high. This allows us to treat in parallel the semi-quantum and the full quantum models.

The whole linear space of quantum states within the full quantum problem has dimension $2(2N + 1)$ and can be described in terms of decoupled basis $|M_N, \pm k\rangle$, $|M_N| \leq N$ or in terms of coupled basis $|M_J = M_N \pm k, M_N, \pm k\rangle$.

The decoupled basis is suitable to use if we want to classify states according to eigenvalues of the "vibrational" operator $V_z = \begin{pmatrix} k & 0 \\ 0 & -k \end{pmatrix}$ as a classifying operator. The operator V_z plays the role of effective "spin operators" together with $V_+ = \begin{pmatrix} 0 & 1 \\ 0 & 0 \end{pmatrix}$ and $V_- = \begin{pmatrix} 0 & 0 \\ 1 & 0 \end{pmatrix}$.

The operator V_z has two eigenvalues $\pm k$. It splits $2(2N + 1)$ quantum states into two bands with the same number of states in the band according to its eigenvalue. The operators $V_\pm$ are formally defined as operators transforming vibrational functions $V_+|-k\rangle = |k\rangle$, $V_-|k\rangle = |-k\rangle$. Using $N_z, N_\pm$ rotational operators an SO(2) invariant operator constructed from rotational and vibrational operators in the simplest form can be written as $\mathbf{NV} = N_z V_z + V_+ N_-^{2k} + V_- N_+^{2k}$. This operator can be used as classifying operator within a coupled rotation–vibrational basis. One of the resulting bands consists of $2(N + k) + 1$ eigenstates, whereas another band has $2(N - k) + 1$ eigenstates.

Table 4 Band structures for a model with four quantum states with SO(2) symmetry ±1, ±3

N	Cycles	Chern number				Band center			
1	1^4	0	0	0	0	−3	−1	1	3
2	2, 1^3	2	−2	0	0	−2	−2	1	3
3		4	0	−4	0	−1	−1	−1	3
4		6	0	0	−6	0	−1	1	0
5		0	2	−2	0	−3	0	0	3
6		0	4	0	−4	−3	1	1	1
7		0	0	2	−2	−3	−1	2	2
8	2^2	2	−2	2	−2	−1	−1	1	1
9		4	4	−4	−4	−1	1	−1	1
10		6	2	−2	−6	0	0	0	0
11	3, 1	2	2	−4	0	−2	0	−1	3
12		4	−2	−2	0	−1	−2	0	3
13		4	0	2	−6	−1	−1	2	0
14		6	0	−4	−2	0	−1	−1	2
15		2	4	0	−6	−2	1	1	0
16		6	−2	0	−4	0	−2	1	1
17		0	2	2	−4	−3	0	2	1
18		0	4	−2	−2	−3	1	0	2
19	4	2	2	2	−6	−2	0	2	0
20		2	4	−2	−4	−2	1	2	−1
21		4	−2	+4	−6	−1	0	1	0
22		4	2	−4	−2	−1	2	1	−2
23		6	−2	−2	−2	0	2	0	−2
24		6	−4	2	−4	0	1	0	−1

Chern numbers and center positions for each of four bands are given for all 24 possible band structures

To describe the transformation from one band system to another one, as it is schematically shown in Fig. 7, we suggest the following explicit polynomial form of the operator describing the wall-crossing

$$H_{\text{wall cross}} = a \prod_{\alpha=0}^{2k-1} (N_z + V_z - (N + k - \alpha)) + b \left(V_- N_+^{2k} + V_+ N_-^{2k}\right). \quad (10)$$

This operator is SO(2) invariant and consequently commutes with J_z. The operator (10) has $2k$ zero eigenvalues associated with the eigenfunctions of the J_z operator with eigenvalues $N + k, N + k - 1, \ldots, N - k + 1$.

Eigenstates with zero eigenvalue of the local Hamiltonian (10) are named zero-mode states. They are responsible for topological phase transitions.

Crossing a wall in the control parameter space gives rise to a deformation of the model Hamiltonians in such a manner that the zero energy modes disappear in the full quantum model and that the degeneracy of eigenvalues disappears in the semi-quantum model. In general, it is possible to imagine several different situations. In the case

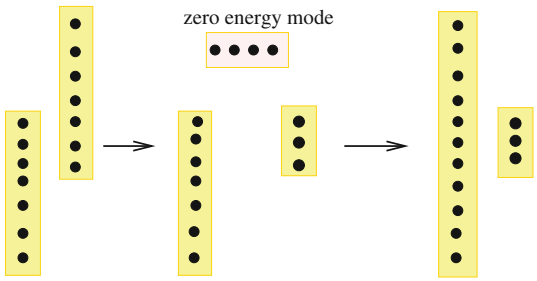

Fig. 7 Rearrangement of bands through formation of zero-mode states in the case of sufficiently high J values. For this figure $J = 3$ and $m_1 = -2, m_2 = 2$. Quantum states are shown by *black fill dots*

of one zero eigenvalue (the case with $k = 1/2$), under the variation of control parameters corresponding to the crossing of the boundary, this zero eigenvalue simply crosses the zero energy either from the positive side to the negative side or vice versa. This is a generic behavior.

In the case of two zero eigenvalues, the scenario of their behavior under the variation of control parameters can be similar. It is possible that two eigenvalues come from the same side (positive or negative), become degenerate at zero, and go to another side crossing the zero. This scenario repeats the generic scenario with one zero eigenvalue except that the zero eigenvalue becomes degenerate and the redistribution consists of two eigenvalues. Such a scenario was discussed on a concrete example of a molecular system in [3] for the CF_4 molecule, where the redistribution of two sixfold clusters was observed between two bands. The fact of sixfold quasi-degeneracy is naturally not important in our present context. It is a consequence of finite cubic symmetry. The important point here is the fact of a simultaneous transfer of two clusters. This means that for each degeneracy point and, in other words, for each wall-crossing model Hamiltonian two zero eigenvalues are formed. In contrast, transfer of only one cluster (or of only one of two levels for each local Hamiltonian) between these bands is forbidden by symmetry. Formation of several zero-mode states is illustrated schematically in Fig. 7.

Another possible scenario with two zero eigenvalues corresponds to two eigenvalues coming to zero from different sides (one from the positive and another from the negative). After crossing the boundary, the two zero eigenvalues leave again to two different sides. The cumulative effect of crossing the boundary is: no redistribution of energy levels between bands. This situation can be compared with the spin Hall effect, where Hall currents related to electrons with spin projections $+1/2$ and $-1/2$ are nonzero but opposite and the net effect is zero. Apparently such a situation cannot appear in a problem with $m_1 - m_2 \neq 0$. We need to combine the case with $m_1 - m_2 = 0$ with additional symmetry responsible for the formation of zero energy mode. Note that the requirement

$m_1 - m_2 = 0$ (in case of zero Chern numbers for each band) for such scenario appears for the case of the axial symmetry group $SO(2)$. In case of a finite symmetry group, the numbers of states in two bands can be different, but the formation of two zero energy states coming along the deformation from two different bands remains possible.

References

1. Arnold VI (1995) Remarks on eigenvalues and eigenvectors of Hermitian matrices, Berry phase, adiabatic connections and quantum Hall effect. Selecta Mathematica 1:1–19
2. Berry MV (1984) Quantal phase factor accompanying adiabatic changes. Proc R Soc Lond A 392:45–57
3. Brodersen S, Zhilinskii B (1995) Transfer of clusters between the vibrational components of CF_4. J Mol Spectrosc 169:1–17
4. Broer HW, Cushman RH, Fassò F, Takens F (2007) Geometry of KAM-tori for nearly integrable Hamiltonian systems. Ergod Theory Dyn Syst 27:725–741
5. Caspers WJ (2008) Degeneracy of the eigenvalues of hermitian matrices. J Phys Conf Ser 104:012032
6. Chen X, Gu Z-C, Liu Z-X, Wen X-G (2012) Symmetry protected topological orders and the group cohomology of their symmetry group. Science 338:1604–1606
7. Cushman RH, Duistermaat JJ (1988) The quantum mechanical spherical pendulum. Bull Am Math Soc 19:475–479
8. Efstathiou K, Sadovskii D (2010) Normalization and global analysis of perturbations of the hydrogen atom. Rev Mod Phys 82:2099–2154
9. Faure F, Zhilinskii B (2000) Topological Chern indices in molecular spectra. Phys Rev Lett 85:960–963
10. Faure F, Zhilinskii B (2002) Topologically coupled energy bands in molecules. Phys Lett A 302:242–252
11. Shapere A, Wilczek F (eds) (1989) Geometric phases in physics. World Scientific, Singapore
12. Faddeev LD, Popov VN (1967) Feynman diagrams for the Yang–Mills field. Phys Lett B 25:29–30
13. Harter W (1993) Principles of symmetry, dynamics, and spectroscopy. Wiley Interscience, New York
14. Hasan MZ, Kane CL (2010) Topological insulators. Rev Mod Phys 82:3045–3067
15. Iwai T, Zhilinskii B (2011) Energy bands: Chern numbers and symmetry. Ann Phys (NY) 326:3013–3066
16. Iwai T, Zhilinskii B (2012) Rearrangement of energy bands: Chern numbers in the presence of cubic symmetry. Acta Appl Math 120:153–175
17. Iwai T, Zhilinskii B (2013) Qualitative features of the rearrangement of molecular energy spectra from a "wall-crossing" perspective. Phys Lett A 377:2481–2486
18. Iwai T, Zhilinskii B (2014) Chern number modification in crossing the boundary between different band structures. Three band model with cubic symmetry. Submitted for publication
19. Kane CL, Mele EJ (2005) Z_2 topological order and the quantum spin Hall effect. Phys Rev Lett 95:146802
20. Kitaev A (2009) Periodic table for topological insulators and superconductors. AIP Conf Proc 1134:22–30
21. Kohmoto M (1985) Topological invariant and the quantization of the Hall conductance. Ann Phys (NY) 160:343–354
22. Kontsevich M, Soibelman Y (2013) Wall-crossing structures in Donaldson–Thomas invariants, integrable systems and mirror symmetry. arXiv:1303.3253 to appear in Lecture Notes in Mathematics
23. Michel L, Zhilinskii B (2001) Symmetry, invariants topology. Basic tools. Phys Rep 341:11–84
24. Moore JE, Balents L (2007) Topological invariants of time-reversal-invariant band structures. Phys Rev B 75:121306(R)
25. Pavlichenkov I, Zhilinskii B (1988) Critical phenomena in rotational spectra. Ann Phys (NY) 184:1–32
26. Pavlov-Verevkin VB, Sadovskii DA, Zhilinskii BI (1988) On the dynamical meaning of diabolic points. Europhys Lett 6:573–78
27. Sadovskii D, Zhilinskii B (1999) Monodromy, diabolic points, and angular momentum coupling. Phys Lett A 256:235–44
28. Sadovskii D, Zhilinskii B (2006) Quantum monodromy, its generalizations and molecular manifestations. Mol Phys 104:2595–2615
29. Shrivastava KN (2004) Negative-spin quasiparticles in quantum Hall effect. Phys Lett A 326:469–472
30. van Tonder A (2002) Ghost as negative spinors. Nucl Phys B 645:371–386
31. Vu Ngoc S (1999) Quantum monodromy in integrable systems. Commun Math Phys 203:465–479
32. Zhilinskii B (2001) Symmetry, invariants and topology in molecular models. Phys Rep 341:85–172
33. Zhilinskii B (2011) Quantum bifurcations. In: Meyers R (ed) Mathematics of complexity and dynamical systems. Springer, New York, pp 1438–1456
34. Zhilinskii B, Brodersen S (1994) The symmetry of the vibrational components in T_d molecules. J Mol Spectrosc 163:326–338

Theor Chem Acc (2014) 133:1504
DOI 10.1007/s00214-014-1504-7

REGULAR ARTICLE

Vibrational energy flow across heme–cytochrome *c* and cytochrome *c*–water interfaces

Johnson K. Agbo · Yao Xu · Ping Zhang · John E. Straub · David M. Leitner

Received: 2 April 2014 / Accepted: 8 May 2014 / Published online: 31 May 2014

Abstract We examine vibrational energy transfer across the heme–protein and protein–solvent interfaces of cytochrome *c*, using, as appropriate, classical, semiclassical, and quantum approaches. To characterize energy flow across the interface between the heme and the rest of cytochrome *c*, we calculate communication maps for the protein in its native structure as well as two structures with Met80 dissociated from the heme at 300 K. The response to excess energy in the heme is mediated by covalent and hydrogen bonds to the heme, as well as several through-space interactions, including those involving the dissociated Met80. This observation suggests no energy flow bottleneck between the heme and Met80 that would impede rebinding kinetics at 300 K. We examine the possibility of additional bottlenecks to energy flow by calculating the temperature dependence of the ergodicity threshold in an imidazole-ligated Fe-porphyrin system that constitutes the core of the heme–histidine complex. The ergodic threshold, which we calculate quantum mechanically, corresponds to a temperature of about 140 K. We also address the flow of excess vibrational energy from the protein to the solvent. We calculate the thermal boundary conductance between cytochrome *c* and water semiclassically over a range of temperatures and find that the protein–water interface poses no greater resistance to thermal flow than the protein itself.

Keywords Vibrational energy flow · Thermal boundary conductance · Communication maps · Diffuse mismatch model

1 Introduction

Pathways and bottlenecks to energy flow in proteins mediate chemical reaction kinetics including allosteric transitions, charge transfer, and ligand binding and dissociation [1–9]. For this reason, there have been numerous experimental and computational studies of vibrational energy relaxation in heme proteins [10–22]. Cytochrome *c*, a heme protein consisting of a single polypeptide chain containing 104 amino acid residues organized into a series of five α helices and six β turns, is an important participant in electron transfer for ATP synthesis in mitochondria and as signal amplifier in cell apoptosis [23]. The heme active site in cytochrome *c* has a six-coordinate low-spin iron, with His18 and Met80 bound as internal ligands. A number of experimental studies [24–26] have elucidated its ultrafast dynamics following photoexcitation, sometimes leading to ligand dissociation and recombination. Recent computational work has explored the non-adiabatic transitions involved in ligand recombination using ab initio potential energy surfaces [27] revealing heterogeneity in the rebinding kinetics determined by protein and solvent structure and temperature [28]. The rebinding kinetics can

Dedicated to Professor Greg Ezra and published as part of the special collection of articles celebrating his 60th birthday.

J. K. Agbo
Department of Chemistry and Physics, Coastal Carolina University, Conway, SC 29528-6054, USA

Y. Xu · D. M. Leitner (✉)
Department of Chemistry and Chemical Physics Program, University of Nevada, Reno, NV 89557, USA
e-mail: dml@unr.edu

P. Zhang · J. E. Straub (✉)
Department of Chemistry, Boston University, Boston, MA 02215, USA
e-mail: straub@bu.edu

also be influenced by energy flow. Bu and Straub reported detailed molecular dynamics (MD) simulations of vibrational energy relaxation from the heme of cytochrome *c* in its native state [29]. In this article, we further study vibrational energy flow in cytochrome *c*, both in its native structure and in two structures with Met80 dissociated from the heme. We examine, using classical, semiclassical, and quantum methods, vibrational energy transfer across two interfaces: (1) between the heme and the rest of cytochrome *c* when Met80 is bonded and dissociated from the heme, and (2) the interface between cytochrome *c* and water.

Bottlenecks to vibrational energy transfer in a molecule as large as a protein can occur on different length scales. On the scale of a residue or cofactor, energy redistribution among vibrational modes within such a subspace of the protein depends on anharmonic coupling and a local density of states made up of these modes. Quantum mechanical first-order time-dependent perturbation theory can be adopted to calculate energy transfer by anharmonic coupling [30–32], an approach that becomes valid when the product of the anharmonic coupling and local density of states is at least of order 1 [33, 34]. When this criterion is not met, energy may still flow but the dynamics can be quite complex in molecules of even modest size [35–38]. On larger length scales, we may be interested in energy flow through residues of the protein, for instance, how bonds or other interactions between residues influence redistribution of excess energy in different parts of the protein [29, 39]. At even larger length scales, we can consider vibrational energy flow between the protein as a whole and the solvent, e.g., to address how excess energy already distributed within the protein flows into the solvent environment and whether additional resistance to energy redistribution is encountered at the protein–solvent interface [40–42].

In our study of energy flow across the heme–protein interface, we calculate communication maps [43], which we use to determine the response of the protein to excess energy in the heme at 300 K when Met80 is bound to and dissociated from the heme. Met80-heme rebinding kinetics depends on whether the Met80 orientation to the heme is upward or downward, i.e., the upward structure does not bind to the heme and must isomerize to the downward to bind [27, 28]. Isomerization kinetics can be mediated by energy flow in each structure as well as the barrier between structures [44–50], so we examine if an energy flow bottleneck is introduced when Met80 is dissociated from the heme. In the native structure, Met80 responds more rapidly than any other residue to excess energy in the heme. We find the response time to be diminished but still quite rapid when Met80 is dissociated from the heme, so that, at least at temperatures near 300 K, there appears to be no energy flow bottleneck between the heme and Met80. Dissociation of Met80 from the heme does not affect the response of other parts of the protein to excess vibrational energy in the heme.

Another way in which energy flow could influence the rate constant for Met80-heme rebinding involves limited or slow energy relaxation within the heme itself, which might occur at low temperature. We can think of the binding region as a system of many coupled nonlinear oscillators, which may exhibit ergodicity only above an energy threshold [51–55]. We examine the energy and temperature dependence of ergodicity quantum mechanically in an imidazole-ligated Fe-porphyrin system that forms the binding region of the heme. Vibrational relaxation in that system was studied by Straub and coworkers using quantum mechanical time-dependent perturbation theory [31]. We use the vibrational frequencies calculated in that work to estimate the temperature-dependent ergodicity threshold, which we find to be near 140 K. We thus expect limited or sluggish energy flow within the binding region at lower temperatures.

Having examined how excess energy flows from the heme into the rest of the protein, we consider energy flow across the boundary between cytochrome *c* and solvent. We coarse grain the system beyond the level of the residues and address thermal transport across the interface of the protein and bulk water. Thermal transport within proteins has been studied by MD simulations [56–58], computational approaches based on the vibrational modes of the system [45, 59, 60], and experimentally by time-resolved spectroscopy [61–64]. Below we adopt a semiclassical approach [65] to calculate the resistance to thermal flow across the cytochrome *c*–water interface and compare the result with the resistance to thermal flow in proteins computed earlier [60] to determine whether the flow of excess vibrational energy in cytochrome *c* is impeded more by the protein itself or its interface with water.

In the following section, we summarize the calculation of communication maps to describe the response of cytochrome *c* to excess vibrational energy in the heme and thermal boundary conductance at the cytochrome *c*–water interface. In Sect. 3, we present and discuss our results. Concluding remarks are given in Sect. 4.

2 Methods

2.1 Communication maps and molecular simulations

Protein structures and calculation of normal modes, which was carried out using the CHARMM simulation package with the CHARMM28 force field, have been described in previous work by two of us [27, 28]. The sequence of

1HRC from the PDB was used to define the human cytochrome *c* system, and the crystal structure was taken as the initial configuration. Using the normal modes for cytochrome *c* in the native structure and two dissociated structures, i.e., upward and downward [27, 28], we computed frequency-resolved communication maps. The calculation of communication maps has been detailed elsewhere [43], and in this subsection, we summarize the method. Thermal transport coefficients have been computed for molecules and other nanoscale objects using a number of approaches [66–68]. For coarse-graining a sizable molecular system such as a protein, a useful starting point is the heat current operator in harmonic approximation [69]

$$S = \sum_{\alpha,\beta} \mathbf{S}_{\alpha\beta} a_\alpha^\dagger a_\beta, \tag{1}$$

where α and β are two modes of the protein, and $a^\dagger$ and a are, respectively, raising and lowering operators. The coefficient, $\mathbf{S}_{\alpha\beta}$, corresponding to the protein as a whole can be expressed in terms of the Hessian matrix, **H**, and eigenmodes, **e**, of the object. We break the coefficient up into contributions from various regions. The contribution to the energy flux between regions A and A' to the matrix elements of **S** is [43]

$$\mathbf{S}_{\alpha\beta}^{\{AA'\}} = \frac{i\hbar(\omega_\alpha + \omega_\beta)}{4V\sqrt{\omega_\alpha \omega_\beta}} \sum_{r,r' \in (x,y,z)} \sum_{l,l' \in AA'} e_l^\alpha H_{rr'}^{ll'} (\boldsymbol{R}_l - \boldsymbol{R}_{l'}) e_{l'}^\beta \tag{2}$$

where $\mathbf{R}_l$ is the position of atom l and r is a coordinate (x, y or z). When the regions A and A' span the protein, Eq. (2) expresses the matrix elements of the heat current operator for the whole system in harmonic approximation given in Ref. [69]. Similarly, we can sum over all regions to obtain $\mathbf{S}_{\infty\beta}$ for the whole molecule. Considering only energy flow between the local regions A and A', we write the local energy diffusivity in mode α in harmonic approximation as

$$D_\alpha^{\{AA'\}} = \frac{\pi V^2}{3\hbar^2 \omega_\alpha^2} \sum_{\beta \neq \alpha} \left| S_{\alpha\beta}^{\{AA'\}} \right|^2 \delta(\omega_\alpha - \omega_\beta). \tag{3}$$

When A and A' span the molecule, Eq. (3) gives the mode diffusivity, from which the coefficient of thermal conductivity, κ, can be expressed for the whole molecule, $\kappa = \Sigma_\alpha C_\alpha D_\alpha$, where C_α is the heat capacity per unit volume of the molecule for mode α, given by $C_\alpha = k_B(\beta\hbar\omega_\alpha)^2 \frac{e^{\beta\hbar\omega_\alpha}}{(e^{\beta\hbar\omega_\alpha}-1)^2}$. Otherwise $D_\alpha^{\{AA'\}}$ is a local mode diffusivity for energy flow between A and A'. The coefficient of thermal conductivity has been calculated for proteins [45, 59, 60], and here, we identify the regions of the protein that primarily contribute to thermal transport through the molecule. For a practical calculation on a finite-sized system, we substitute a rectangular window of width η for the delta function, which should be large enough to envelop several vibrational modes. For the results presented here, we calculated the mode diffusivity using $\eta = 15\ \mathrm{cm}^{-1}$, which is large enough to include many modes in the averaging; results for D_α did not change significantly with larger η. Communication maps can then be constructed by plotting $D_\alpha^{\{AA'\}}$ for all A and A' at frequencies, ω_α. We note that we have considered the extent to which anharmonicity might affect the pathways we calculate in the communication maps in a previous study. In a recent calculation of communication maps for PYP [70], we identified the same energy transport pathways from the chromophore as Ishikura and Yamato [71] did using an anharmonic treatment.

In Sect. 3, we use communication maps to locate energy transport channels that include the heme. We present results for the thermal average over the frequency-resolved communication maps for the structures at 300 K, using for averaging the communication maps constructed at 50, 100 cm^{-1}, and continuing in 50 cm^{-1} intervals until 400 cm^{-1}, above which the communication maps contribute very little to the thermal average due to the small values of $D_\alpha^{\{AA'\}}$ at higher frequency. Each of these frequency-resolved maps is actually an average over maps for 4 modes closest in frequency to the designated frequency. The thermally averaged communication map is obtained assigning a Boltzmann weight to the frequency-resolved communication maps and is specifically calculated as $D^{\{AA'\}} = \int d\omega \rho(\omega) D^{\{AA'\}}(\omega) e^{-\hbar\omega/k_B T}$. Using the thermally averaged frequency-resolved communication map, we calculate, in addition to the local thermal diffusivity, a response rate of one residue to vibrational excitation in another, corresponding to the inverse of the first mean passage time, which we define as $D^{\{AA'\}}/R^2$ [14], where R is the distance from the center of mass of A to the center of mass of A'.

To complement the analysis of energy transport using communication maps, we also carried out classical non-equilibrium simulations of energy transport from the heme. We in effect heated the Fe and neighboring atoms of the porphyrin to 300 K and followed the transfer of energy over the next few picoseconds to the rest of the molecule, which was initially at 0 K. Similar starting conditions have been applied in earlier molecular simulations of proteins to elucidate energy transport pathways [72] and by us for a homodimeric hemoglobin [14]. We carried out this analysis in harmonic approximation to provide a realistic representation of the thermal population of the vibrational modes of the protein. On the short times of this analysis, there is no time for configurational changes of the protein or confined water molecules [73]. Details of our non-equilibrium simulation approach, including other applications to heme proteins, are given in Refs. [60, 74, 75].

2.2 Cytochrome *c*–water thermal boundary conductance

The thermal boundary conductance, h_{Bd}, between two subsystems, 1 and 2, the inverse of the thermal boundary resistance or Kapitza resistance [65, 76], is expressed in terms of the heat flow, $\dot{Q}$, driven by the difference in temperature, ΔT, between the two sides of the interface and the area of the interface, A, $h_{Bd} = \frac{\dot{Q}}{A\Delta T}$. Heat flow across the interface can be expressed in harmonic approximation in terms of the vibrational excitations, each with energy $\hbar\omega$, that pass through it. The vibrational mode density per unit volume on side j is $\bar{\rho}_j(\omega)$ and the mode occupation number is $n(\omega, T) = (\exp(\beta\hbar\omega) - 1)^{-1}$, where $\beta = 1/k_B T$ and the speed of propagation on side j is $v_j(\omega)$. The thermal boundary conductance is then expressed as [76] $h_{Bd} = \frac{1}{4}\frac{\mathrm{d}}{\mathrm{d}T}\int d\omega \hbar\omega v_1(\omega)\bar{\rho}_1(\omega)n(\omega, T)\alpha(\omega)$, where $\alpha(\omega)$ is the transmission probability. In a convenient approach to eliminating the transmission probability, $\alpha(\omega)$, the diffuse mismatch model assumes that after crossing the boundary, a vibrational excitation has no memory of which side of the interface it emerged from, i.e., there is diffuse scattering of vibrational energy at the boundary between the protein and water, giving [76]

$$h_{Bd} = \frac{1}{4}k_B \int d\omega(\beta\hbar\omega)^2 \times \frac{v_1(\omega)v_2(\omega)\bar{\rho}_1(\omega)\bar{\rho}_2(\omega)}{(v_1(\omega)\bar{\rho}_1(\omega) + v_2(\omega)\bar{\rho}_2(\omega))}\frac{e^{\beta\hbar\omega}}{(e^{\beta\hbar\omega} - 1)^2}. \quad (4)$$

We apply Eq. (4) to estimate the boundary conductance at the interface between cytochrome *c* and water. For the calculations discussed in the following section, the volume of the protein is estimated assuming a sphere with radius corresponding to the protein's radius of gyration, which for cytochrome *c* is 14 Å. We have used the vibrational mode density of cytochrome *c* reported in Ref. [74] and for water in Ref. [77], both calculated in harmonic approximation. For the speed of sound in water and cytochrome *c*, we have used the values 15 Å ps^{-1} [77] and 22 Å ps^{-1} [41, 74], respectively.

3 Results and discussion

3.1 Communication maps of vibrational energy flow from heme into protein

Before discussing the communication maps, we first examine results of non-equilibrium simulations of vibrational energy flow from the center of the heme to the rest of the protein. In Fig. 1, we plot the time evolution to 3 ps of vibrational energy in cytochrome *c*, which is initially cold everywhere except the Fe atom and the atoms of the porphyrin directly bonded to it.

The non-equilibrium simulations were carried out for the native structure of cytochrome *c* and can be directly compared with earlier MD simulations of vibrational energy flow in cytochrome *c* carried out by Bu and Straub

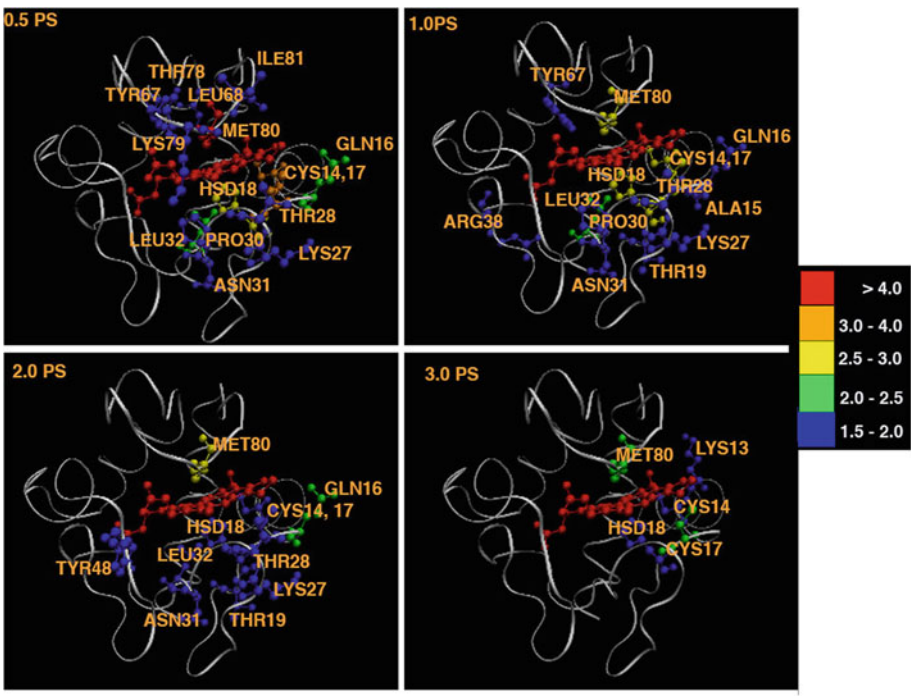

Fig. 1 Snapshots of non-equilibrium molecular simulations of vibrational energy flow in cytochrome *c* (structure with Met80 bonded to the heme). The *color code* corresponds to percentage of total energy in the residue that is indicated

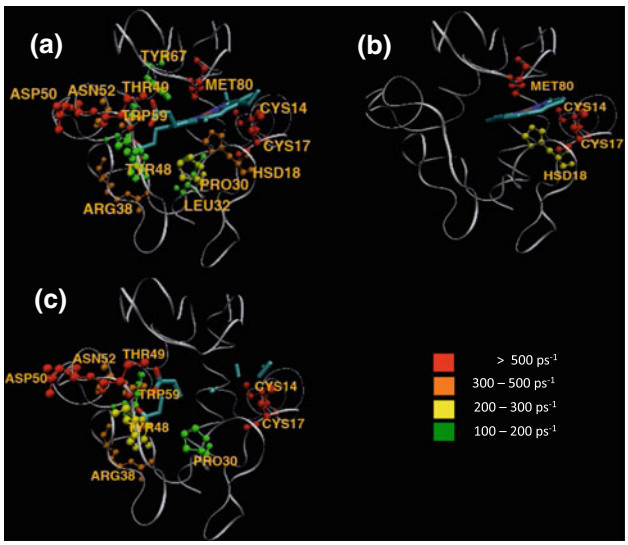

Fig. 2 Largest values of D/R^2 between the heme, or parts of the heme, and protein residues obtained from communication maps of cytochrome *c* at 300 K. In **a**, the heme is complete, whereas in **b** and **c** the largest D/R^2 values are plotted for interactions between the residues and the porphyrin ring and heme side chains, respectively

[29]. In that study, the entire heme was heated initially, whereas in the simulations we present here, we have considered energy flow from a "hot" region consisting only the Fe and a few atoms of the porphyrin. By 1 ps, we observe that more than 10 % of the total energy in the protein is contained in the Cys14, Cys17, His18, and Met80, i.e., those residues covalently bonded to the heme. However, there is little energy flow into the residues that hydrogen bond to the heme, residues that Bu and Straub [29] found to open up additional energy transport pathways from the heme. The difference is likely due to the different initial conditions in these two studies. By 2–3 ps, we observe that excess energy originally in the heme is found mainly in the two cysteines and Met80.

We calculated communication maps for cytochrome *c*, not only in its native state with Met80 bonded to the heme, but also for two structures where Met80 is dissociated, which we refer to as upward and downward due to the orientation of Met80 with respect to the heme. The response of the protein to excess energy in the heme, and to excess energy in different parts of the heme, obtained from the communication maps, is plotted in Figs. 2 and 3. We define the response rate of one residue to vibrational excitation in another as $D^{\{AA'\}}/R^2$, where R is the distance from the center of mass of A to the center of mass of A', and $D^{\{AA'\}}$ is the local energy diffusivity between A and A'. The largest response rates from the heme that we observed were of order 0.1 fs^{-1}.

Figure 2a shows the residues that respond fastest to excess vibrational energy in the heme of the bonded form of cytochrome *c* based on the communication maps, which are seen to include Cys14, Cys17, and Met80, all covalently bonded to the heme. Other residues that respond particularly rapidly include Thr49 and Asp50, which are located on the periphery of the heme and hydrogen bond to the side chains, as well as Trp59, which has been probed by Mizutani coworkers by picosecond time-resolved anti-Stokes ultraviolet resonance Raman (UVRR) measurements [26]. In the UVRR experiments, an energy transfer time of 1–3 ps from the heme to Trp59 was found. To examine whether or not the response of these residues is due to excess energy in the Fe-porphyrin portion of the heme or the heme side chains, we computed communication maps in which we separated these two parts of the heme. $D^{\{AA'\}}/R^2$ for the response to excess energy in the Fe-porphyrin is plotted in Fig. 2b, and for the response to excess energy in the heme side chains in Fig. 2c. We observe that the fast response of Met80 is due to interaction with Fe-porphyrin, whereas the fast response of the cysteine residues is due to interaction with both the porphyrin and the side chains. The fast response of Thr49, Asp50, Trp59, as well as some other residues that are peripheral to the heme is due to the interaction with the heme side chains. Similarly, through-space interactions with the heme appear to originate from the heme side chains, e.g., Arg38, which was also found by Bu and Straub [29] to funnel energy from the heme. The results of the communication maps, in which the response to excess energy in the heme core and the heme side chains were separately examined, are consistent with the flow of energy found in the non-equilibrium simulations plotted in Fig. 1. In the latter, only the center of the porphyrin was initially hot, revealing an energy transport pathway through the two cysteines and Met80 but none through Thr49 or Asp50.

We consider now the effect of Met80 dissociation on the response of the protein to excess energy in the heme. Figure 3 compares the response rates for excess energy in the heme for the bonded (Fig. 3a) and upward (Fig. 3b) forms and for excess energy in only the porphyrin region of the bonded (Fig. 3c) and upward orientations of Met80 with respect to the heme (Fig. 3d) (The results for the upward and downward orientations are very similar and only the former are shown.). The most striking difference between the bonded and the unbonded forms is the reduction in the response time of Met80 to excess vibrational energy in the heme when Met80 is not bonded. Indeed, Met80 goes from the residue that responds fastest to excitation in the Fe-porphyrin portion of the heme to a residue that responds more slowly than either of the cysteines or His18 when Met80 is dissociated from the heme.

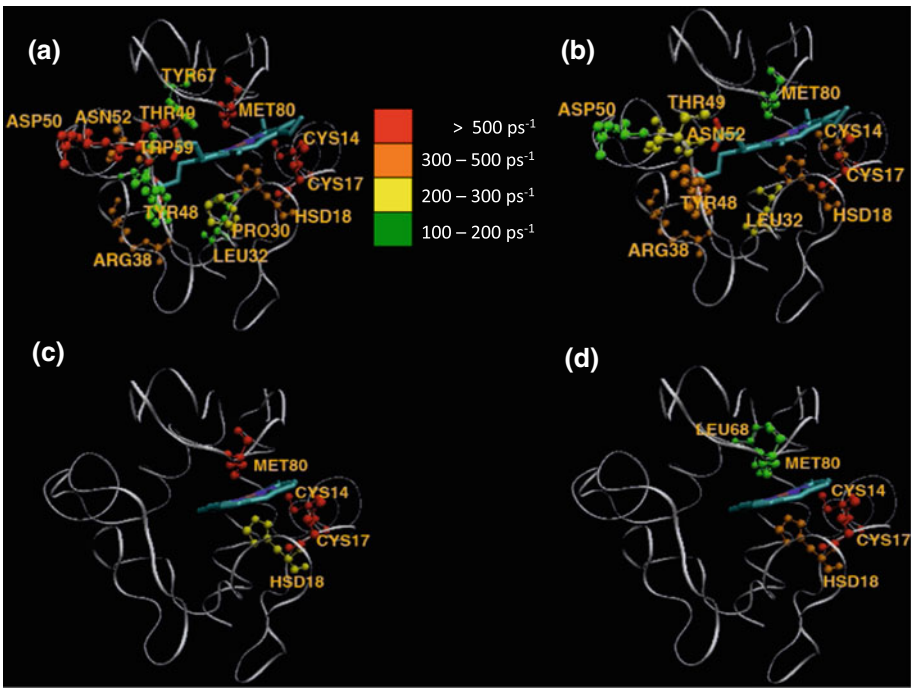

Fig. 3 Communication map predictions of the hot residues following excitation of the ring portion of the heme in the bonded (**a**) and (**c**) and the dissociated (**b**) and (**d**) systems. As in Fig. 2, the largest heme residue D/R^2 values are plotted for the full heme (**a**) and (**b**) and for the porphyrin region only (**c**) and (**d**). The bonded structure exhibits much faster energy flow into Met80 than the dissociated system, though communication with Met80 remains quite rapid even without the chemical bond between the heme and Met80

Nevertheless, we still observe a significant through-space response of Met80 to excess energy in the heme, comparable to the response rate of other nearby residues, some of which hydrogen bond to the heme. The rapid response of Met80 to excess energy in the heme indicates that the rate constant for rebinding of Met80 to the heme is not regulated by bottlenecks to vibrational energy flow between them at 300 K.

When the temperature is low, however, bottlenecks to vibrational energy flow within the heme itself could emerge. At low temperatures, anharmonic coupling among the vibrational modes of the heme might not be sufficiently large to ensure rapid energy flow. Straub and coworkers carried out quantum mechanical time-dependent perturbation calculations of vibrational relaxation in an imidazole-ligated Fe-porphyrin system (Fig. 4), examining the anisotropic relaxation from specific vibrational modes of the complex. Using the vibrational mode frequencies that they report, we can estimate the internal energy in this complex that is needed for ergodic flow of vibrational energy in this molecule using local random matrix theory (LRMT) [33, 34]. LRMT predicts that the ergodicity threshold depends on a *local* density of states, not the total vibrational density of states of the molecule. The ergodicity threshold occurs where the product of the local density of states and the size of the anharmonic matrix elements coupling states on the energy shell is of order 1, or when [33, 34]

$$T(E) \equiv \frac{2\pi}{3} \sum_{Q} \left(\langle |V_Q| \rangle \rho_Q \right)^2 > 1, \tag{5}$$

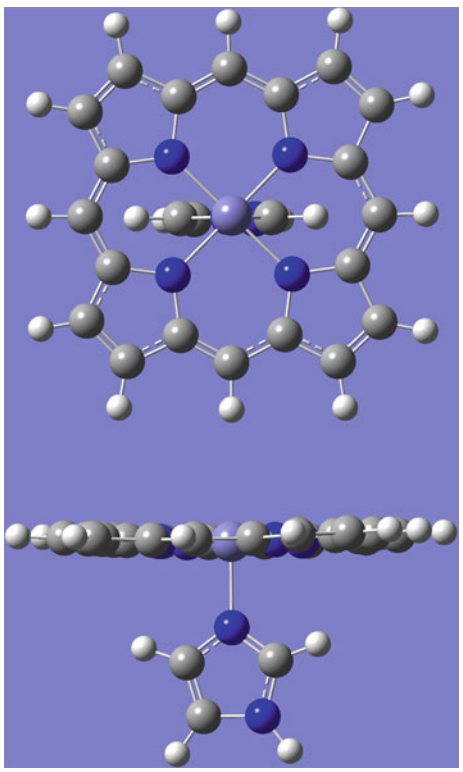

Fig. 4 Top (*top*) and side (*bottom*) views of the Fe-porphyrin system studied by Straub and coworkers [31]. Using the vibrational frequencies reported in Ref. [31], we estimate the total energy required for irreversible energy flow in this molecule

where Q is the distance in terms of quantum numbers between two states coupled by the set of matrix elements, V_Q, and ρ_Q is the local density of states. Cubic anharmonic terms couple

states at most a distance $Q = 3$ in vibrational quantum number space, as a cubic term can transfer one quantum of energy from one mode to two quanta in other modes.

To estimate the ergodicity threshold in terms of the vibrational frequencies of the system, we make use of a scaling relation to estimate average anharmonic matrix elements, V_{ij}, coupling states $|i\rangle$ and $|j\rangle$. The assumption underlying the scaling is the expectation and observation that coupling between states that lie a "distance" Q from one another in quantum number space, where $Q = \sum_\alpha v_\alpha$, and v_α is the occupation number difference in mode α between the two vibrational states, decrease with Q roughly as $V_{ij} \sim C^{-Q}$, where $C > 1$ [78]. Gruebele and coworkers found empirically that for modest-sized organic molecules [78]

$$V_{ij} = \prod_\alpha R_\alpha^{v_\alpha}, \quad R_\alpha \approx \frac{a^{1/Q}}{b}(\omega_\alpha n_\alpha)^{1/2}, \tag{6}$$

which yields the expected exponential decrease in the matrix elements with Q while accounting for the occupation of individual modes. In Eq. 6, n_α is the number of quanta in mode α, ν_α is the occupation number difference in mode α between two vibrational states, and a and b are constants. For V_{ij} expressed in cm^{-1}, a and b are chosen to be 3,050 and 270, respectively. We have compared estimates using Eq. (6) for the anharmonic constants with ab initio calculations of the anharmonic constants in peptide–water complexes and found that, on average, the results are quite similar [79].

The value of $T(E)$ calculated with Eq. (5) depends on the energy, E, of the molecule. Since we consider the heme at a given temperature, we take the thermal energy to be $\langle E\rangle = \sum_\alpha \langle n_\alpha\rangle \hbar\omega_\alpha$, where the temperature-dependent mode occupation, $\langle n_\alpha\rangle$, is given by $\langle n_\alpha\rangle = \left(e^{\hbar\omega/k_BT} - 1\right)^{-1}$.

The result we obtain for $T(E)$ for the imidazole-ligated Fe-porphyrin complex is plotted in Fig. 5. We find the ergodicity threshold for this system at energy of about 1,040 cm^{-1}. The corresponding temperature dependence of T is plotted in the inset to Fig. 5, where we estimate the temperature of the ergodicity threshold to be around 140 K. That temperature lies below the protein dynamical transition of around 180 K, so that at all temperatures where conformational transitions are relatively facile we expect vibrational energy flow within the heme to be facile as well. The rate of energy flow from an initially excited state is dictated by the local density of states to which it is coupled [33, 34], which mediates the mode-specific pathways observed in calculations [31].

3.2 Cytochrome *c*–water thermal boundary conductance

The coefficient of thermal conductivity for several proteins has been computed in linear response approximation from

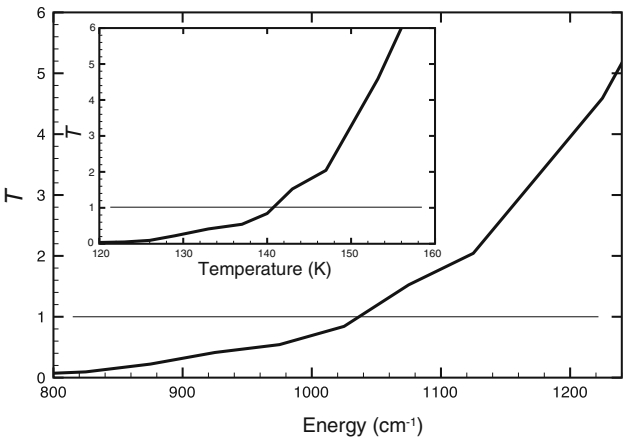

Fig. 5 Transition parameter, T, as a function of total energy in the imidazole-ligated Fe-porphyrin system shown in Fig. 2. The ergodicity transition occurs at the energy where $T = 1$, indicated by the horizontal line, which in this molecule appears around 1,200 cm^{-1}. Inset shows T as a function of temperature, where again the critical $T = 1$ is indicated by a horizontal line. The ergodicity threshold is found for this molecule to be around 140 K

two different approaches, both yielding values of 0.1–0.3 W m^{-1} K^{-1} [40, 60], much smaller than the thermal conductivity of water, which is about 0.6 W m^{-1} K^{-1}. Here, we examine whether the boundary between cytochrome c and water introduces additional resistance to vibrational energy flow beyond the resistance to thermal flow in the protein.

We calculated the thermal boundary conductance, h_{Bd}, for cytochrome c and water with Eq. (4) from 200 to 320 K and plot the result in Fig. 6. In earlier studies, we calculated the thermal boundary conductance between myoglobin and water [41] and between GFP and water [42]. The former turns out to be about 1 % larger than the values we found for cytochrome c and water, so essentially indistinguishable from the cytochrome c–water results plotted in Fig. 6. However, the results for the GFP–water interface that we calculated in the same way are different, and we plot them in Fig. 6 with our calculations for cytochrome c and water. For the cytochrome c–water interface, we find a modest increase in boundary conductance over the plotted range of temperature, from about 240 MW K^{-1} m^{-2} at 200 K to about 300 MW K^{-1} m^{-2} at 320 K, with a value of 299 MW K^{-1} m^{-2} at 300 K. This compares with about 260 MW K^{-1} m^{-2} at 200 K to about 340 MW K^{-1} m^{-2} at 320 K for the GFP–water interface, with a value at 300 K of 329 MW K^{-1} m^{-2}, which is about 10 % larger than the thermal boundary conductance we computed for the cytochrome c–water interface. While we are not aware of molecular simulation studies of the thermal boundary conductance between cytochrome c and water with which to compare, we note the values that we compute at 300 K

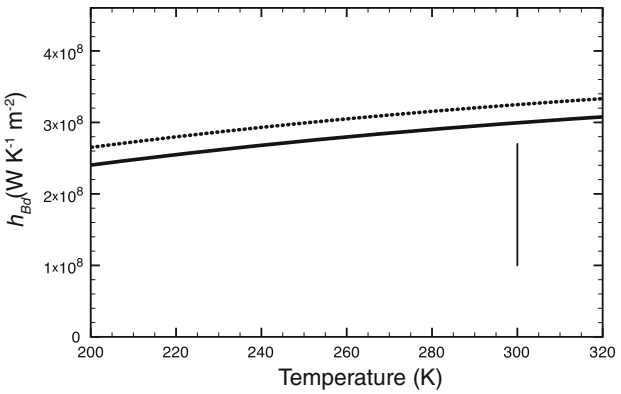

Fig. 6 Boundary thermal conductance, h_{Bd}, calculated for cytochrome *c* and water (*solid curve*), with the result for GFP and water (*dotted curve*) plotted for comparison. The vertical line at 300 K represents the range of values for h_{Bd} obtained by molecular simulations for four different proteins reported in Ref. [40]

are reasonably consistent with those computed for four different proteins (including GFP but not cytochrome *c*) by molecular simulations at 300 K and reported in Ref. [40]. We plot the range of those boundary conductance values in Fig. 6 for comparison.

The thermal boundary conductance between cytochrome *c* and water is roughly 2–3 times as large as the thermal boundary conductance computed for the interface between water and a monolayer of hydrocarbon chains with –OH head groups [80]. Vibrational energy transport across the cytochrome *c*–water interface is relatively efficient compared with interfaces involving other organic molecules that hydrogen bond to water.

The relative thermal resistance within a protein to thermal resistance at the boundary between the protein and water is given by the dimensionless Biot number, Bi, defined as $\mathrm{Bi} = h_{Bd}L/\kappa$, where L is a length scale, often taken as the volume to surface area, and κ is the coefficient of thermal conductivity [40]. At 300 K, we find $h_{Bd} = 299$ MW K^{-1} m^{-2}. While we have not computed the coefficient of thermal conductivity for cytochrome *c*, we use as a representative value $\kappa = 0.25$ W K^{-1} m^{-1}, obtained for myoglobin in an earlier study [60]. We approximate the length, L, as the volume to surface area, $R/3$, which, using a 14 Å radius of gyration noted earlier, is about 0.5 nm for cytochrome *c*. These estimates yield a value for the Biot number of $\mathrm{Bi} \approx 0.6$, so that thermal resistance at the protein–water interface is comparable, perhaps a bit smaller, than thermal resistance in cytochrome *c*.

4 Concluding remarks

We have examined vibrational energy transfer across the heme–protein and protein–water interfaces of cytochrome *c*. To characterize energy flow across the heme–protein interface, we calculated frequency-resolved communication maps for cytochrome *c* in its native structure as well as two forms of the protein with Met80 dissociated from the heme and computed the thermal average at 300 K. We found the response of cytochrome *c* in its native structure at 300 K to excess energy in the heme to be mediated primarily by covalent and hydrogen bonds to the heme, as well as several specific through-space interactions with the heme side chains. Included in the latter is Trp59, which has been probed by Mizutani coworkers by picosecond time-resolved anti-Stokes UVRR measurements [26]. The communication maps reveal that Trp59 lies along an energy transport pathway that emerges from the heme side chains, consistent with the picosecond response time to excitation of the heme observed in the UVRR experiments [26]. In earlier work, we found vibrational energy transport pathways to be robust with respect to thermal motion of proteins around their native structure [81]. However, the energy transport pathways in cytochrome *c*, like those for electron transfer [82], could be altered when this protein interacts with its cellular environment.

The communication maps indicted that energy flow from the heme to Met80 remains rapid when it is dissociated from the heme, though not as fast as when it is covalently bonded. The rapid energy flow between heme and dissociated Met80 that we found at 300 K suggests no energy flow bottleneck between them, though bottlenecks may emerge at lower temperature, even within the binding region itself. To examine the latter possibility, we calculated the temperature dependence of the ergodicity threshold in an imidazole-ligated Fe-porphyrin system that constitutes the core of the heme–histidine complex, which we found to correspond to about 140 K, well below the protein dynamical transition of roughly 180 K.

We also addressed vibrational energy flow from cytochrome *c* into the solvent, adopting a more coarse-grained perspective than our computational study of the response of the protein to excess vibrational energy in the heme. We calculated the thermal boundary conductance between cytochrome *c* and water over a wide range of temperatures and found that the interface between the protein and water poses no greater resistance to thermal flow than the protein itself.

Acknowledgments Support from the National Science Foundation (NSF CHE-0910669 and CHE-1361776 to DML, CHE-1114676 to JES) is gratefully acknowledged.

References

1. Leitner DM, Straub JE (2009) Proteins: energy, heat and signal flow. Taylor and Francis Press, New York

2. Smock RG, Gierasch LM (2009) Sending signals dynamically. Science 324:198–203
3. Fujisaki H, Straub JE (2005) Vibrational energy relaxation in proteins. Proc Natl Acad Sci (USA) 102:7626–7631
4. Leitner DM (2008) Energy flow in proteins. Ann Rev Phys Chem 59:233–259
5. Gunasekaran K, Ma B, Nussinov R (2004) Is allostery an intrinsic property of all dynamic proteins? Proteins Struct Func Bioinform 57:433–443
6. Nussinov R, Tsai C-J (2012) Allostery in disease and in drug discovery. Cell 153:293–305
7. Agarwal PK (2005) Role of protein dynamics in reaction rate enhancement by enzymes. J Am Chem Soc 127:15248–15256
8. Fang C, Frontiera RR, Tran R, Mathies RA (2009) Mapping GFP structure evolution during proton transfer with femtosecond Raman spectroscopy. Nature 462:200–205
9. Buchli B, Waldauer SA, Walser R, Donten ML, Pfister R, Bloechliger N, Steiner S, Caflisch A, Zerbe O, Hamm P (2013) Kinetic response of a photoperturbed allosteric protein. Proc Natl Acad Sci USA 110:11725–11730
10. Nagy AM, Raicu V, Miller RJD (2005) Nonlinear optical studies of heme protein dynamics: implications for proteins as hybrid states of matter. Biochim Biophys Acta 1749:148–172
11. Sagnella DE, Straub JE, Jackson TA, Lim M, Anfinrud PA (1999) Vibrational population relaxation of carbon monoxide in the heme pocket of carbonmonoxy myoglobin: comparison of time-resolved mid-IR absorbance experiments and molecular dynamics simulations. Proc Natl Acad Sci USA 96:14324–14329
12. Henry ER, Eaton WA, Hochstrasser RM (1986) Molecular dynamics simulations of cooling in laser-excited heme proteins. Proc Natl Acad Sci USA 83:8982–8986
13. Lian T, Locke B, Kholodenko Y, Hochstrasser RM (1994) Energy flow from solute to solvent probed by femtosecond ir spectroscopy: malachite green and heme protein solutions. J Phys Chem 98:11648–11656
14. Gnanasekaran R, Agbo JK, Leitner DM (2011) Communication maps computed for homodimeric hemoglobin: computational study of water-mediated energy transport in proteins. J Chem Phys 135:065103
15. Champion PM (2005) Following the flow of energy in biomolecules. Science 310:980–982
16. Sagnella DE, Straub JE (2001) Directed energy "funneling" mechanism for heme cooling following ligand photolysis or direct excitation in solvated carbonmonoxy myoglobin. J Phys Chem B 105:7057–7063
17. Takayanagi M, Okumura H, Nagaoka M (2007) Anisotropic structural relaxation and its correlation with the excess energy diffusion in the incipient process of photodissociated MbCO: high-resolution analysis via ensemble perturbation method. J Phys Chem B 111:864–869
18. Nagaoka M, Yu I, Takayanagi M (2009) Energy flow analysis in proteins via ensemble molecular dynamics simulations: time-resolved vibrational analysis and surficial Kirkwood-Buff Theory. In: Leitner DM, Straub JE (eds) Proteins: energy, heat and signal flow. Taylor & Francis Group, CRC Press, Boca Raton, pp 169–196
19. Mizutani Y, Kitagawa T (1997) Direct observation of cooling of heme upon photodissociation of carbonmonoxy myoglobin. Science 278:443–446
20. Koyama M, Neya S, Mizutani Y (2006) Role of heme propionates of myoglobin in vibrational energy relaxation. Chem Phys Lett 430:404–408
21. Sato A, Mizutani Y (2005) Picosecond structural dynamics of myoglobin following photodissociation of carbon monoxide as revealed by ultraviolet time-resolved resonance Raman spectroscopy. Biochem 44:14709–14714
22. Ye X, Demidov A, Champion PM (2002) Measurements of the photodissociation quantum yields of MbNO and MbO2 and the vibrational relaxation of the six-coordinate heme species. J Am Chem Soc 124:5914–5924
23. Ow Y-LP, Green DR, Hao Z, Mak TW (2008) Cytochrome *c*: functions beyond respiration. Nat Rev Mol Cell Biol 9:532–542
24. Vos MH (2008) Ultrafast dynamics of ligands within heme proteins. Biochim Biophys Acta 1777:15–31
25. Zang C, Stevens JA, Link JJ, Guo L, Wang L, Zhong D (2009) Ultrafast proteinquake dynamics in cytochrome *c*. J Am Chem Soc 131:2846–2852
26. Fujii N, Mizuno M, Mizutani Y (2011) Direct observation of vibrational energy flow in cytochrome *c*. J Phys Chem B 115:13057–13064
27. Zhang P, Malolepsza E, Straub JE (2012) Dynamics of methionine ligand rebinding in cytochrome *c*. J Phys Chem B 116:6980–6990
28. Zhang P, Ahn SW, Straub JE (2013) "Strange kinetics" in the temperature dependence of methionine ligand rebinding dynamics in cytochrome *c*. J Phys Chem B 117:7190–7202
29. Bu L, Straub JE (2003) Simulating vibrational energy flow in proteins: relaxation rate and mechanism for heme cooling in cytochrome *c*. J Phys Chem B 107:12339–12345
30. Zhang Y, Fujisaki H, Straub JE (2009) Mode specific vibrational energy relaxation of amide I and II modes in N-methylacetamide/water clusters: the intra- and inter-molecular energy transfer mechanisms. J Phys Chem A 113:3051–3060
31. Zhang Y, Fujisaki H, Straub JE (2009) Direct evidence for mode-specific vibrational energy relaxation from quantum time-dependent perturbation theory. I. Five-coordinate ferrous iron porphydin model. J Chem Phys 130:025102
32. Leitner DM (2001) Vibrational energy transfer in helices. Phys Rev Lett 87:188102
33. Leitner DM, Wolynes PG (1996) Statistical properties of localized vibrational eigenstates. Chem Phys Lett 258:18–24
34. Leitner DM, Wolynes PG (1997) Vibrational mixing and energy flow in polyatomic molecules: quantitative prediction using local random matrix theory. J Phys Chem A 101:541–548
35. Keshavamurthy S (2013) Scaling perspective on intramolecular vibrational energy flow: analogies, insights and challenges. Adv Chem Phys 153:43–110
36. Semparithi A, Keshavamurthy S (2006) Intramolecular vibrational energy redistributions as diffusion in state space: classical-quantum correspondence. J Chem Phys 125:141101
37. Leitner DM, Gruebele M (2008) A quantum model of restricted vibrational energy flow on the way to the transition state in unimolecular reactions. Mol Phys 106:433–442
38. Gruebele M, Bigwood R (1998) Molecular vibrational energy flow: beyond the golden rule. Int Rev Phys Chem 17:91–145
39. Bu L, Straub JE (2003) Vibrational energy relaxation of 'tailored' hemes in myoglobin following ligand photolysis supports energy funneling mechanism of heme 'cooling'. J Phys Chem B 107:10634–10639
40. Lervik A, Bresme F, Kjelstrup S, Bedeaux D, Rubi JM (2010) Heat transfer in protein–water interfaces. Phys Chem Chem Phys 12:1610–1617
41. Leitner DM (2013) Thermal boundary conductance and rectification in molecules. J Phys Chem B 117:12820–12828
42. Xu Y, Leitner DM (2014) Vibrational energy flow through the green fluorescent protein water interface: communication maps and thermal boundary conductance. J Phys Chem B. doi:10.1021/jp412141z
43. Leitner DM (2009) Frequency resolved communication maps for proteins and other nanoscale materials. J Chem Phys 130:195101
44. Berne BJ, Borkovec M, Straub JE (1988) Classical and modern methods in reaction rate theory. J Phys Chem 92:3711–3725

45. Leitner DM (2005) Heat transport in molecules and reaction kinetics: the role of quantum energy flow and localization. Adv Chem Phys 130B:205–256
46. Komatsuzaki T, Baba A, Kawai S, Toda M, Straub JE, Berry RS (2011) Ergodic problems for real complex systems in chemical physics. Adv Chem Phys 145:171–220
47. Leitner DM, Matsunaga Y, Li C-B, Komatsuzaki T, Shojiguchi A, Toda M (2011) Non-brownian phase space dynamics of molecules, the nature of their vibrational states, and non-RRKM kinetics. Adv Chem Phys 145:83–122
48. Li CB, Matsunaga Y, Toda M, Komatsuzaki T (2005) Phase space reaction network on a multisaddle energy landscape: HCN isomerization. J Chem Phys 123:184301
49. Shojiguchi A, Li CB, Komatsuzaki T, Toda M (2007) Fractional behavior in multi-dimensional Hamiltonian systems describing reactions. Phys Rev E 76:056205
50. Toda M (2005) Global aspects of chemical reactions in multidimensional phase space. Adv Chem Phys 130A:337–399
51. Ezra GS, Martens CC, Fried LE (1987) Semiclassical quantization of polyatomic molecules: some recent developments. J Phys Chem 91:3721–3730
52. Uzer T (1991) Theories of intramolecular vibrational energy transfer. Phys Rep 199(2):73–146
53. Keshavamurthy S, Ezra GS (1997) Eigenstate assignments and the quantum-classical correspondence for highly-excited vibrational states of the Baggot H_2O Hamiltonian. J Chem Phys 107:156–179
54. Leitner DM, Wolynes PG (1996) Vibrational relaxation and energy localization in polyatomics: effects of high-order resonances on flow rates and the quantum ergodicity transition. J Chem Phys 105:11226–11236
55. Logan DE, Wolynes PG (1990) Quantum localization and energy flow in many-dimensional Fermi resonant systems. J Chem Phys 93:4994–5012
56. Lervik A, Bresme F, Kjelstrup S (2009) Heat transfer in soft nanoscale interfaces: the influence of interface curvature. Soft Matter 5:2407–2414
57. Nguyen PH, Park SM, Stock G (2010) Nonequilibrium molecular dynamics simulation of the energy transfer through a peptide helix. J Chem Phys 132:025102
58. Nguyen PH, Hamm P, Stock G (2009) Nonequilibrium molecular dynamics simulation of photoinduced energy flow in peptides: theory meets experiment. In: Leitner DM, Straub JE (eds) Proteins: energy, heat and signal flow. Taylor & Francis Group, CRC Press, Boca Raton, pp 149–168
59. Yu X, Leitner DM (2003) Vibrational energy transfer and heat conduction in a protein. J Phys Chem B 107:1698–1707
60. Yu X, Leitner DM (2005) Heat flow in proteins: computation of thermal transport coefficients. J Chem Phys 122:054902
61. Botan V, Backus EHG, Pfister R, Moretto A, Crisma M, Toniolo C, Nguyen PH, Stock G, Hamm P (2007) Energy transport in peptide helices. Proc Natl Acad Sci USA 104:12749–12754
62. Kholodenko Y, Volk M, Gooding E, Hochstrasser RM (2000) Energy dissipation and relaxation processes in deoxymyoglobin after photoexcitation in the Soret region. Chem Phys 259:71–87
63. Helbing J, Devereux M, Nienhaus K, Nienhaus GU, Hamm P, Meuwly M (2012) Temperature dependence of the heat diffusivity of proteins. J Phys Chem A 116:2620–2628
64. Müller-Werkmeister HM, Bredenbeck J (2014) A donor-acceptor pair for the real time study of vibrational energy transfer in proteins. Phys Chem Chem Phys 16:3261–3266
65. Hopkins PE (2013) Thermal transport across solid interfaces with nanoscale imperfections: effects of roughness, disorder, dislocations and bonding on thermal boundary conductance (Review Article). ISRN Mech Eng, 2013: 682586
66. Buldum A, Leitner DM, Ciraci S (1999) Thermal conduction through a molecule. Europhys Lett 47:208–212
67. Segal D, Nitzan A, Hänggi P (2003) Thermal conductance through molecular wires. J Chem Phys 119:6840–6855
68. Leitner DM, Wolynes PG (2000) Heat flow through an insulating nanocrystal. Phys Rev E 61:2902–2908
69. Allen PB, Feldman JL (1993) Thermal conductivity of disordered harmonic solids. Phys Rev B 48:12581–12588
70. Xu Y, Leitner DM (2014) Communication maps of vibrational energy transport in photoactive yellow protein. J Phys Chem A. doi:10.1021/jp411281y
71. Ishikura T, Yamato T (2006) Energy transfer pathways relevant for long-range intramolecular signaling of photosensory protein revealed by microscopic energy conductivity analysis. Chem Phys Lett 432:533–537
72. Ota N, Agard DA (2005) Intramolecular signaling pathways revealed by modeling anisotropic thermal diffusion. J Mol Biol 351:345–354
73. Gnanasekaran R, Xu Y, Leitner DM (2010) Dynamics of water clusters confined in proteins: a molecular dynamics simulation study of interfacial waters in a dimeric hemoglobin. J Phys Chem B 114:16989–16996
74. Yu X, Leitner DM (2003) Anomalous diffusion of vibrational energy in proteins. J Chem Phys 119:12673–12679
75. Yu X, Leitner DM (2006) Thermal conductivity computed for vitreous silica and methyl-doped silica above the plateau. Phys Rev B 74:184305
76. Swartz ET, Pohl RO (1989) Thermal boundary resistance. Rev Mod Phys 61:605–668
77. Yu X, Leitner DM (2005) Thermal transport coefficients for liquid and glassy water computer from a harmonic aqueous glass. J Chem Phys 123:104503
78. Bigwood R, Gruebele M, Leitner DM, Wolynes PG (1998) The vibrational energy flow transition in organic molecules: theory meets experiment. Proc Natl Acad Sci USA 95:5960–5967
79. Agbo JK, Leitner DM, Myshakin EM, Jordan KD (2007) Quantum energy flow and the kinetics of water shuttling between hydrogen bonding sites on trans-formanilide (TFA). J Chem Phys 127:064315
80. Acharya H, Mozdzierz NJ, Keblinski P, Garde S (2012) How chemistry, nanoscale roughness, and the direction of heat flow affect thermal conductance of solid–water interfaces. Ind Eng Chem Res 51:1767–1773
81. Agbo JK, Gnanasekaran R, Leitner DM (2014) Communication maps: exploring energy transport through proteins and water. Isr J Chem. doi:10.1002/ijch.201300139
82. Volkov AM, vanNuland NAJ (2012) Electron transfer interactome of cytochrome *c*. PLoS Comput Biol 8:e1002807

Theor Chem Acc (2014) 133:1575
DOI 10.1007/s00214-014-1575-5

REGULAR ARTICLE

Quantum molecular dynamics simulations of liquid benzene using orbital optimization

Nazar Ileri · Laurence E. Fried

Received: 22 April 2014 / Accepted: 26 August 2014 / Published online: 25 September 2014

Abstract The structure of liquid benzene is investigated by quantum molecular dynamics simulations. Results using variationally optimized numerical pseudo-atomic orbitals are compared to those of generic optimized orbitals. The accuracy of the first-principle calculations is compared with recent experimental findings. Simulations using minimal basis sets with optimized orbitals are shown to successfully predict the local structure of liquid benzene, while simulations with non-optimized minimal basis sets have significant errors in the structure of the first solvation shell. The use of a minimal optimized basis set considerably speeds up simulations, while preserving much of the accuracy of a larger basis set formed by generic orbitals. The transferability of the optimized orbitals is also explored under different environmental conditions.

Keywords Liquid benzene · Ab initio simulations · Orbital optimization · Krylov · Direct diagonalization

1 Introduction

Benzene is an important organic solvent that finds uses in many industrial and scientific applications. It is the simplest aromatic hydrocarbon, constituting the building blocks of many important complex molecules. Furthermore, it provides an important example of aromatic π–π interactions, which have been of great interest to numerous fields including crystal packing [1], drug design [2], molecular recognition [3], and DNA/RNA base stacking [4]. Due to the aromatic π-bonding and electron delocalization, benzene has exceptional stability at ambient conditions.

Detailed knowledge of the structural properties of benzene is necessary for better understanding of π-interactions in condensed matter. Solid state benzene is well-known to have a herringbone pattern [5–7]. The structure of an isolated benzene dimer in the gas phase [8–16] has also received much attention; both experimental and theoretical results indicate almost isoenergetic, parallel displaced, and T-shaped configurations. The T-shaped configuration is accepted as the true global energy minimum today [12, 17–19]. Benzene in the liquid state, however, is less well understood. Theoretical [20] and experimental studies by X-ray diffraction [21–23] and neutron diffraction [24–27] techniques on the structure of liquid benzene have shown that the local ordering in liquid benzene is mostly perpendicular L-shaped [21, 22, 24] and/or T-shaped [23, 26, 27]. More recently, a parallel displaced and a perpendicular Y-shaped arrangement have been proposed [25] at separations <0.5 and >0.5 nm, respectively, by high-resolution neutron diffraction experiments supported with empirical potential structure refinement analysis. In addition, the perpendicular T-shaped configuration is reported to occur only as a saddle point in the liquid state [25].

Due to the lack of conclusive experimental data, numerous computational studies have been performed to shed light on the structural properties of liquid benzene. In particular, a number of studies have employed the molecular dynamics (MD) [28–30] and Monte Carlo (MC) [31, 32] techniques with empirical force fields. However, results obtained greatly depend on the force fields used. Conventional atom-centered force fields generally predict random

Dedicated to Professor Greg Ezra and published as part of the special collection of articles celebrating his 60th birthday.

N. Ileri · L. E. Fried (✉)
Physical and Life Sciences Directorate, Lawrence Livermore National Laboratory, Livermore, CA 94550, USA
e-mail: fried1@llnl.gov

or slightly favor perpendicular orientations [25, 33, 34]. A charge-separated all-atom force field [31] based on the Hunter and Sanders model [35], where a charge distribution above and below the aromatic ring represents the π-electrons, has resulted in perpendicular configurations being strongly preferred [31, 36, 37]. Recently, Fu and Tian [28] have compared different force fields and concluded that separation of charges or fitting the ab initio pairwise potentials does not necessarily guarantee the reliability of the force fields. They obtained the best fit to the latest experimental results [25] with the optimized potentials for liquid simulations (OPLS-AA) force field.

Density functional theory (DFT)-based ab initio MD simulations have been widely used to study the structural properties of ionic liquids, which often contain complex ring structures [38–40]. It has also been shown to provide an accurate description of π-aromatic interactions in benzene [14, 41, 42]. However, DFT–MD simulations scale poorly with computational effort and hence are practically limited to relatively small system sizes (several hundred atoms) and very short time periods (<10 ps). Liquid state simulations present particular challenges, due to the possibility of slow equilibration times and significant system size effects. Therefore, structural studies of benzene by DFT–MD simulations have mostly focused on the benzene dimer and small benzene clusters [41, 43–45]. Only recently, phase changes in solid benzene at pressures up to 300 GPa [46] as well as in shock-compressed liquid benzene (up to 70 GPa) [47] have been investigated by DFT–MD, which has been proven to be particularly suitable for the study of the chemical reactions in condensed and gas phases [48, 49].

First-principles DFT calculations generally scale as the third power of the number of atoms present in the simulation cell. Therefore, simulations of large and complex systems by DFT–MD necessitate the use of linear-scaling methods (O(N)), where the computations scale only linearly with the system size. Variationally optimized numerical atomic orbitals, which we will refer to as optimized atomic orbitals (OAO), have been shown to provide efficient and accurate localized orbitals as a basis set, suitable for linear-scaling methods [50–53]. OAO have been well documented and successfully employed in the simulation studies of isolated molecules and biomolecules [51, 54] as well as solids [51, 55], but there are few examples for neat molecular liquids. Recently, liquid water simulations [53] have been performed using improved polarization orbitals with a screened Coulomb confinement potential developed for water-based systems [52]. In addition, solid–liquid interface simulations of an electrochemical system containing propylene carbonate have been conducted by combining effective-screening medium method with O(N) DFT [55].

To this end, here, we study the structure of liquid benzene by ab initio MD simulations. This approach avoids the many adjustable parameters involved with empirical force fields, while allowing for the possibility of chemical reaction at extreme temperatures and pressures. Numerical atomic orbitals are variationally optimized specifically for benzene, based on the force theorem. The benzene-specific optimized orbitals are used as a basis set in comparison with generic orbitals. The generic orbitals are optimized from pseudo-atomic orbitals across a wide range of chemical conditions. The transferability of the OAO is tested under different environmental conditions. Effects of long-range interatomic London dispersion interactions are investigated. We show that orbital optimization considerably improves the calculations of a molecular liquid with a fixed basis set. The simulations with a minimal optimized basis set are substantially faster than those of a larger basis set formed by generic orbitals, yet retain much of the accuracy of the larger basis.

2 Computational details

The initial configuration of liquid benzene was obtained by MD simulations using OPLS-AA empirical force field [56, 57] as implemented in the GROMACS software package [58, 59]. Procedures were based on the simulations conducted by Fu et al. [28]. Ten benzene molecules were generated in a cubic simulation box of size 1.484 nm^3 with periodic boundary conditions, setting the density equal to the experimental value [60]. The system was energy minimized for 5,000 steps using the conjugate gradient minimization algorithm, with one steepest descent step for every ten conjugate gradient steps. Then, the equilibration and production runs were performed at 300 K temperature and 1 atm pressure in an NPT ensemble, each for 10 ns and with a time step of 1 fs. The temperature and pressure of the system were controlled by a Nose–Hoover thermostat [61, 62] and a Parrinello–Rahman isotropic barostat [63, 64] with a coupling time of 0.5 and 2.0 ps, respectively. A 0.5-nm cutoff distance was applied for Van der Waals interactions with a long-range dispersion correction for energy. Coulomb interactions were calculated by the particle-mesh Ewald (PME) method using a 0.5-nm cutoff for real space, a 0.12-nm grid spacing, and a PME order of 8. All bonds were constrained with the P-LINCS algorithm [65, 66]. A final density of 861 kg/m^3 was achieved in the production run, which is in good agreement with the experimental value of 876.5 kg/m^3.

Ab initio MD simulations of benzene were performed using the OpenMX software package [50, 51, 54, 67, 68], based on Kohn–Sham DFT [69], and basis set consisting of a linear combination of localized pseudo-atomic

orbitals. The Perdew–Bruke–Ernzerhof (PBE) exchange–correlation functional [70] within the generalized gradient approximation was adopted. Norm-conserving pseudopotentials proposed by Morrison et al. [71] are employed. The pseudo-atomic orbitals, generated by a confinement potential scheme [50, 51, 54, 67], had a cutoff radius of 5.0 a.u (except for calculations referred to below as PBE/DZP-7, where the cutoff radius was set to 7.0 a.u) for both hydrogen and carbon atoms. In principle, the complete basis set limit is approached as both the number of orbitals per atom and the cutoff radius are increased. For each element, single valence (commonly referred to as single zeta or SZ), double valence plus single polarization (DZP), and triple valence plus single polarization orbitals (TZP)-(H:s3p1, C:s3p3d1) as well as optimized contracted single valence orbitals (H:s1, C:s1p1) obtained from the generic (H:s6, C:s6p6) basis set; generic orbitals are the optimized pseudo-atomic orbitals provided by OpenMX) produced by the orbital optimization method [50, 51, 54] were used for the basis set. The DFT-D2 method [72] was employed to include the Van der Waals interaction. For orbital optimization, atomic basis orbitals with the same element type were optimized using the same orbital. The maximum number of self-consistent field iterations and the self-consistence field convergence criterion were 100 and 10^{-4} (Hartree/bohr)^2, respectively.

For calculations using optimized orbitals, a system size of 80 benzene molecules were also studied by replicating fully equilibrated configurations of ten molecules in three dimensions. The starting configurations were achieved through the same basis set as the one employed in larger system size. The real-space grid technique [73] was used to calculate the Hamiltonian matrix elements within an accuracy of 10^{-6} Hartree. A cutoff energy of 150 Ry was chosen in the numerical integrations and in the solution of Poisson's equation using the fast Fourier transformation algorithm (FFT). Unlike the small system size (10 benzene molecules) where the direct diagonalization method was used, large system calculations employed the linear-scaling Krylov subspace method [74] with the radius of a sphere centered on each atom and the dimension of the Krylov subspace set to 0.5 nm and 400, respectively. The radius of 0.5 nm was selected among the investigated parameters of 0.5, 0.6, 0.7 nm, since the simulations were faster and the results were only slightly different from those with a larger sphere radius. The dimension of the Krylov subspace, on the other hand, was set to the default value of the software. A cubic periodic boundary simulation cell was used and the MD time step was set to 0.5 fs, in all simulations. Three different temperature and density conditions were studied as follows: (300 K, 861 kg/m^3), (573 K, 570 kg/m^3), and (814 K, 1,400 kg/m^3). The electron and ion temperatures were set equal in order to achieve local thermodynamic equilibrium. All geometries were optimized by the steepest descent algorithm until the forces were $<10^{-4}$ a.u. Equilibration runs were performed in an NVT ensemble by scaling the velocities [75] for 2 ps and subsequently by the Nose–Hoover method [61, 62, 76] for 8 ps. The mass of heat bath for the Nose–Hoover thermostat was set to 100 a.u. Properties were calculated using the data from the final 8 ps Nose–Hoover MD runs after the equilibrium is achieved.

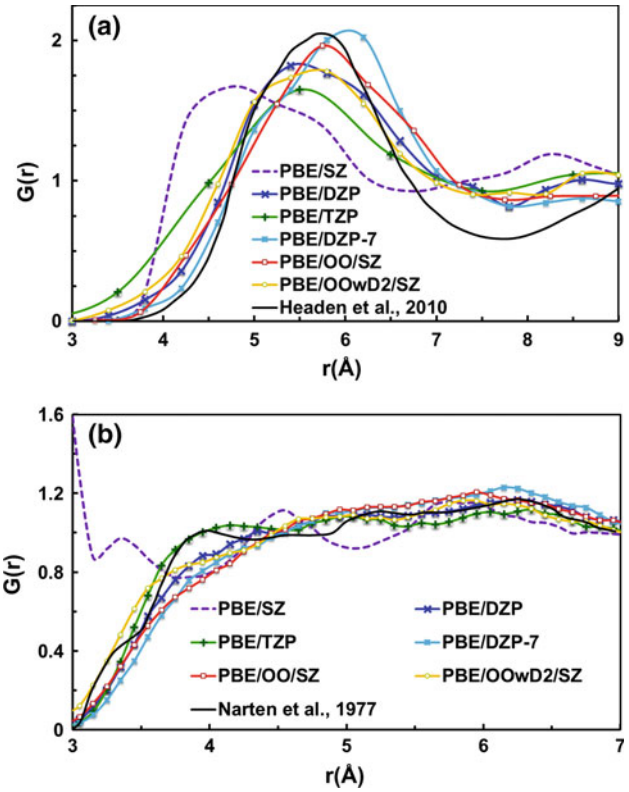

Fig. 1 RDFs of **a** the COM of benzene molecules, **b** C–C atom pairs. Experimental data cited from **a** Ref. [25] and **b** ref [22]. The best fits to experimental results are obtained with **a** PBE/OO/SZ and **c** PBE/TZP

3 Results and discussion

The radial distribution functions (RDFs) of the center of mass (COM) of benzene molecules as well as the C atoms pairs for the ten molecule system are given in Fig. 1. The COM-RDFs provide general information on the size and number of molecules within the first solvation shell (Fig. 1a). It has been calculated by the relation $G(r) = V/N^2 \sum_{i<j}\delta(r - r_{ij})$ and compared to the experimental findings reported by Headen et al. [25]. Computations with the optimized single valence orbitals (PBE/OO/SZ) have predicted the best $G(r)$ values when compared to

experiment. A coordination number of approximately 12 in the first solvation shell is obtained with all calculations in agreement with the experimental value, except for the single valence orbitals (PBE/SZ) where only nine nearest neighbors are found. Similarly, the differences in the peak positions are calculated to be within 0.3 Å, excluding PBE/SZ where the difference is ~1 Å. The best peak positions are attained with the optimized single valence orbitals with and without the DFT-D2 method (PBE/OOwD2/SZ and PBE/OO/SZ respectively). In contrast, the best fit to the first minimum outside of the first shell is achieved through double valence orbitals with polarization (PBE/DZP and PBE/DZP-7) as well as PBE/OO/SZ. The difference in the first minimum compared to the experimental value is less than 0.3 Å with PBE/OO/SZ, PBE/DZP-7, and PBE/TZP. Similar to COM-RDFs, C atom pair RDFs (Fig. 1b) provide overall features of liquid structure obtained through different basis sets, but in greater detail. Besides, experimental C atom pair RDFs are generally easier to measure and more accurate compared to the COM-RDFs, which is a weighted average of C–C, C–H, and H–H RDFs [26]. All triple and double valence orbitals with polarization (PBE/DZP-7, PBE/TZP, and PBE/DZP) predict the first three peaks of the RDF (the peak positions were reported as 4.0, 5.2, and 6.3 Å by Narten et al. [21, 22]) within 0.3 Å deviation. The best first peak estimate is obtained with PBE/TZP at 4.1 Å, while the best second and third peak estimates are achieved at about 5.2 Å with PBE/DZP and PBE/DZP-7 and at 6.3 Å with PBE/DZP, respectively. In general, PBE/TZP calculations have resulted in the best intensity profile, while PBE/SZ has yielded in the worst profile as well as the peak positions, which are observed at r values more than 0.5 Å before reported values. This is indicative of a large effective attraction between neighboring benzene molecules, perhaps produced by basis set superposition error. Unlike generic single zeta orbitals (PBE/SZ), optimized single zeta orbitals (both PBE/OO/SZ and PBE/OOwD2/SZ) provide satisfying results, although they fail to locate the first peak of the C–C RDFs. Particularly, the intensity results of PBE/OOwD2/SZ are in good agreement with both PBE/DZP and PBE/TZP computations. The second and the third peaks are found to be at 5.0 and 6.0 Å with PBE/OO/SZ, and at 5.1 and 6.0 Å with PBE/OOwD2/SZ, respectively.

The simulated structure of liquid benzene is further investigated by the radial-angular pair distribution function (RADF), which gives some information on the degree of orientational order [25, 29, 30] (Fig. 2). The RADF has been computed for the minimum angles between the normals of aromatic planes using the equation $g(r,\theta) = 1/N\rho 4\pi r^2 \sin\theta \Delta r \Delta\theta \ [\Sigma_i \Sigma_{i\neq j} \delta(r - r_{ij}) \delta(\theta - \theta_{ij})]$, where ρ is the bulk number density, Δr and $\Delta\theta$ are the radial and angular resolution. In accordance with the experimental and computational findings [22, 23, 25, 28, 31], PBE/DZP-7, PBE/SZ, PBE/OOwD2/SZ, and PBE/OO/SZ calculations show a preference for perpendicular ordering in the first shell with the highest $g(r,\theta)$ values at $\theta \sim 90°$. The main peaks are obtained at 5.8, 4.8, 5.3, and 5.8 Å, respectively. Similar to Headen's findings [25] a shoulder is observed at $r \sim 4$ Å at low angles with PBE/DZP-7, PBE/OO/SZ, and PBE/OOwD2/SZ (Fig. 2d–f), indicating the existence of a parallel molecular arrangement at small molecular separations. On the other hand, the first peaks are shifted to $r \sim 4$ Å at $\theta < 20°$, with PBE/DZP and PBE/TZP calculations (Fig. 2b, c) while they remain at 5.8 and 5.3 Å, respectively, at $\theta > 20°$. Indeed, the peak values estimated for PBE/DZP and PBE/TZP at $r \sim 4$ Å and $\theta < 20°$ are much greater than the values obtained at $\theta \sim 90°$, showing higher preference for parallel ordering with increasing basis set size. Analysis of the simulation trajectories has revealed that Y-shaped and distorted L-shaped configurations with separation distances $r > 0.5$ nm (Fig. 3a) are the predominant geometry throughout the simulation time with PBE/DZP-7, PBE/SZ, PBE/OO/SZ, and PBE/OOwD2/SZ calculations although parallel displaced configurations (Fig. 3b) are also observed at smaller separations. Conversely, benzene molecules mainly arrange themselves in a parallel displaced configuration with PBE/DZP and PBE/TZP calculations resulting in large $g(r,\theta)$ estimates at low r and θ. This indicates that the structure of fluid can be successfully reproduced with a large basis set having orbital cutoff radius of 7.0 a.u., although a smaller radius OO/SZ calculation perform as well in capturing the overall coordination number and the detailed structure of the liquid.

Benzene has been shown to be nearly isotropic in the first solvation shell, with two anisotropic effects, i.e. parallel ordering at $r < 5$ Å and perpendicular ordering at $r > 5$ Å, almost canceling each other [25]. Therefore, the number of benzene molecules in the first solvation shell ($0 < r < 7.5$ Å), as well as at small ($0 < r < 5$ Å) and large separations (5 Å $< r <$ 6 Å) within the first shell, is calculated as function of molecular orientations (Fig. 4) and compared to that of an isotropic liquid in the defined region. For PBE/SZ only, the r values are shifted by 1 Å due to a significant shift in COM-RDF values. In other words, total number of molecules are computed as a function of θ for molecular separations $0 < r <$ 6.5 Å, $0 < r <$ 4 Å, and 4 Å $< r <$ 5 Å, for a better comparison of isotropy in the first shells. Unlike the experiments [25], the configurational distributions obtained in the first shell are anisotropic in all simulations (Fig. 4a). This is in accordance with the recent computational findings by Takeuchi et al. [77] and is attributed to the reduced perturbation effects induced by a small system size and lesser π–π interactions. At smaller molecular separations ($r < 5$ Å; $r <$ 4 Å

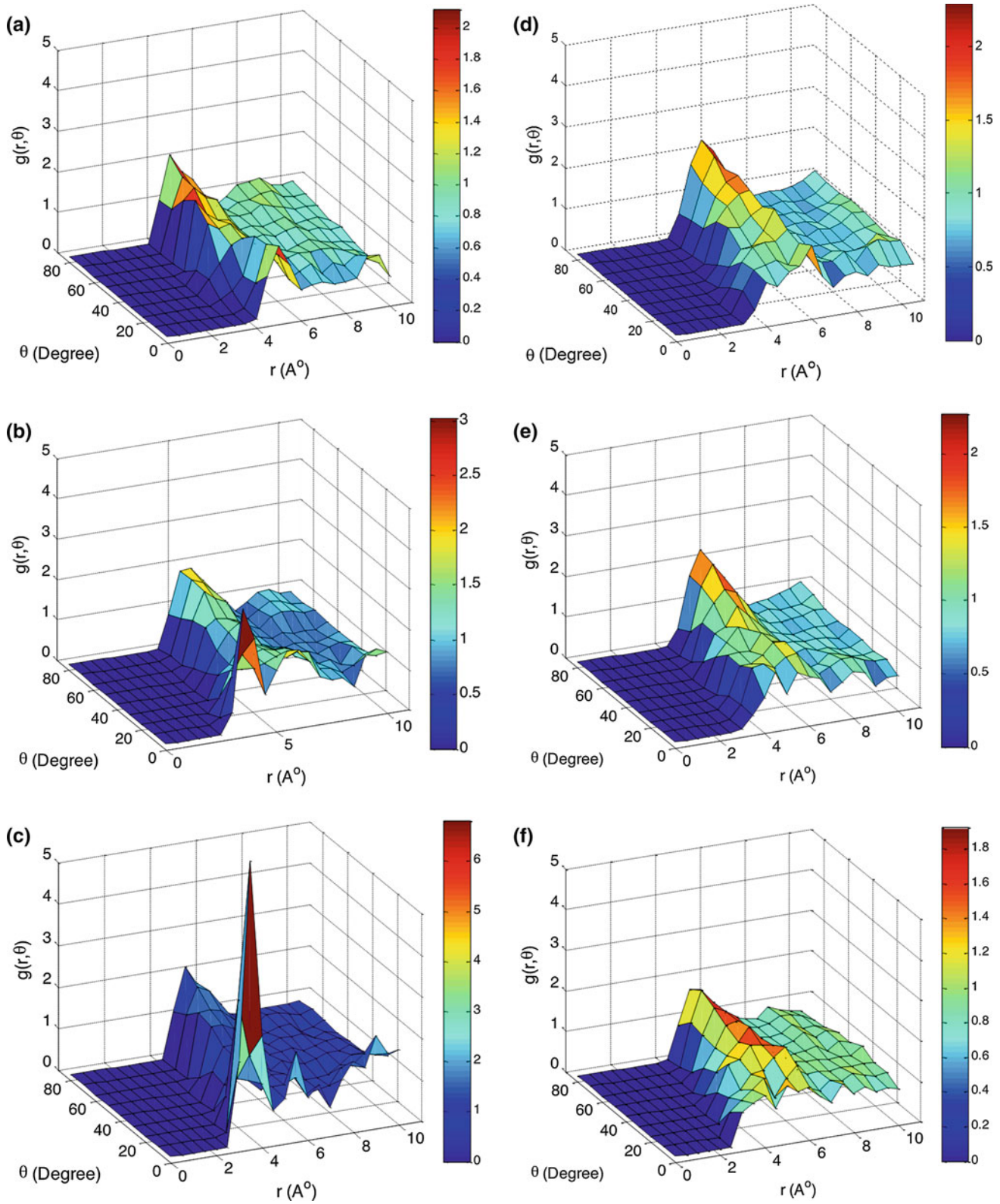

Fig. 2 Radial angular distribution functions for the COM of benzene molecules with **a** PBE/SZ, **b** PBE/DZP, **c** PBE/TZP, **d** PBE/DZP-7, **e** PBE/OO/SZ, **f** PBE/OOwD2/SZ. The radial and angular resolution is $\Delta r = 1$ Å, $\Delta\theta = 10°$ in (**d**), and $\Delta r = 0.5$ Å, $\Delta\theta = 10°$ in all other cases. PBE/DZP-7, PBE/SZ, PBE/OO/SZ, and PBE/OOwD2/SZ calculations show a higher preference for perpendicular molecular ordering, while PBE/DZP and PBE/TZP show a higher preference for parallel molecular arrangements. At small angles, PBE/DZP-7, PBE/OO/SZ, and PBE/OOwD2 have a shoulder next to main peak at $r \approx 4$ Å in accordance with ref [25] findings. The first peak is completely shifted to $r \approx 4$ Å with PBE/DZP and PBE/TZP

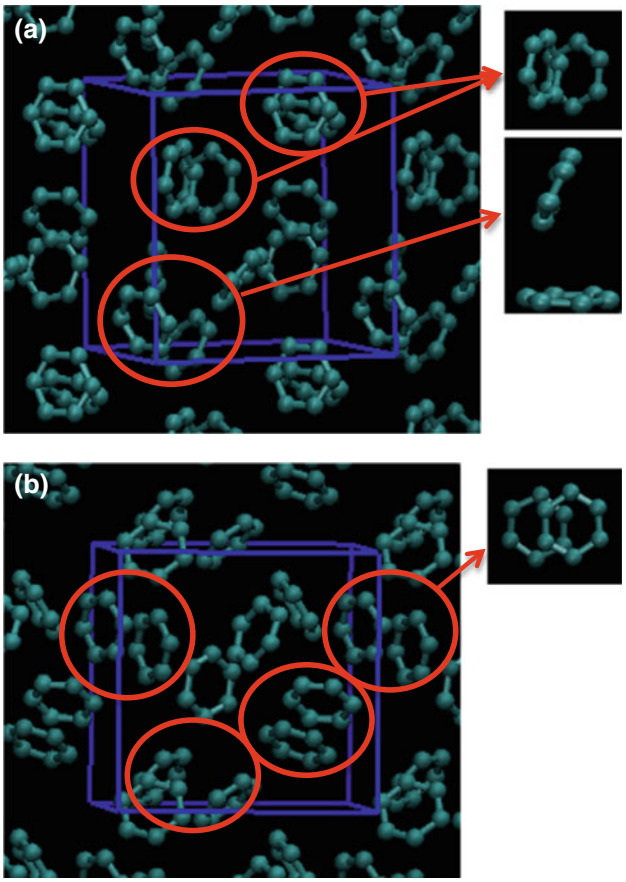

Fig. 3 **a** Perpendicular Y-shaped and distorted L-shaped ordering are the predominant geometry observed with PBE/DZP-7, PBE/SZ, PBE/OO/SZ, and PBE/OOwD2/SZ calculations. **b** Parallel displaced configuration is the predominant geometry observed with PBE/DZP and PBE/TZP calculations

for PBE/SZ), all simulations predict parallel arrangements (Fig. 4c). Profiles obtained by PBE/DZP-7, PBE/OO/SZ, and PBE/OOwD2/SZ are specifically in good agreement with Headen's findings [25]. PBE/DZP and PBE/TZP, on the other hand, show significantly higher preference for parallel displaced stacking and hence have the peak values exceeding the isotropic curve at much narrower angles ($\theta < 30°$). At larger separations within the first shell (Fig. 4e), only PBE/DZP, PBE/DZP-7, PBE/TZP, and PBE/OO/SZ show a small anisotropy toward perpendicular arrangement with the curves slightly exceeding the isotropic ones at angles $\theta > 65°$, $\theta > 85°$, $\theta > 80°$, and $\theta > 85°$, respectively. Although the number of molecules increases with increasing θ, calculated values are mainly lower than or in line with the isotropic estimates with PBE/OOwD2/SZ and PBE/SZ calculations.

Using the variationally optimized orbitals, the effect of simulation cell size on calculations was also investigated. An O(N) scheme based on a Krylov subspace method

Fig. 4 Number of benzene molecules as function of angle between ▶ aromatic planes **a** in the first coordination shell ($0 < r < 6.5$ Å for PBE/SZ and $0 < r < 7.5$ Å, for all others), **b** between $0 < r < 5$ Å ($0 < r < 4$ Å for PBE/SZ), and **d** between 5 Å $< r <$ 6 Å (4 Å $< r <$ 5 Å for PBE/SZ) are compared to the isotropic distributions within the defined region. Calculated distributions are compared with the experimental distributions reported by Headen et al. [25]. For the sake of simplicity, only the experimental isotropic distribution is given in (**a**) and (**b**), as the calculated curves are in general very similar to experimental findings. **c** Distributions of PBE/SZ given in graph **b** are enlarged for a better resolution and compared with the calculated isotropic distribution. **e** Distributions obtained for PBE/SZ, PBE/TZP, and PBE/OOwD2/SZ in graph **d** are enlarged for a better resolution and compared with the corresponding isotropic curves. The isotropic curves for PBE/OO/SZ and PBE/DZP-7 between 5 Å $< r <$ 6 Å (not shown) are overlapping with the isotropic curve of PBE/OOwD2/SZ given in (**e**). The best fit to the Headen et al. is obtained through PBE/DZP-7 and PBE/OO/SZ calculations

implemented in OpenMX [74] was used for the large system size. This scheme is ~6X faster than calculations with the O(N^3) direct diagonalization method (11 vs 68 s per MD step using 960 MPI processes with two threads per process). In addition, nearly the same C–C RDFs are obtained using both methods (Fig. 5a). We also compared $G(r)$ for a system containing 10 benzene molecules with a system of 80 benzene molecules. No significant difference in C–C RDF profiles is observed with different simulation cell size (Fig. 5b). Similarly, the first peak and the first minimum positions in COM-RDFs remain the same with large system PBE/OO/SZ (PBE/OO/SZ/80) calculations compared with small system calculations (Fig. 5c). However, a shift in the peak position by ~0.4 Å is observed with 80-benzene-molecule PBE/OOwD2/SZ simulations (PBE/OOwD2/SZ/80) compared to PBE/OOwD2/SZ calculations of 10 benzene molecules (Fig. 5c). The shift in the curve is attributed to an increase in attractive forces in the system.

Data presented so far reveal that simulations with a basis set constructed of variationally optimized numerical atomic orbitals yield radial structural properties in good general agreement with experiment and with results with larger basis sets. The detailed orientational structure of the fluid, as measured by $g(r,\theta)$, shows stronger dependence on the basis set than $G(r)$. In addition, the single zeta simulations are faster and hence computationally much cheaper. Using 120 MPI processors with two threads, computational times required for running one MD step to simulate 10 benzene molecules is 5.2, 13.7, 20.4, 32.4, 5.1, and 6.2 s with PBE/SZ, PBE/DZP, PBE/TZP, PBE/DZP-7, PBE/OO/SZ, and PBE/OOwD2/SZ, respectively. Similarly, using 960 MPI processors with two threads and employing the direct diagonalization method, the times needed to simulate one MD step of 80 benzene molecules is 346 and 68 s with PBE/DZP and PBE/OO/SZ, respectively.

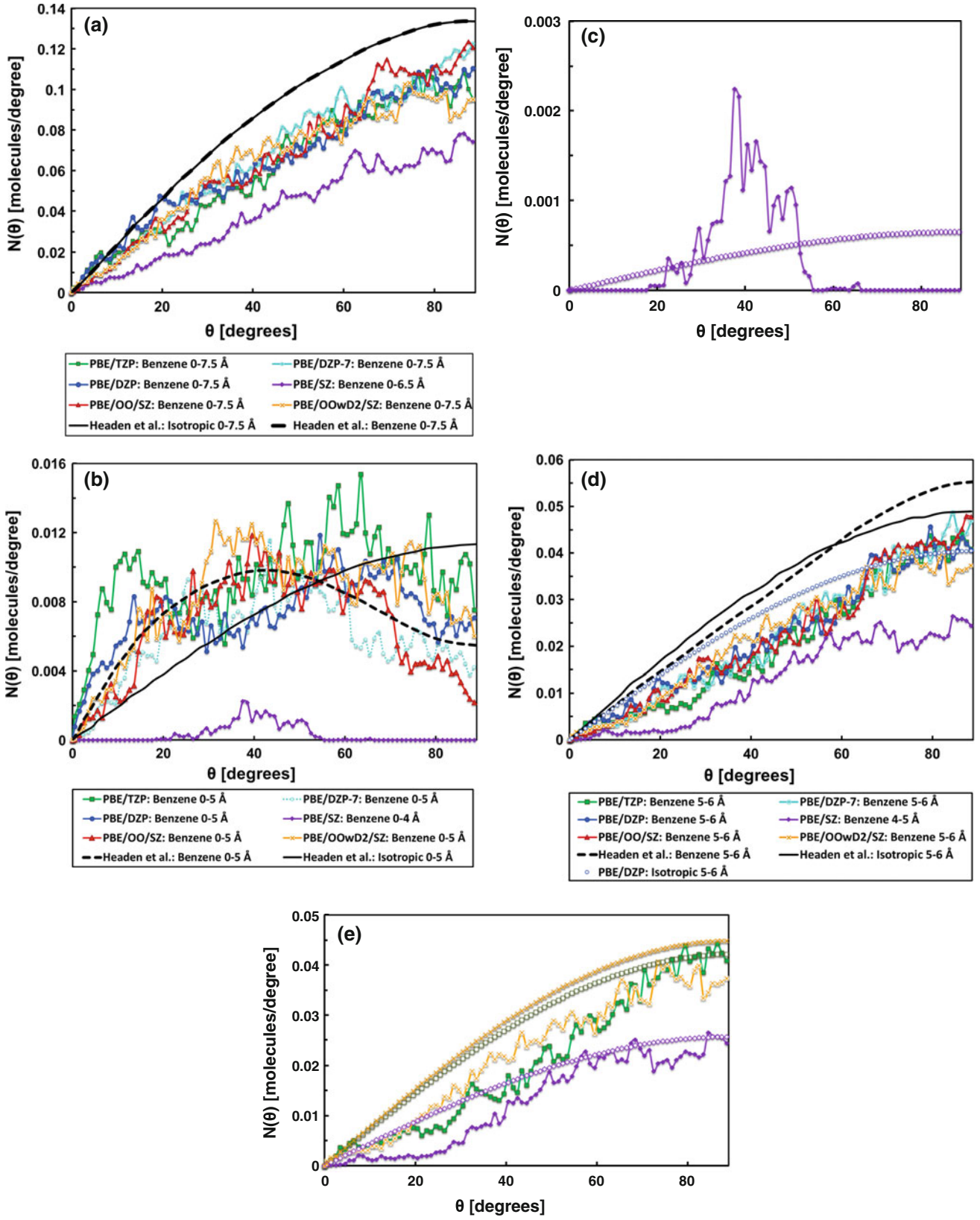
(a)
N(θ) [molecules/degree]
θ [degrees]
PBE/TZP: Benzene 0-7.5 Å
PBE/DZP-7: Benzene 0-7.5 Å
PBE/DZP: Benzene 0-7.5 Å
PBE/SZ: Benzene 0-6.5 Å
PBE/OO/SZ: Benzene 0-7.5 Å
PBE/OOwD2/SZ: Benzene 0-7.5 Å
Headen et al.: Isotropic 0-7.5 Å
Headen et al.: Benzene 0-7.5 Å
(c)
N(θ) [molecules/degree]
θ [degrees]
(b)
N(θ) [molecules/degree]
θ [degrees]
PBE/TZP: Benzene 0-5 Å
PBE/DZP-7: Benzene 0-5 Å
PBE/DZP: Benzene 0-5 Å
PBE/SZ: Benzene 0-4 Å
PBE/OO/SZ: Benzene 0-5 Å
PBE/OOwD2/SZ: Benzene 0-5 Å
Headen et al.: Benzene 0-5 Å
Headen et al.: Isotropic 0-5 Å
(d)
N(θ) [molecules/degree]
θ [degrees]
PBE/TZP: Benzene 5-6 Å
PBE/DZP-7: Benzene 5-6 Å
PBE/DZP: Benzene 5-6 Å
PBE/SZ: Benzene 4-5 Å
PBE/OO/SZ: Benzene 5-6 Å
PBE/OOwD2/SZ: Benzene 5-6 Å
Headen et al.: Benzene 5-6 Å
Headen et al.: Isotropic 5-6 Å
PBE/DZP: Isotropic 5-6 Å
(e)
N(θ) [molecules/degree]
θ [degrees]

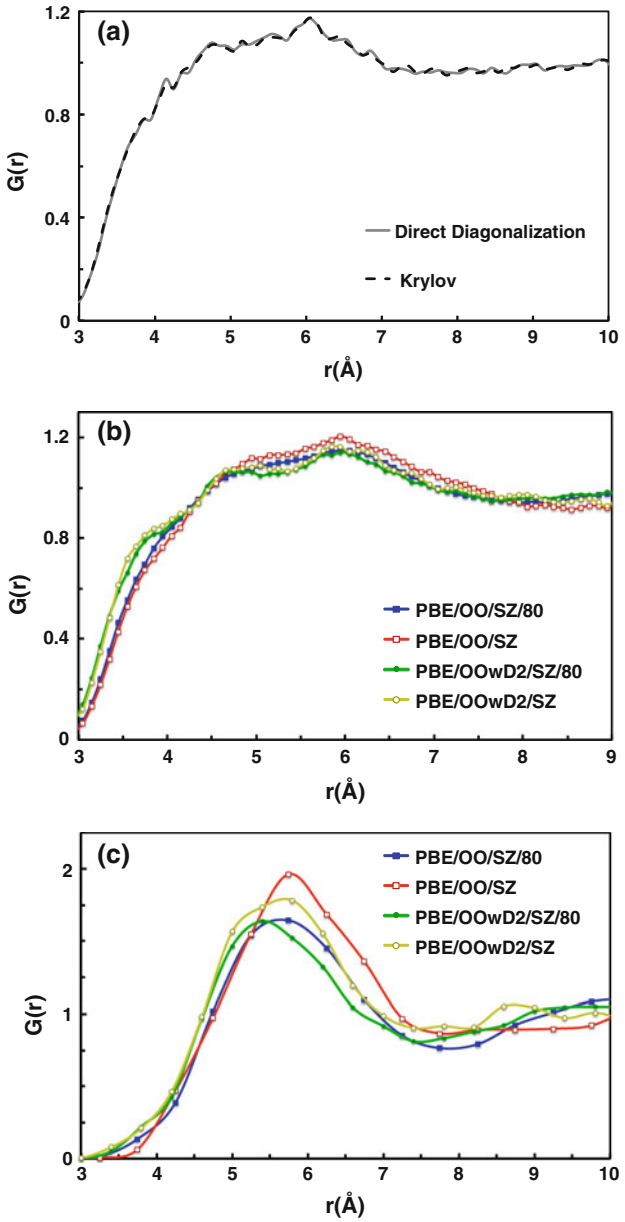

Fig. 5 **a** Comparison of the Krylov diagonalization method versus the direct diagonalization method. Intermolecular C–C pair distribution functions were obtained by 2-ps PBE/OO/SZ calculations in a system with 80 benzene molecules. **b** Intermolecular C–C pair distribution functions obtained with 80 benzene molecules versus 10 benzene molecules using variationally optimized orbitals (PBE/OO/SZ and PBE/OOwD2/SZ). **c** COM distribution functions obtained with 80 benzene molecules versus 10 benzene molecules using variationally optimized orbitals (PBE/OO/SZ and PBE/OOwD2/SZ). The COM $G(r)$ is more sensitive to system size than the C–C $G(r)$

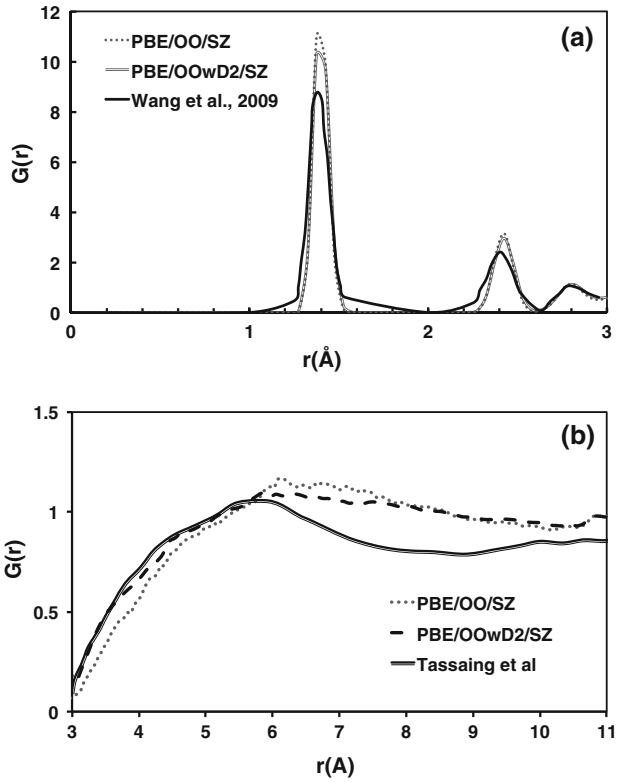

Fig. 6 Orbital optimization results in successful predictions under different conditions. **a** Intramolecular C–C pair distribution functions for benzene at 814 K and 1400 kg/m^3. Results of optimized orbital calculations are compared to the computational findings of Ref. [47]. **b** Intermolecular RDFs for supercritical benzene at 573 K and 570.2 kg/m^3. Results of optimized orbital calculations are compared to the experimental findings from Ref. [26]

It is also important to have a basis set that performs well under different environments to circumvent the need to develop several basis sets for each specific condition. Therefore, we have tested the transferability of variationally optimized orbitals at temperatures 573 K (density: 570.2 kg/m^3) and 814 K (density: 1,400 kg/m^3) and compared the results with the reported values (cf. Fig. 6). Figure 6a depicts the intramolecular C–C pair distribution functions for benzene at 814 K. Both PBE/OO/SZ and PBE/OOwD2/SZ have yielded in accurate predictions compared to Wang et al. findings where the phase transition in liquid benzene is studied by a detailed quantum MD simulation. The second peak is found to deviate <0.1 Å, whereas the first and third peaks exactly fit the first and third peak positions of Wang et al. [47]. Figure 6b, on the other hand, shows the intermolecular C–C pair RDF for supercritical benzene at 573 K. The profiles obtained by PBE/OO/SZ and PBE/OOwD2/SZ simulations are in good agreement with the calculated values by Tassaing et al. [26] especially at $r < 6$ Å. PBE/OOwD2/SZ better predicts the C–C $G(r)$ at ambient conditions (see Fig. 1b) than at supercritical conditions. The peak positions are calculated to be within 0.35 Å of Tassaing's results. Slightly higher $G(r)$ values are found at $r > 6$ Å with both cases compared to Tassaing's findings, which is attributed to the slight differences in system densities. Overall, optimized orbitals have good

transferability properties and yield in accurate results at different conditions.

4 Conclusions

First-principles MD simulations were performed to study the structure of liquid benzene. Variationally optimized numerical atomic orbitals based on the force theorem were used as a basis set in conjunction with the generic optimized orbitals. The accuracy of the simulations was compared with the recent experimental findings reported by Headen et al. based on neutron diffraction measurements. The local structure of benzene, with parallel displaced arrangements at small separations and Y-shaped geometry at larger separations, is successfully reproduced using basis sets with variationally optimized orbitals (PBE/OO/SZ and PBE/OOwD2/SZ). Among the simulations with the larger basis sets only calculations with double valence single polarization orbitals having a cutoff 7.0 a.u demonstrated matching local structure. The smaller basis set size has substantially increased the simulation speed by at least a factor of 2–6 compared to a larger basis set of generic orbitals. Yet, the accuracy is significantly improved or at least preserved compared to the accuracy of the same size or a larger basis set formed by generic orbitals, respectively. PBE/OO/SZ is found to predict the local ordering in benzene slightly better than PBE/OOwD2/SZ, while PBE/OOwD2/SZ is observed to yield in better C–C RDF profiles. The order-N Krylov technique is found to perform well for molecular liquids, with only a factor of 2 increase in the wall time per simulation step between a 120 and 960 atom system. The transferability of the variationally optimized orbitals is also explored under different environmental conditions and shown to result in accurate predictions at different conditions. Overall, DFT simulations using orbital optimization are shown to be efficient and accurate in predicting the structure of molecular liquid benzene. Further studies will assess the applicability of simulation methodology employed here, using order-N DFT methods and compact optimized basis functions, to the study of condensed phase chemical reactivity.

Acknowledgments This work was performed under the auspices of the U.S. Department of Energy by Lawrence Livermore National Laboratory under Contract DE-AC52-07NA27344. Laurence E. Fried thanks Prof. Gregory S. Ezra for his patient encouragement and guidance at Cornell University.

References

1. Vallee R et al (2000) Nonlinear optical properties and crystalline orientation of 2-methyl-4-nitroaniline layers grown on nanostructured poly(tetrafluoroethylene) substrates. J Am Chem Soc 122(28):6701–6709
2. Meyer EA, Castellano RK, Diederich F (2003) Interactions with aromatic rings in chemical and biological recognition. Angew Chem Int Ed 42(11):1210–1250
3. Baker CM, Grant GH (2007) Role of aromatic amino acids in protein–nucleic acid recognition. Biopolymers 85(5–6):456–470
4. Hunter CA (1993) Aromatic interactions in proteins, DNA and synthetic receptors. Philos Trans R Soc Mathe Phys Eng Sci 345(1674):77–85
5. Cox EG, Smith JAS (1954) Crystal structure of benzene at-3-degrees-C. Nature 173(4393):75
6. Cox EG, Cruickshank DWJ, Smith JAS (1955) Crystal structure of benzene—new type of systematic error in precision X-ray crystal analysis. Nature 175(4461):766
7. Cox EG, Cruickshank DWJ, Smith JAS (1958) The crystal structure of benzene at-3-degrees-C. Proc R Soc Lond Ser Mathe Phys Sci 247(1248):1–21
8. Janda KC et al (1975) Benzene dimer—polar molecule. J Chem Phys 63(4):1419–1421
9. Steed JM, Dixon TA, Klemperer W (1979) Molecular-beam studies of benzene dimer, hexafluorobenzene dimer and benzene–hexafluorobenzene. J Chem Phys 70(11):4940–4946
10. Hopkins JB, Powers DE, Smalley RE (1981) Mass-selective 2-color photo-ionization of benzene clusters. J Phys Chem 85(25):3739–3742
11. Langridgesmith PRR et al (1981) Ultraviolet-spectra of benzene clusters. J Phys Chem 85(25):3742–3746
12. Venturo VA, Felker PM (1993) Intermolecular Raman bands in the ground-state of benzene dimer. J Chem Phys 99(1):748–751
13. Hobza P, Selzle HL, Schlag EW (1996) Potential energy surface for the benzene dimer. Results of ab initio CCSD(T) calculations show two nearly isoenergetic structures: T-shaped and parallel-displaced. J Phys Chem 100(48):18790–18794
14. Sato T, Tsuneda T, Hirao K (2005) A density-functional study on pi-aromatic interaction: benzene dimer and naphthalene dimer. J Chem Phys 123(10):104307
15. Sinnokrot MO, Sherrill CD (2006) High-accuracy quantum mechanical studies of pi–pi interactions in benzene dimers. J Phys Chem A 110(37):10656–10668
16. van der Avoird A et al (2010) Vibration–rotation–tunneling states of the benzene dimer: an ab initio study. Phys Chem Chem Phys 12(29):8219–8240
17. Henson BF et al (1992) Raman-vibronic double-resonance spectroscopy of benzene dimer isotopomers. J Chem Phys 97(4):2189–2208
18. Erlekam U et al (2006) An experimental value for the B-1u C–H stretch mode in benzene. J Chem Phys 124(17):171101
19. Tsuzuki S et al (2005) Ab initio calculations of structures and interaction energies of toluene dimers including CCSD(T) level electron correlation correction. J Chem Phys 122(14):144323
20. Lowden LJ, Chandler D (1974) Theory of intermolecular pair correlations for molecular liquids—applications to liquids carbon-tetrachloride, carbon-disulfide, carbon diselenide, and benzene. J Chem Phys 61(12):5228–5241
21. Narten AH (1968) Diffraction pattern and structure of liquid benzene. J Chem Phys 48(4):1630–1634
22. Narten AH (1977) X-ray-diffraction pattern and models of liquid benzene. J Chem Phys 67(5):2102–2108
23. Katayama M et al (2010) Liquid structure of benzene and its derivatives as studied by means of X-ray scattering. Phys Chem Liq 48(6):797–809
24. Bartsch E et al (1985) A neutron and X-ray-diffraction study of the binary-liquid aromatic system benzene-hexafluorobenzene.1. The pure components. Ber Bunsen Ges Phys Chem Chem Phys 89(2):147–156

25. Headen TF et al (2010) Structure of pi–pi interactions in aromatic liquids. J Am Chem Soc 132(16):5735–5742
26. Tassaing T et al (2000) The structure of liquid and supercritical benzene as studied by neutron diffraction and molecular dynamics. J Chem Phys 113(9):3757–3765
27. Misawa M, Fukunaga T (1990) Structure of liquid benzene and naphthalene studied by pulsed neutron total scattering. J Chem Phys 93(5):3495–3502
28. Fu C-F, Tian SX (2011) A comparative study for molecular dynamics simulations of liquid benzene. J Chem Theory Comput 7(7):2240–2252
29. Bogdan TV (2006) Atom-atomic potentials and the correlation distribution functions for modeling liquid benzene by the molecular dynamics methods. Russ J Phys Chem 80:S14–S20
30. Chelli R et al (2001) The fast dynamics of benzene in the liquid phase—Part II. A molecular dynamics simulation. Phys Chem Chem Phys 3(14):2803–2810
31. Baker CM, Grant GH (2006) The structure of liquid benzene. J Chem Theory Comput 2(4):947–955
32. Coutinho K, Canuto S, Zerner MC (1997) Calculation of the absorption spectrum of benzene in condensed phase. A study of the solvent effects. Int J Quantum Chem 65(5):885–891
33. Jorgensen WL et al (1993) Monte-Carlo simulations of pure liquid substituted benzenes with OPLS potential functions. J Comput Chem 14(2):206–215
34. Cabaco MI et al (1997) Neutron diffraction and molecular dynamics study of liquid benzene and its fluorinated derivatives as a function of temperature. J Phys Chem B 101(35):6977–6987
35. Hunter CA, Sanders JKM (1990) The nature of pi–pi interactions. J Am Chem Soc 112(14):5525–5534
36. Righini R (1993) Ultrafast optical kerr-effect in liquids and solids. Science 262(5138):1386–1390
37. Zorkii PM, Lanshina LV, Bogdan TV (2008) Computer simulation and diffraction studies of the structure of liquid benzene. J Struct Chem 49(3):524–547
38. Forsman J, Woodward CE, Trulsson M (2011) A classical density functional theory of ionic liquids. J Phys Chem B 115(16):4606–4612
39. Song Z, Wang H, Xing L (2009) Density functional theory study of the ionic liquid [emim]OH and complexes [emim]OH(H2O) n (n = 1,2). J Solut Chem 38(9):1139–1154
40. Umebayashi Y et al (2009) Raman spectroscopic study, DFT calculations and MD simulations on the conformational isomerism of N-Alkyl-N-methylpyrrolidinium Bis-(trifluoromethanesulfonyl) amide ionic liquids. J Phys Chem B 113(13):4338–4346
41. Waller MP et al (2006) Hybrid density functional theory for pi-stacking interactions: application to benzenes, pyridines, and DNA bases. J Comput Chem 27(4):491–504
42. Yan Z, Truhlar DG (2005) How well can new-generation density functional methods describe stacking interactions in biological systems? Phys Chem Chem Phys 7(14):2701–2705
43. Tachikawa H (2013) Double pi-pi stacking dynamics of benzene trimer cation: direct ab initio molecular dynamics (AIMD) study. Theor Chem Acc 132(7):1374
44. Sherrill CD, Takatani T, Hohenstein EG (2009) An assessment of theoretical methods for nonbonded interactions: comparison to complete basis set limit coupled-cluster potential energy curves for the benzene dimer, the methane dimer, benzene-methane, and benzene-H2S. J Phys Chem A 113(38):10146–10159
45. Pitonak M et al (2008) Benzene dimer: high-level wave function and density functional theory calculations. J Chem Theory Comput 4(11):1829–1834
46. Wen X-D, Hoffmann R, Ashcroft NW (2011) Benzene under high pressure: a story of molecular crystals transforming to saturated networks, with a possible intermediate metallic phase. J Am Chem Soc 133(23):9023–9035
47. Wang C, Zhang P (2010) The equation of state and nonmetal–metal transition of benzene under shock compression. J Appl Phys 107(8):083502
48. Goldman N et al (2005) Bonding in the superionic phase of water. Phys Rev Lett 94(21):217801
49. Schwegler E et al (2008) Melting of ice under pressure. Proc Natl Acad Sci U S A 105(39):14779–14783
50. Ozaki T (2003) Variationally optimized atomic orbitals for large-scale electronic structures. Phys Rev B 67(15):155108
51. Ozaki T, Kino H (2004) Numerical atomic basis orbitals from H to Kr. Phys Rev B 69(19):195113
52. Junquera J et al (2001) Numerical atomic orbitals for linear-scaling calculations. Phys Rev B 64(23):235111
53. Corsetti F et al (2013) Optimal finite-range atomic basis sets for liquid water and ice. J Phys: Condens Matter 25(43):435504
54. Ozaki T, Kino H (2004) Variationally optimized basis orbitals for biological molecules. J Chem Phys 121(22):10879–10888
55. Ohwaki T et al (2012) Large-scale first-principles molecular dynamics for electrochemical systems with O(N) methods. J Chem Phys 136(13):134101
56. Jorgensen WL, Tiradorives J (1988) The OPLS potential functions for proteins—energy minimizations for crystals of cyclic-peptides and crambin. J Am Chem Soc 110(6):1657–1666
57. Jorgensen WL, Severance DL (1990) Aromatic aromatic interactions—free-energy profiles for the benzene dimer in water, chloroform, and liquid benzene. J Am Chem Soc 112(12):4768–4774
58. Van der Spoel D et al (2005) GROMACS: fast, flexible, and free. J Comput Chem 26(16):1701–1718
59. Hess B (2009) GROMACS 4: algorithms for highly efficient, load-balanced, and scalable molecular simulation. Abstracts of Papers of the American Chemical Society 237
60. NISTChemistryWebBook. http://webbook.nist.gov/chemistry
61. Nose S (1984) A molecular-dynamics method for simulations in the canonical ensemble. Mol Phys 52(2):255–268
62. Hoover WG (1985) Canonical dynamics—equilibrium phase-space distributions. Phys Rev A 31(3):1695–1697
63. Parrinello M, Rahman A (1981) Polymorphic transitions in single-crystals—a new molecular-dynamics method. J Appl Phys 52(12):7182–7190
64. Nose S, Klein ML (1983) Constant pressure molecular-dynamics for molecular-systems. Mol Phys 50(5):1055–1076
65. Hess B et al (1997) LINCS: a linear constraint solver for molecular simulations. J Comput Chem 18(12):1463–1472
66. Hess B (2008) P-LINCS: a parallel linear constraint solver for molecular simulation. J Chem Theory Comput 4(1):116–122
67. Ozaki T, Kino H (2005) Efficient projector expansion for the ab initio LCAO method. Phys Rev B 72(4):045121
68. OpenMX. http://www.openmx-square.org/
69. Hohenberg P, Kohn W (1964) Inhomogeneous electron gas. Phys Rev B 136(3B):B864
70. Perdew JP, Burke K, Ernzerhof M (1996) Generalized gradient approximation made simple. Phys Rev Lett 77(18):3865–3868
71. Morrison I, Bylander DM, Kleinman L (1993) Nonlocal hermitian norm-conserving vanderbilt pseudopotential. Phys Rev B 47(11):6728–6731
72. Grimme S (2006) Semiempirical GGA-type density functional constructed with a long-range dispersion correction. J Comput Chem 27(15):1787–1799
73. Soler JM et al (2002) The SIESTA method for ab initio order-N materials simulation. J Phys: Condens Matter 14(11):2745–2779
74. Ozaki T (2006) O(N) Krylov-subspace method for large-scale ab initio electronic structure calculations. Physical Review B 74(24):245101

75. Woodcock LV (1971) Isothermal molecular dynamics calculations for liquid salts. Chem Phys Lett 10(3):257–261
76. Nose S (1984) A unified formulation of the constant temperature molecular-dynamics methods. J Chem Phys 81(1):511–519
77. Takeuchi H (2012) Structural features of small benzene clusters (C6H6)(n) (n <= 30) as investigated with the All-Atom OPLS potential. J Phys Chem A 116(41):10172–10181

Theor Chem Acc (2014) 133:1525
DOI 10.1007/s00214-014-1525-2

REGULAR ARTICLE

Effect of a chiral electrostatic cavity on product selection in a reaction with a bifurcating reaction path

Barry K. Carpenter

Received: 9 April 2014 / Accepted: 19 June 2014 / Published online: 2 July 2014

Abstract The possibility of influencing the selection of product-forming branches in a reaction with a bifurcating reaction path is explored. The reaction chosen is a substituted version of the well-known ring opening of singlet cyclopropanylidene. The substituents are arranged such that the starting carbene is meso (i.e., achiral) but the products are enantiomeric allenes. The question being posed is whether optical activity can be induced in the products by choosing the reaction to occur within a chirally disposed set of point charges. Direct-dynamics trajectory calculations are used to address the problem. It is found that, on a microscopic level, the point charges have a very significant effect on the choice of bifurcation branch. However, when the individual microscopic effects are averaged, to take account of free rotation of the molecule with respect to the charge array, the net effect is small (about 3 % enantiomeric excess after 500 fs). Nevertheless, even this small effect is larger than one might have predicted on the basis of an earlier analysis of electrostatic contributions to the interactions between chiral molecules. The reason is that the present simulation involves a concentric arrangement of chiral, polar objects, whereas the earlier analysis considered only a side-by-side arrangement. Through the use of numerical simulation, it is shown that two freely rotating arrays of chiral point charges exhibit larger diastereomeric discrimination when the arrays are concentric than when they are not, even for comparable average distances between the charges.

Keywords Direct dynamics · Optical activity induction · Reaction path bifurcation

1 Introduction

It has been known for several decades that certain reactions lack unique intrinsic reaction coordinates (IRCs), i.e., steepest-descent paths in mass-weighted coordinates, because, in each case, the path bifurcates on the "downhill" slope after a rate-determining transition state [1]. If the bifurcation branches lead to symmetry-related minima, then the branching occurs at a so-called valley-ridge inflection (VRI) point [2]. A related phenomenon can occur on surfaces with product minima of unequal energy. In these cases, a unique IRC can be defined—leading to one of the two products—but the other minimum may nevertheless be accessible along a path that leads monotonically downhill from the rate-determining transition state [3]. From the point of view of reaction dynamics, the symmetrical case with the true IRC bifurcation is not qualitatively different from the unsymmetrical one, and so for the purposes of the present discussion, the two cases are combined and characterized as potential energy surfaces with reaction-path bifurcation.

In recent years, a vast number of reactions exhibiting path bifurcation have been identified [3–12]. They encompass a wide range of chemical and biochemical transformations, including some of the classical "named" reactions of organic chemistry [13–16]. Despite their frequent occurrence, the factors that control the branching ratio to the two products in these reactions are very poorly understood. For one interesting case of experimental study and theoretical analysis, see [17].

A recent investigation of a simple two degree-of-freedom model for a potential energy surface with a bifurcating

Dedicated to Professor Greg Ezra and published as part of the special collection of articles celebrating his 60th birthday.

B. K. Carpenter (✉)
School of Chemistry, Cardiff University, Cardiff CF10 3AT, UK
e-mail: carpenterb1@cardiff.ac.uk

reaction path has shown that there can be extreme sensitivity of the outcome to very small changes in parameters [18]. First, the IRC might lead to the deeper or the shallower of the two product minima, and the switch from one to the other can be caused by tiny changes in relative position of the stationary points, even when their relative energies are kept constant. Second, trajectory calculations reveal that the product ratio can show an extreme and nonmonotonic dependence on the efficiency with which kinetic energy is dissipated during the trajectory transit. This dissipation represents a simple model for solvent–solute energy exchange in a liquid-phase reaction, and so the discovery implies the possibility of very large changes in product ratio for relatively modest changes in solvent properties [18].

More generally, the picture that emerges is that reactions with bifurcating reaction paths may exhibit hypersensitivity to a variety of external perturbations. Although such hypersensitivity would potentially present a problem for prediction of reaction outcomes, it might also represent an opportunity for unusual control of the reaction through relatively modest variation of conditions. It is this latter feature that is investigated in the present paper. Specifically, the question of optical activity induction through the use of external electric fields is explored by way of direct-dynamics trajectory simulation.

2 Computational details

All electronic structure calculations reported in this paper used the B3LYP hybrid density functional [19] (for the particular implementations of B3LYP used by different electronic structure programs, see [20]) with a 6/31G(d) basis set [21]. Propagation of the trajectories was accomplished by direct dynamics, using broken-symmetry unrestricted Kohn–Sham orbitals. These were employed because some trajectories were found to enter regions of the potential energy surface near a seam of intersection with an upper surface, and in these regions, some means of handling nondynamic electron correlation was necessary [22].

Quasiclassical trajectories were initiated by normal-mode sampling from a canonical ensemble at 298 K, in the vicinity of the ring-opening transition state. Rotations were treated classically. A given trajectory was run with a randomly rotated (*R*) configuration of point charges. The point charges had values of 0.2, −0.4, 0.8, and −0.6 in units of the absolute charge on the electron. They were tetrahedrally arranged on the surface of a sphere of radius 5 Å about the molecular center of mass. The point charges were kept fixed with respect to the laboratory frame during each trajectory, but the molecule was allowed to rotate within the charged cavity. Exactly the same set of initial conditions (geometry and initial momenta of the atoms) was then rerun, but with the Cartesian coordinates of the point charges being inverted, to give the (*S*) configuration. A total of 3,200 trajectories (1,600 pairs) were run. All calculations were carried out with the Gaussian 09 suite of programs [23].

3 Results and discussion

The reaction chosen for study was a variant of the classic case of IRC bifurcation first studied by Ruedenberg and coworkers—the ring opening of a singlet-state cyclopropanylidene [4]. The variation employed for the present study was that fluoro and methyl substituents replaced the hydrogen atoms of the prototype. The substituents were arranged in a meso configuration, as shown in Fig. 1, thereby defining the carbene to be achiral.

The ring opening of singlet cyclopropanylidenes initially follows a disrotatory path, maintaining C_s symmetry. This stereochemistry is easily understood because, to a first approximation, the divalent carbon has a lone-pair in the plane of the ring, and an empty 2*p* orbital perpendicular to the plane. The latter feature makes the carbene electronically akin to a cyclopropyl cation, for which the Woodward–Hoffmann rules predict disrotatory ring opening [24]. However, for the carbene, the disrotatory stereochemistry cannot proceed all the way to the products, because that would lead to allenes in which all four of the substituents were in the same plane. In order to reach the equilibrium allene geometry (D_{2d} in the parent case, but C_2 in this substituted example), the reaction path has to bifurcate. For the reaction considered here, bifurcation branches lead to opposite enantiomers of the product allene. The question addressed in the present calculations is whether introduction of a chiral electric field, accomplished with four point charges of unequal magnitude, can cause one of the two enantiomers to be favored in the reaction—i.e., whether optical activity can be induced in the product through the agency of the electric field. The chosen point-charge model for the field could be considered to represent the electrostatic component of the carbene's interaction with a chiral solvent.

An important paper by Craig and Schipper on the electrostatic contribution to interactions between chiral molecules would appear at first sight not to offer much encouragement for this project [25]. These authors show that: "Electrostatic discrimination in the freely rotating systems has a leading term in the inverse seventeenth power of the separation and can be disregarded." However, closer reading of their analysis reveals two reasons for retaining some hope of success. First, Craig and Schipper considered two limiting cases in their analysis: A freely rotating case in

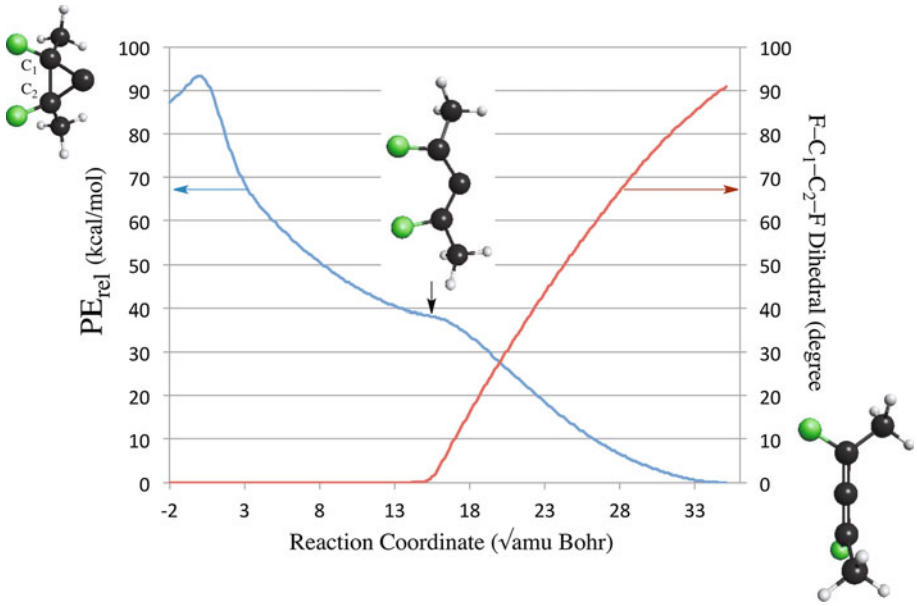

Fig. 1 One branch of the bifurcating intrinsic reaction coordinate for the ring opening of singlet meso-difluorodimethylcyclopropanylidene. The *blue line* plots the potential energy and the *red line* tracks the $F–C_1–C_2–F$ dihedral angle. The bifurcation occurs near the point where the dihedral angle ceases to be zero. Calculations were carried out using a B3LYP/6-31G(d) electronic structure model

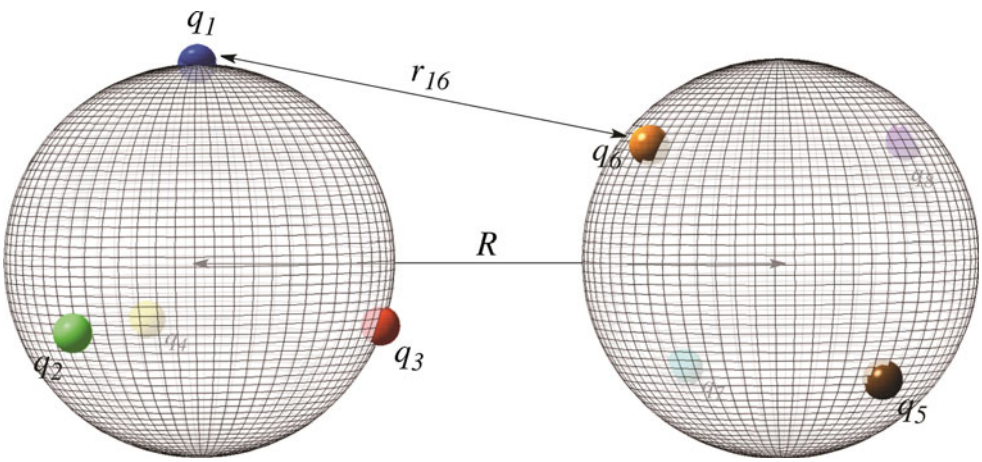

Fig. 2 Side-by-side arrangement of tetrahedral point-charge arrays considered in Model 1, as described in the text

which the total interaction between the chiral molecules was $\ll kT$ and a "locked-up" case in which the interaction energy was $\gg kT$ [25]. Their conclusion about the negligible contribution from electrostatics applied only to the former. However, one might wonder whether the conditions required for their freely rotating case would commonly be met by real polar, chiral molecules. For example, one may note that two point charges of only ± 0.1 times the electron charge at a distance of 3.5 Å in a vacuum would have an interaction energy of 1.6 kT at 298 K. Typical point-charge equivalents in real polar molecules are often substantially larger than ± 0.1, and approach of the molecules to within 3.5 Å is fully compatible with the van der Waals radii of common elements [26]. The second reason for hope is that Craig and Schipper did not investigate the arrangement of point charges most relevant to the present problem, namely that of two concentric spheres of different radius. The inner sphere might represent a chiral solute molecule and the outer sphere the chiral solvent cavity in which it resides.

In order to address these two issues, simple numerical models have been employed. In both cases, one considers the interaction of two point-charge arrays on spheres of varying radius or separation. For each sphere, there are four point charges of unequal magnitude, summing to zero. The point charges on each sphere maintain a fixed tetrahedral arrangement, but one sphere is free to rotate with respect to the other. In Model 1, which is the closer analogy to the Craig and Schipper analysis, the spheres have fixed radii of 1 Å but varying separation, R (Fig. 2).

In Model 2, the spheres are concentric, with the inner one maintaining the radius of 1 Å but the outer one now having a variable radius (Fig. 3).

In each case, the question to be addressed is whether there is a detectable Coulombic energy difference between charge arrays of different relative chirality when each is

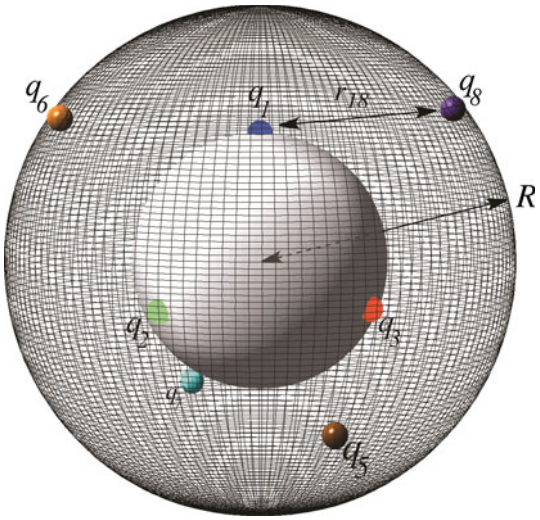

Fig. 3 Concentric arrangement of tetrahedral point-charge arrays considered in Model 2, as described in the text

allowed to explore all possible rotational orientations with respect to the other.

For both models, one can write as follows:

$$\langle V\rangle = \frac{\int_{-\pi}^{\pi}\int_{-\pi/2}^{\pi/2}\int_{-\pi}^{\pi} V\alpha\beta\gamma e^{\frac{V_{\alpha\beta\gamma}}{kT}}\mathrm{d}\alpha\mathrm{d}\beta\mathrm{d}\gamma}{\int_{-\pi}^{\pi}\int_{-\pi/2}^{\pi/2}\int_{-\pi}^{\pi} e^{\frac{V_{\alpha\beta\gamma}}{kT}}\mathrm{d}\alpha\mathrm{d}\beta\mathrm{d}\gamma}$$

$$V_{\alpha\beta\gamma} = \sum_{i=1}^{4}\sum_{j=5}^{8}\frac{q_i q_j}{r_{ij}(\alpha,\beta,\gamma)}$$

Here, $\langle V\rangle$ is the average total potential energy at a given value of R, $q_1 - q_4$ are the values of the point charges on sphere 1, and $q_5 - q_8$ are the values of the point charges on sphere 2; α, β, and γ are the Euler angles for intrinsic rotation of sphere 2 with respect to sphere 1. The Boltzmann weighting of the individual $V_{\alpha\beta\gamma}$ terms obviates the need to consider separate free-rotation and locked-up extremes, because at small R a few $|V_{\alpha\beta\gamma}|$ will be $\gg kT$, and for the attractive interactions, those orientations will be given high weighting factors. By contrast, at large R where all $|V_{\alpha\beta\gamma}| \ll kT$, all orientations will be given roughly equal weights.

The charges on sphere 1 were chosen to be $q_1 = 0.05$, $q_2 = -0.1$, $q_3 = 0.2$, $q_4 = -0.15$ and for sphere 2 $q_5 = 0.1$, $q_6 = -0.2$, $q_7 = 0.4$, $q_8 = -0.3$, all in units of the absolute value of the charge on the electron. The expression for $\langle V\rangle$ was evaluated by Monte Carlo integration, using a temperature of 298 K for the Boltzmann weightings. If one assigns Cahn–Ingold–Prelog priorities [27] according to the absolute magnitudes of the point charges, then the interaction potentials for the charge arrays depicted in Figs. 2 and 3 could be classified as V_{RR}. In order to calculate V_{RS}, the Cartesian coordinates of the point charges on sphere 2 were inverted and the integral recomputed. The difference between these two quantities defines the chiral discrimination energy, which was evaluated as a function of the distance R between 2.01 and 15 Å for the two models (The lower limit was set to 2.01 Å to avoid the infinities that can obviously occur for model 1 at $R = 2$ Å). The results are displayed in Fig. 4.

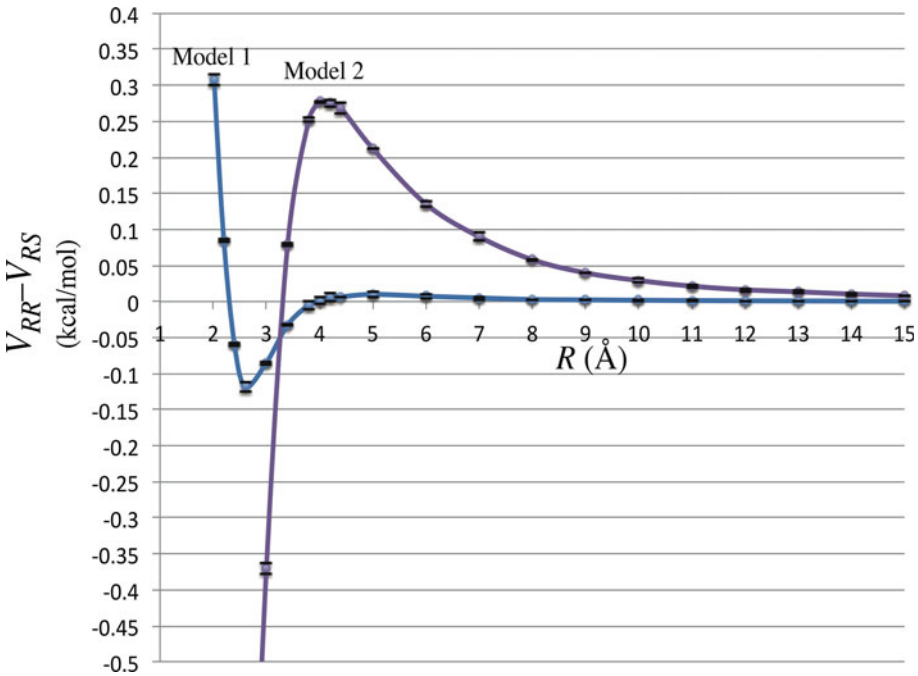

Fig. 4 Diastereomeric differences in interaction energy for chiral tetrahedral arrays of point charges as a function of distance and arrangement (side-by-side in Model 1 and concentric in Model 2). *Horizontal bars* above and below each point represent standard errors from the Monte Carlo integration

Interestingly, the quantity V_{RR}–V_{RS} changes sign as a function of distance for both models. Of more importance for the present purposes, however, is the fact that the chiral discrimination drops to near zero in model 1, beyond about 4 Å, which is the distance at which the Boltzmann-weighted average interaction energy between the spheres has a value ~kT. This is simply a numerical demonstration of the Craig and Schipper result [25].

By contrast, in model 2, one sees a much slower drop off of the chiral discrimination with distance. In this model, the average interaction energy between the spheres has a value of kT at ~7.5 Å. From this model, it seems plausible that the electrostatic interaction of a chiral, polar molecule with a chiral, polar solvent could be larger than one might have anticipated from just pairwise interaction between chiral molecules in the manner analyzed by Craig and Schipper.

The next step was to evaluate the role of a chiral cavity of point charges, akin to model 2 above, on the product selection in the ring opening of meso-difluorodimethylcyclopropanylidene. As discussed below, it was recognized to be important to get as close as possible to convergence for the trajectory calculations, but that took a good deal of computational effort (~10^5 processor hours in the present example). Because convergence is reached faster for larger charge effects, the point charges were given values of 0.2, −0.4, 0.8, and −0.6 times the absolute value of the charge on the electron. They were tetrahedrally arranged on the surface of a sphere of fixed radius 5 Å, about the center of mass of the carbene. This choice of origin ensured that the molecule could not escape the sphere at any time during a trajectory.

The thermodynamic effect of the chiral charged cavity on the product allenes was evaluated by carrying out B3LYP/6-31G(d) single-point energy evaluations for each enantiomer of the allene within each enantiomer of the chiral charge arrangement at randomly chosen relative rotations. Again, the average energy was evaluated by Boltzmann weighting the individual orientations at 298 K. The result is shown in Fig. 5. For simplicity, the labels on the lines refer only to the (*R*) enantiomer of the allene, although the calculations actually included both enantiomers. The outcome of the calculations was a predicted thermodynamic preference of 0.84 ± 0.03 kcal/mol for the (*R*) allene to be in the (*R*) charged cavity at 298 K.

Attention was now turned to evaluation of the chiral charge effect on the trajectories for ring opening of the carbene. Several decisions had to be made about these calculations. The first was whether to include the charge interactions in the sampling of initial states. One could argue that it would be a more realistic simulation of a reaction in a chiral solvent to do so, but in the end the decision was made to impose the chiral charge effects only after the reactive trajectories had started. The reasoning was that

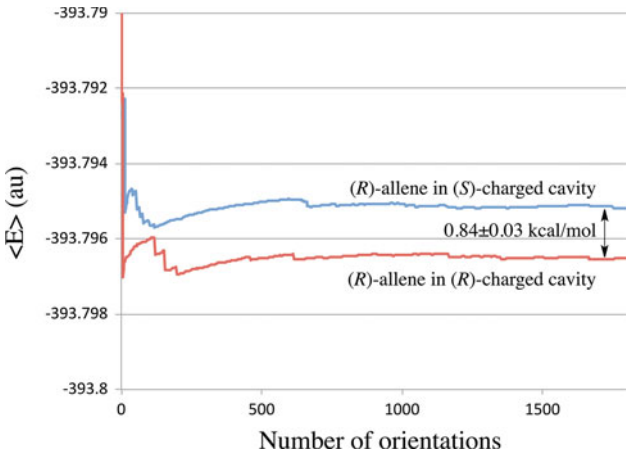

Fig. 5 Boltzmann-weighted running average of energies for the two enantiomers of a chiral charge array surrounding one enantiomer of a chiral, polar allene, as a function of the number of relative rotational orientations sampled

the purpose of the study was not to create a realistic model for a chiral solvent, but rather to investigate the influence of one component of such a medium on one aspect of the reaction—namely its ability to influence the choice of path near the VRI. Inclusion of the chiral charges in the selection of initial conditions would have convoluted a second effect into the one of principal interest and thereby complicated the analysis of the final outcome. Calculations already under way, involving explicit chiral solvent molecules, will include the effect on selection of initial conditions.

The second necessary decision concerned the duration of each trajectory. In the absence of any means to dissipate kinetic energy, the trajectories would obviously afford the products in the thermodynamic ratio if run for an infinite length of time. That is clearly neither interesting nor practical. In the end, the selection of the termination time, 500 fs, was a largely a pragmatic one, mandated by the computational effort of the project. In order to assess any time dependence of the results, the effect after 500 fs was compared with that when the trajectories first encountered a product well (defined as having a F–C_1–C_2–F dihedral angle of ±90°), which occurred, on average, at ~150 fs.

A total of 1,600 trajectory pairs (see Sect. 2) were run. The results are summarized in Fig. 6.

The average enantiomeric excess plotted in Fig. 6 is calculated as the quantity $(N_{RR} + N_{SS} - N_{RS} - N_{SR})/(N_{RR} + N_{SS} + N_{RS} + N_{SR})$, where N counts the number of trajectories of a particular class, the first subscript specifies the chirality of the allene formed and the second specifies the chirality of the point-charge array. Although it is apparent that complete convergence of the results would require an even larger set of trajectories than considered in the

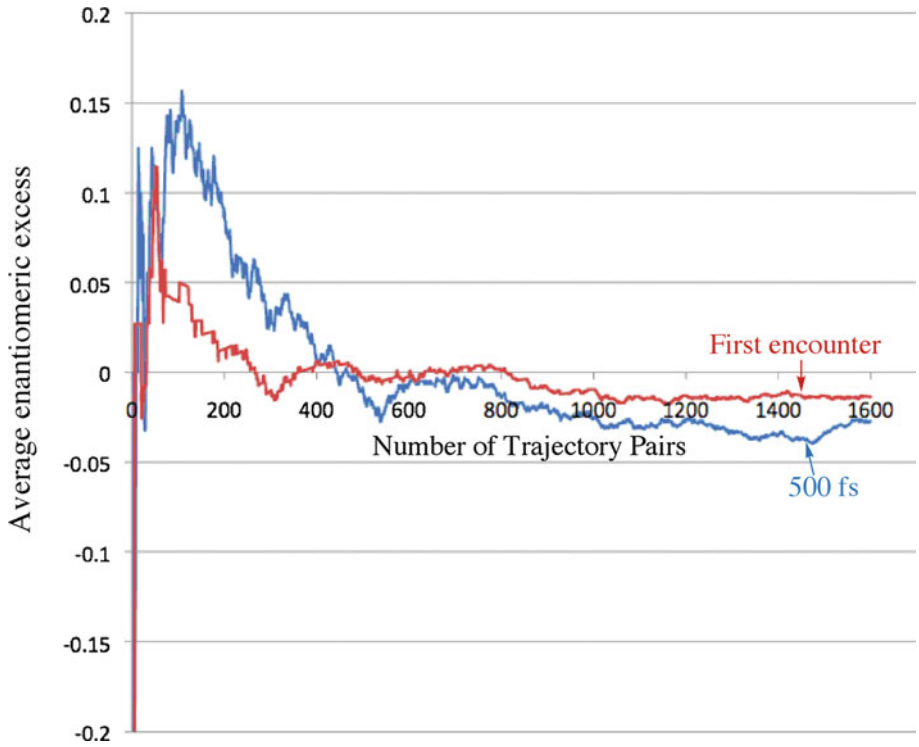

Fig. 6 Running average of enantiomeric excess (see text for definition) as a function of the number of trajectory pairs computed

present work, it seems safe to make the qualitative conclusions outlined below.

The first obvious conclusion is that the effect is small. At 500 fs, one sees an enantiomeric excess of about 3 %, and upon first encounter of a trajectory with a product minimum, it is only about half that. These are substantially smaller numbers than the expected value at equilibrium. If one assumes that the free energy difference between the favored [i.e., (*R*) allene in (*R*) charged cavity or (*S*) allene in (*S*) cavity] and disfavored (the alternative pairs) combinations is equal to the energy difference reported in Fig. 5, then the equilibrium enantiomeric excess at 298 K should be 61 %. Given that the enantiomeric excess appears to increase with time, and that the increase is in the direction favored at equilibrium, one can conclude that the principal effect of the point charge arrays considered in this simulation is thermodynamic. As the trajectories cross from one product well to the other, they tend to stay with higher probability in the well of lower energy. The overall effect on the initial selection of those wells is very small, at least for the particular system studied here. In a system where energy was being lost to the bath, there would come a time when there was no longer sufficient energy to cross from one product well to the other. Whether that occurred prior to equilibrium would be a very system-specific issue, but in general it seems likely that the final enantiomeric excess for the product allenes would be in the same direction as that favored at equilibrium, but possibly smaller in absolute magnitude.

The small average effect of the point charges seen in the present work masks a much larger microscopic effect between trajectory pairs. For pairs of trajectories with identical initial geometries and momenta assigned to the atoms, 18.2 % exhibited a dependence of the first-selected product on the chirality of the charge array, and at 500 fs, the chiral discrimination rose to 42.1 %. Trajectories that exhibited chiral discrimination upon first encounter with a product well typically separated from each other almost from the outset, as illustrated in Fig. 7a. They showed paths that were close to mirror images of each other. By contrast, trajectories experiencing the chiral discrimination later on in the time evolution typically started out on very similar paths, but then separated and followed non-mirror image paths. This is illustrated in Fig. 7b.

This behavior can be understood by considering the relative magnitudes of internal and external forces acting on the atoms. If a trajectory were started exactly at the stationary point for the ring-opening transition state, and with no initial momenta assigned to the atoms, then only external forces due to the charges would be acting on the atoms at the beginning of the trajectory. Since the molecular geometry at the stationary point is achiral, the enantiomeric charge arrays would necessarily impose enantiomeric sets of forces, leading to mirror image trajectories. In the opposite limit, where there were no external forces but there were initial momenta applied to the atoms, the two trajectories would have to be identical, since the starting conditions would be identical. The real situation is somewhere

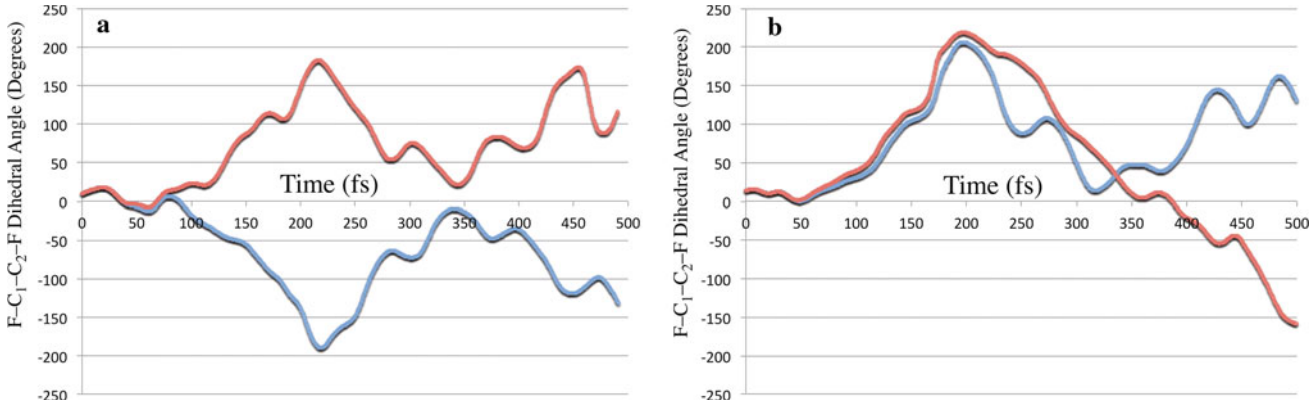

Fig. 7 Influence of charge arrays of opposite chirality on trajectories started with identical geometries and momenta. **a** The separation is almost immediate, and the paths followed are close to being mirror images. **b** The separation is delayed and the paths are not mirror images

between these two limits. The orientation of the charge arrays with respect to the molecule for the trajectories in Fig. 7a is such that the dipole-quadrupole combinations (vide infra) are near maximal and lead to external forces that outweigh the internal ones. By contrast, the orientation for the trajectories in Fig. 7b is such that the internal forces are initially larger than the external ones and so the trajectories start out on very similar paths. As the molecule rotates with respect to the charge array, the external forces increase in magnitude until they outweigh the internal ones and start to cause chiral discrimination. But by now, the molecules are chiral (i.e., far from the abscissa of Fig. 7b) and so the enantiomeric charge arrays no longer have mirror image effects on the trajectories.

The seeming inconsistency between microscopic and macroscopic effects of the chiral charge arrays is presumably related to the difference between "locked-up" and freely rotating limits in the Craig and Schipper analysis. When pairs of chiral polar objects are held in fixed relative orientations, the leading chiral term in the multipole expansion of their interaction energy is a dipole-quadrupole combination [25]. This term can favor *RR* or *RS* interactions and can be substantial in magnitude, but when the chiral objects are allowed to rotate freely with respect to each other, the net effect averages to near zero. In the present case, a similar effect apparently occurs between a chiral molecule and a chiral charged cavity; in the freely rotating situation, the residual discrimination is small but nonzero, in line with the expectations from the simple models introduced at the beginning of this paper.

The interactions between freely rotating molecules of different relative chirality are found experimentally to be much larger than the negligible electrostatic effect predicted from the Craig and Schipper analysis. This presumably implies that other contributors, particularly dispersion interactions, are principally responsible for the chiral discrimination [28]. It seems reasonable to expect that the same will be true for the system studied here, and that the simulation of the ring opening in the presence of explicit chiral solvent molecules—a calculation presently underway—could yield effects greater than seen for just the electrostatic interactions considered here.

4 Conclusions

The diastereomeric energy differences between chiral arrays of point charges are found, through numerical simulation, to be larger for concentric arrangements than non-concentric ones even when the average distance between charges is comparable. This implies that the cavity in a chiral solvent might exert a larger electrostatic discrimination between enantiomeric solutes than one would have expected on the basis of pairwise interaction between chiral molecules. When trajectories for a reaction with a bifurcating reaction path leading to enantiomeric products are run in the presence of a surrounding chiral array of point charges, it is found that large microscopic effects on the product selection occur. However, when the results are averaged to take account of relative rotation of the molecule and the charged cavity, the net result is much smaller.

Acknowledgments Support of this work by the EPSRC (Grant No. EP/K000489/1) is gratefully acknowledged. Computational work was carried out on the Raven HPC cluster at the Advanced Research Computing facility of Cardiff University.

References

1. Valtazanos P, Ruedenberg K (1986) Theor Chim Acta 69:281
2. Quapp W (2003) J Theor Comput Chem 2:385

3. Rehbein J, Carpenter BK (2011) Phys Chem Chem Phys 13:20906
4. Valtazanos P, Elbert ST, Xantheas S, Ruedenberg K (1991) Theor Chim Acta 78:287
5. Shaik S, Danovich D, Sastry GN, Ayala PY, Schlegel HB (1997) J Am Chem Soc 119:9237
6. Taketsugu T, Yanai T, Hirao K, Gordon MS (1998) Theochem J Mol Struct 451:163
7. Castano O, Palmeiro R, Frutos LM, Luisandres J (2002) J Comput Chem 23:732
8. Zhou C, Birney DM (2002) Org Lett 4:3279
9. Birney DM (2010) Curr Org Chem 14:1658
10. Ess DH, Wheeler SE, Iafe RG, Xu L, Celebi-Olcum N, Houk KN (2008) Angew Chem Int Ed 47:7592
11. Hong YJ, Tantillo DJ (2009) Nat Chem 1:384
12. Hong YJ, Tantillo DJ (2014) Nat Chem 6:104
13. Katori T, Itoh S, Sato M, Yamataka H (2010) J Am Chem Soc 132:3413
14. Yamataka H, Sato M, Hasegawa H, Ammal SC (2010) Faraday Discuss 145:327
15. Yamamoto Y, Hasegawa H, Yamataka H (2011) J Org Chem 76:4652
16. Akimoto R, Tokugawa T, Yamamoto Y, Yamataka H (2012) J Org Chem 77:4073
17. Bogle XS, Singleton DA (2012) Org Lett 14:2528
18. Collins P, Carpenter BK, Ezra GS, Wiggins S (2013) J Chem Phys 139:154108
19. Stephens PJ, Devlin FJ, Chabalowski CF, Frisch MJ (1994) J Phys Chem 98:11623
20. Hertwig RH, Koch W (1997) Chem Phys Lett 268:345
21. Francl MM, Pietro WJ, Hehre WJ, Binkley JS, Gordon MS, Defrees DJ, Pople JA (1982) J Chem Phys 77:3654
22. Cremer D (2001) Mol Phys 99:1899
23. Frisch MJ, Trucks GW, Schlegel HB, Scuseria GE, Robb MA, Cheeseman JR, Scalmani G, Barone V, Mennucci B, Petersson GA et al (2009) Gaussian 09, revision D.1. Gaussian, Inc., Wallingford
24. Clark DT, Armstron DR (1969) Theor Chim Acta 13:365
25. Craig DP, Schipper PE (1975) Proc R Soc Lond Ser A 342:19
26. Alvarez S (2013) Dalton Trans 42:8617
27. Cahn RS, Ingold CK, Prelog V (1956) Experientia 12:81
28. Craig DP, Power EA, Thirunam T (1971) Proc R Soc Lond Ser A 322:165

Theor Chem Acc (2014) 133:1495
DOI 10.1007/s00214-014-1495-4

REGULAR ARTICLE

Computer simulation of quantum dynamics in a classical spin environment

Alessandro Sergi

Received: 15 March 2014 / Accepted: 25 April 2014 / Published online: 20 May 2014

Abstract In this paper, a formalism for studying the dynamics of quantum systems coupled to classical spin environments is reviewed. The theory is based on generalized antisymmetric brackets and naturally predicts open-path off-diagonal geometric phases in the evolution of the density matrix. It is shown that such geometric phases must also be considered in the quantum–classical Liouville equation for a classical bath with canonical phase space coordinates; this occurs whenever the adiabatics basis is complex (as in the case of a magnetic field coupled to the quantum subsystem). When the quantum subsystem is weakly coupled to the spin environment, non-adiabatic transitions can be neglected and one can construct an effective non-Markovian computer simulation scheme for open quantum system dynamics in classical spin environments. In order to tackle this case, integration algorithms based on the symmetric Trotter factorization of the classical-like spin propagator are derived. Such algorithms are applied to a model comprising a quantum two-level system coupled to a single classical spin in an external magnetic field. Starting from an excited state, the population difference and the coherences of this two-state model are simulated in time while the dynamics of the classical spin is monitored in detail. It is the author's opinion that the numerical evidence provided in this paper is a first step toward developing the simulation of quantum dynamics in classical spin environments into an effective tool. In turn, the ability to simulate such a dynamics can have a positive impact on various fields, among which, for example, nanoscience.

Keywords Quantum–classical systems · Spin dynamics · Time-reversible integrator

1 Introduction

The computer simulation of systems of interest to nanoscience requires to consider in detail the environment surrounding, for example, the quantum reactive centers [1], the Josephson junctions [2] or the quantum dots [3–5]. Environments can be represented either by means of bosonic degrees of freedom [6] or by spinors [7] (or also by a combination of the two types of coordinates). In practice, following accurately the dynamics of both the relevant system and the surrounding environment (bath) leads to a theoretical/computational approach that is complementary to the study of master equations [8–14].

A scheme to perform the computer simulation of quantum systems coupled to classical spin baths was introduced in [15]. The approach of Ref. [15] can be classified within the quantum–classical approximations [16–20] to quantum dynamics since it is based on a quantum–classical Liouville equation [21–27] for a classical spin bath. It is interesting that the formalism in [15] does not require to approximate the memory function of the

Dedicated to Professor Greg Ezra and published as part of the special collection of articles celebrating his 60th birthday.

This work is based upon research supported by the National Research Foundation of South Africa.

A. Sergi (✉)
School of Chemistry and Physics, University of KwaZulu-Natal, Private Bag X01, Scottsville, Pietermaritzburg 3209, South Africa
e-mail: sergi@ukzn.ac.za

A. Sergi
National Institute of Theoretical Physics (NITheP), Durban, KwaZulu-Natal, South Africa

environment since the bath degrees of freedom are described explicitly, in the spirit of molecular dynamics simulations [28, 29]. From this point of view, the approach of Ref. [15] provides a non-Markovian route to the simulation of quantum effects in classical spin baths. It is worthy of note that the formalism in [15] was naturally devised exploiting the mathematical structure provided by generalized antisymmetric brackets [30–32]. Such brackets have also been used to formulate the statistical mechanics of systems with thermodynamic [33–35] and holonomic constraints [36, 37] in classical mechanics.

In the regime of weak coupling, the adiabatic basis is particularly suited for numerical studies. When such a basis is complex (e.g., in the presence of magnetic dipoles and fields), it has been shown that the formalism of Ref. [15] naturally predicts an open [38, 39] geometric phase [40–43] in the evolution of the off-diagonal matrix elements of operators.

In this paper, three topics will be dealt with. The first is that, when the adiabatic basis is complex, also the quantum–classical Liouville equation in a classical bath with canonical (position/momentum) coordinates possesses an open geometric phase term for the off-diagonal matrix elements. The second is a brief review of the formalism for the quantum dynamics of systems in classical spin baths, as introduced in Ref. [15]. The third is the explicit formulation of integration algorithms, based on the symmetric Trotter factorization [44–46] of the classical spin propagator. It is worth noting that the classical-like spin dynamics could also have been integrated by means of the elegant measure-preserving algorithms invented by Ezra [47–49]. In order to illustrate the algorithms, a specific model comprising a quantum two-level system coupled to a classical spin is studied and numerical results are reported. It is the author's opinion that the numerical algorithms presented here are a first significant step toward developing the theory introduced in Ref. [15] into an effective tool for studying quantum nanosystems.

This paper is organized as follow. In Sect. 2, the formulation of quantum–classical dynamics of quantum systems in environments represented by canonically conjugate variables is summarized. It is shown that, when the basis is complex, one has to consider a geometric phase in the evolution of the off-diagonal matrix elements also in this case. In Sect. 3, it is briefly reviewed how the quantum–classical theory of Sect. 2 can be generalized to describe quantum systems in classical spin baths. The model system simulated in this paper is introduced in Sect. 4. Its time-reversible integrators, on the various energy surfaces, are developed in Sect. 5. The detailed algorithms for integration on the (1, 1), (2, 2) and (1, 2) surfaces are given in the Appendices 1–3. The details and the results of the calculations on the model are discussed in Sect. 6. Finally, conclusions and perspectives are given in Sect. 7.

2 Quantum–classical Liouville equation in a complex adiabatic basis

Consider a quantum system whose Hamiltonian operator $\hat{H}(\{\xi\})$ is defined in terms of a set of quantum operators $\hat{\xi}_i, i = 1, \ldots, n$ and assume that the quantum degrees of freedom interact with a classical bath which can be represented by canonical phase space coordinates $X = (R, P)$. Such classical coordinates enter the definition of the bath classical Hamiltonian $H_B(X)$. It is worth stating clearly that in this section, a multidimensional notation is adopted. According to this, for example, the symbol R stands for $(R_1, R_2, \ldots)$, and a scalar products such as $P \cdot P$ stand for $\sum_I P_I^2$. Such a multidimensional notation will be abandoned in favor of a more explicit notation in the next sections. The interaction between the quantum subsystem and the classical bath is given in terms of a coupling term $\hat{H}_C(\{\xi\}, X)$. The total Hamiltonian (which must be a constant of motion) describing the coupled quantum subsystem plus classical bath can be written as

$$\hat{\mathcal{H}}(X) = \hat{H}(\{\xi\}) + \hat{H}_{\mathrm{C}}(\{\xi\}, X) + H_{\mathrm{B}}(X). \tag{1}$$

Accordingly, one is also led to introduce a quantum–classical density matrix $\hat{\rho}_{\mathrm{QC}}(X)$ and quantum–classical operators $\hat{\chi}_{\mathrm{QC}}(X)$. The evolution in time, in a Schrödinger-like dynamical picture, can be postulated as

$$\begin{aligned}\frac{\partial}{\partial t}\hat{\rho}_{\mathrm{QC}}(X,t) &= -\frac{i}{\hbar}\left[\hat{\mathcal{H}}(X) \quad \hat{\rho}_{\mathrm{QC}}(X,t)\right]\boldsymbol{\mathcal{D}}\begin{bmatrix}\hat{\mathcal{H}}(X)\\ \hat{\rho}_{\mathrm{QC}}(X,t)\end{bmatrix},\\ &= -\frac{i}{\hbar}\left[\hat{\mathcal{H}}(X), \hat{\rho}_{\mathrm{QC}}(X,t)\right]_{\boldsymbol{\mathcal{D}}}.\end{aligned} \tag{2}$$

In Eq. (2), the antisymmetric matrix operator $\mathcal{D}$ has been introduced. It is defined as

$$\mathcal{D} = \begin{bmatrix} 0 & 1 + \frac{i\hbar}{2}\frac{\overleftarrow{\partial}}{\partial X_I}\mathcal{B}_{IJ}\frac{\overrightarrow{\partial}}{\partial X_J}\\ -1 - \frac{i\hbar}{2}\frac{\overleftarrow{\partial}}{\partial X_I}\mathcal{B}_{IJ}\frac{\overrightarrow{\partial}}{\partial X_J} & 0\end{bmatrix}, \tag{3}$$

where

$$\boldsymbol{\mathcal{B}} = \begin{bmatrix} 0 & 1\\ -1 & 0\end{bmatrix} \tag{4}$$

is the symplectic matrix. The arrows over the partial derivative symbols in Eq. (2) denote in which direction the partial derivative operator must act. Moreover, in Eq. (2)

and in the following, the sum over repeated indices is implied. Equation (2), which is just the quantum–classical Liouville equation [21–27] written in matrix form, defines what is known as quantum–classical bracket [16–20] or non-Hamiltonian commutator [30]. The bracket couples the dynamics of the phase space degrees of freedom with that of the quantum operators; it takes into account both the conservation of the energy and the quantum back-reaction. Moreover, when there is no coupling, i.e., $\hat{H}_{\mathrm{C}} = 0$, the bracket makes the quantum system evolve in terms of the standard quantum commutator and the classical bath through the Poisson bracket.

The quantum–classical bracket in Eq. (2) does not satisfy the Jacobi relation, and this, in turn, leads to the lack of time-translation invariance of the algebra defined in terms of the bracket itself [30, 50]. Less abstract consequences of such mathematical features are that the coordinates of the bath, which are classical at time zero, acquire quantum phases as time flows. With respect to this, one has to consider the bracket as an approximation to the correct quantum dynamics of the total system (subsystem plus bath). Such a dynamics, although correct in principle, would not be calculable so that, following the philosophy of *approximated theoretical complexity* (as discussed in [51]), the quantum–classical bracket can be invoked as an effective tool in order to perform computer simulations that would be otherwise impossible. In practice, fast bath decoherence may alleviate the theoretical problems associated with the acquisition of quantum phase terms by the variables that should stay classical and, indeed, the quantum–classical bracket, or quantum–classical Liouville equation, is used for many applications in chemistry and physics [16–27]. It is worth reminding that the non-Lie (or, as they are also called, non-Hamiltonian) brackets, with their lack of time-translation invariance, are also used as technical tools to impose thermodynamical (such as constant temperature and/or pressure) [33–35] and holonomic constraints [36, 37] in classical molecular dynamics calculations [28, 29].

The abstract equations of motion in (2) can be represented in the adiabatic basis. Upon writing the total Hamiltonian as $\hat{\mathcal{H}}(X) = (P^2/2M) + \hat{h}(R)$, such a basis is defined by the eigenvalue problem $\hat{h}(R)|\alpha;R\rangle = E_\alpha(R)|\alpha;R\rangle$. In the adiabatic basis, the quantum–classical evolution reads

$$\frac{\partial}{\partial t}\hat{\rho}_{\alpha\alpha'}(X,t) = -\sum_{\beta\beta'}\big[i\omega_{\alpha\alpha'} + iL_{\alpha\alpha'}\delta_{\alpha\beta}\delta_{\alpha'\beta'} + J_{\alpha\alpha',\beta\beta'}\big]\hat{\rho}_{\beta\beta'}(X,t). \tag{5}$$

In Eq. (5), the symbol $\omega_{\alpha\alpha'}(R) = [E_\alpha(R) - E_{\alpha'}(R)]/\hbar$ denotes the Bohr frequency,

$$iL_{\alpha\alpha'} = \frac{P}{M}\cdot\frac{\partial}{\partial R} + \frac{1}{2}\left(F_W^{\alpha} + F_W^{\alpha'}\right)\cdot\frac{\partial}{\partial P}, \tag{6}$$

is the classical-like Liouville operator for the bath degrees of freedom, $F_W^{\alpha} = -\langle\alpha;R|(\partial\hat{h}/\partial R)|\alpha;R\rangle$ is the Helmann–Feynman force, and

$$J_{\alpha\alpha',\beta\beta'} = \frac{P}{M}\cdot d_{\alpha\beta}\left(1 + \frac{1}{2}S_{\alpha\beta}\cdot\frac{\partial}{\partial P}\right)\delta_{\alpha'\beta'} + \frac{P}{M}\cdot d^*_{\alpha'\beta'}\left(1 + \frac{1}{2}S^*_{\alpha'\beta'}\cdot\frac{\partial}{\partial P}\right)\delta_{\alpha\beta}, \tag{7}$$

is the transition operator, responsible for the non-adiabatic transitions between the energy levels of the quantum subsystem, as a result of the coupling to the bath. The symbol $d_{\alpha\beta} = \langle\alpha|\partial/\partial R|\beta\rangle$ denotes the non-adiabatic coupling vector. In Eq. (7), the vector $S_{\alpha\beta} = \hat{d}_{\alpha\beta}(E_\alpha - E_\beta)(\hat{d}_{\alpha\beta}\cdot P/M)^{-1}$ together with its complex conjugate $S^*_{\alpha'\beta'}$ has been defined (the symbol $\hat{d}_{\alpha\beta}$ denotes the normalization of the coupling vector over the space of all R coordinates).

The coupling vector has the property $d_{\alpha\beta} = -d^*_{\beta\alpha}$ so that, when the adiabatic basis is real, $d_{\alpha\alpha} = 0$ and the transition operator in Eq. (7) is purely off-diagonal. However, when the basis is complex (e.g., when the symmetry under time inversion is broken, for example, because of a magnetic field), $d_{\alpha\alpha}$ is not zero and is purely imaginary

$$d_{\alpha\alpha} = i\phi_{\alpha\alpha} \neq 0. \tag{8}$$

One can see that a phase $\phi_{\alpha\alpha}$ is naturally emerging from the representation of the quantum–classical Liouville equation in a complex basis. Hence, in a complex adiabatic basis, Eq. (5) can be rewritten as

$$\frac{\partial}{\partial t}\hat{\rho}_{\alpha\alpha'}(X,t) = -\sum_{\beta\beta'}\Big[i\omega_{\alpha\alpha'} + i\frac{P}{M}(\phi_{\alpha\alpha} - \phi_{\alpha'\alpha'}). + iL_{\alpha\alpha'}\delta_{\alpha\beta}\delta_{\alpha'\beta'} + J^{\mathrm{od}}_{\alpha\alpha',\beta\beta'}\Big]\hat{\rho}_{\beta\beta'}(X,t). \tag{9}$$

where $J^{\mathrm{od}}_{\alpha\alpha',\beta\beta'}$ is the off-diagonal part of the transition operator

$$J^{\mathrm{od}}_{\alpha\alpha',\beta\beta'} = \frac{P}{M}\cdot d_{\alpha\beta}[1-\delta_{\alpha\beta}]\left(1 + \frac{1}{2}S_{\alpha\beta}\cdot\frac{\partial}{\partial P}\right)\delta_{\alpha'\beta'} + \frac{P}{M}\cdot d^*_{\alpha'\beta'}[1-\delta_{\alpha'\beta'}]\left(1 + \frac{1}{2}S^*_{\alpha'\beta'}\cdot\frac{\partial}{\partial P}\right)\delta_{\alpha\beta}, \tag{10}$$

While the phase $\omega_{\alpha\alpha}$ has a dynamical source, the phase $\phi_{\alpha\alpha}$ has a geometric origin and it is analogous to the famous Berry phase [40–42]. Hence, Eq. (9) is the quantum–classical Liouville equation displaying geometric phase effects. In principle, such phases are also present for open paths [52] of the classical environment and they are off-diagonal in nature [53–55].

3 Quantum–classical spin dynamics

Consider a classical spin vector $\mathbf{S}$ with components S_I, $I = x, y, z$, whose energy is described by the Hamiltonian be $H_{\rm SB}(\mathbf{S})$. It is known that the equations of motion can be written in matrix form as

$$\dot{S}_I = \mathcal{B}^{\rm S}_{IJ} \frac{\partial H_{\rm SB}}{\partial S_J}, \tag{11}$$

where

$$\boldsymbol{\mathcal{B}}^{\rm S} = \begin{bmatrix} 0 & S_z & -S_y \\ -S_z & 0 & S_x \\ S_y & -S_x & 0 \end{bmatrix}. \tag{12}$$

The antisymmetric matrix $\boldsymbol{\mathcal{B}}^{\rm S}$ can also be written in a compact way as

$$\mathcal{B}^{\rm S}_{IJ} = \epsilon_{IJK} S_K. \tag{13}$$

The equations of motion (11) preserve the Casimir $C_2 = \mathbf{S}\cdot\mathbf{S}$ for any arbitrary Hamiltonian $H_{\rm SB}(\mathbf{S})$. They also have a zero phase space compressibility

$$\kappa = \frac{\partial \dot{S}_I}{\partial S_I}\epsilon_{IJK}\delta_{KJ}\frac{\partial H_{\rm SB}}{\partial S_J} + \mathcal{B}^{\rm S}_{IJ}\frac{\partial^2 H_{\rm SB}}{\partial S_I \partial S_J} = 0. \tag{14}$$

The equations of motion can also be written in the form

$$\dot{S}_I = \{S_I, H_{\rm SB}\}_{\boldsymbol{\mathcal{B}}^{\rm s}}, \tag{15}$$

upon introducing a non-canonical bracket defined as

$$\{A, B\}_{\boldsymbol{\mathcal{B}}^{\rm s}} = \frac{\partial A}{\partial S_I}\mathcal{B}^{\rm S}_{IJ}\frac{\partial B}{\partial S_J}, \tag{16}$$

where $A = A(\mathbf{S})$ and $B = B(\mathbf{S})$ are arbitrary functions of the spin degrees of freedom.

Let us assume that the classical spin system is interacting with the quantum system with Hamiltonian operator $\hat{H}(\{\hat{\chi}\})$ through an interaction of the form $\hat{H}_{\rm c}(\{\hat{\chi}\}, \mathbf{S})$ The total Hamiltonian operator of the quantum subsystem in the classical spin bath can be written analogously to Eq. (1)

$$\hat{\mathcal{H}}(\mathbf{S}) = \hat{H}(\{\hat{\chi}\}) + \hat{H}_{\rm C}(\{\hat{\chi}\}, \mathbf{S}) + H_{\rm SB}(\mathbf{S}). \tag{17}$$

The evolution of the density matrix $\hat{\rho}(\mathbf{S})$ of the quantum system in the classical bath can be postulated in the form

$$\begin{aligned} \frac{\partial}{\partial t}\hat{\rho}(\mathbf{S}, t) &= -\frac{i}{\hbar}\begin{bmatrix} \hat{\mathcal{H}}(\mathbf{S}) & \hat{\rho}(\mathbf{S}, t) \end{bmatrix} \cdot \mathcal{D}^{\rm S} \cdot \begin{bmatrix} \hat{\mathcal{H}}(\mathbf{S}) \\ \hat{\rho}(\mathbf{S}, t) \end{bmatrix}, \\ &= -\frac{i}{\hbar}\left[\hat{\mathcal{H}}(\mathbf{S}), \hat{\rho}(\mathbf{S}, t)\right]_{\mathcal{D}^{\rm s}} \end{aligned} \tag{18}$$

where

$$\mathcal{D}^{\rm S} = \begin{bmatrix} 0 & 1 + \frac{i\hbar}{2}\frac{\overleftarrow{\partial}}{\partial S_I}\mathcal{B}^{\rm S}_{IJ}\frac{\overrightarrow{\partial}}{\partial S_J} \\ -1 - \frac{i\hbar}{2}\frac{\overleftarrow{\partial}}{\partial S_I}\mathcal{B}^{\rm S}_{IJ}\frac{\overrightarrow{\partial}}{\partial S_J} & 0 \end{bmatrix}. \tag{19}$$

The right-hand side of Eq. (18) introduces a quantum–classical bracket for a quantum subsystem in a classical spin bath.

In order to represent the abstract Eq. (18), the quantum–classical Hamiltonian of Eq. (17) can be rewritten as

$$\hat{\mathcal{H}}(\mathbf{S}) = \hat{h}(\mathbf{S}) + H_{\rm SB}(\mathbf{S}). \tag{20}$$

Accordingly, the adiabatic basis is defined by the eigenvalue equation

$$\hat{h}(\mathbf{S})|\alpha; \mathbf{S}\rangle = E_\alpha(\mathbf{S})|\alpha; \mathbf{S}\rangle. \tag{21}$$

However, at variance with the case of the canonical coordinate bath discussed in Sect. 2, where it depended only on the positions R (and not on the conjugate momenta P), the adiabatic basis defined by Eq. (21) depends on all the non-canonical spin coordinates $\mathbf{S}$. Hence, in the spin adiabatic basis, Eq. (18) becomes

$$\begin{aligned} \partial_t \rho_{\alpha\alpha'} = &-i\omega_{\alpha\alpha'}\rho_{\alpha\alpha'} - \mathcal{B}^{\rm S}_{IJ}\frac{\partial H_{\rm SB}}{\partial S_J}\left\langle \alpha; \mathbf{S}\left|\frac{\partial \hat{\rho}}{\partial S_I}\right|\alpha'; \mathbf{S}\right\rangle \\ &+ \frac{1}{2}\mathcal{B}^{\rm S}_{IJ}\left\langle \alpha; \mathbf{S}\left|\frac{\partial \hat{h}}{\partial S_I}\frac{\partial \hat{\rho}}{\partial S_J}\right|\alpha'; \mathbf{S}\right\rangle \\ &- \frac{1}{2}\mathcal{B}^{\rm S}_{IJ}\left\langle \alpha; \mathbf{S}\left|\frac{\partial \hat{\rho}}{\partial S_I}\frac{\partial \hat{h}}{\partial S_J}\right|\alpha'; \mathbf{S}\right\rangle, \end{aligned} \tag{22}$$

where the antisymmetry of $\boldsymbol{\mathcal{B}}^{\rm S}$ has been used. As it was done in Sect. 2, a coupling vector can be defined as

$$d^I_{\sigma\alpha} = \left\langle \sigma; \mathbf{S}\left|\frac{\overrightarrow{\partial}}{\partial S_I}\right|\alpha; \mathbf{S}\right\rangle, \tag{23}$$

where the index I of the spin components, has been left explicit. The following identities can be easily found

$$\begin{aligned} \left\langle \alpha; \mathbf{S}\left|\frac{\partial \hat{\rho}}{\partial S_I}\right|\alpha'; \mathbf{S}\right\rangle = &\frac{\partial \rho_{\alpha\alpha'}}{\partial S_I} + d^I_{\alpha\sigma}\rho_{\sigma\alpha'} \\ &- \rho_{\alpha\sigma'}d^I_{\sigma'\alpha'}, \end{aligned} \tag{24}$$

$$\left\langle \alpha; \mathbf{S}\left|\frac{\partial \hat{h}}{\partial S_I}\right|\sigma; \mathbf{S}\right\rangle = \frac{\partial h_{\alpha\sigma}}{\partial S_I} - \Delta E_{\alpha\sigma}d^I_{\alpha\sigma}, \tag{25}$$

where $\Delta E_{\alpha\sigma} = E_\alpha - E_\sigma$. With the help of Eqs. (24) and (25), the equations of motion can be written as

$$
\begin{aligned}
\partial_t \rho_{\alpha\alpha'} = & -i\omega_{\alpha\alpha'}\rho_{\alpha\alpha'} - \mathcal{B}^{\mathrm{S}}_{IJ}\frac{\partial H_{\mathrm{SB}}}{\partial S_J}\frac{\partial \rho_{\alpha\alpha'}}{\partial S_I} - \frac{1}{2}\mathcal{B}^{\mathrm{S}}_{IJ}\frac{\partial E_\alpha}{\partial S_J}\frac{\partial \rho_{\alpha\alpha'}}{\partial S_I} \\
& - \frac{1}{2}\mathcal{B}^{\mathrm{S}}_{IJ}\frac{\partial E_{\alpha'}}{\partial S_J}\frac{\partial \rho_{\alpha\alpha'}}{\partial S_I} - \Bigg(-\mathcal{B}^{\mathrm{S}}_{IJ}\frac{\partial H_{\mathrm{SB}}}{\partial S_J} d^I_{\alpha\beta}\delta_{\alpha'\beta'} \\
& - \mathcal{B}^{\mathrm{S}}_{IJ}\frac{\partial H_{\mathrm{SB}}}{\partial S_J} d^{I*}_{\alpha'\beta'}\delta_{\alpha\beta} - \frac{1}{2}\mathcal{B}^{\mathrm{S}}_{IJ}\Delta E_{\alpha\beta} d^I_{\alpha\beta}\frac{\partial}{\partial S_J}\delta_{\alpha'\beta'} \\
& - \frac{1}{2}\mathcal{B}^{\mathrm{S}}_{IJ}\Delta E_{\alpha'\beta'} d^{I*}_{\beta'\alpha'}\frac{\partial}{\partial S_J}\delta_{\alpha\beta}\Bigg)\rho_{\beta\beta'} \\
& + \frac{1}{2}\mathcal{B}^{\mathrm{S}}_{IJ}\Bigg(\frac{\partial E_\alpha}{\partial S_I} d^J_{\alpha\beta}\delta_{\alpha'\beta'} - \frac{\partial E_\alpha}{\partial S_I} d^J_{\beta'\alpha'}\delta_{\alpha\beta} \\
& - \Delta E_{\alpha\sigma} d^I_{\alpha\sigma} d^J_{\sigma\beta}\rho_{\beta\alpha'} + \Delta E_{\alpha\beta} d^I_{\alpha\beta} d^J_{\beta'\alpha'}\Bigg)\rho_{\beta\beta'} \\
& - \frac{1}{2}\mathcal{B}^{\mathrm{S}}_{IJ}\Bigg(\frac{\partial E_{\alpha'}}{\partial S_J} d^I_{\alpha\beta}\delta_{\alpha'\beta'} - \frac{\partial E_{\alpha'}}{\partial S_J} d^I_{\beta'\alpha'}\delta_{\alpha\beta} \\
& + \Delta E_{\sigma'\alpha'} d^J_{\sigma'\alpha'} d^I_{\beta'\sigma'}\delta_{\alpha\beta} - \Delta E_{\beta'\alpha'} d^J_{\beta'\alpha'} d^I_{\alpha\beta}\Bigg)\rho_{\beta\beta'}.
\end{aligned}
\tag{26}
$$

At this stage, it is useful to introduce a classical-like spin Liouville operator:

$$
\begin{aligned}
L_{\alpha\alpha'} &= \left(\mathcal{B}^{\mathrm{S}}_{IJ}\frac{\partial H_{\mathrm{SB}}}{\partial S_J}\frac{\partial}{\partial S_I} + \frac{1}{2}\mathcal{B}^{\mathrm{S}}_{IJ}\frac{\partial E_{\alpha'}}{\partial S_J}\frac{\partial}{\partial S_I} + \frac{1}{2}\mathcal{B}^{\mathrm{S}}_{IJ}\frac{\partial E_\alpha}{\partial S_J}\frac{\partial}{\partial S_I}\right) \\
&= \mathcal{B}^{\mathrm{S}}_{IJ}\frac{\partial H^{\mathrm{S}}_{\alpha\alpha'}}{\partial S_J}\frac{\partial}{\partial S_I} = \left\{\ldots, H^{\mathrm{S}}_{\alpha\alpha'}\right\}_{\boldsymbol{\mathcal{B}}^{\mathrm{S}}},
\end{aligned}
\tag{27}
$$

where the matrix elements of the total system Hamiltonian on the adiabatic surfaces are denoted as

$$
H^{\mathrm{S}}_{\alpha\alpha'} = H_{\mathrm{SB}} + \frac{1}{2}(E_\alpha + E_{\alpha'}). \tag{28}
$$

A transition operator for the spin bath can be defined as

$$
\begin{aligned}
J_{\alpha\alpha',\beta\beta'} = & \mathcal{B}^{\mathrm{S}}_{IJ}\frac{\partial H_{\mathrm{SB}}}{\partial S_J} d^I_{\alpha\beta}\delta_{\beta'\alpha'} + \frac{1}{2}\mathcal{B}^{\mathrm{S}}_{IJ}\Delta E_{\alpha\beta} d^I_{\alpha\beta}\frac{\partial}{\partial S_J}\delta_{\alpha'\beta'} \\
& + \mathcal{B}^{\mathrm{S}}_{IJ}\frac{\partial H_{\mathrm{SB}}}{\partial S_J} d^{I*}_{\alpha'\beta'}\delta_{\alpha\beta} + \frac{1}{2}\mathcal{B}^{\mathrm{S}}_{IJ}\Delta E_{\alpha'\beta'} d^{I*}_{\alpha'\beta'}\frac{\partial}{\partial S_J}\delta_{\alpha\beta}.
\end{aligned}
\tag{29}
$$

The operator in Eq. (29) goes to the transition operator in Eq. (10) when canonical variables are considered. In the case of a spin bath, in order to take properly into account non-adiabatic effects, a higher-order transition operator (acting together with $J_{\alpha\alpha',\beta\beta'}$) must be considered. Such an operator is

$$
\begin{aligned}
\mathcal{S}_{\alpha\alpha',\beta\beta'} = & \frac{1}{2}\mathcal{B}^{\mathrm{S}}_{IJ}\frac{\partial(E_\alpha + E_{\alpha'})}{\partial S_I} d^J_{\alpha\beta}\delta_{\alpha'\beta'} \\
& + \frac{1}{2}\mathcal{B}^{\mathrm{S}}_{IJ}\frac{\partial(E_\alpha + E_{\alpha'})}{\partial S_I} d^{J*}_{\alpha'\beta'}\delta_{\alpha\beta} \\
& - \frac{1}{2}\mathcal{B}^{\mathrm{S}}_{IJ}\Delta E_{\alpha\sigma} d^I_{\alpha\sigma} d^J_{\sigma\beta}\delta_{\beta\alpha'} - \frac{1}{2}\mathcal{B}^{\mathrm{S}}_{IJ}\Delta E_{\alpha\beta} d^I_{\alpha\beta} d^{J*}_{\alpha'\beta'} \\
& - \frac{1}{2}\mathcal{B}^{\mathrm{S}}_{IJ}\Delta E_{\alpha'\sigma'} d^{I*}_{\alpha'\sigma'} d^{J*}_{\sigma'\beta'}\delta_{\alpha\beta} \\
& - \frac{1}{2}\mathcal{B}^{\mathrm{S}}_{IJ}\Delta E_{\alpha'\beta'} d^{I*}_{\alpha'\beta'} d^J_{\alpha\beta}.
\end{aligned}
\tag{30}
$$

The operator in Eq. (30) is identically zero for canonical conjugate variables. Using Eqs. (27–30), the equation of motion reads

$$
\begin{aligned}
\partial_t \rho_{\alpha\alpha'} = & \sum_{\beta\beta'}\big(-i\omega_{\alpha\alpha'}\delta_{\alpha\beta}\delta_{\alpha\alpha'} - L_{\alpha\alpha'}\delta_{\alpha\beta}\delta_{\alpha\alpha'} - J_{\alpha\alpha',\beta\beta'} \\
& + \mathcal{S}_{\alpha\alpha',\beta\beta'}\big)\rho_{\beta\beta'}.
\end{aligned}
\tag{31}
$$

The general equations of motion (31) are difficult to integrate if one desires to take into account non-adiabatic corrections. However, in the case of weak coupling between the spin bath and the quantum subsystem, one is allowed to take the adiabatic limit of the operators in Eqs. (29) and (30). This is performed by assuming that the off-diagonal elements of $d_{\alpha\alpha'}$ (which couple different adiabatic energy surfaces) are negligible. In such a case, one obtains

$$
\begin{aligned}
J^{\mathrm{ad}}_{\alpha\alpha',\beta\beta'} &= -\mathcal{B}^{\mathrm{S}}_{IJ}\frac{\partial H_{\mathrm{SB}}}{\partial S_J}\big(d^I_{\alpha\alpha} + d^{I*}_{\alpha'\alpha'}\big)\delta_{\alpha\beta}\delta_{\beta'\alpha'} \\
&= -i\mathcal{B}^{\mathrm{S}}_{IJ}\frac{\partial H_{\mathrm{SB}}}{\partial S_J}\big(\Phi^I_{\alpha\alpha} - \Phi^I_{\alpha'\alpha'}\big)\delta_{\alpha\beta}\delta_{\beta'\alpha'},
\end{aligned}
\tag{32}
$$

where, using the fact that $d^I_{\alpha\alpha}$ is purely imaginary, a phase

$$
\Phi^I_{\alpha\alpha'} = -id^I_{\alpha\alpha'} \tag{33}
$$

has been introduced in a manner analogous to that when the bath has a representation in terms of canonical variables. In a similar way, one can take the adiabatic limit of the $\mathcal{S}_{\alpha\alpha',\beta\beta'}$ in Eq. (30):

$$
\mathcal{S}^{\mathrm{ad}}_{\alpha\alpha',\beta\beta'} = -\frac{i}{2}\mathcal{B}^{\mathrm{S}}_{IJ}\frac{\partial(E_\alpha + E_{\alpha'})}{\partial S_J}\big(\Phi^I_{\alpha\alpha} - \Phi^I_{\alpha'\alpha'}\big)\delta_{\alpha\alpha}\delta_{\alpha'\alpha'}. \tag{34}
$$

Hence, in the weak-coupling (adiabatic) limit, the equation of motion reads

$$
\begin{aligned}
\frac{\partial}{\partial t}\rho_{\alpha\alpha'} = & \Bigg[-i\omega_{\alpha\alpha'} - i\mathcal{B}^{\mathrm{S}}_{IJ}\frac{\partial H^{\mathrm{S}}_{\alpha\alpha'}}{\partial S_J}\big(\Phi^I_{\alpha\alpha} - \Phi^I_{\alpha'\alpha'}\big) \\
& - \mathcal{B}^{\mathrm{S}}_{IJ}\frac{\partial H^{\mathrm{S}}_{\alpha\alpha'}}{\partial S_J}\frac{\partial}{\partial S_I}\Bigg]\rho_{\alpha\alpha'}.
\end{aligned}
\tag{35}
$$

In the absence of explicit time-dependence in the basis set, Eq. (35) can be rewritten as

$$
\begin{aligned}
\partial_t \rho_{\alpha\alpha'} = & \Bigg[-i\omega_{\alpha\alpha'} - \left(\left\langle \alpha, \mathbf{S}\middle|\frac{\mathrm{d}}{\mathrm{d}t}\middle|\alpha, \mathbf{S}\right\rangle - \left\langle \alpha', \mathbf{S}\middle|\frac{\mathrm{d}}{\mathrm{d}t}\middle|\alpha', \mathbf{S}\right\rangle\right) \\
& - \mathcal{B}^{\mathrm{S}}_{IJ}\frac{\partial H^{\mathrm{S}}_{\alpha\alpha'}}{\partial S_J}\frac{\partial}{\partial S_I}\Bigg]\rho_{\alpha\alpha'}.
\end{aligned}
\tag{36}
$$

Using the Dyson identity, this can be written in propagator form as

$$\rho_{\alpha\alpha'}(t) = \exp\left[-i\int_{t_0}^{t} \mathrm{d}t'\omega_{\alpha\alpha'}(t')\right] \times \exp\left[-\int_{t_0}^{t} \mathrm{d}t'\left(\left\langle \alpha,\mathbf{S}\left|\frac{\mathrm{d}}{\mathrm{d}t'}\right|\alpha,\mathbf{S}\right\rangle - \left\langle \alpha',\mathbf{S}\left|\frac{\mathrm{d}}{\mathrm{d}t'}\right|\alpha',\mathbf{S}\right\rangle\right)\right] \times \exp\left[-(t-t_0)\mathcal{B}^{\ddagger\mathrm{S}}_{IJ}\frac{\partial H^{\mathrm{S}}_{\alpha\alpha'}}{\partial S_J}\frac{\partial}{\partial S_I}\right]\rho_{\alpha\alpha'}(t_0). \tag{37}$$

Equation (37) provides the adiabatic approximation of the quantum–classical Liouville equations in spin baths. The geometric phase arises from the time integral of the term $\langle\alpha,\mathbf{S}|(\mathrm{d}/\mathrm{d}t)|\alpha,\mathbf{S}\rangle - \langle\alpha',\mathbf{S}|(\mathrm{d}/\mathrm{d}t)|\alpha',\mathbf{S}\rangle$, which is purely off-diagonal.

4 Quantum–classical spin model

Consider a quantum two-level system represented by the Pauli matrices

$$\sigma_x = \begin{bmatrix} 0 & 1 \\ 1 & 0 \end{bmatrix}, \quad \sigma_y = \begin{bmatrix} 0 & -i \\ i & 0 \end{bmatrix}, \quad \sigma_z = \begin{bmatrix} 1 & 0 \\ 0 & -1 \end{bmatrix}, \tag{38}$$

and a classical spin with components $\mathbf{S} = (S_x, S_y, S_z)$ immersed in a constant magnetic field $\mathbf{B} = (0, 0, b)$. Hence, consider a model defined by the total Hamiltonian below

$$\begin{aligned}\hat{H}(\mathbf{S}) &= -\Omega\sigma_x - c_1 b\sigma_z - \mu\mathbf{S}\cdot\boldsymbol{\sigma} - c_2 bS_z + \frac{S_z^2}{2} \\ &= \hat{h}(\mathbf{S}) - c_2 bS_z + \frac{S_z^2}{2},\end{aligned} \tag{39}$$

where $\boldsymbol{\sigma} = (\sigma_x, \sigma_y, \sigma_z)$, and c_1, c_2 are coupling coefficients.

Upon defining

$$\gamma = c_1 b + \mu S_z, \tag{40}$$

$$\eta = -\mu S_y, \tag{41}$$

$$\tilde{\Omega} = \Omega + \mu S_x, \tag{42}$$

one can write the eigenvalues of the Hamiltonian (39) as

$$E_1 = +\sqrt{\tilde{\Omega}^2 + \gamma^2 + \eta^2}, \tag{43}$$

$$E_2 = -\sqrt{\tilde{\Omega}^2 + \gamma^2 + \eta^2}, \tag{44}$$

and the eigenvectors as

$$|E_1\rangle = \frac{1}{\sqrt{2(1+|\tilde{G}|^2)}}\begin{pmatrix} 1+\tilde{G}^* \\ \tilde{G}-1 \end{pmatrix}, \tag{45}$$

$$|E_2\rangle = \frac{1}{\sqrt{2(1+|\tilde{G}|^2)}}\begin{pmatrix} 1-\tilde{G}^* \\ 1+\tilde{G} \end{pmatrix}, \tag{46}$$

where $\tilde{G} = G + i\eta/\gamma$, and

$$G = \frac{-\tilde{\Omega} + \sqrt{\tilde{\Omega}^2 + \gamma^2 + \eta^2}}{\gamma}. \tag{47}$$

4.1 Dynamics on the adiabatic surfaces

In a Heisenberg-like picture of the dynamics, quantum–classical operators $\hat{\chi}(\mathbf{S}, t))$, depending on the classical spin coordinates, evolve in time while the density matrix remain stationary. From the equation of motion for the density matrix given in (37), one can easily obtain the evolution equation for the operator in the adiabatic basis. For clarity, it is useful to write explicitly

$$\chi_{\alpha\alpha'}(t) = \exp\left[i\int_{t_0}^{t} \mathrm{d}t'\omega_{\alpha\alpha'}(t')\right] \times \exp\left[\int_{t_0}^{t} \mathrm{d}t'\left(\left\langle \alpha,S\left|\frac{\mathrm{d}}{\mathrm{d}t'}\right|\alpha,S\right\rangle - \left\langle \alpha',S\left|\frac{\mathrm{d}}{\mathrm{d}t'}\right|\alpha',S\right\rangle\right)\right] \times \exp\left[(t-t_0)\mathcal{B}^{\mathrm{S}}_{IJ}\frac{\partial H^{\mathrm{S}}_{\alpha\alpha'}}{\partial S_J}\frac{\partial}{\partial S_I}\right]\chi_{\alpha\alpha'}(t_0). \tag{48}$$

The equation of motion (48) can be simulated on the computer in terms of classical-like trajectories evolving on adiabatic energy surfaces. The classical-like spin Liouville operator defined in (27) determines the equations of motion

$$\dot{S}_x = S_z\frac{\partial H_{\alpha\alpha'}}{\partial S_y} - S_y\frac{\partial H_{\alpha\alpha'}}{\partial S_z}, \tag{49}$$

$$\dot{S}_y = -S_z\frac{\partial H_{\alpha\alpha'}}{\partial S_x} + S_x\frac{\partial H_{\alpha\alpha'}}{\partial S_z}, \tag{50}$$

$$\dot{S}_z = S_y\frac{\partial H_{\alpha\alpha'}}{\partial S_x} - S_x\frac{\partial H_{\alpha\alpha'}}{\partial S_y}, \tag{51}$$

where $H_{\alpha\alpha'}$ are the adiabatic surface Hamiltonians. For the model in Eq. (39), these can be written explicitly as

$$H_{11} = \frac{S_z^2}{2} - c_2 bS_z + \sqrt{\tilde{\Omega}^2 + \gamma^2 + \eta^2}, \tag{52}$$

$$H_{12} = H_{21} = \frac{S_z^2}{2} - c_2 bS_z, \tag{53}$$

$$H_{22} = \frac{S_z^2}{2} - c_2 bS_z - \sqrt{\tilde{\Omega}^2 + \gamma^2 + \eta^2}, \tag{54}$$

where γ, η and $\tilde{\Omega}$ have been defined in Eqs. (40–42).

In order to write explicitly the equations of motion for the spin onto the three energy surfaces, one needs to calculate the derivatives of the Hamiltonians H_{11}, H_{12} and H_{22} with respect to the spin components (S_x, S_y, S_z). On the (1, 1) surface one finds:

$$\frac{\partial H_{11}}{\partial S_x} = \frac{\mu(\Omega + S_x)}{\sqrt{(\Omega + \mu S_x)^2 + \mu^2 S_y^2 + (\mu S_z - c_1 b)^2}}, \tag{55}$$

$$\frac{\partial H_{11}}{\partial S_y} = \frac{\mu^2 S_y}{\sqrt{(\Omega + \mu S_x)^2 + \mu^2 S_y^2 + (\mu S_z - c_1 b)^2}}, \tag{56}$$

$$\frac{\partial H_{11}}{\partial S_z} = S_z - c_2 b + \frac{\mu(b + \mu S_z)}{\sqrt{(\Omega + \mu S_x)^2 + \mu^2 S_y^2 + (\mu S_z - c_1 b)^2}}. \tag{57}$$

On the (1, 2) and (2, 1) surfaces, one finds:

$$\frac{\partial H_{12}}{\partial S_x} = \frac{\partial H_{21}}{\partial S_x} = 0. \tag{58}$$

$$\frac{\partial H_{12}}{\partial S_y} = \frac{\partial H_{21}}{\partial S_y} = 0. \tag{59}$$

$$\frac{\partial H_{12}}{\partial S_z} = \frac{\partial H_{21}}{\partial S_z} = S_z - c_2 b, \tag{60}$$

while on the (2, 2) surface one finds:

$$\frac{\partial H_{22}}{\partial S_x} = -\frac{\mu(\Omega + S_x)}{\sqrt{(\Omega + \mu S_x)^2 + \mu^2 S_y^2 + (\mu S_z - c_1 b)^2}}, \tag{61}$$

$$\frac{\partial H_{22}}{\partial S_y} = -\frac{\mu^2 S_y}{\sqrt{(\Omega + \mu S_x)^2 + \mu^2 S_y^2 + (\mu S_z - c_1 b)^2}}, \tag{62}$$

$$\frac{\partial H_{22}}{\partial S_z} = S_z - c_2 b - \frac{\mu(b + \mu S_z)}{\sqrt{(\Omega + \mu S_x)^2 + \mu^2 S_y^2 + (\mu S_z - c_1 b)^2}}. \tag{63}$$

At this stage, in order to simplify the expression of the gradients of the adiabatic surface Hamiltonians, one can use the identity

$$(\Omega + \mu S_x)^2 + \mu^2 S_y^2 + (\mu S_z - c_1 b)^2 = \Omega^2 + c_1^2 b^2 + 2\mu(\Omega S_x - c_1 b S_z) + \mu^2 \mathbf{S}^2. \tag{64}$$

As a matter of fact, the equations of motion (49–51) conserve the Casimir $\mathbf{S}^2 = S_M S_M$ for an arbitrary Hamiltonian $H_{\alpha\alpha'}$. To see this, one can rewrite the matrix $\boldsymbol{\mathcal{B}}^S$ in Eq. (12) as $\mathcal{B}^S_{IJ} = \epsilon_{IJK} S_K$ (where ϵ_{IJK} is the completely antisymmetric tensor) and obtain

$$\frac{\mathrm{d}}{\mathrm{d}t}\mathbf{S}^2 = \frac{\partial S_M S_M}{\partial S_I}\mathcal{B}^S_{IJ}\frac{\partial H_{\alpha\alpha'}}{\partial S_J} = -2\epsilon_{MJK} S_M S_K \frac{\partial H_{\alpha\alpha'}}{\partial S_J} = 0, \tag{65}$$

where in the last step an odd permutations of the indices of ϵ_{KJM} has been performed. Since $\mathbf{S^2}$ is a constant of motion, one can define

$$C^2 = \Omega^2 + c_1^2 b^2 + \mu^2 \mathbf{S}^2, \tag{66}$$

so that

$$\tilde{\Omega}^2 + \gamma^2 + \eta^2 = C^2 + 2\mu(\Omega S_x - c_1 b S_z). \tag{67}$$

Hence, the derivatives of the adiabatic surfaces can be rewritten as follows. On the (1,1) surface, one has:

$$\frac{\partial H_{11}}{\partial S_x} = \frac{\mu(\Omega + S_x)}{\sqrt{C^2 + 2\mu(\Omega S_x - c_1 b S_z)}}, \tag{68}$$

$$\frac{\partial H_{11}}{\partial S_y} = \frac{\mu^2 S_y}{\sqrt{C^2 + 2\mu(\Omega S_x - c_1 b S_z)}}, \tag{69}$$

$$\frac{\partial H_{11}}{\partial S_z} = S_z - c_2 b + \frac{\mu(b + \mu S_z)}{\sqrt{C^2 + 2\mu(\Omega S_x - c_1 b S_z)}}. \tag{70}$$

On the (1, 2) and (2, 1) surfaces, one has:

$$\frac{\partial H_{12}}{\partial S_x} = \frac{\partial H_{21}}{\partial S_x} = 0, \tag{71}$$

$$\frac{\partial H_{12}}{\partial S_y} = \frac{\partial H_{21}}{\partial S_y} = 0, \tag{72}$$

$$\frac{\partial H_{12}}{\partial S_z} = \frac{\partial H_{21}}{\partial S_z} = S_z - c_2 b, \tag{73}$$

and on the (2, 2) surface, one has:

$$\frac{\partial H_{22}}{\partial S_x} = -\frac{\mu(\Omega + S_x)}{\sqrt{C^2 + 2\mu(\Omega S_x - c_1 b S_z)}}, \tag{74}$$

$$\frac{\partial H_{22}}{\partial S_y} = -\frac{\mu^2 S_y}{\sqrt{C^2 + 2\mu(\Omega S_x - c_1 b S_z)}}, \tag{75}$$

$$\frac{\partial H_{22}}{\partial S_z} = S_z - c_2 b - \frac{\mu(b + \mu S_z)}{\sqrt{C^2 + 2\mu(\Omega S_x - c_1 b S_z)}}. \tag{76}$$

5 Time-reversible integrators

A different set of equations of motion corresponds to each adiabatic energy surface. Hence, one has to find different algorithms of integration on each surface. In the following, the Liouville propagator on each surface is factorized and the associated time-reversible algorithm for the spin dynamics is derived. It is worth noting that within a purely

classical context, other authors have considered alternative schemes of integration [56–58]. At the same time, while what follows is based on the basic symmetric Trotter factorization of the evolution operator, in order to integrate the spin dynamics, one could have used the elegant time-reversible measure-preserving algorithms invented by Ezra [47–49].

5.1 Reversible integrator on the (1, 1) adiabatic surface

The equations of motion on the (1, 1) surface can be written explicitly as

$$\dot{S}_x = \frac{\mu^2 S_y S_z - \mu S_y(b+\mu S_z)}{\sqrt{C^2 + 2\mu(\Omega S_x - c_1 b S_z)}} - S_y(S_z - c_2 b), \tag{77}$$

$$\dot{S}_y = \frac{\mu S_x(b+\mu S_z) - \mu(\Omega + S_x)S_z}{\sqrt{C^2 + 2\mu(\Omega S_x - c_1 b S_z)}} + S_x(S_z - c_2 b), \tag{78}$$

$$\dot{S}_z = \frac{\mu(\Omega + S_x)S_y - \mu^2 S_x S_y}{\sqrt{C^2 + 2\mu(\Omega S_x - c_1 b S_z)}}. \tag{79}$$

From Eqs. (77–79), one can easily find the corresponding Liouville operators

$$L^{S_x}_{1,(1,1)} = \frac{\mu^2 S_y S_z - \mu S_y(b+\mu S_z)}{\sqrt{C^2 + 2\mu(\Omega S_x - c_1 b S_z)}} \frac{\partial}{\partial S_x}, \tag{80}$$

$$L^{S_x}_{2,(1,1)} = -S_y(S_z - c_2 b)\frac{\partial}{\partial S_x}, \tag{81}$$

$$L^{S_y}_{(1,1)} = \left[\frac{\mu S_x(b+\mu S_z) - \mu(\Omega + S_x)S_z}{\sqrt{C^2 + 2\mu(\Omega S_x - c_1 b S_z)}} + S_x(S_z - c_2 b)\right]\frac{\partial}{\partial S_y}, \tag{82}$$

$$L^{S_z}_{(1,1)} = \frac{\mu(\Omega + S_x)S_y - \mu^2 S_x S_y}{\sqrt{C^2 + 2\mu(\Omega S_x - c_1 b S_z)}} \frac{\partial}{\partial S_z}, \tag{83}$$

and the propagators

$$U^{S_x}_{1,(1,1)}(\tau) = \exp\left[\tau \frac{\mu^2 S_y S_z - \mu S_y(b+\mu S_z)}{\sqrt{C^2 + 2\mu(\Omega S_x - c_1 b S_z)}} \frac{\partial}{\partial S_x}\right], \tag{84}$$

$$U^{S_x}_{2,(1,1)}(\tau) = \exp\left[-\tau S_y(S_z - c_2 b)\frac{\partial}{\partial S_x}\right], \tag{85}$$

$$U^{S_y}_{(1,1)}(\tau) = \exp\left\{\tau\left[\frac{\mu S_x(b+\mu S_z) - \mu(\Omega + S_x)S_z}{\sqrt{C^2 + 2\mu(\Omega S_x - c_1 b S_z)}} + S_x(S_z - c_2 b)\right]\frac{\partial}{\partial S_y}\right\}, \tag{86}$$

$$U^{S_z}_{(1,1)}(\tau) = \exp\left[\tau \frac{\mu(\Omega + S_x)S_y - \mu^2 S_x S_y}{\sqrt{C^2 + 2\mu(\Omega S_x - c_1 b S_z)}} \frac{\partial}{\partial S_z}\right]. \tag{87}$$

The action of $U^{S_x}_{1,(1,1)}(\tau) = \exp[\tau L^{S_x}_{1,(1,1)}]$ on S_x can be found by means of the analytical integration of the equation of motion associated with the Liouville operator $L^{S_x}_{1,(1,1)}$ in Eq. (80). In pseudo-code form, one obtains

$$U^{S_x}_{1,(1,1)}(\tau): \begin{cases} S_x \rightarrow \frac{1}{C_1}\left\{\frac{3}{2}C_1 C_3 \tau + [C_2 + C_1 S_x(0)]^{\frac{3}{2}}\right\}^{\frac{2}{3}} \\ -\frac{C_2}{C_1}, \end{cases} \tag{88}$$

where

$$C_1 = 2\mu\Omega, \tag{89}$$

$$C_2 = C^2 - 2\mu c_1 b S_z, \tag{90}$$

$$C_3 = \mu^2 S_y S_z - \mu S_y(b + \mu S_z). \tag{91}$$

The actions of $U^{S_x}_{2,(1,1)}(\tau) = \exp[\tau L^{S_x}_{2,(1,1)}]$ and $U^{S_y}_{(1,1)}(\tau) = \exp[\tau L^{S_y}_{(1,1)}]$ on S_x and S_y, respectively, are simple variable shifts which can be written in pseudo-code form as

$$U^{S_x}_{2,(1,1)}(\tau): \{S_x \rightarrow S_x - \tau S_y(S_z - c_2 b), \tag{92}$$

$$U^{S_y}_{(1,1)}(\tau): \begin{cases} S_y \rightarrow S_y + \tau\left[\frac{\mu S_x(b+\mu S_z) - \mu(\Omega + S_x)S_z}{\sqrt{C^2 + 2\mu(\Omega S_x - c_1 b S_z)}} + S_x(S_z - c_2 b)\right]. \end{cases} \tag{93}$$

The action of $U^{S_z}_{(1,1)}(\tau) = \exp[\tau L^{S_z}_{(1,1)}]$ on S_z can also be determined by the analytical integration of the corresponding equation of motion

$$\dot{S}_z = \frac{\mu(\Omega + S_x)S_y - \mu^2 S_x S_y}{\sqrt{C^2 + 2\mu(\Omega S_x - c_1 b S_z)}} = \frac{B_3}{\sqrt{B_2 - B_1 S_z}}, \tag{94}$$

where one has defined

$$B_1 = 2\mu c_1 b, \tag{95}$$

$$B_2 = C^2 + 2\mu\Omega S_x, \tag{96}$$

$$B_3 = \mu(\Omega + S_x)S_y - \mu^2 S_x S_y. \tag{97}$$

One finds

$$U^{S_z}_{(1,1)}(\tau): \begin{cases} S_z \rightarrow \frac{B_2}{B_1} \\ -\frac{1}{B_1}\left\{[B_2 - B_1 S_z]^{\frac{3}{2}} - \frac{3B_1 B_3 \tau}{2}\right\}^{\frac{2}{3}}. \end{cases} \tag{98}$$

Finally, one can consider three propagators on the (1, 1) surface:

$$U^1_{(1,1)}(\tau) = U^{S_x}_{1,(1,1)}\left(\frac{\tau}{4}\right) U^{S_x}_{2,(1,1)}\left(\frac{\tau}{2}\right) U^{S_x}_{1,(1,1)}\left(\frac{\tau}{4}\right) \times U^{S_y}_{(1,1)}\left(\frac{\tau}{2}\right) U^{S_z}_{(1,1)}(\tau) U^{S_y}_{(1,1)}\left(\frac{\tau}{2}\right) \times U^{S_x}_{1,(1,1)}\left(\frac{\tau}{4}\right) U^{S_x}_{2,(1,1)}\left(\frac{\tau}{2}\right) U^{S_x}_{1,(1,1)}\left(\frac{\tau}{4}\right), \tag{99}$$

$$U^2_{(1,1)}(\tau) = U^{S_z}_{(1,1)}\left(\frac{\tau}{2}\right) U^{S_x}_{1,(1,1)}\left(\frac{\tau}{4}\right) U^{S_x}_{2,(1,1)}\left(\frac{\tau}{2}\right) \times U^{S_x}_{1,(1,1)}\left(\frac{\tau}{4}\right) U^{S_y}_{(1,1)}(\tau) U^{S_x}_{1,(1,1)}\left(\frac{\tau}{4}\right) \times U^{S_x}_{2,(1,1)}\left(\frac{\tau}{2}\right) U^{S_x}_{1,(1,1)}\left(\frac{\tau}{4}\right) U^{S_z}_{(1,1)}\left(\frac{\tau}{2}\right), \tag{100}$$

$$U^3_{(1,1)}(\tau) = U^{S_y}_{(1,1)}\left(\frac{\tau}{4}\right) U^{S_z}_{(1,1)}\left(\frac{\tau}{2}\right) U^{S_y}_{(1,1)}\left(\frac{\tau}{4}\right) \times U^{S_x}_{1,(1,1)}\left(\frac{\tau}{2}\right) U^{S_x}_{2,(1,1)}(\tau) U^{S_x}_{1,(1,1)}\left(\frac{\tau}{2}\right) \times U^{S_y}_{(1,1)}\left(\frac{\tau}{4}\right) U^{S_z}_{(1,1)}\left(\frac{\tau}{2}\right) U^{S_y}_{(1,1)}\left(\frac{\tau}{4}\right), \tag{101}$$

and write the corresponding integration algorithm. Each of the three propagators $U^k_{(1,1)}(\tau), k = 1, \ldots, 3$, can be used to obtain a different propagation algorithm. In order to obtain a more uniform sampling of phase space, one can also act with a different $U^k_{(1,1)}(\tau)$ at each successive time step τ.

5.2 Reversible integrator on the (2, 2) adiabatic surface

The equations of motion on the (2, 2) surface are

$$\dot{S}_x = \frac{\mu S_y(b + \mu S_z) - \mu^2 S_y S_z}{\sqrt{C^2 + 2\mu(\Omega S_x - c_1 b S_z)}} - S_y(S_z - c_2 b), \tag{102}$$

$$\dot{S}_y = \frac{\mu(\Omega + S_x)S_z - \mu S_x(b + \mu S_z)}{\sqrt{C^2 + 2\mu(\Omega S_x - c_1 b S_z)}} + S_x(S_z - c_2 b), \tag{103}$$

$$\dot{S}_z = \frac{\mu^2 S_x S_y - \mu(\Omega + S_x)S_y}{\sqrt{C^2 + 2\mu(\Omega S_x - c_1 b S_z)}}. \tag{104}$$

From Eqs. (102–104), one can easily write the corresponding Liouville operators

$$L^{S_x}_{1,(2,2)} = -\frac{C_3}{\sqrt{C_2 + C_1 S_x}} \frac{\partial}{\partial S_x}, \tag{105}$$

$$L^{S_x}_{2,(2,2)} = -S_y(S_z - c_2 b)\frac{\partial}{\partial S_x}, \tag{106}$$

$$L^{S_y}_{(2,2)} = \left[\frac{\mu(\Omega + S_x)S_z - \mu S_x(b + \mu S_z)}{\sqrt{C^2 + 2\mu(\Omega S_x - c_1 b S_z)}} + S_x(S_z - c_2 b)\right]\frac{\partial}{\partial S_y}, \tag{107}$$

$$L^{S_z}_{(2,2)} = -\frac{B_3}{\sqrt{B_2 - B_1 S_z}} \frac{\partial}{\partial S_z}, \tag{108}$$

where C_1, C_2, C_3 have been defined in Eqs. (89–91) and B_1, B_2, B_3 have been defined in Eqs. (95–97). The propagators for the (2, 2) adiabatic surface can be written as

$$U^{S_x}_{1,(2,2)}(\tau) = \exp\left[-\tau \frac{C_3}{\sqrt{C_2 + C_1 S_x}} \frac{\partial}{\partial S_x}\right], \tag{109}$$

$$U^{S_x}_{2,(2,2)}(\tau) = \exp\left[-\tau S_y(S_z - c_2 b)\frac{\partial}{\partial S_x}\right], \tag{110}$$

$$U^{S_y}_{(2,2)}(\tau) = \exp\left\{\tau\left[\frac{\mu(\Omega + S_x)S_z - \mu S_x(b + \mu S_z)}{\sqrt{C^2 + 2\mu(\Omega S_x - c_1 b S_z)}} + S_x(S_z - c_2 b)\right]\frac{\partial}{\partial S_y}\right\}, \tag{111}$$

$$U^{S_z}_{(2,2)}(\tau) = \exp\left[-\tau \frac{B_3}{\sqrt{B_2 - B_1 S_z}} \frac{\partial}{\partial S_z}\right], \tag{112}$$

where C_1, C_2, C_3 have been defined in Eqs. (89–91) and B_1, B_2, B_3 have been defined in Eqs. (95–97).

The action of $U^{S_x}_{1,(2,2)}(\tau) = \exp[L^{S_x}_{1,(2,2)}]$ on S_x is determined by integrating analytically the equation of motion associated with the Liouville operator in (105). In pseudo-code form, such action can be written as

$$U^{S_x}_{1,(2,2)}(\tau): \begin{cases} S_x \rightarrow \frac{1}{C_1}\left[-\frac{3}{2}C_1 C_3 \tau + (C_2 + C_1 S_x)^{3/2}\right]^{2/3} \\ \quad -\frac{C_2}{C_1}. \end{cases} \tag{113}$$

Similarly, the action of $U^{S_z}_{(2,2)}(\tau) = \exp[L^{S_z}_{(2,2)}]$ on S_z is determined by integrating analytically the equation of motion associated with the Liouville operator in (108):

$$U^{S_z}_{(2,2)}(\tau): \left\{ S_z \rightarrow \frac{B_2}{B_1} - \frac{1}{B_1}\left[(B_2 - B_1 S_z)^{\frac{3}{2}} + \frac{3}{2}B_1 B_3 \tau\right]^{\frac{2}{3}}. \right. \tag{114}$$

The propagators $U^{S_y}_{(2,2)}(\tau)$ and $U^{S_z}_{(2,2)}(\tau)$ generate simple time shifts of the appropriate spin coordinates:

$$U^{S_x}_{2,(2,2)}(\tau): \{S_x \rightarrow S_x - \tau S_y(S_z - c_2 b). \tag{115}$$

$$U^{S_y}_{(2,2)}(\tau): \begin{cases} S_y \rightarrow S_y + \tau\left[\frac{\mu(\Omega + S_x)S_z - \mu S_x(b + \mu S_z)}{\sqrt{C^2 + 2\mu(\Omega S_x - c_1 b S_z)}} + S_x(S_z - c_2 b)\right]. \end{cases} \tag{116}$$

Finally, one can consider the following three propagators on the (2, 2) surface:

$$U^1_{(2,2)}(\tau) = U^{S_x}_{1,(2,2)}\left(\frac{\tau}{4}\right) U^{S_x}_{2,(2,2)}\left(\frac{\tau}{2}\right) U^{S_x}_{1,(2,2)}\left(\frac{\tau}{4}\right) \times U^{S_y}_{(2,2)}\left(\frac{\tau}{2}\right) U^{S_z}_{(2,2)}(\tau) U^{S_y}_{(2,2)}\left(\frac{\tau}{2}\right) \times U^{S_x}_{1,(2,2)}\left(\frac{\tau}{4}\right) U^{S_x}_{2,(2,2)}\left(\frac{\tau}{2}\right) U^{S_x}_{1,(2,2)}\left(\frac{\tau}{4}\right), \quad (117)$$

$$U^2_{(2,2)}(\tau) = U^{S_z}_{(2,2)}\left(\frac{\tau}{2}\right) U^{S_x}_{1,(2,2)}\left(\frac{\tau}{4}\right) U^{S_x}_{2,(2,2)}\left(\frac{\tau}{2}\right) \times U^{S_x}_{1,(2,2)}\left(\frac{\tau}{4}\right) U^{S_y}_{(2,2)}(\tau) U^{S_x}_{1,(2,2)}\left(\frac{\tau}{4}\right) \times U^{S_x}_{2,(2,2)}\left(\frac{\tau}{2}\right) U^{S_x}_{1,(2,2)}\left(\frac{\tau}{4}\right) U^{S_z}_{(2,2)}\left(\frac{\tau}{2}\right), \quad (118)$$

$$U^3_{(2,2)}(\tau) = U^{S_y}_{(2,2)}\left(\frac{\tau}{4}\right) U^{S_z}_{(2,2)}\left(\frac{\tau}{2}\right) U^{S_y}_{(2,2)}\left(\frac{\tau}{4}\right) \times U^{S_x}_{1,(2,2)}\left(\frac{\tau}{2}\right) U^{S_x}_{2,(2,2)}(\tau) U^{S_x}_{1,(2,2)}\left(\frac{\tau}{2}\right) \times U^{S_y}_{(2,2)}\left(\frac{\tau}{4}\right) U^{S_z}_{(2,2)}\left(\frac{\tau}{2}\right) U^{S_y}_{(2,2)}\left(\frac{\tau}{4}\right), \quad (119)$$

These allow one to find the algorithm of propagation on the (2, 2) surface. Each of the three propagators $U^k_{(2,2)}(\tau)$, $k = 1, \ldots, 3$, can be used to obtain a different propagation algorithm. In order to obtain a more uniform sampling of phase space, one can also act with a different $U^k_{(2,2)}(\tau)$ at each successive time step τ.

5.3 Reversible integrators on the (1, 2) adiabatic surface

The equations of motion on the (1, 2) adiabatic energy surface are

$$\dot{S}_x = -S_y(S_z - c_2 b), \quad (120)$$

$$\dot{S}_y = S_x(S_z - c_2 b), \quad (121)$$

$$\dot{S}_z = 0. \quad (122)$$

They are identical to the equations of motion on the (2, 1) energy surface. The Liouville operators associated with the Eqs. (120) and (121) are:

$$L^{S_x}_{(1,2)} = -S_y(S_z - c_2 b)\frac{\partial}{\partial S_x}, \quad (123)$$

$$L^{S_y}_{(1,2)} = S_x(S_z - c_2)\frac{\partial}{\partial S_y}. \quad (124)$$

The associated propagators are:

$$U^{S_x}_{(1,2)}(\tau) = \exp\left[-\tau S_y(S_z - c_2 b)\frac{\partial}{\partial S_x}\right], \quad (125)$$

$$U^{S_y}_{(1,2)}(\tau) = \exp\left[\tau S_x(S_z - c_2 b)\frac{\partial}{\partial S_y}\right]. \quad (126)$$

Finally, one can consider the following total propagators on the (1, 2) surface:

$$U^1_{(1,2)}(\tau) = U^{S_x}_{(1,2)}\left(\frac{\tau}{2}\right) U^{S_y}_{(1,2)}(\tau) U^{S_x}_{(1,2)}\left(\frac{\tau}{2}\right), \quad (127)$$

$$U^2_{(1,2)}(\tau) = U^{S_y}_{(1,2)}\left(\frac{\tau}{2}\right) U^{S_x}_{(1,2)}(\tau) U^{S_y}_{(1,2)}\left(\frac{\tau}{2}\right), \quad (128)$$

and easily write the algorithm of integration. Each of the two propagators $U^k_{(1,2)}(\tau), k = 1, 2$, can be used to obtain a different propagation algorithm. In order to obtain a more uniform sampling of phase space, one can also act with a different $U^k_{(1,2)}(\tau)$ at each successive time step τ.

6 Numerical results

In order to analyze the quantum dynamics of the model, one can calculate averages in the Heisenberg-like picture:

$$\langle \hat{\chi} \rangle_t = \sum_{\alpha\alpha'} \int \mathrm{d}^3\mathbf{S}\, \rho_{\alpha\alpha'}(\mathbf{S}) \chi_{\alpha'\alpha}(\mathbf{S}, t) \quad (129)$$

where $\hat{\chi}(\mathbf{S}, t)$ is the chosen observable (which is evolved in time), also depending on the classical spin coordinates $\mathbf{S} = (S_x, S_y, S_z)$, and $\mathrm{d}^3\mathbf{S} = \mathrm{d}S_x \mathrm{d}S_y \mathrm{d}S_z$. For the sake of illustrating the integration algorithms derived in Sect. 5, it is assumed that at time $t = 0$, the spin and the quantum systems are decoupled so that the initial density matrix is

$$\hat{\rho}(\mathbf{S}) = \hat{\rho}_\mathrm{s} \otimes \sqrt{\frac{\beta}{2\pi}} \exp[-\beta S_z^2], \quad (130)$$

where $\hat{\rho}_\mathrm{s}$ is the density matrix of the isolated quantum subsystem. In order to study the evolution of both the population difference between the excited and ground state of the model and the coherence of the initial superposition between such states, it is assumed that the quantum subsystem is in a superposition of states at $t = 0$ that is represented in the basis of σ_z by the state vector

$$|\Psi\rangle = \frac{\sqrt{5}}{5}[2|1\rangle - |2\rangle]. \quad (131)$$

The associated density matrix has components

$$\boldsymbol{\rho}_\mathrm{s} = \begin{bmatrix} 4/5 & -2/5 \\ -2/5 & 1/5 \end{bmatrix}. \quad (132)$$

According to such choices, the dynamics will display both population and coherence oscillations.

The density matrix in the adiabatic basis takes the form

$$\boldsymbol{\rho}^\mathrm{ad}_\mathrm{s} = \frac{1}{\mathcal{N}} \begin{bmatrix} \rho_{11} & \rho_{12} \\ \rho^*_{12} & \rho_{22} \end{bmatrix}, \quad (133)$$

where, using the definition of G given in Eq. (47),

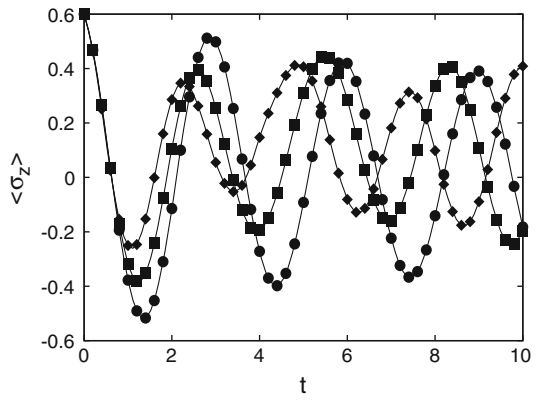

Fig. 1 Time evolution of the population difference $\langle\sigma_z(t)\rangle$ for $\beta = 0.3, \Omega = 1, b = 1, c_1 = 0.01, c_2 = 0.1$. The coefficient μ takes the values 0.25, 0.5 and 0.74 for *black circles*, *squares* and *diamonds*, respectively. The *lines* are drawn to help the eye

$$\rho_{11} = \frac{1}{5}\left[\frac{9\eta^2}{\gamma^2} + (3+G)^2\right], \tag{134}$$

$$\rho_{22} = \frac{1}{5}\left[\frac{\eta^2}{\gamma^2} + (1-G)^2\right], \tag{135}$$

$$\rho_{12} = -\frac{[3i\eta + \gamma(3+G)][-i\eta + \gamma(-1+3G)]}{5\gamma^2}, \tag{136}$$

$$\mathcal{N} = 2(1 + G^2 + \eta^2/\gamma^2). \tag{137}$$

One can use spherical coordinates

$$S_x = S\sin(\theta)\cos(\phi) \tag{138}$$

$$S_y = S\sin(\phi)\sin(\theta) \tag{139}$$

$$S_z = S\cos(\theta) \tag{140}$$

in order to sample the Boltzmann weight on S_z as

$$\exp\left[-\beta\frac{S_z^2}{2}\right] = \exp\left[-\beta\frac{\cos^2\theta}{2}\right] \tag{141}$$

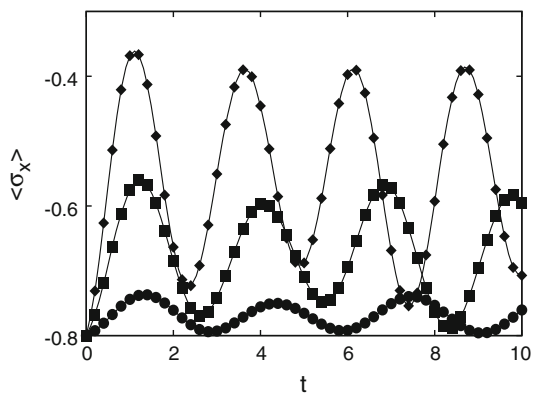

Fig. 2 Time evolution of the coherence $\langle\sigma_x(t)\rangle$ for $\beta = 0.3, \Omega = 1, b = 1, c_1 = 0.01, c_2 = 0.1$. The coefficient μ takes the values 0.25, 0.5 and 0.74 for *black circles*, *squares* and *diamonds*, respectively. The *lines* are drawn to help the eye

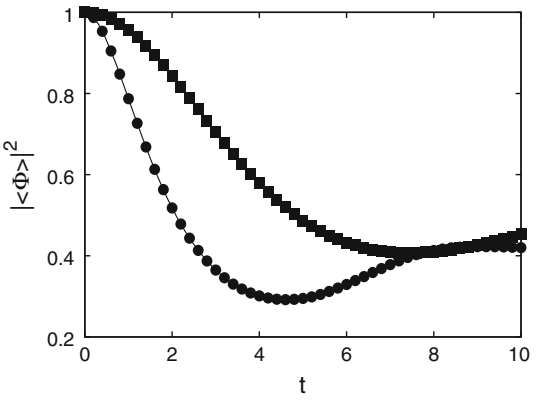

Fig. 3 Time evolution of the modulus square of the average phase for $\beta = 0.3, \Omega = 1, b = 1, c_1 = 0.01, c_2 = 0.1, \mu = 0.25$; the *black circles* denote the results for the geometric phase while the *black squares* denote the results for the Bohr phase

by sampling $\cos(\theta)$ uniformly between $(-1, 1)$ and to sample the angle ϕ uniformly between $(0, 2\pi)$.

The observables $\sigma_z(\mathbf{S}, t)$ and $\sigma_x(\mathbf{S}, t)$ are evolved in the adiabatic basis, and the calculation of their trace, according to Eq. (129), provides the population and the coherence evolution, respectively.

Calculations were performed for $\beta = 0.3, \Omega = 1, b = 1$, $c_1 = 0.01, c_2 = 0.1$. The coefficient μ was varied and took the values 0.25, 0.5 and 0.74. The values of the parameters are given in dimensionless units. Figure 1 shows the behavior of the population as a function of time when the coupling μ is varied. The damping increases as the coupling increases. Figure 2 displays the time evolution of the coherence when the coupling is varied. The coherence oscillations are greater for greater coupling. Since the two-level system is coupled to a single rotating classical spin, no real dissipation is expected

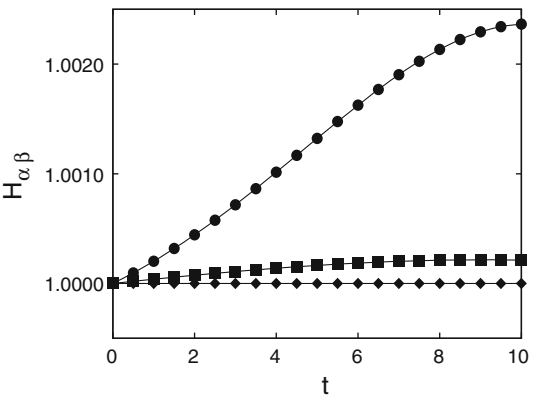

Fig. 4 Adiabatic surface Hamiltonians versus time. The *black circles* denote the curve for $\alpha = 1$ and $\beta = 1$ (excited state dynamics); the *square* denote the curve for $\alpha = 2$ and $\beta = 2$ (ground state dynamics) while the *black diamonds* denote the curve $\alpha = 1$ and $\beta = 2$ (mean surface dynamics). The *continues line* are for helping the eye. The parameters specifying the calculations are $\beta = 0.3, \Omega = 1,\ b = 1$, $c_1 = 0.01, c_2 = 0.1, \mu = 0.75$. The *black circles* denote the results for the geometric phase while the *black*

when monitoring the dynamics of the two-level system only. In Fig. 3, the time evolution of the moduli square of the average of the Bohr and geometric phases is shown. No major geometric effect was expected for the model studied. Finally, the stability of the integration algorithm introduced in Sect. (5) is illustrated in Fig. 4. A numerical integration time step $\tau = 0.001$ (in dimensionless units) was used in all the calculation performed. The Trotter symmetric factorization discussed in Sect. (5) was combined with a fifth-order Yoshida scheme [59]. As expected, the more stable numerical integration is achieved on the (1, 2) mean energy surface. This arises from the absence of quantum effects on the mean surface of the model in Eq. (39). As quantum effects increase, going from the ground state (2, 2) to the excited state (1, 1), the stability of the numerical integration somewhat diminishes but remains satisfactory over the whole time interval explored. The numerical conservation of the spin modulus is almost perfect on all the three adiabatic energy surfaces.

7 Conclusions and perspectives

In this paper, a formalism for studying the dynamics of quantum systems coupled to classical spin environments has been reviewed. The theory is based on generalized antisymmetric brackets and naturally predicts the existence of open-path off-diagonal geometric phases in the dynamics of the density matrix. It has also been shown that such geometric phases must be considered in the quantum–classical Liouville equation, expressed by means of canonical phase space coordinates, whenever the adiabatics basis is complex (as in the case of a magnetic field coupled to the quantum subsystem).

When the quantum subsystem is weakly coupled to the spin environment, non-adiabatic transitions can be neglected. In such a case, one can construct an effective non-Markovian computer simulation scheme for open quantum system dynamics in a classical spin environment. In this paper, a detailed derivation of integration algorithms based on the symmetric Trotter factorization of the classical-like spin propagator has been given. Such algorithms have been applied to a model system comprising a quantum two-level system coupled to a single classical spin in an external magnetic field. The numerical integration conserves the spin modulus perfectly and the spin energy satisfactorily during the entire time interval explored. Starting from an excited state, the population difference and the coherences of the two-state model have been simulated and studied in function of the strength of the coupling parameter between the spin and the two-level system.

One could look at the numerical evidence provided in this paper as a first step toward developing the simulation schemes for quantum dynamics in classical spin environments into an effective tool for studying systems of interest in nanoscience.

Acknowledgments The author is grateful to G. S. Ezra for many discussions, encouragement and support received in the past few years.

Appendix 1: Integration algorithm on the (1, 1) surface

In pseudo-code form, the algorithm provided by $U^{1}_{(1,1)}(\tau)$ is:

$$U^{S_x}_{1,(1,1)}\left(\frac{\tau}{4}\right): \begin{cases} S_x \to \frac{1}{C_1}\left\{\frac{3}{2}C_1C_3\frac{\tau}{4} + [C_2 + C_1S_x]^{\frac{3}{2}}\right\}^{\frac{2}{3}} \\ \quad -\frac{C_2}{C_1}, \end{cases} \tag{142}$$

$$U^{S_x}_{2,(1,1)}\left(\frac{\tau}{2}\right): \left\{S_x \to S_x - \frac{\tau}{2}S_y(S_z - c_2b), \right. \tag{143}$$

$$U^{S_x}_{1,(1,1)}\left(\frac{\tau}{4}\right): \begin{cases} S_x \to \frac{1}{C_1}\left\{\frac{3}{2}C_1C_3\frac{\tau}{4} + [C_2 + C_1S_x]^{\frac{3}{2}}\right\}^{\frac{2}{3}} \\ \quad -\frac{C_2}{C_1}, \end{cases} \tag{144}$$

$$U^{S_y}_{(1,1)}\left(\frac{\tau}{2}\right): \begin{cases} S_y \to S_y + \frac{\tau}{2}\left[\frac{\mu S_x(b+\mu S_z) - \mu(\Omega + S_x)S_z}{\sqrt{C^2 + 2\mu(\Omega S_x - c_1bS_z)}}\right. \\ \qquad \left. + S_x(S_z - c_2b)\right], \end{cases} \tag{145}$$

$$U^{S_z}_{(1,1)}(\tau): \begin{cases} S_z \to \frac{B_2}{B_1} - \frac{1}{B_1}\left[(B_2 - B_1S_z)^{\frac{3}{2}}\right. \\ \qquad \left. - \frac{3B_1B_3\tau}{2}\right]^{\frac{2}{3}}, \end{cases} \tag{146}$$

$$U^{S_y}_{(1,1)}\left(\frac{\tau}{2}\right): \begin{cases} S_y \to S_y + \frac{\tau}{2}\left[\frac{\mu S_x(b+\mu S_z) - \mu(\Omega + S_x)S_z}{\sqrt{C^2 + 2\mu(\Omega S_x - c_1bS_z)}}\right. \\ \qquad \left. + S_x(S_z - c_2b)\right], \end{cases} \tag{147}$$

$$U^{S_x}_{2,(1,1)}\left(\frac{\tau}{2}\right): \left\{S_x \to S_x - \frac{\tau}{2}S_y(S_z - c_2b), \right. \tag{148}$$

$$U^{S_x}_{1,(1,1)}\left(\frac{\tau}{4}\right):\begin{cases} S_x \to \frac{1}{C_1}\left\{\frac{3}{2}C_1C_3\frac{\tau}{4}+[C_2+C_1S_x]^{\frac{3}{2}}\right\}^{\frac{2}{3}} \\ \quad -\frac{C_2}{C_1}, \end{cases} \tag{149}$$

$$U^{S_x}_{1,(1,1)}\left(\frac{\tau}{4}\right):\begin{cases} S_x \to \frac{1}{C_1}\left\{\frac{3}{2}C_1C_3\frac{\tau}{4}+[C_2+C_1S_x]^{\frac{3}{2}}\right\}^{\frac{2}{3}} \\ \quad -\frac{C_2}{C_1}. \end{cases} \tag{150}$$

The algorithm provided by $U^2_{(1,1)}(\tau)$ is:

$$U^{S_z}_{(1,1)}\left(\frac{\tau}{2}\right):\begin{cases} S_z \to \frac{B_2}{B_1} \\ \quad -\frac{1}{B_1}\left\{[B_2-B_1S_z]^{\frac{3}{2}}-\frac{3B_1B_3\tau}{4}\right\}^{\frac{2}{3}}, \end{cases} \tag{151}$$

$$U^{S_x}_{1,(1,1)}\left(\frac{\tau}{4}\right):\begin{cases} S_x \to \frac{1}{C_1}\left\{\frac{3}{2}C_1C_3\frac{\tau}{4}+[C_2+C_1S_x]^{\frac{3}{2}}\right\}^{\frac{2}{3}} \\ \quad -\frac{C_2}{C_1}, \end{cases} \tag{152}$$

$$U^{S_x}_{2,(1,1)}\left(\frac{\tau}{2}\right):\left\{S_x \to S_x-\frac{\tau}{2}S_y(S_z-c_2b), \right. \tag{153}$$

$$U^{S_x}_{1,(1,1)}\left(\frac{\tau}{4}\right):\begin{cases} S_x \to \frac{1}{C_1}\left\{\frac{3}{2}C_1C_3\frac{\tau}{4}+[C_2+C_1S_x]^{\frac{3}{2}}\right\}^{\frac{2}{3}} \\ \quad -\frac{C_2}{C_1}, \end{cases} \tag{154}$$

$$U^{S_y}_{(1,1)}(\tau):\begin{cases} S_y \to S_y+\tau\left[\frac{\mu S_x(b+\mu S_z)-\mu(\Omega+S_x)S_z}{\sqrt{C^2+2\mu(\Omega S_x-c_1bS_z)}}\right. \\ \qquad\qquad \left.+S_x(S_z-c_2b)\right], \end{cases} \tag{155}$$

$$U^{S_x}_{1,(1,1)}\left(\frac{\tau}{4}\right):\begin{cases} S_x \to \frac{1}{C_1}\left\{\frac{3}{2}C_1C_3\frac{\tau}{4}+[C_2+C_1S_x]^{\frac{3}{2}}\right\}^{\frac{2}{3}} \\ \quad -\frac{C_2}{C_1}, \end{cases} \tag{156}$$

$$U^{S_x}_{2,(1,1)}\left(\frac{\tau}{2}\right):\left\{S_x \to S_x-\frac{\tau}{2}S_y(S_z-c_2b), \right. \tag{157}$$

$$U^{S_x}_{1,(1,1)}\left(\frac{\tau}{4}\right):\begin{cases} S_x \to \frac{1}{C_1}\left\{\frac{3}{2}C_1C_3\frac{\tau}{4}+[C_2+C_1S_x]^{\frac{3}{2}}\right\}^{\frac{2}{3}} \\ \quad -\frac{C_2}{C_1}, \end{cases} \tag{158}$$

$$U^{S_z}_{(1,1)}\left(\frac{\tau}{2}\right):\begin{cases} S_z \to \frac{B_2}{B_1} \\ \quad -\frac{1}{B_1}\left\{[B_2-B_1S_z]^{\frac{3}{2}}-\frac{3B_1B_3\tau}{4}\right\}^{\frac{2}{3}}. \end{cases} \tag{159}$$

The algorithm provided by $U^3_{(1,1)}(\tau)$ is:

$$U^{S_y}_{(1,1)}\left(\frac{\tau}{4}\right):\begin{cases} S_y \to S_y+\frac{\tau}{4}\left[\frac{\mu S_x(b+\mu S_z)-\mu(\Omega+S_x)S_z}{\sqrt{C^2+2\mu(\Omega S_x-c_1bS_z)}}\right. \\ \qquad\qquad \left.+S_x(S_z-c_2b)\right], \end{cases} \tag{160}$$

$$U^{S_z}_{(1,1)}\left(\frac{\tau}{2}\right):\begin{cases} S_z \to \frac{B_2}{B_1} \\ \quad -\frac{1}{B_1}\left[(B_2-B_1S_z)^{\frac{3}{2}}-\frac{3B_1B_3\tau}{4}\right]^{\frac{2}{3}}, \end{cases} \tag{161}$$

$$U^{S_y}_{(1,1)}\left(\frac{\tau}{4}\right):\begin{cases} S_y \to S_y+\frac{\tau}{4}\left[\frac{\mu S_x(b+\mu S_z)-\mu(\Omega+S_x)S_z}{\sqrt{C^2+2\mu(\Omega S_x-c_1bS_z)}}\right. \\ \qquad\qquad \left.+S_x(S_z-c_2b)\right], \end{cases} \tag{162}$$

$$U^{S_x}_{1,(1,1)}\left(\frac{\tau}{2}\right):\begin{cases} S_x \to \frac{1}{C_1}\left\{\frac{3}{2}C_1C_3\frac{\tau}{2}+[C_2+C_1S_x]^{\frac{3}{2}}\right\}^{\frac{2}{3}} \\ \quad -\frac{C_2}{C_1}, \end{cases} \tag{163}$$

$$U^{S_x}_{2,(1,1)}(\tau):\left\{S_x \to S_x-\tau S_y(S_z-c_2b), \right. \tag{164}$$

$$U^{S_x}_{1,(1,1)}\left(\frac{\tau}{2}\right):\begin{cases} S_x \to \frac{1}{C_1}\left\{\frac{3}{2}C_1C_3\frac{\tau}{2}+[C_2+C_1S_x]^{\frac{3}{2}}\right\}^{\frac{2}{3}} \\ \quad -\frac{C_2}{C_1}, \end{cases} \tag{165}$$

$$U^{S_y}_{(1,1)}\left(\frac{\tau}{4}\right):\begin{cases} S_y \to S_y+\frac{\tau}{4}\left[\frac{\mu S_x(b+\mu S_z)-\mu(\Omega+S_x)S_z}{\sqrt{C^2+2\mu(\Omega S_x-c_1bS_z)}}\right. \\ \qquad\qquad \left.+S_x(S_z-c_2b)\right], \end{cases} \tag{166}$$

$$U^{S_z}_{(1,1)}\left(\frac{\tau}{2}\right):\begin{cases} S_z \to \dfrac{B_2}{B_1} \\ \quad -\dfrac{1}{B_1}\left[(B_2 - B_1 S_z)^{\frac{3}{2}} - \dfrac{3B_1B_3\tau}{4}\right]^{\frac{2}{3}}, \end{cases} \tag{167}$$

$$U^{S_y}_{(1,1)}\left(\frac{\tau}{4}\right):\begin{cases} S_y \to S_y + \dfrac{\tau}{4}\left[\dfrac{\mu S_x(b+\mu S_z) - \mu(\Omega + S_x)S_z}{\sqrt{C^2 + 2\mu(\Omega S_x - c_1 b S_z)}}\right. \\ \qquad\qquad \left. + S_x(S_z - c_2 b)\right]. \end{cases} \tag{168}$$

Appendix 2: Integration algorithm on the (2, 2) surface

The algorithm provided by $U^1_{(2,2)}(\tau)$ is

$$U^{S_x}_{1,(2,2)}\left(\frac{\tau}{4}\right):\begin{cases} S_x \to \dfrac{1}{C_1}\left[-\dfrac{3}{2}C_1C_3\dfrac{\tau}{4} + (C_2 + C_1S_x)^{\frac{3}{2}}\right]^{\frac{2}{3}} \\ \quad -\dfrac{C_2}{C_1}, \end{cases} \tag{169}$$

$$U^{S_x}_{2,(2,2)}\left(\frac{\tau}{2}\right):\left\{S_x \to S_x - \frac{\tau}{2}S_y(S_z - c_2 b), \right. \tag{170}$$

$$U^{S_x}_{1,(2,2)}\left(\frac{\tau}{4}\right):\begin{cases} S_x \to \dfrac{1}{C_1}\left[-\dfrac{3}{2}C_1C_3\dfrac{\tau}{4} + (C_2 + C_1S_x)^{\frac{3}{2}}\right]^{\frac{2}{3}} \\ \quad -\dfrac{C_2}{C_1}, \end{cases} \tag{171}$$

$$U^{S_y}_{(2,2)}\left(\frac{\tau}{2}\right):\begin{cases} S_y \to S_y + \dfrac{\tau}{2}\left[\dfrac{\mu(\Omega + S_x)S_z - \mu S_x(b+\mu S_z)}{\sqrt{C^2 + 2\mu(\Omega S_x - c_1 b S_z)}}\right. \\ \qquad\qquad \left. + S_x(S_z - c_2 b)\right], \end{cases} \tag{172}$$

$$U^{S_z}_{(2,2)}(\tau):\begin{cases} S_z \to \dfrac{B_2}{B_1} \\ \quad -\dfrac{1}{B_1}\left[(B_2 - B_1 S_z)^{\frac{3}{2}} + \dfrac{3}{2}B_1B_3\tau\right]^{\frac{2}{3}}, \end{cases} \tag{173}$$

$$U^{S_y}_{(2,2)}\left(\frac{\tau}{2}\right):\begin{cases} S_y \to S_y + \dfrac{\tau}{2}\left[\dfrac{\mu(\Omega + S_x)S_z - \mu S_x(b+\mu S_z)}{\sqrt{C^2 + 2\mu(\Omega S_x - c_1 b S_z)}}\right. \\ \qquad\qquad \left. + S_x(S_z - c_2 b)\right], \end{cases} \tag{174}$$

$$U^{S_x}_{1,(2,2)}\left(\frac{\tau}{4}\right):\begin{cases} S_x \to \dfrac{1}{C_1}\left[-\dfrac{3}{2}C_1C_3\dfrac{\tau}{4} + (C_2 + C_1S_x)^{\frac{3}{2}}\right]^{\frac{2}{3}} \\ \quad -\dfrac{C_2}{C_1}, \end{cases} \tag{175}$$

$$U^{S_x}_{2,(2,2)}\left(\frac{\tau}{2}\right):\left\{S_x \to S_x - \frac{\tau}{2}S_y(S_z - c_2 b), \right. \tag{176}$$

$$U^{S_x}_{1,(2,2)}\left(\frac{\tau}{4}\right):\begin{cases} S_x \to \dfrac{1}{C_1}\left[-\dfrac{3}{2}C_1C_3\dfrac{\tau}{4} + (C_2 + C_1S_x)^{\frac{3}{2}}\right]^{\frac{2}{3}} \\ \quad -\dfrac{C_2}{C_1}. \end{cases} \tag{177}$$

The algorithm provided by $U^2_{(2,2)}(\tau)$ is

$$U^{S_z}_{(2,2)}\left(\frac{\tau}{2}\right):\begin{cases} S_z \to \dfrac{B_2}{B_1} \\ \quad -\dfrac{1}{B_1}\left[(B_2 - B_1 S_z)^{\frac{3}{2}} + \dfrac{3}{2}B_1B_3\dfrac{\tau}{2}\right]^{\frac{2}{3}}, \end{cases} \tag{178}$$

$$U^{S_x}_{1,(2,2)}\left(\frac{\tau}{4}\right):\begin{cases} S_x \to \dfrac{1}{C_1}\left[-\dfrac{3}{2}C_1C_3\dfrac{\tau}{4} + (C_2 + C_1S_x)^{\frac{3}{2}}\right]^{\frac{2}{3}}, \\ \quad -\dfrac{C_2}{C_1}, \end{cases} \tag{179}$$

$$U^{S_x}_{2,(2,2)}\left(\frac{\tau}{2}\right):\left\{S_x \to S_x - \frac{\tau}{2}S_y(S_z - c_2 b), \right. \tag{180}$$

$$U^{S_x}_{1,(2,2)}\left(\frac{\tau}{4}\right):\begin{cases} S_x \to \dfrac{1}{C_1}\left[-\dfrac{3}{2}C_1C_3\dfrac{\tau}{4} + (C_2 + C_1S_x)^{\frac{3}{2}}\right]^{\frac{2}{3}} \\ \quad -\dfrac{C_2}{C_1}, \end{cases} \tag{181}$$

$$U^{S_y}_{(2,2)}(\tau):\begin{cases} S_y \to S_y + \tau\left[\dfrac{\mu(\Omega + S_x)S_z - \mu S_x(b+\mu S_z)}{\sqrt{C^2 + 2\mu(\Omega S_x - c_1 b S_z)}}\right. \\ \qquad\qquad \left. + S_x(S_z - c_2 b)\right], \end{cases} \tag{182}$$

$$U^{S_x}_{1,(2,2)}\left(\frac{\tau}{4}\right):\begin{cases} S_x \to \dfrac{1}{C_1}\left[-\dfrac{3}{2}C_1C_3\dfrac{\tau}{4} + (C_2 + C_1S_x)^{\frac{3}{2}}\right]^{\frac{2}{3}} \\ \quad -\dfrac{C_2}{C_1}, \end{cases} \tag{183}$$

$$U^{S_x}_{2,(2,2)}\left(\frac{\tau}{2}\right):\left\{S_x \to S_x - \frac{\tau}{2}S_y(S_z - c_2 b), \right. \tag{184}$$

$$U^{S_x}_{1,(2,2)}\left(\frac{\tau}{4}\right):\begin{cases} S_x \to \dfrac{1}{C_1}\left[-\dfrac{3}{2}C_1C_3\dfrac{\tau}{4} + (C_2 + C_1S_x)^{\frac{3}{2}}\right]^{\frac{2}{3}} \\ \quad -\dfrac{C_2}{C_1}, \end{cases} \tag{185}$$

$$U^{S_z}_{(2,2)}\left(\frac{\tau}{2}\right):\begin{cases} S_z \to \dfrac{B_2}{B_1} \\ \quad -\dfrac{1}{B_1}\left[(B_2 - B_1 S_z)^{3/2} + \dfrac{3}{2}B_1B_3\dfrac{\tau}{2}\right]^{2/3}. \end{cases} \tag{186}$$

The algorithm provided by $U^3_{(2,2)}(\tau)$ is

$$U^{S_y}_{(2,2)}\left(\frac{\tau}{4}\right):\begin{cases} S_y \to S_y + \dfrac{\tau}{4}\left[\dfrac{\mu(\Omega+S_x)S_z - \mu S_x(b+\mu S_z)}{\sqrt{C^2+2\mu(\Omega S_x - c_1 b S_z)}}\right. \\ \qquad\qquad \left. + S_x(S_z - c_2 b)\right], \end{cases} \tag{187}$$

$$U^{S_z}_{(2,2)}\left(\frac{\tau}{2}\right):\begin{cases} S_z \to \dfrac{B_2}{B_1} \\ \quad -\dfrac{1}{B_1}\left[(B_2 - B_1 S_z)^{\frac{3}{2}} + \dfrac{3}{2}B_1 B_3 \dfrac{\tau}{2}\right]^{\frac{2}{3}}, \end{cases} \tag{188}$$

$$U^{S_y}_{(2,2)}\left(\frac{\tau}{4}\right):\begin{cases} S_y \to S_y + \dfrac{\tau}{4}\left[\dfrac{\mu(\Omega+S_x)S_z - \mu S_x(b+\mu S_z)}{\sqrt{C^2+2\mu(\Omega S_x - c_1 b S_z)}}\right. \\ \qquad\qquad \left. + S_x(S_z - c_2 b)\right], \end{cases} \tag{189}$$

$$U^{S_x}_{1,(2,2)}\left(\frac{\tau}{2}\right):\begin{cases} S_x \to \dfrac{1}{C_1}\left[-\dfrac{3}{2}C_1 C_3 \dfrac{\tau}{2} + (C_2 + C_1 S_x)^{\frac{3}{2}}\right]^{\frac{2}{3}} \\ -\dfrac{C_2}{C_1}, \end{cases} \tag{190}$$

$$U^{S_x}_{2,(2,2)}(\tau):\left\{S_x \to S_x - \tau S_y(S_z - c_2 b), \right. \tag{191}$$

$$U^{S_x}_{1,(2,2)}\left(\frac{\tau}{2}\right):\begin{cases} S_x \to \dfrac{1}{C_1}\left[-\dfrac{3}{2}C_1 C_3 \dfrac{\tau}{2} + (C_2 + C_1 S_x)^{\frac{3}{2}}\right]^{\frac{2}{3}} \\ -\dfrac{C_2}{C_1}, \end{cases} \tag{192}$$

$$U^{S_y}_{(2,2)}\left(\frac{\tau}{4}\right):\begin{cases} S_y \to S_y + \dfrac{\tau}{4}\left[\dfrac{\mu(\Omega+S_x)S_z - \mu S_x(b+\mu S_z)}{\sqrt{C^2+2\mu(\Omega S_x - c_1 b S_z)}}\right. \\ \qquad\qquad \left. + S_x(S_z - c_2 b)\right], \end{cases} \tag{193}$$

$$U^{S_z}_{(2,2)}\left(\frac{\tau}{2}\right):\begin{cases} S_z \to \dfrac{B_2}{B_1} \\ \quad -\dfrac{1}{B_1}\left[(B_2 - B_1 S_z)^{\frac{3}{2}} + \dfrac{3}{2}B_1 B_3 \dfrac{\tau}{2}\right]^{\frac{2}{3}}, \end{cases} \tag{194}$$

$$U^{S_y}_{(2,2)}\left(\frac{\tau}{4}\right):\begin{cases} S_y \to S_y + \dfrac{\tau}{4}\left[\dfrac{\mu(\Omega+S_x)S_z - \mu S_x(b+\mu S_z)}{\sqrt{C^2+2\mu(\Omega S_x - c_1 b S_z)}}\right. \\ \qquad\qquad \left. + S_x(S_z - c_2 b)\right]. \end{cases} \tag{195}$$

Appendix 3: Integration algorithm on the $(1,2)$ surface

The algorithm provided by $U^1_{(1,2)}(\tau)$ is

$$U^{S_x}_{(1,2)}\left(\frac{\tau}{2}\right):\left\{S_x \to S_x - \frac{\tau}{2}S_y(S_z - c_2 b), \right. \tag{196}$$

$$U^{S_y}_{(1,2)}(\tau):\left\{S_y \to S_y + \tau S_x(S_z - c_2 b), \right. \tag{197}$$

$$U^{S_x}_{(1,2)}\left(\frac{\tau}{2}\right):\left\{S_x \to S_x - \frac{\tau}{2}S_y(S_z - c_2 b). \right. \tag{198}$$

The algorithm provided by $U^2_{(1,2)}(\tau)$ is

$$U^{S_y}_{(1,2)}\left(\frac{\tau}{2}\right):\left\{S_y \to S_y + \frac{\tau}{2}S_x(S_z - c_2 b), \right. \tag{199}$$

$$U^{S_x}_{(1,2)}(\tau):\left\{S_x \to S_x - \tau S_y(S_z - c_2 b), \right. \tag{200}$$

$$U^{S_y}_{(1,2)}\left(\frac{\tau}{2}\right):\left\{S_y \to S_y + \frac{\tau}{2}S_x(S_z - c_2 b). \right. \tag{201}$$

References

1. Kapral R, Sergi A (2005) Dynamics of condensed phase proton and electron transfer processes, vol. 1, ch. 92. In: Rieth M, Schommers W (eds) Handbook of theoretical and computational nanotechnology. American Scientific Publishers, Valencia, CA
2. Likharev KK (1996) Dynamics of Josephson junctions and circuits. CRC Press, Amsterdam
3. Hayashi T, Fujisawa T, Cheong HD, Jeong YH, Hirayama Y (2003) Coherent manipulation of electronic states in a double quantum dot. Phys Rev Lett 91:226804
4. Petta JR, Johnson AC, Marcus CM, Hanson MP, Gossard AC (2004) Manipulation of a single charge in a double quantum dot. Phys Rev Lett 93:186802
5. Petta JR, Johnson AC, Taylor JM, Laird EA, Yacoby A, Lukin MD, Marcus CM, Hanson MP, Gossard AC (2005) Coherent manipulation of coupled electron spins in semiconductor quantum dots. Science 309:2180–2184
6. Leggett AJ, Chakravarty S, Dorsey AT, Fisher MPA, Garg A, Zwerger W (1987) Dynamics of the dissipative two-state system. Rev Mod Phys 59:1–85
7. Prokof'ev NV, Stamp PCE (2000) Theory of the spin bath. Rep Prog Phys 63:669–726
8. Breuer H-P, Petruccione F (2002) The theory of open quantum systems. Oxford University Press, Oxford
9. Ottinger HC (2005) Beyond equilibrium thermodynamics. Wiley, Hoboken
10. Ottinger HC (2000) Derivation of a two-generator framework of nonequilibrium thermodynamics for quantum system. Phys Rev E 62:4720
11. Ottinger HC (2010) Nonlinear thermodynamic quantum master equation: properties and examples. Phys Rev A 82:052119
12. Ottinger HC (2011) Euro Phys. Lett. 94:10006
13. Ottinger HC (2012) Stochastic process behind nonlinear thermodynamic quantum master equation. I. Mean-field construction. Phys Rev A 86:032101
14. Flakowski J, Schweizer M, Ottinger HC (2012) Stochastic process behind nonlinear thermodynamic quantum master equation. II. Simulation. Phys Rev A 86:032102
15. Sergi A (2013) Communication: quantum dynamics in classical spin baths. J Chem Phys 139:031101
16. Anderson A (1995) Quantum backreaction on "classical" variables. Phys Rev Lett 74:621–625
17. Prezhdo O, Kisil VV (1997) Mixing quantum and classical mechanics. Phys Rev A 56:162–176
18. Zhang WY, Balescu R (1988) Statistical mechanics of a spin polarized plasma. J Plasma Phys 40:199–213

19. Balescu R, Zhang WY (1988) Kinetic equation, spin hydrodynamics and collisional depolarization rate in a spin-polarized plasma. J Plasma Phys 40:215–234
20. Osborn TA, Kondrat'eva MF, Tabisz GC, McQuarrie BR (1999) Mixed Weyl symbol calculus and spectral line shape theory. J Phys A 32:4149–4169
21. Gerasimenko VI (1982) Dynamical equations of quantum–classical systems. Teoret Mat Fiz 50:77–87
22. Boucher W, Traschen J (1988) Semiclassical physics and quantum fluctuations. Phys Rev D 37:3522–3532
23. Martens CC, Fang J-Y (1996) Semiclassical limit molecular dynamics on multiple electronic surfaces. J Chem Phys 106:4918–4930
24. Kapral R, Ciccotti G (1999) Mixed quantum–classical dynamics. J Chem Phys 110:8919–8929
25. Horenko I, Salzmann C, Schmidt B, Schutte C (2002) Quantum–classical Liouville approach to molecular dynamics: surface hopping gaussian phase-space packets. J Chem Phys 117:11075–11088
26. Shi Q, Geva E (2004) A derivation of the mixed quantum–classical liouville equation from the influence functional formalism. J Chem Phys 121:3393–3404
27. Sergi A, Sinayskiy I, Petruccione F (2009) Numerical and analytical approach to the quantum dynamics of two coupled spins in bosonic baths. Phys Rev A 80:012108
28. Allen MP, Tildesley DJ (2009) Computer simulation of liquids. Oxford University Press, Oxford
29. Frenkel D, Smit B (2002) Understanding molecular simulation. Academic Press, London
30. Sergi A (2005) Non-Hamiltonian commutators in quantum mechanics. Phys Rev E 72:066125
31. Sergi A (2007) Deterministic constant-temperature dynamics for dissipative quantum systems. J Phys A: Math Theor 40:F347–F354
32. Sergi A (2006) Statistical mechanics of quantum–classical systems with holonomic constraints. J Chem Phys 124:024110
33. Sergi A, Ferrario M (2001) Non-Hamiltonian equations of motion with a conserved energy. Phys Rev E 64:056125
34. Sergi A (2003) Non-Hamiltonian equilibrium statistical mechanics. Phys Rev E 67:021101
35. Sergi A, Giaquinta PV (2007) On the geometry and entropy of non-Hamiltonian phase space. J Stat Mech Theory Exp 02:P02013
36. Sergi A (2004) Generalized bracket formulation of constrained dynamics in phase space. Phys Rev E 69:021109
37. Sergi A (2005) Phase space flows for non-Hamiltonian systems with constraints. Phys Rev E 72:031104
38. de Polavieja GG, Sjöqvist E (1998) Extending the quantal adiabatic theorem: geometry of noncyclic motion. Am J Phys 66:431–438
39. Mead CA, Truhlar DG (1979) On the determination of born-oppenheimer nuclear motion wave functions including complications due to conical intersections and identical nuclei. J Chem Phys 70:2284–2296
40. Berry MV (1984) Quantal phase factors accompanying adiabatic changes. Proc R Soc Lond Ser A 392:45–57
41. Shapere A, Wilczek F (eds) (1989) Geometric phases in physics. World Scientific, Singapore
42. Mead CA (1992) The geometric phase in molecular systems. Rev Mod Phys 64:51–85
43. Kuratsuji H, Iida S (1985) Effective action for adiabatic process. Prog Theor Phys 74:439–445
44. Tuckerman M, Martyna GJ, Berne BJ (1992) Reversible multiple time scale molecular dynamics. J Chem Phys 97:1990–2001
45. Martyna GJ, Tuckerman M, Tobias DJ, Klein ML (1996) Explicit reversible integrators for extended systems dynamics. Mol Phys 87:1117–1157
46. Sergi A, Ferrario M, Costa D (1999) Reversible integrators for basic extended system molecular dynamics. Mol Phys 97:825–832
47. Ezra GS (2006) Reversible measure-preserving integrators for non-Hamiltonian systems. J Chem Phys 125:034104
48. Sergi A, Ezra GS (2010) Bulgac-Kusnezov-Nose-Hoover thermostats. Phys Rev E 81:036705
49. Sergi A, Ezra GS, Bulgac–Kusnezov–Nosé-Hoover thermostats for spins, unpublished
50. Nielsen S, Kapral R, Ciccotti G (2001) Statistical mechanics of quantum–classical systems. J Chem Phys 115:5805–5815
51. Sergi A, Giaquinta PV (2007) On computational strategies in molecular dynamics simulation. Phys Essays 20:629–640
52. Pati AK (1998) Adiabatic berry phase and Hannay angle for open paths. Ann Phys 270:178–197
53. Filipp S, Sjöqvist E (2003) Off-diagonal generalization of the mixed-state geometric phase. Phys Rev A 68:042112
54. Englman R, Yahalom A, Baer M (2000) The open path phase for degenerate and non-degenerate systems and its relation to the wave function and its modulus. Eur Phys J D 8:1–7
55. Manini N, Pistolesi F (2000) Off-diagonal geometric phases. Phys Rev Lett 85:3067–3071
56. Frank J, Huang W (1997) Leimkuhler geometric integrators for classical spin systems. J Comput Phys 133:160–172
57. Krech M, Bunker A, Landau DP (1998) Fast spin dynamics algorithms for classical spin systems. Comput Phys Commun 111:1–13
58. Steinigeweg R, Schmidt H-J (2006) Symplectic integrators for classical spin systems comput. Phys Commun 174:853–861
59. Yoshida H (1990) Construction of higher order symplectic integrators. Phys Lett A 150:262–268

Theor Chem Acc (2014) 133:1543
DOI 10.1007/s00214-014-1543-0

REGULAR ARTICLE

Ions in liquid metal clusters

R. Stephen Berry · Boris M. Smirnov

Received: 10 March 2014 / Accepted: 12 July 2014 / Published online: 12 August 2014

Abstract From the results of computer simulations, especially of 13-atom metal clusters by molecular dynamics, we derive a theory of the solid–liquid phase transition in metal clusters that connects to the jellium model. We analyze the nature of the ion's behavior in liquid clusters. As a result, we find a dynamical coexistence among the cluster's configurational states create the liquid aggregate state of this cluster. It follows from the entropy analysis that motions of the ions in liquid metal clusters explore a selective set of ion configurations, rather than following independent motions in a self-consistent cluster field.

Keywords Metal clusters · Phase transitions · Melting · Jellium

1 Introduction

A system of a small finite number of bound atoms, a cluster, may be used—cautiously—as a model for macroscopic systems of bound atoms, to guide our understanding of the nature of some phenomena these systems exhibit. We consider from this standpoint the phase transitions between the solid and liquid aggregate states. It is convenient to represent the phase transition as a transition between cluster configurational states or sets thereof; each configurational state corresponds to a local minimum of the potential energy surface (PES) of this system as a function of atomic coordinates; typically, the cluster's PES is characterized by many local minima. One can relate the cluster's solid and liquid states directly to one or some combination of configurational states. According to the definition of the liquid aggregate state, one or several cluster atoms may move about the cluster on a time scale short compared with that in which atoms remain "in their knots' in the solid aggregate state.

Evidently, the global minimum of the PES corresponds to the most stable solid form of the cluster; other local minima may also act as metastable solid forms. Our goal here is to analyze the nature of the liquid aggregate state of clusters. To understand the nature of the phase transition to this state in clusters, we consider clusters consisting of 13 atoms. Indeed, 13 is the lowest magic number of atoms for many clusters, for which the first icosahedral shell is completed. Of course, some kinds of 13-atom clusters have other structures, and there are even conflicting results from simulations regarding which structure is the global minimum for certain kinds of clusters, such as Au_{13} [1–3]; different computational methods sometimes give different results. However, one can safely generalize by recognizing that many kinds of clusters have several low-lying, locally stable structures with similar energies.

Configurational excitation is characterized by an energy higher than that of the global minimum, which, for some kinds of clusters, this means with energy above the structure with a maximum number of nearest neighbors. For many clusters, this is the lowest-energy solid state and may be separated from the first excited configurational state by a sizeable energy gap. This simplifies the analysis and allows

Dedicated to Professor Greg Ezra and published as part of the special collection of articles celebrating his 60th birthday.

R. S. Berry (✉)
Department of Chemistry, University of Chicago,
5735 South Ellis Avenue, Chicago, IL 60637, USA
e-mail: berry@uchicago.edu

B. M. Smirnov
Institute for High Temperatures, Izhorskaya 13/19,
Moscow 127412, Russia

us to understand the nature of the solid–liquid phase transition from the microscopic standpoint. In particular, one can understand in this case the influence of the character of atom interactions in clusters on the phase transition. Here, we will compare the phase transitions in Lennard–Jones and metal clusters. To obtain the numerical parameters of the cluster phase transition, we largely use the results of molecular dynamics simulations. Specifically, we use the results for Lennard–Jones clusters [4, 5] and metal clusters [6].

Properties of clusters which differentiate them from macroscopic atomic systems are important because of the insights they give us regarding phase transitions. First of all, in contrast to bulk atomic systems, under conditions near those of the traditional point of phase transition, i.e., the point of equal chemical potential of both phases, clusters exhibit dynamic coexistence of two or more phases [4, 5, 7–10]. Next, the contribution of thermal motion of atoms is important for parameters of the phase transition. In particular, in the case of the 13-atom Lennard–Jones clusters, ignoring the thermal motion of atoms in the solid–liquid phase transition yields a predicted melting point off from the correct one by a factor of two [11]. The contribution of thermal motion of atoms to the entropy jump reveals a different character of atom oscillations in the solid and liquid cluster states [13, 14]. For example, the anharmonicity of vibrations plays a significant role in determining the entropic contribution to many cluster phase transitions [11]. The inclusion of anharmonic contributions was developed by Doye and Wales [12]. Hence, the nature of atomic or ionic oscillations in clusters is important for phase transitions, and, on the other hand, information about the phase transition opens the possibility of revealing the character of cluster oscillations at the phase transition. The goal of this paper is to analyze the character of ionic oscillations in 13-atom metal clusters in phase transitions from molecular dynamics simulations [6, 15–17].

We consider the phase transition in clusters from the microscopic standpoint as the transition between configurational cluster states or, more strictly, sets thereof. Configurational cluster states are characterized by the topography of the PES [18], the energy of the system as a function of nuclear coordinates, within the Born–Oppenheimer approximation. Typically, the PES has many local minima [19–21]. Then, one can often consider the melting phase transition of a cluster as the transition between lowest configurational states, as it is shown in Fig. 1 for a 13-atom cluster with pairwise interatomic interactions [22], where interaction between nearest neighbors dominates. In this case, the ground configuration cluster state corresponds to the icosahedral structure [23] with a central atom and 12 surface atoms, which form a completed atom shell. In the first configurational excited state, one atom transfers onto the cluster surface. The promoted atom may move relatively freely about the surface and, equally important, may exchange with any of the other atoms in the icosahedral shell. Although as a result of this transition surface atoms shift slowly relative to the vibrational frequency, and the energy parameters of the phase transition depend on the form of the pair interaction potential, the qualitative character of this transition is identical for various interaction potentials. So, in this case, one atom transfers in an excited atom shell; in this case, there are no other, intermediate configurational cluster states.

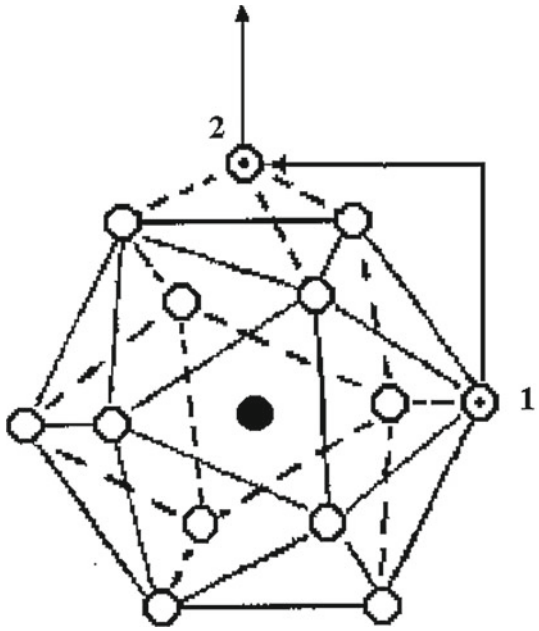

Fig. 1 The character of the lowest configurational excitations of the 13-atom icosahedral cluster, a single-atom promotion from the 12-atom shell to the surface [22]. Numbers *1* and *2* indicate positions of a transferring atom for the solid and liquid aggregate states of the cluster

According to computer simulation of 13-atom metal clusters [6, 15–17], their ground states most commonly exhibit icosahedral structure. Next, the lowest configuration state is separated from the ground state by an energetic gap, similar to clusters with pairwise interactions of atoms. But in contrast to these clusters, the lowest configurational states of metal clusters are not separated from subsequent excited configurational states by large energy gaps. The difference between these types of clusters is demonstrated schematically in Fig. 2. For this reason, the lowest-energy liquid aggregate states of metal clusters typically consist of many configurational states, in contrast to clusters with a pairwise atom interaction. (Of course, the higher-energy liquid states of dielectric clusters include many configurational states, with all the atoms capable of moving relatively easily.) We below take into account this fact in the

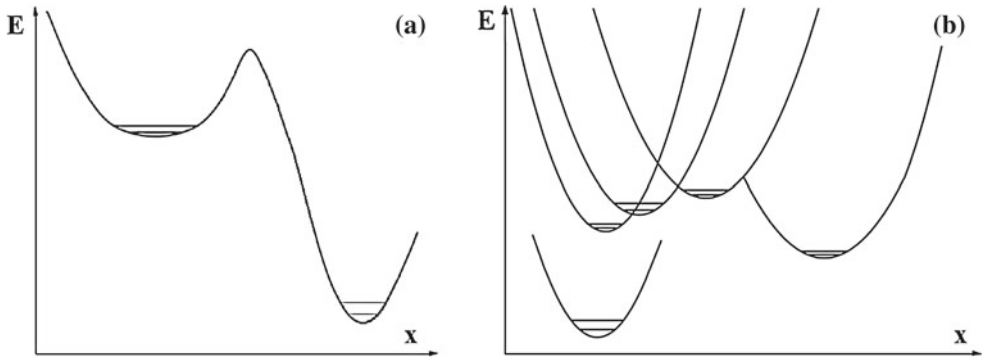

Fig. 2 Character of configurational excitation in a dielectric cluster (**a**) with one excited configurational state of a certain symmetry and for a metal cluster (**b**) with a large number of isomers, i.e., with a large number of excited configurational states of similar excitation energies. The coordinate x in the multidimensional space of nuclear coordinates joins the global cluster PES (potential surface energy) minimum with an indicated local minimum of the PES

analysis of thermal motion of atoms in the low-energy liquid state of 13-atom metal clusters. Our analysis is based on the results of computer simulations of metal clusters [6, 15–17] conducted with the Sutton–Chen interaction potential [24]. These molecular dynamics simulations take into account the thermal motion of atoms.

In this paper, we analyze the character and role of atom oscillations in some 13-atom metal clusters. Comparing the melting phase transition of these clusters with that of clusters for which interaction between nearest neighbors dominates, we construct an analogous theory of the phase transitions in metal clusters, accounting for the importance of the thermal motion of ions within these clusters for the phase transitions and for the importance of the multiplicity of configurational states that contribute to the liquid state. For the qualitative understanding of ion oscillations in the liquid aggregate state, we use various models of atomic systems. The 13-atom cluster has been chosen because its closed-shell structure is likely to be a better model as a parallel (and contrast) to bulk materials than would be clusters with partially filled outer shells and consequent high atomic mobility.

2 Phase transitions in metal clusters

Let us construct the theory of the phase transition in metal clusters by analogy with the phase transition in clusters with a pair interaction of atoms as a result of transition between two configuration states (for example, [22]). The latter case is represented in Fig. 1. The entropy jump at the phase transition ΔS in this case is the sum of the configurational ΔS_o and the thermal ΔS_t parts

$$\Delta S = \Delta S_o + \Delta S_t \tag{1}$$

The configurational part ΔS_o is independent of the cluster temperature (the temperature of atomic oscillations), i.e., this value corresponds to the entropy jump at zero temperature. In particular, in the case of Fig. 1, the configurational part accounting for the number of possibilities for this configurational transition is the product of the number of positions in the occupied atomic shell that can form a vacancy (12) and the number of atomic positions on the cluster surface, where this atom does not border a vacancy (15), i.e., $\Delta S_o = \ln(12 \cdot 15) = 5.2$. The thermal part ΔS_{ot} of the entropy jump results from the fact that the excited configurational state has a looser atomic structure than the ground state. (Note that we are using units in which the Boltzmann constant k_B is unity.)

In constructing the entropy for metal clusters, along with the terms of formula (1), we add a term accounting for the appearance of new configurational states with increasing cluster energy. Thus, the entropy difference ΔS for the liquid and solid state near the melting point takes the form

$$\Delta S = \Delta S_o + \Delta S_t + \Delta S_c, \tag{2}$$

where ΔS_o is the entropy jump at zero temperature, ΔS_t is the contribution of thermal motion of atoms in the entropy jump, and ΔS_c is the additional entropy due to accessible configurational states. According to the definition, the melting point T_m is given by

$$\Delta S_m = \frac{\Delta E(T_m)}{T_m}, \tag{3}$$

where ΔS_m is the jump of the total entropy at the melting point, $\Delta E(T_m)$ is a change of the configurational energy at the melting point.

Note that the energy gap between the solid and liquid states of metals is typically small compared with usual total cluster energies. In particular, the ratio of the melting enthalpy of bulk systems per atom, ΔH_{fus} to the atomic binding energy ε_o in this macroscopic system of atoms is equal approximately 0.04 for metals Ni, Cu, Ag, Au and 0.2

for argon. A similar difference holds for clusters as well. This low energy gap for metal clusters does not separate the solid and liquid aggregate states of clusters on the scale of fluctuations in computer simulations [6, 15–17] of 13-atom metal clusters, in contrast to Lennard–Jones clusters [4, 5]. Correspondingly, computer simulations of metal clusters provide less information than the counterpart simulations of dielectric clusters with interatomic pair interactions.

Considering clusters as atomic systems with many internal degrees of freedom, we can introduce some thermodynamic parameters. In the case of the cluster phase transition between two aggregate states, it is convenient to use the ratio p of probabilities based on partition functions $Z_{\rm sol}$ and $Z_{\rm liq}$ for these aggregate states, that is, the ratio of probabilities of cluster location in these aggregate states

$$p = \frac{Z_{\rm liq}}{Z_{\rm sol}} = \exp\left(\Delta S - \frac{\Delta E}{T}\right), \tag{4}$$

where ΔS is the entropy jump as a result of the phase transition, ΔE is the energy difference for aggregate states, and the cluster temperature T is that associated with atomic vibrations. In the case of metal clusters, the entropy and energy jumps are distributed over several configurational states in the liquid aggregate state, and the ratio is given by

$$p(T) = \int \exp\left(\Delta S_k - \frac{\Delta E}{T}\right) g(T)\mathrm{d}k, \tag{5}$$

where $\Delta E(n)$ is the excitation energy for a given configurational state, $k(E)$ is the number of configurational states with excitation energy below E, $\Delta S_k = \ln g_k$ accounts for the statistical weight g_k of a given configurational state due to its symmetry, and the factor $\ln g(T) = \Delta S_{\rm t}$ characterizes the ratio of statistical weights of the liquid and solid states due to thermal motion of atoms, where $g(0) = 1$.

Let us represent the dependence of the energy of configurational excitation $\Delta E(k)$ on an isomer number k, the number of configurational excitations with excitation energy below $\Delta E(k)$, as

$$\Delta E(k) = \Delta_{\rm o} + \Delta_1 \left(\frac{k}{k_{\rm o}}\right)^{\alpha}, \tag{6}$$

and for definiteness, we arbitrarily take $k_{\rm o} = 100$. This dependence uses three parameters and is represented in Fig. 3 for clusters Ni_{13}, Ag_{13}, Au_{13}. In addition, Table 1 contains parameters of this formula for the indicated clusters, where $E_{\rm b}$ is the total binding energy of atoms in these clusters at zero temperature. The melting points $T_{\rm m}$ of clusters in Table 1 follow from the temperature dependence of the correlation function [4, 8, 9, 25] for the fractional fluctuation of the mean square distance between cluster atoms; this has a sharp jump at the melting point, typically from 0.1 or below to about 0.2. In addition, according to the traditional melting point definition $p(T_{\rm m}) = 1$.

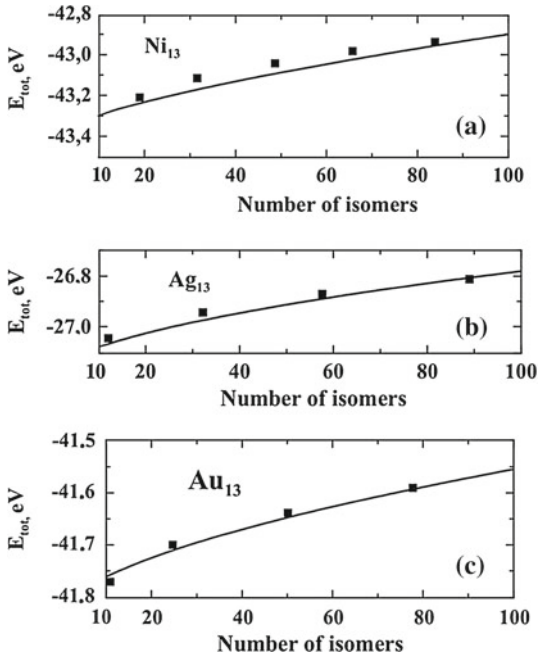

Fig. 3 The number of isomers with the excitation energy below an indicated value for metal clusters according to numerical evaluations [6] and approximation (6). **a** Ni_{13}, **b** Ag_{13}, **c** Au_{13} (*squares* correspond to explicit evaluations, *solid curves* to the approximations of the evaluations). The total energy of cluster atoms for the solid aggregate state is $E_{\rm o} = -44.1$ eV for Ni_{13}, $E_{\rm o} = -27.9$ eV for Ag_{13}, and $E_{\rm o} = -42.0$ eV for Au_{13}

Table 1 Parameters of melting of 13-atom metal clusters for $k_{\rm o} = 100$

Cluster	Ni_{13}	Ag_{13}	Au_{13}
$E_{\rm b}$ (eV)	44.11	27.87	41.96
$\Delta_{\rm o}$ (eV)	0.73	0.66	0.13
$\Delta_{\rm o}/E_{\rm b}$ (%)	1.6	2.4	0.31
Δ_1 (eV)	0.50	0.42	0.28
α	0.68	0.55	0.58
$\Gamma(1/\alpha)$	0.89	0.94	0.91
$T_{\rm m}$ (K)	860	820	250
$\overline{\Delta E(T_{\rm m})}$ (eV)	0.84	0.79	0.16
$g(T_{\rm m})$	2.4×10^3	1.7×10^3	430
$\delta T_{\rm m}$ (K)	200	200	70
$\overline{k}$	13	16	4
$\Delta S_{\rm t}$	7.8	7.4	6.1
$\Delta S_{\rm m}$	11.2	11.3	9.3
$\Delta S_{\rm t}/\Delta S_{\rm m}$ (%)	70	66	65

Evaluating the integral (5) with the dependence (6) for the energy of cluster excitation, we obtain

$$p(T) = \frac{k_{\rm o} g(T)}{\alpha \Gamma\left(\frac{1}{\alpha}\right)} \exp\left(-\frac{\Delta_{\rm o}}{T}\right)\left(\frac{T}{\Delta_1}\right)^{1/\alpha} \tag{7}$$

The relation $p(T_m) = 1$ gives

$$g(T_m) = \frac{\alpha}{k_o \Gamma\left(\frac{1}{\alpha}\right)} \left(\frac{\Delta_1}{T_m}\right)^{1/\alpha} \exp\left(\frac{\Delta_o}{T_m}\right), \quad (8)$$

$$\Delta S_t(T_m) = \ln g(T_m)$$

and from this, we find a contribution to the entropy jump $\Delta S_t(T_m) = \ln g(T_m)$ which comes from the thermal motion of atoms. Table 1 shows the values $\Delta S_t(T_m)$ for the clusters under consideration here.

The average excitation energy $\overline{\Delta E}$ at a given temperature for transition into the liquid state is a sum of the energy gap between the ground and lowest configurational excited state Δ_o, and the energy of configurational excitation within the liquid state. We consider the vibrational energy contribution separately, below. On the basis of formula (6), we have for the energy change at this transition

$$\overline{\Delta E} = \int \exp\left(-\frac{\Delta E(k)}{T}\right) g(T) E(k) \mathrm{d}k = \Delta_o + \frac{Tp(T)}{\alpha},$$

and at the melting point, this value is

$$\overline{\Delta E(T_m)} = \Delta_o + \frac{T_m}{\alpha} \quad (9)$$

Substituting this energy change at the melting point in formula (3), we determine the entropy jump ΔS_m at the melting point T_m; its values are given in Table 1. In addition, the further contribution to the entropy jump due to thermal motion of atoms $\Delta S_t(T_m)/\Delta S_m$, given in Table 1, exhibits the role of atomic vibrations in the phase transitions of metal clusters.

Let us analyze one more aspect of the cluster behavior at melting, which is connected with coexistence of phases. For convenience, we assume that coexistence of phases is observable in the range [26]

$$0.1 < p(T) < 10 \quad (10)$$

According to formula (10), given that the basic temperature dependence for the ratio of populations of the liquid and solid states $p(T)$ has the form $p(T) \sim \exp(-\Delta E/T)$, we find the width of the observable coexistence range (10) of the solid and liquid phases δT_m

$$\delta T_m = \frac{T_m^2 \ln 10}{\Delta E} \quad (11)$$

i.e., we assume $\delta T_m \ll T_m$, and the solid and liquid phases coexist in observable quantities within the temperature range from $T_m - \delta T_m$ up to $T_m + \delta T_m$. Table 1 contains the temperature range δT_m for phase coexistence. We see that for 13-atom metal clusters, phase coexistence is observable within a relatively wide range of temperatures.

In evaluating the integral (5), we assume that the phase transition is determined by many configurational states, which form the liquid aggregate state, so that we have a continuous dependence $\Delta E(n)$. An average number of isomers partaking in the phase transition is given by

$$\overline{k} = k_o \left(\frac{T_m}{\Delta_1}\right)^{1/\alpha} \frac{\Gamma(2/\alpha)}{\Gamma(1/\alpha)},$$

and Table 2 contains values of this parameter which justify the method used. In contrast, the liquid state of a dielectric cluster of atoms with pairwise interactions at first melting involves only one small set of excited configurational states, which is separated from other, higher excited configurational states by a significant energy gap. Hence, the phase transition in such clusters may be described by the model of two configurational states [14, 27, 28]. On the contrary, the liquid aggregate state of metal clusters includes many configurational states whose number increases even with relatively small increases in the cluster's excitation.

It is also possible to take a different course, and distinguish the lowest state characterized by a single particle's promotion to mobility from a fully liquid state, in which all or most of the particles are simultaneously mobile. This distinction is especially useful for clusters of 50 or more atoms, which display a clear "surface-melted" phase between the solid and true liquid [29]. Here, because the single promoted atom can exchange readily with a surface atom, so all the particles, with the possible exception of the central atom, can participate in the liquid-like motion, we consider the single-particle excitation as the onset of melting for the 13-atom cluster.

Let us analyze the reliability of the data of Table 2, which is based on the Sutton–Chen potential [30] as a model for atomic interactions in a metal cluster. Comparison for 13-atom metal clusters with the results of other models shows that the cluster structure coincides in the nickel and silver case, whereas calculations [31–37] for gold clusters with various models do not give the same sequences of cluster structures. This sequence of configurational states of the 13-atom gold cluster according to calculations [6], which we use above, differs from that of measurements of the cluster mobility [38] for charged gold clusters. Moreover, using the melting point of the

Table 2 Parameters of the jellium model for 13-atom metal clusters

Cluster	Ni_{13}	Ag_{13}	Au_{13}
r_W (Å) [55]	1.44	1.66	1.65
Θ_D (K) [53]	450	225	165
S_{sol}	81	103	67
$\Delta V_{sol}/V_o$	0.03	0.05	0.008
$\Delta V/V_{sol}$	0.1	0.07	0.09
$\hbar\omega_{br}$ (K)	490	270	380
ν	1.5	1.4	3.2

13-atom gold cluster and the density of the energy of configurationally excited states according to calculations [6] leads to contradictions. However, the neutral and charged clusters may not have the same sequence of structures, so some caution is required here. Note that the determination of the melting point may be based on the dependence of the root-mean-square bond length fluctuation δ that has a jump from 0.05 to 0.26 at the temperature $T = 400$ K [16]. Evaluation of the melting point in paper [15] on the basis of the Gupta potential gives $T_\mathrm{m} = 417$ K, whereas the value $T_\mathrm{m} = 247$ K is obtained on the basis of the embedded atom model. Previous calculations [39] using the Gupta potential led to $T = 680$ K. This dispersion of the melting point values testifies to the low accuracy of energy parameters for the Au_{13} cluster. In order to bring the estimated melting point into accord with other energy parameters used in computer simulations [6], we take the melting point of the cluster Au_{13} to be $T_\mathrm{m} = 250$ K. Note that this corresponds to the isothermal regime of cluster melting. In the adiabatic regime of cluster melting, its temperature at cluster melting varies from 250 to 450 K. Under these conditions, the contribution of thermal atomic motion to the entropy jump is 65 %, as in the other cases. But the accuracy in the gold case is low.

3 Interactions in metal clusters

Let us consider metal clusters from another standpoint. Our task is now to adjust the data from the phase transition in metal clusters to the character of interactions in this cluster. Because of the large number of stable excited configurations of metal clusters, which correspond to local minima of the PES, the atomic shell model does not describe metal clusters well. The density of levels related to locally stable cluster states is relatively large for metal clusters, and the number of configurational states available to the liquid increases with increasing excitation energy (or the cluster temperature).

The interaction within the cluster includes both exchange interaction between electrons and electrostatic interactions of the electrons and ions; the sum of these interactions gives a self-consistent field that acts on ions. Averaging over stable configurations with similar excitation energies in the liquid aggregate state, we find that ions can occupy a limited volume inside the cluster, i.e., can move over a certain region in a self-consistent cluster field. This liquid state includes many configurations. A simple model for describing the metal clusters is the jellium model [40–49] in which electrons are distributed over a certain region, and ions move in a self-consistent field inside this region due to their thermal energy. The jellium model is analogous to the Thomson atomic model [50], in which the positive charge is distributed over the atom volume, and electrons float in this volume. Within the framework of the jellium model, one can represent a metal cluster as a metallic plasma located inside a ball of a radius R that is given by

$$R = r_\mathrm{W} n^{1/3}, \tag{12}$$

where r_W is the Wigner–Seitz radius, and n is the number of cluster atoms. We assume in this formula according to the Wigner–Seitz concept [51, 52] that competition between exchange and electrostatic interactions in metal clusters is the same as in the bulk metal and that leads to a specific volume for each electron–ion pair. Note that usually the jellium model is applied to the solid aggregate state of metal clusters and allows one to determine magic numbers of metal clusters. These depend on the character of exchange and electrostatic interactions inside the cluster. But it seems even more appropriate to apply the jellium model to the liquid state of metal clusters because ions, due to their thermal motion, occupy a certain volume inside the cluster.

Since oscillatory motion of ions inside the metal cluster gives a contribution to the entropy jump at the phase transition, data for the phase transition allow us to analyze the character of thermal motion of ions in metal clusters. For this analysis, we consider first a simple model in which the cluster ions may move freely in the effective volume V of the cluster. One can use the general expression for the partition function Z_n of ions and their entropy S_n for the system of n ions (for example, [53, 54])

$$S_n = T\frac{\partial \ln Z_n}{\partial T} + \ln Z_n, \quad Z_n = \frac{V^n}{n!}\left(\frac{mT}{2\pi\hbar^2}\right)^{3n/2}, \tag{13}$$

where m is the atomic mass. In the limit of large number n of cluster ions, we use the Stirling formula

$$n! = \sqrt{2\pi} n^{n+1/2} \exp(-n), \tag{14}$$

that gives for the partition function Z_n of the system of n cluster ions

$$Z_n = \frac{(V/n)^n \exp(n)}{\sqrt{2\pi n}}\left(\frac{mT}{2\pi\hbar^2}\right)^{3n/2}, \tag{15}$$

and the cluster entropy is

$$S_n = \frac{5n}{2} + n\ln\left[\frac{V}{n}\left(\frac{mT}{2\pi\hbar^2}\right)^{3/2}\right] - \frac{1}{2}\ln(2\pi n), \tag{16}$$

where V is the total volume accessible to the ions.

The above model with a region of free ionic motion inside the cluster is enough rough, and we use it only for a qualitative description of the ion behavior inside metal clusters. This model shows that because cluster oscillations are essential and give a contribution to the entropy jump

at the phase transition, parameters of the phase transition depend on the atomic mass. This model also explains why electrons do not influence on the phase transition parameters. One can use a more realistic model, considering ions to be oscillating in the region of their equilibrium locations. Then, the entropy part due to ion oscillations is expressed through the vibrational spectrum parameters, which, by analogy with the crystal entropy, is given by (for example, [56])

$$\begin{aligned} S_{\mathrm{sol}} &= \frac{12\pi^4}{5} n \left(\frac{T}{\Theta_{\mathrm{D}}}\right)^3, \quad T \ll \Theta_{\mathrm{D}}; \\ S_{\mathrm{sol}} &= 3n \ln\left(\frac{T}{\Theta_{\mathrm{D}}}\right) + 4n, \quad T \gg \Theta_{\mathrm{D}}, \quad n \gg 1, \end{aligned} \tag{17}$$

where Θ_{D} is the Debye temperature. (By analogy with the traditional definition for bulk matter, the term is used here for the energy of excitation of the highest-frequency vibrational mode.) Though this formula is not suitable for 13-atom clusters near the melting point, it gives a correct order of magnitude. The values of the entropy according to formula (17) and the Debye temperatures for bulk metals are given in Table 2. We see that the cluster entropy according to formula (17) exceeds the entropy jump at melting of metal clusters (Table 1) by one order of magnitude.

One can compare this with the cluster volume $V_{\mathrm{o}} = 4\pi r_{\mathrm{W}}^n/3$, and the ratio of these volumes in Table 2 testifies to the small volume inside the cluster where ions may be found. We note that the volume V within the framework of this model is the difference of volumes occupied by ions in the liquid and solid states, rather than the ion volume for the liquid aggregate state.

Assuming the variation in the volume of free ion motion ΔV as a result of cluster melting is small, we obtain from formula (16)

$$\frac{\Delta V}{V} = \frac{\Delta S_{\mathrm{t}}}{S_n} \tag{18}$$

Estimations for the change of the volume ΔV of free ion motion in liquid metal clusters from the corresponding volume in the solid cluster are given in Table 2. These were obtained on the basis of the above data. We see that this change is relatively small.

Along with the Debye temperature of the bulk metal Θ_{D}, we take as a characteristic of cluster oscillations the energy of breathing vibrations of the 13-atom cluster $\hbar\omega_{\mathrm{br}}$ which is expressed here in temperature units. Breathing vibrations are atomic motions in which the distances between all the 12 surface atoms in the 13-atom cluster remain identical in the course of those vibrations. Assuming interaction between nearest neighbors to be dominated in this 13-atom cluster, one can connect the frequency of breathing vibrations ω_{br} with the vibration frequency ω_{o} in the diatomic molecule consisting of the same atoms. This connection under the above condition has the form [57] $\omega_{\mathrm{br}} = 1.37\omega_{\mathrm{o}}$; the values of $\hbar\omega_{\mathrm{br}}$ are given in Table 2. Note that both values, Θ_{D} and $\hbar\omega_{\mathrm{br}}$, are characteristics of cluster oscillations, and the degree of coincidence of their values testifies to the degree of their utility. Again, we obtain a low accuracy in the gold case. In addition, the energy of cluster vibrational excitation is compared with the melting point expressed in energy units. This means that a restricted number of oscillations of a given mode give a contribution to the entropy jump.

Thus, because a typical energy of cluster vibrations can be related to the melting point expressed in energetic units, we can estimate the extent of new vibrational excitation that is added as a result of the phase transition. Let us introduce a typical number of those additional cluster vibrations v on the basis of the (assumed) formula

$$g(T_{\mathrm{m}}) = \overline{k} \cdot v^{\overline{k}} \tag{19}$$

Table 2 contains the values of v according to formula (18), which confirm the above conclusion about the restricted additional number of vibration excitations for each mode.

One can add to this one more fact regarding small excitations of cluster oscillations in the liquid aggregate state at temperatures near the melting point. A 13-atom cluster is characterized by 33 $(3n - 6)$ vibration degrees of freedom. Note that the value v in Table 2 is the additional number of vibrational states per configurational state. Thus, the reduced number of additional vibrations with respect to zero oscillations is $v/33$. One can see that this value is small, which testifies to the relatively small extent of excitation of oscillations for the liquid aggregate states. We thus conclude that although atomic oscillations in metal clusters are important for the solid–liquid phase transition, the actual excess excitation of atomic oscillations associated with melting is relatively small.

Let us apply this conclusion for the jellium model to the liquid state of metal clusters. This model supposes that a self-consistent cluster field is created, which contains the electrons and ions. The size of the spatial distribution of an electron is of the order of the Wigner–Seitz radius, whereas ions occupy small regions near their equilibrium positions. As for ion oscillations in a metal cluster, there are two extreme possibilities: independent vibrations or completely correlated, collective vibrations. Because the vibrational modes are not classified in detail, the latter case is the better first approximation. Moreover, by analogy with the phase coexistence in Lennard–Jones clusters [4, 5, 7–10], one can assume the dynamical coexistence of configurationally excited states in the liquid aggregate state. This means that at every time, a metal cluster is located in some local basin associated with a configuration, and transitions

between various excited configurational states proceed with time.

4 Phase transitions in dielectric and metal clusters

Our task here is to infer the implications of the results of computer simulations of metal clusters. Because the numerical analyses of the melting phase transition in metal clusters have not separated the solid and liquid aggregate states in the range of their coexistence, in contrast to 13-atom Lennard–Jones clusters, they provide us only with information about ionic oscillations at the melting point. As a conclusion, we infer that the entropy jump in the melting of 13-atom metal clusters is less than the entropy of each aggregate state, and vibrational states in the liquid are excited only weakly at the phase transition.

In the case of 13-atom Lennard–Jones clusters, the solid and liquid states may be separated in the computer simulations [4, 5]. This allows one to determine the entropy jump not only at the melting point, but over a wider range of phase coexistence [58]. At the melting point, we have in accordance with formula (1) for the entropy jump at the phase transition in the 13-atom Lennard–Jones clusters, $\Delta S_o = 5.2$, $\Delta S_t = 3.8$. This shows that the contribution to the entropy jump from atomic vibrations in this Lennard-Jones cluster is approximately 40 % and that is comparable to the vibrational contribution to the entropy for metal clusters of about 70 %. The total entropy jump at the melting point is similar for metal and Lennard–Jones clusters. Therefore, the melting point expressed in energetic units is close to the energy gap Δ_o between the ground and first excited configuration states for Lennard–Jones clusters, as well as for metal clusters. On the contrary, the ratio of the energy gap Δ_o between the lowest configurational states to the total binding energy E_b of cluster atoms is about 0.2 for the Ar_{13} cluster and approximately 0.04 for the metal clusters under consideration [59]. One more difference in the phase transitions between 13-atom clusters with pairwise atomic interactions and metal clusters is this; while the lowest states of metal clusters exhibit shell structure, this behavior is not realized for excited configurational states of 13-atom metal clusters. Rather, metal clusters exhibit a large number of excited configurational states with similar energies in their liquid state.

One can expect that a certain contribution to the entropy jump at the solid–liquid phase transition in Lennard–Jones follows from vibrations involving a transferred atom promoted to the cluster surface. The entropy jump for these clusters due to thermal motion of atoms is relatively small, because only a few vibration levels are able to contribute. This allows one to represent precisely the character of motion of a promoted atom in the lowest liquid aggregate state of this cluster. Then, a transferred atom oscillates in one of 15 potential wells on the cluster surface, which is formed by interaction of a transferred atom and surface atoms of this cluster. Atomic transitions into neighboring wells proceed after many atomic oscillations in a given well.

Thus, one can see some specifics and analogies in thermal motion of nuclei in metal clusters and clusters with interatomic pair interactions. In considering oscillations of atoms in Lennard–Jones clusters or other clusters with interatomic pair interactions for which interactions between nearest neighbors dominate, one can state that these oscillations has a character different from those in metal clusters, but in both cases, these oscillations include only several vibrational levels for each mode. We note also that the entropy of a bulk atomic system has a power dependence on the temperature ($\sim T^3$) at low temperatures compared with the vibration energy, whereas for clusters, this dependence is exponential.

As for 13-atom metal clusters, configurational states can be considered states of atomic oscillation around local equilibrium positions. According to this analysis, interaction between ions is important for these oscillations. It is important that configurational excitations in metal clusters correspond to local minima of the PES for these clusters with relatively small excitation energies, while in the case of the Lennard–Jones cluster, the lowest configurational excitation corresponds to transition of one atom into an excited atomic shell.

5 Conclusion

In considering the phase transitions in metal clusters, we use 13-atom clusters as guides. These clusters are convenient for modeling because of their small size and because the liquid state is separated from the solid one by a sizeable energy gap since the outer shell of the solid is completed, with icosahedral structure. Clusters consisting of 13 atoms are convenient for simulation because these clusters have two clearly distinct aggregate states and, because of particle exchanges, all the atoms of the surface shell partake in the phase transition. Combining the results of computer simulation of clusters with an appropriate theory of the phase transition in clusters, one can find the part of the entropy jump, which arises from the change of thermal ionic motion in a cluster due to its restructuring. This gives a useful insight toward understanding the behavior of the ions in metal clusters.

Since the liquid aggregate state of metal clusters includes a variety of many ion configurations, the liquid aggregate state involves the dynamic coexistence of these configurations. This means that at each time, one configuration state

is realized, and then, transitions into other configurational states take place. Simultaneous with transition into a certain configuration state, a specific vibrational cluster state is established, with nuclei oscillating around equilibrium nuclear positions. Transitions between such vibrational state are possible so long as the cluster resides in a given configurational state. Since the vibrational energy is limited at the phase transition, only a relatively few vibrational states are realized for cluster oscillations in a given configurational state.

Using the cluster jellium model, one can construct configurational cluster states by introducing a self-consistent field between cluster electrons and ions. This self-consistent field establishes the configurational states as minima of the PES. Thermal motion of ions in these configurational states as ion oscillations in the cluster field corresponds to ion oscillations around equilibrium positions; they make a significant contribution to the entropy of the phase transition in metal clusters, and in this way is established a connection between the behavior of cluster ions and the cluster's melting phase transition.

References

1. Piotrowski MJ, Piquini P, Da Silva JLF (2010) Phys Rev B 81(1–14):155466
2. Larsen AH, Kleis J, Thygesen KS, Nrskov JK, Jacobsen KW (2011) Phys Rev B 84(1–13):245429
3. Chou JP, Hsing CR, Wei CM, Cheng C, Chang CM (2013) J Phys Condens Matter 25(1–8):125305
4. Jellinek J, Beck TL, Berry RS (1986) J Chem Phys 84:2783–2794
5. Davis HL, Jellinek J, Berry RS (1987) J Chem Phys 86:6456–6469
6. Arslan H, Güven MH (2005) N J Phys 7:60
7. Berry RS, Jellinek J, Natanson G (1984) Phys Rev A 30:919–931
8. Berry RS, Beck TL, Davis HL, Jellinek J (1988) Adv Chem Phys 90(Part 2):75–138
9. Berry RS (1993) Chem Rev 93:2379–2394
10. Berry RS (1999) In: Jellinek J (ed) Theory of atomic and molecular clusters. Springer, Berlin, pp 1–26
11. Berry RS, Smirnov BM (2013) Phys Rep 527:205–250
12. Doye JPK, Wales DJ (1995) J Chem Phys 102:9659–9672
13. Berry RS, Smirnov BM (2004) JETP 98:366–373
14. Berry RS, Smirnov BM (2005) Phys Uspekhi 48:345–388
15. Sebetci A, Guvenc ZB (2004) Model Simul Mater Sci Eng 12:1131–1138
16. Arslan H, Güven MH (2006) Acta Phys Slovac 56:511–520
17. Yildirim EK, Atis M, Guvenc ZB (2007) Phys Scr 75:111–118
18. Wales DJ (2003) Energy landscapes. Cambridge University Press, Cambridge
19. Hoare MR, Pal P (1971) Adv Phys 20:161–196
20. Hoare MR, Pal P (1975) Adv Phys 24:645–678
21. Hoare MR (1979) Adv Chem Phys 40:49–135
22. Smirnov BM, Berry RS (2008) Phase transitions of simple systems. Springer, Berlin
23. Mackay AL (1962) Acta Crystallogr 15:916–918
24. Sutton AP, Finnis MW, Pettifor DG, Ohta Y (1988) J Phys C 21:35–66
25. Zhou Y, Karplus M, Ball KD, Berry RS (2002) J Chem Phys 116:2323–2329
26. Berry RS, Smirnov BM (2009) Low Temp Phys 35:256–264
27. Berry RS, Smirnov BM (2001) J Chem Phys 114:6816–6823
28. Berry RS, Smirnov BM (2005) J Noncryst Sol 351:1543–1550
29. Cheng HP, Berry RS (1992) Phys Rev A 45:7969–7980
30. Sutton AP, Chen J (1990) Philos Mag Lett 61:139–146
31. Häberlen OD, Chung S-C, Stener M, Rösch N (1997) J Chem Phys 106:5189–5201
32. Doye JPK, Wales DJ (1997) J Chem Soc Faraday Trans 93:4233–4243
33. Doye JPK, Wales DJ (1998) N J Chem 22:733–744
34. Wilson NT, Johnston RL (2000) Eur Phys J D 12:161–169
35. Darby S, Mortimer-Jones TV, Johnston RL, Roberts C (2002) J Chem Phys 116:1536–1550
36. Wang J, Wang G, Zhao J (2002) Phys Rev B 66(1–6):035418
37. Oviedo J, Palmer RE (2002) J Chem Phys 117:9548–9551
38. Johansson MP, Lechtken A, Schooss D, Kappes MM, Furche F (2008) Phys Rev A 77(1–7):053202
39. Garzon IL, Jellinek J (1993) Z Phys D 26:316–318
40. Ekardt W (1984) Phys Rev B 29:1558–1564
41. Ekardt W (1985) Phys Rev B 31:6360–6370
42. Chou MY, Cohen ML (1986) Phys Lett A 113:420–424
43. Manninen M (1986) Phys Rev B 34:6886–6894
44. Cohen ML, Chou MY, Knight WD, de Heer WA (1987) J Phys Chem 91:3141–3149
45. Yannouleas C, Broglia RA, Brack M, Bortignon PF (1989) Phys Rev Lett 63:255–258
46. Brack M (1989) Phys Rev B 39:3533–3542
47. Nishioka H, Hansen K, Mottelson BR (1990) Phys Rev B 42:9377–9386
48. Genzken O, Brack M (1991) Phys Rev Lett 67:3286–3289
49. de Heer WA (1993) Rev Mod Phys 65:611–676
50. Thomson JJ (1904) Philos Mag 7:237
51. Wigner EP, Seitz F (1934) Phys Rev 46:509–524
52. Wigner EP (1934) Phys Rev 46:1002–1011
53. Kittel C (1970) Thermal physics. Wiley, New York
54. Kittel C, Kroemer H (1980) Thermal physics. Wiley, New York
55. Smirnov BM (1999) Clusters and small particles in gases and plasmas. Springer, New York
56. Landau LD, Lifshitz EM (1980) Statistical physics, vol 1. Pergamon Press, Oxford
57. Smirnov BM (2006) Principles of statistical physics. Wiley VCH, Berlin
58. Berry RS, Smirnov BM (2009) J Chem Phys 130(1–8):064302
59. Berry RS, Smirnov BM (2009) Phys Uspekhi 52:137–164